

Astrophysical Signatures from small-scale Structure of Axion Dark Matter

Dissertation zur Erlangung des Doktorgrades an der Fakultät für Mathematik, Informatik und Naturwissenschaften der Universität Hamburg

vorgelegt von

Dennis Maseizik

aus Bielefeld

Hamburg, 2025

Gutachter der Dissertation:

Prof. Dr. Günter Sigl

Prof. Dr. Robi Banerjee

Gutachter der Disputation:

Prof. Dr. Günter Sigl

Prof. Dr. Robi Banerjee

Prof. Dr. Jochen Liske

Prof. Dr. Thomas Konstandin

Prof. Dr. Oliver Gerberding

Datum der Disputation: 15.10.2025

Vorsitzender des Prüfungsausschusses:

Prof. Dr. Jochen Liske

Vorsitzender des Promotionsausschusses:

Prof. Dr. Wolfgang Parak

Dekan der Fakultät für Mathematik,

Informatik und Naturwissenschaften:

Prof. Dr.-Ing. Norbert Ritter



 $^{\odot}$ 2025 Dennis Maseizik

Dieses Werk ist lizenziert unter einer

Creative Commons Namensnennung 4.0 International Lizenz:

 $\verb|http://creativecommons.org/licenses/by/4.0/|$

Eidesstattliche Versicherung / Declaration on oath

Hiermit versichere ich an Eides statt, die vorliegende Dissertationsschrift selbst verfasst und

keine anderen als die angegebenen Hilfsmittel und Quellen benutzt zu haben.

Sofern im Zuge der Erstellung der vorliegenden Dissertationsschrift generative Künstliche

Intelligenz (gKI) basierte elektronische Hilfsmittel verwendet wurden, versichere ich, dass

meine eigene Leistung im Vordergrund stand und dass eine vollständige Dokumentation

aller verwendeten Hilfsmittel gemäß der Guten wissenschaftlichen Praxis vorliegt. Ich trage

die Verantwortung für eventuell durch die gKI generierte fehlerhafte oder verzerrte Inhalte,

fehlerhafte Referenzen, Verstöße gegen das Datenschutz- und Urheberrecht oder Plagiate.

I hereby declare on oath that I have written the present dissertation independently and have

used no resources or aids other than those indicated.

Insofar as generative artificial intelligence (gAI) based electronic tools were used in the

preparation of this dissertation, I affirm that my own contribution was paramount and that a complete documentation of all tools used is provided in accordance with the principles of

good scientific practice. I accept responsibility for any potentially erroneous or biased content

generated by gAI, incorrect references, violations of data protection and copyright laws or

plagiarism.

Hamburg, den 17.05.2025

Ort, Datum | Place, date

Unterschrift | Signature

D. Mosesth

Zusammenfassung

Axionen sind schwach wechselwirkende pseudo-skalare Teilchen, die ursprünglich im Zusammenhang mit der Peccei-Quinn-Lösung des starken CP-Problems der QCD postuliert wurden. Im kosmologischen Kontext stellen Axionen eine vielversprechende Lösung für die Erklärung der fehlenden dunklen Materie im aktuellen Standardmodell des Universums dar. Wenn das kosmische Axionfeld erst nach der kosmologischen Inflation etabliert wird - wie in dieser Arbeit angenommen - führen die daraus resultierenden Fluktuationen in der axionischen Materiedichte zur Bildung kompakter massiver Strukturen. Auf kleinen Skalen führen diese Strukturen zur Bildung von Axionen-Miniclustern und Axionen-Sternen – äußerst massedichten Objekten, die voraussichtlich später die Entstehungsorte von Galaxien durch aufeinanderfolgende Minicluster-Merger bestimmen. Es wird daher erwartet, dass die Halos aus dunkler Materie in typischen Galaxien eine vielfältige Substruktur leichter und mittelschwerer Minicluster aufweisen, in deren Zentrum jeweils ein Axionen-Stern vorhanden ist. Diese zentralen Axionen-Sterne haben hohe Dichten, die ihre mögliche Detektion durch parametrische Resonanz und relativistische Teilchen-Emission ermöglichen.

In dieser Arbeit erweitern wir vorangegangene Studien über die Massen- und Größenverteilung der Minicluster-Population durch ihre Übertragung auf Dunkle-Materie-Halos von Galaxien mit besonderem Schwerpunkt auf den Eigenschaften ihrer zentralen Axionen-Sterne. Ausgehend von den Eigenschaften galaktischer Axionen-Sterne berechnen wir die erwarteten Ereignisraten für verschiedene Signaturen, die durch Kollisionen zwischen Neutronensternen, Miniclustern und Axionen-Sternen entstehen. Wir betrachten Axion-Massen im Bereich von $10^{-12} \,\mathrm{eV} \le m_a \le 10^{-2} \,\mathrm{eV}$ mit unterschiedlicher Abhängigkeit $m_a(T)$ von der kosmologischen Temperatur. Unsere Analyse legt nahe, dass Signaturen aus Kollisionen zwischen Substrukturen aus axionischer dunkler Materie und Neutronensternen in der Milchstraße voraussichtlich nicht nachweisbar sind. Stattdessen leiten wir in dieser Arbeit neuartige Detektionsmethoden her, die das kontinuierliche Massenwachstum von Axionen-Sternen in Miniclustern nutzen. Wir zeigen, dass langfristige Massenakkretion von Axionen-Sternen beobachtbare Signale sowohl durch parametrische Resonanz als auch durch wiederkehrende Bosenovae liefern kann. Durch die Abschätzung der erwarteten Häufigkeit von akkretierenden Axionen-Sternen in unserer Galaxie zeigen wir, dass galaktische Radiolinien für eine große Bandbreite an Axion-Massen und Axion-Photon-Kopplungen vorhergesagt werden. Darüber hinaus legen unsere Ergebnisse nahe, dass die Häufigkeit galaktischer Bosenovae ausreichen kann, um ihren Nachweis in zukünftigen Breitband-Detektoren für axionische dunkle Materie zu ermöglichen.

Abstract

Axions are weakly interacting pseudo-scalar particles originally motivated by the Peccei-Quinn solution of the strong CP problem of QCD. In the context of cosmology, axions provide a compelling solution to explain the missing dark matter in the standard model of the universe. When the cosmic axion field is established after the inflationary epoch as assumed in this work, the resulting fluctuations in the axion matter density source the formation of compact structures. On small scales, these structures lead to the formation of axion miniclusters and axion stars - highly overdense objects, which are expected to source the sites of galaxy formation at late times through consecutive minicluster mergers. As a consequence, the dark matter halos of standard galaxies are expected to exhibit a rich substructure of lighter and inter-mediate mass miniclusters, each hosting a single axion star core. These axion star cores have large central densities that allow for their possible detection through parametric resonance and relativistic axion emission.

In this work, we extend earlier investigations on the mass and size distribution of the minicluster population to galaxy dark matter halos with special emphasis on the properties of their axion star cores. Inferring the properties of galactic axion stars, we calculate the expected event rates for different signatures given by collisions between neutron stars, miniclusters and axion stars. We consider axion masses in the range $10^{-12} \,\mathrm{eV} \le m_a \le 10^{-2} \,\mathrm{eV}$ with various scenarios for the cosmological temperature evolution of $m_a(T)$. Our analysis suggests that signatures from collisions of neutron stars with miniclusters and axion stars are unlikely to be detected in the Milky Way. Instead we provide novel detection schemes by exploiting the continuous mass growth of the axion star cores. We show that long-time mass accretion of axion stars can provide observable signals from both parametric resonance and re-occurring bosenovae. Evaluating the expected axion star abundance of our galaxy, we demonstrate that galactic radio lines are predicted for a large range of axion masses and axion-photon couplings. Similarly, we find that the rate of galactic bosenovae may be sufficient to allow for their detection in future broadband axion dark matter searches.

Acronyms

ALP Axion-like Particle

AS Axion Star

ASMF Axion Star Mass Function ASMC Axion-Star-Minicluster

CDM Cold Dark Matter

CMB Cosmic Microwave Background

CP Charge-Parity Symmetry

DM Dark Matter

EKG Einstein-Klein-Gordon
 EOM Equation of Motion
 FDM Fuzzy Dark Matter
 GP Gross-Pitaevskii

GPP Gross-Pitaevskii-Poisson

HMF Halo Mass Function

 ΛCDM Λ Cold Dark Matter Model

MC Axion Minicluster

MW Milky Way

MCMF Minicluster Mass Function

NFW Navarro-Frenk-White

NS Neutron Star PQ Peccei-Quinn

QCD Quantum Chromodynamics

SP Schrödinger-Poisson

Conventions

Terminology:

 $\begin{array}{lll} Axions & \widehat{=} & \text{Axion-like Particles, including the QCD axion} \\ ALPs & \widehat{=} & \text{Axion-like Particles other than the QCD axion} \end{array}$

Metric Tensor:

$$\operatorname{sgn}(g_{\mu\nu}) = (-+++)$$

Natural units:

$$\hbar = c = 1$$

Publications

Journal Papers

- Dennis Maseizik and Günter Sigl. "Distributions and collision rates of ALP stars in the Milky Way". In: *Phys. Rev. D* 110.8 (2024), p. 083015. DOI: 10.1103/PhysRevD.110.083015. arXiv: 2404.07908 [astro-ph.CO]
 - Author contributions: Dennis Maseizik performed numerical and analytical calculations, prepared the figures and wrote the manuscript. Günter Sigl supervised the research, provided the formalism for estimates on the cosmological event rates and reviewed the manuscript.
- Dennis Maseizik, Sagnik Mondal, Hyeonseok Seong, and Günter Sigl. "Radio lines from accreting axion stars". In: Journal of Cosmology and Astroparticle Physics 2025.05 (2025), p. 033. DOI: 10.1088/1475-7516/2025/05/033. arXiv: 2409.13121 [hep-ph]

 Author contributions: Dennis Maseizik performed numerical and analytical calculations, implemented the accretion rates and flux predictions, prepared the data, produced part of the figures and developed the framework of resonant ASMC systems. Hyeonseok Seong performed numerical and analytical calculations for the experimental detectability and resonance criteria, produced the potential constraints and schematic figures, improved the framework of the paper and wrote the manuscript. Sagnik Mondal performed analytical calculations for the accretion rates and resonance criteria, derived the accretion rates for the external accretion model and improved the framework of resonant ASMC systems. Günter Sigl supervised the research, provided the incentive to combine parametric resonance with axion star accretion and reviewed the manuscript.
- Dennis Maseizik, Joshua Eby, Hyeonseok Seong, and Günter Sigl. "Detectability of accretion-induced bosenovae in the Milky Way". In: *Phys. Rev. D* 111.6 (2025), p. 063017. DOI: 10.1103/PhysRevD.111.063017. arXiv: 2410.13082 [hep-ph]

 Author contributions: Dennis Maseizik performed the numerical and analytical calculations, implemented the accretion rates and Bosenova predictions, produced the figures, developed the framework of accreting ASMC systems and wrote the manuscript. Joshua Eby performed numerical and analytical calculations for the experimental detectability and burst properties, contributed the framework of derivative and non-derivative couplings and wrote the manuscript. Hyeonseok Seong improved the framework of accretion rates, performed consistency checks, contributed to the discussion and reviewed the manuscript. Günter Sigl supervised the research, contributed to the discussion and reviewed the manuscript.

Conference Proceedings

• Günter Sigl, Dennis Maseizik, and Hyeonseok Seong. "Glowing Axion Stars at Radio Frequencies". In: *PoS* COSMICWISPers (2024), p. 026. DOI: 10.22323/1.454.0026

1	Inti	roduction 1
2	Axi	on Dark Matter
	2.1	The strong CP Problem
	2.2	The Peccei-Quinn Mechanism and the QCD Axion
	2.3	Axion Models and Interactions
	2.4	Axion-like Particles
	2.5	Axion Dark Matter Production
		2.5.1 Thermal Production
		2.5.2 Misalignment Mechanism
		2.5.3 Decay of Topological Defects
	2.6	Axion Structure Formation
	2.7	Experimental Searches
	,	2.7.1 Axion-Photon Coupling
		2.7.2 Axion-Nucleon Coupling
		21112 Timon Patrician Coupling
3	Axi	on Miniclusters 29
	3.1	Gross-Pitaevskii Poisson System
	3.2	Spherical Collapse Model
	3.3	Linear Growth of Matter Perturbations
	3.4	Press-Schechter Formalism
	3.5	Minicluster Evolution
		3.5.1 Numerical Simulations
		3.5.2 Parametrization for Mass Distributions
	3.6	Galactic Minicluster Mass Distribution
		3.6.1 General approach for axion-like Particles
		3.6.2 Generalized Minicluster Mass Distributions
		3.6.3 Tidal Disruption in stellar Encounters
	3.7	Core-Halo Relation
4		on Stars 55
	4.1	Mass-Radius Relation
	4.2	Axion Star Formation
	4.3	Axion Star Mass Growth
		4.3.1 Power-Law Fits
		4.3.2 Self-similar Attractor Model
	4.4	Bosenovae
	4.5	Parametric Resonance
	4.6	Core-Halo Relation of Axion Stars
		4.6.1 Modification of virial Velocities
		4.6.2 Modification of specific Energies
	4.7	Galactic Axion Star Mass Distribution
		4.7.1 Low-Mass Cutoffs in Axion Star Distributions
		4.7.2 Axion Star Mass Distributions

5	Sign	natures of Axion Stars 91
	5.1	Mass-integrated Collision Rates
	5.2	Neutron-Star-Axion-Star Collisions
		5.2.1 Signals of Neutron-Star-Axion-Star Transients
		5.2.2 Galactic Signal Rates and Neutron Star Evolution
	5.3	Neutron-Star-Minicluster Collisions
		5.3.1 Signals from Neutron-Star-Minicluster Transients
		5.3.2 Galactic Signal Rates of Neutron-Star-Minicluster Collisions 104
	5.4	Axion Star Mergers and relativistic Bursts
		5.4.1 Axion Star Merger Dynamics
		5.4.2 Axion Star Merger Rates
	5.5	Parametric Resonance and Axion Star Accretion
	0.0	5.5.1 Signals from parametrically resonant Axion Stars
		5.5.2 Abundance of parametrically resonant Axion Stars
	5.6	Cosmological Event Rates
	5.7	Implications for Axion Searches
	0.1	implications for fixion scarcines
6	Rac	lio Lines from Axion Stars 127
_	6.1	Mass Distribution of resonant Systems
	6.2	External Minicluster Accretion Model
	6.3	Internal Minicluster Accretion Model
	6.4	Line Emission & galactic Radio Backgrounds
	0.1	6.4.1 Galactic Radio Background
		6.4.2 Spectral Flux from External Accretion
		6.4.3 Spectral Flux from Internal Accretion
		6.4.4 Gravitational Detuning
	6.5	
	0.5	Constraints on the Axion-photon Coupling
		6.5.1 Approaches to Background Comparison
		6.5.2 Constraints from External Accretion
		6.5.3 Constraints from Internal Accretion
	c c	6.5.4 Directional Dependence of resonant Emission
	6.6	Outlook on Axion Star Radio Lines
7	Cal	actic Axion Novae 157
•	7.1	Mass Growth Modeling
	7.1	Detectability of galactic Axion Bursts
	1.2	
		7.2.1 Burst Properties and Propagation
	7.9	v
	7.3	Non-Derivative Couplings
	7.4	Derivative Couplings
	7.5	Outlook on Detection of Bosenovae
8	Cor	nclusion & Outlook 173
J	8.1	Conclusion
	8.2	Outlook & Implications for Future Research
	0.4	Outlook & implications for ruthe nescardles

\mathbf{A}	Cos	mological Context	177
	A.1	Table of important Parameters	177
	A.2	Schematic Summary of Contents	178
	A.3	Relativistic Degrees of Freedom	
	A.4	Navarro-Frank-White Profile	179
	A.5	Ground States of the Schrödinger-Poisson System	180
	A.6	Rescaling of the Schrödinger Poisson system	180
	A.7	Galactic Neutron Star Distribution	
	A.8	Madelung Transformation	
В	Nur	nerical Methods	183
	B.1	Operator-Splitting Methods	183
	B.2	Three-dimensional Grid Setup	
	В.3	Discrete Fourier Transform and Discrete Observables	
	B.4	Pseudo-spectral Operator-splitting Scheme	
	B.5	Application to Axion Star Condensation	
	B.6	Outlook on numerical Simulations for Future Research	
\mathbf{C}	\mathbf{Add}	litional Information on Mass Distributions	195
	C.1	Properties of galactic Miniclusters	195
		Properties of galactic Axion Stars	
D	Ana	dytical Calculations on Axion Stars	199
		Parametric Resonance	199
	D.2	Derivation of Axion Star Resonance Mass	201
	D.3	Derivation of Axion Star Radius Cutoff	203
Bi	bliog	graphy	205
Ac	knov	wledgments	227

Introduction

The cosmological standard model ranks among the most important scientific achievements since it encompasses our fundamental understanding of the laws of nature. It provides an important framework prescribing the interpretation of various observational data and explains the cosmic history from the early universe until today. The most recent fundamental shift in our understanding of the universe occurred in 1998, when its accelerated expansion was discovered through recession velocities of type 1A supernovae [5]. After that, dark energy (Λ) was understood to be a major contribution to the total energy budget of the universe, next to cold dark matter (CDM), in the so-called Λ CDM model.

The Λ CDM model is the most simple and most well-tested cosmological model that stands up to observational challenges from decades of astronomical observations. Despite its great success in explaining precision measurements of the cosmic microwave background and the homogeneity of the present-day universe, the Λ CDM model still faces a series of fundamental challenges. These challenges include the Hubble tension arising from different measurements of the present-day expansion rate of the universe [6], the nature of dark energy and most importantly for this work, the unknown nature of the name-giving cold dark matter (DM) component.

The first evidence for the existence of dark matter came through observations in the kinematics of galaxy clusters by Fritz Zwicky [7] in the 1930s. Ever since then, a large amount of experimental data has consolidated the need for a larger matter component, mainly through measurements of galaxy rotation curves [8–10], combined observations of the Bullet cluster [11, 12] and CMB measurements [13, 14]. Within the last decades, extensive searches for different dark matter candidates like massive compact halo objects (MACHOS), primordial black holes and weakly interacting massive particles (WIMPs) have been performed. Despite these efforts, neither WIMPs nor any other dark matter particles have been found so far, which raised scientific interest in new models and explanations. Among the most elegant and well-motivated of these is the QCD axion, a weakly interacting pseudo-scalar particle that was proposed by Peccei and Quinn in the 1970s to explain the strong CP problem of quantum chromodynamics [15, 16]. Analogous to the QCD axion, there exist many other extensions of the standard model, which also introduce a spontaneously broken global shift symmetry [17, 18] and a corresponding pseudo-Nambu-Goldstone boson that can serve as dark matter. These so-called axion-like particles are generally very light but can be produced abundantly via the non-thermal vacuum realignment mechanism [19-21], in which the energy stored in the oscillations of the early axion field behaves like cold dark matter at low cosmological temperatures. The subsequent evolution of the matter density perturbations sourced by the axion field is fundamentally different depending on if the symmetry breaking occurred before or after cosmic inflation. When the global symmetry remains unbroken during inflation as will be assumed in this work, the axion field takes different values across a Hubble patch leading to the collapse of large matter overdensities around matter-radiation equality [22].

The objects formed from these overdensities are called axion miniclusters [23, 24]. They exhibit a large range of masses, with typical values $\mathcal{M} \sim 10^{-12}\,M_{\odot}$ for $m_a \sim 50\,\mu\text{eV}$, and are expected to host a dense core of condensed axions, called an axion star, or soliton [25, 26]. Miniclusters have been shown to form heavier structures through consecutive mergers throughout the cosmological evolution [27] and could thereby source the sites of galaxy formation at late times. Just like their minicluster counterparts in N-body simulations [27–29], the galaxy-sized dark matter halos formed from such mergers are expected to exhibit a rich substructure of lighter and intermediate-mass miniclusters [30]. This scenario has important implications for experimental observations of dark matter in our galaxy: First, the collisions of these objects with earth-based detectors could lead to observable signals in axion DM search experiments. Secondly and importantly for this work, axion stars on the verge of instability, can source the emission of either radio bursts [31–34] or relativistic axion particles [35, 36]. Miniclusters, which host an unstable axion star in their center can therefore allow for either confirmation or exclusion of different axion models through (non-)observation of the resulting axion star signals.

In this work, we introduce the galactic DM substructure and more specifically the axion star population of the Milky Way in a hierarchical approach: We start from the production of axion dark matter in the early universe and consider the galactic dark matter halo of the Milky Way to be composed out of a large population of lighter and heavy axion miniclusters, each of which can host up to a single axion star core. Axion stars in return have been considered to yield observable signatures through a variety of mechanisms, namely through spontaneous decay of axions into photons, relativistic axion emission during collapse and radio amplified radio conversion in the presence of the strong magnetic fields of neutron stars. The major goal of this work is to provide a complete evaluation of the aforementioned, most important axion star signatures and their detectability. A second part of this work is dedicated to the development of new detection strategies, which exploit the mass growth of axion star cores.

For this, we start by introducing the fundamental properties of different axion models together with different production and detection mechanisms of axion matter density perturbations in Chap. 2. Chap. 3 summarizes how current knowledge on the formation and evolution of axion miniclusters can be applied to estimate their present-day mass distribution in the galactic dark matter halo. The resulting properties of galactic miniclusters are thereafter used to infer the mass distribution of their respective axion star cores in Chap. 4. In Chap. 5 the combined properties of axion stars and miniclusters can then be used to re-evaluate the detectability of various signatures through calculation of the mass-integrated collision rates with astrophysical sources. The resulting findings motivate the development of new observational methods for accreting axion stars in Chap. 6 and Chap. 7. First, Chap. 6 focusses on the development of two major accretion mechanisms for isolated and non-isolated axion-star-minicluster systems. Both of these mechanisms are shown to induce substantial mass growth and resulting spontaneous decay in axion stars, which is detectable with existing radio telescopes like LOFAR and FAST according to our analysis. An equivalent approach is taken in Chap. 7, where the continuous mass growth of axion stars leads to numerous, re-occurring axion bursts within the Milky Way, which can potentially be detected using future broadband axion searches. Lastly, the results of this work are summarized together with possible improvements in Chap. 8.

For the sake of clarity, we provide a schematic overview of the total structure and content of this work in Fig. A.1 and App. A.2. The different minicluster- and axion star parameters used in this thesis are summarized together with their respective definitions in Tab. A.1.

Axion Dark Matter

This chapter serves as a basic introduction of both the cosmological QCD axion and other axion-like particles - together more broadly referred to as *axions* in this thesis (see Conventions). Such particles are both motivated by the ongoing search for the missing dark matter in our universe and by other, model-dependent considerations, most importantly by the solution of the strong CP problem in the case of the QCD axion. The strong CP problem will be introduced in Sec. 2.1 together with the Peccei-Quinn mechanism in Sec. 2.2. Sec. 2.3 summarizes the interactions between different axion models and the standard model. The generalization to axion-like particles and their fundamental properties are introduced in Sec. 2.4. Different production mechanisms of axion dark matter and its role in the cosmological evolution are summarized in Sec. 2.5 and Sec. 2.6, with special emphasis on the axion misalignment mechanism. Lastly, Sec. 2.7 gives a summary of the most relevant experimental techniques designed to either detect or exclude different axion models, and more specifically their predicted axion small-scale structure. The content of this chapter is based on more elaborate reviews such as Ref.s [37–39] for the strong CP problem and Ref.s [40–49] for the cosmological axion.

2.1 The strong CP Problem

Soon after the theory of Quantum Chromo-Dynamics (QCD) was established as the fundamental theory of strong interactions, it was understood that the general QCD Lagrangian could contain a term which violates invariance under time reversal (T) and parity (P) transformations. This equivalently CP violating term (with CP denoting the combined transformation of charge conjugation (C) and parity) is generally referred to as the θ -term with Lagrangian

$$\mathcal{L}_{\theta} = \theta \, \frac{\alpha_s}{8\pi} G^a_{\mu\nu} \tilde{G}^{a,\mu\nu} \subset \mathcal{L}_{\text{QCD}} \,, \tag{2.1}$$

where $\alpha_s = g_s^2/(4\pi)$ is the strong fine-structure constant and g_s the strong coupling. The field strength tensor $G^a_{\mu\nu} = \partial^\mu G^{a\nu} - \partial^\nu G^{a\mu} - g_s f^{abc} [G^{b\mu}, G^{c\nu}]$ is built from the gluon field $G^{a\mu}$ and the structure constants f^{abc} of the gauge group of QCD. Its dual is defined as $\tilde{G}^{a\mu\nu} = \epsilon^{\mu\nu\alpha\beta} G^a_{\alpha\beta}/2$ and importantly, θ is expected to be an order one parameter, which serves as a measure of the strength of CP violation in QCD [37].

Another contribution to the strong CP problem arises from the quark mass Lagrangian

$$\mathcal{L}_M = \bar{q}_{iR} M_{ij} q_{jL} + h.c. \tag{2.2}$$

with indices L and R labelling the left- and right-handed helicity states of the quark fields q_i . Since, the quark mass matrix M_{ij} is generally complex, a chiral transformation $q \to \exp(i\alpha\gamma_5/2)q$ of the quark fields with the Dirac matrix $\gamma_5 = i\gamma_0\gamma_1\gamma_2\gamma_3$ is needed to change to a physical basis by diagonalization of M_{ij} . These chiral transformations change the θ vacuum state of QCD by introducing a rotation [37]

$$e^{i\alpha\gamma_5} |\theta\rangle = |\theta + \alpha\rangle .$$
 (2.3)

The shift required to render the quark masses real and positive is $\alpha = \arg(\det M)$, so that the total contribution to the CP violating $\bar{\theta}$ -term including the effects of chiral transformations is 2π -periodic with

$$\bar{\theta} = \theta + \arg(\det M), \qquad (2.4)$$

taking values $\bar{\theta} \in [-\pi, \pi]$ and where $\bar{\theta} = 0$ amounts to no violation of the CP symmetry of QCD [37, 50]. The general $\bar{\theta}$ -term and the corresponding violation of CP symmetry for $\bar{\theta} \neq 0$ induce an electric dipole moment for the neutron which is roughly on the order of

$$d_n \sim \frac{\bar{\theta}em_u m_d}{m_n^2(m_u + m_d)} \sim 10^{-16} \,\bar{\theta} \,e\,\mathrm{cm}\,,$$
 (2.5)

with the electron charge e, the neutron mass m_n and the masses m_u, m_d of the up- and down quarks [51]. Experimental measurements of this dipole moment yield an upper bound of $|d_n| < 1.8 \cdot 10^{-26} e$ cm [52], which amounts to the stringent constraint $|\bar{\theta}| \lesssim 10^{-10}$ for the $\bar{\theta}$ -parameter in Eq. (2.4). Since the natural expectation for $\bar{\theta} \in [-\pi, \pi]$ is an $\mathcal{O}(1)$ number, the apparently exact CP symmetry of QCD constitutes a fine-tuning problem raising the question why the observed value of $\bar{\theta}$ is so extremely small.

2.2 The Peccei-Quinn Mechanism and the QCD Axion

The easiest possible solution to the strong CP problem of QCD is to assume that one of the quarks is massless. In this case $\det M = 0$ and the $\arg(\det M)$ term in Eq. (2.4) becomes arbitrary, allowing one to set $\bar{\theta} = 0$ for any θ . However it was quickly found that the lightest quark mass in the standard model is that of the up quark with $m_u = 2.2 \pm 0.5 \,\text{MeV}$ [53], which effectively ruled out the massless quark explanation.

Another, more viable solution was proposed by Peccei and Quinn (PQ) in the 1970s, who introduced a new axial $U(1)_{PQ}$ symmetry which is broken at some energy scale f_a , often referred to as the *decay constant* [15]. Under this symmetry, the newly defined complex scalar field

$$\varphi(x) = \varphi_0(x) e^{i\phi(x)/f_a} \tag{2.6}$$

transforms according to

$$\varphi(x) \to e^{i\alpha} \varphi(x) \,, \tag{2.7}$$

where the field φ is decomposed into the radial mode $\varphi_0(x)$ and a pseudo-scalar field $\phi(x)$. Similar to the Higgs mechanism, the field φ has a symmetry breaking potential, where the $U(1)_{PQ}$ symmetry is spontaneously broken by the vacuum expectation value $\langle \varphi \rangle = f_a$. The pseudo Nambu-Goldstone boson associated to this symmetry breaking, $\phi(x)$, is known as the

axion [15, 17]. It can be shown that the corresponding axion Lagrangian contains the crucially important axion-gluon interaction term

$$\mathcal{L}_{agg} = \frac{\alpha_s}{8\pi} \frac{\phi}{f_a} G_{\mu\nu} \tilde{G}^{\mu\nu} \,. \tag{2.8}$$

This term encompasses a solution of the strong CP problem since it provides a similar contribution than the theta-term in Eq. (2.1) and Eq. (2.4) [15, 37]. The cancellation of the CP violation contained in \mathcal{L}_{θ} , \mathcal{L}_{M} and \mathcal{L}_{agg} can also be seen from the axion potential $V(\phi)$, which is inherited from the Lagrangian Eq. (2.8). A simplified but common assumption for the cosmological axion potential is [40, 41, 54]

$$V(\phi) = m_{\pi}^{2} f_{\pi}^{2} \frac{m_{u} m_{d}}{m_{u}^{2} + m_{d}^{2}} \left[1 - \cos\left(\bar{\theta} + \frac{\phi}{f_{a}}\right) \right], \tag{2.9}$$

whereas its exact form has to be computed numerically from instantons [54] or chiral perturbation theory [55]. It is given in terms of the pion mass and decay constant m_{π} , f_{π} and exhibits a CP conserving minimum at $\langle \phi \rangle = -\bar{\theta} f_a$. The strong CP problem of QCD is thus solved dynamically by the field $\phi(x)$ relaxing to its potential minimum, where the shift $\phi \to \phi + \langle \phi \rangle$ cancels the CP violating contributions from Eq. (2.1) and Eq. (2.2). Accordingly, one can also interpret the PQ solution as a promoting of the static CP violation parameter $\bar{\theta}$ to a dynamical field $\bar{\theta} \to \phi(x)/f_a$. Apart from solving the CP problem, the axion potential Eq. (2.9) induces an axion mass

$$m_a^2 = \frac{\partial^2 V(\phi)}{\partial \phi^2} \bigg|_{\min(\phi)} = \frac{m_\pi^2 f_\pi^2}{f_a^2} \frac{m_u m_d}{m_u^2 + m_d^2},$$
 (2.10)

with Eq. (2.10) implying $m_a^2 f_a^2 = \text{const.}$ Inserting standard model values for the known parameters m_u , m_d , m_π , f_π , the zero-temperature axion mass from Eq. (2.10) is commonly expressed in terms of the decay constant as [56]

$$m_a \approx 50 \,\mu\text{eV}\left(\frac{1.2 \cdot 10^{11} \,\text{GeV}}{f_a}\right)$$
 (2.11)

where in this work we assume a representative value of $m_a = 50 \,\mu\text{eV}$, in good agreement with Ref.s [28, 30, 43, 57]. More generally and above the QCD confinement scale, the axion potential V derived from the Lagrangian Eq. (2.8) evolves with the cosmological temperature T as

$$V(\phi, T) = m_a^2(T) f_a^2 \left[1 - \cos\left(\frac{\phi N_{\text{DW}}}{f_a}\right) \right], \qquad (2.12)$$

where $N_{\rm DW}=1$ is the domain wall number and the temperature dependent axion mass

$$m_a^2(T) = \frac{\chi(T)}{f_a^2}$$
 (2.13)

is given in terms of the topological susceptibility $\chi(T)$ of QCD [54]. Note that the axion field in Eq. (2.12) has already been shifted compared to Eq. (2.9). For temperatures below the QCD scale $T < T_{\rm QCD} \approx 180 \,\mathrm{MeV}$ [54], $m_a(T)$ approaches its zero-temperature value from Eq. (2.11).

Conversely, $\chi(T)$ evolves beyond the QCD confinement scale, rendering the axion effectively mass-less at high temperatures. Wantz and Shellard [54] reported the scaling

$$\chi(T) = \alpha_a \Lambda_a^4 \left(\frac{T}{\Lambda_a}\right)^{-2n} \quad , \quad T > \Lambda_a$$
(2.14)

of the susceptibility, with coefficient $\alpha_a = 1.68 \cdot 10^{-7}$, temperature index n = 3.34 and $\Lambda_a = 400 \,\text{MeV}$. This means that the axion mass temperature evolution in Eq. (2.13) can be parametrized by a power law according to

$$m_a(T) = \frac{\sqrt{\alpha_a} \Lambda_a^2}{f_a} \left(\frac{T}{\Lambda_a}\right)^{-n} \simeq m_{a,0} \left(\frac{T}{\Lambda_a}\right)^{-n} , \quad T > \Lambda_a$$
 (2.15)

where $m_{a,0} \equiv m_a(T=0)$ is the zero-temperature axion mass and the decay constant f_a was estimated from the zero-temperature relation Eq. (2.13) as $f_a \sim \sqrt{\chi(0)}/m_{a,0} \sim \sqrt{\alpha_a}\Lambda_a^2/m_{a,0}$ [58]. Unless the temperature dependence is explicitly written out, we refer to the low-temperature value of the axion mass, i.e. $m_a \equiv m_{a,0}$. In Sec. 2.5, this parametrization of $m_a(T)$ will be used to determine the present-day axion abundance for a given set of parameters α_a , n, Λ_a , which in turn have to be found numerically from QCD lattice calculations [41, 54].

2.3 Axion Models and Interactions

In this section we will examine the coupling of different axion models to standard model particles. It should be noted that the original Peccei-Quinn-Weinberg-Wilczek (PQWW) axion involving only a single additional complex scalar field is excluded by experiments. As we will see, axion couplings to the standard model are proportional to $1/f_a$, which is why the original PQWW axion with $f_a \sim 100\,\text{GeV}$ on the order of the electroweak phase transition was quickly ruled out by laboratory experiments [59, 60]. A solution to this problem was the invention of so-called invisible axion models, for which the PQ scale is introduced independently of the electroweak scale. This allows for much larger axion decay constants $f_a \gg 100\,\text{GeV}$, which lead to smaller couplings to the standard model, that have not been ruled out yet [19, 61].

Many of these models can be assigned to one of two different categories: the Kim-Shifman-Vainshtein-Zakharov (KSVZ) type axions introducing heavy quarks next to a PQ scalar, and the Dine-Fischler-Srednicki-Zhitnitsky (DFSZ) type models, which introduce an additional Higgs field next to the PQ scalar [41]. Conveniently, the zero-temperature axion mass, which is derived from the axion-gluon coupling Eq. (2.8), is essentially model-independent. The simple explanation for this is the fact that the Lagrangian \mathcal{L}_{agg} , which gives rise to the axion potential and which is required to cancel the CP-violating $\bar{\theta}$ term, has to be model-independent in order to solve the strong CP problem consistently.

In this work and in the context of axion small-scale structure, we will focus on the case of KSVZ-type models with domain wall number $N_{\rm DW}=1$, for which miniclusters are a generic prediction in standard QCD axion models [58]. For DFSZ-type axion models with $N_{\rm DW}>1$ on the other hand, the axion relic density can be enhanced above $\Lambda {\rm CDM}$ values, as explained in more detail in Subsec. 2.5.3. Independent of the QCD axion model at hand, the total Lagrangian contains the terms

$$\mathcal{L}_{\text{ind}} = -\frac{1}{2} \partial_{\mu} \phi \partial^{\mu} \phi + \frac{\alpha_s}{8\pi} \frac{\phi}{f_a} G_{\mu\nu} \tilde{G}^{\mu\nu} \subset \mathcal{L}_a$$
 (2.16)

which amount to a kinetic term plus the Lagrangian \mathcal{L}_{agg} from Eq. (2.8). At low energies, the phenomenologically most relevant couplings to the standard model are given by the modeldependent axion interactions with photons, nucleons, protons and electrons $(\gamma, f = n, p, e)$

$$\mathcal{L}_{a\gamma\gamma} = -\frac{g_{a\gamma\gamma}}{4} \phi F^{\mu\nu} \tilde{F}_{\mu\nu} \,, \tag{2.17}$$

$$\mathcal{L}_{aff} = \sum_{f=n,p,e} \frac{g_{aff}}{2m_f} \partial_{\mu} \phi \overline{\Psi}_f \gamma^{\mu} \gamma_5 \Psi_f , \qquad (2.18)$$

$$\mathcal{L}_{af\gamma} = -i \sum_{f=n,p} \frac{g_{af\gamma}}{2m_f} \phi F^{\mu\nu} \overline{\Psi}_f \sigma_{\mu\nu} \gamma_5 \Psi_f , \qquad (2.19)$$

where $F^{\mu\nu}$, $\tilde{F}_{\mu\nu}$ are the electromagnetic field strength tensor and its dual respectively, Ψ_f are fermion wave functions and $\sigma_{\mu\nu}$ is the spin operator. Here, $g_{a\gamma\gamma}$ is the axion-photon coupling, g_{aff} is the coupling to fermions and $g_{af\gamma}$ is the mixed coupling leading to the neutron electric dipole moment. Note that $g_{a\gamma\gamma}$, $g_{af\gamma}$ have mass dimension -1, while g_{aff} is dimensionless by definition. The coupling strengths in Eq. (2.17) - Eq. (2.19) are often expressed in terms of the dimensionless coupling constants $C_{a\gamma\gamma}$, C_{aff} and $C_{af\gamma}$ defined by

$$g_{a\gamma\gamma} \equiv \frac{\alpha}{2\pi} \frac{C_{a\gamma\gamma}}{f_a} \quad , \quad g_{aff} \equiv \frac{C_{aff} m_f}{f_a} \quad , \quad g_{af\gamma} \equiv \frac{C_{af\gamma}}{f_a} \, ,$$
 (2.20)

where all couplings g scale inversely with f_a as mentioned before.

Phenomenologically most relevant for this work is the axion-photon coupling coefficient

$$C_{a\gamma\gamma} = \frac{E}{N} - 1.92(4),$$
 (2.21)

where E/N = is the model-dependent ratio between the electromagnetic anomaly number E and the number of color anomalies N. KSVZ-type models usually have E/N=0, while classical DFSZ models have E/N = 8/3. The above coefficient yields the axion-photon coupling constant

$$g_{a\gamma\gamma} = \left[0.203(3)\frac{E}{N} - 0.39(1)\right] \frac{m_a}{\text{GeV}^2},$$
 (2.22)

of the decay process $a \to \gamma + \gamma$.

In the KSVZ axion model, which we focus on in this work, the axion-nucleon and axion-electron coupling constants C_{aff} take the values [43, 62, 63]

$$C_{ann}^{KSVZ} = -0.02(3),$$
 (2.23)

$$C_{ann}^{\text{KSVZ}} = -0.02(3),$$
 (2.23)
 $C_{app}^{\text{KSVZ}} = -0.47(3),$ (2.24)

$$C_{aee}^{\rm KSVZ} = \frac{3\alpha_s^2}{4\pi^2} \left[\frac{E}{N} \ln \left(\frac{f_a}{m_e} \right) - 1.92 \ln \left(\frac{1 \,\text{GeV}}{m_e} \right) \right] \,. \tag{2.25}$$

(2.26)

For completeness, we also give the corresponding coefficients for DFSZ type models which are found to be [62, 63]

$$C_{ann}^{\rm DFSZ} = 0.254 + 0.414 \sin^2 \beta \pm 0.025$$
 (2.27)

$$C_{app}^{\text{DFSZ}} = 0.617 + 0.435 \sin^2 \beta \pm 0.025$$
 (2.28)

$$C_{aee}^{\text{DFSZ}} = \frac{\sin^2 \beta}{3} \,, \tag{2.29}$$

(2.30)

where β is an angular parameter related to the vacuum expectation value of the Higgs field. Lastly, the model-independent axion-photon-nucleon couplings [62, 63]

$$C_{an\gamma} = -C_{ap\gamma} = (3.7 \pm 1.5) \cdot 10^{-3}$$
 (2.31)

of the neutron and proton have equal magnitudes and opposite signs.

Note that the QCD axion models introduced in this section obey specific relations Eq. (2.20) between their coupling constants $g_{a\gamma\gamma}$, g_{aff} , $g_{af\gamma}$ and the decay constant f_a of the PQ symmetry breaking. Taking into account Eq. (2.11), this means that the mass m_a of the QCD axion fixes both its decay constant f_a and the standard model couplings $g_{a\gamma\gamma}$, g_{aff} , $g_{af\gamma}$ The search for axion models constituting the missing cold dark matter thus amounts to optimizing the parameter range for m_a to fix the present-day axion abundance to the correct value (see also Sec. 2.5). This so-called cosmological axion mass band lies in the range $10^{-6} \text{ eV} \leq m_a \leq 10^{-4} \text{ eV}$.

2.4 Axion-like Particles

The ongoing search for dark matter and the realization that the QCD axion provides an excellent dark matter candidate motivated the definition of a broader class of particles with similar properties than the previous QCD axion models. These so-called *axion-like particles* (ALPs, or often simply termed axions) are typically massive pseudo-scalar particles that are either generated dynamically like the QCD axion or that are present in the universe from the beginning. Axion-like particles can arise naturally as the pseudo-Nambu-Goldstone bosons from extensions of the standard model, where an approximate symmetry becomes spontaneously broken. The introduction of ALPs can hence be seen as a generic class of axion-like dark matter candidates, that do not solve the strong CP problem and which are often motivated rather by their simple nature and their CDM like behavior at low temperatures.

Generally, ALPs can appear in many different extensions of the standard model, like SUSY theories [64] or string theoretical models [65–67], which is why we take a simplified approach in the following and refer to Ref. [68] for a detailed review on the topic. A common assumption is that the ALP potential inherited from some strongly interacting sector is similar to the QCD instanton potential from Eq. (2.12), i.e.

$$V_{\rm A}(\phi_A) \sim \Lambda^4 \left[1 - \cos\left(\frac{\phi_A}{f_A}\right) \right] ,$$
 (2.32)

which gives a similar relation for the ALP mass m_A

$$m_A^2 = \frac{\partial^2 V_{\mathcal{A}}(\phi_A)}{\partial \phi_A^2} \bigg|_{\min(\phi_A)} = \frac{\Lambda^4}{f_A^2}, \qquad (2.33)$$

and where Λ^4 takes the role of the topological susceptibility $\chi(T)$ in Eq. (2.13).

Opposed to the QCD axion models in Sec. 2.3, ALPs can have arbitrary combinations of the parameters m_A , f_A and $g_{a\gamma\gamma}$, g_{aff} , $g_{af\gamma}$, largely enhancing their possible parameter space. Due to their Nambu-Goldstone nature, ALP couplings are suppressed by the symmetry breaking scale f_A , yielding feeble interactions for large f_A as in the case of the QCD axion.

In the context of arbitrary ALP models, the temperature evolution of the quantity $\Lambda(T)$ in Eq. (2.33), which governs the temperature evolution of the ALP mass, is strongly model-dependent. We deal with this model-dependence following the approach in Ref.s [58] and [54] by introducing a parametrization of the form

$$m_A(T) = m_{A,0} \left(\frac{T}{\Lambda_0}\right)^{-n} \quad , \quad T > \Lambda_0 \tag{2.34}$$

to describe the temperature evolution of the ALP mass m_A with zero-temperature value $m_{A,0} \equiv m_A(T=0)$ in terms of the temperature index n and a reference scale Λ_0 . Note that this parametrization is equivalent to the QCD axion mass scaling in Eq. (2.15).

While the QCD axion has $m_{a,0} \approx 21 \,\mu\text{eV}$, n = 3.34 and $\Lambda_0 = \Lambda_a = 400 \,\text{MeV}$ according to the instanton liquid model in Ref. [54], the ALP parameters $m_{A,0}$, n and Λ_0 are essentially unconstrained. Eq. (2.34) can therefore be interpreted as a generalization of the QCD axion relation Eq. (2.15), where each ALP model has a different set of parameters $m_{A,0}$, n and Λ_0 determining the evolution of m_A with T. Based on the zero-temperature scaling of the QCD axion in Eq. (2.13), we assume $\Lambda_0 \equiv \Lambda(T=0) \sim \sqrt{m_{A,0} f_A}$ for the general ALP mass temperature evolution in Eq. (2.34)¹.

In this work and in the following, the term axions refers to the general class of axion-like particles, including the QCD axion, whereas the term ALPs refers to axion-like particles specifically.

2.5 Axion Dark Matter Production

In the previous sections we have introduced the QCD axion as the pseudo-Nambu-Goldstone boson of a spontaneously broken $U(1)_{PQ}$ symmetry which solves the strong CP problem. Similarly, ALPs can be generated as the pseudo-Nambu-Goldstone bosons of more general symmetry breaking, with both mechanisms being described by some high energy scale f_a . In a cosmological context, the symmetry breaking will take place in the early universe with the axion field dynamic and subsequent dark matter production depending strongly on the hierarchy of f_a and other cosmological temperature scales. The most relevant such scale is the temperature of the universe during inflation, given by the Gibbons-Hawking temperature of the de-Sitter horizon

$$T_I = \frac{H_I}{2\pi} \,, \tag{2.35}$$

which is defined in terms of the inflationary Hubble scale H_I [41, 69]. It is common to distinguish axion models and their subsequent evolution as CDM into two scenarios: those with a pre-inflationary symmetry breaking, i.e. $f_a > T_I$ and those with a post-inflationary PQ transition, where $f_a < T_I$. We use this distinction to describe axion DM production by the misalignment

¹Note that here for the QCD axion $\Lambda_0 \neq \Lambda_a$, which agrees roughly with the scaling $\Lambda_0 \sim 2.5 \sqrt{m_{A,0} f_A}$ reported in Ref. [58].

mechanism in Subsec. 2.5.2, but restrict our analysis to the post-inflationary case for the majority of our study.

As for this section, we start by introducing the thermal production of relic axions in Subsec. 2.5.1 and put special emphasis on the misalignment mechanism in Subsec. 2.5.2. As it turns out, the latter provides an excellent explanation linking the axion field to the expected abundance of cold dark matter in our universe. We also summarize how the decay of the axion string-domain-wall network leads to additional axion DM production in Subsec. 2.5.3 and how it seeds the formation of small-scale DM structures in Sec. 2.6.

2.5.1 Thermal Production

There are different thermal processes in the plasma of the early universe, which can contribute to the production of relic axions, mainly derived from their interactions with quarks, gluons and pions. In the case of the QCD axion, the most relevant among them is given by pion-scattering $\pi + \pi \leftrightarrow \pi + a$ [22, 41]. Pion-scattering becomes relevant after hadronization at temperatures $T \lesssim 200 \,\text{MeV}$. Compared to the QCD axion, ALPs are often more weakly coupled to the strongly interacting sector, which is why the abundance of thermal ALPs is strongly model-dependent. For simplicity, we will thus only consider the thermal production of QCD axions in the following. Once the interaction rate for pion-scattering drops below the Hubble expansion rate, the number density of relic axions is fixed by freeze-out at the decoupling temperature. Thermal axions have to be out of equilibrium by recombination, i.e. for $T > 0.26 \,\text{eV} \gg m_a$, when they are still relativistic. Thermally produced axions with sub-eV mass will thus contribute to the total energy budget of the universe in the form of some yet unobserved 'dark radiation' component. This is why the relic density of thermal axions is often expressed in terms of the excess number of neutrino species $\Delta N_{\text{eff}} = N_{\text{eff}} - 3.044$ by writing [42, 70, 71]

$$\rho_{a,\text{th}} = \rho_{\text{rad}} - \rho_{\gamma} - \rho_{\nu} = \frac{7}{8} \left(\frac{4}{11}\right)^{4/3} \Delta N_{\text{eff}} \rho_{\gamma}, \qquad (2.36)$$

where $N_{\rm eff}$ is the effective number of neutrino flavours. Here, $\rho_{\rm rad}$ denotes the total relativistic energy density composed out of photons in the cosmic microwave background (CMB) with density ρ_{γ} , the $N_{\nu}=3$ neutrino species constituting ρ_{ν} and thermal axions with relic density $\rho_{a,\rm th}$. Using the conservation of the comoving entropy density, one can show that any light, weakly interacting scalar particle will contribute to the dark radiation component by an amount [70]

$$\Delta N_{\text{eff}} = \frac{4}{7} \left[\frac{11}{4} \frac{g_{\star,S}(T_{\nu})}{g_{\star,S}(T_d)} \right]^{4/3} \approx 0.027 \left[\frac{106.75}{g_{\star,S}(T_d)} \right]^{4/3} , \qquad (2.37)$$

where $g_{\star,S}(T_d)$ is the number of entropic degrees of freedom at the decoupling temperature T_d . Since the standard model has $g_{\star,S}(T) \lesssim g_{\star,S}(T \gtrsim 3m_{\rm top}) = 106.75$ for temperatures above the top-quark mass $T \gtrsim 100\,{\rm GeV}$, it can be seen from Eq. (2.37) that the QCD axion should contribute at least with $\Delta N_{\rm eff} \approx 0.027$ to the effective number of neutrinos $N_{\rm eff}$.

For the QCD axion, thermal production becomes more efficient when the axion-pion coupling gets larger. Recalling the inverse scaling of the standard model couplings in Eq. (2.20) with f_a , this means that a smaller symmetry breaking scale f_a will enhance the thermal axion abundance. The required value for the thermal axion population to become visible in future galaxy redshift

surveys [72] is $f_a \sim 10^7$ GeV, corresponding to $m_a \geq 0.15$ eV [41]. On the other hand, stellar cooling constrains the decay constant to $f_a > 10^9$ GeV, where the thermal relic abundance is essentially negligible. Depending on the ALP model, thermal production may however become significant for other axion-like dark matter candidates, see e.g. Ref.s [41, 42, 70] for a more detailed discussion.

2.5.2 Misalignment Mechanism

In the previous subsection we have summarized how axions can contribute to the total energy budget of the universe in the form of hot dark matter. However cosmological observations of both the cosmic microwave background and the matter power spectrum in the ΛCDM model strongly constrain the abundance of relativistic DM particles. Instead they suggest that the majority of the matter component should be non-relativistic, or cold [73]. As we will see in this subsection, the vacuum realignment of the axion field provides an excellent mechanism for axion CDM to be produced abundantly [19, 20, 74]. To demonstrate the vacuum realignment mechanism, we start with the derivation of the equation of motion (EOM) for the axion field in an expanding universe. Neglecting axion self-interactions and couplings to standard model particles, the EOM can be obtained from the Lagrangian [41]

$$\mathcal{L}_{\theta} = f_a^2 \left[-\frac{1}{2} \partial_{\mu} \theta \partial^{\mu} \theta - V(\theta, T) \right] , \qquad (2.38)$$

where $g_{\mu\nu}$ is the metric tensor and $V(\theta,T)$ is the axion potential from Eq. (2.12). Note that the axion field has been rescaled to $\theta = \phi/f_a$ here. Taking the Friedman-Lemaitre-Robertson-Walker metric with zero curvature

$$ds^{2} = -dt^{2} + a^{2}(t) \left(dr^{2} + r^{2} d\Omega^{2} \right), \qquad (2.39)$$

and scale factor a(t), the equation of motion for θ becomes

$$\ddot{\theta} + 3H\dot{\theta} - \frac{1}{a^2}\nabla^2\theta + \frac{\partial V(\theta)}{\partial\theta} = 0, \qquad (2.40)$$

where $H = \dot{a}/a$ is the Hubble constant. The stress energy tensor of the axion field is

$$T^{\mu\nu} = f_a^2 \partial^\mu \partial^\nu \theta + f_a^2 g^{\mu\nu} \left[-\frac{1}{2} \partial_\alpha \theta \partial^\alpha \theta - V(\theta, T) \right] , \qquad (2.41)$$

which yields the axion energy density ρ_a and pressure P_a [41]

$$\rho_a = f_a^2 \left[\frac{1}{2} \dot{\theta}^2 + \frac{1}{2a^2} (\nabla \theta)^2 + V(\theta, T) \right] , \qquad (2.42)$$

$$P_a = f_a^2 \left[\frac{1}{2} \dot{\theta}^2 - \frac{1}{6a^2} (\nabla \theta)^2 - V(\theta, T) \right]. \tag{2.43}$$

The basic principle of the misalignment mechanism can be understood from Eq. (2.40), Eq. (2.42) and Eq. (2.43): Assuming a small displacement, i.e. a small initial angle $\theta = \theta_I \ll 1$ for the axion field, one can perform a Taylor expansion and write $V(\theta, T) \approx m_a^2(T)\theta^2/2$. This so-called

harmonic approximation linearizes the EOM and allows for a simplified analytical treatment of the misalignment mechanism. Applying it to the homogeneous axion field with $\nabla \theta = 0$, Eq. (2.40) reduces to the differential equation of a damped harmonic oscillator

$$\ddot{\theta} + 3H(T)\dot{\theta} + m_a^2(T)\theta = 0, \qquad (2.44)$$

where the Hubble friction term $\propto 3H(T)$ takes the role of the damping and where the axion mass $m_a(T)$ evolves according to Eq. (2.15). At early times and before the QCD phase transition, the axion is effectively massless $m_a(T) \approx 0$. This means that for $T \gg T_{\rm QCD}$, the homogeneous field evolution is dominated by the Hubble drag, with $3H(T) \gg m_a(T)$, so that the axion field remains essentially frozen at its initial value $\theta = \theta_I \in [-\pi, \pi]$. Looking at Eq. (2.42) and Eq. (2.43) for $T \gg T_{\rm QCD}$, $\dot{\theta} = 0$ and $\nabla \theta = 0$, it can be seen that the axion field in the harmonic approximation has $\rho_a = -P_a$ in this epoch, which implies the same equation of state $w = P/\rho = -1$ as dark energy.

In the second part of its evolution, the axion starts to oscillate around the time when $3H(T_{\rm osc}) = m_a(T_{\rm osc})$, with a frequency $\sim m_a$. The temperature $T_{\rm osc}$ defining equality between axion mass and Hubble drag is called the oscillation temperature. After the onset of axion oscillations, the field θ behaves like CDM. The subsequent dynamical evolution of the field θ and its density fluctuations differs drastically depending on the hierarchy between the temperature scales of inflation and PQ symmetry breaking. We will thus make use of Eq. (2.35) to distinguish between the pre- and post-inflationary symmetry breaking scenarios in the following.

Before treating the two different scenarios in more detail, we can estimate the relic abundance of axions produced from the misalignment mechanism as a function of the initial misalignment angle θ_I using the harmonic approximation. Once the axion oscillations begin and for slow variation of $m_a(T)$, the comoving axion number density $n_a(T) = \rho_a(T)/m_a(T)$ becomes conserved [41]. This allows us to express the present-day axion density at $T = T_0 = 2.725 \,\mathrm{K}$ [14]

$$n_a(T_0) = n_a(T_{\text{osc}}) \left(\frac{a_{\text{osc}}}{a_0}\right)^3 \tag{2.45}$$

in terms of the number density and scale factor $a_{\rm osc} = a(T_{\rm osc})$ at the temperature $T_{\rm osc}$. Assuming that the homogeneous field with $\nabla \theta = 0$ and initial value θ_I does not change significantly until $T_{\rm osc}$, i.e. $\dot{\theta}_i \approx 0$, Eq. (2.42) yields the number density

$$n_a(T_{\rm osc}) = \frac{\rho_a(T_{\rm osc})}{m_a(T_{\rm osc})} \approx \frac{1}{2} m_a(T_{\rm osc}) f_a^2 \theta_I^2$$
(2.46)

from the mass density $\rho_a(T_{\rm osc})$. Together with $\rho_a(T_0) = m_a(T_0)n_a(T_0)$ one obtains

$$\rho_a(T_0) = \frac{1}{2} \theta_I^2 f_a^2 m_a(T_0) m_a(T_{\text{osc}}) \left(\frac{a_0}{a_{\text{osc}}}\right)^{-3}$$
(2.47)

$$= \frac{1}{2} \theta_I^2 f_a^2 m_a(T_0) m_a(T_{\text{osc}}) \left[\frac{g_{\star,S}(T_0) T_0^3}{g_{\star,S}(T_{\text{osc}}) T_{\text{osc}}^3} \right], \qquad (2.48)$$

where in the last expression we have used the conservation $g_{\star,S}(T)T^3a^3 = \text{const}$ of the comoving entropy. It can be shown by taking the average $\langle \cdot \rangle$ over the field oscillations, that the averaged axion pressure is $\langle P_a \rangle = 0$ [41, 75] and that the corresponding time-dependent equation of state

oscillates around w = 0. Together with the conservation of the comoving number density n_a , the axion field thus behaves like CDM at $T \lesssim T_{\rm osc}$.

The remaining quantity needed to obtain the relic density Eq. (2.47) for a given axion model with characteristic parameters m_a , f_a , n and initial angle θ_I is the oscillation temperature $T_{\rm osc}$. In the QCD axion case with m_a obeying Eq. (2.15), the defining condition $3H(T_{\rm osc}) = m_a(T_{\rm osc})$ can be rearranged to find the expression [42]

$$T_{\rm osc} = \left(\sqrt{\frac{10}{\pi^2 g_{\star,R}(T_{\rm osc})}} m_a M_{\rm Pl}\right)^{\frac{2}{2n+4}} T_{\rm QCD}^{\frac{2n}{2n+4}}, \qquad (2.49)$$

where $M_{\rm Pl}=1/\sqrt{8\pi G}$ is the reduced Planck mass. The typical oscillation temperature is of order $T_{\rm osc}\sim 1\,{\rm GeV}$ for representative axion parameters $m_a\sim 10^{-5}\,{\rm eV}$, $T_{\rm QCD}\sim 180\,{\rm MeV}$ and n=4. Re-expressing Eq. (2.47) in terms of the critical density $\rho_c=3H^2M_{\rm Pl}^2$ yields the axion relic density contribution

$$\Omega_a^{\text{mis}} = \frac{m_a(T_0)m_a(T_{\text{osc}})f_a^2\theta_I^2}{6H_0^2M_{\text{Pl}}^2} \left[\frac{g_{\star,S}(T_0)T_0^3}{g_{\star,S}(T_{\text{osc}})T_{\text{osc}}^3} \right]$$
(2.50)

produced from the misalignment mechanism. For the QCD axion, m_a and f_a are related by Eq. (2.11), while the temperature evolution of $m_a(T)$ described by n, Λ_a sets the oscillation temperature $T_{\rm osc}$. However in the most general case of axion-like particles, m_A and f_A can take independent values so that the oscillation temperature needs to be calculated numerically. This can be done by equating the ALP mass temperature evolution $m_A(T)$ in Eq. (2.34) as $m_A(T) = 3H(T)$ with H(T) obtained from the second Friedmann equation

$$3H(T)^2 M_{\rm Pl}^2 = \frac{\pi^2}{30} g_{\star,R}(T) T^4 \,, \tag{2.51}$$

where $g_{\star,R}(T)$ are the relativistic degrees of freedom. In this work we use the fits by Wantz & Shellard [54] for $g_{\star,i}$ with i=R,S parametrized by

$$g_{*,i} = \exp\left[a_0^i + \sum_{j=1}^5 a_{j,1}^i \left(1.0 + \tanh\frac{\tilde{T} - a_{j,2}^i}{a_{j,3}^i}\right)\right], \quad \tilde{T} = \ln\frac{T}{1 \text{ GeV}}.$$
 (2.52)

The corresponding fit parameters a_j^i in Tab. A.2 are accurate up to $\lesssim 4\%$ precision around the QCD phase transition and up to roughly 1% elsewhere [54].

With the determination of the oscillation temperature for QCD axions and ALPs outlined above, Eq. (2.50) allows us to estimate the relic abundance Ω_a^{mis} for arbitrary axion models, i.e. for different combinations of m_A, n, f_A . The remaining quantity needed to fix Ω_a^{mis} is the initial misalignment angle $\theta_I \in [-\pi, \pi]$ entering quadratically in Eq. (2.50). As mentioned before, understanding the dynamical evolution of the axion field and its initial conditions prescribed by θ_I leads us to study the pre- and post-inflationary scenarios for both QCD axions and ALPs in the following.

Pre-inflationary Scenario

We start with the pre-inflationary case depicted in Fig. 2.1 on the left. In this scenario, the PQ symmetry (or any other relevant symmetry for ALPs) is broken before the onset of inflation,

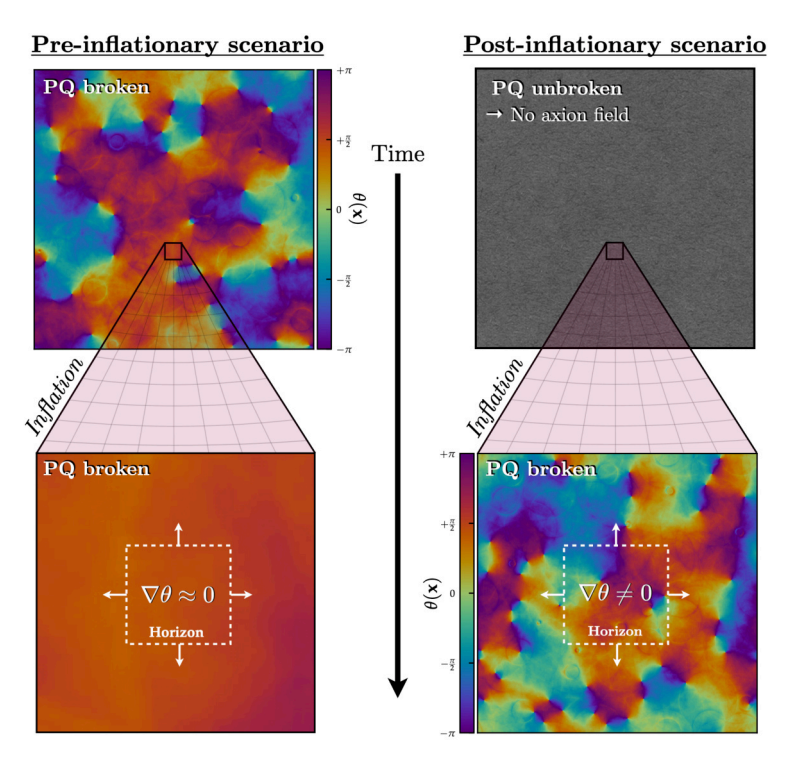


Figure 2.1: Conceptual diagram demonstrating the axion field evolution depending on the time of PQ symmetry breaking, taken from Ref. [42]. Left: In the pre-inflationary case, the axion field gets broken at some scale $f_a > T_I$ and the rapid expansion during inflation leaves a roughly uniform $\nabla \theta \approx 0$ distribution of θ in the current Hubble patch. Right: When the PQ symmetry is broken after inflation $f_a < T_I$, the same horizon is filled with a random ensemble of values for $\theta \in [-\pi, \pi]$ so that $\nabla \theta \neq 0$.

 $f_a > T_I$, with the Gibbons-Hawking temperature T_I from Eq. (2.35). Once the temperature drops below f_a , the PQ symmetry becomes spontaneously broken. At this point, each causally disconnected Hubble patch with horizon size $R_H \sim 1/H$ takes a different value for the initial misalignment angle, with θ_I being randomly drawn from a uniform distribution between $[-\pi,\pi]$. As argued above, the axion field remains frozen at its initial value $\theta=\theta_I$ as long as $m_a(T) < 3H(T)$ and the axion energy density is roughly given by $\rho_a \simeq f_a^2 m_a^2(T)\theta_I^2/2$.

Simultaneously, the universe continues to cool down followed by a rapid expansion during inflation, which stretches out the Hubble patches with different initial values of θ_I . As a consequence, the present-day Hubble volume in this scenario exhibits a uniform value of θ_I everywhere, with $\nabla\theta\approx0$, as indicated by the zoomed in panel in the bottom left of Fig. 2.1.

In the pre-inflationary scenario, the value of θ_I in our universe is completely random and it sets the relic abundance of the pre-inflationary misalingment production according to Eq. (2.50). The dependence of Ω_a^{mis} on θ_I can be intuitively understood from the fact that the energy stored in the axion field oscillations depends directly on the initial misalignment angle, with which the field started to oscillate. This means that with some fine-tuning of θ_I one can set Ω_a^{mis} to almost arbitrary values. As a consequence, the predictive power of the pre-inflationary scenario is arguably compromised (see Ref.s [76, 77] for discussions on the topic). Importantly for this work, we will hereafter focus on the post-inflationary scenario, where the ambiguity in the choice of θ_I vanishes.

Post-inflationary Scenario

In the second scenario, the PQ symmetry remains unbroken throughout the inflationary period, i.e. $f_a < T_I$ as shown by the absence of the axion field in the gray panel on the right of Fig. 2.1. After inflation, the radiation temperature eventually drops below f_a and similarly to before, the axion field is established with θ_I taking random values on the interval $[-\pi, \pi]$. The important difference here is that in the post-inflationary scenario, many regions with different θ_I are contained within a single Hubble horizon so that generally $\nabla \theta \neq 0$. It is thus most reasonable to consider the spatially averaged background energy density

$$\bar{\rho}_a = \frac{1}{V} \int d^3x \, \rho_a(\mathbf{x}) \tag{2.53}$$

instead of its local counterpart ρ_a from Eq. (2.47). Note that this is equivalent to averaging over different Hubble patches with different θ_I . Therefore using the averaged energy density, one can follow the same steps that led to the relic abundance in Eq. (2.50) by means of the replacement $\rho_a \to \bar{\rho}_a$. We can estimate that

$$\bar{\rho}_a(T) \simeq \frac{1}{2} f_a^2 m_a \left(T_{\text{osc}} \right) m_a(T) \left(\frac{a \left(T_{\text{osc}} \right)}{a(T)} \right)^3 \left\langle \theta_{\text{I}}^2 \right\rangle, \tag{2.54}$$

where the randomly drawn average value of θ_I^2 over a Hubble patch is now given by

$$\langle \theta_{\rm I}^2 \rangle = \int_{-\pi}^{+\pi} d\theta \mathcal{F}(\theta) \theta^2 = \frac{\pi^2}{3}$$
 (2.55)

with a flat distribution function $\mathcal{F}(\theta) = 1/(2\pi)$. In principle, the resulting modification of the relic abundance Ω_a^{mis} in Eq. (2.50) amounts to a replacement $\theta_I^2 \to \langle \theta_I^2 \rangle = \pi^2/3$. There are however additional modifications to Ω_a^{mis} in the post-inflationary scenario that we will need to take into account as well.

The first such modification arises from the fact that Eq. (2.50) has been computed from the harmonic axion potential $V(\theta) = m_a^2(T)\theta^2/2$, which is valid for $\theta_I \ll 1$. However when the initial displacement angle becomes large, $\theta_I \sim 1$, anharmonic corrections caused by the axion's self-interactions become relevant. In this case, the axion potential will be flattened for larger θ_I and the onset of oscillations at $T_{\rm osc}$ will be delayed [41]. This results in the relic abundance being increased compared to the prediction in the harmonic approximation. The corresponding anharmonic corrections are usually taken into account by assuming $g_{\star,R} = {\rm const}$ over the timescale on which anharmonic corrections change $T_{\rm osc}$ [58]. Under this assumption, the correction to $T_{\rm osc}$ can be calculated analytically performing the replacement

$$\rho_a^{\text{mis}} \to \mathcal{F}_{\text{an}}(\theta_I) \, \rho_a^{\text{mis}}$$
(2.56)

with the anharmonic correction function

$$\mathcal{F}_{\rm an}(\theta_I) = \left[\ln \left(\frac{e}{p(\theta_I)} \right) \right]^q , \qquad (2.57)$$

where the power index

$$q = \frac{3}{2} - \frac{n}{2n+4} \tag{2.58}$$

is given in terms of the axion mass temperature index n from Eq. (2.34) [58]. The polynomial fitting function

$$p(\theta) = 1 - \left(\frac{\theta}{\pi}\right)^4 \tag{2.59}$$

obtained from Ref. [58] was matched to the solution of the EOM in Eq. (2.40) for a homogeneous axion field with a cosine potential of the form in Eq. (2.32). Note that as expected $\mathcal{F}_{an} \to 0$ for small θ and that $\mathcal{F}_{an}(\theta)$ is monotonically increasing for $\theta \to \pi$. Applying Eq. (2.56) amounts to replacing θ_I^2 in Eq. (2.50) by

$$\langle \theta_I^2 \mathcal{F}_{\rm an} (\theta_I) \rangle = \frac{1}{2\pi} \int_{-\pi}^{\pi} d\theta \mathcal{F}_{\rm an} (\theta) \theta^2 \equiv c_{\rm an} \frac{\pi^2}{3} \,.$$
 (2.60)

Comparing with Eq. (2.55), it can be seen that the coefficient $c_{\rm an}$ effectively accounts for the anharmonic corrections from the axion cosine potential. Rearranging Eq. (2.60), the value of $c_{\rm an}$ can be obtained from the polynomial fit $p(\theta)$ by writing

$$c_{\rm an} = \frac{3}{2\pi^3} \int_{-\pi}^{\pi} d\theta \,\theta^2 \left[\ln \left(\frac{e}{1 - \left(\frac{\theta}{\pi} \right)^4} \right) \right]^{\frac{3}{2} - \frac{n}{2n+4}} \,. \tag{2.61}$$

Note that here, $c_{\rm an}$ only depends on the axion mass temperature index n. For the extended relic abundance $\Omega_a^{\rm an}$ including anharmonic corrections, we obtain the result

$$\Omega_a^{\rm an} = \frac{m_a(T_0)m_a(T_{\rm osc})f_a^2}{6H_0^2M_{\rm Pl}^2} \frac{c_{\rm an} \,\pi^2}{3} \left[\frac{g_{\star,s}(T_0)T_0^3}{g_{\star,s}(T_{\rm osc})T_{\rm osc}^3} \right] \,, \tag{2.62}$$

which is independent of the initial angle θ_I as opposed to Eq. (2.50) for the pre-inflationary case. As a consequence, the predicted total relic abundance $\Omega_a^{\rm an}$ is completely set by the three model-dependent axion parameters m_a, n, f_a , where the remaining constants Λ_a and Λ_0 in Eq. (2.15) and Eq. (2.34) are fixed by QCD calculations or the approximate relation $\Lambda_0 \simeq \sqrt{m_A f_a}$ for ALPs respectively.

We conclude by emphasizing that the random values of θ_I seeded by the PQ symmetry breaking in the bottom right panel of Fig. 2.1 contribute large $\mathcal{O}(1)$ fluctuations in the energy density of the axion field $\rho_a(\boldsymbol{x})$. These fluctuations extend over scales on the order of the horizon at the time when QCD instanton effects give rise to the axion potential and most importantly for this work, they are expected to seed the formation of so-called axion miniclusters, which we treat in more detail in Chap. 3. Before moving on to the formation of axion small-scale structure and its possible detection, there is yet another production mechanism contributing to the total relic abundance, that needs to be taken into account.

We also mention for completeness, that next to the standard misalignment mechanism from this subsection with $\dot{\theta}=0$, there exist similar models in which the axion field has a non-zero initial velocity $|\dot{\theta}|>0$. This so-called *kinetic misalignment mechanism* is explored in Ref.s [78–81], but not considered in this thesis for simplicity.

2.5.3 Decay of Topological Defects

A third production mechanism of axion dark matter arises from the gradient term proportional to $\nabla \theta$ in Eq. (2.40) and from the resulting non-linear axion field dynamics in the *post-inflationary* scenario. In this scenario and after the PQ symmetry breaking, the continuous axion field $\theta(\boldsymbol{x})$ will adopt randomly chosen angles at different locations \boldsymbol{x} within a Hubble patch. As a consequence of this randomness, there should exist some points in space, where the surrounding axion field happens to wrap around the entire range of $\theta \in [-\pi, \pi]$.

At these particular points, the complex scalar field φ will be forced into the center of the complex plane at $|\varphi| = 0$, i.e. on top of the Mexican hat potential, where the PQ symmetry is effectively restored and the angle θ is undefined. The resulting field configuration turns out to be stable due to the 2π -winding of θ as long as the potential $V(\theta, T)$ has no preferred value of θ , or equivalently, as long as the axion remains massless. In three dimensions, the singular points with $|\varphi| = 0$ connect along a one-dimensional line that is commonly referred to as an axion string [82–84].

The energy contained in the cores of axion strings is set by the radial shape of the complex field $\varphi(x)$ defined by Eq. (2.6), Eq. (2.40), Eq. (2.12) with $\theta = a/f_a$ and is thereby closely related to the decay constant f_a [42]. It is commonly expressed in terms of the string tension μ_s , which is given in units of energy per unit length. After the PQ symmetry breaking at $T \simeq f_a$ and before the QCD phase transition, the string tension can be calculated using the EOM from Eq. (2.40) together with the cosmological horizon as a large-scale cutoff $r_{\text{max}} = H(t)^{-1}$ for the string size, which gives $\mu_s \sim f_a^2$ [22, 42, 85]. Accordingly, the cosmic string network can potentially store a considerable amount of energy [86, 87], where the exact contributions need to be calculated from extensive numerical calculations [87–97].

Once the axion acquires a mass around $T \sim T_{\rm osc}$, the potential $V(\theta,T)$ develops a CP-conserving minimum at $\theta=0$, that allows the cosmic strings to unravel themselves due to the existence of a preferred value for θ . This is often visualized as a tilting of the Mexican hat potential, where due to the tilting, $V(\theta,T)$ exhibits an absolute minimum at $\theta=0$ and a quasi-stable maximum at the saddle point $\theta=\pm\pi$. The resulting decay of axion strings contributes to the dark matter relic abundance and occurs until the axion field oscillates around the minimum $\theta=0$ everywhere. During the decay of axion strings, another topological defect arises in locations, where the axion field gets stuck at the saddle point $\theta=\pm\pi$. The two-dimensional surfaces where this happens are called domain walls because they separate different regions ('domains') of the universe, in which the axion field rolls down either along the positive $\theta\in[0,\pi]$ or negative set of values $\theta\in[-\pi,0]$ of the shift-symmetric field $\theta\in[-\pi,\pi]$. Importantly, domain wall decay can provide an additional energy contribution to the relic abundance Ω_a .

Fig. 2.2 shows a visualization of the string- and domain wall network from numerical simulations of the QCD axion field in the post-inflationary scenario with $m_a = 50 \,\mu\text{eV}$ before and after the axion mass becomes relevant at T_{osc} , taken from Ref.s [28, 42]. At temperatures $T > T_{\text{osc}}$ in the left panel, cosmic strings can be seen to form as the red-colored filaments with larger densities given by $\ln(\rho_a/\bar{\rho}_a)$. After the onset of axion oscillations at $T \lesssim T_{\text{osc}}$, domain walls can be seen to form as the yellow colored surfaces connecting cosmic strings. Throughout the onset of axion oscillations, both of these structures will decay, thereby stir up the cosmic axion field and lead to additional production of axion DM compared to the case with $\nabla \theta = 0$.

The calculation of the axion abundance resulting from the decay of strings and domain walls

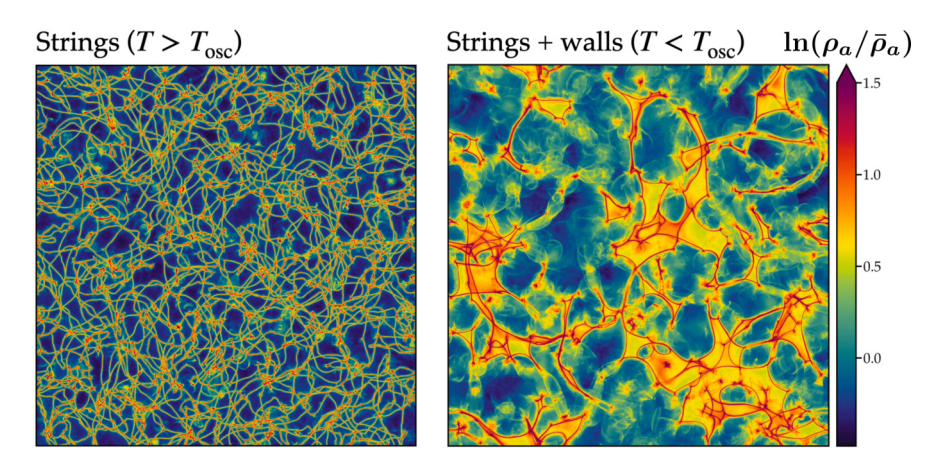


Figure 2.2: Visualization of the string- and domain wall network taken from Ref. [42] as reproduced from the simulations in Ref. [28] for the QCD axion with $m_a = 50 \,\mu\text{eV}$. The color scaling indicates the logarithmic overdensity $\ln(\rho_a/\bar{\rho}_a)$. Axion strings appear at $T > T_{\text{osc}}$ as the red colored filaments, while domain walls form later at $T < T_{\text{osc}}$ as seen by the yellow surfaces bound by red strings.

requires sophisticated numerical simulations of the complex PQ field. As it turns out, these simulations are extremely challenging because they need to resolve string cores with a typical width $\Delta x \sim f_a^{-1}$ in a system of box size $L \sim H(t)^{-1}$, eventually reaching $L/\Delta x \sim 10^{28}$ for the QCD axion [42]. This means that late-time extrapolation of the simulated results, specifically of the power spectrum of string-radiated axions, is necessary due to numerical limitations. Additional complication arises from the determination of the initial conditions and by use of different numerical techniques, see e.g. Ref.s [28, 97–99] for detailed discussions on the topic.

Summarizing the different production mechanisms of axion dark matter, including axion production from the misalignment mechanism in Eq. (2.62) and from the decay of topological defects parametrized by α_{dec} , the total axion relic abundance can be written as [41]

$$\Omega_a^{\text{tot}} h^2 = (1 + \alpha_{\text{dec}}) \Omega_a^{\text{an}} h^2 , \qquad (2.63)$$

where predictions for the parameter $\alpha_{\rm dec}$ range from 0.16 to 186 [92, 100–102]. The large uncertainty in the determination of $\alpha_{\rm dec}$ is related to the inconclusiveness of the numerical simulations discussed above. In this work we follow Ref.s [92] and [58] by assuming an intermediate value of order-one, namely $\alpha_{\rm dec} = 2.48$ obtained from the calculations in Ref. [103]. It should be emphasized that improved numerical simulations are needed to ultimately resolve uncertainties in the production of axion dark matter from topological defects. For now and fixing $\alpha_{\rm dec} = 2.48$, we can finally write the total relic abundance as

$$\Omega_a^{\text{tot}} = (1 + \alpha_{\text{dec}}) \frac{m_a(T_0) m_a(T_{\text{osc}}) f_a^2}{6H_0^2 M_{\text{Pl}}^2} \frac{c_{\text{an}} \pi^2}{3} \left[\frac{g_{\star,s}(T_0) T_0^3}{g_{\star,s}(T_{\text{osc}}) T_{\text{osc}}^3} \right], \tag{2.64}$$

with $T_0 = 2.725 \,\mathrm{K}$ and where both the misalignment mechanism with anharmonic corrections and the decay of the combined string-domain-wall network around T_{osc} are taken into account. Note that the above treatment of topological defects was given for the case $N_{\mathrm{DW}} = 1$ considered in this work. In a more general context with $N_{\mathrm{DW}} > 1$, the N_{DW} minima of $V(\theta, T)$ become degenerate, rendering domain walls stable. In contradiction to cosmological observations, stable

domain walls tend to quickly dominate the energy budget of the universe. This property of axion models with $N_{\rm DW} > 1$ is called the *domain wall problem*, see also Ref.s [42, 104] for discussions and possible solutions.

2.6 Axion Structure Formation

Before moving on to its phenomenological aspects, we briefly summarize the cosmological evolution of the axion field and how it gives rise to observable axion small-scale structure in the present-day universe. At some high temperature $T \sim f_a < T_I$, the spontaneous symmetry breaking of the QCD axion- or ALP field occurs, where for the masses $10^{-12} \, \text{eV} \le m_a \le 10^{-2} \, \text{eV}$ and for the axion models considered in this work, the decay constant lies in the range $10^{10} \, \text{GeV} \le f_a \le 10^{13} \, \text{GeV}$ (c.f. Fig. 3.7). After the PQ symmetry breaking and a period of inflation, the initial misalignment angle $\theta_I \in [-\pi, \pi]$ takes random values over a Hubble patch. The randomness of the axion field $\theta(x)$ sources topological defects, which decay around $T \sim T_{\text{osc}}$ with model-dependent oscillation temperatures in the range $1 \, \text{MeV} \le T_{\text{osc}} \le 10^2 \, \text{GeV}$. Around the same time, the energy stored in the axion oscillations with misalignment angle $\theta = \theta_I$ will give rise to the production of dark matter while the axion field oscillates around its zero-temperature value $\theta = 0$.

The inhomogeneous initial conditions of the axion field and the subsequent decay of the string-domain-wall network for $N_{\rm DW}=1$ turn out to source large isocurvature fluctuations in the axion energy density. As soon as the axion acquires a mass around $T_{\rm osc}$, these density fluctuations become matter density perturbations seeding the formation of dark matter structure. The resulting perturbations are large in amplitude with $\Phi = \rho_a/\bar{\rho}_a - 1 \sim \mathcal{O}(1)$ but small in size. They collapse gravitationally around matter-radiation equality and are generally referred to as axion miniclusters to distinguish them from the large-scale dark matter halos formed at late times. Their rich phenomenology and substructure is laid out in more detail in Chap. 3 and Chap. 4.

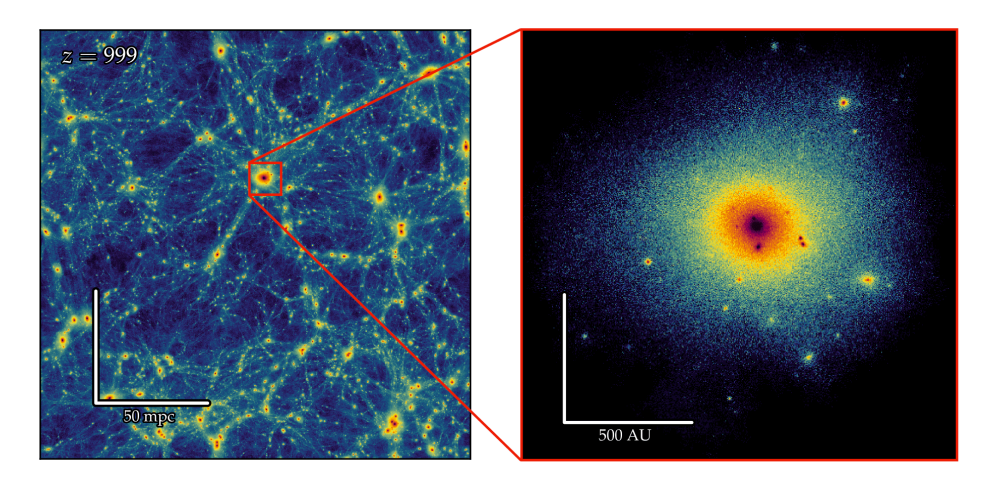


Figure 2.3: Snapshots of the merging of miniclusters at redshift z = 999 after the collapse of minicluster seeds around $z \gtrsim z_{\rm eq} \simeq 3402$, taken from Ref. [42] and based on the simulations in Ref. [105]. The zoomed in panel shows a significantly heavier and larger minicluster containing a rich substructure of light and intermediate mass miniclusters. Such heavy miniclusters are expected to evolve into the sites of galaxy formation at late times, motivating our study of the NFW dark matter halo in Chap. 3.

For the purpose of this section, we briefly demonstrate how axion small-scale structure emerges from the initial density perturbations of the inhomogeneous axion field in Fig. 2.3.

Fig. 2.3 shows a visualization of the cosmic structures formed by merging miniclusters in the N-body simulations performed in Ref. [105] and taken from Ref. [42]. The node and filament structure of the matter overdensities in Fig. 2.3 was sourced by the initial axion field $\theta_I(x)$ and by the subsequent formation and decay of the axion string-domain-wall network depicted in Fig. 2.2. After the gravitational collapse of the axion matter perturbations into miniclusters around matter-radiation equality redshft $z \gtrsim z_{\rm eq} \simeq 3402$, the miniclusters evolve to form heavier structures through successive merger events and tidal disruption.

An example for a high-mass minicluster formed by such mergers is shown in the zoomed in panel on the right of Fig. 2.3, where a central dense core and several lower-mass miniclusters can be seen to be embedded in the larger structure. The evolution of the minicluster distribution will be treated in detail in Chap. 3. For now we emphasize that the successive mergers of these objects lead to the formation of increasingly massive and large structures, which eventually seed the sites of galaxy formation in the late universe.

2.7 Experimental Searches

Before moving on to the details of axion small-scale structure and its detection prospects, we will summarize the fundamental aspects of the most relevant astrophysical and laboratory axion searches in this section. Based on the different interactions of the axion field with standard model particles introduced in Sec. 2.3, we distinguish experiments exploiting the axion-photon coupling $g_{a\gamma\gamma}$ from Eq. (2.17) in Subsec. 2.7.1 from those using the axion-fermion coupling g_{aff} in Eq. (2.18) and Subsec. 2.7.2.

We focus on the case of the axion-photon interaction in Subsec. 2.7.1 since most of the observation methods of galactic axion DM structures in this work are based on it. For the analysis of galactic axion burst signals in Chap. 7 and Ref. [3], we also briefly mention the concept of spin-precession experiments as an example for DM searches exploiting axion-fermion couplings in Subsec. 2.7.2.

2.7.1 Axion-Photon Coupling

The phenomenologically most relevant interaction relies on the coupling $g_{a\gamma\gamma}$ between axions and photons as described in the Lagrangian from Eq. (2.17). This interaction gives rise to the decay of an axion into two photons, $a \to \gamma + \gamma$. Due to the large lifetime of axion DM particles, the corresponding interaction rate for this process is generally very small. On the other hand, and in the presence of a strong magnetic field, axions may be converted into photons (and vice versa). This process is known as the axion Primakoff effect [106].

The Primakoff effect serves as the starting point for three major types of axion experiments, which were proposed in the seminal paper in Ref. [107] by Pierre Sikivie. The three classifications are called *Light-Shining-through-a-Wall* (LSW), *helioscope* and *haloscope* experiments. In a fourth scenario, the magnetic field needed for the conversion of axions may also be provided by an active neutron star, which encounters an axion overdensity or a minicluster. For the considerations in this work, we focus on the above four types of DM detection schemes, but we emphasize the large range of existing and upcoming axion-photon searches, see e.g Ref.s [41, 42, 44, 45, 48] for detailed reviews on the topic.

Light-shining-through-a-Wall Experiments

LSW type experiments rely on the partial conversion of photons into axions (and vice versa), which occurs when photons from a high-intensity laser beam travel along a transverse magnetic field. Axions are hereby produced from the traversing laser beam in the *production region* shown in the left of Fig. 2.4. The newly produced axions can then travel through an optically opaque barrier or 'wall' indicated by the black solid bar in the center of Fig. 2.4 to be subsequently converted back into photons in the *reconversion region* on the right. For coherent conversion

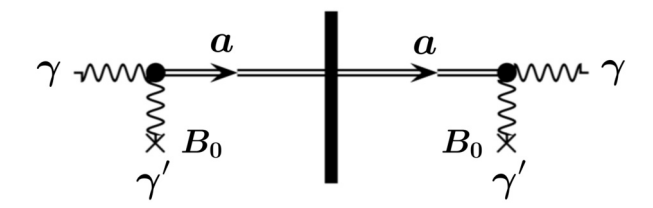


Figure 2.4: Schematic representation of an LSW type experiment with production (left) and reconversion regions (right) separated by an optical barrier indicated by the black bar, taken from Ref. [44].

 $m_a \ll \sqrt{2\pi\omega/L}$ in a transverse magnetic field of strength B_0 and length L, the conversion probabilities of the production and reconversion region are approximately given by

$$\mathcal{P}(\gamma \to a) \simeq \left(\frac{g_{a\gamma\gamma}BL}{2}\right)^2 \simeq \mathcal{P}(a \to \gamma),$$
 (2.65)

where ω is the photon energy and the observed power will be proportional to $\mathcal{P}(\gamma \to a \to \gamma) = \mathcal{P}(a \to \gamma)^2$ [44, 45]. The conversion probabilities in Eq. (2.65) can be significantly amplified by using resonators like optical cavities in the production and regeneration regions through a process called resonant regeneration [45, 108–110]. In the case of resonant regeneration, the total conversion probability gains an additional factor of $\mathcal{P}(\gamma \to a \to \gamma) \propto \beta_P \beta_R$, where $\beta_P, \beta_R \sim 10^4$ are the power built up factors of the production and reconversion regions respectively. The corresponding enhancement $\beta_P \beta_R \propto Q^2$ scales with the quality factor Q measuring the number of round trips a typical photon can take before exiting the cavity.

Important LSW experiments include the ongoing ALPS-II experiment [111], its predecessor the ALPS-I experiment [112] and OSQAR [113]. LSW experiments are broadband in nature, but have the disadvantage of being limited in sensitivity due to the scaling $\mathcal{P}(\gamma \to a \to \gamma) \propto g_{a\gamma\gamma}^4$ of the double conversion process.

Helioscopes

Helioscope DM searches can be understood from the right part of the LSW scheme in Fig. 2.4: The fundamental idea in this class of experiments is to convert solar axions, which are produced from interactions between thermal photons and the Coulomb fields of nuclei in the solar plasma. Due to the temperature $T \sim 1 \,\text{keV}$ of the solar core [114], the observed solar axion flux lies in the keV-energy range, with a peak around an energy of $E_a \simeq 3 \,\text{keV}$ for the simplest case² involving

²More specifically this is the case for the KSVZ-type axion models considered in this work. For DFSZ models on the other hand, the axion-electron coupling is usually dominant, leading to a peak around $E \sim 1 \, \text{keV}$, see Ref.s [115, 116] for details.

only Primakoff conversion in the solar plasma [117]. In a static magnetic field, the energy of the reconverted photon is equal to the energy of the incoming axion, $E_{\gamma} = E_a \sim \text{keV}$, so that X-ray detectors are used to detect the converted solar axion flux.

Opposed to LSW and haloscope searches, helioscopes have to follow the suns trajectory across the horizon throughout an observation. The experimental setup is therefore embedded on a movable platform, which carries a long cylindrical dipole magnet with a homogeneous field of strength B and length L. Similarly to Eq. (2.65), the conversion probability of a reference helioscope may be written as [45, 107]

$$\mathcal{P}(a \to \gamma) = 2.6 \cdot 10^{-17} \left(\frac{g_{a\gamma}}{10^{-10} \text{GeV}^{-1}} \right)^2 \left(\frac{B_e}{10 \text{ T}} \right)^2 \left(\frac{L}{10 \text{ m}} \right)^2 \mathcal{F}$$
 (2.66)

where the form factor \mathcal{F} measures the coherence of the conversion. In vacuum, and for coherent conversion $m_a \ll \sqrt{2\pi\omega/L}$ along the entire magnetic field of length L the form factor is $\mathcal{F} = 1$. Some of the most important helioscope experiments are CAST [118], the upcoming babyIAXO [119] and its final stage, IAXO [120].

Haloscopes

Similar to helioscopes, haloscopes exploit the axion-photon conversion probability $\mathcal{P}(a \to \gamma)$ to obtain a photon signal from an incoming flux of axions. An important difference compared to helioscopes is the fact that haloscope experiments aim to convert axions from DM overdensities in the galactic NFW halo. This implies that haloscopes rely on the assumption that axions constitute the missing dark matter in the universe. They can be used to constrain the product $g_{a\gamma\gamma}\sqrt{\rho_a/\rho_{\rm dm}}$, where $0 < \rho_a/\rho_{\rm dm} \le 1$ is the fraction of the local axion dark matter density relative to the local DM density $\rho_{\rm dm} \simeq 0.45 \, {\rm GeV \, cm^{-3}}$ [121]. Accordingly, the sensitivity of haloscope experiments decreases if axions are a subdominant component, i.e. for $\rho_a/\rho_{\rm dm} < 1$. With the axion being one of the most well motivated dark matter candidates, we will assume $\rho_a/\rho_{\rm dm} \simeq 1$ in the following (see also Sec. 3.2).

Haloscopes play a particularly important role in the observation of the local axion small-scale structure, because they can directly probe fluctuations in the local axion DM density. Such fluctuations can be caused by the inhomogeneous local axion field (c.f. Sec. 2.5) axion miniclusters (c.f. Chap. 3), axion stars (c.f. Chap. 4) and relativistic axion bursts (c.f. Chap. 7).

In general, DM axions are non-relativistic, with a velocity dispersion on the order of $\sigma_v \sim 10^{-3}$ related to the virial velocity of the NFW halo of the Milky Way. The local axion spectrum with angular frequency

$$\omega_a = E_a = m_a + \frac{1}{2}m_a v^2 = m_a \left(1 + \mathcal{O}\left(10^{-6}\right)\right)$$
 (2.67)

is therefore expected to be close to monochromatic, which allows for the use of microwave cavities with a large quality factor Q to enhance the signal power through resonant conversion. Given the large range of possible axion masses under consideration, the resonance frequency of the cavity has to be tunable to the axion mass within a frequency width of $\Delta f \sim m_a/Q$. This resonance matching is responsible for the characteristic line-like structure of haloscope constraints on $g_{a\gamma\gamma}$.

The design of haloscope experiments capable of achieving resonance for larger $m_a > \mu eV$ is technically challenging because higher frequencies require smaller cavity volumes, which in return

yield a smaller signal power. Conversely, smaller axion masses $m_a < \mu \text{eV}$ require large cavity volumes for which suitable large magnets are difficult and expensive to design [45]. To deal with these challenges, a large range of different experiments are under development. Among the most important examples are traditional microwave cavity searches like ADMX [122] and FLASH [123], dish antenna experiments based on the concept from Ref. [124] like BRASS [125] or BREAD [126] and dielectric haloscopes [127] like MADMAX [128, 129]. For the purpose of

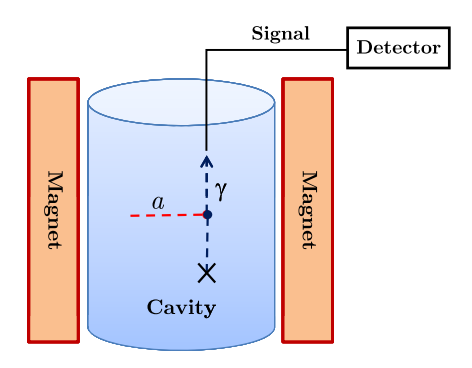


Figure 2.5: Schematic arrangement of an axion haloscope experiment, modified from Ref. [45]. The two parallel magnets in red source the homogeneous magnetic field B leading to a resonant conversion of axions with suitable mass $m_a \approx \omega$, where ω is the tuned frequency of the cavity in blue.

this thesis, we focus on the conventional haloscope design from Ref. [107] and refer to other experiments in Chap. 7 if needed.

The basic microwave cavity design depicted in blue in Fig. 2.5 consists of a homogeneous magnetic field with strength B surrounding the blue cavity with volume V and a tunable resonance frequency. When the cavity frequency matches m_a , the axion-photon conversion gets enhanced by a factor proportional to the quality factor Q of the cavity. The resulting signal power in the mass band $m_a \pm m_a/Q$ is given by [45, 107]

$$P_s \sim \rho_a \frac{g_{a\gamma\gamma}^2 B_0^2}{m_a} V \mathcal{C} Q \,, \tag{2.68}$$

where \mathcal{C} is the geometric factor of the resonant mode, assuming that the DM bandwidth is smaller than the width of the cavity resonance, $\sigma_v^2 \lesssim 1/Q$. For ADMX-like parameters with $\rho_a = 0.45\,\mathrm{GeV}\,\mathrm{cm}^{-3},\ g_{a\gamma\gamma} \sim 10^{-14}\,\mathrm{GeV}^{-1},\ B_0 \sim 7\,\mathrm{T},\ m_a \sim 50\,\mu\mathrm{eV},\ V \sim 140\,\mathrm{l},\ \mathcal{C} = 0.4$ and Q = 50000, the expected power is roughly on the order of $P_s \sim 10^{-21}\,\mathrm{W}$ [122]. For QCD axions, the signal power P_s is typically much smaller than the system noise

$$P_n = T_{\text{sys}} \, \Delta f = T_{\text{sys}} \frac{m_a \sigma_v^2}{2\pi} \sim 10^{-19} \left(\frac{T_{\text{sys}}}{\text{K}}\right) \left(\frac{m_a}{50 \,\mu\text{eV}}\right),\tag{2.69}$$

where the noise temperature T_{sys} accounts for amplifier and thermal fluctuations in the detector [45]. This means that haloscope experiments have to rely on large observation times t_{obs} to sufficiently increase the signal to noise ratio, given by Dicke's radiometer Equation

$$\frac{S}{N} = \frac{P_s}{T_{\text{sys}}} \sqrt{\frac{t_{\text{obs}}}{\Delta f}}.$$
 (2.70)

The large amount of measurements with a narrow width of $\Delta f = m_a/Q$ required to scan across a considerable parameter range in m_a and the observation times $t_{\rm obs} = (S/N)^2 (T_{\rm sys}/P_s)^2 \Delta f$ imply experimental run times on the order of months to years [45, 122].

It should be noted that the above microwave cavity experiments, by construction, require establishing a precise resonance between axion mass and the cavity resonance. Due to the narrow width of this resonance and because of the long measurement times required, both spectral and time-dependent modulations of the axion DM density are hard to obtain. However time varying, $\mathcal{O}(1)$ background fluctuations of the local axion field and its expected modulations arising from the occurrence of galactic axion bursts (see Chap. 7) motivate the additional development of broadband DM searches. The experimental details of these searches are beyond the scope of this work and can be found in Ref.s [124, 127] and [125, 126, 128]. We briefly summarize the fundamental concepts and differences compared to microwave cavity searches but refer to Ref.s [44, 45, 114] for reviews on the topic.

The concept of dish antennas as introduced in Ref. [124] relies on the fact that a time-dependent axion field $\phi(t)$ induces a homogeneous electric field

$$\mathbf{E}_{\mathbf{a}}(t) = -g_{a\gamma\gamma}\mathbf{B}_{0}\phi(t) \tag{2.71}$$

in the presence of a locally homogeneous magnetic field \mathbf{B}_0 . In this case, the axion field and its induced electric field $\mathbf{E}_a(t)$ parallel to \mathbf{B}_0 oscillate at a frequency $\omega_a \sim m_a$. For conducting or dielectric media, the effective field \mathbf{E}_a decreases due to polarization effects and free charge currents in the medium, compared to the vacuum case in Eq. (2.71). It can be shown from the axion-modified Maxwell equations, that the continuity of fields at the boundaries of different media is ensured through the emission of almost monochromatic photons with frequency $f = m_a/(2\pi)$. When the magnetic field is aligned parallel to the boundary of the medium, e.g. along a metallic mirror, the electromagnetic wave is emitted perpendicular to the mirror surface as shown in the left panel of Fig. 2.6. The BRASS experiment [125] uses this concept and a spherical metallic mirror to focus the emitted photons in the center of curvature of the dish. The resulting power emitted from a dish with surface A is [45]

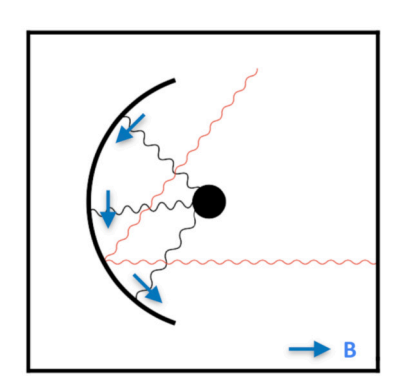
$$P_{\gamma} = \frac{A|\mathbf{E}_a|^2}{2} = \frac{Ag_{a\gamma\gamma}|\mathbf{B}_0|^2}{2} \tag{2.72}$$

$$\sim 10^{-27} \frac{W}{\mathrm{m}^2} \left(\frac{g_{a\gamma}}{10^{-14} \mathrm{GeV}^{-1}} \right)^2 \left(\frac{50 \,\mu\mathrm{eV}}{m_a} \right)^2 \left(\frac{|\mathbf{B}_0|}{10 \,\mathrm{T}} \right)^2 \left(\frac{A}{m^2} \right) , \qquad (2.73)$$

which implies that stronger magnetic fields and larger dishes can be used to increase the observed signal strength.

Dielectric haloscopes are designed to achieve both of the above effects by employing a series of parallel dielectric discs between a mirror and a receiver as depicted in the right panel of Fig. 2.6. In this configuration, each of the parallel, transparent dielectric disks takes the role of a single dish antenna, which emits photons perpendicular to its surface. The emitted electromagnetic waves will be reflected by and transmitted through the surrounding disks before eventually reaching the receiver. Additionally, the separation of the disks can be optimized to amplify the emitted power of photons in the dielectric haloscope.

Since the axion-induced electric field in Eq. (2.71) and the resulting photon-emission from the



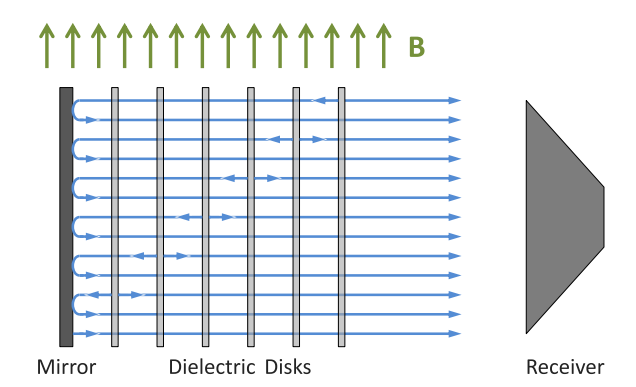


Figure 2.6: Left: Concept of a dish antenna with a spherical metallic mirror and parallel magnetic field B, similar to the one used by the BRASS collaboration [125], taken from Ref. [44]. Right: Mirror and disk arrangement of a dielectric haloscope with parallel B-field [130], similar to the setup of MADMAX [129].

boundary surface occur for a whole range of axion masses and photon frequencies $f = m_a/(2\pi)$, the broadband detection range is mostly limited by the receiver. The dielectric haloscope experiment of the MADMAX collaboration [128] aims to probe the range $40 \,\mu\text{eV} \lesssim m_a \lesssim 400 \,\mu\text{eV}$ with DSFZ sensitivity [131, 132]. Likewise the dish antenna experiment of the BRASS collaboration aims to explore QCD axion models in the range $50 \,\mu\text{eV} \lesssim m_a \lesssim \text{meV}$ [125] while the BREAD collaboration focuses on the range $20 \,\text{meV} \lesssim m_a \lesssim 0.1 \,\text{meV}$ [44, 126, 133]. Importantly for the considerations in Chap. 7, all three of these experiments can operate in broadband-mode.

Neutron Star Collisions

A common property of most axion-photon search experiments is the use of a strong magnetic field to enhance the conversion probabilities arising from the Primakoff effect. In an astrophysical context, a sufficiently strong magnetic field may similarly be provided by an active neutron star encountering an axion DM overdensity, e.g. in a galactic transient event. As we will see in Chap. 5, such events can potentially occur numerously between galactic miniclusters and neutron stars and they have been conjectured to provide measurable radio bursts within observation times on the order of a year [134–137].

Fig. 2.7 shows a graphical representation of an axion particle entering the vicinity $r \lesssim \pm 120 \,\mathrm{km}$ of an active neutron star in gray, where the spatially dependent plasma frequency $\omega_p(\mathbf{r})$ of the neutron star magnetosphere in eV is indicated by the color gradient. The representative trajectory of an incoming axion in purple ends at the conversion surface R_c , defined by equality of axion mass and plasma frequency, $\omega_p(\mathbf{r}) \approx m_a \approx \mu \mathrm{eV}$. At this distance, the conversion probability is greatly enhanced, leading to the effective production of radio photons with frequency $f = m_a/(4\pi)$ as indicated by the purple outgoing wave.

The plasma frequency ω_p is related to the modified dispersion relation of photons traveling through a plasma, which generates an effective photon mass. It is given in terms of the spatially dependent number density of electrons $n_e(\mathbf{r})$ by [138]

$$\omega_p(\mathbf{r}) = \sqrt{\frac{4\pi\alpha_{EM}n_e(\mathbf{r})}{m_e}},\tag{2.74}$$

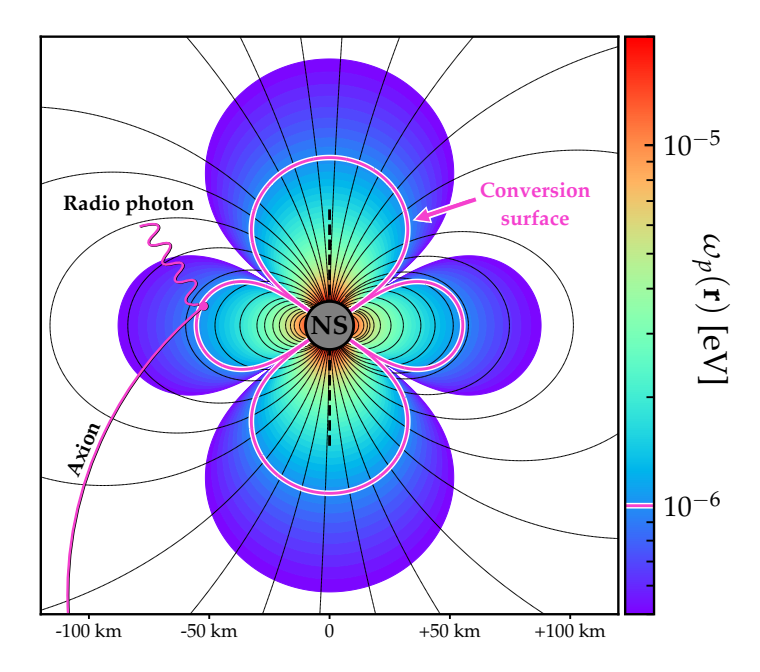


Figure 2.7: Visualization of the neutron star magnetosphere in the Goldreich-Julian model taken from Ref. [42]. The color-coding indicates the spatially dependent plasma frequency $\omega_p(\mathbf{r})$ of the NS magnetosphere and the pink contour line indicates the conversion surface where $\omega_p(\mathbf{r}) \approx m_a \approx \mu \text{eV}$. A representative trajectory of an axion particle reaching the conversion surface R_c and being converted into a radio photon is depicted in purple.

where $\alpha_{EM} \approx 1/137$ is the fine structure constant and the electron mass is $m_e = 511 \,\mathrm{keV}$ [53]. The most simple approach to model the electron density $n_e(\mathbf{r})$ in a rotating neutron star with an aligned, co-rotating magnetosphere is given by the Goldreich-Julian model [139]. In this model, the strong rotating magnetic field induces electric surface fields that lead to the extraction of charges from the neutron star surface. The extracted charges form a current along the magnetic field lines and constitute the plasma in the stars magnetosphere. Associated with the electric fields induced on the neutron star surface, is the so-called Goldreich-Julian charge density

$$n_{\rm GJ}(\mathbf{r}) = \frac{2\mathbf{\Omega}_{NS} \cdot \mathbf{B}}{e} \frac{1}{1 - \Omega_{NS}^2 r^2 \sin^2 \theta},$$
(2.75)

where $\Omega_{NS} = (2\pi/P_{NS})\hat{\mathbf{z}}$ is the angular rotation vector of the neutron star magnetic field with period P_{NS} and velocity $v = \Omega r \sin \theta$ at a polar angle θ relative to the z-axis. Importantly, for $\mathbf{B} \parallel \Omega_{NS}$ and at the magnetic poles $\theta = 0, \pi$, Eq.(2.75) simplifies to $n_{\text{GJ}} = 2\Omega_{NS}B/e$.

The co-rotating magnetic field **B** is generally modeled as a (misaligned) dipole with field strength B_0 at the NS surface and $B \sim B_0 (r/r_{NS})^3$ beyond. For typical neutron stars, the rotation period is on the order of $P_{NS} \sim O(s)$ and the magnetic field strength at the surface lies in the range $B_0 \sim 10^{13} - 10^{14}$ Gauss. A common assumption that we apply in this work is to set the electron density $n_e = |n_{GJ}|$ to be equal to the absolute of the Goldreich-Julian charge density given by Eq. (2.75) [140, 141]. From this approach, one can derive the conversion surface R_c of the neutron star, where $\omega_p(\mathbf{r}) \approx m_a$ and axion-photon conversion is resonantly enhanced by the magnetosphere. The detailed formula for a magnetic field configuration, which is misaligned with respect to the rotation axis was derived in Ref. [140], who found $R_c \sim 100 \,\mathrm{km}$ for $m_a \simeq \mu \mathrm{eV}$

and typical neutron stars with $r_{NS} = 1$, $B_0 = 10^{14}$ Gauss, P = 1 s.

Most importantly for this work, effective axion-photon conversion in a NS transient event requires sufficiently large plasma frequencies ω_p and thus large enough B_0 to fulfil the resonance condition $\omega_p \approx m_a$ for a given axion mass m_a . As will be shown in Chap. 5, this condition drastically limits the fraction of neutron star encounters producing radio signals in our galaxy.

2.7.2 Axion-Nucleon Coupling

Different to haloscope-type experiments who exploit the axion-photon coupling in Eq. (2.17), spin precession experiments utilize the axion-fermion couplings from Eq. (2.18) and Eq. (2.19) to obtain an axion DM signal using nuclear magnetic resonance (NMR) techniques. In preparation of the analysis in Chap. 7, we summarize the basic concept of the cosmic axion-spin precession experiment (CASPEr) [142] in this section. More specifically we will constrain our analysis to the CASPEr Wind search [142] looking for couplings of the form in Eq. (2.18). The full potential of CASPEr and other axion-spin experiments can be read up in Ref.s [142, 143]. It can be shown that the relevant Lagrangian \mathcal{L}_{aff} for nucleons $f = N \equiv n, p$ in Eq. (2.18) results in a non-relativistic Hamiltonian [143]

$$H_{aN} = g_{aN} \nabla \phi(\mathbf{r}, t) \cdot \boldsymbol{\sigma}_N, \qquad (2.76)$$

which is similar to the potential energy $H_e \supset -\mu_B \mathbf{B} \cdot \boldsymbol{\sigma}^3$ of an electron with spin operator $\boldsymbol{\sigma}$ in a magnetic field \mathbf{B} , where $\mu_B = e/(2m_e)$ is the Bohr magneton. Eq. (2.76) thus describes the interaction of nuclear spins with an oscillating 'pseudo-magnetic field' generated by the gradient $\nabla \phi(\mathbf{r},t)$ of the axion field. The magnitude of this gradient can be estimated from the momentum operator $\mathbf{p} = -i\nabla$, which gives

$$|\nabla \phi| \approx m_a v \phi_0 \quad , \tag{2.77}$$

where ϕ_0 is the amplitude of the oscillating axion field with $\phi(t) \approx \phi_0 \cos(\omega_a t)$ at leading order and $v \simeq 10^{-3}$ is the relative velocity of the incoming axion flux. Since the corresponding values of ϕ_0 and v are locally dependent on the galactic position of earth-based experiments, spin precession searches like CASPEr Wind rely on the assumption that axions constitute the galactic DM. The resulting flux of dark matter particles arriving at earth as described by Eq. (2.77) is often called the axion wind. It acts as a pseudo-magnetic field directed along \mathbf{v} [143] and induces an energy-shift H_{aN} to the nuclear spins in an NMR experiment. Expressing ϕ_0 by assuming an axion-dominated DM energy density $\rho_{\rm dm} \simeq m_a^2 \phi_0^2/2 \simeq 0.4 \,{\rm GeV}\,{\rm cm}^{-3}$, the corresponding time-dependent value of H_{aN} can be estimated to be on the order of [143]

$$H_{aN} \simeq g_{aN} \sqrt{2\rho_{\rm dm}} \cos(\omega_a t) \mathbf{v} \cdot \boldsymbol{\sigma}_N.$$
 (2.78)

The induced energy shift in Eq. (2.78) is small, but it can be measured using NMR techniques as depicted in Fig. 2.8. In this approach, the sample of nuclear spins is embedded in an homogeneous background magnetic field \mathbf{B}_0 in red that determines the Larmor frequency $\Omega_L = \gamma_n |\mathbf{B}_0|$ with which the spins precess around the direction of \mathbf{B}_0 . As long as the leading field \mathbf{B}_0 is misaligned with the axion-induced pseudo-magnetic field $\mathbf{B}_a \propto g_{aNN} \sqrt{2\rho_{\rm DM}} \mathbf{v}$ in green, the spins can be tipped away from their initial orientation. This tipping occurs when $\omega_a \approx \Omega_L$ and the

³Where the g-factor of the electron was approximated to $g \approx 2$.

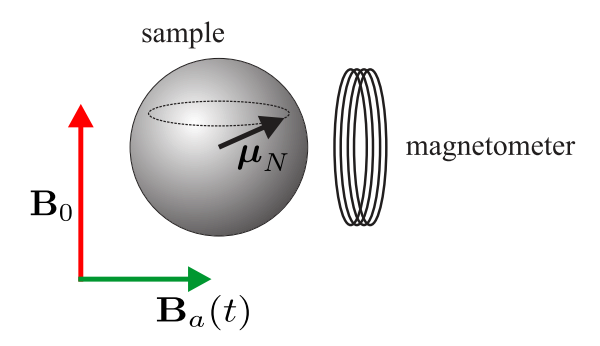


Figure 2.8: Schematic representation of the CASPEr Wind arrangement, taken from Ref. [142]: The leading field \mathbf{B}_0 in red determines the Larmor frequency $\Omega_L = \gamma |\mathbf{B}_0|$ of the spin sample. When the axion wind induces a pseudo-magnetic field \mathbf{B}_a in green, which has a resonant oscillation frequency $\omega_a \approx \Omega_L$, the spins will be tipped away from \mathbf{B}_0 . The amplitude of the magnetic field arising from the precessing magnetic dipoles $\boldsymbol{\mu}_N$ in the spin ensemble can then be detected using a magnetometer.

oscillations of the axion field match the Larmor frequency of the background magnetic field. In the laboratory frame, the nuclear spins with magnetic dipole moments μ_N can then be seen to precess around \mathbf{B}_0 , as indicated by the gray sphere and black arrow in Fig. 2.8.

For experimental detection, a magnetometer can be used to measure the transverse magnetization arising from the ensemble of polarized spins with magnetic dipoles μ_N in the sample. Due to the dependence of the Larmor frequency Ω_L on $|\mathbf{B}_0|$, the axion mass to be probed can be set by tuning the strength of the leading field $|\mathbf{B}_0|$ [44, 45].

Axion Miniclusters

As was already pointed out in Sec. 2.5 and Sec. 2.6, the post-inflationary symmetry breaking of the axion field is characterized by the emergence of large inhomogeneities. The density perturbations seeded by these inhomogeneities generate significant deviations from standard CDM on small scales due to the formation of dense axion miniclusters [23–25, 28–30, 144–148]. On galactic scales, miniclusters are expected to constitute the NFW dark matter halos of galaxies, which implies that a significant number of these objects could be contained in our galactic environment.

This scenario has important phenomenological consequences for possible observations of axion DM: First, miniclusters (or minicluster remnants, sometimes called *tidal streams*) in the solar neighbourhood can induce fluctuations of the local dark matter density $\rho_{\rm dm}$ probed in earth-based detectors [42, 149, 150]. Secondly, galactic miniclusters and their solitonic cores can collide with other astrophysical objects like neutron stars producing bursts of radio photons [134, 136, 140, 151–157]. And most importantly for this work, we can employ various existing knowledge on galactic miniclusters to constrain the properties of their accreting axion star cores to develop new detection strategies for axion dark matter in Chap. 4 to Chap. 7.

In this chapter, we summarize the current status of analytical and numerical research on the formation, evolution and present-day properties of axion miniclusters. We start by introducing the equations of motion governing the non-relativistic evolution of axion DM with and without self-interactions in Sec. 3.1. Sec. 3.2 incorporates the spherical collapse model describing the formation of miniclusters around matter-radiation equality. After their formation, miniclusters evolve during the matter dominated epoch, where the analytical description of their mass distribution is summarized in Sec. 3.3 and Sec. 3.4. In Sec. 3.5, we consider the full range of minicluster masses predicted from numerical simulations in Subsec. 3.5.1 and analytical calculations in Subsec. 3.5.2. From this, we infer the estimated properties of the galactic minicluster distribution in the NFW dark matter halo of the Milky Way at present-day redshift in Sec. 3.6. Lastly in Sec. 3.7, we introduce the canonical core-halo mass relation linking the properties of miniclusters to those of their axion star cores in Chap. 4. The combined content presented in this chapter and in Chap. 2 constitutes the green shaded panels in the schematic summary of Fig. A.1.

3.1 Gross-Pitaevskii Poisson System

As laid out in Chap. 2, the early universe evolution of the axion field from the symmetry breaking around $T \sim f_a$ until the onset of axion oscillations at $T \sim T_{\rm osc}$ is dominated by non-linear axion self interactions and the formation of topological defects. Later, at $T < T_{\rm osc}$ after the axion mass becomes relevant and topological defects have decayed, the remaining fluctuations in the matter density will collapse gravitationally and decouple from the Hubble flow. At these

temperatures, the axion field behaves like cold dark matter, which allows for a non-relativistic treatment, which we introduce in the following.

We follow the derivation of the non-relativistic EOM for the QCD axion similar to the calculations in Ref.s [33, 158–161] and modify the approach to include axion-like particles by also considering arbitrary combinations of m_a and f_a , next to the QCD axion relation Eq. (2.11). More precisely, this thesis closely follows the approach in Ref. [1], which lays the foundation for the subsequent publications, Ref. [2] and Ref. [3], all of which are part of this thesis.

The total Lagrangian density of the self-gravitating axion field in Eq. (2.38) can be written as

$$\mathcal{L} = \sqrt{-g} \left[-\frac{g_{\mu\nu}}{2} \partial^{\mu} \phi \partial^{\nu} \phi - V(\phi) + \frac{R}{16\pi G} \right], \qquad (3.1)$$

where the Ricci scalar R accounts for the evolution of the metric $g_{\mu\nu}$ and $G = 1/\left(8\pi M_{\rm Pl}^2\right)$ is the gravitational constant. From the Lagrangian in Eq. (3.1) one obtains the relativistic equations of motion

$$R^{\mu\nu} - \frac{1}{2}g^{\mu\nu} = 8\pi G T_a^{\mu\nu} \,, \tag{3.2}$$

$$\frac{1}{\sqrt{g}}\partial_{\mu}\left[\sqrt{-g}g^{\mu\nu}\partial_{\nu}\right]\phi + V'(\phi) = 0, \qquad (3.3)$$

which are often called the *Einstein-Klein-Gordon* equations (EKG) [162]. Eq. (3.3) describes the evolution of the axion field, while the Einstein Eq. (3.2) determines the geometry of spacetime as a function of the stress energy tensor $T^{\mu\nu}$ of the axion field from Eq. (2.41). A crucial step in the derivation of the non-relativistic EOM is to make appropriate assumptions for the axion potential $V(\phi)$ from Eq. (2.12), the metric tensor $g^{\mu\nu}$ and the axion field ϕ . Starting with $V(\phi)$, we can expand the axion potential around the CP-conserving minimum $\phi = 0$, keeping only the two leading-order terms

$$V(\phi) = m_a^2 f_a^2 \left[1 - \cos\left(\frac{\phi}{f_a}\right) \right] = \frac{m_a^2}{2} \phi^2 + \frac{\lambda}{4!} \phi^4 + \mathcal{O}\left(\lambda^2 \phi^6 / m_a^2\right), \tag{3.4}$$

where we have introduced the quartic coupling constant

$$\lambda = -c_{\lambda} \frac{m_a^2}{f_a^2} \tag{3.5}$$

of the attractive self-interaction with $\lambda < 0$. For the case of the QCD axion, the constant c_{λ} depends on the up- and down quark masses m_u , m_d with $c_{\lambda} = 1 - 3m_u m_d/(m_u^2 + m_d^2) \approx 0.3$ according to more accurate calculations using chiral perturbation theory and lattice QCD [33, 43]. More generally and for the case of axion-like particles, c_{λ} is an $\mathcal{O} \sim 1$ parameter, which is why we assume $c_{\lambda} = 1$ for different axion models in the following [41, 158] This also coincides with the standard dilute instanton gas approximation for the QCD axion.

As will be shown in Chap. 4, the second-order term in Eq. (3.4) is crucial for the stability of axion matter fluctuations, because it describes the self-interactions of the axion field. The other relevant force is the gravitational interaction of axions, where in the context of miniclusters, a Newtonian treatment is sufficient. This can be seen by estimating the magnitude of the Newtonian potential $\Phi_N \sim G\mathcal{M}_0/\mathcal{R} \ll 1$ using the characteristic minicluster mass $\mathcal{M}_0 \sim$

 $10^{-12} M_{\odot}$ and radius $\mathcal{R} \sim 10^7 \,\mathrm{km}$ (see Sec. 3.2). In the Newtonian limit and for vanishing anisotropic stress, the metric can be written as [163]

$$ds^{2} = -(1 + 2\Phi_{N})dt^{2} + (1 - 2\Phi_{N})\delta_{ij}dx^{i}dx^{j}, \qquad (3.6)$$

with $\sqrt{-g} \approx 1 - 2\Phi_N$ and $R \approx 2(\nabla \Phi_N)^2$. Expressing $g^{\mu\nu}$ using Eq. (3.6), the Lagrangian of the axion field from Eq. (3.1) reduces to

$$\mathcal{L} = \frac{(\nabla \Phi_N)^2}{8\pi G} + \frac{1 - 4\Phi_N}{2}\dot{\phi}^2 - \frac{(\nabla \phi)^2}{2} - (1 - 2\Phi_N)V(\phi), \qquad (3.7)$$

where $V(\phi)$ obeys the Taylor expansion from Eq. (3.4). The third assumption to be made in this section relates to the axion field ϕ in Eq. (3.7). At temperatures below $T_{\rm osc}$, the axion field behaves like cold dark matter, where we assume that its relic density is $\Omega_a h^2 \simeq \Omega_c h^2 = 0.12$ [14]. From this, we can infer the occupation number of CDM axions by estimating its de-Broglie wavelength as

$$\lambda_{\rm dB} = \frac{2\pi}{m_a v} = 29.8 \,\mathrm{m} \left(\frac{50 \,\mu\text{eV}}{m_a}\right) \left(\frac{250 \,\mathrm{km/s}}{v}\right) \,,$$
 (3.8)

which together with the local axion DM density $\rho_a = \rho_{\rm dm}$ yields

$$\mathcal{N}_a \sim \frac{\rho_{\rm dm}}{m_a} \lambda_{\rm dB}^3 \sim 10^{23} \left(\frac{50 \,\mu \rm eV}{m_a}\right)^4 \left(\frac{250 \,\rm km/s}{v}\right)^3$$
 (3.9)

for the number of particles in a de Broglie volume $V \sim \lambda_{\rm dB}^3$. Considering only sub-eV axion masses, the occupation number \mathcal{N}_a turns out to be so large that the system is best described by classical waves, similar to how the large occupation number of photons in electromagnetism motivates a classical treatment of the electric and magnetic fields. Furthermore the axion field is also highly non-relativistic with a typical minicluster escape velocity on the order of $v_{\rm esc} \sim \sqrt{G\mathcal{M}_0/\mathcal{R}} \sim 10^{-9} \ll 1$. Thus expressing the classical real (pseudo-)scalar field ϕ in terms of a slowly varying complex scalar field $\psi(\mathbf{x},t)$ one can write [161, 164, 165]

$$\phi(\boldsymbol{x},t) = \frac{1}{\sqrt{2m_a}} \left[\psi(\boldsymbol{x},t)e^{-im_a t} + \psi^*(\boldsymbol{x},t)e^{im_a t} \right]. \tag{3.10}$$

with $|\dot{\psi}| \ll m\psi$ and $|\ddot{\psi}| \ll m^2\psi$ so that m_a is the dominant energy scale in the problem. Inserting Eq. (3.10) into the Lagrangian Eq. (3.7), the rapidly oscillating terms proportional to $e^{\pm im_a t}$ may be neglected since they average to zero over time. This way, the non-relativistic evolution of the complex field ψ can be shown to follow the *Gross-Pitaevskii-Poisson* system (GPP):

$$i\frac{\partial\psi}{\partial t} = -\frac{1}{2m_a}\Delta\psi + m_a\Phi_N\psi - \frac{|\lambda|}{8m_a^2}|\psi|^2\psi, \qquad (3.11)$$

$$\Delta\Phi_N = 4\pi G m_a |\psi|^2 \,, \tag{3.12}$$

where the Newtonian potential Φ_N in Eq. (3.12) is sourced by the matter density $\rho_a = m_a |\psi|^2$ of the non-relativistic axion field [158]. The same matter density can be used to determine the total number and mass of the system according to

$$N = \int d^3x |\psi|^2 \quad , \quad M = m_a \int d^3x |\psi|^2 \,, \tag{3.13}$$

both of which are conserved quantities. Other important conservation laws relate to the total energy E and angular momentum L of the system [166]. The conservation of energy and the stationary solutions to the GPP system are examined in detail in Sec. 4.1.

Note that the GPP system Eq. (3.11) and Eq. (3.12) is given for attractive self-interactions $\lambda < 0$ explicitly. In a more general context, repulsive self-interactions have $\lambda > 0$, while in the specific case of $\lambda = 0$ the system reduces to the *Schrödinger-Poisson* system

$$i\frac{\partial\psi}{\partial t} = -\frac{1}{2m_a}\Delta\psi + m_a\Phi_N\psi\,, (3.14)$$

$$\Delta\Phi_N = 4\pi G m_a |\psi|^2 \,, \tag{3.15}$$

which is commonly used in numerical simulations and for axion miniclusters with smaller densities $|\psi|$ and negligibly weak self-interactions (see also App. B and e.g. Ref.s [30, 167–172]). We emphasize that both the GPP and the SP equations are classical by nature due to the large occupation numbers of the axion field., as explained in Ref. [173].

Lastly, the solutions to the GPP equations, Eq. (3.11), Eq. (3.12) - and those of the SP system for $\lambda = 0$ - obey a scaling symmetry of the form

$$\{\mathbf{r}, t, \psi, E, \Phi_N, \lambda\} \to \{\mu^{-1}\mathbf{r}, \mu^{-2}t \,\mu^2\psi, \mu^2 E, \mu^2 \Phi_N, \mu^{-2}\lambda\},$$
 (3.16)

with an arbitrary, non-zero shift parameter μ [174]. Essentially, the symmetry in Eq. (3.16) can be used to transform a given solution of the GPP system onto another solution with a different density profile $\rho = m_a |\psi|^2$ but the same $\lambda^2 \rho$ [174]. We focus on the derivation of the stationary solutions in Sec. 4.1 and continue with the formation of miniclusters in the next section.

3.2 Spherical Collapse Model

The gravitational collapse of miniclusters is seeded by density fluctuations in the axion field, which emerge at temperatures around $T \sim T_{\rm osc}$. Until matter-radiation equality, the horizon-sized patches with initial overdensities $\Phi = \rho_a/\bar{\rho}_a - 1$ will collapse forming highly overdense objects, which are called axion miniclusters. Their characteristic size is given by the horizon size at $T = T_{\rm osc}$, which leads to radii on the order of $\mathcal{R} \sim 1/H(T_{\rm osc}) \sim 10^7\,\mathrm{km}$. The corresponding typical mass is set by the mass enclosed within a sphere with radius $\mathcal{R} \sim 1/H(T_{\rm osc})$, which implies $\mathcal{M} \sim 10^{-12}\,M_{\odot}$ for $m_a = 50\,\mu\mathrm{eV}$ and the QCD axion. Typical miniclusters have $\Phi \sim 1$ and collapse redshifts $z_c \sim z_{\rm eq}$, where more generally $\Phi \in (0, 10^4]$ is expected from numerical calculations [28, 175].

Since Φ stays roughly constant during the radiation-dominated epoch, the spherical collapse model can be used to estimate the central minicluster density $\rho_{\rm mc}$ as a function of Φ . The equation of motion for a spherical region in a flat universe with radiation density $\rho_{\rm rad}$ and matter density ρ_m is [24]

$$\ddot{r} = -\frac{8\pi G \rho_{\rm rad}}{3} r - \frac{G\mathcal{M}}{r^2} \,, \tag{3.17}$$

where r denotes the radius of the region and \mathcal{M} is its enclosed mass. Eq. (3.17) can be rephrased by changing to conformal time $d\eta = dt/a(t)$ and expressing the radius $r = a(\eta)R_{\xi}(\eta)\xi$ in terms of a comoving shell with label ξ , where $R_{\xi}(\eta)$ measures the deviation of the shell motion from the Hubble flow. Using the Friedmann equations for a flat universe and the densities $\rho_{\rm rad} = \rho_{\rm eq}(a_{\rm eq}/a)^4$, $\rho_{\rm m} = \rho_{\rm eq}(a_{\rm eq}/a)^3$ set by the value $\rho_{\rm eq}$ at matter-radiation equality, one obtains the equation of motion [24]

$$aR_{\xi}'' + a'R_{\xi}' + \left(\frac{G\mathcal{M}}{\xi^3 R_{\xi}^2} - \frac{4\pi G}{3} a^3 \rho_m R_{\xi}\right) = 0.$$
 (3.18)

The total mass enclosed within a comoving shell ξ can be parametrized as

$$\mathcal{M} = \frac{4\pi}{3} \rho_{\rm eq} a_{\rm eq}^3 \left[1 + \Phi(\xi) \right] \xi^3 \,, \tag{3.19}$$

which together with the definition $x = a/a_{eq}$ yields

$$x(1+x)\frac{d^2R_{\xi}}{dx^2} + \left(1 + \frac{3}{2}x\right)\frac{dR_{\xi}}{dx} + \frac{1}{2}\left(\frac{1+\Phi}{R_{\xi}^2} - R_{\xi}\right) = 0.$$
 (3.20)

Eq. (3.20) was solved numerically in Ref. [24], but an analytic solution may be found by expanding R_{ξ} in a power series to second order in x. Using this assumption, Eq. (3.20) reduces to

$$R_{\xi} = 1 - \frac{\Phi x}{2} - \frac{\Phi^2 x^2}{8} \,. \tag{3.21}$$

For $\dot{r} = 0$ in Eq. (3.17), or equivalently at $R_{\xi} + x dR_{\xi}/dx$ in Eq. (3.20), the spherical fluctuation with size r switches from an expanding to a collapsing sphere. To second order in Eq. (3.21), the scale factor and matter density corresponding to this turn-around are given by

$$x_{\rm ta} = \frac{C_x}{\Phi}, \quad \text{and} \quad \rho_{\rm ta} = C_\rho \rho_{\rm eq} \frac{\Phi^3}{3\xi^2} \frac{d}{d\xi} (1 + \Phi) \xi^3,$$
 (3.22)

where the parameters C_x and C_ρ are determined numerically. Using the numerical result $C_\rho \simeq 17$ from Ref. [24] and considering that the virial radius is half of the turn-around radius, the central density of the minicluster with initial overdensity Φ is roughly

$$\rho_{\rm mc} \simeq 140 \,\rho_{\rm eq} \,\Phi^3 \,(1+\Phi) \simeq 7 \cdot 10^6 \,\Phi^3 (1+\Phi) \left(\frac{\Omega_a h^2}{0.12}\right)^4 \frac{\rm GeV}{\rm cm^3} \,,$$
(3.23)

where the factor 2 from the virial radius yields a relative factor 8 between the virial density and $\rho_{\rm ta}$. The characteristic density in Eq. (3.23) is of crucial importance for the analysis in this work. It determines both the density and radius of the collapsed miniclusters as a function of $\Phi \in (0, 10^4]$.

Note that as discussed in Ref.s [29, 30, 176], the radial density profiles of typical miniclusters can be well-fit using the NFW profile from Eq. (A.1). Their expected concentration parameters $c = r_{\rm vir}/R_s$ with the virial and scale radius $r_{\rm vir}$, R_s range from $160 \lesssim c \lesssim 400$ depending on the minicluster mass \mathcal{M} and for $m_a = 50\,\mu\text{eV}$ [28–30]. Since the scaling of the minicluster concentration c with \mathcal{M} , Φ , m_a and z is not generally known, we rely on a homogeneous sphere model for the minicluster profile throughout this work. Deviations from the NFW profile of dense miniclusters exhibiting a steeper central slope at late times were recently discussed in

Ref. [175].

Assuming a spherically homogeneous profile with total mass $\mathcal{M} = 4\pi/3\rho_{\rm mc}\mathcal{R}^3$, the characteristic minicluster radius

$$\mathcal{R} \simeq \frac{3.4 \cdot 10^7}{\Phi (1 + \Phi)^{1/3}} \left(\frac{\mathcal{M}}{10^{-12} M_{\odot}}\right)^{1/3} \text{ km}$$
 (3.24)

is easily obtained as a function of the overdensity parameter Φ from Eq. (3.25). In order to determine the range of \mathcal{R} , both knowledge on the distribution of Φ and \mathcal{M} is required. Starting with \mathcal{M} , the distribution and time evolution of minicluster masses is a major source of uncertainty. A summary of semi-analytical methods following the work in Ref. [58] is presented in Sec. 3.3 to Sec. 3.6. As for now, the characteristic mass \mathcal{M}_0 of miniclusters can be estimated from the amount of axion dark matter contained within a spherical region of radius $R \sim 1/H(T_{\rm osc})$. Using a spherical geometry for the minicluster collapse and writing the comoving horizon size in terms of the comoving wavenumber $k_{\rm osc} = aH(T_{\rm osc})$, one obtains

$$\mathcal{M}_0 = \bar{\rho}_a \frac{4\pi}{3} \left(\frac{\pi}{k_{\text{osc}}}\right)^3 \,, \tag{3.25}$$

which is equivalent to other definitions of \mathcal{M}_0 , e.g. in Ref. [146], up to a geometrical factor of $4\pi^4/3 \simeq 130$ [58]. The range of minicluster masses is typically centered around $\mathcal{M} \sim \mathcal{M}_0$ and it will be determined in the following sections.

Continuing with the second open parameter in Eq. (3.24), the distribution of the initial minicluster overdensity Φ was calculated from Eq. (2.40) in the simulations of Ref. [146]. We follow

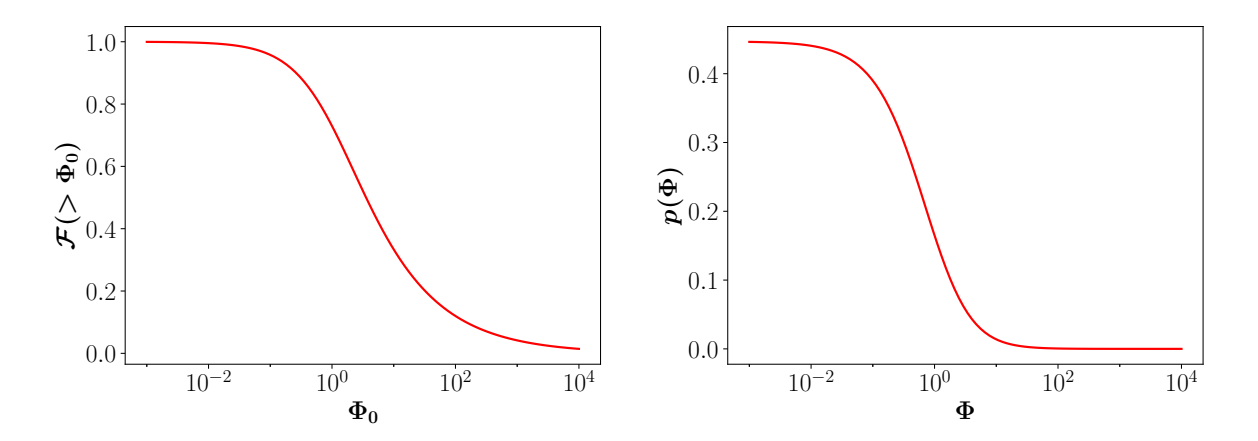


Figure 3.1: Left: Initial cumulative mass fraction $\mathcal{F}(>\Phi_0)$ of miniclusters with $\Phi>\Phi_0$. Right: Probability distribution $p_{\Phi}(\Phi)$ of objects with initial overdensity parameter Φ following Ref.s [2, 58, 146].

the approach of Ref. [58], who showed that the mass fraction of miniclusters with $\Phi > \Phi_0$ from Ref. [146] is well-fit by a Pearson-VII-type distribution of the form

$$\mathcal{F}(>\Phi_0) \simeq \frac{1}{[1 + (\Phi_0/a_1)]^{a2}},$$
 (3.26)

with $a_1 \simeq 1.023$ and $a_2 \simeq 0.462$. From the initial cumulative mass fraction in Eq. (3.26), we can derive the initial probability distribution:

$$p_{\Phi}(\Phi) = \frac{a_2}{a_1(1 + \Phi/a_1)^{a_2+1}},\tag{3.27}$$

as a function of Φ . It can be seen from the left panel of Fig. 3.1, that roughly 70% of the miniclusters form with initial overdensities $\Phi > 1$ and that approximately 14% of miniclusters form with large overdensities of $\Phi > 10$ [146]. The distribution of Φ depicted in the right panel of Fig. 3.1 will be applied to the minicluster population of the galactic DM halo in Chap. 6 and Chap. 7. Before, we continue to constrain the remaining free parameter from Eq. (3.24): the range of minicluster masses \mathcal{M} and its evolution over time.

3.3 Linear Growth of Matter Perturbations

The linear growth of miniclusters with the initial properties from Sec. 3.2 can be understood by considering the growth of axion matter perturbations in an expanding universe. In this section we recall the most fundamental results on the dynamics of linear axion fluctuations from cosmological perturbation theory following Ref.s [41, 177, 178]. Considering the continuity and Euler equations of a relativistic fluid, the EOM describing the linear growth of the time-dependent matter perturbations $\delta_a(t) = \rho_a(t)/\bar{\rho}_a(t) - 1$ in an axion-dominated universe for $T \ll T_{\rm osc}$ can be shown to take the form [41, 177]

$$\ddot{\delta}_a + 2H\dot{\delta}_a + \left(\frac{k^2c_s^2}{a^2} - 4\pi G\rho_a\right)\delta_a = 0, \qquad (3.28)$$

where c_s is the sound speed of the fluid. Eq. (3.28) describes an oscillator with a time-dependent damping, that expresses the competition between pressure and gravitational collapse. Matter perturbations δ_a will thus experience a different evolution depending on the scaling of the first and second term in round brackets. The axion Jeans scale k_J is defined as the scale, where the pressure term $c_s^2 k^2 \delta_a / a^2$ and the gravitational term cancel each other. Entering the axion effective sound speed $c_s^2 \approx k^2/(4m_a^2 a^2)$, one obtains

$$k_J = \left[16\pi G a^4 \bar{\rho}_a(a)\right]^{1/4} m_a^{1/2}.$$
 (3.29)

The scale-dependent behavior of the density fluctuations can also be understood by considering the solutions to Eq. (3.28). Using the axion effective sound speed and expressing H for a matter dominated universe one obtains [41]

$$\delta_a = C_+ D_+(k, a) + C_- D_-(k, a), \qquad (3.30)$$

where C_{\pm} carry information on the initial conditions and the solutions $D_{\pm}(k, a)$ are the growing and decaying modes respectively. The exact form and time-dependent behavior of $D_{\pm}(k, a)$ can be found in Ref. [178]. For this work, we summarize that modes with $k < k_J$ will grow linearly after matter-radiation equality, similar to the standard cold dark matter case.

The modes with $k > k_J$ on the other hand separate into two different categories: First, the largest wavenumbers $k > k_J(a_0)$ correspond to fluctuations which are still smaller than the

present-day Jeans scale. They show an oscillating behavior in D_+ , D_- with constant amplitude over time, thus suppressing structure formation on very small scales. Secondly, modes in the range $k_J(a_{eq}) \le k \le k_J(a_0)$ oscillate as long as they remain below the a-dependent Jeans scale $k_J(a)$. As soon as they move above the Jeans scale, these modes show the usual growing and decaying modes $D_+(k,a)$ and $D_-(k,a)$.

This observation has two important consequences: First, axion dark matter differs from standard CDM on scales below the Jeans scale $k > k_J$ and secondly, it exhibits a CDM-like behavior on large scales in the limit $k^2c_s^2 \to 0$ with a growing mode $\delta \propto a$ and decaying mode $\delta_a \propto a^{-3/2}$. Importantly for this work, the similarity to standard CDM allows us to employ analytical linear growth models to the mass distribution of miniclusters in the next section.

3.4 Press-Schechter Formalism

As mentioned in Sec. 3.2, miniclusters are expected to form over a wide range of masses until matter-radiation equality. While the characteristic quantities from Sec. 3.2 provide order-of-magnitude estimates for typical minicluster properties, a more precise knowledge of the mass and size distribution of these objects is required. This is specifically important due to the ongoing tidal interactions and mergers between miniclusters that dominate their evolution in the matter-dominated epoch and which lead to the formation of heavier structures over time. The standard approach to model the linear mass growth of axion miniclusters is given by the *Press-Schechter* formalism [179, 180].

Calculations involving a spherically symmetric perturbation in a flat, matter-dominated universe show that a linearly evolved overdensity δ has collapsed into a halo or minicluster once $\delta(\mathbf{x},t) > \delta_c = 1.686$ [181]. Using the linear growth model from Sec. 3.3, the time-dependence of the density contrast can be expressed in terms of the growing mode $D(t) \approx D_+(t)$ as $\delta(\mathbf{x},t) = D(t)\delta_0(\mathbf{x})$, which is valid at late times $t \gg t_0^{-1}$.

This simple collapse criterion serves as the main assumption in the estimation of the mass distribution of collapsed objects in the Press-Schechter approach. An important first step in this formalism is to smooth the density field $\delta(\mathbf{x}, R)$ with a window function $W(\mathbf{x}, R_f)$

$$\delta_s(\mathbf{x}, R_f) = \int d^3 x' \, \delta_0\left(\mathbf{x}'\right) W\left(\mathbf{x} + \mathbf{x}', R_f\right) , \qquad (3.31)$$

which amounts to a filtering of $\delta(\mathbf{x}, R_f)$ on a length scale R_f through convolution with $W(\mathbf{x}, R_f)$. In this framework all points in space satisfying $\delta_s(\mathbf{x}, R_f, t) > \delta_c$ are considered to be part of a minicluster. There exist different choices for the window function W, with the two most prominent being the spherical top hat filter and the Gaussian filter

$$W(\mathbf{x}, R_f) = \frac{1}{(2\pi)^{3/2} R_f^3} \exp\left(\frac{-|\mathbf{x}|^2}{2R_f^2}\right)$$
(3.32)

used in Ref. [58] and in Sec. 3.6 of this work. The variance $\sigma^2(R_f)$ of the density field $\delta_s(\mathbf{x}, R_f, t)$ smoothed on a scale R_f can be expressed in terms of the linear power spectrum P(k) as

$$\sigma^2(R_f) = \langle \delta_s^2(\mathbf{x}, R_f) \rangle = \frac{1}{2\pi^2} \int_0^\infty dk k^2 P(k) W^2(kR_f) , \qquad (3.33)$$

¹Note that this is equivalent to the common formulation of a time-dependent collapse barrier $\delta_c(t) = \delta_c/D(t)$, for the initial overdensity with threshold $\delta_0(\mathbf{x}) > \delta_c(t)$.

where $W(kR_f) = \exp(-k^2R_f^2/2)$ is the Fourier transform of the window function $W(\mathbf{x}, R_f)$. Since the smoothing length R_f is directly related to the mass $M = C_f \bar{\rho} R_f^3$ of the structure with a filter-dependent constant $C_f = (2\pi)^{3/2}$, the variance $\sigma^2(M) = \sigma^2(R)$ is often called the mass variance.

Press and Schechter [179] postulated that the probability $\mathcal{P}[>\delta_c]$ to find $\delta_s(\mathbf{x}, M, t) > \delta_c$ at a given time t is equal to the mass fraction $\mathcal{F}[>M]$ contained in objects with mass greater than M. For a Gaussian density field, the probability is found to be [182]

$$\mathcal{P}\left[>\delta_{c}\right] = \frac{1}{\sqrt{2\pi}\sigma(M)} \int_{\delta_{c}}^{\infty} d\delta \exp\left[-\frac{\delta^{2}}{2\sigma(M)^{2}}\right] = \frac{1}{2}\operatorname{erfc}\left[\frac{\delta_{c}(t)}{2\sigma(M)}\right], \tag{3.34}$$

with the complementary error function $\operatorname{erfc}(x) = 1 - \operatorname{erf}(x)$. The mass function n(M,t)dM gives the number of objects with masses in the range [M,M+dM] per comoving volume, with $n(M,t) = dn/dM = 1/Mdn/d\ln M$. This can be used to equate the mass function using the fraction of mass $\partial \mathcal{F}/\partial MdM$ contained in structures with masses in the range [M,M+dM]:

$$n(M,t)dM = \frac{\bar{\rho}}{M} \frac{\partial F(>M)}{\partial M} dM, \qquad (3.35)$$

where $\bar{\rho}$ is the comoving background density. Taking into account an additional fudge factor 2, the relation between the probability $\mathcal{P}(>\delta_c)$ and the mass fraction of objects more massive than M is $F(>M) = 2\mathcal{P}[>\delta_c]$. This relation yields the Press-Schechter halo mass function [58]

$$\frac{dn}{d\ln M} = 2\bar{\rho}\frac{\partial \mathcal{P}(>\delta_{\rm c})}{\partial M} = \sqrt{\frac{2}{\pi}}\frac{\bar{\rho}}{M}\frac{\delta_{\rm c}}{\sigma(M)}\exp\left(-\frac{\delta_{\rm c}^2}{2\sigma(M)^2}\right)\left|\frac{d\ln\sigma(M)}{d\ln M}\right|,\tag{3.36}$$

which gives the comoving number density of objects per logarithmic mass interval as a function of M and where it was used that $\partial \mathcal{P}/\partial M = \partial \mathcal{P}/\partial \sigma(M)|d\sigma(M)/dM|$. The time dependence of the mass function in Eq. (3.36) enters through the linear growth factor D(t), which determines the time evolution of the smoothed density field $\delta_s(t)$ and the mass variance $\sigma(M)$.

Note also that Eq. (3.36) was derived using a spherical collapse model. There exist extensions of the simple Press-Schechter approach introduced in this section, namely the ellipsoidal collapse model by Sheth and Tormen [183], which provides better agreement with N-body simulations [171]. As argued in Ref. [58], the use of the Press-Schechter approach in Eq. (3.36) provides a reasonable estimate for the linear growth of the minicluster mass function due to the large underlying uncertainties (see Subsec. 3.5.2 for a more detailed discussion).

3.5 Minicluster Evolution

In the previous sections, we have introduced the spherical collapse model of Ref. [23] and showed how it can be used to estimate characteristic minicluster properties for different axion masses or models. From this, the next step is to infer the present-day properties of miniclusters with special emphasis on the *minicluster* (halo) mass function (MCMF) using the Press-Schechter approach from Sec. 3.4 and Ref. [58].

In this context, it is useful to divide the evolution of the axion field into three distinct stages: First, in the early universe, the axion field arises from the spontaneous symmetry breaking around $T \sim f_a$ and acquires a mass around $T \sim T_{\rm osc}$ leading to the formation of topological

defects as summarized in Sec. 2.5. This stage and the emergence of early minicluster seeds has been investigated by means of lattice simulations following Eq. (2.40) in Ref.s [23, 28, 184]. In the second stage, the system is dominated by the gravitational force, which allows for the use of N-body simulations in the context of miniclusters [29, 30]. Lastly, and in the third stage, minicluster mergers lead to the formation of large-scale dark matter halos seeding the formation of galaxies at late times. In this section, we discuss the results from N-body simulations obtained from the second stage in Subsec. 3.5.1 following Ref. [30]. Subsequently in Subsec. 3.5.2, we apply the predictions from Ref. [58] to estimate the properties of axion miniclusters in the third evolutionary stage, i.e. in the present-day universe.

3.5.1 Numerical Simulations

Starting with the gravitational evolution of the MCMF, this section summarizes the numerical results found in Ref.s [30] and [29]. The authors of Ref. [30] used the initial conditions from the lattice simulations in Ref. [185] together with the GAGDET-3 code [185] to trace the evolution of the QCD axion density perturbations with $m_a = 50 \,\mu\text{eV}$ from redshift $z \sim 10^6$ down to z = 99. The redshift-dependent evolution of the MCMF reproduced from the corresponding N-body simulations is shown in Fig. 3.2, where the left and right panels depict the mass distribution of structures before and after matter-radiation equality $z_{\rm eq} \simeq 3402$.

In the left panel of Fig. 3.2, it can be seen that the MCMF at early times, $z \sim 10^6$ in blue, peaks at the lower masses close to the low-mass resolution cutoff at $\mathcal{M} \sim 10^{-15} M_{\odot}$. The miniclusters

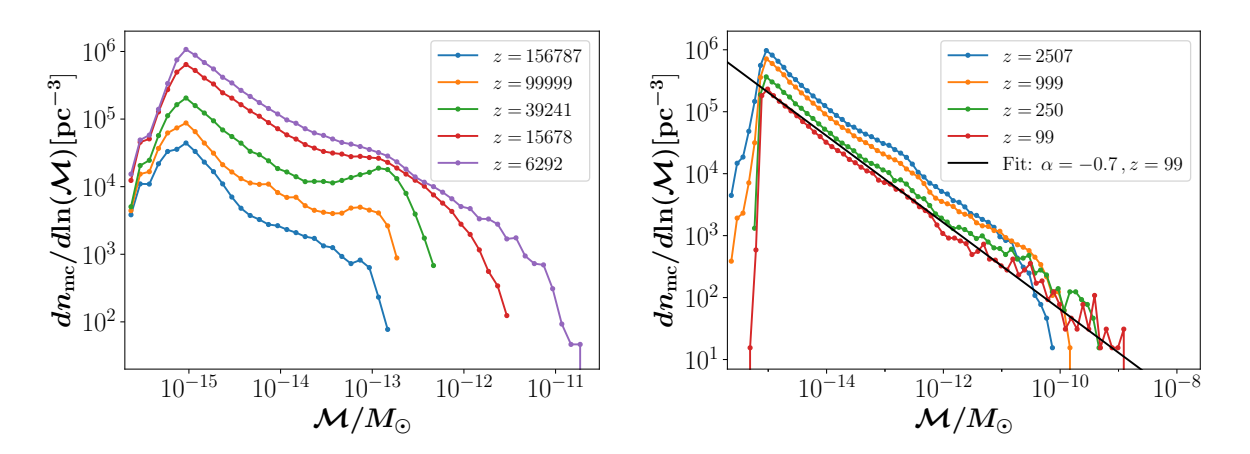


Figure 3.2: Evolution of the minicluster mass function with redshift z before (left) and after (right) matter-radiation equality $z_{\rm eq} \simeq 3402$. A power-law fit with slope $\alpha \simeq -0.7$ following Eq. (3.37) is applied to the z = 99 data in black. The data is taken from the numerical N-body simulations of miniclusters in the post-inflationary scenario performed in Ref. [30] for the QCD axion mass $m_a = 50 \,\mu\text{eV}$.

forming at these large redshifts $z\gg z_{\rm eq}$ amount to structures, which are deeply non-linear and thus characterized by large initial overdensities $\Phi\gg 1$. As mentioned before and as shown in Fig. 3.1, the majority of the overall collapsed objects has moderate overdensities $\Phi\sim 1$, which is why most miniclusters collapse around comparatively lower redshifts $z\sim z_{\rm eq}$ in purple. Accordingly at lower redshift z, the overall number of collapsed objects grows quickly and the MCMF develops a pronounced second peak at $\mathcal{M}\gtrsim 10^{-13}\,M_{\odot}$ around $z\sim 4\cdot 10^4$. This second

peak corresponds to the canonical miniclusters with characteristic masses $\mathcal{M} \sim \mathcal{M}_0$ predicted by Eq. (3.25). Until matter-radiation equality, the evolution of the MCMF exhibits a continuous growth in amplitude due to the ongoing collapse of minicluster seeds and a simultaneous extension towards the high-mass end $\mathcal{M} \sim 10^{-11} M_{\odot}$. Note that similar results were obtained in the N-body simulations performed in Ref. [29].

Around redshifts $z \sim z_{\rm eq} \simeq 3402$, the second peak has been flattened out and the MCMF is well-fit by a power-law with slope index $\alpha = -0.7$ [30]

$$\frac{dn}{d\ln \mathcal{M}} \propto \mathcal{M}^{\alpha} \,. \tag{3.37}$$

Finally and after matter-radiation equality, the overall (comoving) number density of miniclusters decreases due to tidal interactions and minicluster mergers, which simultaneously raise the high-mass end of the MCMF to $\mathcal{M} \sim 10^{-9} M_{\odot}$ at the lowest redshift z = 99. The evolution of the MCMF following Eq. (3.37) has several important consequences for this work, namely:

- 1. The MC mass distribution peaks towards the lower masses, presumably extending to masses lower than the resolution cutoff mass $\mathcal{M} \sim 10^{-15}\,M_{\odot}$
- 2. A slope index $\alpha = -0.7$ can be used to characterize the MCMF for $z < z_{\rm eq}$
- 3. The range $\{\mathcal{M}\}$ of minicluster masses changes over time due to gravitational interactions
- 4. Large-scale dark matter haloes are expected to have a (sub-)minicluster population similar to the late-time MCMF at z = 99 in the right panel of Fig. 3.2 in red

We note that point 4 in the above enumeration is not directly evident from the MCMF in Fig. 3.2. This observation is best made by counting the number of sub-miniclusters, which are embedded within the virial radius of a heavier 'host' minicluster with $\mathcal{M}_{\text{host}} > \mathcal{M}_{\text{sub}}$. From this we obtain the global sub-halo MCMF depicted in figure Fig. 3.3 as a function of the host minicluster mass $\mathcal{M}_{\text{host}}$. As can be seen in Fig. 3.3, the evolution of the sub-halo MCMF is approximately frozen after matter-radiation equality. The high-mass end $\mathcal{M}_{\text{sub}} \gtrsim 10^{-12} M_{\odot}$ of the MCMF is subject to large uncertainty due to the low number of samples in the simulation volume. Importantly for this work and point 4., the fitted slope-index $\alpha = -0.7$ of the host MCMF in the right panel of Fig. 3.2 also remains approximately valid for the global population of sub-miniclusters as seen by the black line in Fig. 3.3.

The conclusion to draw from this observation, is that the approximate power-law slope of the (sub-halo) MCMF can be assumed to also apply at late times in the following. This assumption has the important consequence that the galactic NFW halo of the Milky Way (and those of other standard spiral galaxies) are expected to host a large number of miniclusters with a wide range of masses $\{\mathcal{M}\}$ and an MCMF slope index α at z=0 due to their host minicluster nature. It should however be emphasized that there is an underlying uncertainty on the exact value of the slope parameter $-0.7 \lesssim \alpha \lesssim -1/2$ [29, 30, 58] depending on the initial conditions,

of the slope parameter $-0.7 \lesssim \alpha \lesssim -1/2$ [29, 30, 58] depending on the initial conditions, the method of investigation and on the mass range $\{\mathcal{M}\}$ under consideration. Since N-body simulations can not be performed until present-day redshift $z \sim 0$, it is common to extrapolate their power-law behavior at $z \lesssim 100$ down to z = 0. N-body simulations predict $\alpha \simeq 0.7$ [30], while $\alpha - 0.6$ [180] and $\alpha = -1/2$ [58] are obtained from semi-analytical models. Crucially for the considerations in this work, additional predictions estimating the present-day range of \mathcal{M}

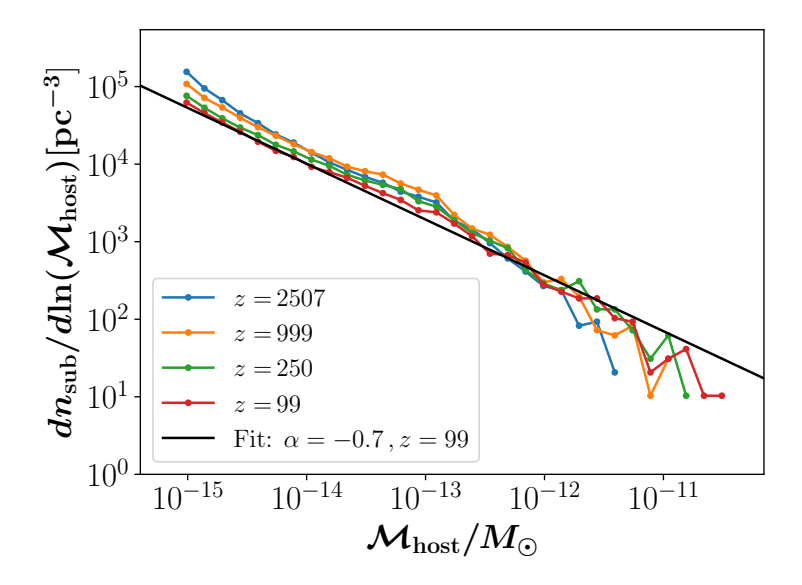


Figure 3.3: Evolution of the global sub-halo MCMF at redshifts $z < z_{\rm eq}$ as a function of the parent halo mass $\mathcal{M}_{\rm host}$ for $m_a = 50\,\mu\text{eV}$. A power-law fit with slope $\alpha = -0.7$ following Eq. (3.37) is applied to the z = 99 data in black. The data was extracted from the numerical N-body simulations performed in Ref. [30].

for different axion models m_a , n, f_a are needed (c.f. Sec. 2.4). Such predictions are best obtained from semi-analytical considerations, which will be introduced in Subsec. 3.5.2.

As for this section dealing with the MCMF evolution in N-body simulations, we conclude that the initial mass distribution which is established around $z \simeq z_{\rm eq}$, is determined by the initial power spectrum of axion density perturbations [28, 184]. Subsequently in the matter-dominated epoch, the MCMF evolves due to tidal disruption and minicluster mergers leading to the formation of increasingly heavy structures over time. This leads to an extension of the mass range towards larger minicluster masses \mathcal{M} , where the power-law slope α established at $z_{\rm eq}$ is expected to remain roughly preserved at $z < z_{\rm eq}$.

3.5.2 Parametrization for Mass Distributions

In the previous subsection, we have shown how numerical simulations can be used to predict that the MCMF evolves with a roughly constant slope index $\alpha = -0.7$. In this section, we follow the semi-analytic Press-Schechter approach from Ref. [58] to motivate the second representative value $\alpha = -1/2$ of the MCMF slope considered in this work. More specifically, we summarize the steps performed in Ref. [58] leading to the parametrization of the z=0 mass distribution of miniclusters, which we will use to infer the galactic MCMF in the following sections.

The authors of Ref. [58] used a Gaussian window function of the form in Eq. (3.32) to smooth the axion density field, for which the mass contained within a comoving volume of radius R is $\mathcal{M} = (2\pi)^{3/2} \bar{\rho}_a R^3$. In their framework with a constant collapse threshold $\delta_c = 1.686$, the

statistics of the smoothed density field $\delta_a(\eta)^2$ following Eq. (3.31) are characterized by the time-dependent power spectrum $P(k,\eta)$ according to the relation

$$\langle |\delta_a(\mathbf{x}, \eta)|^2 \rangle = \int \frac{d^3k}{(2\pi)^3} P(k, \eta) , \qquad (3.38)$$

where the (conformal) time-dependence η is inherited from the linear growing or oscillating modes of Eq. (3.28). The initial power spectrum at the temperature $T_{\rm osc}$ when the axion matter density perturbations are established is truncated at the comoving size $k_{\rm osc} = aH(T_{\rm osc})$ of the horizon at $T_{\rm osc}$ according to

$$P_0(k) \equiv P(k, \eta_{\rm osc}) = \frac{24\pi^2}{5k_{\rm osc}^3} \Theta(k_{\rm osc} - k),$$
 (3.39)

where $\theta(x)$ is the Heaviside function [58]. Expressing the evolution $P(k, \eta) = P_0(k)\mathcal{T}^2(k, \eta)$ in terms of the isocurvature transfer function $\mathcal{T}(k, \eta)$ from Ref. [186] together with the Heaviside initial power spectrum $P_0(k)$, the mass variance evolves with time as

$$\sigma^{2}(\mathcal{M}, \eta) = \int \frac{k^{2}dk}{2\pi^{2}} P_{0}(k) \mathcal{T}^{2}(k, \eta) |W(k, \mathcal{M})|^{2}, \qquad (3.40)$$

which exhibits a scaling of $\sigma(\mathcal{M}) \propto \mathcal{M}^{-1/2}$. More details on the calculation and properties of the mass variance $\sigma(\mathcal{M})$ can be found in Ref. [58]. Since the present-day $\eta = \eta_0$ overdensity from linear growth scales as $\delta(\eta_0) \propto D(\eta_0)/D(\eta_{eq})\delta(\eta_{eq}) = \delta(\eta_{eq})/D(\eta_{eq})$ and from $\sigma^2 \propto \delta^2$ in Eq. (3.33), it follows that the mass variance at z = 0 is simply given by

$$\sigma^2(\mathcal{M}, z = 0) = \frac{\sigma^2(\mathcal{M}, z_{\text{eq}})}{D^2(z_{\text{eq}})},$$
(3.41)

with the initial mass variance $\sigma(\mathcal{M}, z_{eq})$ and the linear growth factor $D(z_{eq})$. The linear growth factor of cold dark matter in a flat universe with $\Omega_{\Lambda} = 1 - \Omega_m$ is

$$D(z) = \frac{\Omega_m}{\tilde{D}(0)} \frac{5}{2} \frac{H(z)}{H_0} \int_z^{\infty} dz' \left[\frac{H(z')}{(1+z')H_0} \right]^{-3} , \qquad (3.42)$$

which is normalized to unity at z = 0 and where $\tilde{D}(0)$ is the corresponding growth factor before normalization [58].

Using the time-dependent mass variance of the Gaussian filtered density field from Eq. (3.40), the authors of Ref. [58] calculated the redshift-dependent evolution of the MCMF for different m_a , f_a , n from z_{eq} until present-day redshift z=0. Details on the calculation can be found in Ref. [58] and the references therein; as for this work, we will only demonstrate their results and apply them to axion-like particles in the following.

The evolution of a representative MCMF given for an axion with $m_a = 10^{-7}$ eV and temperature-independent mass evolution n = 0 following Eq. (2.34) is depicted in Fig. 3.4.

²Note that compared to the general Press-Schechter formalism in Sec. 3.4 we have switched to conformal time $dt = ad\eta$ here.

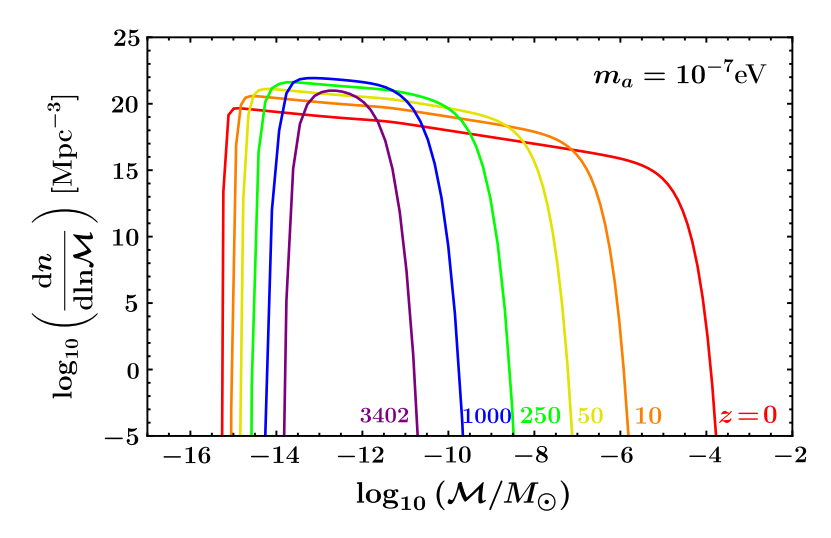


Figure 3.4: Evolution of the MCMF with redshift z obtained from the Press-Schechter approach in Ref. [58] for $m_a = 10^{-7}$ eV and n = 0 in Eq. (2.34). The MCMF is established at matter-radiation equality $z_{\rm eq} \simeq 3402$ and broadens over time due to tidal interactions as indicated by the colored lines.

It can be clearly seen from the initial MCMF at $z=z_{\rm eq}\simeq 3402$ in purple that the mass distribution of miniclusters is comparably narrow and roughly centered around the characteristic MC mass $\mathcal{M}_0 \simeq 10^{-12} M_{\odot}$ at early times. Towards lower redshift, the MCMF broadens due to the ongoing collapse of density seeds with modes in the range $k_J(\eta_{\rm eq}) < k < k_J(\eta_0)$ and due to the formation of heavier structures from minicluster mergers. Eventually, at redshift z=0 in red, the present-day MCMF is established, thus providing an analytical estimate for the present-day range of minicluster masses from linear growth predictions.

As it turns out, the predicted MC mass range at z=0 indicated by the red line in Fig. 3.4 can be expressed in terms of the characteristic mass \mathcal{M}_0 from Eq. (3.25) and in terms of the Jeans

$$\mathcal{M}_J = 1.4 \cdot 10^{-18} M_{\odot} \left(\frac{m_a}{50 \,\mu\text{eV}}\right)^{-3/2} \left(\frac{\Omega_m}{0.32}\right)^{1/4} \left(\frac{h}{0.67}\right)^{1/2} ,$$
 (3.43)

which is derived from the Jeans scale in Eq. (3.29). Specifically, in the case of the z=0 MCMF and for different choices of m_a, n, f_a , the authors of Ref. [58] showed that the mass range of miniclusters can be parametrized using an upper and a lower mass bound $\mathcal{M}_{J,\text{min}}$ and \mathcal{M}_{max} respectively.

These two limiting masses are indicated by the red dashed lines and red notations in Fig. 3.5, together with the z=0 MCMF taken from Fig. 3.4 in black lines. Comparing the analytical MCMF to the lower and upper mass bounds $\mathcal{M}_{J,\text{min}}$, \mathcal{M}_{max} in red, a good agreement in the predicted mass ranges can be seen. As was shown in Ref. [58], the lower mass bound is related to the redshift-dependent Jeans mass \mathcal{M}_J by

$$\mathcal{M}_{J,\min}(m_a)\Big|_{z=0} \approx \mathcal{M}_J \left[\frac{1.8}{7.5 + \log_{10} D(z=0)} \right]^2$$
 (3.44)

$$\approx 8.3 \cdot 10^{-20} \, M_{\odot} \left(\frac{m_a}{50 \, \mu \text{eV}} \right)^{-3/2} \left(\frac{\Omega_m}{0.32} \right)^{1/4} \left(\frac{h}{0.67} \right)^{1/2} \,, \tag{3.45}$$

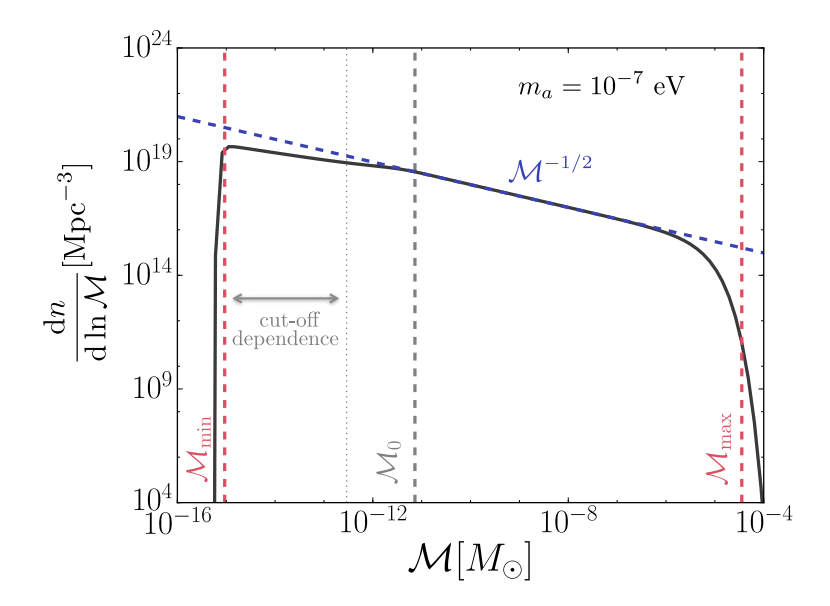


Figure 3.5: Parametrization of the MCMF in black at present-day redshift z = 0 for $m_a = 10^{-7}$ eV, taken from Ref. [58]. The characteristic MC mass \mathcal{M}_0 is indicated by the gray dashed line and the blue dashed line shows the power-law fit from Eq. (3.37) with slope index $\alpha = -1/2$. The absolute low- and high-mass cutoffs from the Jeans limit $\mathcal{M}_{\min} = \mathcal{M}_{J,\min}$ in Eq. (3.45) and from linear growth, \mathcal{M}_{\max} in Eq. (3.46), are shown in red dashed lines.

where the index J indicates the connection to \mathcal{M}_J and Eq. (3.45) will only be evaluated at z=0 in this work. Below this mass scale, miniclusters do not form by gravitational collapse. The corresponding upper mass bound can also be expressed in terms of the linear growth factor D(z) from Eq. (3.42) according to [58]

$$\mathcal{M}_{\text{max}}(m_a, n)\Big|_{z=0} \approx 4.9 \cdot 10^6 \,\mathcal{M}_0(m_a, n) \, D(z=0)^2 \,,$$
 (3.46)

where we have indicated an additional dependence on the axion mass temperature evolution index n - opposed to the temperature-independent lower mass bound in Eq. (3.45). The upper mass bound \mathcal{M}_{max} is related to the linear growth of structures with $\mathcal{M} \sim \mathcal{M}_0$ at z_{eq} , that leads to the occurrence of high-mass MCs with $\mathcal{M} \gg \mathcal{M}_0$ at late times. Note that the definition of \mathcal{M}_{max} depends on the characteristic MC mass \mathcal{M}_0 from Eq. (3.25). Therefore, the mass distribution of miniclusters at z=0 can be parametrized by the three masses $\mathcal{M}_{J,\text{min}}$, \mathcal{M}_0 and \mathcal{M}_{max} - together with the slope index $\alpha=-1/2$ in Fig. 3.5 [58].

Between the minimum and maximum minicluster masses $\mathcal{M}_{J,\text{min}}$ and \mathcal{M}_{max} , the MCMF slope in Fig. 3.5 is well-fit by a power-law of the form in Eq. (3.37) with $\alpha = -1/2$ indicated by the blue dashed line, except for the lowest masses with \mathcal{M} below the gray dotted line ³. The corresponding low-mass tail has $\mathcal{M} \lesssim \mathcal{M}_0/25$ and exhibits a *cut-off dependence* as mentioned by the gray arrows in Fig. 3.5.

This cutoff dependence is expected to modify the MCMF slope at the low-mass tail to a degree, which strongly depends on the initial power spectrum in Eq. (3.39) and on the applied window

³The discrepancy between the $\alpha=-0.7$ scaling observed in Subsec. 3.5.1 at $z\gtrsim 100$ and linear growth predictions with $\alpha=-1/2$ at z=0 is currently unresolved.

function in Eq. (3.31). A detailed discussion on the impact of different filters on the MCMF can be found in Ref. [58]. In this work, we briefly summarize the most important uncertainties leading to the cutoff dependence at $\mathcal{M} \lesssim \mathcal{M}_0/25$ for the Gaussian filter and Heaviside power spectrum:

On scales $\mathcal{M} < \mathcal{M}_0$ the density field $\delta(\eta)$ is highly non-Gaussian, which means that the standard Press-Schechter formalism can not be applied for these matter perturbations. Independent of the Gaussianity of the field, a cutoff in the MCMF is expected from the truncated axion power spectrum in Eq. (3.39) for $\mathcal{M} \lesssim \mathcal{M}_0$. Indications for this cutoff were found in numerical simulations [187] and from the filter-dependence observed in Ref. [58]. Using the parametrization introduced in Subsec. 3.5.2 based on the Gaussian window function and Heaviside initial power spectrum, Fairbairn & Marsh [58] found that this cutoff dependence becomes relevant below an approximate \mathcal{M}_0 -cutoff scale

$$\mathcal{M}_{0,\min} \equiv \mathcal{M}_0 / 25, \qquad (3.47)$$

where the index '0' indicates the connection to the characteristic mass \mathcal{M}_0 . To account for the large uncertainties in the low-mass tail of the MCMF Eq. (3.47), we will consider two different low- \mathcal{M} cutoffs in the following: First the cut-off prediction in Eq. (3.47) proportional to \mathcal{M}_0 and secondly the Jeans mass cutoff $\mathcal{M}_{J,\text{min}}$ introduced in Eq. (3.45). In the range where $\mathcal{M}_0/25 \le \mathcal{M} \le \mathcal{M}_{\text{mass}}$, the MCMF can be parametrized by a power-law with

In the range where $\mathcal{M}_0/25 \leq \mathcal{M} \leq \mathcal{M}_{\text{max}}$, the MCMF can be parametrized by a power-law with $\alpha = -1/2$ with good precision (c.f. Fig. 3.5). For simplicity, we also apply the scaling $\alpha = -1/2$ in the range $\mathcal{M}_{J,\text{min}} \leq \mathcal{M} \leq \mathcal{M}_{\text{max}}$ with the Jeans cutoff $\mathcal{M}_{J,\text{min}}$, similar to what was done in Ref.s [136, 188].

3.6 Galactic Minicluster Mass Distribution

With the combined numerical and analytical predictions for the evolution of miniclusters from Sec. 3.3 to Subsec. 3.5.2, we are now in a position to extrapolate their initial properties from Sec. 3.1 and Sec. 3.2 to the hypothetical present-day population of galactic sub-miniclusters in the NFW halo of the Milky Way. Analogous to the approach in Ref.s [58] and [1], we consider different classes of axion models in the range $10^{-12} \, \text{eV} \le m_a \le 10^{-3} \, \text{eV}$ with QCD-like potentials from Eq. (2.32) and a modified temperature dependence n of the axion mass $m_a(T)$ in Eq. (2.34). We introduce the characterization of different axion models following Ref. [58] in Subsec. 3.6.1 and apply the resulting MC mass predictions for different models m_a, n, f_a to the Milky Way DM halo in Subsec. 3.6.2 following Ref. [1]. In Subsec. 3.6.3, we also consider the impact of tidal disruption on the long-time survival of miniclusters.

3.6.1 General approach for axion-like Particles

Our implementation of different axion models (i.e. of ALP DM models, including the QCD axion) is best understood by listing the three characteristic quantities that allow for the parametrization of the z=0 MCMF in Subsec. 3.5.2, namely: α , $\mathcal{M}_{J,\text{min}}$ and \mathcal{M}_0 .

The first is the power law scaling α from Eq. (3.37), where the corresponding slope indices $\alpha = \{-1/2, -0.7\}$ considered in this work are motivated by the analytic and numerical predictions from Fig. 3.2 and Fig. 3.5 respectively. Secondly and thirdly, the low-mass bound $\mathcal{M}_{J,\text{min}}$ in Eq. (3.45) only depends on the axion mass m_a , while the high-mass bound \mathcal{M}_{max} in Eq. (3.46)

also depends on the characteristic MC mass \mathcal{M}_0 from Eq. (3.25).

This characteristic mass scale measures the amount of dark matter contained within a Hubble horizon around $T \sim T_{\rm osc}$. Following Eq. (3.25), the dependence of \mathcal{M}_0 on $T_{\rm osc}$ is encoded in the comoving wavenumber

$$k_{\text{osc}} = a(T_{\text{osc}})H(T_{\text{osc}}) = \left[\frac{g_{\star,S}(T_0)}{g_{\star,S}(T_{\text{osc}})}\right]^{1/3} \frac{T_0}{T_{\text{osc}}}H(T_{\text{osc}})$$
 (3.48)

at $T = T_{\rm osc}$ and where $g_{\star,S}(T)$ are the entropic degrees of freedom from Ref. [54] and Tab. A.2. Eq. (3.48) clearly depends on the oscillation temperature $T_{\rm osc}$, which can be determined analytically only for the QCD axion case (see Eq. (2.49)). For our considerations involving axion-like particles, the oscillation temperature needs to be calculated numerically by equating the temperature-dependent scaling of the axion mass in Eq. (2.34) with the Hubble drag from Eq. (2.40), i.e. $3H(T_{\rm osc}) = m_a(T_{\rm osc})$, as explained in Subsec. 2.5.2. The left-hand side of this equation can be obtained from the second Friedmann Eq. (2.51) using the fit for $g_{\star,R}(T)$ in Tab. A.2.

Moving on to the right-hand side, the remaining quantity needed to determine the temperature which gives $3H(T)=m_a(T)$ is the temperature scale Λ_0 defined in Eq. (2.34). As mentioned before, this quantity is equivalent to the QCD susceptibility in Eq. (2.14), which specifies the zero-temperature m_a - f_a relation from Eq. (2.11) (see Sec. 2.3 for details). For the generalization to axion-like particles, we adopt the approach from Ref. [58] by assuming the simplified QCD-like scaling $\Lambda_0 = \sqrt{m_a f_a}$. Note that in the specific case of the QCD axion, this temperature scale is given by $\Lambda \simeq 2.5 \sqrt{m_a f_a}$ [58], which is well within the uncertainties of the linear growth predictions from Subsec. 3.5.2.

Following this procedure, we can calculate $T_{\rm osc}$, $k_{\rm osc}$ and \mathcal{M}_0 for any combination of the three parameters m_a , f_a , n, or equivalently for arbitrary axion-like models with properties defined in Sec. 2.3. However since we are interested mainly in axion-like dark matter candidates which should have order-one relic abundance $\Omega_a h^2 \sim \Omega_c h^2 \sim 0.12$, we can use the total relic abundance $\Omega_a^{\rm tot}(f_a)$ from Eq. (2.64) to fix the symmetry breaking scale f_a in the following. The corresponding requirement $\Omega_a(f_a)h^2 \stackrel{!}{=} 0.12$ for f_a is equivalent to the consideration of axion models, which constitute 100% of the missing dark matter.

In this approach, we characterize each axion model by choosing a set of parameters (m_a, n) from the range $10^{-12} \text{ eV} \le m_a \le 10^{-3} \text{ eV}$ and for three characteristic values of $n = \{0, 1, 3.34\}$, where n = 3.34, $m_a \approx 50 \,\mu\text{eV}$ roughly corresponds to the numerical calculation of the QCD axion in Ref. [54]. Since the aforementioned generalization of axion-like DM candidates is crucial for the analysis in the following chapters, we summarize the fundamental steps performed for each axion model (m_a, n) in short below:

- 1. Choose an axion model (m_a, n) with $m_a \equiv m_{a,0} = m_a(T=0)$ and n defined in Eq. (2.34)
- 2. For this model, determine f_a by requiring 100% DM abundance $\Omega_a^{\text{tot}}(f_a)h^2 \stackrel{!}{=} 0.12$ using
 - the total relic abundance $\Omega_a^{\rm tot}(f_a)$ from Eq. (2.64)
 - with $T_{\rm osc}$ from $3H(T_{\rm osc})=m_a(T_{\rm osc})$ and $\Lambda_0=\sqrt{m_af_a}$ in Eq. (2.34),
 - H(T) from Eq. (2.51) and $m_a(T)$ from Eq. (2.34)
- 3. Determine $T_{\rm osc}$ again for the above specific value of f_a and $\Lambda_0 = \sqrt{m_a f_a}$

- 4. From this calculate $k_{\rm osc}$ according to Eq. (3.48)
- 5. Using k_{osc} calculate the characteristic MC mass $\mathcal{M}_0(m_a, n)$ in Eq. (3.25)
- 6. Apply the Press-Schechter predictions from Sec. 3.4
 - With $\alpha = -1/2$ (or $\alpha = -0.7$ in some cases) for the MCMF slope, Eq. (3.37)
 - With low-mass cutoffs $\mathcal{M}_{J,\text{min}}$ or $\mathcal{M}_{0,\text{min}}$ from Eq. (3.45) or Eq. (3.47)
 - and the high-mass cutoff \mathcal{M}_{max} of the MCMF in Eq. (3.46)
- 7. Obtain the galactic MCMF by normalization to the Milky Way DM halo (see Sec. 3.6)

We emphasize the dependence of T_{osc} , \mathcal{M}_0 , \mathcal{M}_{max} and $\mathcal{M}_{0,\text{min}}$ on the axion parameters (m_a, f_a, n) , where in our formalism the dependence reduces to (m_a, n) as explained above. The application of the generalized axion-model approach to the hypothetical minicluster distribution of the Milky Way in point 7. will be presented in Subsec. 3.6.2. Note also that the entire range of steps 1. to 7. in the above enumeration is displayed in green panels in the schematic representation of Fig. A.1.

Before moving on to galactic minicluster properties, we continue by plotting our results for $T_{\rm osc}$ and f_a in Fig. 3.6. As seen in the left panel of Fig. 3.6, the oscillation temperature decreases

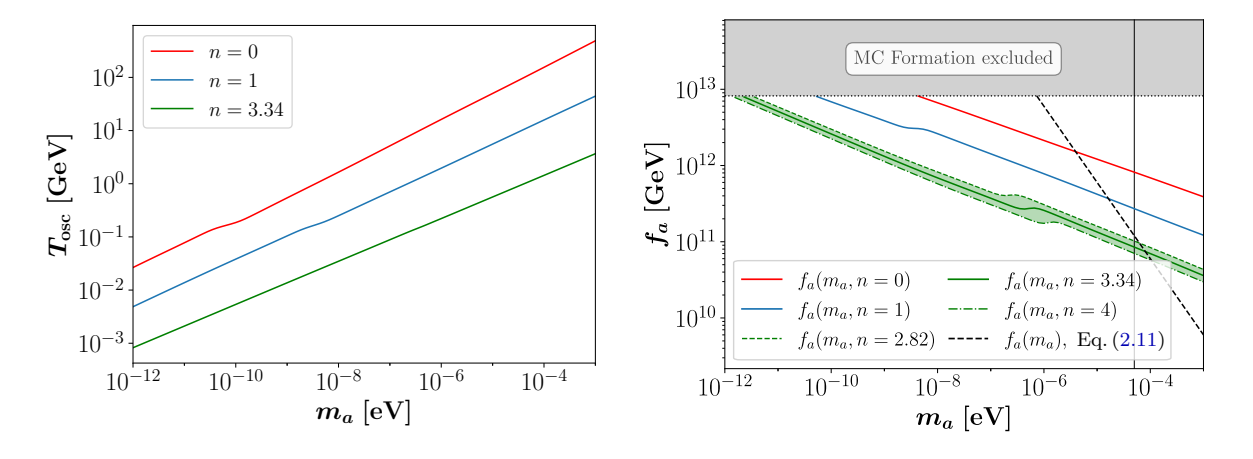


Figure 3.6: Left: Oscillation temperature $T_{\rm osc}$ defining the onset of axion oscillations with $3H(T_{\rm osc}) = m_a(T_{\rm osc})$ in Eq. (2.40) obtained from the above procedure following Ref. [58] and Subsec. 2.5.2. Right: decay constant $f_a(m_a,n)$ fixed by matching the relic abundance in Eq. (2.64) at different n in colored lines, compared to the black dashed QCD axion scaling from Eq. (2.11). The green band and lines correspond to different predictions for the temperature index n of the QCD axion [54, 55, 189]. The gray region is excluded by inflationary constraints on the tensor-to-scalar ratio $f_a < 8.2 \cdot 10^{12} \, \text{GeV}$ [58, 190].

with stronger temperature dependence n and for smaller axion masses m_a . This is related to the fact that the temperature of equality with $3H(T)=m_a(T)$ decreases with smaller $m_a(T)$, which in turn decreases both for smaller $m_a=m_{a,0}$ and larger n for $T>\Lambda_0$ in Eq. (2.34). In other words, the axion mass switches on with decreasing temperature and becomes relevant, $m_{a,0}(T/\Lambda_0)^{-n} \sim H(T)$, earlier for larger zero-temperature mass $m_{a,0}$ and smaller temperature-dependence n. For the QCD-axion-like case with $m_a \simeq 50 \,\mu\text{eV}$ and $n \simeq 3.34$ in green, we obtain

 $T_{\rm osc} \sim 1 \, {\rm GeV}$ in agreement with the literature [41, 42, 54].

Additional information is contained in the right panel of Fig. 3.6, where the decay constants giving $\Omega_a^{\rm tot}h^2=0.12$ are shown. To demonstrate the underlying uncertainty in the determination of the temperature index n, we also show the decay constants for n=2.82 obtained from Ref.s [41, 189] and n=4 from the dilute instanton gas model in Ref.s [41, 189]. The spread in f_a arising from different values of n=2.82,3.34,4 is large, but the representative value of n=3.34 from Ref.s [41, 54] lies in between. Our choice of n=3.34 hence provides an intermediate estimate on the possible range of the QCD axion temperature dependence.

We also depict the QCD axion m_a - f_a relation from Eq. (2.11) in black dashed lines and indicate its approximate agreement with axion-like models for $m_a \sim 100 \,\mu\text{eV}$ and $n \simeq 3.34$ by the solid vertical line. For n=3.34, the QCD axion mass lies in the range $50 \,\mu\text{eV} \lesssim m_a \lesssim 200 \,\mu\text{eV}$ [58], where uncertainties in the determination of Ω_a^{tot} (and more specifically α_{dec} and c_n , see also Sec. 2.5) have been taken into account. Since the analysis in this work focuses on the observational prospects of current and next-generation radio-telescopes such as SKA-mid ranging from 350 MHz to 14 GHz, we choose the lower bound of $m_a \approx 50 \,\mu\text{eV}$ for the QCD axion, which amounts to roughly 12 GHz and $f_a \simeq 10^{12} \,\text{GeV}$ [191].

The gray shaded area in Fig. 3.6 is of specific importance for the minicluster scenario considered in this chapter. It is derived from constraints on the tensor-to-scalar ratio r < 0.07 of the CMB [190]. In an inflationary scenario, this ratio constrains the Hubble scale and thus the temperature Eq. (2.35) of the inflationary universe, as demonstrated in Ref.s [192, 193]. To be consistent with the post-inflationary (PQ) scenario assumed in this work (see Sec. 2.5), the symmetry breaking at $T \simeq f_a$ has to occur below $T = f_a < 8.2 \cdot 10^{12} \,\text{GeV}$ [58]. This condition defines the boundary of the gray-shaded area indicated by the black dotted line in the right panel of Fig. 3.6.

To summarize, the post-inflationary constraint $f_a < 8.2 \cdot 10^{12} \,\text{GeV}$ truncates the MC properties \mathcal{M}_0 at some low-mass value of m_a , which depends on the temperature index n. For the remainder of this work, we will omit the gray-shaded region indicating the cutoff in f_a for simplicity. We continue our application to general axion-like models by moving on to point 5 in the above enumeration, i.e. to the determination of $\mathcal{M}_0(m_a, n)$ ⁴.

The characteristic minicluster masses from Eq. (3.25) obtained from $T_{\rm osc}$, f_a and (m_a, n) in Fig. 3.6 are plotted in Fig. 3.7, which shows \mathcal{M}_0 for temperature-independent axions in red and for n=1, n=3.34 in blue and green. The scaling of \mathcal{M}_0 in Fig. 3.7 shows both an increase with decreasing axion mass m_a and an increase with larger n. This can be understood by means of the scaling of $k_{\rm osc}$ in Eq. (3.48) with $T_{\rm osc}$: Considering radiation domination $H(T_{\rm osc}) \sim H_0 \sqrt{\Omega_{\rm rad} a(T_{\rm osc})^{-4}} \propto T_{\rm osc}^2$ and neglecting the change of $g_{\star,S}(T)$ for simplicity, we obtain $k_{\rm osc} \propto H(T_{\rm osc})/T_{\rm osc} \propto T_{\rm osc}$ from Eq. (3.48). Applying this scaling to \mathcal{M}_0 in Eq. (3.25) yields

$$\mathcal{M}_0 \propto k_{\rm osc}^{-3} \propto T_{\rm osc}^3 H(T_{\rm osc})^{-3} \propto T_{\rm osc}^{-3},$$
 (3.49)

which roughly coincides with the scaling of T_{osc} and \mathcal{M}_0 in Fig. 3.6 and Fig. 3.7 (and also with that of k_{osc} obtained in Ref. [58]).

The precise scaling and shape of $\mathcal{M}_0(m_a, n)$ in Fig. 3.7 is caused by the temperature dependence of H(T) in Eq. (2.51), the relativistic degrees of freedom $g_{\star,R}(T)$ in Eq. (2.51) and the

⁴The interested reader may find the results for step 4 and $k_{\rm osc}$ depicted in Ref. [58].

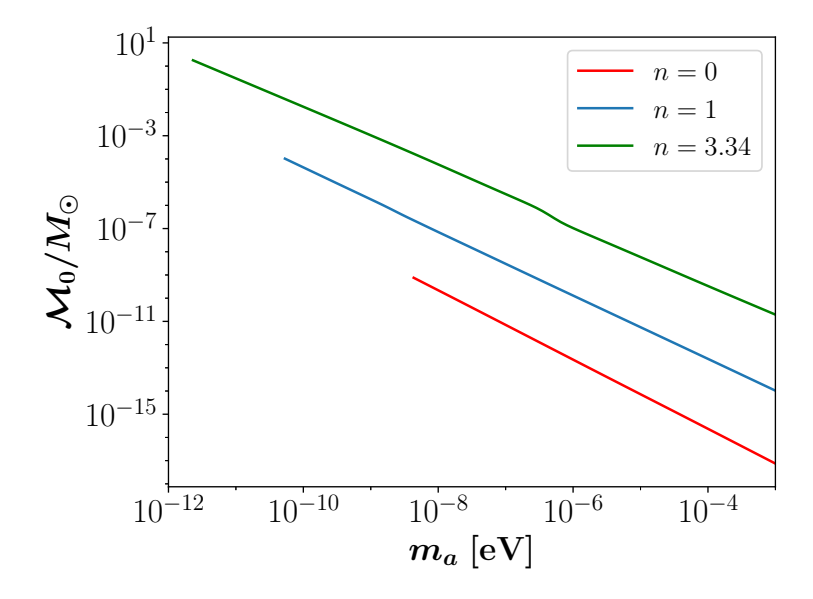


Figure 3.7: Characteristic minicluster mass $\mathcal{M}_0(m_a, n)$ as a function of axion mass m_a and its (colored) temperature dependence n, reproduced from the procedure in Ref. [58], Sec. 3.2 and taken from Ref. [1]. In this plot and in the following figures, the truncation of axion models m_a , n at low axion masses m_a arises from the condition $f_a < 8.2 \cdot 10^{12} \,\text{GeV}$ as shown in Fig. 3.6.

temperature evolution of the axion mass in Eq. (2.34). In the case of temperature-independent axions with n = 0, the characteristic mass can be shown to agree with [58]

$$\mathcal{M}_0(m_a, n = 0) \approx 6.5 \cdot 10^{-16} M_{\odot} \left(\frac{m_a}{50 \,\mu\text{eV}}\right)^{-3/2} \left(\frac{\Omega_c h^2}{0.12}\right) \left(\frac{\Omega_m}{0.32}\right)^{-3/4} \left(\frac{1 + z_{\text{eq}}}{3403}\right)^{3/4}, \quad (3.50)$$

where the scaling $\mathcal{M}_0 \propto m_a^{-3/2}$ will become important at a later point. For n=1,3.34 the scaling of \mathcal{M}_0 is slightly changed due to the different temperature evolution of the axion mass. Nevertheless, even for n>0 the scaling $\mathcal{M}_0 \propto m_a^{-3/2}$ from Eq. (3.50) remains roughly valid. With the characteristic minicluster masses in Fig. 3.7 at hand, the next step to apply the linear growth predictions from Ref. [58] using the MCMF parametrization from Subsec. 3.5.2. This will be done together with the normalization to the galactic DM abundance in the next section.

3.6.2 Generalized Minicluster Mass Distributions

We calculate the MCMF parametrization from Subsec. 3.5.2 for axion miniclusters in the Milky Way dark matter halo using both low-mass cutoffs $\mathcal{M}_{J,\text{min}}$, $\mathcal{M}_{0,\text{min}}$ from Eq. (3.45), Eq. (3.47). This combined treatment of the possible low- \mathcal{M} cutoffs allows us to estimate the phenomenological impact of the MCMF cutoff dependence from Subsec. 3.5.2 in the following chapters. Since also the final slope of the MCMF is subject to open debate, we will assume the Press-Schechter power-law index $\alpha = -1/2$ from Subsec. 3.5.2 unless stated otherwise and consider the case $\alpha = -0.7$ separately later. In the most general way, we can define the normalized minicluster

mass function as

$$\frac{dn}{d\ln\mathcal{M}} = C_n \left(\frac{\mathcal{M}}{\mathcal{M}_{\min}}\right)^{\alpha},\tag{3.51}$$

where $\mathcal{M}_{\min} = \{\mathcal{M}_{J,\min}, \mathcal{M}_{0,\min}\}$ takes the role of a reference MC mass and C_n is a normalization constant to be determined in the following. For simplicity, we will assume that the mass distribution of miniclusters is independent of the galactocentric radial coordinate r.

The total mass of minclusters can then be calculated from Eq. (3.51) by integrating over the MC mass density $dm/d\mathcal{M} = \mathcal{M}dn/d\mathcal{M}$. Assuming a spherically symmetric Milky Way volume $V_{\rm MW} = 4\pi/(3R_{\rm MW}^3)$ with radius $R_{\rm MW} = R_{200} = 237\,\rm kpc$ following the mass models in Ref. [194], we obtain the total MC mass

$$\mathcal{M}_{\text{tot}} = V_{\text{MW}} \int_{\mathcal{M}_{\text{min}}}^{\mathcal{M}_{\text{max}}} d\mathcal{M} C_n \left(\frac{\mathcal{M}}{\mathcal{M}_{\text{min}}} \right)^{\alpha} = V_{\text{MW}} \mathcal{M}_{\text{min}} \frac{C_n}{\alpha + 1} \left[\left(\frac{\mathcal{M}_{\text{max}}}{\mathcal{M}_{\text{min}}} \right)^{\alpha + 1} - 1 \right] . \tag{3.52}$$

The normalization constant C_n from Eq. (3.52) is found by setting $\mathcal{M}_{\text{tot}} \stackrel{!}{=} f_{\text{mc}} \mathcal{M}_{\text{MW}}$, where $f_{\text{mc}} \simeq 0.75$ is equal to the fraction of galactic dark matter contained in miniclusters [30] and $\mathcal{M}_{\text{MW}} = 1.43 \cdot 10^{12} \, M_{\odot}$ is the mass of the Milky Way DM halo taken from Ref. [195]. Using this normalization, the corresponding total number of galactic miniclusters

$$\mathcal{N}_{\text{tot}} = V_{\text{MW}} \int_{\mathcal{M}_{\text{min}}}^{\mathcal{M}_{\text{max}}} d\mathcal{M} \frac{C_n}{\mathcal{M}} \left(\frac{\mathcal{M}}{\mathcal{M}_{\text{min}}} \right)^{\alpha} = V_{\text{MW}} \frac{C_n}{\alpha} \left[\left(\frac{\mathcal{M}_{\text{max}}}{\mathcal{M}_{\text{min}}} \right)^{\alpha} - 1 \right]$$
(3.53)

can be found by integrating over the number density $dn/d\mathcal{M}$. We determine the normalization constant C_n together with the total MC number \mathcal{N}_{tot} for every axion model (m_a, n) and for both cutoffs of the MCMF, i.e. for $\mathcal{M}_{\text{min}} = \mathcal{M}_{0,\text{min}}$ and $\mathcal{M}_{\text{min}} = \mathcal{M}_{J,\text{min}}$. The resulting number of miniclusters is strongly model-dependent and lies in the range $10^{18} \leq \mathcal{N}_{\text{tot}} \leq 10^{26}$ for the QCD axion mass $m_a = 50 \,\mu\text{eV}$ as shown in Fig. C.1.

We show the resulting MCMF obtained for the QCD axion mass $m_a = 50 \,\mu\text{eV}$ and $n = \{0, 1, 3.34\}$ in Fig. 3.8. The different shades and colored lines in Fig. 3.8 refer to the different mass cutoffs of the MCMF, which truncate the MC mass range through \mathcal{M}_{max} in Eq. (3.46), through $\mathcal{M}_{\text{min}} = \mathcal{M}_{0,\text{min}}$ in solid lines and through $\mathcal{M}_{\text{min}} = \mathcal{M}_{J,\text{min}}$ in dashed colored lines. Dotted colored lines and shaded regions indicate the \mathcal{M}_0 -cutoff at $\mathcal{M}_{0,\text{min}} = \mathcal{M}_0/25$. Note that the dashed Jeans mass cutoff $\mathcal{M}_{J,\text{min}}$ in Eq. (3.45) is temperature-independent, while the value of \mathcal{M}_{max} in Eq. (3.46) is directly proportional to \mathcal{M}_0 . Accordingly, the spread of the minicluster mass range in Fig. 3.8 increases with larger \mathcal{M}_0 and specifically for larger n as seen in Fig. 3.7. More importantly, we highlight several fundamental features of the MCMF that are crucial for understanding the properties of galactic axion small-scale structure: First, the MCMF peaks around the low- \mathcal{M} cutoff which means that the MC number and typical mass will be subject to large uncertainty arising from the cutoff dependence discussed in Subsec. 3.5.2. Furthermore, the majority of miniclusters will exhibit masses close to the low- \mathcal{M} cutoff $\mathcal{M} \sim \mathcal{M}_{\text{min}}$.

Secondly, Fig. 3.8 also demonstrates that the intermediate- to high-mass component $\mathcal{M}_0 \lesssim \mathcal{M} \lesssim \mathcal{M}_{max}$ of the MCMF is essentially insensitive to the low-mass cutoffs and to the normalization in Eq. (3.52). The reason for this is the fact that a large majority of the mass relevant for the normalization of the MCMF is contained in the high-mass tail $\mathcal{M} \gg \mathcal{M}_0$. The total number of miniclusters Eq. (3.53) on the other hand is very sensitive to the low-mass cutoff as can be

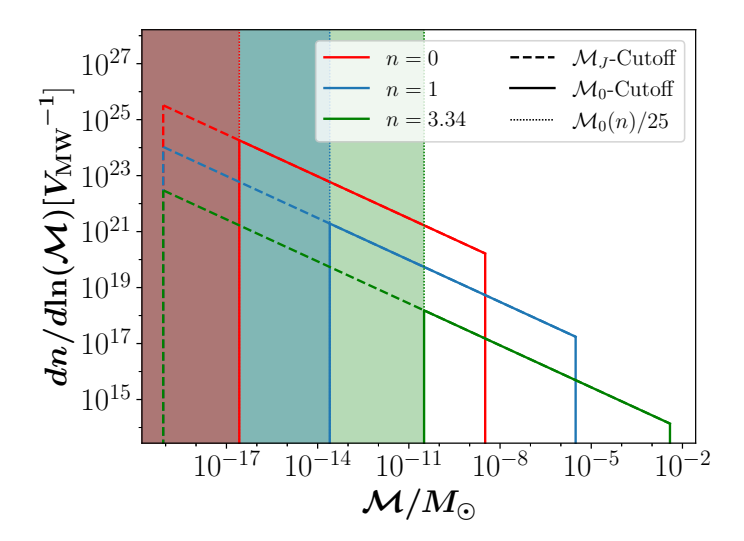


Figure 3.8: MCMF per Milky Way volume obtained using the parametrization from Subsec. 3.5.2 for $m_a = 50 \,\mu\text{eV}$, $\alpha = -1/2$ and different n = 0, 1, 3.34 indicated by colored lines, taken from Ref. [1]. The shaded regions and dotted colored lines denote the low-mass cutoffs given by $\mathcal{M}_{0,\text{min}} = \mathcal{M}_0(n)/25$. Solid lines show the MCMF after applying the $\mathcal{M}_0(n)/25$ -cutoffs while dashed lines display the MCMF with the \mathcal{M}_J -cutoff from Eq. (3.45). Taken from Ref. [1].

understood from Eq. (3.53) and Fig. C.1.

Independent of the low-mass cutoff, large MC masses are predicted in both cases of \mathcal{M}_{\min} , especially for larger values of n. This observation has important implications for DM searches, which we discuss in detail in Chap. 5, Chap. 6 and Chap. 7.

3.6.3 Tidal Disruption in stellar Encounters

In the previous section we have constrained the mass distribution of galactic miniclusters. While we assumed that the MC mass \mathcal{M} and the galactocentric radial coordinate r are independent of each other, we have to consider another effect, which constrains the spatial distribution of axion miniclusters in the Milky Way. This additional effect on the galactic MCMF arises from close encounters between the gravitational fields of stars with $M \sim M_{\odot}$ and the much lighter miniclusters with $\mathcal{M} \ll M_{\odot}$. Owing to the stellar density distribution and the NFW distribution of the dark matter, these events occur most numerously in the vicinity of the galactic center $r \lesssim 1 \,\mathrm{kpc}$. The gravitational dynamics and present-day implications of the tidal interactions of miniclusters with stellar and galactic fields (from the disc and DM halo) have been investigated by numerous studies [42, 149, 150, 188, 196–198].

In this work we employ a simplified approach to model the radial and Φ -dependence of the tidal MC disruption based on the results of Ref.s [188, 197] and Ref. [196] respectively. More precisely we treat the set (\mathcal{M}, Φ, r) of minicluster parameters as independent and consider the r- and Φ -dependence of the resulting survival probabilities separately. Starting with the former, the spatially dependent tidal interactions between stars and miniclusters with typical densities $\Phi \sim 1$ at position r introduce an effective minicluster survival probability $\mathcal{P}_{\text{surv}}(R)$ over long times $t \sim t_H$, as shown in Fig. 3.9 from Ref. [188]. The two colored lines in Fig. 3.9 show two

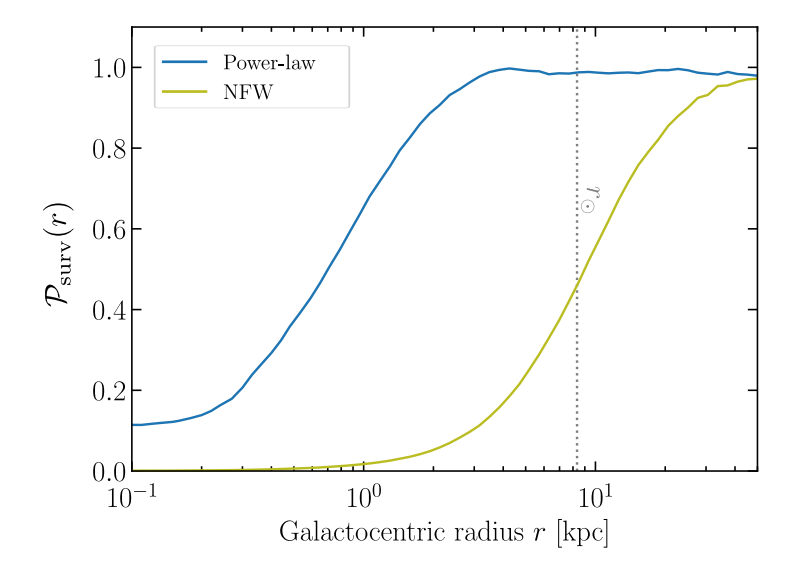


Figure 3.9: Survival probability of galactic miniclusters as a function of the galactocentric radius r, taken from Ref. [188]. The vertical dashed line marks the position of the solar system, while green and blue colors indicate different minicluster profiles.

different minicluster density profiles that were considered in Ref. [188]: First a power-law profile $\rho_{\rm mc} \propto (R_s/r)^{9/4}$ truncated at the spherical radius \mathcal{R} from Eq. (3.24) and secondly the NFW profile from Eq. (A.1). In our analysis, we apply the results from the power-law profile since it provides the same minicluster size \mathcal{R} as Eq. (3.24), but with a more realistic, non-homogeneous density profile.

As can be seen by the blue curve in Fig. 3.9, the survival probability for MCs with a power-law profile is roughly equal to 1 for large radii $r \gtrsim 3\,\mathrm{kpc}$. Below $r \simeq 2\,\mathrm{kpc}$, $\mathcal{P}_{\mathrm{surv}}$ drops rapidly until reaching a $\sim 10\%$ level at $r \sim 0.1\,\mathrm{kpc}$. We use the turnaround point where $\mathcal{P}_{\mathrm{surv}} \simeq 0.5$ at $R_{\mathrm{surv}} \simeq 1\,\mathrm{kpc}$ as a benchmark for our cutoff and assume that an order one fraction of the miniclusters at $r \geq 1\,\mathrm{kpc}$ survive, while all objects below this threshold with $r < 1\,\mathrm{kpc}$ are assumed to be disrupted. Using this approach, the NFW distribution of miniclusters in the Milky Way halo is truncated below

$$r \leq R_{\rm surv} \simeq 1 \,{\rm kpc} \,.$$
 (3.54)

Since this amounts to neglecting the $\sim 10\%$ component of the MCMF close to the galactic center $r < 1\,\mathrm{kpc}$, our approach can be seen as a simplified but conservative modeling of the effects of stellar disruption on miniclusters with a power-law profile and radius \mathcal{R} .

Comparing the results with the green curve and NFW profile miniclusters in Fig. 3.9, the truncation of the MCMF would be at a much higher radial coordinate giving roughly $r_{\rm NFW} \sim R_{\odot} \simeq 8.3\,\rm kpc$. While this effect could significantly lower the predicted event and signal rates in Chap. 5, Chap. 6 and Chap. 7, there is currently no stringent evidence for the NFW profile to apply universally. In a recent study performed in Ref. [175], the authors showed that while miniclusters form with NFW-like density profiles initially, there is evidence that the inner density profiles scale like $\rho_{\rm mc} \sim r^{-2}$ at later times. This result is comparable to the scaling of $\rho_{\rm mc} \sim r^{-9/4}$ assumed for the power-law profile in Ref. [188], and hence provides further motivation for our

choice of the minicluster density profile.

Moving on to the Φ -dependence of the minicluster survival probability, $\mathcal{P}_{\text{surv}}(\Phi)$, we briefly recall the results from Ref. [196] in the following. The authors of Ref. [196] used a superposition of energy eigenstates and the WKB approximation [199, 200] to describe gravitationally bound miniclusters and their interaction with external fields. Ref. [196] estimated the survival fraction of miniclusters in an NFW dark matter halo interacting with the stellar distribution of the Milky Way over cosmic timescales up to $t \sim 10 \,\text{Gyr}$. According to their calculations, stellar disruption at the solar position $r = R_{\odot}$ affects the distribution of the initial overdensity parameter $\Phi \in (0, 10^4]$ according to

$$\mathcal{P}_{\text{surv}}(\Phi) = \frac{1}{2} \left[1 + \tanh\left(\frac{\log_{10}\tilde{\rho}_{\text{mc}}(\Phi) - 4.25}{2}\right) \right], \qquad (3.55)$$

$$\tilde{\rho}_{\rm mc}(\Phi) = \frac{\rho_{\rm mc}(\Phi)}{1M_{\odot} \rm pc^{-3}},\tag{3.56}$$

which is given in terms of the dimensionless minicluster density $\tilde{\rho}_{mc}$ derived from $\rho_{mc}(\Phi)$ in Eq. (3.23) [196]. We demonstrate in Fig. 3.10 that Eq. (3.56) effectively constrains the density

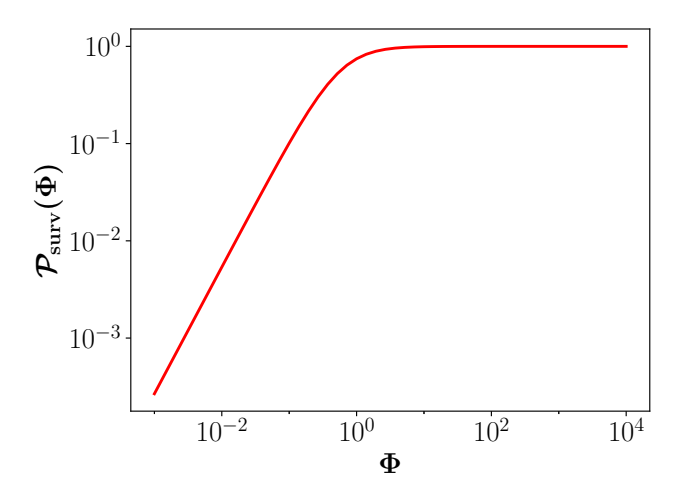


Figure 3.10: Survival probability of MCs as a function of the overdensity parameter Φ from Eq. (3.56), taken from Ref. [2] and reproduced from the results of Ref. [196].

distribution of present-day $t \sim 10 \, \text{Gyr}$ galactic miniclusters to $\Phi \gtrsim 0.5$.

We use the full functional form of $\mathcal{P}_{\text{surv}}(\Phi)$ in our subsequent calculations and extend the result from Ref. [196] obtained at $r \sim R_{\odot}$ to the entire range $r \geq R_{\text{surv}}$ from Eq. (3.54). Improved results could be obtained by investigating the dependence of $\mathcal{P}_{\text{surv}}(\Phi)$ on the three-dimensional galactic cylindrical coordinates ϱ, z, φ . Since such an extensive analysis is beyond the scope of our simple estimations, we will deal with the uncertainties from the combined r- and Φ -dependence of stellar disruption by overestimating the effects from Eq. (3.56) at $r > R_{\odot}$ and possibly underestimating them at smaller radii $R_{\text{surv}} \leq r < R_{\odot}$. On the technical side, our numerical calculations performed in Chap. 5 and following can easily be modified by incorporating improved modeling of galactic minicluster disruption compared to Eq. (3.54) and Eq. (3.56) - once such results become available.

3.7 Core-Halo Relation

The last important property of gravitationally bound miniclusters to be mentioned in this chapter is the formation of a dense solitonic core at the center of a given minicluster, as observed in Ref.s [167–169, 172, 201–206]. The dynamics and evolution of these solitonic cores will be explored in detail in Chap. 4, whereas this section motivates the further investigation of their properties by means of the MCMF and the evolution of their host miniclusters. An example for a composite minicluster-core system is shown in Fig. 3.11, which was taken from the simulations of Ref. [167] for an axion mass $m_a = 10^{-8} \,\text{eV}$ and a box size $L = 0.356 \,\text{pc/h}$. The

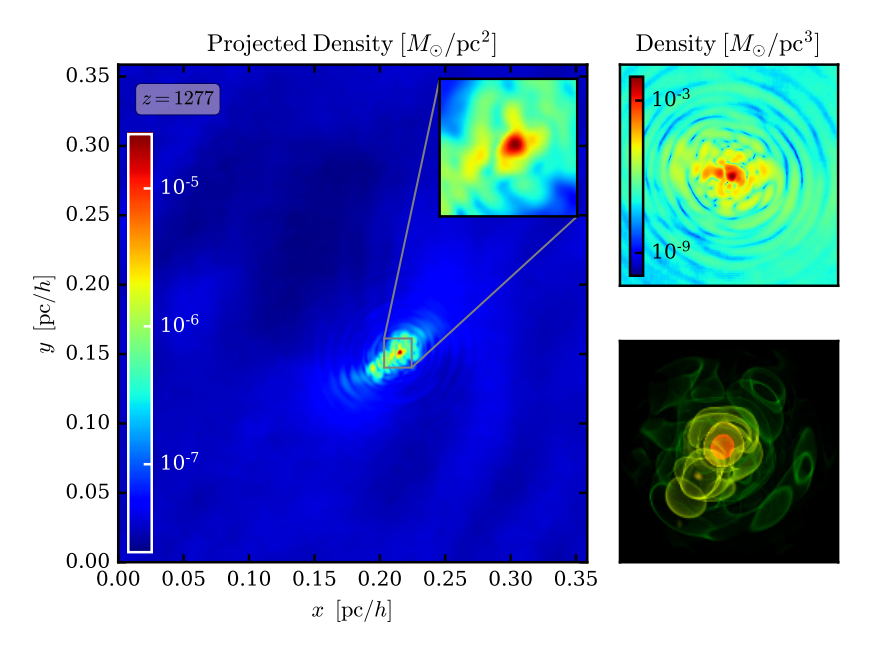


Figure 3.11: Numerical simulation of an axion minicluster with a solitonic core formed around $z \sim z_{\rm eq}$ and shown at z=1277 for $m_a=10^{-8}\,{\rm eV},~\lambda=0$ taken from Ref. [167]. The matter density is given in $M_{\odot}\,{\rm pc}^{-2}$, for a soliton mass $M_{\star}=5.04\cdot 10^{-12}\,M_{\odot}$ and a total mass of $\mathcal{M}=5.98\cdot 10^{-11}\,M_{\odot}$.

authors of Ref. [167] evolved the Schrödinger-Poisson system in an expanding universe to trace the redshift-dependent formation of axion minicluster cores, finding typical formation redshifts $z \sim z_{\rm eq}$ with the example in Fig. 3.11 shown at z=1277. As can be seen by the color grading in Fig. 3.11, the axion star core in red is much denser than the yellow to green minicluster background in which it is embedded. The granular structure of the minicluster is shown in the bottom right panel of Fig. 3.11. It arises from wave interference of the self-gravitating system forming granular overdensities (see also the simulations in Sec. 4.3 and App. B).

Based on the simulations of several composite systems in Ref. [167] with the solitonic cores forming around $z \sim z_{\rm eq}$, we will assume for simplicity that axion stars appear together with their host miniclusters in a virialized state at the collapse redshift $z_c = z_{\rm eq}$. Even more important for this work is the fact that the mass of the red solitonic core in Fig. 3.11 can be related to the total mass (i.e. including that of the core) of its host minicluster in green, as was first shown in the simulations of Ref. [169]. Since the corresponding mass relation was first derived in simulations of ultra-light dark matter with $m_a \sim 10^{-22} \, {\rm eV}$ and $\mathcal{O}({\rm kpc})$ halo sizes, it is commonly referred

to as the *core-halo (mass) relation*. The axion-star core mass M_{\star} predicted by the core-halo relation

$$M_{\star}(z) = \mathcal{M}_{h,\min}(z) \left[\frac{\mathcal{M}}{\mathcal{M}_{h,\min}(z)} \right]^{1/3}$$
(3.57)

depends on the axion mass m_a and the redshift of formation z through the redshift-dependent minimum halo mass

$$\mathcal{M}_{h,\min}(z) = 2.36 \cdot 10^{-16} M_{\odot} \left(\frac{1+z}{1+z_{\rm eq}} \right)^{3/4} \left[\frac{\zeta(z)}{\zeta(z_{\rm eq})} \right]^{1/4} \left(\frac{m_a}{50 \,\mu\text{eV}} \right)^{-3/2} , \quad (3.58)$$

which is defined by requiring $M_{\star} = \mathcal{M}$. Physically, the minimum halo mass $\mathcal{M}_{h,\min}(z)$ represents the lightest halo or minicluster mass, at which the formation of a composite core-halo system with $\mathcal{M} \geq M_{\star}$ can occur at a given redshift. Note also that the factor 1/4 from the original definition in Ref. [169] was dropped here, since we use a different definition of the soliton mass compared to the original authors of Ref. [169].

The quantity $\zeta(z)$ in Eq. (3.58) is the overdensity at virialization [207]

$$\zeta(z) \approx \frac{18\pi^2 + 82[\Omega_m(z) - 1] - 39[\Omega_m(z) - 1]^2}{\Omega_m(z)}$$
(3.59)

in a flat Λ CDM cosmology, which sets the redshift-dependent halo mass according to

$$\mathcal{M} = \frac{4\pi}{3} r_{\text{vir}}^3 \zeta(z) \bar{\rho}_a \,, \tag{3.60}$$

with the comoving virial radius r_{vir} [169]. The matter density parameter

$$\Omega_m(z) = \frac{\Omega_{m,0}(1+z)^3}{\Omega_{m,0}(1+z)^3 + \Omega_{r,0}(1+z)^4 + \Omega_{\Lambda,0}}$$
(3.61)

in Eq. (3.59) depends on the redshift z, which gives $\zeta(z_{\rm eq}) \sim 180$ for our considerations and Planck [14, 167] parameters $\Omega_{m,0} = 0.3089$, $\Omega_{r,0} = 8.486 \cdot 10^{-5}$ and $\Omega_{\Lambda,0} = 0.7$.

To summarize, the results from Ref. [169] established a relation between the mass of the solitonic core and the mass of its host halo, for ultra-light dark matter with $m_a \sim 10^{-22}\,\mathrm{eV}$. Additionally, the authors of Ref. [167] showed that the corresponding mass scaling relation Eq. (3.57) remains valid also for axion miniclusters with masses $m_a = 10^{-8}\,\mathrm{eV}$ and a formation redshift of order $z \sim z_{\rm eq}$, as depicted in Fig. 3.11. Simulations involving composite systems with larger axion masses $m_a \geq 10^{-8}$ are currently not feasible due to numerical limitations in grid resolution and computational performance. However from the scaling symmetry Eq. (3.16) of solutions to the GPP and SP systems Eq. (3.11) and Eq. (3.14) it is expected, that the same scaling which applies in the range $10^{-23}\,\mathrm{eV} \leq m_a \leq 10^{-8}\,\mathrm{eV}$ remains valid also for larger sub-eV masses. This scaling argument motivates the use of the core-halo relation for larger axion masses, like the QCD axion mass $m_a = 50\,\mu\mathrm{eV}$ assumed in this work.

We also emphasize that both the results from Ref. [167] and Ref. [169] were obtained for the Schrödinger-Poisson system, i.e. for $\lambda=0$, which is a good approximation for the gravitationally dominated evolution of the large and dilute host miniclusters. However as we will see in the next chapter, the self-interaction of the axion becomes important when considering the balance of forces that ensures the stability of axion star cores in Sec. 4.1. This complication motivates us to further investigate the validity of the core-halo relation in Eq. (3.57) for axion stars with weak attractive self-interactions in Sec. 4.6.

Axion Stars 4

In the previous chapters we have followed the evolution of small-scale axion structure from the symmetry breaking at $T \sim f_a$ in the early universe, over the production of non-relativistic dark matter at $T \sim T_{\rm osc}$ down to the present-day minicluster distribution of the Milky Way DM halo. These predictions can finally be used together with the core-halo relation from Sec. 3.7 to infer the properties and mass distributions of the most overdense component of axion small-scale structure: so-called *axion stars*, which have been studied extensively in the literature [23, 26, 162, 164, 167, 172, 174, 208–229].

We introduce axion stars as the stationary solutions to the GPP system focusing on the case of weak attractive self-interactions $\lambda < 0$ in Sec. 4.1. The formation and mass growth of axion stars are examined by means of numerical simulations in Sec. 4.2 and Sec. 4.3 respectively. Over time, the continuous accretion of the axion star core from its surroundings can trigger one of two instabilities leading either to the resonant conversion of axions into radio photons in Sec. 4.4 or to the relativistic emission of axion dark matter as shown in Sec. 4.5. Lastly we validate the use of the $\lambda = 0$ core-halo relation for dilute axion stars in Sec. 4.6 and derive the first estimates of the galactic axion star mass distribution from the properties of their host miniclusters in Sec. 4.7.

In terms of the schematic representation in Fig. A.1, this chapter provides the basis for axion star signatures to be investigated in Chap.s 5 to 7 and describes the derivation of the axion star mass distribution shown by the blue shaded panel in Fig. A.1.

4.1 Mass-Radius Relation

In this section, we will extremize the total energy of the system to introduce axion stars as the stationary solutions to the GPP equations, Eq. (3.11) and Eq. (3.12). Depending on the context and on the self-interaction parameter λ , these stationary solutions are generally termed solitons, bose stars ($\lambda = 0$) or ALP/axion stars (typically $\lambda < 0$, like for the QCD axion). As was shown in Ref.s [25, 26, 158, 159, 209, 210, 212, 230–232], the strength of the self-interaction constant λ is crucial to determine the possible range of soliton solutions. While the QCD axion has $\lambda = -c_{\lambda}m_a^2/f_a^2$ set by the decay constant f_a in Eq. (2.11), ALPs can have arbitrary combinations of the parameters m_a , f_a and λ . In this work, we fix $\lambda = -m_a^2/f_a^2$ with $c_{\lambda} = 1$ for ALPs and use the correct dark matter abundance $\Omega_a h^2 = 0.12$ to find f_a as summarized in Subsec. 3.6.1.

Our derivation of the properties of axion stars is closely based on the approach applied in Ref.s [1, 33, 158]. The first step in finding the soliton solutions to the GPP system Eq. (3.11), Eq. (3.12) is to assume an analytic expression for the radially symmetric soliton density profile $\rho_{\star}(r) = m_a |\psi(r)|^2$. There exist a range of choices for the profile ρ_{\star} , many of which were analyzed and compared to numerical ground state solutions in Ref. [231]. Importantly, the

different analytical profiles show $\mathcal{O}(1)$ deviations, which are well within uncertainties arising from the linear growth of axion DM structure, compared to the exact numerical solutions of the GPP system.

Similar to Ref.s [158, 159], we employ a *Gaussian ansatz* for the spherically symmetric wave function

$$\rho_{\star}(r) \equiv m_a |\psi(r)|^2 = \left(\frac{M_{\star}}{\pi^{3/2} R_{\star}^3}\right) e^{-\frac{r^2}{R_{\star}^2}} \tag{4.1}$$

defined in terms of the axion star mass M_{\star} , radius R_{\star} and the radial coordinate r [159]. We choose the Gaussian profile for simplicity but keep our approach general by tracking the corresponding ansatz-specific coefficients $\alpha_{\rm kin}$, $\alpha_{\rm grav}$ and $\alpha_{\rm int}$, which will be introduced in the following. We also confirmed that the resulting soliton solutions predicted from the ansatz in Eq. (4.1) do not deviate significantly from the best-fit sech(x) profile obtained in Ref. [231].

Independent of the specific profile, we can express the Newtonian potential $\Phi_N(\boldsymbol{x},t)$ in Eq. (4.3) through the Green's function for the Poisson Eq. (3.12) [231], and write the different energy contributions of the non-relativistic axion star as

$$E_{\rm kin} = \frac{1}{2m_a} \int d^3x \, |\nabla \psi(\mathbf{x})|^2 = \alpha_{\rm kin} \frac{M_{\star}}{m_a^2 R_{\star}^2}, \tag{4.2}$$

$$E_{\text{grav}} = -\frac{m_a}{2} \int d^3x \, \Phi_N(\boldsymbol{x}) |\psi(\boldsymbol{x})|^2 = -\alpha_{\text{grav}} \frac{GM_{\star}^2}{R_{\star}}, \qquad (4.3)$$

$$E_{\rm int} = \frac{\lambda}{16m_a^2} \int d^3x \, |\psi(\mathbf{x})|^4 = -\alpha_{\rm int} \frac{|\lambda| M_{\star}^2}{m_a^4 R_{\star}^4} \,, \tag{4.4}$$

where the ansatz-specific coefficients

$$\alpha_{\rm kin} = \frac{3}{4}, \quad \alpha_{\rm grav} = \frac{1}{\sqrt{2\pi}}, \quad \alpha_{\rm int} = \frac{1}{32\pi\sqrt{2\pi}}$$
(4.5)

are calculated for the Gaussian profile in Eq. (4.1). The three different energy components in Eq. (4.2), Eq. (4.3) and Eq. (4.4) correspond to the three relevant forces in the system. Stability is ensured by an exact cancellation of the kinetic quantum pressure in Eq. (4.2) by the combined gravitational and attractive self-interactions. Within the Gaussian ansatz, the total energy of the axion star with mass M_{\star} and radius R_{\star} may be written as [159]

$$E_{\star,\text{tot}} = \frac{3M_{\star}}{4m_a^2 R_{\star}^2} - \frac{GM_{\star}^2}{\sqrt{2\pi}R_{\star}} - \frac{|\lambda|M_{\star}^2}{32\pi\sqrt{2\pi}m_a^4 R_{\star}^3}.$$
 (4.6)

Varying the energy $E_{\star,\text{tot}}$ in Eq. (4.6) with respect to the axion star radius R_{\star} , one can find the stationary solutions $\dot{R}_{\star} = \dot{M}_{\star} = 0$ of the GPP equations. Before doing so and for ease of computation, it is useful to transform the physical variables x, t, ψ, Φ_N onto dimensionless quantities of order unity by means of the rescaling [33]

$$x = \widetilde{x}/(\sqrt{G}m_a f_a), \qquad t = \widetilde{t}/(Gm_a f_a^2), \qquad (4.7)$$

$$\psi = \sqrt{Gm_a} f_a^2 \widetilde{\psi} , \qquad \Phi_N = G f_a^2 \widetilde{\Phi}_N , \qquad (4.8)$$

where the rescaled variables are indicated by a tilde and the spatial coordinates y, z transform just like x. The rescaling in Eq. (4.7), Eq. (4.8) excludes all factors G, m_a and λ from Eq. (3.11) and Eq. (3.12), which yields the rescaled Gross-Pitaesvskii-Poisson system

$$i\frac{\partial\widetilde{\psi}}{\partial\widetilde{t}} = -\frac{1}{2}\widetilde{\Delta}\widetilde{\psi} + \widetilde{\Phi}_N\widetilde{\psi} - \frac{1}{8}|\widetilde{\psi}|^2\widetilde{\psi}, \qquad (4.9)$$

$$\widetilde{\Delta}\widetilde{\Phi}_N = 4\pi |\widetilde{\psi}|^2 \,, \tag{4.10}$$

that is often used in numerical simulations (see also App. B). The dimensionless observables of the rescaled GPP system in Eq. (4.9), Eq. (4.10) are connected to their physical counterparts by the relations

$$\widetilde{N} = \frac{Gm_a^2}{f_a\sqrt{G}}N$$
 , $\widetilde{M} = \frac{Gm_a}{f_a\sqrt{G}}M$, (4.11)

$$\widetilde{E}_{\star,\text{tot}} = \frac{m_a}{f_a^3 \sqrt{G}} E_{\star,\text{tot}} \quad , \quad \widetilde{P} = \frac{1}{m_a f_a \sqrt{G}} P \,,$$
 (4.12)

where the total momentum of the system

$$P = \int d^3x \, \psi(\mathbf{x})^* \nabla \psi(\mathbf{x}) \tag{4.13}$$

is important for the numerical simulations to come in Sec. 4.2, Sec. 4.3 and App. B. Using Eq. (4.12) to rewrite the total energy of the axion star in Eq. (4.6) in its dimensionless and profile-independent form yields the total energy relation

$$\widetilde{E}_{\star, \text{tot}}(\widetilde{R}_{\star}) = \alpha_{\text{kin}} \frac{\widetilde{M}_{\star}}{\widetilde{R}_{\star}^{2}} - \alpha_{\text{grav}} \frac{\widetilde{M}_{\star}^{2}}{\widetilde{R}_{\star}} - \alpha_{\text{int}} \frac{\widetilde{M}_{\star}^{2}}{\widetilde{R}_{\star}^{3}}, \qquad (4.14)$$

which we extremize with respect to the star radius \widetilde{R}_{\star} to obtain the rescaled mass-radius relation of axion stars [158, 159]

$$\widetilde{R}_{\star} = \frac{\alpha_{\rm kin} \pm \sqrt{\alpha_{\rm kin}^2 - 3\alpha_{\rm int}\alpha_{\rm grav}\widetilde{M}_{\star}^2}}{\alpha_{\rm grav}\widetilde{M}_{\star}}.$$
(4.15)

The range of axion star radii given by the plus and minus sign in Eq. (4.15) separates the stationary solutions to the GPP system into two distinct branches: First, the *stable dilute branch*, characterized by solutions with a plus sign, and the *unstable dense branch* of axion stars indicated by the minus sign. We also show the resulting branches of the mass-radius relation Eq. (4.18) in Fig. 4.1, where stable soliton solutions are plotted in green and unstable profiles in red lines. The detailed contents of Fig. 4.1 are explained at the end of this section.

The critical point $M_{\star} = \alpha_{\rm kin}/\sqrt{3\alpha_{\rm int}\alpha_{\rm grav}}$ between the two branches constitutes what is commonly referred to as the maximum mass $M_{\star,\lambda}$ and minimum radius $R_{\star,\lambda}$ of stable, dilute axion stars. Scaling back to physical variables we obtain the critical quantities

$$M_{\star,\lambda} = \sqrt{\frac{3}{G}} \frac{2\pi f_a}{m_a} \qquad , \qquad R_{\star,\lambda} = \sqrt{\frac{3}{32\pi G}} \frac{1}{m_a f_a} \,,$$
 (4.16)

where we have entered the specific coefficients $\alpha_{\rm kin}$, $\alpha_{\rm int}$ and $\alpha_{\rm grav}$ of the Gaussian ansatz in Eq. (4.5). For later calculations involving the properties of axion stars we also express the mass-radius relation from Eq. (4.15) in physical units

$$M_{\star} = \frac{\sqrt{2\pi}R_{\star}}{\frac{2m_a^2G}{3}R_{\star}^2 + \frac{1}{16\pi f_z^2}},\tag{4.17}$$

$$R_{\star} = \frac{\alpha_{\rm kin}}{\alpha_{\rm grav} G m_a^2 M_{\star}} \pm \sqrt{\left(\frac{\alpha_{\rm kin}}{\alpha_{\rm grav} G m_a^2 M_{\star}}\right)^2 - \frac{3\alpha_{\rm int}}{\alpha_{\rm grav} G m_a^2 f_a^2}}.$$
 (4.18)

We emphasize that the mass and radius of the axion star M_{\star} , R_{\star} should not be interpreted as an absolute mass and size of the object, but rather as characteristic quantities. In order to determine the total mass enclosed within the soliton profile with boundary conditions $\rho_{\star}(r) \to 0$ for $r \to \infty$, one has to specify a *cutoff radius* at which to truncate the non-vanishing mass density $\rho_{\star}(r) > 0$ at finite r.

We define the cutoff radius $R_{\star,90}$ of the soliton profile as the value of r containing 90% of the total axion star mass, where $R_{\star,90} = 1.76796 R_{\star}$ for the Gaussian profile [158]. In the following sections, we will use $R_{\star,90}$ as the representative value for the physical soliton radius and drop the index '90' thereafter. The physical equivalents $M_{\star}(R_{\star,90})$, $R_{\star,90}$ of Eq. (4.17), Eq. (4.18) are indicated by the black star in Fig. 4.1.

Another important constraint to be considered for soliton solutions on the dense branch with $R_{\star} \leq R_{\star,\lambda}$ is the validity of the non-relativistic approximation inherent to the GPP system Eq. (3.11), Eq. (3.12). With decreasing $\widetilde{R}_{\star} \ll \widetilde{R}_{\star,\lambda} = \sqrt{3\alpha_{\rm int}/\alpha_{\rm grav}}$ in Eq. (4.15), the density of the soliton with $M_{\star} \propto R_{\star}$ increases as $\rho_{\star} \propto M_{\star}/R_{\star}^3 \propto 1/R_{\star}^2$. Eventually and at small enough R_{\star} , the soliton profile reaches a point, where the Taylor expansion in Eq. (3.4) breaks down and higher order terms in the axion potential need to be taken into account. This regime is governed by the relativistic Einstein-Klein-Gordon equations Eq. (3.2), Eq. (3.3), which were solved numerically in Ref. [35].

In the above relativistic limit, the invariance of the Lagrangian density under the transformation $\phi \longrightarrow \phi + 2\pi f_a$ is broken. From this one can infer the non-relativistic condition [231]

$$\frac{\phi_0}{2\pi f_a} = \frac{\psi_0}{\pi f_a \sqrt{2m_a}} = \sqrt{\frac{M_{\star}}{2\pi^{7/2} m_a^2 f_a^2 R_{\star}^3}} = \sqrt{\frac{G f_a^2 \widetilde{M}_{\star}}{2\pi^{7/2} \widetilde{R}_{\star}^3}} \ll 1 \tag{4.19}$$

for the mass M_{\star} and radius R_{\star} of the axion star and where $\psi_0 \equiv \psi(\boldsymbol{x}=0)$ was expressed from the profile in Eq. (4.1). Physically, Eq. (4.19) introduces a lower bound on the dense branch radius

$$R_{\star} \gg \left(\frac{M_{\star}}{2\pi^{7/2}m_a^2 f_a^2}\right)^{1/3}$$
, (4.20)

which we implement in any calculation involving the mass-radius relation of axion stars in the following. Solitons with radii below this bound violate the non-relativistic assumptions from Sec. 3.1 and can therefore not be modeled by the mass-radius relation Eq. (4.17) used in this thesis. The corresponding critical point for the validity of the GPP equations defined by Eq. (4.20) is indicated by the red dot in Fig. 4.1.

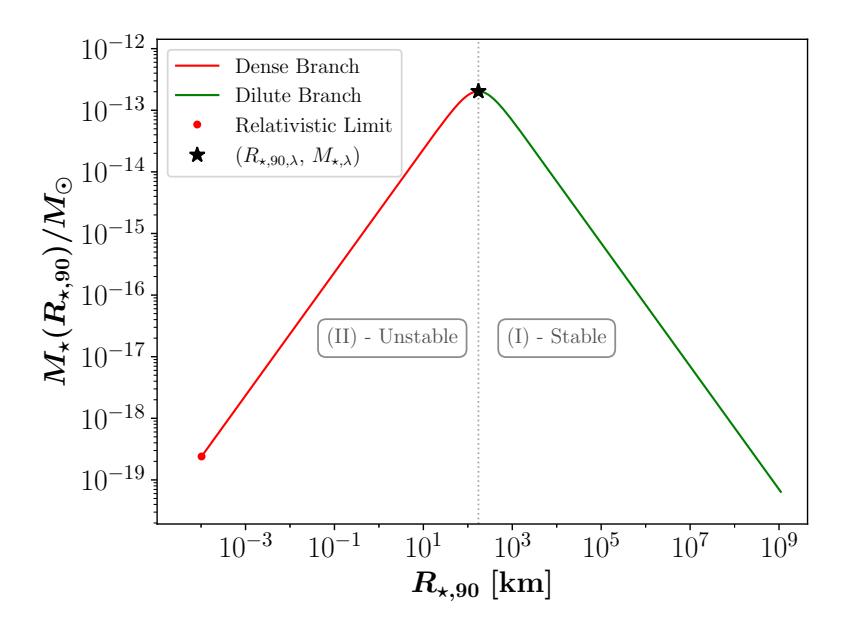


Figure 4.1: Mass-radius relation in Eq. (4.17) for QCD axions with $m_a = 50 \,\mu\text{eV}$ and $f_a \simeq 10^{11} \,\text{GeV}$ using $R_{\star,90}$ as characteristic axion star radius. The dense branch of unstable solutions (II) is given in red, together with the relativistic limit from Eq. (4.20) indicated by the red dot. Stable solutions of dilute axion stars (I) are shown in green, while the critical solution with maximum mass $M_{\star,\lambda}$ and minimum radius $R_{\star,90,\lambda}$, which separates (I) and (II), is labeled with a black star. Taken from Ref. [1].

We summarize the above results in Fig. 4.1, which shows the mass-radius relation Eq. (4.18) of QCD axion stars with $m_a = 50 \,\mu\text{eV}$, n = 3.34 and $f_a \simeq 10^{11} \,\text{GeV}^{-1}$.

By definition of $M_{\star,\lambda}$, $R_{\star,\lambda}$ in Eq. (4.16), the dilute branch solutions (I) in Fig. 4.1 in green are dominated by the self-sourced gravitational force of the axion field in Eq. (3.12), while the dense branch solutions (II) in red are dominated by the short-range forces of the axion self-interaction from Eq. (3.4). More importantly for composite axion-star-minicluster systems (ASMCs), the dilute branch solutions have been shown to be stable against perturbations in the stability analysis of Ref.s [159, 212, 231, 233], whereas solitons on the dense branch are typically unstable against perturbations [35, 209] [36] [234]. This observation leads us to the crucial assumption that the present-day axion star distribution of the galactic dark matter halo should mainly be composed of dilute solitons with $R > R_{\star,\lambda}$.

We also emphasize at this point, that the critical mass $M_{\star,\lambda}$ in Fig. 4.1 does not provide a strict distinction between the stable and unstable soliton solutions. Instead the numerical analysis performed in Ref. [235] using the three-dimensional simulations introduced in App. B showed that solutions in the vicinity of the critical point $R_{\star} \sim R_{\star,\lambda}$ can exhibit a semi-stable behavior leading to possible transitions between the two branches under specific perturbations. While these transitions can potentially lead to interesting observable phenomena (see e.g. Sec. 4.4 and Sec. 4.5), they will not be considered in the analysis in this work.

¹The approximate value of the decay constant is related to the QCD-axion-like properties of the axion model with $m_a = 50 \,\mu\text{eV}$, n = 3.34 in Sec. 3.5 and Fig. 3.6.

We conclude that long-lived, stable axion stars should exclusively populate the green branch of solutions in Fig. 4.1, which is why we focus our work on dilute axion stars. Using this assumption together with the mass-radius relation Eq. (4.17), we can fix the axion star radius R_{\star} , profile ρ_{\star} and energy $E_{\star,\text{tot}}$ as a function of its mass M_{\star} for a given axion model with parameters m_a , n and f_a . In principle, the last step in determining the present-day axion star mass distribution is to fix the remaining free axion star parameter - the soliton mass M_{\star} - from the minicluster mass \mathcal{M} . However, the derivation of the present-day core mass distribution requires a deeper understanding of the mass- and time evolution of axion stars, which will be provided in the next sections.

4.2 Axion Star Formation

The obvious starting point in the time evolution of any axion star is its formation, which we assume to always appear in the center of an axion minicluster². In the context of numerical simulations, the formation of axion stars is typically observed from random initial conditions and it has been examined in various studies, e.g. in Ref.s [167, 170, 174, 213]. Since the axions in the soliton populate the same ground state solution with the statistics of a Bose-Einstein condensate, the process of axion star formation is often called *condensation* [237, 238].

In order for the axion ensemble to form a condensate, the system has to establish a locally coherent configuration through gravitational scattering in the Newtonian potential of the inhomogeneous density field. Since the random initial conditions of wave dark matter simulations $(m_a \lesssim \text{eV})$ are characterized by random phases, the time needed to reach a coherent ground state is generally much larger than the gravitational free-fall time

$$\tau_{\rm ff} = \frac{\pi \mathcal{R}^{3/2}}{4\sqrt{GM}} \tag{4.21}$$

of the system with size \mathcal{R} and total mass \mathcal{M} . To see this, we summarize the fundamental analytical calculations and assumptions utilized in the simulations of Ref. [170] in the following. The characteristic timescale for the condensation of a soliton from random, globally homogeneous initial conditions can be calculated in the *kinetic regime*

$$\mathcal{R} \gg \frac{1}{m_a v}$$
 , $\tau_{\rm gr} \gg \frac{1}{m_a v^2}$, (4.22)

where the initial coherence length and time scale of the particles given by the de-Broglie wavelength of the axion field with velocity v are much smaller than the system size \mathcal{R} and the expected formation time τ_{gr} [170] of the condensate.

The authors of Ref.s [170, 215] demonstrated by means of numerical simulations that the time-dependent energy spectrum $F(t,\omega) = d\mathcal{M}/d\omega$ of particles with energy ω evolves according to a Landau kinetic equation. Considering the gravitational scattering rate $\Gamma_{\rm gr} \propto n\sigma_{\rm gr} v \propto 1/\tau_{\rm kin}$ with cross section $\sigma_{\rm gr}$, the kinetic behavior of the numerical simulations motivates the use of

²Note however that there exist also other scenarios, namely the enhanced formation of axion stars from the decay of topological defects at scales near the quantum Jeans scale, which was investigated in Ref. [236]. In this case, the numerous appearance of axion stars with increased relative core masses leads to a significant boost of their relative DM abundance. Their study is complementary to our work involving composite ASMC systems.

the kinetic relaxation time [170]

$$\tau_{\rm gr} \sim \tau_{\rm kin} = \frac{4\sqrt{2}}{\sigma_{\rm gr} v n f},$$
(4.23)

where the bosonic axion system has an occupation number $f \gg 1$, size L and number density $n = N/L^3$. The Rutherford cross section of the gravitational scattering

$$\sigma_{\rm gr} \approx \frac{8\pi (mG)^2 \Lambda}{v^4} \tag{4.24}$$

depends on the Coulomb logarithm $\Lambda = \ln(mvL)$ and the occupation number f in Eq. (4.24)

$$f = \frac{6\pi^2 n}{mv^3} \tag{4.25}$$

accounts for the large phase space densities due to Bose statistics [170, 211]. Putting the above together one obtains the gravitational relaxation time [170]

$$\tau_{\rm gr} = \frac{b\sqrt{2}}{12\pi^3} \frac{mv^6}{G^2 n^2 \Lambda} \sim \frac{10^{10} \,\mathrm{yr}}{\Phi^3 (1+\Phi)} \left(\frac{\mathcal{M}}{10^{-13} M_{\odot}}\right)^2 \left(\frac{m_a}{50 \mu \mathrm{eV}}\right)^3, \tag{4.26}$$

where the coefficient $b \sim 1$, relating $\tau_{\rm gr}$ compared to $\tau_{\rm kin}$, is determined numerically depending on the initial conditions at t=0. Note however that the gravitational relaxation time in Eq. (4.26) only provides a rough estimate of the true formation time $\tau_c \sim \tau_{\rm gr}$ observed in simulations. This statement is best demonstrated by performing the same three-dimensional simulations that were used to validate $\tau_{\rm gr}$ in Ref. [170]. As described in detail in App. B, the numerical simulations of non-relativistic axion stars are often based on a pseudo-spectral operator splitting method similar to Ref.s [170, 239]. The operator splitting scheme essentially decomposes the time evolution operator

$$\mathcal{U} = T \exp\left(-i \int_{t}^{t+\Delta t} dt' \mathcal{H}\right) = T \exp\left\{-i \int_{t}^{t+\Delta t} dt' \left[\frac{\mathbf{k}^{2}}{2m_{a}} + m_{a} \Phi_{N} - \frac{|\lambda|}{8m_{a}^{2}} |\psi|^{2}\right]\right\}, \quad (4.27)$$

of the GPP system in Eq. (3.11), Eq. (3.12) with time ordering operator T into exponentials of the spatial and momentum components $\mathcal{H}_{\mathbf{x}}$, $\mathcal{H}_{\mathbf{k}}$ of the total Hamiltonian

$$\mathcal{H} = -\frac{\nabla^2}{2m_a} + m_a \Phi_N - \frac{|\lambda|}{8m_a^2} |\psi|^2 = \mathcal{H}_{\mathbf{x}} + \mathcal{H}_{\mathbf{k}}, \qquad (4.28)$$

$$\mathcal{H}_{\mathbf{x}} = m_a \Phi_N - \frac{|\lambda|}{8m_a^2} |\psi|^2 \quad , \quad \mathcal{H}_{\mathbf{k}} = -\frac{\nabla^2}{2m_a} \,. \tag{4.29}$$

The above separation of the Hamiltonian \mathcal{H} facilitates the calculation of the energy expectation value and other observables in position and in Fourier space, where $\langle \psi | \mathcal{H}_{\mathbf{x}} | \psi \rangle$ and $\langle \psi_{\mathbf{k}} | \mathcal{H}_{\mathbf{k}} | \psi_{\mathbf{k}} \rangle$ become diagonal. In this approach, the wave function $\psi(\mathbf{x}, t + \Delta t) = \mathcal{U}\psi(t)$ - or its Fourier space equivalent $\psi_{\mathbf{k}}(\mathbf{k}, t)$ - may be evolved in time through repeated Fourier transforms and combined multiplication with exponentials $\exp(-i\mathcal{H}_i dt)$ of the Hamiltonian components $\mathcal{H}_{\mathbf{x}}$ and $\mathcal{H}_{\mathbf{k}}$ in the

corresponding eigenspace i. For this, the time evolution operator \mathcal{U} needs to be 'split up' into an ordered series of products of the second-order representation

$$\exp\left[-i(\mathcal{H}_{\mathbf{x}} + \mathcal{H}_{\mathbf{k}})dt\right] = \exp\left(-i\frac{\mathcal{H}_{\mathbf{k}}}{2}dt\right) \cdot \exp\left(-i\mathcal{H}_{\mathbf{x}}dt\right) \cdot \exp\left(-i\frac{\mathcal{H}_{\mathbf{k}}}{2}dt\right) + \mathcal{O}(dt^{3})$$
(4.30)

at each discrete timestep dt in Eq. (4.27). Note that the identity in Eq. (4.30) can be directly obtained by applying the Baker-Campbell-Hausdorff formula in Eq. (B.8) to the product $\exp(A) \exp(B)$ as explained in App. B and Ref. [239].

Although the method used in the simulations in this thesis is of higher order $\mathcal{O}(dt^4)$, all of the fourth- to 8th-order schemes from App. B are based on the second-order splitting in Eq. (4.30). We refer to App. B for a detailed explanation of the grid discretization and operator splitting methods of the numerical GPP system in three-dimensional simulations. For now and given a three-dimensional grid with resolution N_x , the numerical system can be evolved in time to arbitrary t using a discrete step size Δt and repeated Fourier transforms to compute the energy eigenvalues and their exponentials $\exp(-i\mathcal{H}_i dt)$ in the respective (diagonal) basis i.

With the numerical time evolution being prescribed by Eq. (4.27) and Eq. (4.30), the final state of the system is completely determined by the initial state $\psi_0(\mathbf{x})$ - apart from small numerical errors. The initial wavefunction in return is typically specified in Fourier space, where two approaches are common in the literature [170, 174, 213]: First the Gaussian initial distribution

$$\widetilde{\psi}_0(\widetilde{\mathbf{k}}) = 2\sqrt{2}\pi^{3/4}\sqrt{\widetilde{N}}\exp\left(-\frac{\widetilde{\mathbf{k}}^2}{2} + i\theta_r(\mathbf{k})\right)$$
 (4.31)

where the initial phase $\theta_r(\widetilde{\mathbf{k}}) \in [0, 2\pi]$ is randomly drawn from a uniform distribution at each point $\widetilde{\mathbf{k}}$ on the momentum space grid. And secondly, the δ -distributed wave function

$$|\psi_0(\mathbf{k})|^2 \propto \delta_D(|\mathbf{k}| - m_a v_0), \qquad (4.32)$$

which constitutes the surface of a sphere with radius $|\mathbf{k}| = m_a v_0$ equal to the characteristic momentum $k_0 = m_a v_0$ of the system and again with random phases $\theta_r \in [0, 2\pi]$. For the Gaussian and δ -distributions considered in this section, we obtained b = 0.9 and b = 0.6 respectively, which agrees with the predictions from the original work, Ref. [170]. Note that in Eq. (4.31) and in the following, numerical variables of the simulations are prescribed in rescaled units following Eq. (4.8) for $\lambda \neq 0$ and Eq. (A.5) for $\lambda = 0$.

We demonstrate the initial configuration and subsequent evolution of a δ -distributed system in Fig. 4.2, which was obtained using the pseudo-spectral algorithm from App. B. Fig. 4.2 shows different two-dimensional planes \tilde{z} in position space, at which the soliton is situated at a given \tilde{t} . The three-dimensional grid was set up with a resolution of $N_x=256^3$ and initialized with a δ -distributed initial field for a rescaled system size $\tilde{L}=44$ and particle number $\tilde{N}=55$ shown in the top left panel. As before, the quantities labeled by a tilde indicate the dimensionless variables obtained from the rescaling in Eq. (4.8). We use rescaled coordinates to evolve the m_a -independent GPP system in Eq. (4.9), Eq. (4.10) for negligible self-interactions $\lambda=0$ and choose \tilde{N}, \tilde{L} appropriately such that the resulting soliton mass \tilde{M}_{\star} corresponds to a dilute soliton with $M_{\star} \simeq 1.9 \cdot 10^{-14} \, M_{\odot}$ after $\tilde{t}=10^4$ for $m_a=50 \, \mu {\rm eV}, \, f_a \simeq 10^{11} \, {\rm GeV}$ and $v_0 \simeq 10^{-9} \, ^3$. The mass of

³Here, the physical mass-dependence of the rescaled GPP system is absorbed in the rescaling Eq. (4.58). As soon as we relate the m_a -independent simulation to a specific axion model, the axion parameters m_a , f_a determine the physical system properties of the simulation.

the total system is $\mathcal{M} \simeq 1.5 \cdot 10^{-13} \, M_{\odot}$ and its length is $L = 1.7 \cdot 10^5 \, \mathrm{km}$ for the aforementioned QCD axion parameters. Note that the soliton mass growth is substantial, since the initial core mass at $\tilde{t} = 2500$ shown in orange in Fig. B.3 with $\tilde{N} \simeq 2$ is roughly $M_{\star} \simeq 5 \cdot 10^{-15} \, M_{\odot}$. For the operator splitting and time coordinate, we use the fourth-order scheme from Eq.s (B.18), (B.19) and $\Delta \tilde{t} = 0.01$, where a more detailed analysis of this simulation can be found in App. B.

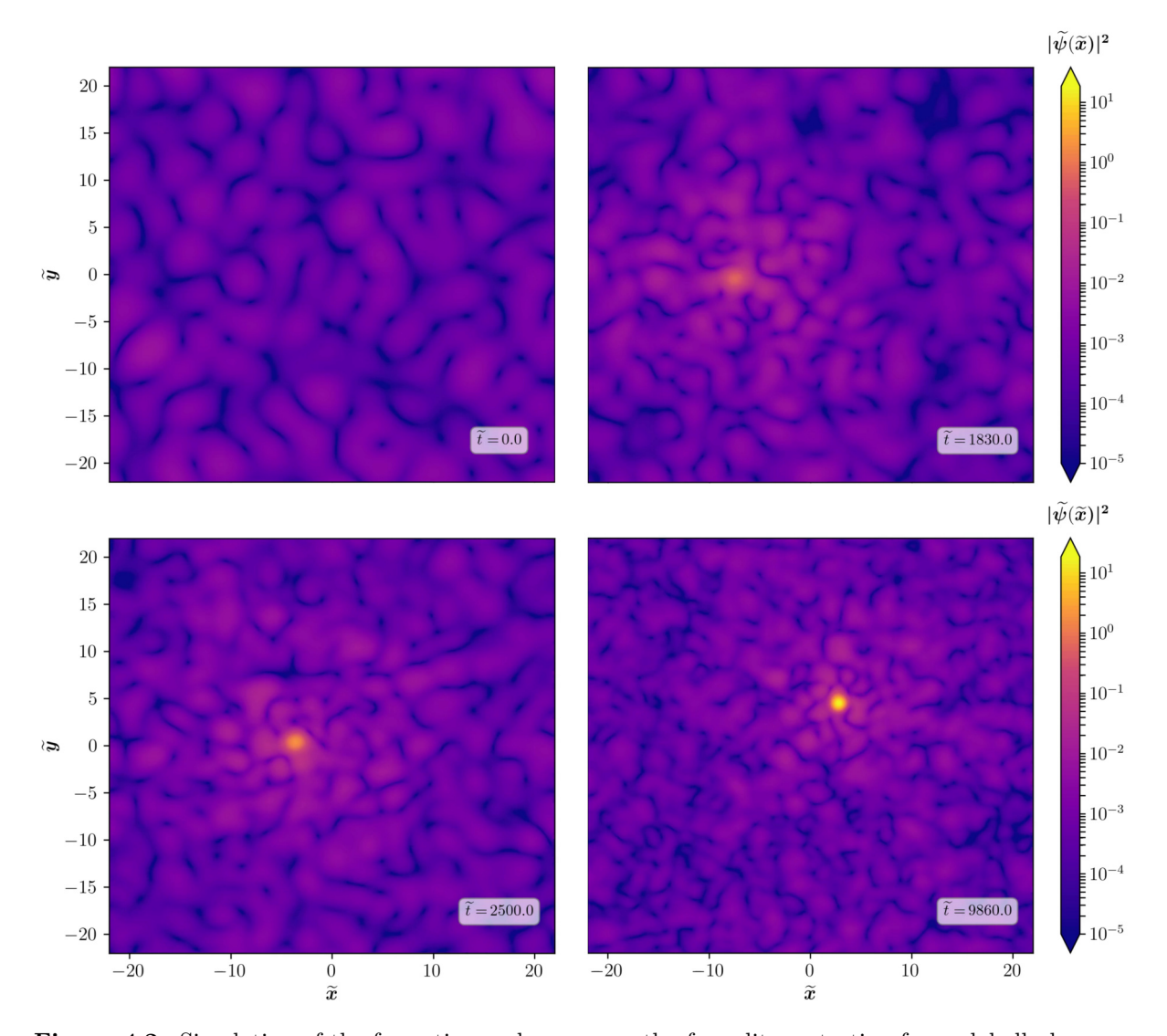


Figure 4.2: Simulation of the formation and mass growth of a soliton, starting from globally homogeneous, random initial conditions as in Eq. (4.32). The simulation was run for $\lambda = 0$, $\widetilde{L} = 44$, $\widetilde{N} = 55$ on an $N_x = 256^3$ grid with timesteps $\Delta \widetilde{t} = 0.01$ and predicted condensation time $\widetilde{\tau}_{gr} \simeq 1445$. Initial conditions are shown in the top left panel, followed by the formed soliton at different times $\widetilde{t} = 1830, 2500, 9860$.

Initially, the system is globally homogeneous, with random fluctuations on scales $k \sim k_0$ and random phases θ_r , as seen in the top left panel of Fig. 4.2. After an amount of time, which roughly agrees with the predicted condensation time $\tilde{\tau}_{\rm gr} \simeq 1445$, a spherical object can be seen to have formed in the top right panel. The physical formation time of the soliton is $\tau_{\rm gr} \simeq 600 \, {\rm yrs}$ for QCD

axion parameters. It is surrounded by spherical overdensities, which interact with the soliton and are sometimes referred to as gravitationally bound quasi-particles or granular overdensities due to their Brownian-like motion in the global Newtonian potential. Over time, the newly formed soliton grows in mass leading to an increase of the maximal density $\max_{\widetilde{x}} |\widetilde{\psi}(\widetilde{t}, \widetilde{x})|^2$ as seen by the yellow color in the bottom panels of Fig. 4.2. The time-dependent mass growth of this object will be analyzed in more detail in the following section.

4.3 Axion Star Mass Growth

Once a given axion star has formed inside of its host minicluster around the condensation time $\tau_c \simeq \tau_{\rm gr}$, it begins to accrete mass from the surrounding density field through repeated interactions with the granular quasi-particle overdensities observed in Fig. 4.2. The rate of mass growth of the soliton depends mainly on the time $t > \tau_{\rm gr}$ and secondly on the minicluster parameters $\mathcal{M}, \Phi, \mathcal{R}$ as well as on the axion model m_a, n setting the former.

Importantly for this work, the continuous accretion of the axion star from some initial value $M_{\star,0} = M_{\star}(\tau_{\rm gr})$ can drive the composite ASMC system to criticality, leading to observable phenomena through soliton instability (see Sec. 4.4 and Sec. 4.5). In this section we introduce two approaches to model the mass evolution of axion stars: First the power-law fits for $M_{\star}(t)$ in Subsec. 4.3.1 and secondly the semi-analytical attractor model investigated in Ref. [170], which provides a crucial framework for the accretion estimates in Chap.s 6, 7 as shown by the yellow bottom panel in Fig. A.1.

4.3.1 Power-Law Fits

The first observations of soliton mass growth in numerical simulations relate to the early stage of accretion, right after condensation and at times $t \gtrsim \tau_{\rm gr}$. At these early times, the axion star acquires mass from the surrounding gas of particles leading to a time-dependent mass growth similar to [170]

$$M_{\star}(t) \simeq M_{\star,0} \left(\frac{t - \tau_{\rm gr}}{\tau_{\rm gr}}\right)^{1/2},$$
 (4.33)

where $M_{\star,0}$ is the initial mass at formation $t = \tau_{\rm gr}$. The above growth rate was confirmed in numerous studies [167, 170, 174, 213, 215] including our simulations using the pseudo-spectral method in App. B.

Fig. 4.3 shows the maximum field density $\max_{\widetilde{\mathbf{x}}} |\widetilde{\psi}(\widetilde{\mathbf{x}})|^2$ obtained from the long-time evolution of the condensed soliton in Sec. 4.2 and Fig. 4.2 using the code from App. B. The numerical results in red show a rapid increase of the maximal density after $\widetilde{t} \simeq 1000$ and demonstrate that the numerically determined collapse time $\widetilde{\tau}_c = 1325 \simeq \widetilde{\tau}_{\rm gr}$ is in good agreement with the prediction $\widetilde{\tau}_{\rm gr} \approx 1445$ from Eq. (4.26). It can further be seen from the scaling $M_{\star}(t) \propto \rho_{\star}(t,0)^{1/4}$ [174] that the power-law scaling in Eq. (4.33) implies roughly $\rho_{\star}(t,0) \propto t^{1/2}$, as indicated by the black dashed line in Fig. 4.3 [174]. Similarly, the dotted line corresponds to the density scaling inferred from Eq. (4.33) with a fitting constant $\widetilde{\tau}_0 = 1000$. In both cases, the soliton growth is roughly approximated by the predictions $\widetilde{\rho}_{\star} \propto \widetilde{t}^2$ and Eq. (4.33) for $\widetilde{t} \gtrsim 2000$.

Note that as a consequence of the mass-radius relation in Eq. (4.17), the mass increase of the dilute soliton induces a decrease of its radius $R_{\star} \sim 1/M_{\star}$, as is best observed in the radial profile

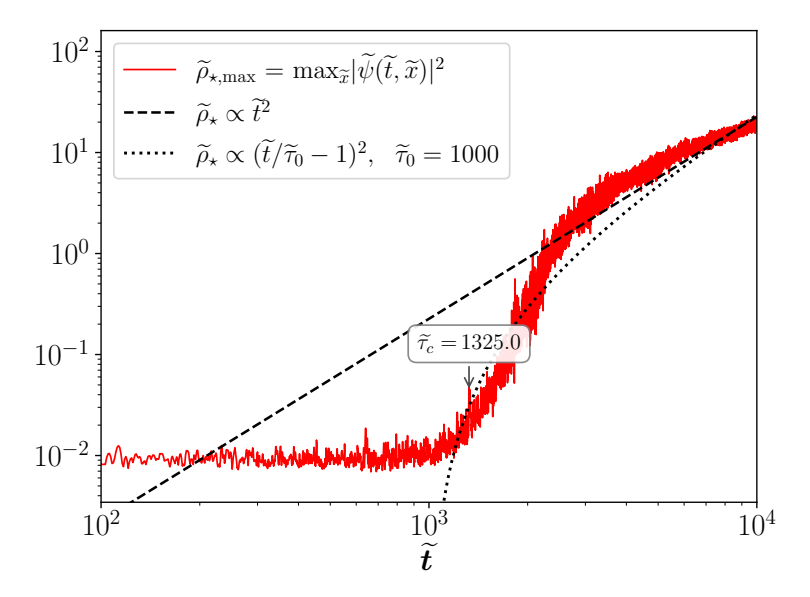


Figure 4.3: Maximum density $\max_{\widetilde{x}} |\widetilde{\psi}(\widetilde{t},\widetilde{\mathbf{x}})|^2$ of the three-dimensional grid in the simulation from Fig. 4.2 and App. B, as a function of rescaled simulation time \widetilde{t} . The numerical results in red are compared to a simple power-law scaling $\widetilde{\rho}_{\star} \propto \widetilde{t}^2$ in black dashed lines and the actual scaling from Eq. (4.33) in the black dotted line. Note that here we have replaced the gravitational condensation time $\widetilde{\tau}_{\rm gr}$ in Eq. (4.33) with a fitting constant $\widetilde{\tau}_0 = 1000$ due to large uncertainties in the numerical determination of $\tau_{\rm gr}$.

plot of $|\widetilde{\psi}(\widetilde{r})|$ at different \widetilde{t} in Fig. B.2. Most importantly, the mass growth in Fig. 4.3 starts to saturate around the latest simulation times $\widetilde{t} \lesssim 10^4$, which indicates a possible transition to a third stage of axion star evolution (after formation and early mass growth $\propto t^2$).

This observation raises the crucial question whether the power-law scaling in Eq. (4.33) continues indefinitely or whether the growth rate changes after long times $\tilde{t} \gg \tilde{\tau}_{\rm gr}$. To answer this question, it makes sense to consider the expected equilibrium configuration of the SP or GPP system, where the size of the overdensities is approximately equal to the soliton size $R_{\star, \rm vir}$ corresponding to a mass $M_{\star, \rm vir}$. In this particular state of balance, the accretion rate of the virialized soliton is expected to drop. A natural prediction for the time $\tau_{\rm sat}$, where the mass growth rate saturates, may be obtained by setting the virial velocity of the $\lambda = 0$ soliton [49, 171]

$$v_{\star, \text{vir}} \simeq GM_{\star}m_a$$
 (4.34)

equal to the virial velocity

$$v_{\rm mc, vir} \simeq \sqrt{\frac{GM}{\mathcal{R}}}$$
 (4.35)

of its host minicluster. Inserting Eq. (4.34) for v in Eq. (4.26) and assuming the power-law from Eq. (4.33) to hold, one obtains the mass growth law [167, 171, 174]

$$M_{\star}(t_{\rm star}) \simeq M_{\star, \rm vir} \left(\frac{t_{\rm star}}{\tau_{\rm sat}}\right)^{1/8}$$
 (4.36)

of the saturated axion star at $t > \tau_{\rm sat}$ with the saturation time [167]

$$\tau_{\text{sat}} = \frac{b\sqrt{2}}{12\pi^3} \frac{mv_{\star,\text{sat}}^6}{G^2 n^2 \ln(mv_b \mathcal{R})},$$
(4.37)

where $M_{\star, \text{vir}}$ is the boson star mass at $t = \tau_{\text{sat}}$ and $v_{\star, \text{sat}} = v_{\star, \text{vir}}(M_{\star, \text{vir}})$.

Due to the significant amount of computational power required to reach the saturated stage $t > \tau_{\rm sat}$ and due to lack of numerical resources, we do not reproduce the power-law from Eq. (4.36) in our simulations. Instead we summarize the result of the original work, Ref. [174], confirming that the late-time accretion indeed saturates at $M_{\star}(t) \propto t^{1/8}$ in Fig. 4.4.

Figure Fig. 4.4 shows the averaged time-dependent central densities $\rho_{\star}(t,0) \propto M_{\star}^4(t)$ of solitons formed in a series of simulations with box sizes $\tilde{L}=25,20,18,15$ and different particle numbers $\tilde{N}=691,754,817,880,942,1005,1131$. The shaded regions indicate the $1-\sigma$ intervals of

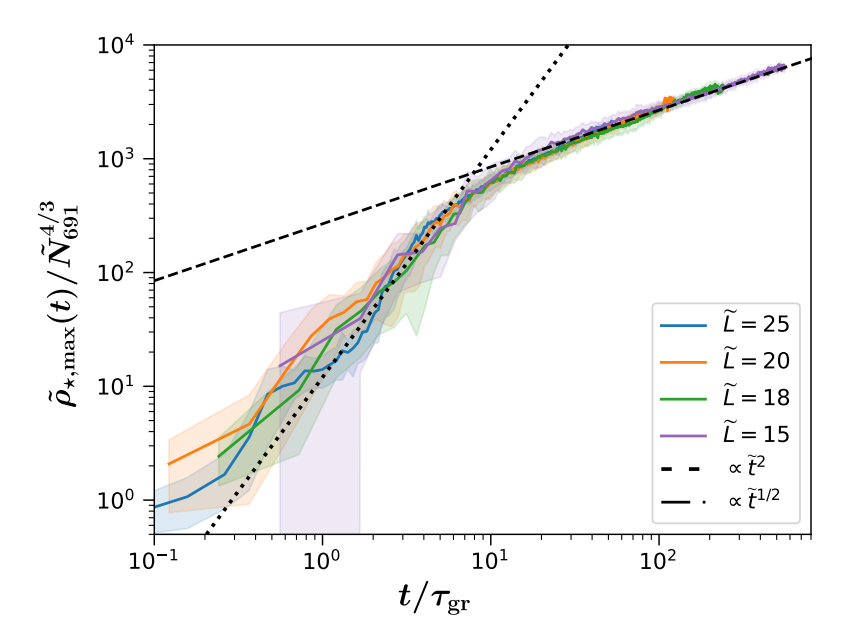


Figure 4.4: Averaged central densities $\widetilde{\rho}_{\star}(t,0)$ for different solitons formed in numerical simulations at fixed $\widetilde{L}=25,20,18,15$ and for different $\widetilde{N}=691,754,817,880,942,1005,1131$, taken from Ref. [174]. The black lines show the power-law predictions from Eq. (4.33) and Eq. (4.36), respectively. Shaded regions indicate the $1-\sigma$ intervals of the averaged simulations at different \widetilde{N} and same \widetilde{L} . The densities are normalized to a power of the total mass $\widetilde{N}_{691}=\widetilde{N}/691$ for better representation.

the averaged densities at fixed \widetilde{L} and the density is normalized to a power of the total mass $\widetilde{N}_{691} = \widetilde{N}/691$.

Due to the large overall densities in the system, the axion stars form almost immediately $\tau_{\rm gr} \sim \tau_{\rm ff}$ and thereafter accrete with the predicted scalings $\rho_{\star}(t,0) \propto t^2$ and $t^{1/2}$ shown in dotted and dashed lines. This is opposed to the numerical system in Fig. 4.2 and App. B, which has a significantly lower density n and thus larger $\tau_{\rm gr}$ in Eq. (4.26). We emphasize however that the decrease of $\tau_{\rm gr}$ in terms of the parameters \widetilde{N} , \widetilde{L} comes at the cost of drastically smaller required timesteps $\Delta t \lesssim 10^{-5}$, so that even the simulations in Fig. 4.4 require immense computation times compared to Fig. 4.3.

Lastly, the power law deviations, which occur around the transition region $\tilde{t} \sim \tilde{\tau}_{\rm sat}$ at the intersection of the dotted and dashed black lines, indicate the need for an improved modeling of the mass growth rates. Such an improved model providing a smooth time evolution of the soliton mass will be introduced in the next subsection.

4.3.2 Self-similar Attractor Model

The first detailed model of the time- and \mathcal{M} -dependent mass growth of an axion star is the self-similar attractor model introduced in Ref. [240], which we summarize in this subsection. Similar to the power-law fits from Subsec. 4.3.1, this model was tested in numerical simulations of the Schrödinger-Poisson system Eq. (3.14), Eq. (3.15), which amounts to negligible self-interactions $\lambda = 0$. Since axion miniclusters are dominated by gravitational forces [167, 241], and since the self-interaction of their dilute axion star cores in our considerations is relatively weak⁴, we will use the $\lambda = 0$ attractor model also for the ASMC systems with weak attractive self-interactions $\lambda < 0$.

A more detailed discussion on the minicluster- and core energy deviations induced by additional consideration of the self-interaction energy in Eq. (4.4) compared to the $\lambda=0$ case can be found in Sec. 4.6. To summarize, we find that even in the most extreme case $M_{\star}=M_{\star,\lambda}$, the self-interaction only contributes 1/3 of the total system energy. Compared to the large uncertainties arising from the linear growth in Subsec. 3.5.2, this justifies the use of the $\lambda=0$ attractor model as an order-of-magnitude estimate for the true axion star growth rate in the following.

Coming back to the derivation of the original authors, who considered solitons with $\lambda=0$, it is helpful to consider the energy spectrum $F(t,\omega)=d\mathcal{M}/d\omega$ of the boson mass distribution over different energies ω . As originally shown in the related Ref. [170], the energy spectrum develops a sharp peak with $\omega<0$ at the time of condensation. Physically, the mass and energy of this peak correspond to the soliton mass and potential energy of the gravitationally bound axion star. An explicit example of the spectrum evaluated at two different points in time $t\approx 3.2\tau_{\rm gr}$ in pink and $t\approx 10.9\tau_{\rm gr}$ in blue is depicted in Fig. 4.5.

The energy spectrum in Fig. 4.5 is given in rescaled units with dimension one, namely $\tilde{F} = 2\omega_0 F/\mathcal{M}$ and $\tilde{\omega} = \omega/(2\omega_0)$, where $\omega_0 = mv_0^2/2$ is the characteristic energy of the particles. Two more important features in the spectrum in Fig. 4.5 are the bath component of the ambient, gravitationally unbound particles in the simulation at $\tilde{\omega} > 0$ and the bound states with $\tilde{\omega} \lesssim 0$, which constitute the granular environment of the soliton seen in Fig. 4.2.

Over time and comparing the pink and blue spectra, the system can be seen to evolve into a configuration with a more strongly bound bose star, indicated by the blue peak at smaller $\tilde{\omega}$ and a thermal bath with an increased high- ω tail extending to the largest particle energies $\tilde{\omega} \sim 5$. The total mass of the system can be found by integrating over the above two and a third component, which gives a total system mass $\mathcal{M} = M_{\star} + M_{\odot} + M_b$, where M_{\odot} describes the excited bound states in the vicinity of the soliton and M_b is the mass of the bath or background. A crucial observation in the derivation of the mass growth model is the realization that the time-dependent spectra in Fig. 4.5 exhibit a scaling symmetry of the form [240]

$$\tilde{F}(t,\tilde{\omega}) = a_s F_s(b_s \tilde{\omega}), \quad a_s = \tau^{-1/D_s}, \quad b_s = \tau^{2/D_s - 1}$$
 (4.38)

⁴That is, by definition of the stable dilute branch of axion stars in Sec. 4.1 and $\lambda = -m_a^2/f_a^2$, which we have limited our analysis to.

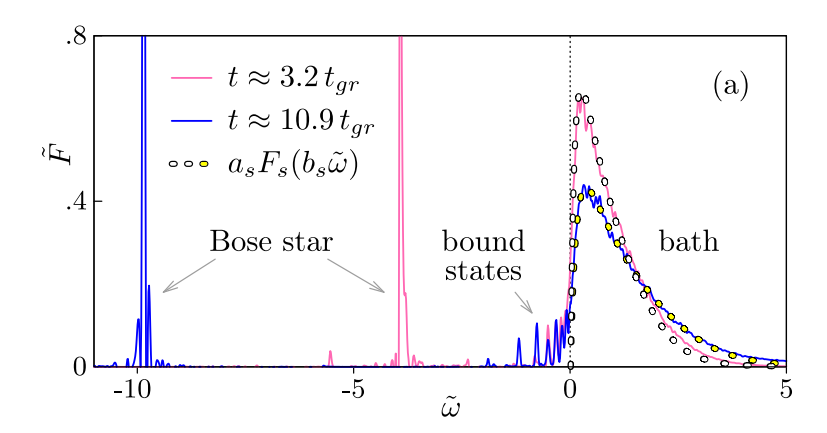


Figure 4.5: Simulated rescaled energy spectra $\tilde{F} = 2\omega_0 F/\mathcal{M}$ at two different points in time after condensation: $t \approx 3.2\tau_{\rm gr}$ in pink and $t \approx 10.9\tau_{\rm gr}$ in blue. The sharp peaks at negative energies $\tilde{\omega}$ correspond to bose stars (i.e. with $\lambda = 0$) and the bell-shaped curves represent the bath at different times. The latter of which can be parametrized by the rescaling in Eq. (4.38) as shown by the white circles. The figure was taken from Ref. [240].

where $\tau = t/\tau_{\rm gr}$ is the relative time coordinate and $D_s = 2.8$ is a numerical coefficient. The parametrization of the time-dependent spectra using Eq. (4.38) with the self-similar scaling function $F_s(\omega_s)$ is indicated by the white circles in Fig. 4.5.

Importantly, the rescaling in Eq. (4.38) describes a time-dependent mass $M_b \propto \tau^{k_M}$ of the bath and a corresponding energy $E_b \propto \tau^{k_E}$ with power-law parameters [240]

$$k_M = 1 - 3/D_s, \quad k_E = 2 - 5/D_s, \quad 3k_E - 5k_M = 1$$
 (4.39)

Physically, this means that some fraction of the particles in the bath will eventually lose energy through gravitational scattering and become bound to either the soliton M_{\star} or to a quasi-particle overdensity in its surrounding M_{\odot} . The scaling in Eq. (4.39) can then be used to derive an equation of motion for the resulting mass growth of the total system.

A crucial step here is to assume that the weakly time-dependent scaling parameters from Eq. (4.38) are given by $D_s = D_s(\tau)$, $k_M(\tau) = d \ln M_b/d \ln \tau$ and $k_E(\tau) = d \ln E_b/d \ln \tau$ and that at different times τ they satisfy the relation $3k_E - 5k_M \approx 1$ in Eq. (4.39). Then writing the mass of the soliton and its quasi-particle environment as $M_{\circledast} = M_{\star} + M_{\odot}$, the conservation of the total mass $M_b = \mathcal{M} - M_{\circledast}$ and energy $E_b = \mathcal{E} - E_{\circledast}$ of the system give $d \ln \tau \approx 3d \ln (\mathcal{E} - E_{\circledast}) - 5d \ln (\mathcal{M} - M_{\circledast})$, which after integration yields

$$\left(1 - \frac{E_{\circledast}}{\mathcal{E}}\right)^3 \left(1 - \frac{M_{\circledast}}{\mathcal{M}}\right)^{-5} \approx \frac{\tau - \tau_i}{\tau_{\star}},$$
(4.40)

where $E_{\circledast} = E_{\star} + E_{\circlearrowleft}$, \mathcal{E} is the total energy and τ_{\star} an integration constant to be determined later⁵. Since the excited states in M_{\circlearrowleft} carry relatively little energy, the energy of the bose star and its environment in Eq. (4.40) may be approximated as $E_{\circledast} \approx E_{\star} = -\gamma M_{\star}^3$ with $\gamma \approx 0.0542 m_a^2 G^2$.

⁵Note here that for consistency with other chapters, the '*' symbols used in this work correspond to the index 'bs' in Ref. [240], while the symbol '®' replaces the '*' symbol in Ref. [240].

Additionally defining $\epsilon^2 = \mathcal{E}/(\gamma \mathcal{M}^3)$ one finally obtains the mass growth equation

$$\left[1 + \frac{M_{\star}^{3}}{\epsilon^{2} \mathcal{M}^{3}}\right]^{3} \left[1 - \frac{M_{\odot}}{\mathcal{M}} - \frac{M_{\star}}{\mathcal{M}}\right]^{-5} \approx \frac{\tau - \tau_{i}}{\tau_{\star}}$$
(4.41)

of the self-similar attractor [240]. The quantities $\tau_i \approx -0.1$ and τ_{\star} in Eq. (4.41) are empiric fitting parameters where the integration constant $\tau_{\star} \approx (1 - \tau_i) (1 - M_{\odot}/\mathcal{M})^5$ is fixed by the initial condition $M_{\star} = 0$ at $\tau = 1$.

Taking all of the above together, we show a comparison between different simulations of the self-similar system in Eq. (4.41) with relative energies $\epsilon \approx 0.186$ and $\epsilon \approx 0.074$ in Fig. 4.6. The

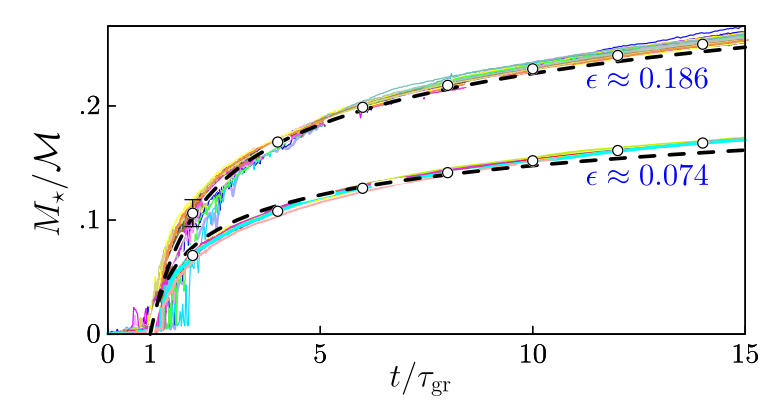


Figure 4.6: Time-dependent soliton mass $M_{\star}(t)$ obtained from 22 simulations with different $\mathcal{M}, \widetilde{L}, \tau_{\rm gr}$ but same $\epsilon \approx 0.186$ and $\epsilon \approx 0.074$ in colored lines, taken from Ref. [240]. The dashed black lines indicate the predictions from Eq. (4.41) after fixing τ_{\star} from the initial conditions. White circles indicate the average over different simulations with same ϵ .

corresponding predictions from the mass growth model in Eq. (4.41) are shown in black dashed lines and can be seen to agree well with the different numerical simulations in colored lines. The same remains true for the averaged numerical data at same ϵ , as seen by the white empty circles in Fig. 4.6. Similar to the results in Fig. 4.3 and Fig. 4.4, the largest disagreement can be observed at early times $t \sim \tau_{\rm gr}$, where the system is most sensitive to the random nature of the initial conditions from Sec. 4.2.

For completeness and for later considerations, Eq. (4.41) can be used to derive the mass growth rate [2]

$$\frac{\delta M_{\star}}{\delta t} \simeq \frac{\left(1 - \frac{M_{\star}}{\mathcal{M}}\right)^{6}}{\left[5 + \frac{1}{\epsilon^{2}} \left(\frac{M_{\star}}{\mathcal{M}}\right)^{2} \left(9 - 4\frac{M_{\star}}{\mathcal{M}}\right)\right] \left[1 + \frac{1}{\epsilon^{2}} \left(\frac{M_{\star}}{\mathcal{M}}\right)^{3}\right]^{2}} \frac{\mathcal{M}}{1.1 \tau_{gr}},$$
(4.42)

of the axion star core in a composite ASMC system with ϵ determined by [240]

$$\epsilon \simeq 0.008 \sqrt{\Phi} (1 + \Phi)^{1/6} \left(\frac{10^{-13} M_{\odot}}{\mathcal{M}} \right)^{2/3} \left(\frac{50 \,\mu\text{eV}}{m_a} \right)$$
 (4.43)

and where the small contribution of the excited states around the soliton was neglected. This means that for a given axion model m_a , n, the accretion rate in Eq. (4.42) generally depends on

three parameters: the minicluster density parameter Φ , the minicluster mass \mathcal{M} and the axion star mass M_{\star} . As already pointed out in Sec. 3.2, we assume the two parameters \mathcal{M} and Φ to be independent from each other and from the galactocentric radial coordinate r for simplicity. At this stage, \mathcal{M} is prescribed from the MCMF in Subsec. 3.6.2 and $\Phi \in (0, 10^4]$ is known from the simulations in Ref. [146]. The remaining parameter, M_{\star} will be fixed in section Sec. 4.7. For now, we show the accretion rates from Eq. (4.42) after normalization to the characteristic value $\mathcal{M}/\tau_{\rm gr}$ in Eq. (4.42) for the two classes of systems in Fig. 4.6 with $\epsilon \approx 0.186$ and $\epsilon \approx 0.074$ in orange and blue. Importantly for the analysis in this work, the accretion rates are initially

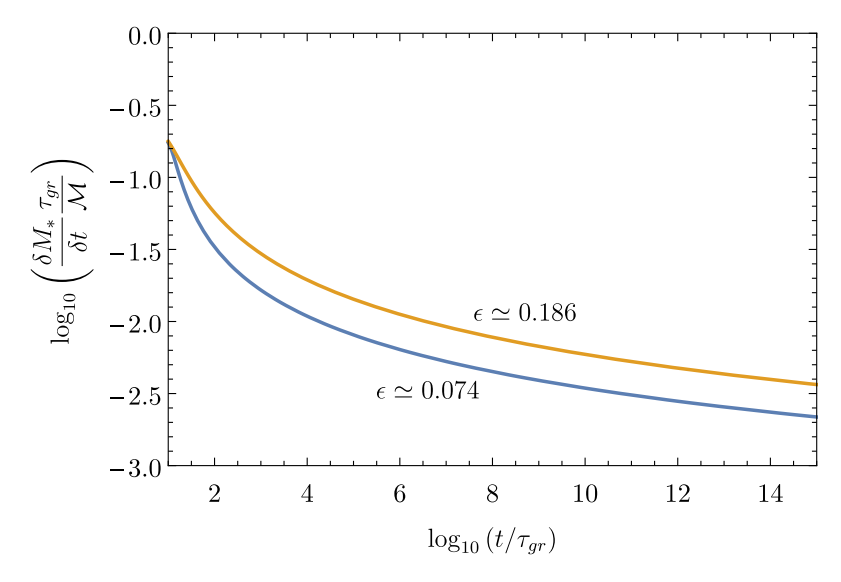


Figure 4.7: Predicted accretion rates of the solitons in Fig. 4.6 with $\epsilon \approx 0.186$ in orange and $\epsilon \approx 0.074$ in blue, taken from Ref. [2]. The growth rates are normalized by $\mathcal{M}/\tau_{\rm gr}$ following Eq. (4.42).

large, shortly after the time of condensation, and drop significantly at large values of $t \gg \tau_{\rm gr}$. Even at the latest times $t \gg \tau_{\rm gr}$, the accretion remains sufficiently large for the star mass to change considerably over long timescales $t \sim t_H$ as will be shown in Chap. 7. This means that after forming with some initial mass $M_{\star,0}$, the axion star will continue to accrete over time until potentially reaching one of the two critical mass thresholds to be explored in the following two sections.

4.4 Bosenovae

The first and most important critical soliton mass was already introduced in the derivation of the mass-radius relation in Sec. 4.1: the maximum stable axion star mass due to self-interactions, $M_{\star,\lambda}$ in Eq. (4.16). Physically, the stationary solution with $M_{\star,\lambda}$, $R_{\star,\lambda}$ describes the point of approximate equipartition between the gravitational energy $E_{\text{grav}}(M_{\star})$ from Eq. (4.3) and the self-interaction energy $E_{\text{int}}(M_{\star})$ from Eq. (4.4).

Once an axion star exceeds the critical mass $M_{\star} > M_{\star,\lambda}$, the self-interaction potential of the axion in Eq. (2.9) triggers relativistic multi-particle interactions in a process commonly referred to as a *Bosenova* or axion nova [35, 209, 212, 217, 225, 234, 242–244]. During the ensuing collapse of the super-critical soliton, relativistic axions are generated in repeated cycles of collapse, particle emission and expansion until the resulting mass-loss drives the system to become

sub-critical, $M_{\star} \leq M_{\star,\lambda}$, again. Due to the relativistic nature of the field dynamics, the non-relativistic pseudo-spectral method from App. B is insufficient to trace the Bosenova process. Instead, the full Einstein-Klein-Gordon equations, Eq. (3.2), Eq. (3.3) need to be solved numerically.

In the following, we recall the most important results from Ref. [35], who solved the spherically symmetric relativistic field equations for a marginally super-critical solution M_{\star} , R_{\star} numerically. The resulting collapse of a super-critical axion star is depicted in Fig. 4.8, which shows the time-dependent evolution of the central density $\rho(t,0)$. In this case, the super-criticality

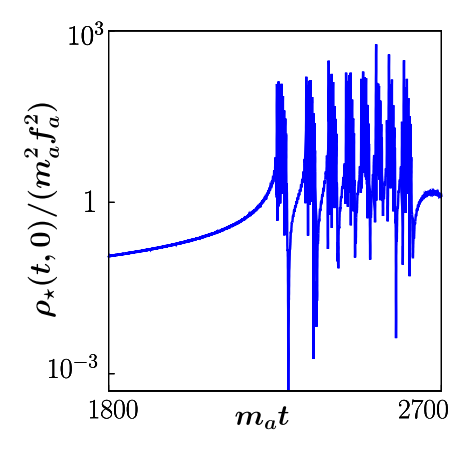


Figure 4.8: Time-dependent central soliton density $\rho_{\star}(t,0)$ during one of several collapse cycles from the relativistic simulations for $m_a \approx 2 \cdot 10^{-9} \,\text{eV}$, $f_a \approx 3 \cdot 10^{15} \,\text{GeV}$ and $c_{\lambda} \approx 0.44$, taken from Ref. [35]. The time coordinate is normalized by the characteristic time scale $\tau \sim 1/(m_a c^2)$ of the relativistic particles.

was achieved by performing a transformation $\psi(r) \to \gamma \psi(\gamma r)$ with $\gamma = 1 - 10^{-4}$ on the critical soliton profile with initial mass $M_{\star,\lambda}$ [35].

The numerical parameters correspond to an axion model with $m_a \approx 2 \cdot 10^{-9} \, \text{eV}$, $f_a \approx 3 \cdot 10^{15} \, \text{GeV}$. Note also that the authors used a different coupling constant $c_{\lambda} = (1 + y^2 - y)/(1 + y^2)^2 \approx 0.44$ with $y = m_u/m_d \approx 0.56$, compared to our simplified assumption of $c_{\lambda} = 1$ for the quartic coupling in Eq. (3.4). As argued in Subsec. 3.6.1, the exact value of c_{λ} setting the coupling $\lambda = -c_{\lambda}m_a^2/f_a^2$ is not expected to drastically alter the qualitative evolution of the system since the corresponding critical mass in Eq. (4.16) scales as $M_{\star,\lambda} \propto 1/\sqrt{\lambda} \propto 1/\sqrt{c_{\lambda}}$. From a different perspective, the leading order peak in Fig. 4.10 has the lowest $k/m_a \approx 2.4$, which suggests that higher order processes in λ are subdominant, see also Eq. (3.4). The axion model simulated in Ref. [240] is therefore in rough correspondence with the models considered in this work.

At early times, the soliton exhibits an increase in central density compared to the initial value $m_a t = 1800$ of the normalized time coordinate. At a central density of $\rho_{\star}(t,0)/(m_a^2 f_a^2) \sim 10^2$, the relativistic collapse and subsequent emission of relativistic particles from the soliton lead to a sudden drop in density down to $\rho_{\star}(t,0)/(m_a^2 f_a^2) \sim 10^{-3}$. This collapse process repeats itself $N_c = 8$ times until enough axion matter is depleted for the star to relax to a stable configuration $M_{\star} \leq M_{\star,\lambda}$. As was shown in the simulations of Ref. [35], the process in Fig. 4.8 involving $N_c = 8$ collapse cycles can also occur repeatedly, with the number of cycles $N_{\star} \sim 5$ depending on the initial mass $M_{\star} > M_{\star,\lambda}$ of the super-critical soliton configuration [240].

⁶Specifically, the authors of Ref. [240] compared two simulations with different f_a , leading to different $M_{\star,\lambda}$ in Eq. (4.16) and $N_{\star} = 5, 7$ collapse cycles.

Additional insight on the production of relativistic waves in the system can be obtained by inspecting the radially symmetric soliton profile $\rho_{\star}(r,t)$ at different times t in Fig. 4.9. The

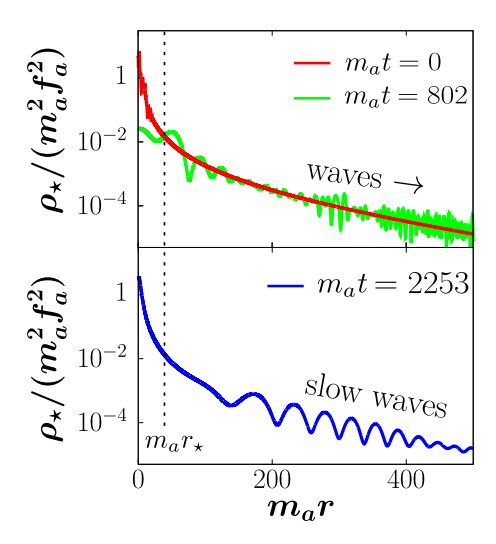


Figure 4.9: Radial axion star profile $\rho_{\star}(r,t)$ at different times t=0,802,2253 in red, green and blue colors, taken from the relativistic simulations of Ref. [35]. The text indicates the generation of relativistic (green) and non-relativistic (blue) waves in the system, which become visible in the soliton profile. Note that between the different points in time t=0,802,2253, several collapse cycles of the form in Fig. 4.8 have occurred in the meantime.

red line in Fig. 4.9 shows the initial soliton profile at $m_a t = 0$, which soon develops into the green profile around $m_a t = 802$ once the production of relativistic waves in the central region $\rho_{\star}(t,0)$ commences. These relativistic waves with $k/m_a \gg v_{\rm esc}$, with the escape velocity $v_{\rm esc}$, will quickly leave the central region thereby transporting energy away from the soliton core. The emission of relativistic particles in Fig. 4.8 is accompanied by the production of non-relativistic modes which are shown as slow density waves in the bottom panel and blue curve of Fig. 4.9. These low energy waves can partially escape the system if their wavenumbers fulfill the inequality $k/m_a > v_{\rm esc}$. However most of the non-relativistic waves with $k/m_a < v_{\rm esc}$ are eventually captured again by the soliton remnant, so that $M_{\star}(t_f) \simeq 0.7 M_{\star}(t=0)$ at the final simulation time t_f [240]. As outlined above, the production of high- and low energy waves, the subsequent soliton dilution and its re-collapse repeat itself multiple times during the evolution of a super-critical system.

An important measure of the bosenova dynamics is given by the energy spectrum $d\mathcal{E}/dk$ of emitted axions shown in Fig. 4.10. The solid line in blue shows the energy spectrum obtained from the simulations of the collapsing axion star, compared to a power-law fit $d\mathcal{E}/dk \propto k^{-2.3}$ shown by the black dashed line. It can clearly be seen, that the energy spectrum exhibits four well pronounced peaks with an approximate width of $\Delta k \approx m_a$.

Different peaks are indicated by the red colored shades and lines respectively, whereas the peaks are centered around the characteristic values $k/m_a \approx 2.4, 3.9, 5.5, 7.1$. The amplitude of the spectrum in Fig. 4.10 is normalized by the scaling of the leading-peak component at $k/m_a \approx 2.4$

$$\frac{\mathcal{E}_{2.4}}{m_a} = \int_{1.9}^{2.9} d(k/m_a) \frac{d\mathcal{E}}{dk} \approx 3400 N_{\star} \frac{f_a^2}{m_a^2} \propto N_{\star} \frac{f_a^2}{m_a^2} \tag{4.44}$$

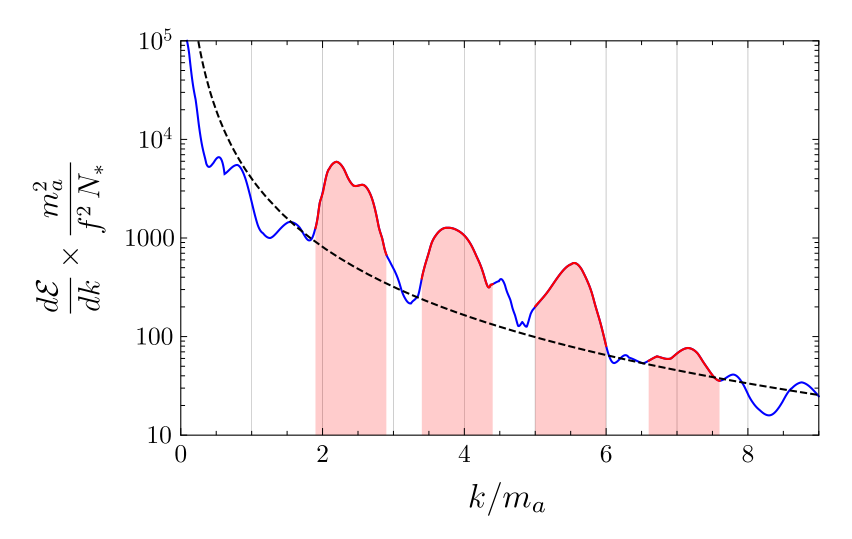


Figure 4.10: Energy spectrum of emitted axions in a bosenova in solid lines together with a power-law fit of the form $d\mathcal{E}/dk \propto k^{-2.3}$ in black dashed lines. The leading peaks of the spectrum with width $\Delta k \approx m_a$ are indicated by the red lines and shaded regions, which are centered around $k/m_a \approx 2.4, 3.9, 5.5, 7.1$. This figure was taken from Ref. [36] and reproduced from the data in Ref. [240].

with $\Delta k = m_a$ and the explosion number $N_{\star} = \mathcal{O}(\text{few})$ [36]. After several repeated collapse cycles involving N_{\star} explosions for $m_a \approx 2 \cdot 10^{-9} \, \text{eV}$, $f_a \approx 3 \cdot 10^{15} \, \text{GeV}$ as above, the authors of Ref. [35] showed that the total energy loss of the system may be well-fit by the linear parametrization

$$f_{\rm em} \equiv \frac{\mathcal{E}_{\rm loss}}{M_{\star,\lambda}} \approx 0.3 + 830 \frac{f_a}{m_{\rm Pl}} \quad , \quad \frac{f_a}{m_{\rm Pl}} \lesssim 10^{-3} \,,$$
 (4.45)

where $m_{\rm Pl}$ is the Planck mass. The final state of the soliton with initial super-critical mass $M_{\star} \geq M_{\star,\lambda}$ in Eq. (4.45) - after experiencing an energy loss $\mathcal{E}_{\rm loss}$ - corresponds to a diffuse gravitationally bound configuration. In different simulations, collapsing axion stars have been observed to lose between 30% and 60% of their mass through axion emission [35].

For simplicity, we will use the conservative estimate $f_{\rm em} = 0.3$ of the emitted energy of a bosenova in the following [3]. Another important scale relates to the duration of a single axion burst emitted from a bosenova event at the source, which is approximately given by

$$\delta t_{\rm burst} \approx \frac{400}{m_a} \approx 6 \, \rm ns \left(\frac{50 \, \mu eV}{m_a} \right)$$
 (4.46)

and which we use in the considerations of axion burst detection in Chap. 7.

4.5 Parametric Resonance

Moving on to the second critical soliton mass, this section deals with the modification of the Maxwell equations in the presence of a homogeneous axion field. The basic goal is to derive a simplified resonance criterion for solitons, similar to what was done in Ref.s [31–33]. Opposed to the critical mass $M_{\star,\lambda}$ from Eq. (4.16) and Sec. 4.4 due to the self-interaction instability, the critical mass in this section represents the onset of resonant conversion of gravitationally bound

axions in the soliton into photons under specific conditions.

To understand these conditions, it is useful to start from the Lagrangian $\mathcal{L}_{a\gamma\gamma}$ from Eq. (2.17) describing the interaction of the electromagnetic field in the presence of an axion field ϕ . Varying the Lagrangian in Eq. (2.17) with respect to the four vector potential $A^{\mu} = (A_0, \mathbf{A})$ and neglecting gradients of the non-relativistic axion field ϕ , which is slowly varying in space $|\nabla \phi| \ll |\partial_t \phi|$, one obtains the equation of motion

$$\ddot{\mathbf{A}}_{\mathbf{k}} + k^2 \mathbf{A}_{\mathbf{k}} + g_{a\gamma\gamma} i \mathbf{k} \int \frac{d^3 k'}{(2\pi)^3} \partial_t \phi_{\mathbf{k} - \mathbf{k}'} \mathbf{A}_{\mathbf{k}'} = 0$$
(4.47)

in Fourier space [32]. Here, the two degrees of freedom of the propagating photon are described by \mathbf{A} , where the corresponding vector potential is formulated in the Coulomb gauge, $\nabla \cdot \mathbf{A} = 0$. The next step is to assume the time- and k-dependence of the axion field in Eq. (4.47). Physically, the system under consideration is a soliton with a Gaussian profile $\rho_{\star}(r)$ of the form in Eq. (4.1), which depends on the soliton mass M_{\star} . However as was shown in the detailed study of Ref. [32], the condition for resonant axion-photon conversion inside of the soliton may be qualitatively described by considering a homogeneous axion field

$$\phi(t) = \phi_0 \cos(\omega_0 t) \tag{4.48}$$

with field amplitude ϕ_0 and an oscillation frequency $\omega_0 \approx m_a$. It is therefore sufficient to insert the homogeneous axion field ϕ from Eq. (4.48) into Eq. (4.47) while expressing the vector potential **A** in terms of time-dependent mode functions $s_{\mathbf{k}}(t)$ (see App. D.1 and Ref. [32] for details). Using these assumptions, the different polarizations decouple and the corresponding mode functions can be shown satisfy so-called *Mathieu equation* [32]

$$\ddot{s}_{k} + \left[k^{2} - g_{a\gamma\gamma} \omega_{0} k \phi_{0} \sin(\omega_{0} t)\right] s_{k} \equiv \ddot{s}_{k} + \omega_{k}^{2}(t) s_{k} = 0,$$
(4.49)

which describes an oscillator with a periodic pump frequency $\omega_k^2(t) = \omega_k^2(t+T)$ and period $T = 2\pi/\omega_0$. According to common literature [245, 246], the solutions to the Mathieu equation exhibit a band structure of stable, oscillating and unstable, exponentially growing solutions. These solutions can be written in the general form

$$s_{\mathbf{k}}(t) = P_{\mathbf{k}}(t)e^{\mu_k t} + P_{\mathbf{k}}(-t)e^{-\mu_k t},$$
 (4.50)

where $P_{\mathbf{k}}(t)$ is a periodic function of time and the parameter μ_k is called the *Floquet exponent*. Importantly for our considerations of resonant axion-photon conversion, the real component of the Floquet exponent μ_k is responsible for the exponentially growing modes.

At small amplitudes, $k/\omega_0 \gg g_{a\gamma\gamma}\phi_0/2$, the resulting spectrum of narrow resonant bands is composed of equally spaced lines with decreasing width, centered around $k^2 \approx (n\omega_0/2)^2$ for $n \in \mathbb{N}^+$. We demonstrate the derivation of the corresponding EOM in App. D.1 by employing the small-amplitude analysis from Ref.s [32, 33]. As for the resonance condition, we summarize that the exponential growth of the photon occupation number from Eq. (4.50) is dominated by the first instability band with n=1, which has the largest width and Floquet exponent $\mu_k^{(n)}$, respectively. Following the derivation in App. D.1, one obtains the exponential growth rate [32]

$$\mu_k^{(1)} = \sqrt{\frac{g_{a\gamma\gamma}^2 k^2 \phi_0^2}{4} - \frac{\left(k^2 - \frac{\omega_0^2}{4}\right)^2}{\omega_0^2}}$$
 (4.51)

of the first instability band at n = 1. The width of this resonant band can be found from the wavenumbers k, where $\mu_k = 0$ and the resonance gets shut off. Denoting the lower and upper edges of the band with minus and plus signs, the edges of the first instability band are given by

$$k_{\pm}^{(1)} = \sqrt{\frac{\omega_0^2}{4} + \frac{g_{a\gamma\gamma}^2 \omega_0^2 \phi_0^2}{16}} \pm \frac{g_{a\gamma\gamma} \omega_0 \phi_0}{4} = k_c^{(1)} \pm \frac{\Delta k^{(1)}}{2}, \qquad (4.52)$$

where $k_c^{(1)}$ is the center of the n=1 band and the corresponding bandwidth $\Delta k^{(1)}$ is proportional to the axion-photon coupling constant $g_{a\gamma\gamma}$:

$$\Delta k^{(1)} = k_{+}^{(1)} - k_{-}^{(1)} = \frac{g_{a\gamma\gamma} \,\omega_0 \,\phi_0}{2} \,. \tag{4.53}$$

For small amplitudes $k/\omega_0 \gg g_{a\gamma\gamma}\phi_0/2$, the central wavenumber

$$k_c^{(1)} = \omega_0/2\sqrt{1 + g_{a\gamma\gamma}^2 \phi_0^2/2}$$
 (4.54)

with $\omega_0 \approx m_a$ is approximately equal to half the axion mass $k_c^{(1)} \approx m_a/2$. At this specific value of $k = k_c^{(1)} \approx m_a/2$, the growth exponent in Eq. (4.51) takes its maximum value of

$$\mu_H \approx \frac{g_{a\gamma\gamma} \, m_a \, \phi_0}{4} \,, \tag{4.55}$$

where the subscript H emphasizes that this result was obtained for the homogeneous axion field in Eq. (4.48). Note that the n=1 instability band considered in this section represents the decay process $a \to \gamma + \gamma$, which does not include effects of Bose enhancement and therefore does not depend on the number of previously produced particles. Similarly, the second instability band with n=2 and $\omega=\omega_0$ in Eq. (D.11) amounts to the process $a+a\to\gamma+\gamma$. For the small amplitudes considered in this section however, higher order processes n>1 are suppressed compared to the first instability band so that the leading-order resonance described in Eq. (4.55) is sufficient to find the resonance condition we are interested in.

Coming back to the relevant case of solitons with a non-homogeneous profile $\rho_{\star}(r)$, Ref. [32] investigated the parametric resonance of axion stars by exploiting the spherical symmetry of the problem. According to their numerical calculations, the corresponding maximum growth rate μ_{\star} of the spherically symmetric soliton is approximately given by

$$\mu_{\star} \approx \begin{cases} \mu_H - \mu_{\rm esc}, & \mu_H > \mu_{\rm esc} \\ 0, & \mu_H < \mu_{\rm esc} \end{cases} , \tag{4.56}$$

where μ_H is the maximum growth rate of the homogeneous condensate in Eq. (4.55) and $\mu_{\rm esc} \approx 1/(2R_{\star})$ is the photon escape rate of the soliton with characteristic radius R_{\star} . For the Gaussian radial profile in Eq. (4.1) assumed in this work, the axion field amplitude ϕ_0 in Eq. (4.55) can be obtained from the wavefunction $\psi(r)$ following Eq. (3.10) and

$$\phi_0 = \sqrt{\frac{2}{m_a}} \psi_0 = \sqrt{\frac{2M_{\star}}{m_a^2 \pi^{3/2} R_{\star}^3}} \,. \tag{4.57}$$

Inserting the above expression for ϕ_0 together with $\mu_{\rm esc} \approx 1/(2R_{\star})$ and μ_H from Eq. (4.55), the resonance condition $\mu_H > \mu_{\rm esc}$ in Eq. (4.56) can be rephrased into the condition [2, 33]

$$g_{a\gamma\gamma}f_a > 0.42 \left[\frac{c_{\lambda}g(\alpha_{\star})}{\alpha_{\star}}\right]^{1/2}$$
 (4.58)

for the axion parameters $g_{a\gamma\gamma}$, $\lambda = -c_{\lambda}m_a^2/f_a^2$ and f_a . Here the parameter $\alpha_{\star} \in (0,1]$ and the function $g(\alpha_{\star}) = (1 + \sqrt{1 - \alpha_{\star}^2})/\alpha_{\star}$ were used to express the soliton mass M_{\star} and radius R_{\star} [33]

$$M_{\star} = \alpha_{\star} M_{\star,\lambda} \tag{4.59}$$

$$R_{\star} = g(\alpha_{\star}) R_{\star,\lambda} \,, \tag{4.60}$$

in terms of the mass-radius relation Eq. (4.17) and the critical quantities $M_{\star,\lambda}$, $R_{\star,\lambda}$ from Eq. (4.16) ⁷.

Since α_{\star} , $g(\alpha_{\star})$ are essentially functions of M_{\star} , R_{\star} with the critical quantities $M_{\star,\lambda}$, $R_{\star,\lambda}$ being fixed at each axion model m_a , n, the condition Eq. (4.58) can be rephrased into a mass requirement for the axion star mass $M_{\star} \geq M_{\star,\gamma}$. Thus entering M_{\star} , R_{\star} from Eq. (4.59), using the mass-radius relation from Eq. (4.17) and rearranging for M_{\star} , we obtain the critical mass [2]

$$M_{\star,\gamma} \simeq 5.94 \cdot 10^{-14} M_{\odot} \left(\frac{50 \,\mu\text{eV}}{m_a} \right) \left(\frac{10^{-11} \text{GeV}^{-1}}{g_{a\gamma\gamma}} \right)^2 \left(\frac{10^{11} \text{GeV}}{f_a} \right) \sqrt{\left(\frac{g_{a\gamma\gamma} f_a}{0.42} \right)^2 - \frac{c_{\lambda}}{2}} , \quad (4.61)$$

beyond which the decay of axions into photons in the soliton leads to a parametric resonance with exponential enhancement of the photon occupation number with μ_{\star} given by Eq. (4.56). The detailed derivation of $M_{\star,\gamma}$ can be found in App. D.2.

Importantly, axion stars with $M_{\star} > M_{\star,\gamma}$ can act as resonant amplifiers of ambient photons with frequencies $f \simeq m_a/(4\pi)$ through cascade-like stimulated emission. The essential picture here is that a photon with suitable frequency f passing through the soliton with radius R_{\star} can stimulate the emission of another photon, which excites emission of another photon along traveling a distance $\sim R_{\star}$ and so forth.

Accordingly, axion stars with $M_{\star} > M_{\star,\gamma}$ acquire an additional mechanism of energy emission, which is triggered rapidly after reaching $M_{\star,\gamma}$ and which has directly observable consequences. We demonstrate numerical predictions for the expected radio emission of resonant axion stars in Subsec. 5.5.1 and explore the combined predictions arising from the continuous mass growth of axion stars in Sec. 4.3 triggering the instability above $M_{\star,\gamma}$ in Chap. 6. Before doing so however, we need to establish a formalism to derive the mass distribution of axion stars from that of their host miniclusters in Chap. 3. This will be done in the remaining sections of this chapter.

4.6 Core-Halo Relation of Axion Stars

The missing link connecting the mass distribution of galactic miniclusters from Sec. 3.6 to the properties of their axion star cores was already introduced in Sec. 3.7. However there is a crucial limitation inherent to the canonical core-halo relation in Eq. (3.57), which is related to the fact that it was derived for negligible self-interactions, $\lambda = 0$, specifically [169]. An

⁷Note that the different proportionality constant in Eq. (4.58) is due to the fact that Ref.s [32, 33] used a $\operatorname{sech}(x)$ profile opposed to the Gaussian profile used in Eq. (4.1) and Ref. [2].

important question, which arises naturally for the ASMC systems with weak self-interactions $\lambda = -m_a^2/f_a^2 < 0$ considered in this work, is whether and to what extent the mass relation Eq. (3.57) may be applied for soliton cores with a λ -dependent mass-radius relation of the form in Eq. (4.17). To answer this question, we take two different approaches for estimating the expected modification of the core-halo relation from Eq. (3.57), under the influence of weak attractive self-interactions. Both of the approaches in Subsec. 4.6.1 and Subsec. 4.6.2 are based on the analytical calculations in Ref.s [241, 247, 248], which will be used to infer constraints on the applicability of the $\lambda = 0$ relation from Ref. [169] as a function of M_{\star} , \mathcal{M} and m_a , n.

We emphasize, that the derivation and simulation of an extended core-halo relation for self-interacting systems are beyond the scope of this work. Furthermore it is important to note here that the canonical core-halo relation in Eq. (3.57) is far from universal. To this date, there is an ongoing discussion on the meaning and distinction of different core-halo scalings $M_{\star} \propto \mathcal{M}^{\beta}$ with $1/3 \leq \beta \leq 2/3$ [169, 204, 249]. The major conclusion seems to be that the observed scaling depends sensitively on the initial conditions and the merger history of the simulation. We direct the attention of the interested reader to Ref.s [241, 247–249] for detailed reviews on the topic and to Ref.s [205, 206, 250, 251] for recent investigations.

Since our considerations involve axion minicluster systems forming around redshifts $z \sim z_{\rm eq}$, we use the canonical relation in Eq. (3.57), which was numerically confirmed for $z \sim z_{\rm eq}$ in the minicluster simulations of Ref. [167]. In a more general context, our approach in deriving the ASMF in Sec. 4.7 and Fig. A.1 is strongly modular, so that any update on the mass relation of axion stars could be easily implemented.

4.6.1 Modification of virial Velocities

We start with the first of two equivalent approaches in the derivation of the $M_{\star} \propto \mathcal{M}^{1/3}$ scaling. This first approach is based on the assumption that the virial velocity of the total system equilibrates with the characteristic velocity of the soliton, $v_{\star, \text{vir}} \simeq v_{\text{mc,vir}}$ at late times [171, 174]. Using the virial velocity of a gravitating sphere for the minicluster in Eq. (4.35) together with the soliton groundstate property from Eq. (4.34), one can directly obtain the $\beta = 1/3$ scaling by expressing the radius as $\mathcal{R} = [3\mathcal{M}/(4\pi\rho_{\text{mc}})]^{1/3}$.

Note however that the groundstate solution of the Schrödinger-Poisson system used to derive $v_{\star, \text{vir}}$ deviates from Eq. (4.34) in the general case $|\lambda| \neq 0$. This is why the authors of Ref. [247] modified the standard assumption $v_{\star, \text{vir}} \simeq v_{\text{mc,vir}}$ for the virial velocities of the star and total system by introducing a modified *virialization condition* of the form

$$\frac{GM_{\star}}{R_{\star}} \simeq D_h \frac{G\mathcal{M}}{\mathcal{R}} \,, \tag{4.62}$$

where the perturbative coefficient D_h is determined by matching the $\lambda=0$ results to those of Schive et al. [169]. In this approach, both the minicluster and its soliton core are modeled as spherical overdensities, where the deviations from the standard virialization condition are contained in the effective modification constant D_h . In the following, we summarize the results from Ref. [247], who presented a redshift-independent extension of the core-halo relation Eq. (3.57) for arbitrary $|\lambda| > 0$ based on the analytical approaches in Ref.s [169] and [249].

Combining Eq. (4.62) with the mass-radius relation of self-interacting axion stars in Eq. (4.17), the authors of Ref. [247] showed that the extended core-halo relation scales as $M_{\star} \propto \sqrt{1 + \Delta \lambda(\mathcal{M})}$

at z = 0, where the corresponding perturbation term

$$\Delta \lambda = 1.48 \cdot 10^{-9} \left(\frac{f_a}{10^{11} \,\text{GeV}} \right)^{-2} \left(\frac{\mathcal{M}}{10^{-13} M_{\odot}} \right)^{2/3} \tag{4.63}$$

quantifies the expected modification of M_{\star} compared to Eq. (3.57) and Eq. (3.58). We apply the

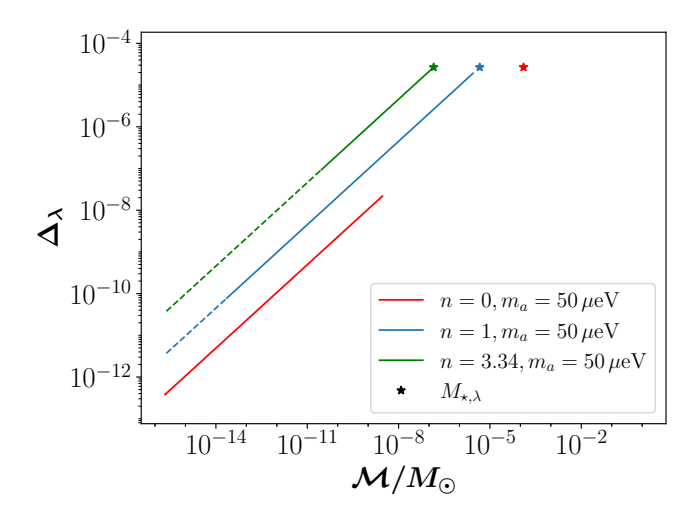


Figure 4.11: Perturbation term $\Delta\lambda(\mathcal{M}, f_a)$ from Eq. (4.63) measuring the modification of $M_{\star}(\mathcal{M})$ at $|\lambda| > 0$ compared to the $\lambda = 0$ mass relation in Eq. (3.57). Both with colors indicating different values for the axion mass m_a and its temperature dependence n. The ranges of M_{\star} obtained with the \mathcal{M}_{0} - and \mathcal{M}_{J} -cutoffs from Subsec. 3.5.2 are shown in solid and dashed lines. Stars correspond to the maximum stable AS mass $M_{\star,\lambda}$ from Eq. (4.16). The figure was taken from Ref. [1].

perturbative measure $\Delta\lambda$ from Eq. (4.63) to redshift $z=z_{\rm eq}$ in Fig. 4.11 for $m_a=50\,\mu{\rm eV}$ and find that the predicted modification due to self-interactions λ remains negligible $\Delta\lambda\leq 3\cdot 10^{-5}$ for every $m_a, n=0,1,3.34$ and for every stable branch soliton with mass M_{\star} .

The colored lines in Fig. 4.11 indicate the different axion star mass ranges predicted from the two low-mass cutoffs of the MCMF in Sec. 3.5, where solid lines correspond to the \mathcal{M}_0 -cutoff from Eq. (3.47) and dashed lines show the \mathcal{M}_J -cutoff from Eq. (3.45). As a consequence of the scaling of \mathcal{M}_{max} in Eq. (3.46) with \mathcal{M}_0 and n (see also Fig. 3.7), the range of AS masses for n = 1, 3.34 in blue and green extends to larger M_{\star} compared to the temperature-independent cases in red.

We generally confirm that for all axion models m_a, n under consideration, the contribution of $\Delta \lambda$ remains negligible. For the specific case of $m_a = 50 \,\mu\text{eV}$ in Fig. 4.11, the perturbation parameter reaches its maximum value of $\Delta \lambda \simeq 3 \cdot 10^{-5}$ at $M_{\star} = M_{\star,\lambda}$.

This result is not surprising since we had limited our analysis to the dilute stable branch of axion stars, which is characterized by dominance of gravity over short-range interactions. Let us emphasize here that, in contrast, the smallness of $\Delta\lambda$ would break down entirely on the dense branch, where axion self-interactions become the dominant force in the system. The long-term stability of the dilute component in the mass radius relation in Fig. 4.1 thus provides a natural parameter space in which the $\lambda=0$ relation Eq. (3.57) remains applicable.

Nevertheless, some modifications of the core-halo relation in Eq. (3.57) are expected to occur

once the star mass approaches the critical point $M_{\star} = M_{\star,\lambda}$, where both gravitational and self-interacting contributions become comparably important. This is why we additionally employ a second, more conservative approach to estimate possible modifications to the core-halo relation in Subsec. 4.6.2.

4.6.2 Modification of specific Energies

The second approach to derive the mass relation Eq. (3.57) is given by the approximate equality of the specific energies E_{\star}/M_{\star} and ε/M of the soliton and its host minicluster respectively. This scaling was originally observed in the numerical simulations of Ref. [169], which established the canonical $\beta = 1/3$ relation. As was shown in Ref. [241], the virialization condition $v_{\star, \text{vir}} \simeq v_{\text{mc,vir}}$ is equivalent to the requirement

$$\frac{|E_{\star,\text{tot}}|}{M_{\star}} \simeq \frac{|\mathcal{E}|}{\mathcal{M}} \stackrel{E_{\star,\text{tot}} \sim E_{\text{grav}}}{\Longrightarrow} \frac{GM_{\star}}{R_{\star}} \simeq \frac{G\mathcal{M}}{\mathcal{R}}$$
(4.64)

for the specific energies of the composite ASMC system. The total star energy $E_{\star,\text{tot}}$ in Eq. (4.64) is typically assumed to be on the order of the gravitational binding energy E_{grav} from Eq. (4.3) [169, 247]. This assumption remains valid for most of the dilute branch solitons with $M_{\star} \ll M_{\star,\lambda}$, which are considered for the galactic ASMF. Instead of the modified virialization approach from Subsec. 4.6.1 and Eq. (4.62) we can thus consider the changes in $E_{\star,\text{tot}}$ and \mathcal{E} to measure the effective modification of the core mass relation in Eq. (3.57).

Starting with the right-hand side of Eq. (4.64), which measures the change $\Delta \mathcal{E}$ in the minicluster energy, we can argue that for typical ASMC systems with overdensity parameter $\Phi \sim 1$, the minicluster density $\rho_{\rm mc}$ in Eq. (3.23) will be much lower than that of their axion star cores $\rho_{\star} \lesssim M_{\star,\lambda}/R_{\star}^3 \sim 10^{23} \,\mathrm{GeV/cm^3}$, where we have used QCD axion parameters $m_a = 50 \mu\,\mathrm{eV}$ and n = 3.34. In these dilute systems, the short-range self-interaction will be negligible compared to the long-range gravitational force (see also Ref. [247] for a detailed calculation). Physically, the self-interaction energy of the minicluster in the Hamiltonian of Eq. (4.9) scales with a higher power of the small field $E_{\rm int} \propto |\widetilde{\psi}|^4$ compared to the gravitational scaling $E_{\rm grav} \propto |\widetilde{\psi}|^2$ with $|\widetilde{\psi}| < 1$ as depicted in Fig. 4.2.

Thus assuming $\Delta \mathcal{E} \ll \mathcal{E}$ for the host miniclusters, the relevant energy shift in the equilibrium state described by Eq. (4.64) is simply given by the left-hand side contribution

$$\Delta E_{\star} \equiv |E_{\star, \text{tot}} - E_{\star, \text{tot}}(\lambda = 0)| = |E_{\text{int}}|, \qquad (4.65)$$

where $E_{\star,\mathrm{tot}}(\lambda=0)$ is the Schrödinger-Poisson soliton energy evaluated at $\lambda=0$. We show the relative energy shifts $|\Delta E_{\star}/E_{\mathrm{grav}}|=E_{\mathrm{int}}/E_{\mathrm{grav}}$ appearing in the specific energy ansatz from Eq. (4.64) in Fig. 4.12, again for $m_a=50\,\mu\mathrm{eV}$ and n=0,1,3.34. Like before, the range of masses M_{\star} in Fig. 4.12 corresponds to the core-masses derived from the MCMF in Fig. 3.8 using the core-halo relation in Eq. (3.57) with the \mathcal{M}_J -cutoff in dashed and the \mathcal{M}_0 -cutoff in solid colored lines. Fig. 4.12 thus demonstrates that the condition in Eq. (4.64) is more stringent than the virial velocity approach from Eq. (4.62) and that it yields qualitatively similar results by predicting negligible energy shifts $|\Delta E_{\star}/E_{\mathrm{grav}}| \ll 1$ for the majority of the soliton mass range M_{\star} .

There is however a small mass range, where M_{\star} becomes similar to the maximum stable mass $M_{\star,\lambda}$ (i.e. close to the gray line and colored stars) and the relative perturbation term

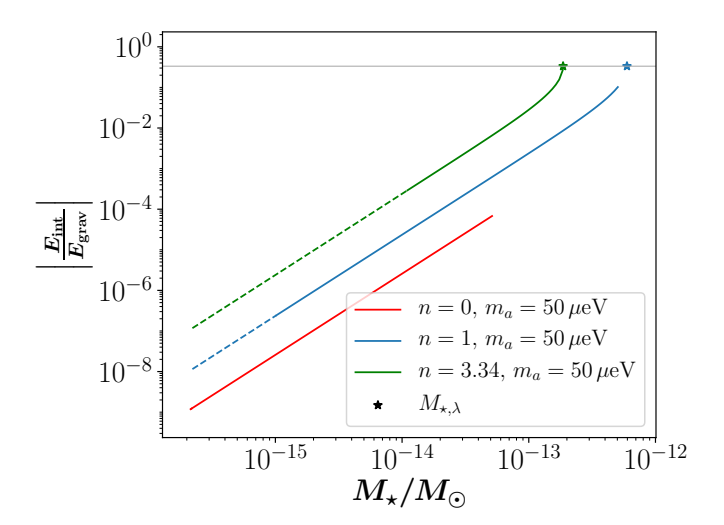


Figure 4.12: Relative core energy fractions $|\Delta E_{\star}/E_{\rm grav}|$ as a function of AS mass M_{\star} reaching up to $|\Delta E_{\star}/E_{\rm grav}| = 1/3$ indicated by the gray line. Stars correspond to the maximum stable AS mass $M_{\star,\lambda}$ from Eq. (4.16). The figure was taken from Ref. [1].

 $|\Delta E_{\star}/E_{\rm grav}| \approx 1/3$ reaches its maximum value. In this mass range, one expects any extended core-halo relation to be modified compared to Eq. (3.57) from Ref. [169]. Importantly for our considerations, even at the critical point $M_{\star} = M_{\star,\lambda}$, the expected energy shift in Eq. (4.64) is of order one. This leads us to the conclusion that the $\lambda = 0$ core-halo relation should still provide us with a reasonable estimate that is well within the large uncertainties of the linear growth MCMF in Sec. 3.5.

To summarize the results of this section, we have checked the applicability of the core-halo relation from Eq. (3.57) using both the virial velocity approach from Ref. [247] in Fig. 4.11 and our more stringent energy modification in Fig. 4.12. In both of these cases we find negligible effects for the majority of soliton masses with $M_{\star} \ll M_{\star,\lambda}$, and limited evidence for order-one modifications at near-critical masses $M_{\star} \sim M_{\star,\lambda}$. Therefore and restricting our analysis of the galactic axion star distribution to dilute stable solitons, we use the canonical mass relation in Eq. (3.57) as an order-of-magnitude estimate for M_{\star} , while keeping in mind the need for an extended core-halo relation for more precise predictions.

4.7 Galactic Axion Star Mass Distribution

Having confirmed the validity of the core-mass relation Sec. 3.7 in the previous section, we are finally in a position to derive the galactic axion star mass distribution from the MCMF in Sec. 3.5. To ensure the physical consistency of our composite ASMC model, we need to obey the minimum mass requirement $\mathcal{M} \geq \mathcal{M}_{h,\text{min}}$ from Eq. (3.58) together with another condition for the size of R_{\star} and \mathcal{R} . These additional cutoffs will be introduced in Subsec. 4.7.1 before we analyze the resulting ASMF in detail in Subsec. 4.7.2.

In terms of the schematic representation of Fig. A.1, we have arrived at the rectangular lightblue panel depicting the determination of the present-day ASMF. This step presents a crucial result for the analysis in this thesis since it allows us to combine previous investigations, namely

numerical results in yellow and experimental limitations in gray panels in Fig. A.1, with the ASMF to infer novel observation methods for axion small-scale structure in Chap. 5 to Chap. 7.

4.7.1 Low-Mass Cutoffs in Axion Star Distributions

Starting with the introduction of the two fundamental consistency requirements of the ASMF, we have assumed that each minicluster can contain up to a single soliton core, whose mass $M_{\star} \subset \mathcal{M}$ is embedded in the composite structure with total mass \mathcal{M} , also referred to as the minicluster mass. Furthermore, the definition of the axion star core requires the object to be situated at the center of the minicluster, which implies that its size is expected to be smaller than the size \mathcal{R} from Eq. (3.24). We formulate these fundamental considerations analytically by demanding two conditions for the existence of a composite ASMC system: First, that the total mass \mathcal{M} entering the core-halo relation in Eq. (3.57) is larger or equal to the mass of its core and secondly that the radius of the axion star should not exceed that of its host minicluster:

$$M_{\star}(\mathcal{M}) \stackrel{!}{\leq} \mathcal{M}, \tag{4.66}$$

$$R_{\star}(M_{\star}) \stackrel{!}{\leq} \mathcal{R} \,, \tag{4.67}$$

where we use the dilute branch mass-radius relation from Eq. (4.18) in the second condition, as before. Note that the mass configuration leading to the equality in Eq. (4.66) was used in Ref. [169] to define the redshift-dependent minimum mass from Eq. (3.58). This means that the corresponding low- M_{\star} cutoff of the ASMF is straight-forwardly obtained by requiring $M_{\star} \geq M_{\star}(\mathcal{M}_{h,\min}) = \mathcal{M}_{h,\min}$ using the core-halo relation and Eq. (3.58).

The second axion star mass threshold relating to Eq. (4.67) can be calculated by solving for M_{\star} , with R_{\star} given by the mass-radius relation Eq. (4.18) and \mathcal{R} from Eq. (3.24). Again demanding equality, $\mathcal{R} \stackrel{!}{=} R_{\star}$, and using Eq. (4.18), Eq. (3.24) and Eq. (3.57), we obtain the critical minimum axion star mass of the radius cutoff with index 'R'

$$M_{\star,R} = 4.87 \cdot 10^{-17} \, M_{\odot} \, \sqrt{\Phi} (1+\Phi)^{1/6} \, \sqrt{\frac{\alpha_{\rm kin} R_{\star,90}}{\alpha_{\rm grav} R_{\star}}} \left(\frac{1+z}{1+z_{\rm eq}}\right)^{1/4} \left[\frac{\zeta(z)}{\zeta(z_{\rm eq})}\right]^{1/12} \left(\frac{m_a}{50 \, \mu \text{eV}}\right)^{-3/2}, \tag{4.68}$$

where we have dropped an additional term which can be neglected as long as the condition

$$f_a \gg 18 \,\text{GeV} \,\sqrt{\Phi} (1+\Phi)^{1/6} \left(\frac{m}{50 \,\mu\text{eV}}\right)^{1/2} \left(\frac{1+z}{1+z_{\text{eq}}}\right)^{1/4} \left[\frac{\zeta(z)}{\zeta(z_{\text{eq}})}\right]^{1/12}$$
 (4.69)

is fulfilled (see App. D.3 for details). We checked that in our framework with $f_a \gtrsim 10^{10}\,\text{GeV}$ following Fig. 3.6 and for an axion mass range of $10^{-12}\,\text{eV} \le m_a \le 10^{-3}\,\text{eV}$, Eq. (4.69) remains valid even for the densest miniclusters with $\Phi \sim 10^4$.

Note that as argued in Ref. [1], our predictions for the radius cutoff do not match the results observed in Ref. [188], who used the same MCMF parametrization and core-halo relation from Subsec. 3.5.2 and Sec. 3.7 at a QCD axion mass of $m_a = 20 \,\mu\text{eV}$. The simple explanation for this discrepancy is the fact that our approach to the core-halo relation Eq. (3.57) was evaluated at redshift $z = z_{\text{eq}}$ compared to the assumption z = 0 applied in Ref. [188]. Using the collapse

redshift z=0, Ref. [188] reported that none of the systems with $\mathcal{M} \leq 5 \cdot 10^{-16} M_{\odot}$ passed the radius cutoff from Eq. (4.67) at $m_a=20\,\mu\text{eV}$ and $\Phi\sim 0.1$. We can compare our result from Eq. (4.68) to their prediction by relating $M_{\star,R}$ to its minicluster equivalent, which gives

$$\mathcal{M}_{R,\min}(z) = 2.07 \cdot 10^{-18} \, M_{\odot} \left(\frac{\alpha_{\rm kin} R_{\star,90}}{\alpha_{\rm grav} R_{\star}} \right)^{3/2} \sqrt{\Phi^{3}(1+\Phi)} \left(\frac{1+z}{1+z_{\rm eq}} \right)^{-3/4} \times \left[\frac{\zeta(z)}{\zeta(z_{\rm eq})} \right]^{-1/4} \left(\frac{m_{a}}{50 \, \mu \text{eV}} \right)^{-3/2} , \tag{4.70}$$

where the coefficients α_i and $R_{\star,90}$ are specific to the Gaussian ansatz in Eq. (4.1). Thus evaluating Eq. (4.70) for z=0 and with m_a , Φ as in Ref. [188], we find $\mathcal{M}_{R,\min}(0)=6.55\cdot 10^{-16}M_{\odot}$ at $m_a=20\,\mu\text{eV}$, $\Phi\sim0.1$, which agrees well with the observation $\mathcal{M}_{R,\min}(0)\approx 5\cdot 10^{-16}\,M_{\odot}$ made in Ref. [188].

The remaining question is which of the two approaches for the collapse redshift $z_c = 0$, $z_{\rm eq}$ should be used. Referring to the formation of axion stars in Fig. 3.11 and Ref. [167], numerical simulations clearly favor $z_c \sim z_{\rm eq}$. This means that the ASMC systems undergo an early collapse around matter-radiation equality after which the gravitationally bound structures decouple from the cosmic expansion, thus freezing the redshift-dependence of the collapsed system at $z = z_{\rm eq}$. Despite this preference, the redshift dependence of the core-halo relation Eq. (3.57) remains subject to open debate, which is why keep track of z in our calculations.

Putting all of the above together, we can use Eq. (3.58) and Eq. (4.70) to calculate the two ASMF cutoffs for different axion models m_a, n . For completeness, we have also added the n-dependent low-mass cutoffs $\mathcal{M}_{0,\text{min}}$ and $\mathcal{M}_{J,\text{min}}$ from Eq. (3.45), Eq. (3.47) to the cutoff masses $\mathcal{M}_{h,\text{min}}$, $\mathcal{M}_{R,\text{min}}$ in Fig. 4.13. It can be seen that essentially all of the AS-cutoff (minicluster) masses

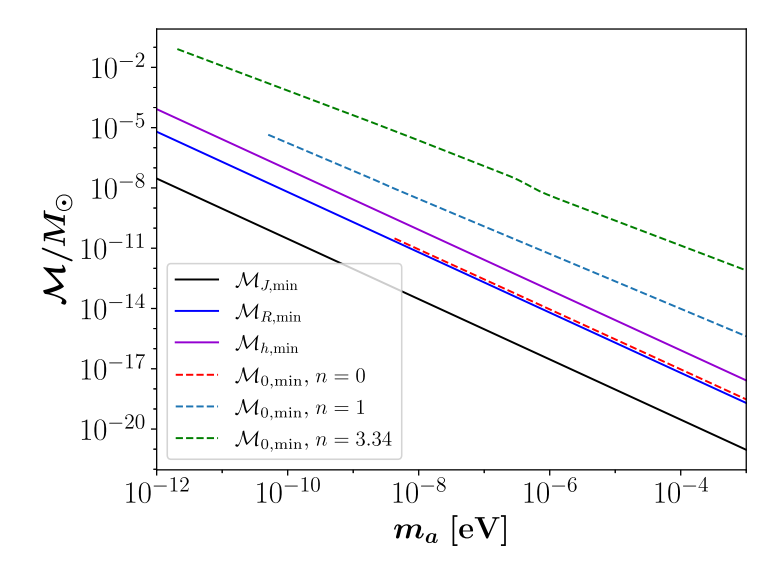


Figure 4.13: Different MC masses setting the low- \mathcal{M} cutoffs of the ASMF at $z=z_{\rm eq}$ as a function of m_a , taken from Ref. [1]. Quantities in solid colored lines are independent of the axion mass temperature index n, while the dashed colored lines show the different n-dependent \mathcal{M}_0 -cutoffs from Eq. (3.47).

in Fig. 4.13 scale as $\mathcal{M} \propto m_a^{-3/2}$, with only minor deviations applying to the to the dashed

colored \mathcal{M}_0 -cutoffs with n > 0 and a modified temperature evolution [58]. In the absence of the \mathcal{M}_0 -cutoff and for n = 0 in red lines, Fig. 4.13 shows that the most stringent requirement for the formation of composite ASMC systems is the purple minimum MC mass $\mathcal{M}_{h,\text{min}}$. Note that this prediction differs from the results in Ref. [188] due to the deviating redshift-dependence of $M_{\star,h}(z)$ and $M_{\star,R}(z)$ in Eq. (3.58) and Eq. (4.68).

In a more general context, the choice of the relevant minicluster threshold masses $\mathcal{M}_{i,\text{min}}$ depends on the specific scenario at hand. While the cutoff masses in Fig. 4.13 apply to any consideration involving axion star cores, we will see in Chap. 6 and Chap. 7 that additional cutoffs become necessary when accretion is taken into account. We also emphasize that the low-mass cutoffs $\mathcal{M}_{h,\text{min}}$, $\mathcal{M}_{R,\text{min}}$ introduced in this section do only apply to axion star core formation i.e. only to the ASMF and not to the MCMF in Subsec. 3.6.2. This fact can be phenomenologically advantageous since the total number of miniclusters in the Milky Way is less constrained than the total number of axion stars, i.e. $\mathcal{N}_{\text{tot}} \geq N_{\star,\text{tot}}$, as we will see in the next section.

Lastly we also implement an additional cutoff to the axion model parameter space m_a, n numerically, where the minimum soliton mass in the ASMF becomes comparable to the maximum stable AS mass, $\min(M_{\star}) \approx M_{\star,\lambda}$, and the gravitational limit of the core-halo relation breaks down for the entire AS population. However this condition only applies to a small region of the low- m_a component of axions with $n \geq 3.34$ and for the \mathcal{M}_0 -cutoff.

4.7.2 Axion Star Mass Distributions

In this subsection, we can finally infer the galactic ASMF from the MCMF for both the \mathcal{M}_J -and the \mathcal{M}_0 -cutoff from Subsec. 3.5.2 under additional consideration of the core-halo cutoff from Eq. (3.58) and the radius cutoff in Eq. (4.68). The results presented in this subsection are taken from Sec. VI.C in Ref. [1]. Analogously to the MCMF in Eq. (3.36), the logarithmic mass distribution of axion stars is defined as the comoving number density $dn_{\star}/d\ln(M_{\star})$ per logarithmic AS mass interval. The ASMF is connected to the MCMF by the relation $dn = dn_{\star}$ [34], which leads to the simple relation

$$\frac{dn_{\star}}{d\ln M_{\star}} = 3\frac{dn}{d\ln \mathcal{M}} \tag{4.71}$$

with the right-hand side defined in Eq. (3.51) and where the factor of 3 comes from the core-halo scaling $M_{\star} \propto \mathcal{M}^{1/3}$ in Eq. (3.57).

Combining this definition with the knowledge from previous sections, we can follow the approach from Fig. A.1 leading to the blue ASMF panel, which we briefly summarize for reasons of comprehensibility: We apply our generalized axion model approach from Chap. 2 and Subsec. 3.6.1, where we determine f_a by requiring $\Omega_a^{\text{tot}} = 0.12$ for a given model m_a, n . For each combination of m_a, n , we infer the characteristic minicluster mass \mathcal{M}_0 and from that the parametrized MCMF from Subsec. 3.5.2, whose total mass in Eq. (3.52) we normalize to the Milky Way mass $\mathcal{M}_{\text{mc,tot}} = f_{\text{mc}} \mathcal{M}_{\text{MW}}$ with $f_{\text{mc}} = 0.75$ [30]. We then apply the $\lambda = 0$ core-halo relation to the MCMF hosting dilute stable axion stars while taking into account the effective low-mass cutoff

$$\mathcal{M}_{\star \min} = \max(\mathcal{M}_{\min}, \mathcal{M}_{h,\min}, \mathcal{M}_{R,\min}) \tag{4.72}$$

of the ASMF given by the MCMF cutoff masses $\mathcal{M}_{\min} = \mathcal{M}_{J,\min}$, $\mathcal{M}_{0,\min}$, together with $\mathcal{M}_{h,\min}$ from Eq. (3.58) and $\mathcal{M}_{R,\min}$ from Eq. (4.70). Only ASMC systems with total masses $\mathcal{M} \geq$

 $\mathcal{M}_{\star,\text{min}}$ are expected to host a stable axion star core according to our previous analysis. The representative ASMF obtained from the host MCMF in Fig. 3.8 for an axion mass $m_a = 50 \,\mu\text{eV}$ and with slope index $\alpha = -1/2$ is shown in Fig. 4.14. For each value of n = 0, 1, 3.34,

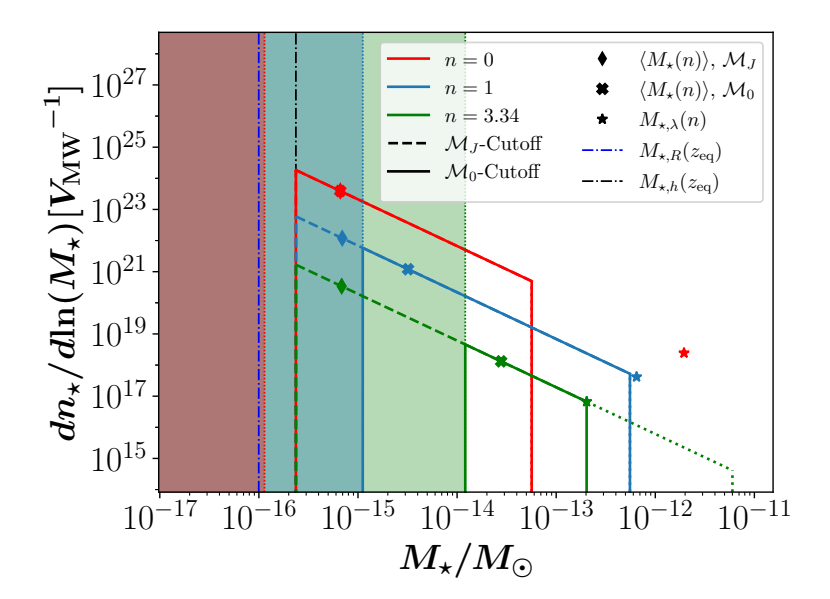


Figure 4.14: ASMF per Milky Way volume obtained from the MCMF for $\alpha = -1/2$ in Fig. 3.8. Colored lines and symbols indicate AS masses at different n = 0, 1, 3.34; the shaded regions and thin dotted colored lines denote the low-mass cutoffs given by $\mathcal{M}_0(m_a, n)/25$. Solid and dashed lines indicate the ASMF with and without applying the \mathcal{M}_0 -cutoffs; dash-dotted lines represent the radius cutoff in Eq. (4.68) in purple and the core-halo cutoff in Eq. (3.58) in black. Colored stars refer to the maximum stable AS mass $M_{\star,\lambda}$ from Eq. (3.57), above which the n = 3.34 component is truncated due to stability (see thick green dotted line). The average AS masses for the two low- \mathcal{M} cutoffs from Subsec. 3.5.2 following Eq. (4.77) are shown in colored diamonds and crosses. Taken from Ref. [1].

the maximum stable AS mass $M_{\star} = M_{\star,\lambda}$ due to self-interactions is indicated with colored stars, while dashed and solid colored lines show the ASMF mass ranges obtained from the two different low- \mathcal{M} cutoffs \mathcal{M}_{\min} in Subsec. 3.5.2.

In the case of n=3.34 in green, we have additionally applied a high-mass cutoff in dotted green lines, where the predicted core mass lies above the maximum stable mass $M_{\star} \geq M_{\star,\lambda}$. The relatively small number of such systems could have reached a critical stage resulting in a bosenova as discussed in Sec. 4.4. In theory, the repeated axion bursts produced during the collapse could introduce sufficient mass-loss for the star to reach a sub-critical configuration again, i.e. $M_{\star} \leq M_{\star,\lambda}$, thus ensuring long-time survival of the corresponding ASMC systems. However, due to their relatively small abundance and from a lack of knowledge about their detailed evolution, we will ignore the super-critical ASMF component in this work.

In agreement with the low- \mathcal{M} cutoffs shown in Fig. 4.13, the red low- M_{\star} component of the n=0 ASMF in Fig. 4.14 is truncated by the core-halo cutoff $\mathcal{M}_{h,\text{min}}$ from Eq. (3.58) for both of the MCMF cutoffs $\mathcal{M}_{\text{min}} = \mathcal{M}_{J,\text{min}}, \mathcal{M}_{0,\text{min}}$ (see the black dash-dotted line in Fig. 4.14 and Fig. 3.8). The other cases n=1,3.34 in blue and green on the other hand, are either cut off by the core-halo mass $\mathcal{M}_{h,\text{min}}$ or the \mathcal{M}_0 -cutoff mass $\mathcal{M}_{0,\text{min}}$. Comparing the low-mass components

of the MCMF and ASMF with the \mathcal{M}_{J} -cutoff in solid lines in Fig. 3.8 and Fig. 4.14, it can be seen that numerous ASMC systems do not pass the effective AS cutoff in Eq. (4.72) due to their total masses being below the minimum threshold $\mathcal{M} < \mathcal{M}_{\star, \min}$.

We also highlight an important feature of the ASMF and MCMF in Fig. 3.8 and Fig. 4.14, which is the approximate independence of the high-mass population $\mathcal{M} > \mathcal{M}_0$ from the low-mass cutoffs \mathcal{M}_{\min} . This observation indicates that even with different \mathcal{M}_{\min} and considering the large uncertainties in the low- \mathcal{M} -cutoffs from Subsec. 3.5.2, the abundance of high-mass ASMC systems predicted from linear growth does not change significantly. The simple explanation for this weak cutoff dependence is the fact that we fix the number of ASMC systems by their total mass \mathcal{M}_{tot} in Eq. (3.52), to which the high-mass tail yields the largest contribution. On the other hand, the total number of objects depends sensitively on the low- \mathcal{M} cutoffs due to the slope index $\alpha = -1/2$ in Eq. (3.51) (c.f. Eq. (3.53), Fig. C.1 and Fig. C.3).

We conclude that the mass range of the ASMF in Fig. 4.14 is determined mainly by the $\mathcal{M}_{0,\min}$, $\mathcal{M}_{h,\min}$ and \mathcal{M}_{\max} -cutoffs with a strong temperature dependence inherited from \mathcal{M}_0 in Fig. 3.7. Additionally defining the core mass range

$$\min(M_{\star}) = M_{\star}(\mathcal{M}_{\star,\min}), \qquad (4.73)$$

$$\max(M_{\star}) = \min(M_{\star}(\mathcal{M}_{\max}), M_{\star, \lambda}) \tag{4.74}$$

of the ASMF using $M_{\star, \text{min}}$ from Eq. (4.72), Eq. (3.46) and Eq. (4.16), we can directly calculate the total mass and number of galactic axion stars cores for different m_a, n , analogous to Eq. (3.52) and Eq. (3.53). A simple integration of the ASMF over M_{\star} yields the following expression for the total mass contained in axion stars

$$M_{\star,\text{tot}} = 4\pi R_{200}^{3} \int_{\min(M_{\star})}^{\max(M_{\star})} dM_{\star} M_{\star} \frac{C_{n} M_{\star}^{3\alpha-1}}{\mathcal{M}_{\min}^{\alpha} \mathcal{M}_{h,\min}^{2\alpha}(z)}$$

$$= \frac{4\pi R_{200}^{3} C_{n}}{3\alpha + 1} \frac{\min(M_{\star})^{3\alpha+1} - \max(M_{\star})^{3\alpha+1}}{\mathcal{M}_{\min}^{\alpha} \mathcal{M}_{h,\min}^{2\alpha}(z)}, \qquad (4.75)$$

where C_n is determined by Eq. (3.52) and Eq. (3.51). Similarly, the total number of axion stars can be obtained from the relation

$$N_{\star,\text{tot}} = 4\pi R_{200}^{3} \int_{\min(M_{\star})}^{\max(M_{\star})} dM_{\star} \frac{C_{n} M_{\star}^{3\alpha - 1}}{\mathcal{M}_{\min}^{\alpha} \mathcal{M}_{h,\min}^{2\alpha}(z)}$$

$$= \frac{4\pi R_{200}^{3} C_{n}}{3\alpha} \frac{\min(M_{\star})^{3\alpha} - \max(M_{\star})^{3\alpha}}{\mathcal{M}_{\min}^{\alpha} \mathcal{M}_{h,\min}^{2\alpha}(z)}.$$
(4.76)

In the following chapters, we repeatedly determine the relevant high- and low-mass cutoffs of both the MCMF and ASMF for every axion model m_a, n with $10^{-12} \,\mathrm{eV} \le m_a \le 10^{-3} \,\mathrm{eV}$ and n = 0, 1, 3.34. The important result from this extensive approach is that we can infer the distribution of various axion star properties M_{\star} , R_{\star} , $N_{\star,\mathrm{tot}}$ as well as their MC equivalents from knowledge of the axion parameters m_a, n alone. We exploit this knowledge and its phenomenological consequences in more detail in Chap. 5 to Chap. 7.

To obtain a better understanding of the physical implications of the ASMF, we continue to evaluate the exemplary case of the QCD axion with $m = 50 \,\mu\text{eV}$ and n = 3.34 from Fig. 3.8 and Fig. 4.14 by supplementing the mass-radius relation from Fig. 4.1 with the ASMF results from

Fig. 4.14. The axion star mass ranges predicted from the \mathcal{M}_{J^-} and \mathcal{M}_0 -cutoff are indicated by the light and dark gray shaded regions in Fig. 4.15. For comparison with previous works, we have additionally plotted the characteristic axion star parameters that were used in earlier literature on axion star phenomenology, namely in Ref.s [33, 134, 135, 137]. The clustering of the

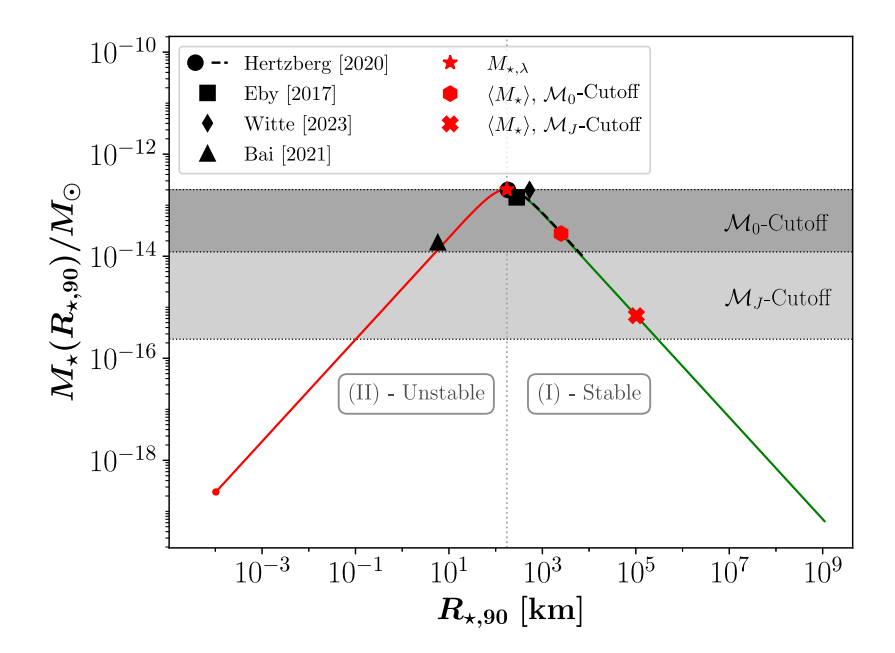


Figure 4.15: Mass-radius relation from Eq. (4.15) with AS properties inferred from the MCMF in Fig. 3.8 using the core-halo relation in Eq. (3.57) for QCD axions with $m_a = 50 \,\mu\text{eV}$, n = 3.34 and $f_a \simeq 10^{11} \,\text{GeV}$. Green and red lines show the stable and unstable branches, black symbols denote the AS parameters used in the literature [33, 134, 135, 137]. Light/dark gray shaded areas and dotted lines correspond to the ASMF with the \mathcal{M}_J -/ \mathcal{M}_0 -cutoff in Fig. 4.14. The upper (dotted) boundary of the shaded areas corresponds to the maximum stable mass $M_{\star,\lambda}$ shown by the red star. Average AS masses from Eq. (4.77) obtained from the two MCMF cutoffs are labeled by red symbols. Taken from Ref. [1].

black symbols in Fig. 4.15 demonstrates that most of the previous authors chose the maximum stable mass $M_{\star,\lambda}$ as a representative value for the expected core mass range.

Our results confirm the existence of such near-critical systems but also indicate that their abundance is generally much lower than previously assumed. The reason for this discrepancy is essentially given by the core-halo scaling $M_{\star} \propto \mathcal{M}^{1/3}$ in Eq. (3.57), which means that a majority of the galactic dark matter is contained in miniclusters but not in their typically much lighter soliton cores with $M_{\star} \leq M_{\star,\lambda}$. This is especially relevant for the intermediate- and high- \mathcal{M} systems in Fig. 3.8 with masses $\mathcal{M} \gg M_{\star,\lambda}$ leading to $M_{\star,\text{tot}} \ll \mathcal{M}_{\text{tot}}$. An additional factor reducing the AS abundance is the negative slope of the MCMF, which peaks at the lowest MC masses $\mathcal{M} \sim \mathcal{M}_{\text{min}}$ well before the core-halo cutoff mass $\mathcal{M}_{h,\text{min}}$ thus restricting the presence of soliton cores in the lightest and most abundant ASMC systems.

The deviations between the assumptions from previous literature in black symbols and our results for M_{\star} , R_{\star} can also be seen by the red cross and hexagon in Fig. 4.15, which indicate the

averaged axion star masses

$$\langle M_{\star} \rangle = \frac{\int_{\min(M_{\star})}^{\max(M_{\star})} dM_{\star} M_{\star} \frac{dn_{\star}}{dM_{\star}}}{\int_{\min(M_{\star})}^{\max(M_{\star})} dM_{\star} \frac{dn_{\star}}{dM_{\star}}}$$
(4.77)

over the mass distribution of the \mathcal{M}_{J} - and \mathcal{M}_{0} -cutoffs respectively. The average soliton radius $\langle R_{\star} \rangle$ corresponding to $\langle M_{\star} \rangle$ is defined as the radius of the averaged mass, i.e.

$$\langle R_{\star} \rangle = R_{\star}(\langle M_{\star} \rangle) \tag{4.78}$$

using the mass-radius relation in Eq. (4.18). Our results for the averaged axion star quantities $\langle M_{\star} \rangle$, $\langle R_{\star} \rangle$ are plotted in Fig. C.4 and Fig. C.5 of App. C. We note that the *n*-dependent average values $\langle M_{\star} \rangle$, $\langle R_{\star} \rangle$ coincide for the \mathcal{M}_{J} -cutoff and n=0,1,3.34, because the vast majority of objects has properties similar to the low-mass cutoff $M_{\star, \text{min}}$.

In most previous studies, the distribution and average mass or radius of axion stars were essentially unknown. This is why the authors of Ref.s [33, 137] calculated the collision and merger rates of such objects in the Milky Way using a parametrization of their relative abundance and typical mass. More specifically, they expressed the number and typical mass of axion stars in terms of two parameters, f_{\star} and ε_{\star} , which are defined as

$$f_{\star} = \frac{M_{\star, \text{tot}}}{\mathcal{M}_{\text{MW}}} \quad , \quad \varepsilon_{\star} = \frac{\langle M_{\star} \rangle}{M_{\star, \lambda}} \,.$$
 (4.79)

Here, $f_{\star} \in [0,1]$ describes the relative dark matter abundance of galactic soliton cores and $\varepsilon_{\star} \in (0,1]$ their typical masses as a fraction of the critical mass $M_{\star,\lambda}$. An understanding of the different assumptions for f_{\star} , ε_{\star} between our work and previous literature is crucial to compare our predictions for galactic signal rates in Chap. 5 to those of Ref.s [135, 137, 188]. We therefore use the numerical results from Eq. (4.75) and Fig. C.4, to directly calculate our linear growth estimates for these two parameters, which are shown in Fig. 4.16 and Fig. 4.17.

Starting with n=0 in red in Fig. 4.16, both of the two low- \mathcal{M} cutoffs in dashed and solid lines coincide, because the core-halo requirement from Eq. (3.58) is more stringent than both $\mathcal{M}_{J,\text{min}}$ and $\mathcal{M}_{0,\text{min}}$. The cases n=1 and n=3.34 on the other hand show significant deviations between the solid and dashed lines in both f_{\star} in Fig. 4.16 and ε_{\star} in Fig. 4.17. Because of the scaling of $\mathcal{M}_{0,\text{min}}$ with \mathcal{M}_0 , n (and the temperature-independence of $\mathcal{M}_{J,\text{min}}$, see also Fig. 3.7), the separation becomes more significant with larger values of n. Physically, a larger \mathcal{M}_0 means that the \mathcal{M}_0 -cutoff truncates a larger fraction of the intermediate-mass range of the ASMF (c.f. Fig. 4.14).

Apart from the cutoff dependence, the strongest impact on f_{\star} and ε_{\star} is given by the temperature index n, which sets the characteristic minicluster mass \mathcal{M}_0 determining both the MCMF and ASMF ranges according to Eq. (3.47). In the case of $f_{\star} \propto M_{\star, \text{tot}}$ shown in Fig. 4.16, the temperature dependence $f_{\star}(n)$ can be explained by the core-halo scaling $M_{\star} \propto \mathcal{M}_0^{1/3}$, which implies that for lager \mathcal{M}_0 , n, the relative contribution of the core mass M_{\star} to each composite system with mass \mathcal{M} decreases. Similarly, looking at the average core mass $\langle M_{\star} \rangle$, which increases with larger \mathcal{M}_{\min} and $\mathcal{M}_{\max} \propto \mathcal{M}_0$, it is straightforward to see that $\varepsilon_{\star} = \langle M_{\star} \rangle / M_{\star, \lambda}$ in Fig. 4.17 will also increase with larger n.

Let us also highlight the precise independence of f_{\star} on m_a for axion models with n=0 in red

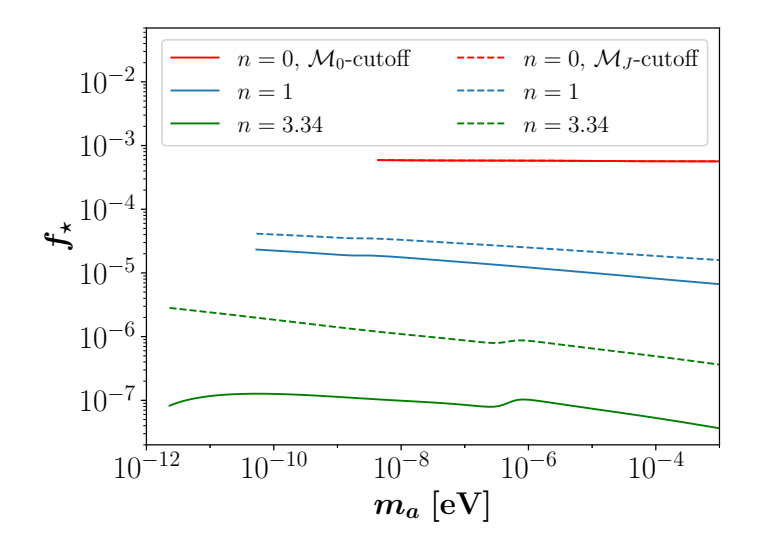


Figure 4.16: Axion star dark matter abundance f_{\star} from Eq. (4.79) at different axion masses m_a and for n = 0, 1, 3.34 in colored lines, taken from Ref. [1]. Dashed/solid lines show the results obtained using the $\mathcal{M}_{J^{-}}/\mathcal{M}_{0}$ -cutoffs of the MCMF from Subsec. 3.5.2, both for $\alpha = -1/2$.

lines of Fig. 4.16. This effect and the weak dependence of the other two cases n=1,3.34 can be understood by considering the scaling $\mathcal{M}_0 \propto m_a^{-3/2}$ of the characteristic mass in Eq. (3.50): The normalization condition $\mathcal{M}_{\text{tot}} = f_{\text{mc}} \mathcal{M}_{\text{MW}}$ with \mathcal{M}_{tot} in Eq. (3.52) implies that the constant C_n in Eq. (3.51) scales as $C_n \propto \mathcal{M}_0^{-1}$.

Neglecting one of the two boundaries of the integral in Eq. (4.75) with $\min(M_{\star})^{-1/2} \gg \max(M_{\star})^{-1/2}$ and inserting the scalings of $\mathcal{M}_{J,\min}$, $\mathcal{M}_{h,\min}$, $\mathcal{M}_0(n=0) \propto m_a^{-3/2}$ from Eq. (3.45), Eq. (3.58), and Eq. (3.50), one arrives at the scaling

$$M_{\star,\text{tot}}(n=0) \propto C_n \mathcal{M}_{h,\min} \mathcal{M}_{\min}^{1/2} \min(M_{\star})^{-1/2}$$

 $\propto \mathcal{M}_0^{-1} m_a^{-3/2} m_a^{-3/4} m_a^{-3/4} \propto \text{const}$ (4.80)

of the total axion star mass, where we have used that $\mathcal{M}_{\min} \propto m_a^{-3/2}$ for the two low- \mathcal{M} cutoffs of the MCMF [1, 58] and inserted $\alpha = -1/2$. Note also that the minimum star mass $\min(M_{\star})$ for n = 0 in Eq. (4.80) is derived from the core-halo cutoff $\mathcal{M}_{h,\min}$, which allowed us to rewrite $\min(M_{\star}) = M_{\star}(\mathcal{M}_{h,\min}) \propto m_a^{-3/2}$ using the core-halo relation and Eq. (3.50).

Since $f_{\star} \propto M_{\star, \text{tot}}$, one directly obtains $f_{\star}(m_a) \propto \text{const}$ from the scaling in Eq. (4.80). For n > 0 in Fig. 4.16, f_{\star} is only roughly constant in m_a , since as argued in Fig. 3.7 before, the scaling $\mathcal{M}_0 \propto m_a^{-3/2}$ is weakly violated by the temperature evolution for n > 0 of the axion mass m_a . This approximate scaling is the reason why f_{\star} in Fig. 4.16 is only approximately independent of m_a for n = 1, 3.34 in blue and green lines.

The important conclusion to draw from this section is that the common assumption $f_{\star} \lesssim 1$ [33, 137] in the literature was proven to be inadequate when dealing with composite ASMC systems in the galactic environment. Conversely, our estimates predict much smaller ranges $10^{-4} \leq f_{\star} \lesssim 1$, potentially suppressing the galactic event rates, which will be examined in more detail in the next chapter. Similarly, a considerable range of axion models m_a, n can reach the

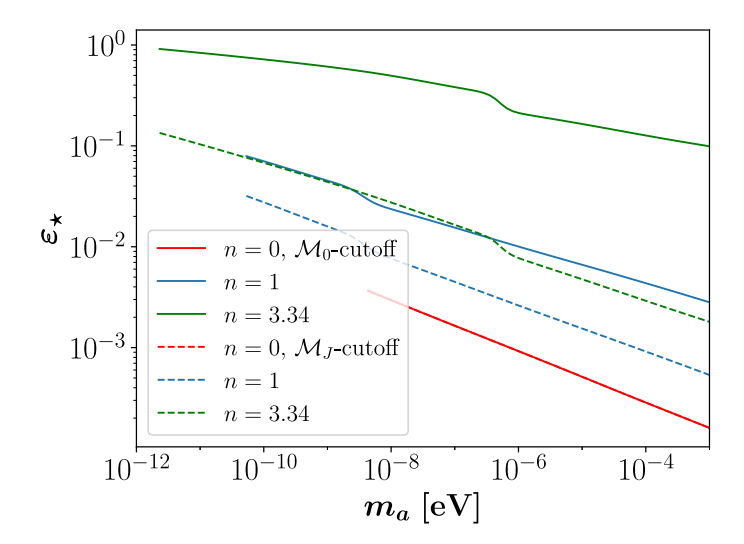


Figure 4.17: Axion star mass parameter ε_{\star} from Eq. (4.79) at different axion masses m_a and for n = 0, 1, 3.34 in colored lines for $\alpha = -1/2$, taken from Ref. [1].

previously anticipated value $\varepsilon_{\star} \sim 1$ for n=1,3.34. Their soliton abundance f_{\star} on the other hand is expected to be strongly suppressed $10^{-7} < f_{\star} < 10^{-4}$ by the larger mass contribution of the host minicluster population for $M_{\star} \propto \mathcal{M}^{1/3}$. In the specific case n=0 of temperature-independent axion masses, we obtain the largest abundance of axion stars $f_{\star} \simeq 10^{-3}$, yet with drastically reduced star masses $\varepsilon_{\star} \lesssim 10^{-3}$, which renders bosenovae and parametric resonance signatures improbable.

In a more general context, the detailed predictions of the properties and distributions of ASMC systems obtained in Subsec. 3.6.2 and Subsec. 4.7.2 represent a crucial improvement in the understanding of galactic axion-small scale structure. To this date, similar results were only obtained in Ref.s [34, 252], who focused on the case $\lambda = 0$. Our results in Subsec. 3.6.2 and Subsec. 4.7.2 demonstrate that the uncertainties in the low- \mathcal{M} cutoff of the MCMF from Subsec. 3.5.2 are essentially irrelevant for the abundance of high-mass ASMC systems in our galaxy. As we will see in Chap. 6 and Chap. 7, these systems are of particular interest for phenomenological observations of the AS instabilities at $M_{\star} = M_{\star,\lambda}, M_{\star,\gamma}$.

Conveniently, also the $\lambda=0$ core-halo relation is expected to remain roughly applicable for most of the long-time stable solitons on the dilute branch in Fig. 4.1. On the other hand, our analysis indicates a strong dependence of the predicted mass and number of axion stars on the exact scaling $\alpha=1/3$ of the core-mass relation $M_{\star} \propto \mathcal{M}^{1/3}$. Better understanding of this relation is especially relevant when considering the long-time accretion of axion star cores as demonstrated in Sec. 4.3 and Ref. [240].

For now, we conclude that our approach of using linear growth predictions for the minicluster mass distributions from Subsec. 3.5.2 and the canonical core-halo mass prediction at $z=z_{\rm eq}$ constitutes a conservative estimate on the true late-time axion star mass distribution. As we will argue in the later chapters, the ongoing accretion from the host minicluster onto its soliton core over a Hubble time is expected to further boost the number of the phenomenologically relevant systems with $M_{\star} \lesssim M_{\star,\gamma}$ in Chap. 6 and $M_{\star} \lesssim M_{\star,\lambda}$ in Chap. 7 respectively.

In the previous chapters, we have applied results from previous investigations on the properties of axion miniclusters to infer the properties of their axion star cores. As shown in Fig. A.1, the major objective of this approach is to estimate the rate and potential detectability of different interactions between axion stars, miniclusters and astrophysical sources in the Milky Way. In the last years, several promising detection methods exploiting the high density and particular properties of axion stars have been proposed.

As for this particular chapter, which is indicated by the red colored rectangle of Fig. A.1, we re-evaluate the expected signal rates of the most promising methods for axion small-scale structure in our galaxy. These are given by the self-interaction instability from Sec. 4.4 and Ref.s [35, 36, 253], the resonant conversion of axion dark matter in the strong magnetic fields of active neutron stars [134–137, 140, 151–157, 214, 254–256] from Fig. 2.7 and the parametric resonance of axion stars [32, 33, 253, 257, 258] in Sec. 4.5.

This chapter therefore serves as an extension of the predictions from previous literature, specifically Ref.s [135, 137, 188, 197], which performed similar estimates on the expected event rates but without detailed knowledge on the mass and size distribution of these objects. Our work improves these predictions by incorporating the full mass distributions of ASs and MCs, the two MCMF cutoffs from Subsec. 3.5.2, the two representative MCMF slopes $\alpha = -1/2$, $\alpha = -0.7$ and different axion models m_a and n. Importantly for this thesis, the results obtained in this chapter will pave the way for the most promising detection prospects, which we examine in Chap. 6 and Chap. 7. The contents of this chapter are taken from Ref. [1].

We start our analysis of the galactic signal rates by summarizing the calculation of the mass-integrated collision rates in Sec. 5.1. The first application of the latter is presented in Sec. 5.2, where we examine the signal rates arising from collisions between neutron stars and axion stars. An analogous evaluation is given for the collisions between axion miniclusters and neutron stars in Sec. 5.3. Sec. 5.4 and Sec. 5.5 focus on the detectability of bosenovae from ASMC mergers and parametric resonance, respectively. Lastly, we also estimate the possible observation of axion star signals from extra-galactic events in Sec. 5.6 before summarizing our results in Sec. 5.7.

5.1 Mass-integrated Collision Rates

Looking at the mass distributions from Fig. 3.8 and Fig. 4.14, it becomes clear that the properties of galactic axion stars and their host miniclusters span across multiple orders of magnitude. Additionally, the spatial distribution of dark matter throughout the galaxy leads to a strong dependence of the number densities n(r), $n_{\star}(r)$ from Eq. (3.51), Eq. (4.71) on the galactocentric radius r. In order to account for the combined mass, size and number density distribution of these objects, we introduce the mass-integrated collision rates of axion stars and miniclusters with astrophysical objects using Milky Way parameters (see App. A).

We use the indices 'i' and 'j' to label encounters between different types of objects, where the symmetry factor

$$S = \begin{cases} \frac{1}{2} & i = j, \\ 1 & i \neq j \end{cases}$$
 (5.1)

prevents double counting in the case that i = j. The total rate of collisions per year and galaxy can thus be obtained by integrating over the galactocentric radius r and over the mass distributions of M_i, M_j according to

$$\Gamma_{i-j} = 4\pi S \int_0^R dr \, r^2 n_i(r) n_j(r) \int dM_i \, p_i(M_i) \int dM_j \, p_j(M_j) \, \langle \sigma_{\text{eff}}(v, M_i, M_j) \, v \rangle_v , \qquad (5.2)$$

where $n_i(r), n_j(r)$ are the radially symmetric number densities of the objects i and j. For our considerations, the radial symmetry holds for axion stars $i = \star$ and miniclusters i = mc, both of which follow the NFW profile in Eq. (A.1). The effective cross section

$$\sigma_{\text{eff}}(v, M_i, M_j, R_i, R_j) = \pi (R_i + R_j)^2 (1 + \eta_{gr})$$
 (5.3)

in Eq. (5.2) depends on the masses and sizes M_i , R_i , where

$$\eta_{\rm gr} = \frac{2G(M_i + M_j)}{(R_i + R_j) v^2} \tag{5.4}$$

is the gravitational enhancement and v is the relative velocity of the collision. The mass distributions of each object i follow a probability distribution function $p_i(M_i)$ obtained from Eq. (3.51) and Eq. (4.71) respectively. Angled brackets $\langle \langle \rangle_v \rangle$ in Eq. (5.2) refer to the average over the distribution of relative velocities. We set the escape velocity of the Milky Way $v_{\rm esc} = 622 \, \rm km s^{-1}$ [194] as an upper limit on v and define the velocity-averaged cross section as

$$\langle \sigma_{\text{eff}}(v)v \rangle_v = 4\pi \int_0^{v_{\text{esc}}} dv \, p_v(v) \sigma_{\text{eff}}(v) v^3$$
 (5.5)

with the Gaussian velocity distribution

$$p_v(v) = \frac{1}{(\pi v_{\text{vir}}^2)^{3/2}} \exp\left(-\frac{v^2}{v_{\text{vir}}^2}\right)$$
 (5.6)

obeying the normalization condition

$$4\pi \int_0^{v_{\rm esc}} dv \, v^2 p_v(v) = 1.$$
 (5.7)

The reference velocity $v_{\rm vir}=239\,{\rm km\,s^{-1}}$ [194] is set to the virial velocity of the MW dark matter halo and the normalization constant $p_v(0)\approx 1/(\pi v_{\rm vir}^2)^{3/2}$ in Eq. (5.6) was approximated for $v_{\rm esc}\gtrsim v_{\rm vir}$ [33].

While the NFW dark matter halo exhibits a spherical symmetry allowing us to integrate Γ_{i-j} according to Eq. (5.2) in the case of AS- and MC collisions, the baryonic matter distribution of the MW follows the well-known disc and bulge profile. For collisions involving neutron stars,

we will thus use cylindrical coordinates instead and express the galactocentric radial coordinate $r = \sqrt{\varrho^2 + \ell^2}$ in terms of its cylindrical counterpart ϱ . Since the spread in observed neutron star masses is small $M_{NS} \sim M_{\odot}$ compared to the MCMF and ASMF, we neglect the corresponding NS mass distribution and assume the typical values of $R_{NS} = 10\,\mathrm{km}$ and $M_{NS} = 1.4\,M_{\odot}$ instead. This assumption is also computationally beneficial, because it ensures that all of the mass-integrated rates amount to four-dimensional integrals (one in v, one to two in M_i, M_j and one to two in space, see Eq. (5.2) and Eq. (5.8) respectively).

Therefore switching to cylindrical coordinates and dropping the dependence on M_j , we only need to integrate over the galactic spatial neutron star distribution $n_{NS}(r)$ according to the analogous definition

$$\Gamma_{i-NS} = 4\pi S \int_0^{R_{\varrho}} d\varrho \, \varrho \int_0^{R_{\ell}} d\ell \, n_{NS}(\varrho, \ell) \, n_i \left(\sqrt{\varrho^2 + \ell^2} \right)$$

$$\times \int dM_i \, p_i(M_i) \, \langle \sigma_{\text{eff}}(v, M_i) \, v \rangle_v , \qquad (5.8)$$

where the boundaries $R_{\varrho} = 50 \,\mathrm{kpc}$, $R_{\ell} = 25 \,\mathrm{kpc}$ are fixed by the fitting functions to observational data from Ref. [259] and Sec. A.7. The number densities n_i used in the following sections are the AS density, MC density and NS density defined by

$$n_{\star}(r) = C_{\star} \,\rho_{NFW}(r),\tag{5.9}$$

$$n_{\rm mc}(r) = C_{\rm mc} \,\rho_{NFW}(r) \,, \tag{5.10}$$

$$n_{NS}(\rho, z) = \frac{C_{NS}}{2\pi\varrho} p_{\varrho}(\varrho) p_{\ell}(\varrho, \ell) , \qquad (5.11)$$

where the normalization constants C_{\star} , $C_{\rm mc}$ with units of inverse mass are set by requiring

$$N_{\star,\text{tot}} = 4\pi \int dr \, r^2 n_{\star}(r) \tag{5.12}$$

$$\mathcal{N}_{\text{tot}} = 4\pi \int dr \, r^2 n_{\text{mc}}(r) \tag{5.13}$$

with $N_{\star,\text{tot}}$, \mathcal{N}_{tot} according to Eq. (4.76) and Eq. (3.53). The neutron star number density and its dimensionless normalization constant C_{NS} on the other hand are determined by requiring

$$N_{NS} = 2 \int_0^{R_{\varrho}} d\varrho \int_0^{R_{\ell}} d\ell \, C_{NS} \, p_{\varrho}(\varrho) \, p_{\ell}(\varrho, \ell) = 10^9$$
 (5.14)

with $p_{\varrho}(\varrho)$, $p_{\ell}(\varrho,\ell)$ taken from the phenomenological fit to the galactic NS distribution introduced in Ref. [259] and summarized in Sec. A.7. Note that the collision rates defined in Eq. (5.2) and Eq. (5.8) are integrated over the mass range of the ASMF/MCMF and over the galactic coordinates r, ϱ, ℓ , which means that they describe the total rate of collisions occurring in the entire AS/MC population per year and galaxy.

We numerically solve the integrals in Eq. (5.2) and Eq. (5.8) using a CPU-parallelized Python algorithm, which determines the boundaries of the mass integrals for $i = \star$, mc automatically from the corresponding ASMF and MCMF in Sec. 4.7 and Subsec. 3.6.2. Same as in the previous chapters, we repeat the procedure for different axion models m_a , n from Subsec. 3.6.1 with $10^{-12} \text{ eV} \leq m_a \leq 10^{-3} \text{ eV}$ and n = 0, 1, 3.34. We start our analysis of the expected signal rates with the neutron star collision rates described by Eq. (5.8) in the following two sections.

5.2 Neutron-Star-Axion-Star Collisions

Over the last years, the resonant conversion of axion dark matter in the strong magnetic fields surrounding active neutron stars has been investigated in numerous studies [134–137, 140, 151–157, 214, 254–256]. We introduced the fundamental mechanism of this process in the theory section on experimental detection in Subsec. 2.7.1 and apply the Goldreich-Julien model for neutron stars to determine their magnetic field properties, similar to what was done in Ref.s [1, 134, 141]. Let us also emphasize that the resonance in this scenario amounts to the equality of axion mass and photon plasma frequency on the conversion surface R_c of the neutron star and that it is fundamentally different from the parametric resonance occurring inside axion stars in Sec. 5.5.

In order to infer the total number of galactic and extra-galactic radio signals from neutron-star-axion-star (NS-AS) encounters, we need to combine the collision rates from Sec. 5.1 with the predicted single event signatures from existing literature. We therefore start by summarizing predictions for the single event signal of a typical NS-AS transient in Subsec. 5.2.1 and combine the resulting information about the transient signal strength with its expected abundance in Subsec. 5.2.2 and Sec. 5.6. The same approach of a combined signal strength and rate analysis will also be taken in the following sections and applied to an extra-galactic context in Sec. 5.6.

5.2.1 Signals of Neutron-Star-Axion-Star Transients

The dynamics of a transient event between a dilute axion star and an active neutron star have been studied in Ref. [135] using Schrödinger-Poisson solvers. In their work, the authors demonstrated that in the presence of the strong gravitational field of the neutron star, both the self-gravity and the kinetic pressure of dilute axion stars can be neglected. Additionally ignoring contributions from self-interactions $\lambda = 0$, they showed that the total system is dominated by tidal forces from the neutron star in head-on collisions. This observation can be understood by comparing the characteristic timescale of the gravitationally interacting axion star [135]

$$\tau_{\star} = \sqrt{\frac{R_{\star}^3}{GM_{\star}}} \tag{5.15}$$

to the crossing time

$$\tau_T \approx \frac{R_{\text{Roche}}}{\sqrt{2GM_{NS}/R_{\text{Roche}} + v_{\infty}^2}},$$
(5.16)

that the AS with velocity $v_{\infty} = 10^{-3}$ at infinity needs to travel from the Roche radius [214]

$$R_{\text{Roche}} = R_{\star} \left(\frac{2M_{NS}}{M_{\star}}\right)^{1/3} \simeq 1.3 \cdot 10^6 \text{ km} \left(\frac{R_{\star}}{10^2 \text{ km}}\right) \left(\frac{M_{NS}}{M_{\odot}}\right)^{1/3} \left(\frac{10^{-12} M_{\odot}}{M_{\star}}\right)^{1/3}$$
 (5.17)

to the NS surface. Physically, the Roche radius represents the distance to the neutron star, where the self-gravitational force of the soliton equals the external tidal force. For QCD axion parameters and dilute axion stars with $M_{\star} \lesssim 10^{-11} \, M_{\odot}$, the crossing time τ_T is smaller than τ_{\star} so that the transient time is too short for the AS dynamics to become relevant, $\tau_T/\tau_{\star} < 1$. Similar effects were also studied extensively in Ref. [209].

Therefore neglecting the energy contributions of the axion star in Eq. (4.2), Eq. (4.3) and Eq. (4.4), Ref. [135] used hydrodynamical N-body simulations of the Schrödinger-Poisson system¹ with an external NS potential to simulate the collision of a soliton of mass $M_{\star} = 10^{-12} M_{\odot}$ and radius $R_{\star} = 2691 \,\mathrm{km}$ with a neutron star of mass $M_{NS} = 1 \,M_{\odot}$ and conversion radius $R_c \sim 100 \,\mathrm{km}$. The resulting dynamics of the collision are shown in Fig. 5.1. In the top panel of

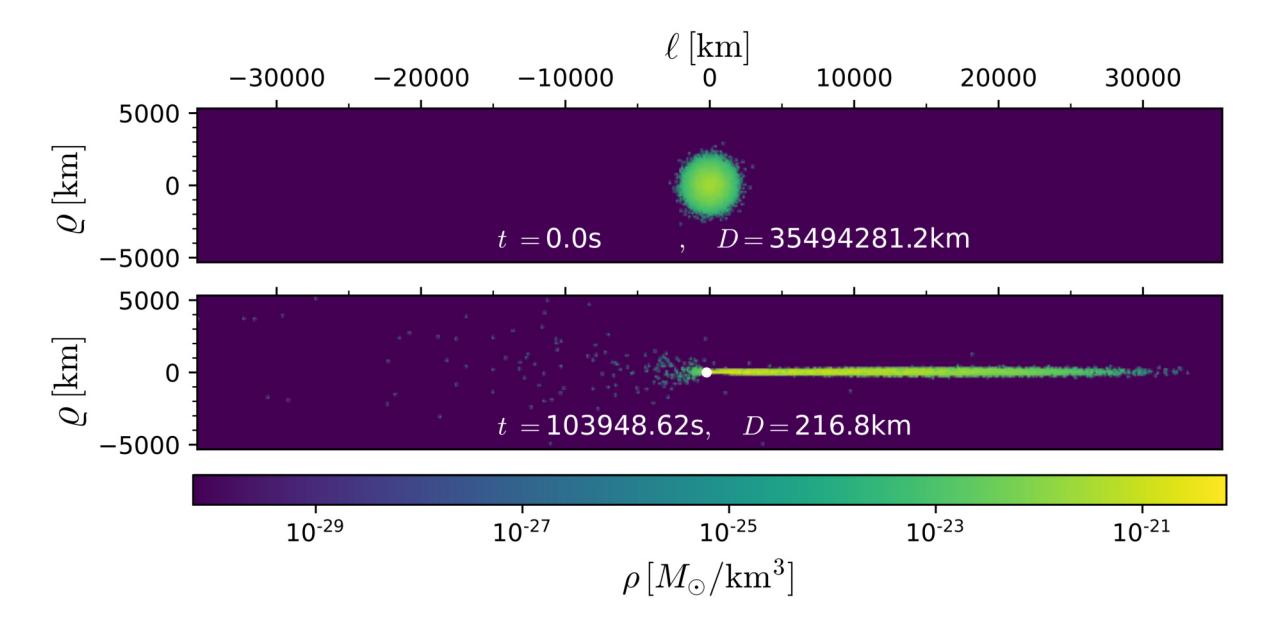


Figure 5.1: Representative head-on collision between an axion star and a neutron star simulated for $m_a = 10^{-5} \, \mathrm{eV}, \, M_\star = 10^{-12} \, M_\odot, \, R_\star = 2691 \, \mathrm{km}, \, M_{NS} = 1 \, M_\odot$ and with an axion star velocity $v_\star = 10^{-3}$ at infinity, taken from Ref. [135]. The two-dimensional mass densities are shown in cylindrical coordinates ϱ, φ, ℓ , where the radial distance ϱ and height ℓ are shown. The white circle in the bottom panel indicates the scale of the conversion radius $R_c \sim 100 \, \mathrm{km}$ of the neutron star.

Fig. 5.1, the dilute axion star is initially in its spherically symmetric ground state configuration with a radial extension of $R_{\star}=2691\,\mathrm{km}$ along both ϱ and ℓ . At $t=0\,\mathrm{s}$, the initial separation between the neutron star- and axion star center is on the order of $D\simeq 3.5\cdot 10^7\,\mathrm{km}$. Later around $t\sim 10^5\,\mathrm{s}$, the axion star approaches a separation of $D\sim 29.000\,\mathrm{km}\sim 10R_{\star}$. By this time, the gravitational perturbation introduced by the neutron star leads to a significant elongation of the soliton profile across a radius of $R_{\star}'\sim 10R_{\star}$ along the ℓ -direction. The bottom panel of Fig. 5.1 shows the time shortly after, when a fraction of the axion star mass has already been scattered by the neutron star. At late times, when the entire soliton profile has crossed the neutron star region, the initially bound axion star configuration is completely disrupted [135].

The key takeaway here is that the stretching of the dilute axion star in the neutron star gravitational field leads to a time modulation of the resulting radio signal from axion-photon conversion on the conversion surface $R_c \sim 100 \,\mathrm{km}$ shown by the white circle in Fig. 5.1. In this context, the duration of the signal $t_s \sim \tau_T$ depends on the size R_{\star} of the axion star and the relative velocity $v \sim 10^{-3}$ of the collision. The signal strength on the other hand scales with the soliton

¹The SP equations can be transformed into continuity and Euler equations using the Madelung transformation in App. A.8.

density ρ_{\star} , which decreases with larger R_{\star} and smaller M_{\star} according to the mass-radius relation of dilute axion stars in Eq. (4.17) with $R_{\star} \propto 1/M_{\star}$.

Recently, the authors of Ref. [134] investigated the brightness, spectral width and time dependence of the radio flux arising from a NS-AS transient event in great detail. To this date, their work represents the most complete analysis of the expected signatures from both NS-AS and NS-MC collisions. We recall their results for the observed radio flux in the following and from

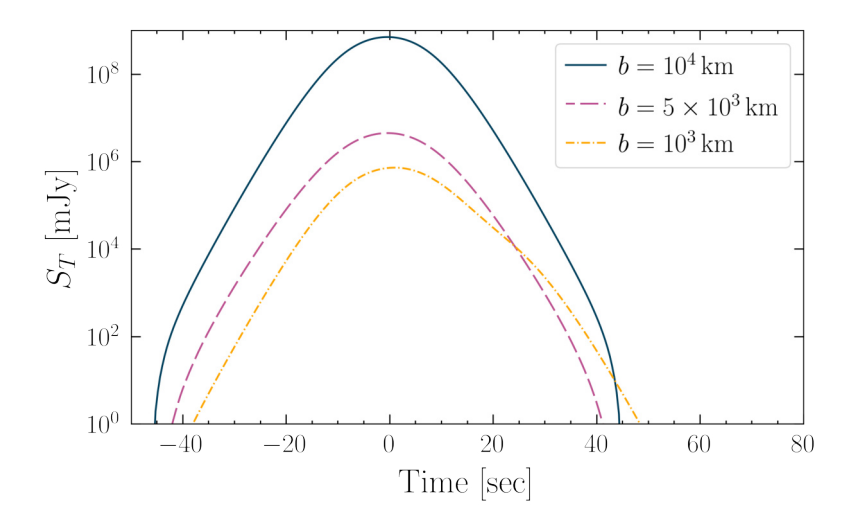


Figure 5.2: Sky-averaged differential flux as a function of the transient time in three NS-AS encounters with different impact parameters $b=10^3$ km, $b=5\cdot 10^3$ km and $b=10^9$ km at an observation distance $d_T=1$ kpc. The representative transient events were simulated for $m_a=26\,\mu\text{eV},\,g_{a\gamma\gamma}=10^{-14}\,\text{GeV}^{-1},\,M_\star=10^{-13}\,M_\odot,\,R_\star=3905\,\text{km}$ assuming an observation bandwidth of $\Delta f_T=10^{-5}\,m_a$. Neutron star and collision parameters are summarized in Tab. 5.1. Taken from Ref. [134].

this infer the galactic signal rates in Subsec. 5.2.2, Subsec. 5.3.2 and the extra-galactic signatures in Sec. 5.6.

The authors of Ref. [134] calculated the rate of resonant conversion occurring inside a neutron star whose Goldreich-Julien charge density follows Eq. (2.75) and whose rotation axis is misaligned by an angle θ_m with respect to the dipolar NS magnetic field **B**. They computed the position- and velocity-dependent resonant photon production rate of axions on the NS conversion surface, assuming a flat axion velocity distribution below the escape velocity of the axion star $v_{\rm esc}(M_{\star})$. The final results obtained for the sky-averaged differential flux observed from three NS-AS collisions with different impact parameters $b=10^3, 5\cdot 10^3, 10^4$ km are shown in Fig. 5.2. For these representative transient events, the NS properties are summarized in Tab. 5.1, whereas the axion mass and coupling are $m_a=26\,\mu\text{eV},\ g_{a\gamma\gamma}=10^{-14}\,\text{GeV}^{-1}$ and the AS parameters are $M_{\star}=10^{-13}\,M_{\odot},\ R_{\star}=3905\,\text{km}$. Fig. 5.2 shows the observed spectral flux densities S_T in the bandwidth $\Delta f_T=10^{-5}\,m_a$ and at a distance of $d_T=1\,\text{kpc}$ in units of mJy.

In all cases, the peak flux densities ranging from $S_T \sim 10^6$ mJy to $S_T \sim 10^8$ mJy are used to determine the t=0 s point of the transient. The total duration of the signal is roughly on the order of $t_s \sim 80$ s, where signals with larger impact parameter b have slightly larger t_s , as seen by the blue line in Fig. 5.2. Remarkably, the blue flux density with the largest impact parameter $b=10^4$ km yields by far the largest peak flux with $S_T \sim 10^8$ mJy. This observation is opposed to the naive expectation, that small impact parameters $b \approx 0$ should provide the largest

Parameter	Value
B_0	$1.6 \cdot 10^{14} \mathrm{G}$
P_{NS}	$3.76\mathrm{s}$
θ_m	$0.2\mathrm{rad}$
v	100 km/s
$ heta_v$	$0\mathrm{rad}$

Table 5.1: Neutron star (collision) parameters used in Fig. 5.2 and Fig. 5.6, both taken from Ref. [134]: The magnetic field strength at the NS surface B_0 , the NS rotational period P_{NS} , the misalignment angle θ_m between magnetic field and rotation axis, the relative velocity of the NS-AS/MC collision v and its orientation with respect to the NS rotation axis θ_v .

axion densities $\rho_{\star}(r \approx 0)$ in the NS region and hence the strongest signals. The explanation for this behavior lies in the non-trivial structure of the axion star velocity distribution and in the trajectories of the infalling axions, which tend to miss the conversion surface for small b [134]. Additionally, NS-AS signals with non-zero impact parameter show stronger sky-averaged flux densities, but also strong anisotropy due to the modified particle trajectories, as discussed in Ref. [134].

For the considerations in this section, we conclude that the radio flux observed from a NS-AS transient event is considerable even at $\mathcal{O}(1\,\mathrm{kpc})$ distances. The strong time modulation of the signal is largely dependent on the orientation and dynamics of the specific collision, where in this work, we neglect the anisotropy of the signals from Ref. [134] and use the results from Fig. 5.2 as benchmark for a representative NS-AS radio signal in Sec. 5.6. Before, the next step is to compute the corresponding encounters rates of the above single event signals in our galaxy.

5.2.2 Galactic Signal Rates and Neutron Star Evolution

The event rates of collisions between axion stars and neutron stars in the Milky Way have been found to be considerable $\Gamma_{\star-NS} > 1\,\mathrm{yr}^{-1}\mathrm{galaxy}^{-1}$ in several earlier studies [135, 137, 188]. The calculations were commonly based on the assumption that an $\mathcal{O}(1\%)$ to $\mathcal{O}(1)$ fraction of dark matter is gravitationally bound in axion stars or miniclusters. We apply our improved modeling of the AS and MC mass distribution to the NS collision rates from Eq. (5.8) for an MCMF slope of $\alpha = -1/2$ using both low-mass cutoffs from Subsec. 3.5.2 in Fig. 5.3.

As before, solid lines indicate the \mathcal{M}_0 -cutoff of the MCMF, while dashed lines show the results using the lower Jeans mass cutoff, $\mathcal{M}_{J,\mathrm{min}}$. The encounter rates in Fig. 5.3 suggest that for larger axion masses m_a and smaller temperature dependence n, a considerable range of axion parameters could be detected. This is firstly due to the fact that for smaller n, the average AS radius $R_{\star} \propto 1/M_{\star}$ is significantly larger, thus enhancing the cross section in Eq. (5.3). Secondly, for lighter structures M_{\star} , \mathcal{M}_0 in Fig. C.4 and Fig. 3.7, the total number of axion stars $N_{\star,\mathrm{tot}} \lesssim \mathcal{N}_{\mathrm{tot}} \propto 1/\mathcal{M}_0$ is increased.

More precisely, the NS-AS collision rates show slightly different scalings with m_a and n depending on the temperature index n, as already explained for $\mathcal{M}_0(m_a, n)$ in Sec. 3.2. In the representative case n = 0, we can use the identities $N_{\star, \text{tot}} \propto \mathcal{M}_0^{-1} \propto m_a^{3/2}$ and $\langle R_{\star} \rangle \propto m_a^{-2} \langle M_{\star} \rangle^{-1} \propto$

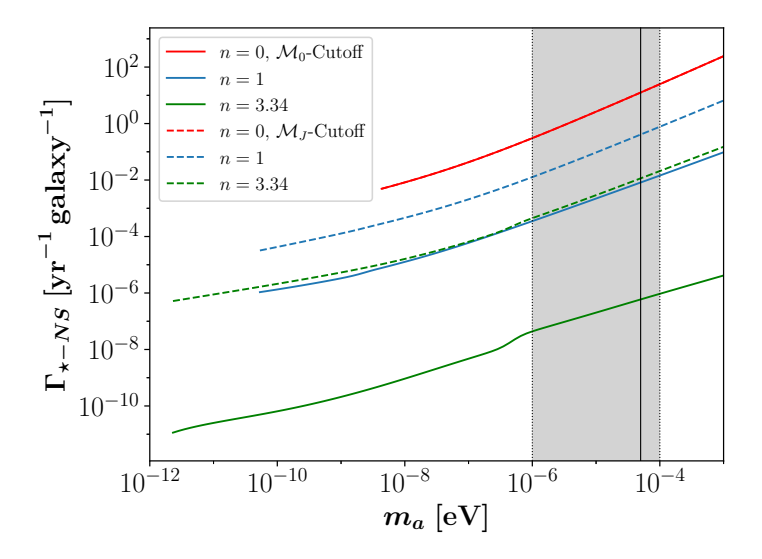


Figure 5.3: Mass-integrated collision rates per year and galaxy between axion stars and neutron stars in the Milky Way as a function of m_a with MCMF power-law index $\alpha = -1/2$, taken from Ref. [1]. Colored lines indicate the temperature index n, solid and dashed lines represent the two different low- \mathcal{M} cutoffs of the MCMF in Subsec. 3.5.2. In this case and in the following figures, the cosmological mass band $10^{-6} \, \text{eV} \le m_a \le 10^{-4} \, \text{eV}$ of the QCD axion is indicated by the gray-shaded region, where the black solid line marks $m_a = 50 \, \mu \text{eV}$.

 $m_a^{-2}\mathcal{M}_0^{-1} \propto m^{-1/2}$ from Eq. (4.75) and Eq. (4.18) to obtain the relations

$$\Gamma_{\star - NS} \Big|_{n=0} \propto \begin{cases} N_{\star, \text{tot}} \langle R_{\star} \rangle^2 \propto m_a^{1/2}, & \eta_{\text{gr}} < 1 \\ N_{\star, \text{tot}} \langle R_{\star} \rangle M_{NS} \propto m_a, & \eta_{\text{gr}} > 1 \end{cases},$$
(5.18)

where we used $M_{NS} \gg M_{\star}$, $M_{NS} =$ const and the results displayed in Fig. C.3, Fig. C.5. The turnaround point between the two scalings is reached when the gravitational enhancement term $\eta_{\rm gr}$ in Eq. (5.3) becomes relevant. The other cases with n>0 roughly follow the same trend, but with different turnarounds for $\eta_{\rm gr}$ and marginally different scalings with m_a from the temperature evolution index n. Note also that for n=0 the results in Fig. 5.3 and Fig. 5.5 are independent of the low- \mathcal{M} cutoff because the minimum MC mass $\mathcal{M}_{h,\min} > \mathcal{M}_{0,\min} > \mathcal{M}_{J,\min}$ from Eq. (3.58) is the dominant constraint on the ASMF.

Summarizing the predictions of Fig. 5.3, the \mathcal{M}_J -cutoff is generally beneficial, because it increases the total number of objects by including the low-mass tail of the MCMF and ASMF in Fig. 3.8, Fig. 4.14. Especially for $m_a \gtrsim 10^{-6}\,\mathrm{eV}$, n=0 and $m_a \gtrsim 10^{-5}\,\mathrm{eV}$, n=1 with the \mathcal{M}_J -cutoff, NS-AS encounters seem to be sufficiently probable to be observed over observation timescales on the order of a decade or less. However the emission of a radio signal from an AS-NS encounter in Subsec. 5.2.1 requires the neutron star to have an active magnetic field with suitable photon plasma frequency $\omega_p \gtrsim m_a$ to allow for the resonant conversion of axions into photons at the NS conversion surface.

In order to quantify the fraction of NS collisions, which are suitable to produce radio signals through resonant conversion of axion DM from galactic ASs and MCs, we introduce the following procedure: We compose a statistically distributed sample population of $N_S = 10^5$ neutron stars,

for which the initial magnetic field strength B_0 , misalignment angle θ_m and rotation frequency $\Omega_{NS} = 2\pi/P_{NS}$ with period P_{NS} are determined from Gaussian distributions in B_0 , θ_m and P_{NS} respectively (see also Tab. 5.1).

For the corresponding distributions, we follow the approach in Ref. [141] by employing the results from the neutron star population synthesis of Ref.s [260, 261]. This way, each of the $N_S = 10^5$ neutron stars in the sample has its initial properties B_0 , θ_m , P_{NS} drawn from the distributions

$$p_B(B_0) = \frac{1}{\sqrt{2\pi\sigma_B^2}} \exp\left[-\frac{\{\log_{10}(B_0) - \mu_B\}^2}{2\sigma_B^2}\right],$$
 (5.19)

$$p_{\theta}(\theta_m) = \sin\left(\frac{\theta_m}{2}\right), \tag{5.20}$$

$$p_P(P_{NS}) = \frac{1}{\sqrt{2\pi\sigma_p^2}} \exp\left[-\frac{(P_{NS} - \mu_p)^2}{2\sigma_p^2}\right],$$
 (5.21)

where B_0 is given in Gauss, θ_m in degrees and P_{NS} in seconds [141]. The fit parameters are $\mu_B = 13.2, \sigma_B = 0.62, \mu_p = 0.22$ and $\sigma_p = 0.42^3$ [260]. With the initial NS properties specified by Eq. (5.19) to Eq. (5.21), the individual time evolution of the total sample is determined by the evolution equations

$$\dot{\theta_m} = -\beta \kappa_2 \frac{B^2}{P_{NS}^2} \sin \theta_m \cos \theta_m \,, \tag{5.22}$$

$$\dot{P_{NS}} = \beta \frac{B^2}{P_{NS}} \left(\kappa_0 + \kappa_1 \sin^2 \theta_m \right) , \qquad (5.23)$$

where $\kappa_0 \sim \kappa_1 \sim \kappa_2 \sim 1$ and $\beta = 6 \cdot 10^{-40} \,\mathrm{s/G^2}$ following Ref. [141]. As for B_0 , the Ohmic dissipation of the dipolar magnetic field with initial strength B_0 leads to an exponential decay

$$B(t) = B_0 \exp(-t/\tau_{\text{Ohm}}), \qquad (5.24)$$

that is characterized by the Ohmic decay constant $\tau_{\rm Ohm}$. Same as in Ref. [141], we assume $\tau_{\rm Ohm} = 1 \, {\rm Myr}$, which gives an approximate average NS lifetime of $t_{NS} \sim 10 \, \tau_{\rm Ohm}$.

In order to obtain a representative NS population from the above evolution model, we assume a constant formation rate over the age of the universe for the $N_S=10^5$ neutron stars with uniformly distributed individual ages $t_i \in [0,10\,\tau_{\rm Ohm})$ and evolve each object i in time until t_i by numerically solving the evolution equations Eq. (5.22) to Eq. (5.24). The constant formation rate and Ohmic decay yield an overall survival suppression factor $f_{surv} \sim 10\,\tau_{\rm Ohm}/t_H \sim 10\,{\rm Myr}/10\,{\rm Gyr} = 10^{-3}$, which has to be combined with an additional resonance factor $f_{res}(m_a)$ accounting for the relative fraction of active neutron stars with a plasma frequency fulfilling the m_a -dependent resonance condition $\omega_p \gtrsim m_a$.

To infer the remaining suppression factor $f_{res}(m_a)$, we need to determine $\omega_p^{(i)}(t_i)$ for each of the neutron stars. This is done by assuming $n_e = |n_{\rm GJ}|$ for the typical electron density, which yields the Goldreich-Julien plasma frequency at the NS surface

$$\omega_p = \sqrt{\frac{4\pi n_{\rm GJ}\alpha_{EM}}{m_e}} = 4\pi \sqrt{\frac{B\alpha_{EM}}{eP_{NS}m_e}},$$
(5.25)

where we have evaluated $n_{\rm GJ} = 2\Omega_{NS}B/e$ from Eq. (2.75) for $\theta = 0, \pi$. We use Eq. (5.25) as an estimate for the locally dependent plasma frequency $\omega_p(\mathbf{r})$, similar to Ref. [141] and use the latter in the resonance condition $\omega_p \gtrsim m_a$ for a given m_a .

Following the above approach we determine the relative NS fraction $f_{res}(m_a)$ numerically by counting the number of neutron stars fulfilling the condition $\omega_p \gtrsim m_a$ for every m_a in the range $10^{-12} \,\mathrm{eV} \leq m_a \leq 10^{-3} \,\mathrm{eV}$. The resulting effective fraction $f_{NS}(m_a) = f_{surv} f_{res}(m_a)$ is plotted in Fig. 5.4. For $m_a \lesssim 10^{-7} \,\mathrm{eV}$, we obtain $f_{res}(m_a) \approx 1$ and the effective NS fraction saturates

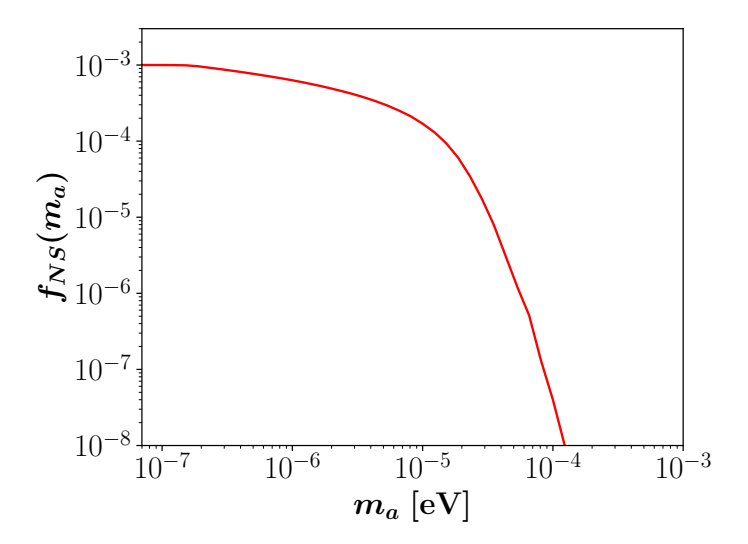


Figure 5.4: Fraction $f_{NS}(m_a)$ of active neutron stars in our mock model, which exhibit a plasma frequency $\omega_p \gtrsim m_a$ enabling the resonant conversion of axions with mass m_a , taken from Ref. [1].

at $f_{NS}(m_a) \approx f_{surv} \approx 10^{-3}$.

On the other hand, in the range $m_a > 10^{-7} \,\mathrm{eV}$ the fraction of objects in the sample fulfilling the resonance condition quickly drops, until reaching $f_{NS}(m_a) \approx 0$ at $m_a \geq 10^{-4} \,\mathrm{eV}$. Since we assume a total number $N_{NS} = 10^9$ in this work, dropping below $f_{NS} \sim 10^{-8}$ effectively excludes NS-collisions from occurring in our galaxy. The m_a -dependence of the suppression rate f_{NS} in Fig. 5.4 has important phenomenological consequences for the detectability of the expected NS-AS encounters. We compute the expected signal rates emitted from galactic NS-AS encounters, which are predicted from our NS population in Fig. 5.4 and from the collision rates in Fig. 5.3 by writing

$$\Gamma_{i-NS}^s = f_{NS} \cdot \Gamma_{i-NS} \tag{5.26}$$

and plot the corresponding results in Fig. 5.5. As a consequence of the scaling $\Gamma_{\star-NS}(m_a) \propto m_a$ in Eq. (5.18), Fig. 5.3 for large m_a and from the NS fraction $f_{NS}(m_a)$, the signal rates in Fig. 5.5 peak around $m_a \approx 10^{-5} \, \text{eV}$. Above these values, $\Gamma^s_{NS-\star}$ quickly drops to zero, as expected from $f_{NS}(m_a)$. Crucially, for every of the axion models m_a, n the signal rates end up well below $\Gamma^s_{NS-\star} = 1 \, \text{yr}^{-1} \, \text{galaxy}^{-1}$. We therefore find that galactic radio signals from NS-AS collisions are expected to be extremely rare, especially for axions with n=3.34 and the QCD axion. Let us emphasize here that the same remains true for a modified MCMF slope of $\alpha=-0.7$, which boosts the signal rates in Fig. 5.5 by n-dependent factors of order $\sim 10 \, \text{to} \sim 100 \, \text{giving}$

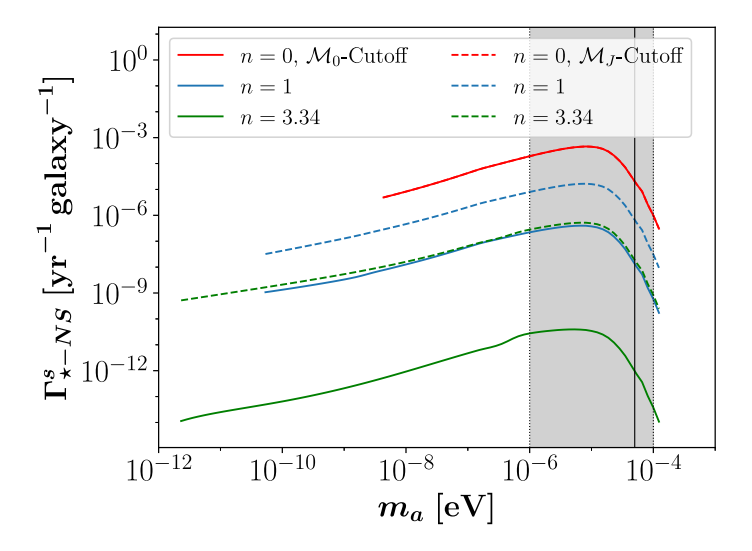


Figure 5.5: Mass-integrated NS-AS signal rates per year and galaxy in the Milky Way, calculated from Fig. 5.3 by applying the NS fraction $f_{NS}(m_a)$ in Eq. (5.26). Colored lines indicate the temperature dependence of the axion mass, solid and dashed lines represent the two different low-mass cutoffs of the MCMF. Taken from Ref. [1].

 $\Gamma_{\star - NS} < 10^{-1} \,\mathrm{yr}^{-1}$ for n = 0 and even smaller rates for n > 0 and the QCD axion. We checked the resulting modifications and confirmed that none of them are sufficient to qualitatively alter the results shown for $\alpha = -1/2$ in Fig. 5.5.

Unless a majority of the galactic dark matter is contained in axion stars rather than in miniclusters (thus yielding $f_{\star} \sim 1$), NS-AS collisions will be far less promising than anticipated. A possible exclusion to this prediction is given by the numerous formation of axion stars from topological defects in Ref. [236], for which the AS abundance would be greatly enhanced, $f_{\star} \sim 1$. As previously mentioned, this mechanism is expected to apply only to specific axion models, which leaves us with the conclusion that NS-AS collisions are generally improbable due to the limited number and size $N_{\star,\text{tot}}$, R_{\star} of the solitons. This observation motivates a similar investigation for the signatures of their larger and more numerous host miniclusters, which we perform in the next section.

5.3 Neutron-Star-Minicluster Collisions

With the signal rates for NS-AS encounters being insufficiently frequent, a reasonable next step is to explore the abundance and signal strength of the resonant axion conversion in the NS magnetosphere during minicluster-NS transients. This idea is especially appealing because the mass $\mathcal{M} \gg M_{\star}$ and size of miniclusters with $\mathcal{R} \sim 10^7 \,\mathrm{km}$ is much larger than that of their AS cores, thus enhancing the cross-section of their interactions. Another advantage is the fact that the size of miniclusters with a spherically homogeneous profile in Eq. (3.24) scales with their mass as $\mathcal{R} \propto \mathcal{M}^{1/3}$, opposed to the inverse mass scaling $R_{\star} \propto 1/M_{\star}$ of dilute axion stars in Eq. (4.17). Owing to the modified scaling behavior of \mathcal{R} in Eq. (5.3), the collision rates of heavier objects are less suppressed by the cross-section in Eq. (5.3) compared to the axion

star case. On the phenomenological site, this can be beneficial, because heavier ASMC systems generally host a denser AS core.

On the other hand, the weaker gravitational binding and large size of miniclusters make these objects more prone to tidal disruption, especially in dense environments such as the galactic bulge. The resulting constraints on the survival of typical miniclusters over long times were discussed in Subsec. 3.6.3 and explored in more detail in Ref.s [136, 188, 196, 197]. On the basis of the results from Ref. [188] in Fig. 3.9, we adopt a simplified approach by truncating the radial distribution of the MC population above the lower integration boundary $R_{\rm surv}=1\,{\rm kpc}$ in Eq. (5.8). Therefore restricting our analysis to miniclusters outside of the galactic bulge, $r>R_{\rm surv}$, we employ the same methods as in Sec. 5.2 using the MC mass and radius distribution obtained from the MCMF and Eq. (3.24). As before, we start by summarizing the single event signal in Subsec. 5.3.1 and combine the resulting detectability with the encounter rates from Eq. (5.8) in Subsec. 5.3.2 and Sec. 5.6.

5.3.1 Signals from Neutron-Star-Minicluster Transients

The collision dynamics in a NS-AS encounter are fundamentally different from the NS-AS event described in Subsec. 5.2.1 and Fig. 5.2. This is mostly because of the greatly enhanced radius $\mathcal{R}/R_{\star} \gg 1$ and mass $\mathcal{M}/M_{\star} \gg 1$ of the axion overdensity undergoing photon conversion. Since $\mathcal{M}_{0} \ll M_{\odot}$ for all axion models m_{a} , n in Fig. 3.7, the gravitational and tidal forces in the interaction are again dominated by the neutron star. The size of the two colliding objects however differs by many orders of magnitude, typically $\mathcal{R}/R_{NS} \sim 10^{7} \,\mathrm{km}/10 \,\mathrm{km} \sim 10^{6}$, which implies that the grid resolution in numerical simulations poses great challenges.

Due to lack of adequate numerical data on the temporal and spatial evolution of NS-MC encounters at the time of writing, we go on to describe the expected collision dynamics qualitatively instead of demonstrating numerical simulations. Comparing the NS-MC scenario to the NS-AS collision in Fig. 5.1 and Fig. 5.2, it is clear that the crossing time τ_T in Eq. (5.16) should be much greater due to the larger size of the minicluster. Accordingly, the resulting signal duration should be orders of magnitude larger $t_s \gg 80\,\mathrm{s}$ than in the NS-AS case. In a similar way, the large radius of the minicluster also increases the maximum impact parameter b leading to radio conversion, which is shown in blue lines in Fig. 5.2 and Fig. 5.6.

On the other hand, and due to the reduced density $\rho_{\rm mc} \sim 10^7 \, {\rm GeV \, cm^{-3}}$ compared to $\rho_{\star} \lesssim M_{\star,\lambda}/R_{\star,\lambda}^3 \sim 10^{23} \, {\rm GeV \, cm^{-3}}$ at $M_{\star} = M_{\star,\lambda}$, the resulting signal strength will be drastically reduced compared to S_T in Fig. 5.2. The dilute nature of the minicluster indicates that it too is expected to experience significant elongation for distances $D \ll R_{\rm Roche}$ well below the Roche radius. An important quantity determining the temporal evolution of the collision and resulting signal is the profile of the miniclusters, which was shown to be well-fit by NFW profiles with an increased concentration in Ref. [30].

Regarding the observed radio conversion signal, we already mentioned in Subsec. 5.2.1 that Ref. [134] provides a detailed analysis of the resulting radio fluxes from both axion stars and miniclusters in NS encounters. We demonstrate their predictions for the sky-averaged differential flux obtained from a collision involving a minicluster with NFW-distributed mass density and the same NS parameters from Tab. 5.1 in Fig. 5.6. In agreement with the aforementioned expectations from the underlying collision dynamics, we find that the signal duration is $t_s \sim 400 \,\mathrm{d}$ for all of the three impact parameters $b = 0, 10^8 \,\mathrm{km}$ and $b = 10^9 \,\mathrm{km}$. The maximum

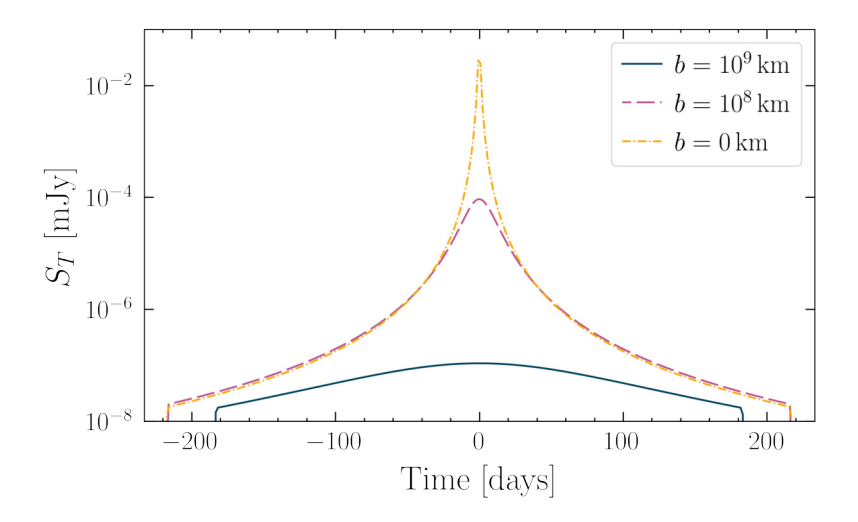


Figure 5.6: Sky-averaged differential flux as a function of the transient time in three NS-MC encounters with different impact parameters b=0 km, $b=10^8$ km and $b=10^9$ km at an observation distance $d_T=1$ kpc. The representative transient event was simulated for $m_a=26\,\mu\text{eV},\ g_{a\gamma\gamma}=10^{-14}\,\text{GeV}^{-1},\ \mathcal{M}=10^{-12}\,M_\odot,\ \mathcal{R}=1.86\cdot10^9$ km assuming an observation bandwidth of $\Delta f_T=10^{-5}\,m_a$. The minicluster density was modeled using an NFW profile, while the neutron star and collision parameters are the same as in Fig. 5.2 and Tab. 5.1. Taken from Ref. [134].

observable impact parameter in blue is $b_{\rm max} \simeq 10^9 \, {\rm km}$ for the minicluster with ${\cal M} = 10^{-12} \, M_{\odot}$, ${\cal R} = 1.86 \cdot 10^9 \, {\rm km}$, and thus much greater than $b_{\rm max} \simeq 10^4 \, {\rm km}$ in Fig. 5.2.

Owing to the modified velocity distribution² and infall dynamics of the larger miniclusters, the dependence of S_T on the impact parameter b is inverted compared to the AS case. A possible explanation for this behavior is the fact that even with $b \gg 0 \,\mathrm{km}$, an order one fraction of the NS conversion surface is surrounded by the axion MC cloud with $\mathcal{R} \gg R_{NS}$ during most of the conversion time t_s .

Looking at the signal strength, we confirm the expectation from the reduced axion density $\rho_{\rm mc} \ll \rho_{\star}$ that the signal is significantly weaker than the AS collision with $S_T \sim 10^{-2} \, {\rm mJy}$ compared to the maximum of $S_T \sim 10^8 \, {\rm mJy}$ from Fig. 5.2. Remarkably for smaller values of b, the slope of the peak in S_T at t=0 d is significantly increased compared to Fig. 5.2. This can be understood from the scaling $\rho_{\rm NFW} \propto 1/r$ below R_s , which enters in the observed flux density $S_T \propto n_{\rm mc} \propto 1/r$, thus greatly enhancing the emission close to the MC center at r=0 kpc.

The expected reduction in brightness also directly implies a reduced detectability, however as we will show in the next part, the resulting collision rates in turn are greatly enhanced. Since $S_T \propto 1/d_T^2$, where $d_T = 1\,\mathrm{kpc}$ in Fig. 5.6, it is clear that the maximum observable distance of NS-MC encounters is much smaller than the AS case. The important question about which observation distances are typical within a given time frame will be answered in the following by computing the encounter rates of the above signals.

²Where we note that for the minicluster, the authors of Ref. [134] assumed a Maxwell-Boltzmann distribution truncated at $v_{\rm esc}(\mathcal{M})$ opposed to the flat truncated AS distribution below $v_{\rm esc}(M_{\star})$ in Fig. 5.2.

5.3.2 Galactic Signal Rates of Neutron-Star-Minicluster Collisions

Starting with the mass-integrated collision rates between neutron stars and miniclusters at galactic distance coordinates R_{ϱ} , $R_{\ell} > R_{\rm surv} = 1 \, \rm kpc$ in Eq. (5.8), we show the results for an MCMF slope of $\alpha = -1/2$ using both low-mass cutoffs in Fig. 5.7. Compared to the analogous

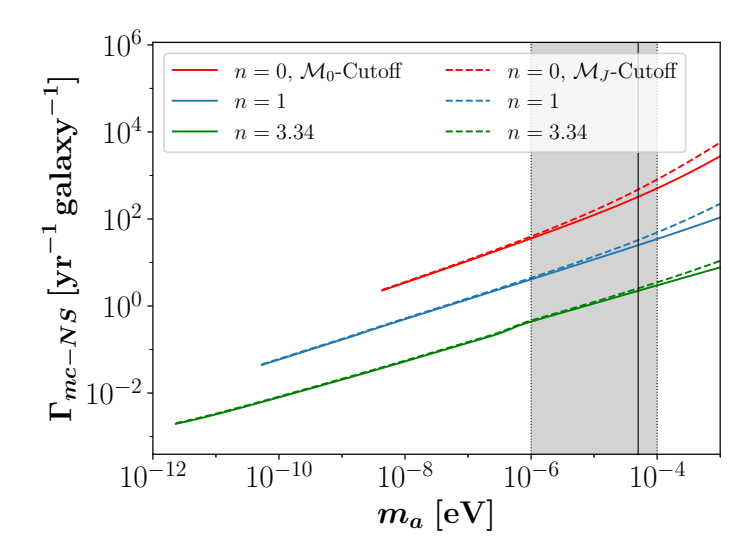


Figure 5.7: Mass-integrated collision rates per year and galaxy between miniclusters and neutron stars as a function of m_a for $\alpha = -1/2$, taken from Ref. [1]. Colored lines indicate the temperature dependence of the axion mass, solid and dashed lines represent the two different low- \mathcal{M} -cutoffs from Subsec. 3.5.2.

AS case in Fig. 5.3, one observes a significant boost in the overall number of collisions per year and galaxy. As argued before, this boost is a direct consequence of the increased number density of MCs, $n_{\rm mc}$ in Eq. (5.8), and of the enhanced cross section for $\mathcal{R} \propto \mathcal{M}^{1/3}$ in Eq. (5.3). The qualitative behavior with m_a, n is similar to the AS case in Fig. 5.3, where both larger m_a and smaller n are beneficial due to the decreased mass and increased number of the objects. Analogous to Eq. (5.18), the n=0 scaling of the NS-MC encounter rates in red in Fig. 5.7 and Fig. 5.9 may be divided into two regimes using $\mathcal{M}_0 \ll M_{NS}$, $\mathcal{N}_{\rm tot} \propto \mathcal{M}_0^{-1}$ and $\mathcal{R} \propto \mathcal{M}^{1/3}$ from Eq. (3.24)

$$\Gamma_{\text{mc-NS}}\Big|_{n=0} \propto \begin{cases} \mathcal{N}_{\text{tot}} \mathcal{R}^2 \propto m_a^{1/2}, & \eta_{\text{gr}} < 1\\ \mathcal{N}_{\text{tot}} \mathcal{R} \propto m_a, & \eta_{\text{gr}} > 1 \end{cases},$$
(5.27)

with a modified turnaround $\eta_{\rm gr} \sim 1$ around the QCD axion mass $m_a \approx 50 \,\mu {\rm eV}$. For the cases n>0 in blue and green a similar trend with slightly different turnaround point $\eta_{\rm gr} \sim 1$ can be seen.

Note that the results in Fig. 5.7 are nearly independent of the low-mass cutoffs $\mathcal{M}_{J,\text{min}}$ and $\mathcal{M}_{0,\text{min}}$ because the major contribution to the mass-integrated collision rates is given by the high-mass tail with $\mathcal{M} \gtrsim \mathcal{M}_0$ and $\mathcal{R}(\mathcal{M}) \gtrsim \mathcal{R}(\mathcal{M}_0)$. Without considering the NS resonance condition $\omega_p \gtrsim m_a$, as done in Fig. 5.7, NS-MC collisions appear rather frequently, reaching $\simeq 4\,\text{yr}^{-1}$ galaxy⁻¹ for the QCD axion with both MCMF cutoffs and up to $\sim 10^3\,\text{yr}^{-1}$ galaxy⁻¹ for n=0 and $m_a=50\,\mu\text{eV}$. Estimating the abundance of the corresponding galactic signal

rates, which we are interested in requires multiplication of $\Gamma_{\text{mc-}NS}$ with f_{NS} from Fig. 5.4. The resulting signal rates obtained from Fig. 5.7 are plotted in Fig. 5.8. Coincidentally as before,

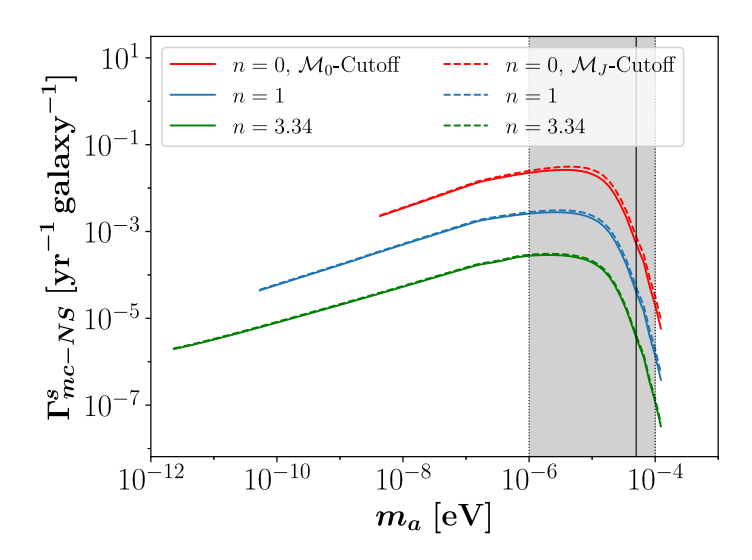


Figure 5.8: Mass-integrated signal rates per year and galaxy, calculated from the encounters between axion miniclusters and neutron stars in Fig. 5.7 by applying the resonance condition $f_{NS}(m_a)$ in Eq. (5.26). Shown as a function of axion mass m_a for $\alpha = -1/2$. This figure is taken from Ref. [1].

the regions where $\Gamma_{mc-NS}(m_a)$ becomes large are strongly suppressed by $f_{NS}(m_a)$ so that the effective rates for producing astrophysical signatures are typically well below 1 per decade for most models m_a , n in Fig. 5.8. The only region, where the signal rates are comparable to one per decade and galaxy is given by n = 0 in red and for $m_a \sim 10^{-5}$ eV, which leaves the general observation of galactic NS-MC encounters very improbable.

We emphasize that this result strongly depends on the power-law index $\alpha = -0.5$ of the MCMF $dn/d \ln \mathcal{M} \propto \mathcal{M}^{\alpha}$ which we have assumed until now. For comparison, the authors of Ref. [136] used a steeper power-law with $\alpha = -0.7$, motivated by numerical simulations of the formation and evolution of miniclusters from Subsec. 3.5.1 and Ref. [30]. For this slope index, the relative contribution of the low- \mathcal{M} components is significantly increased, yielding enhancements by a factor of ~ 10 to ~ 100 for the n-dependent encounter rates of miniclusters. We can confirm the prediction of $\Gamma_{mc-NS} \simeq 4$ /day from Ref. [136], after neglecting the NS resonance and modifying the MC mass range at $m_a = 20 \,\text{eV}$ to $3.3 \cdot 10^{-19} \,M_{\odot} \leq \mathcal{M} \leq 5.1 \cdot 10^{-5} \,M_{\odot}$ with $\alpha = -0.7$. We also note that different to Ref. [136], we use the phenomenological NS distribution fit from

We also note that different to Ref. [136], we use the phenomenological NS distribution fit from Ref. [259] in Sec. A.7 instead of the stellar distribution used by Ref. [136]. The results of our calculations with power-law index $\alpha = -0.7$ are shown in Fig. 5.9.

For the slope index $\alpha = -0.7$ in Fig. 5.9, the low-mass cutoff dependence becomes stronger due to the larger contribution of light miniclusters with $\mathcal{M} < \mathcal{M}_0$, as argued above. The conclusion to draw from our analysis of NS collisions is that despite the very promising encounter rates with ASMC systems, the occurrence of actual signatures from axion-photon conversions is much less common than previously expected. This is especially true for NS-AS collisions which are basically undetectable in the galactic minicluster scenario. For the NS-MC case, detection might still be possible, especially for n = 0, $\alpha = -0.7$ and axion masses around $m_a \simeq 10 \,\mu\text{eV}$ shown

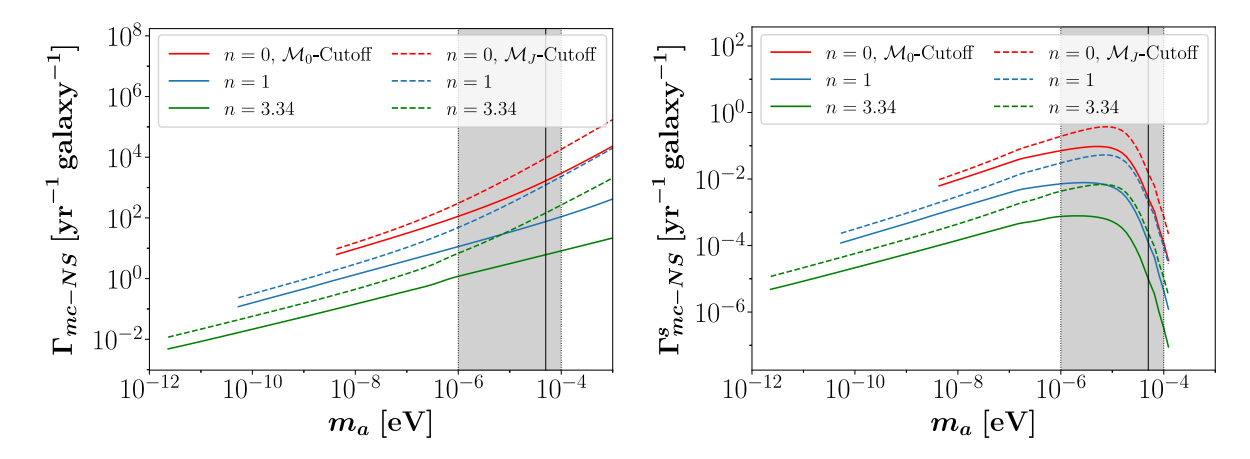


Figure 5.9: Mass-integrated collision- (left) and signal rates (right) per year and galaxy between axion miniclusters and neutron stars as a function of m_a , both taken from Ref. [1]. Calculated for the same parameters as in Fig. 5.7, but for a modified MCMF slope of $\alpha = -0.7$ instead (similar to Fig. 3.2).

in Fig. 5.9. Taking into account the large uncertainties in the NS properties and in the detailed evolution of the minicluster population, the occurrence of radio signals from NS-MC collisions cannot be ultimately ruled out. Our results suggest however, that future research on axion miniclusters should aim to explore new detection mechanisms due to the small expected rates of NS-AS/MC signals in our galaxy.

5.4 Axion Star Mergers and relativistic Bursts

With the galactic detection of radio bursts from axion small-scale structure in neutron star encounters rendered improbable, we direct our attention towards the remaining two major prospects of axion star detection: axion bursts from bosenovae in this section and radio bursts from parametric resonance in Sec. 5.5. The relativistic bursts from axion star core mergers are expected to yield similar signatures to the super-critical solitons from Sec. 4.4, since in both cases the (merged) core mass can reach a super-critical level, $M_{\star} \geq M_{\star,\lambda}$.

An important distinction of the bosenovae occurring in the isolated stars of Sec. 4.4 is that the super-criticality was not introduced through a dynamic process like the gravitational collapse and subsequent soliton merging considered in this section. We therefore summarize the fundamental collision dynamics following the numerical simulations of dilute axion star mergers from App. B in Subsec. 5.4.1 and consider the abundance of the corresponding bursts separately in Subsec. 5.4.2. In the latter section, we explore both the mass-integrated rates for direct mergers of axion stars, with $\Gamma_{\star-\star}$ from Eq. (5.2), as well as that of core mergers following previous host minicluster mergers with rate $\Gamma_{\rm mc-mc}$.

5.4.1 Axion Star Merger Dynamics

Starting with the collision dynamics between two collapsing dilute axion stars, we can employ the numerical methods from App. B to simulate the non-relativistic evolution of the merging system. Analogous simulations were previously performed in Ref.s [31, 33, 172] using similar

numerical methods. It should be noted here that the above references as well as our subsequent analysis focus on the case of dilute, non-relativistic soliton solutions. This regime is distinct from the collapse and signatures of *compact* axion stars, for which the resulting multimessenger merger signal was recently investigated for the first time in Ref.s [34, 253].

Compact axion stars exhibit significantly higher densities thus requiring relativistic simulations, for which the self-interactions are often neglected - as was also done in Ref.s [253, 257]. Our considerations of axion bursts are crucially different from their results, as we are interested in the scalar emission arising from the relativistic multi-particle processes induced by the axion self-interactions with $\lambda < 0$ and the axion potential from Eq. (2.9). The scalar emission observed in Ref.s [253, 257] on the other hand arises only from the relativistic collapse of the compact objects, where no self-interactions $\lambda = 0$ were assumed.

We will therefore rely on the signal predictions from Sec. 4.4 for a qualitative understanding of the resulting axion bursts and demonstrate the non-relativistic collision dynamics leading to the super-criticality of the merged axion star by means of the non-relativistic simulations from App. B. More specifically, we re-simulate the condensation of the $\lambda=0$ SP system with $\widetilde{N}=55, \widetilde{L}=44$ from App. B and Fig. 4.2 until $\widetilde{t}=4000$ in order to obtain a stable soliton configuration including its quasi-particle environment. The total merging system is then composed out of spherical background fluctuations of the axion field, of the soliton core, the excited states around it and of another solitonic object to be specified in the following.

The technical details of the simulation in Fig. 5.10 are presented in App. B and will be summarized together with its time evolution in the following. The condensed axion star core is first evolved until well after the time of condensation, $\tilde{t}=4000\sim 3\tilde{\tau}_{\rm gr}$. After reaching this time, the grid fields get shifted such that the soliton core sits in the origin of the transformed coordinates³. We determined that the initial mass of the central soliton core at $\tilde{\mathbf{x}}=0$, $\tilde{t}=4000$ is roughly $\widetilde{M}_{\star}\approx 5$, which corresponds to $M_{\star}\approx 1.34\cdot 10^{-14}\,M_{\odot}$ for QCD axion parameters $m_a=50\,\mu{\rm eV}$, $f_a\simeq 10^{11}\,{\rm GeV}$.

Next, a spherical object with similar mass $\widetilde{M}_s = 6$ or $M_s \approx 1.6 \cdot 10^{-14} \, M_{\odot}$ and initial velocity $|\widetilde{\mathbf{v}}_0| = \widetilde{v}_y = 1$ is embedded at position $\widetilde{\mathbf{x}} = (0, 17, 0)$ in the volume. The corresponding spherical overdensity with physical velocity $-v_0$ along the y-direction⁴ can be seen together with the condensed soliton system in the top left panel of Fig. 5.10, which shows the axion field density $\widetilde{\rho}(\widetilde{\mathbf{x}}) = |\widetilde{\psi}(\widetilde{\mathbf{x}})|^2$ at different times and $\widetilde{z} \approx 0^5$.

For the numerical implementation of the additional soliton \widetilde{M}_s , we follow the best-fit sech profile obtained in Ref. [231] using the definition

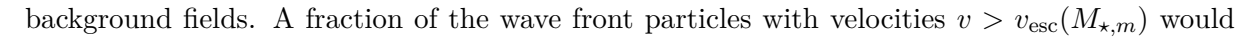
$$\widetilde{\psi}_s(\widetilde{\boldsymbol{x}}) = \widetilde{\psi}_{\text{sech}}(|\widetilde{\boldsymbol{x}}|) \exp(i\widetilde{v}_y\widetilde{y} + i\theta_s),$$
(5.28)

where $\theta_s = 0$ in Fig. 5.10 is a relative phase and $\widetilde{\psi}_{\rm sech}(\widetilde{r} = |\widetilde{\boldsymbol{x}}|)$ is the profile fit from Eq. (B.38). Both of these objects can be seen to have similar size and density in Fig. 5.10, where the actual merger event at $\widetilde{t} \approx 4010$ is depicted in the top right panel. After the solitons have collapsed, a spherically shaped wave front of gravitationally accelerated particles can be seen to spread out from the central simulation region in the bottom left panel of Fig. 5.10. The wave front expands and dilutes over time, as some of the accelerated particles lose energy through scattering in the

³The shift symmetry is ensured by the periodic boundary conditions with $\widetilde{\psi}(\widetilde{\mathbf{x}}) = \widetilde{\psi}(\widetilde{\mathbf{x}} + L\widetilde{\mathbf{n}}_{\widetilde{\mathbf{x}}})$ [170]

⁴For the SP system in Eq. (3.14), Eq. (3.15), v_0 is the reference velocity of the rescaling in App. A.6.

⁵Note that the approximate equality of the position \tilde{z} is related to the stochastic motion of the soliton, which slowly drives it away from the origin after $\tilde{t} = 4000$.



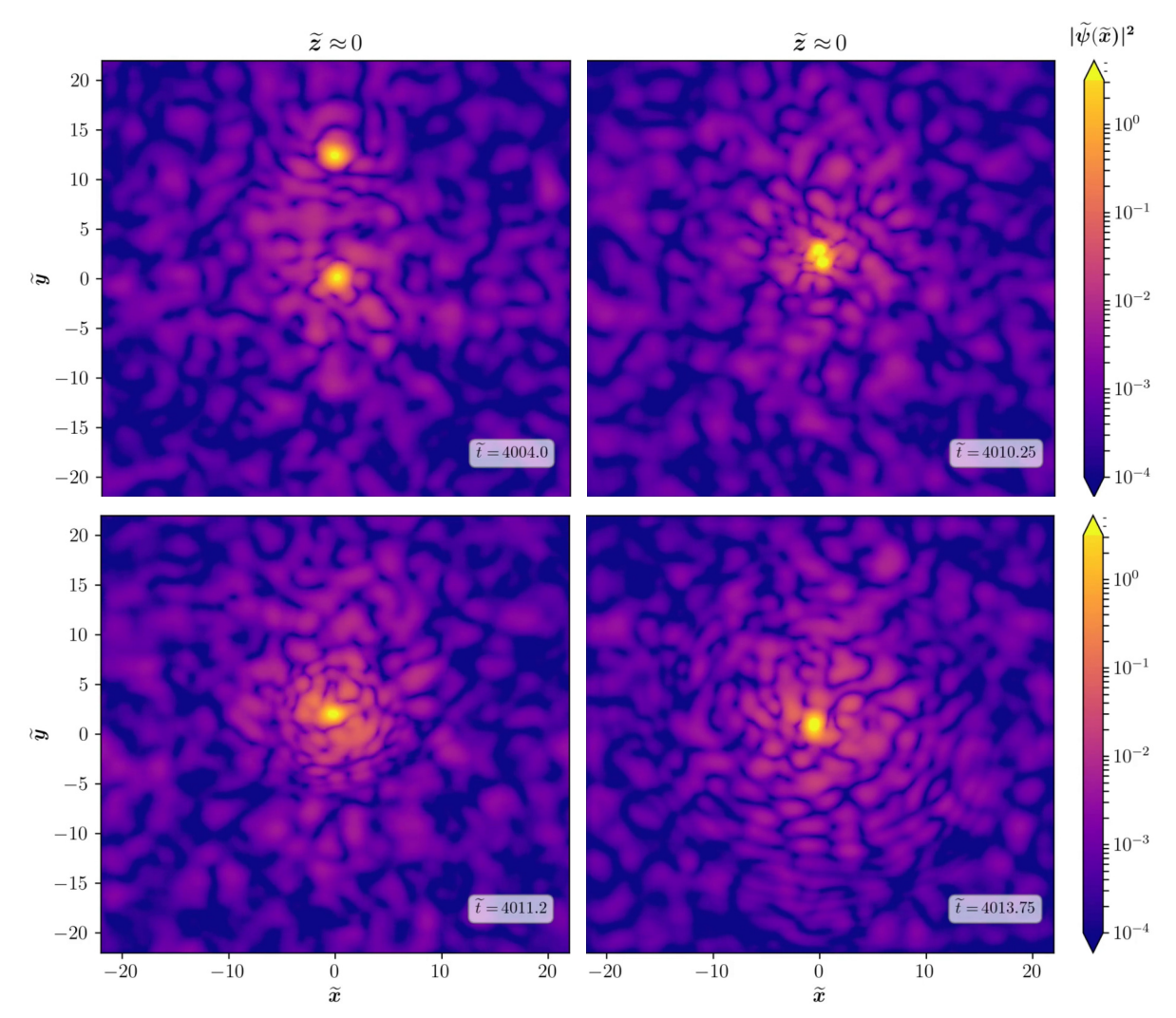


Figure 5.10: Simulation of two sub-critical axion stars with initial masses $\widetilde{M}_{\star} \approx 5$, $\widetilde{M}_{s} = 6$ merging into a stable configuration with $\widetilde{M}_{\star,m} \approx 8 < \widetilde{M}_{\star,\lambda}$ around $\widetilde{t} \approx 4010$ for $\widetilde{\lambda} = 0$. The numerical system is identical with the one simulated in Fig. 4.2 and App. B, except for the spherical object \widetilde{M}_{s} with $\theta_{s} = 0$ in Eq. (5.28), initial position $\widetilde{x}_{0} = \widetilde{z}_{0} = 0$, $\widetilde{y}_{0} = 17$ and velocity $|\widetilde{\mathbf{v}}_{0}| = \widetilde{v}_{y} = 1$. At $\widetilde{t} = 4000$, the condensed soliton M_{\star} is set to the origin $\mathbf{x} = 0$. For QCD axion parameters $m_{a} = 50 \,\mu\text{eV}$, this corresponds to $M_{\star} \approx 1.34 \cdot 10^{-14} \, M_{\odot}$, $M_{s} = 1.6 \cdot 10^{-14} \, M_{\odot}$, with a total merger duration of $t_{m} \approx 6.3 \, \text{yrs}$.

exit the simulation volume after $\widetilde{t}=4015$. The overall collision with $\widetilde{t}=15$ takes roughly 6.3 yrs for QCD axion parameters.

At $\widetilde{t} > 4010$, the two solitons have formed a stable object with merged mass $M_{\star,m} \approx 8$ or $M_{\star,m} \approx 2.14 \cdot 10^{-14} \, M_{\odot}$ for QCD axion properties. The initial momentum of the moving soliton, $M_s v_s$, gets absorbed into the quasi-particle environment of the central core region. We also confirm the mass prediction [33]

$$M_{\star,m} \approx 0.7(M_{\star,1} + M_{\star,2})$$
 (5.29)

for the final merger mass in all of our simulations. We emphasize that for the sub-critical configuration $M_{\star,m} < M_{\star,\lambda}$ simulated in Fig. 5.10, the merged soliton remains stable over long times $\tilde{t} > 4015$.

Accordingly, the simulation in Fig. 5.10 is purely non-relativistic, so that only the gravitational collapse of dilute stars without the self-interaction instability from Fig. 4.8 can be demonstrated. We thus do not investigate the long-time evolution of the merged system, but continue by comparing the dependence of the collision dynamics on the relative phase θ_s of the object \widetilde{M}_s in Eq. (5.28). Since the system at hand is of wavelike nature, the interference between the objects \widetilde{M}_{\star} and \widetilde{M}_s is effectively governed by their relative phase $\theta_{\star} - \theta_s^{\ 6}$.

To demonstrate this effect, we show the results from four different, analogous merger simulations with the same grid parameters from Fig. 5.10 and different θ_s in Fig. 5.11. Remarkably, the

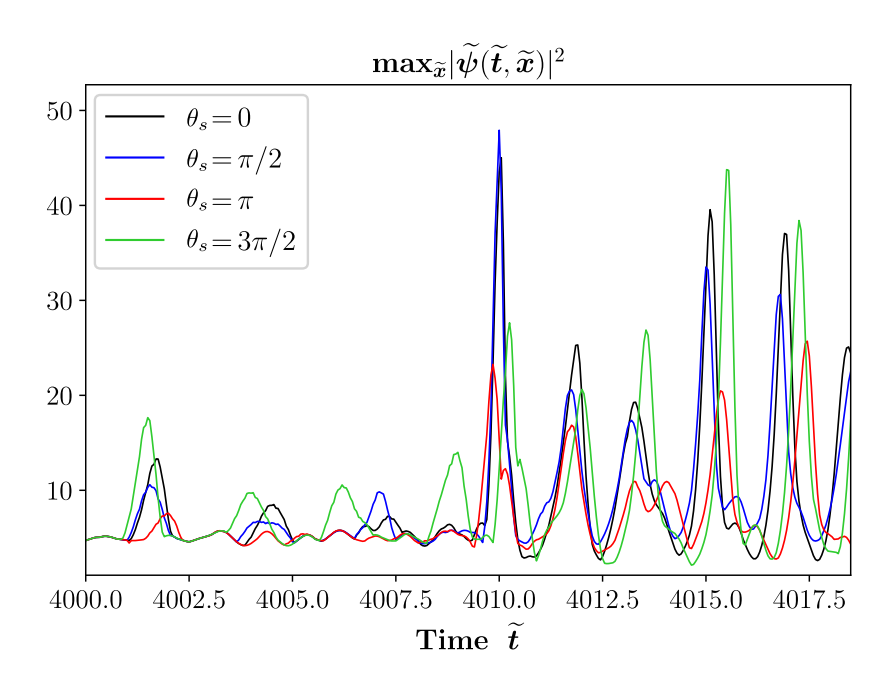


Figure 5.11: Maximum density $\max_{\widetilde{x}} |\widetilde{\psi}(\widetilde{t}, \widetilde{\mathbf{x}})|^2$ over the three-dimensional simulation volume in three merger simulations with the same parameters from Fig. 5.10 but at different $\theta_s = 0, \pi/2, \pi, 3\pi/2$. Different colors indicate different phases θ_s of the soliton wavefunction ψ_s in Eq. (5.28).

resulting collapse around $\tilde{t}=4010$ is most violent for $\theta_s=\pi/2$ in blue lines in Fig. 5.11. This is most likely due to the two soliton profiles having more suitable phases for constructive interference. In contrast, the green curve with $\theta_s=3\pi/2$ shows the largest peaks at earlier times $\tilde{t}<4010$, when the soliton travels through the axion background fluctuations.

This peculiar behavior suggests a separate effect of constructive interference with the background field. Even more remarkable is the fact that the late-time oscillations of the merged soliton at $\tilde{t} > 4010$ in green are also enhanced, compared to the other three phases θ_s in blue, black and red. It could therefore be possible that the phase matching between background field and external soliton plays a particularly important role in the merging process.

For future research, the role of background fluctuations in the merger process would be worth

 $^{^6}$ We do not determine the time-dependent phase θ_{\star} of the condensed core in our simulations.

further investigation. This would be feasible through use of the techniques from App. B with minor additional effort. However for the purpose of this work, we conclude that the collision dynamics of dilute axion stars behave similar to the simulation of sub-critical axion stars in Fig. 5.10 until the self-interaction instability develops. After the instability is triggered, the merged soliton mass is considered to be greater than the critical value of $M_{\star,\lambda}$ from Eq. (4.16) leading to the emission of a relativistic axion burst similar to the one in Fig. 4.10.

An important restriction to this process is that the relative velocity $v < v_{\rm esc}(M_{\star,m})$ required for the formation of a merged soliton with $M_{\star,m} \approx 0.7(M_{\star} + M_s)$ is very small compared to astrophysical scales $v_{\rm vir} \gg v_{\rm esc}(M_{\star,m})$, where $v_{\rm vir} = 239\,{\rm km\,s^{-1}}$ is the virial velocity of the NFW halo. We use this observation to investigate the resulting abundance of the AS merger events in the next section.

5.4.2 Axion Star Merger Rates

With the fundamental collision- and burst dynamics demonstrated in Subsec. 5.4.1 and Sec. 4.4, we will ignore any further details of the bosenova evolution in this subsection and assume that the resulting density fluctuations in the axion dark matter background could potentially be detected by earth based experiments [36, 234]. We dedicate a separate chapter to the detectability of the resulting burst signals in Chap. 7 and motivate the in-depth analysis with estimations of the galactic signal rates in the following.

To estimate how common the occurrence of such axion bursts in our galaxy is, we start by computing the model-dependent (m_a, n) and mass-integrated collision rates for $i = j = \star$, mc in Eq. (5.2) with symmetry factor S = 1/2. The results for direct AS-AS core collisions are shown

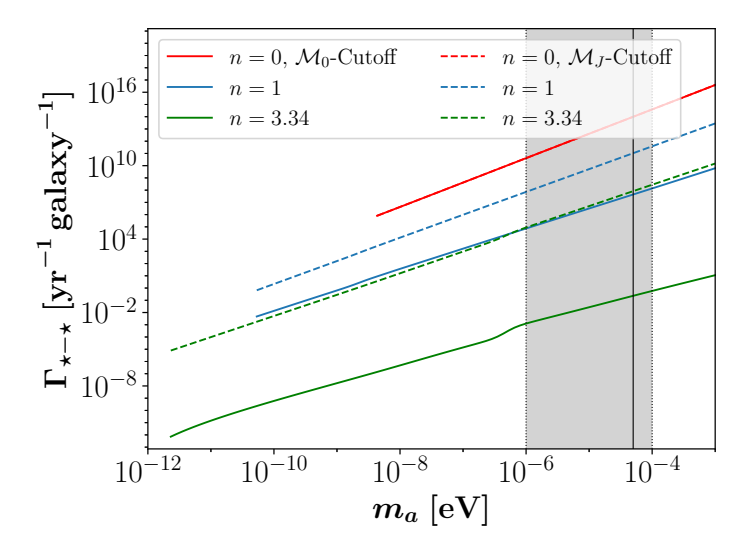


Figure 5.12: Mass-integrated binary collision rates of axion stars per year and galaxy as a function of axion mass m_a , taken from Ref. [1]. Colored lines indicate the temperature dependence of the axion mass, solid and dashed lines represent the two different low- \mathcal{M} cutoffs for $\alpha = -1/2$.

for both MCMF cutoffs in Fig. 5.12 as a function of m_a and n. The collision rates in Fig. 5.12 show a linear scaling with m_a , which can again be explained by simple considerations: For both axion stars and miniclusters, the gravitational enhancement in Eq. (5.4) is negligible, $\eta_{\rm gr} \ll 1$, so that the encounter rates for n=0 in red lines in figures 5.12 with $N_{\star,{\rm tot}} \propto \mathcal{M}_0^{-1}$ and $\langle R_{\star} \rangle \propto m^{-1/2}$ (see Fig. C.5) simply scale as

$$\Gamma_{\star-\star}\Big|_{n=0} \propto N_{\star,\text{tot}}^2 \langle R_{\star} \rangle^2 \propto m_a^2 \,.$$
 (5.30)

The same scaling also applies to the n=0 minicluster rates in red in Fig. 5.14 and Fig. 5.16. For the remaining cases n=1,3.34 in blue and green, the scalings of the binary collision rates with m_a will be marginally different but qualitatively identical as argued before.

Coming back to the predicted encounter rates in Fig. 5.12, we find that for all of the models m_a , n with n=0,1 the resulting collisions are extremely common, $\Gamma_{\star-\star}\gg 1\,\mathrm{yr}^{-1}\,\mathrm{galaxy}^{-1}$. This is especially true for QCD axion masses $m_a=50\,\mu\mathrm{eV}$ and heavier axions, with the only exception given by the two \mathcal{M}_0 -cutoff with temperature index n=3.34 in green dashed lines. As in the previous sections, the \mathcal{M}_J -cutoff produces larger event rates due to the reduced mass and enhanced number of galactic objects, see Fig. C.3. Overall, we can summarize that similar to the previous cases, the occurrence of AS-AS collisions is mostly governed by their abundance and therefore increased for lighter object masses, i.e. for heavier m_a . Equivalent predictions were already made by the authors of Ref. [33]. In contrast, the same statement does not hold true for the case of AS-AS merger rates, which we aim to investigate in this section.

By our definition, mergers are different from collisions in the sense that the final state is a gravitationally bound merged soliton with final mass $M_{\star,m} \simeq 0.7(M_{\star,1}+M_{\star,2})$. The probability for the two solitons involved in an AS-AS collision to merge can be estimated from the ratio of the escape velocity of the binary cores, $v_{\rm esc}(M_{\star,m})$ and the typical velocity $v_{\rm vir}$ of objects in the NFW dark matter halo, which for the scaling in Eq. (5.5) yields

$$\Gamma_{\star - \star}^{m} \sim \left[\frac{v_{\rm esc}(M_{\star})}{v_{\rm vir}} \right]^{4} \Gamma_{\star - \star} \equiv f_{\rm esc} \Gamma_{\star - \star}$$
 (5.31)

for the corresponding merger rate $\Gamma^m_{\star-\star}$. We apply this estimate to our calculation of the total number of AS mergers determined by Eq. (5.2) in Fig. 5.13 by replacing the velocity cutoff $v_{\rm esc}$ in Eq. (5.5) with the escape velocity $v_{\star,\rm esc}(M_{\star,1}+M_{\star,2})\simeq \sqrt{2G(M_{\star,1}+M_{\star,2})/(R_{\star,1}+R_{\star,2})}$ of each binary axion star collision. The corresponding fraction of encounters, which can lead to a merger has an upper bound of

$$f_{\rm esc}(M_{\star}, n = 0) \lesssim \left[\frac{v_{\star, \rm esc}(M_{\star, \lambda})}{v_{\rm vir}}\right]^4 \stackrel{50\,\mu\rm eV}{\sim} \left(\frac{10\,\mathrm{m\,s^{-1}}}{100\,\mathrm{km\,s^{-1}}}\right)^4 \sim 10^{-16}$$
 (5.32)

and it depends on the distribution of AS masses $M_{\star} \leq M_{\star,\lambda}$ in the ASMF, where we have taken the maximum AS properties as an upper bound for n=0 and neglected the impact of the reduced number density at large M_{\star} for simplicity.

Integrating the M_{\star} -dependent suppression factor from Eq. (5.32) over the whole range of AS masses and taking into account the reduced number densities at large values of M_{\star} , the effective suppression can become orders of magnitude smaller than $f_{\rm esc}(M_{\star,\lambda}) \sim 10^{-16}$ - depending on the temperature index n and the low-mass cutoff $\mathcal{M}_{\rm min}$. Accordingly, the AS merger results for an MCMF slope of $\alpha = -1/2$ in Fig. 5.13 are generally many orders of magnitude lower than the corresponding collision rates in Fig. 5.12. More specifically, all of the AS merger rates in

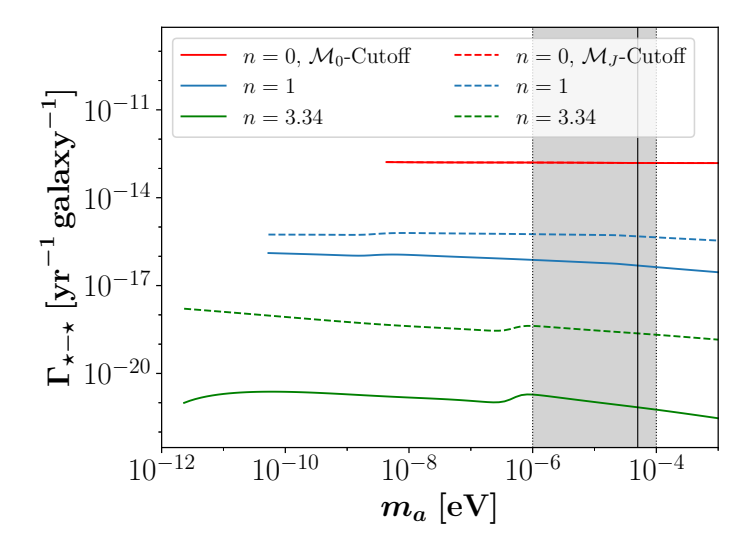


Figure 5.13: Mass-integrated total merger rates of axion stars per year and galaxy as a function of axion mass m_a for $\alpha = -1/2$, taken from Ref. [1]. Successful AS mergers are determined by applying the merged core escape velocity $v_{\star,\text{esc}}(M_{\star,1}+M_{\star,2}) \simeq \sqrt{2G(M_{\star,1}+M_{\star,2})/(R_{\star,1}+R_{\star,2})}$ as a velocity cutoff in Eq. (5.3).

Fig. 5.13 are well below $\Gamma_{\star-\star} < 1/t_H \sim 10^{-10}\,\mathrm{yr^{-1}\,galaxy^{-1}}$, which indicates that these processes are unlikely to occur even over the age of the universe.

The above analysis shows that while galactic axion star encounters in Fig. 5.12 are very common $\Gamma_{\star-\star}\gg 1\,\mathrm{yr}^{-1}$ galaxy⁻¹ for most models except n=3.34 with the \mathcal{M}_0 -cutoff, they are extremely unlikely to ever merge. The simple explanation for this strong suppression are the relatively very small binding energy of axion stars and their large typical velocities in the Milky Way DM halo with velocity dispersion $v_{\rm vir}=239\,\mathrm{km\,s^{-1}}$.

The small escape velocities in return are related to the low masses of axion stars $M_{\star} \ll M_{\odot}$. This observation motivates another equivalent study of merger events in the host minicluster population, which generally exhibits significantly larger masses $\mathcal{M} \gg M_{\star}$ compared to their AS cores, which means that these objects are overall much more likely to merge. Since in the gravitational limit with weak self-interactions $\lambda = -m_a^2/f_a^2$, every minicluster has been shown to host at most a single core (see Fig. 4.2, Fig. 5.10), AS core mergers are guaranteed to appear after a successful host minicluster merger.

Therefore replacing the AS parameters in Eq. (5.2) with the corresponding MC properties and using $v_{\text{mc,esc}}(\mathcal{M}_1 + \mathcal{M}_2) \simeq \sqrt{2G(\mathcal{M}_1 + \mathcal{M}_2)/(\mathcal{R}_1 + \mathcal{R}_2)}$ as a velocity cutoff in Eq. (5.3) instead, we can similarly compute the collision- and merger rates of miniclusters shown in Fig. 5.14 and Fig. 5.15, again for $\alpha = -1/2$. Starting with Fig. 5.14, we find a significant increase in the overall collision rates of miniclusters compared to the AS-AS encounters in Fig. 5.12. This can be understood from two effects: First, the increased number of objects due to the absence of the ASMF cutoffs from Subsec. 4.7.1 in the MCMF and secondly the different scaling of the radius $\mathcal{R} \propto \mathcal{M}^{1/3}$ compared to $R_{\star} \propto 1/M_{\star}$, which enhances the cross section of the intermediate and high-mass component of the MCMF in Eq. (5.3).

Concerning the merger rates of miniclusters, it is important to note here that only MC-MC

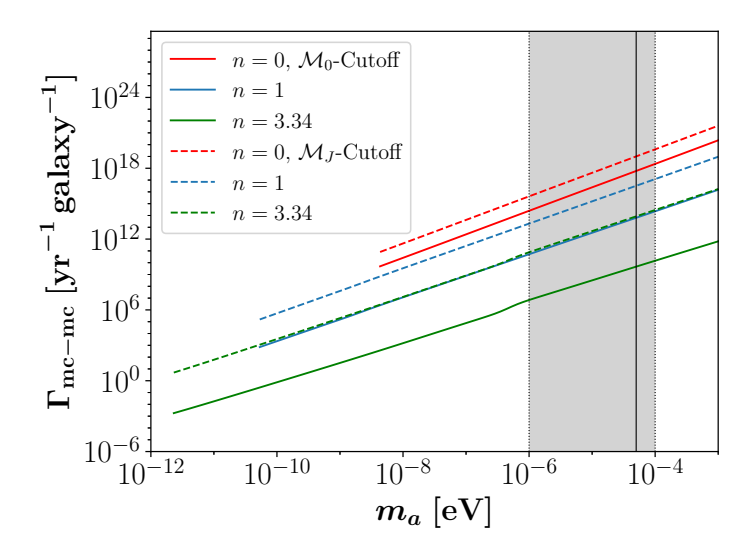


Figure 5.14: Mass-integrated MC collision rates per year and galaxy as a function of axion mass m_a , taken from Ref. [1]. Colored lines indicate the temperature dependence of the axion mass, solid and dashed lines represent the two different low- \mathcal{M} cutoffs for $\alpha = -1/2$.

mergers with a total mass $\mathcal{M}_1 + \mathcal{M}_2 \geq \mathcal{M}(M_{\star,\lambda})$ will safely lead to the production of relativistic bursts (where we have inverted the core-halo relation in Eq. (3.57) to find the MC mass corresponding to $M_{\star,\lambda}$). For this reason we plot the *minicluster bosenova merger rates* in Fig. 5.15 and Fig. 5.16 by only considering collisions, which simultaneously pass the velocity cutoff $v_{\text{mc,esc}}$ and the requirement $\mathcal{M}_1 + \mathcal{M}_2 \geq \mathcal{M}(M_{\star,\lambda})$. In a more general context, the AS cores are not expected to merge simultaneously with their host miniclusters. Nevertheless, the relevant free-fall time of the two AS cores is generally much smaller than the time between two MC collisions, so that we can assume the axion stars to merge quasi-instantaneously to a good approximation (see also the calculation in Sec. 5.6) in the following.

For the case n=1 in blue lines in Fig. 5.15, the bosenova merger rates quickly drop to zero beyond $m_a \gtrsim 10^{-5} \,\mathrm{eV}$ where $2\mathcal{M}_{\mathrm{max}} < \mathcal{M}(M_{\star,\lambda})$. More importantly, the MC signal rates are significantly enhanced in the case of the \mathcal{M}_J -cutoff due to the large total number of MCs, reaching $\Gamma_{\mathrm{mc-mc}} \gtrsim 1 \,\mathrm{yr}^{-1} \,\mathrm{galaxy}^{-1}$ for axions with n=3.34 and at $m_a \approx 50 \,\mu\mathrm{eV}$, $\alpha=-1/2$. The weak dependence of the merger rates on m_a indicates that for larger axion masses and hence smaller $\mathcal{M}_0(m_a)$, the boost from having an increased number of objects $\mathcal{N}_{\mathrm{tot}} \propto 1/\mathcal{M}_0$ roughly cancels with their decreased merger rates due to the smaller typical size $\mathcal{R} \propto \mathcal{M}_0^{1/3}$. The corresponding suppression factor for minicluster merger rates is bound from above by

$$f_{\rm esc}(\mathcal{M}, n = 0) \lesssim \left[\frac{v_{\star, \rm esc}(\mathcal{M}_{\rm max})}{v_{\rm vir}}\right]^4 \stackrel{50 \,\mu\rm eV}{\sim} \left(\frac{100\,\mathrm{m\,s^{-1}}}{100\,\mathrm{km\,s^{-1}}}\right)^4 \sim 10^{-12}\,,$$
 (5.33)

which as expected is orders of magnitude larger than the corresponding factor of the AS case in Eq. (5.32). Here we have again evaluated $f_{\rm esc}(\mathcal{M})$ at the maximum MC mass $\mathcal{M}_{\rm max}$ given by the high-mass cutoff in Eq. (3.46) and neglected the reduced number density $dn/d\mathcal{M}$ at $\mathcal{M} = \mathcal{M}_{\rm max}$ to obtain an upper bound on $f_{\rm esc}$.

Lastly, we note that due to the suppression factor in Eq. (5.33) and its mass-dependence, the

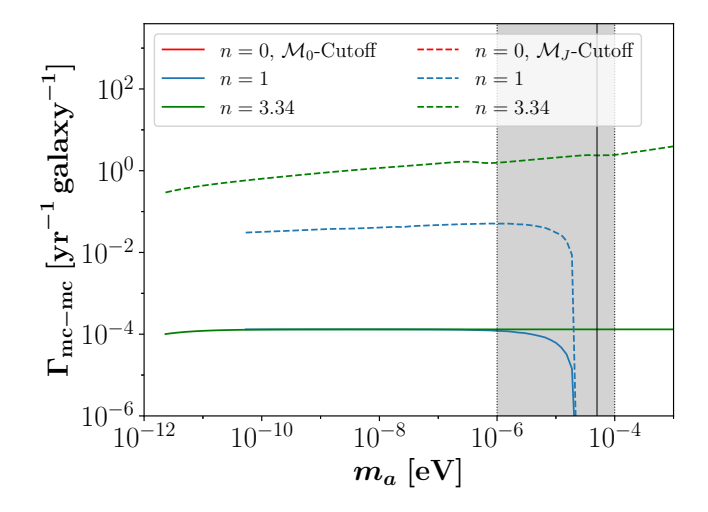


Figure 5.15: Mass-integrated bosenova MC merger rates with $\mathcal{M}_1 + \mathcal{M}_2 \geq \mathcal{M}(M_{\star,\lambda})$ per year and galaxy as a function of axion mass m_a for $\alpha = -1/2$. Successful MC mergers are determined by applying the merged core escape velocity $v_{\text{mc,esc}}(\mathcal{M}_1 + \mathcal{M}_2) \simeq \sqrt{2G(\mathcal{M}_1 + \mathcal{M}_2)/(\mathcal{R}_1 + \mathcal{R}_2)}$ as a velocity cutoff in Eq. (5.3). Taken from Ref. [1].

bosenova rates in Fig. 5.15 are dominated by encounters between the numerous low-mass miniclusters with $\mathcal{M} \simeq \mathcal{M}_{\min}$ and the rare high-mass MCs with $\mathcal{M} \sim \mathcal{M}_{\max}$. To investigate the benefit from an increased number of light MCs with $\mathcal{M} \simeq \mathcal{M}_{\min}$, which can be captured by the heaviest structures, we also plot the results obtained for a modified MCMF slope index $\alpha = -0.7$ from Subsec. 3.5.1. The steeper MCMF slope resulting from assuming $\alpha = -0.7$ in Eq. (3.51) implies a larger relative abundance of the lightest miniclusters $\mathcal{M} \simeq \mathcal{M}_{\min}$.

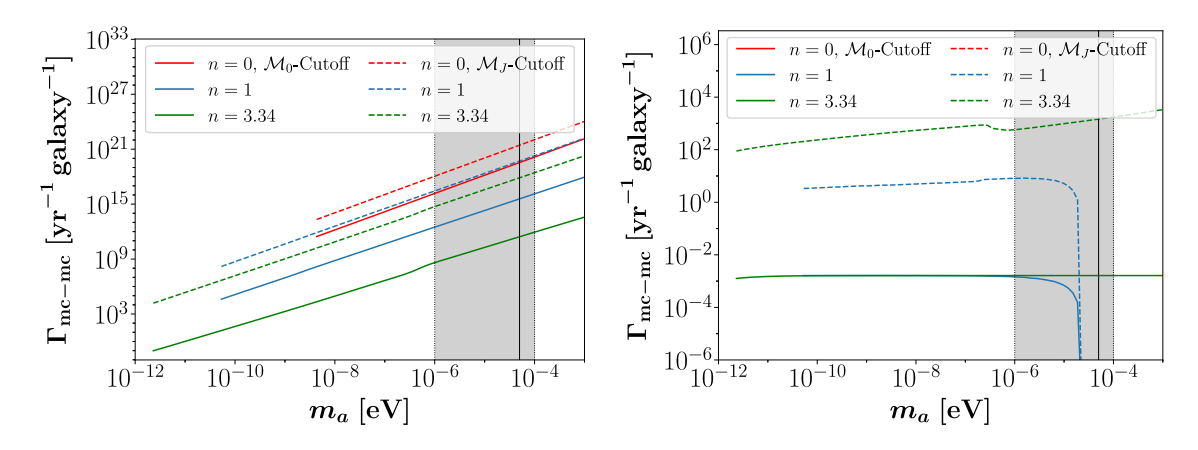


Figure 5.16: Mass-integrated MC collision rates (left) and MC merger rates with $\mathcal{M}_1 + \mathcal{M}_2 \geq \mathcal{M}(M_{\star,\lambda})$ (right) per year and galaxy as a function of m_a , taken from Ref. [1]. Colored lines indicate the temperature dependence of the axion mass, solid and dashed lines represent the two different low- \mathcal{M} cutoffs for $\alpha = -0.7$. Note that MC mergers could also produce radio bursts when $M_{\star,\gamma} < M_{\star,\lambda}$ (see Sec. 5.5).

As a consequence, the total number of miniclusters \mathcal{N}_{tot} is significantly boosted due to the smaller fraction of heavy MCs and hence larger number of light MCs in the Milky Way with

total mass $\mathcal{M}_{\text{tot}} = f_{\text{mc}} M_{\text{MW}}$. For the same reason, the total numbers of MC-MC encounters $\Gamma_{\text{mc-mc}} \propto \mathcal{N}_{\text{tot}}^2$ and bosenova mergers in Fig. 5.16 are strongly enhanced compared to the $\alpha = -1/2$ case in Fig. 5.14 and Fig. 5.15.

We conclude that for the detection of bosenovae from galactic ASMC systems, the low- \mathcal{M} cutoff and the slope index $\alpha = -1/2, -0.7$ of the MCMF have a strong impact on the expected bosenova event rates investigated in this section. Our results suggest that for the QCD axion case $m_a = 50 \,\mu\text{eV}$, n = 3.34 and axions with similar temperature evolution, bosenovae can occur as often as ~ 1 per year for $\alpha = -1/2$ and as often as ~ 3 per day for $\alpha = -0.7$, both with the \mathcal{M}_J -cutoff.

Conversely, for the \mathcal{M}_0 -cutoff the expected merger rates in Fig. 5.15 and Fig. 5.16 are well below one per year - independent of m_a and n. Bosenovae from MC-MC mergers thus require large numbers of miniclusters and benefit from a larger maximum mass \mathcal{M}_{max} as seen for n > 0 in dashed lines in Fig. 5.15 and Fig. 5.16. Even in the cases, where bosenova merger rates are small, other mechanisms such as AS accretion, could still trigger large numbers of bosenovae even for the \mathcal{M}_0 -cutoff. This possibility will be explored in more detail in Chap. 7.

5.5 Parametric Resonance and Axion Star Accretion

The last major axion star signature to be evaluated by means of the galactic ASMF is the parametric resonance of solitons with $M_{\star} \geq M_{\star,\gamma}$ from Eq. (4.61) and Sec. 4.5. Similar to the previous case of the critical mass $M_{\star,\lambda}$, the decay mass $M_{\star,\gamma}$ may be reached through two fundamental processes: First through successful mergers of axion stars, which were found to be sufficiently common in our galaxy for n=1,3.34 with the \mathcal{M}_{J} -cutoff in Subsec. 5.4.2 and secondly through the ongoing mass growth of the solitonic core that was observed in Sec. 4.3. In this section, we investigate both possibilities, while focusing on the second case of axion star accretion, which turns out to be the most promising mechanism. The merger process on the other hand was already discussed in Sec. 5.4, where the AS resonance rates are qualitatively similar as long as $M_{\star,\gamma} \lesssim M_{\star,\lambda}$ and the resonance is not prevented by the relativistic collapse at the maximum stable mass $M_{\star,\lambda}$. As with the previous signatures, we start by demonstrating the electromagnetic signal and luminosity of parametrically resonant solitons in Subsec. 5.5.1. We compute the abundance of the corresponding radio bursts in Subsec. 5.5.2 and estimate their extra-galactic detectability in Sec. 5.6, using the signal strengths from Subsec. 5.5.1.

5.5.1 Signals from parametrically resonant Axion Stars

While the resonance condition for axion stars in Eq. (4.61) could be derived by means of simple considerations and for a homogeneous soliton profile, the computation of the exact properties of the corresponding signal is very challenging to perform. The most complete analysis of the electromagnetic signal from dilute $R_{\star} \gtrsim R_{\star,\lambda}$ and self-interacting $\lambda \neq 0$ axion stars is currently provided in the extensive study of Ref. [31].

Importantly for this work, the authors of Ref. [31] investigated two separate scenarios in which radio emission may be observed from critical solitons: First, when the parametric resonance gets triggered in an axion star with resonant mass $M_{\star} = M_{\star,\gamma} < M_{\star,\lambda}$, as introduced in Sec. 4.5. And secondly, when the increased axion densities ρ_{\star} during the collapse of a non-resonant, unstable soliton with $M_{\star} = M_{\star,\lambda} < M_{\star,\gamma}$ alleviate the resonance condition from Eq. (4.58), leading

to stimulated decay of axions into photons below the resonance mass $M_{\star,\gamma}$. The first case of resonant axion stars on the dilute branch can be described by neglecting self-interactions, i.e. $\lambda = 0$, since the dynamics are governed by the gravitational and electromagnetic interactions. The second case on the other hand involves larger axion field densities and thus requires consideration of the full axion potential from Eq. (2.9).

Starting with the first scenario involving resonant solitons and vanishing self-interactions, we emphasize that the resonance mass for $\lambda=0$ is different to $M_{\star,\gamma}$ due to the absence of self-interactions in the groundstate solution M_s of the SP system. To make clear the distinction between an 'actual' axion star M_{\star} with $\lambda=-m_a^2/f_a^2<0$ and the Schrödinger-Poisson soliton mass M_s for $\lambda=0$, we change the subscript from ' \star , γ ' to 's, γ '. The corresponding $\lambda=0$ Schrödinger-Poisson resonance mass can then be written as [31]

$$M_{s,\gamma} = 7.66 \frac{m_{\rm Pl}}{m_a g_{a\gamma\gamma}} \quad , \quad \lambda \approx 0 \,,$$
 (5.34)

where we note that the parametric resonance process occurring for $M_s \ge M_{s,\gamma}$ is equivalent to the case $M_{\star} \ge M_{\star,\gamma}$ - apart from the modified mass-radius relation for $\lambda < 0$.

The $\lambda = 0$ soliton radius corresponding to the soliton mass M_s can be obtained from numerical calculations of the eigenstates of the Schrödinger-Poisson system Eq. (3.14), Eq. (3.15), which are given in App. A.5. It is commonly expressed in terms of the half-mass radius R_s of the corresponding n = 0 ground state with mass M_s from Eq. (A.2) according to [49]

$$R_s \simeq \frac{4m_{\rm Pl}^2}{M_s m_a^2} = 4r_0 \,,$$
 (5.35)

where the equivalent scale radius $r_0 = m_{\rm Pl}^2/(M_s m_a^2)$ provides a dimensional estimate of the halfmass radius, see also Fig. 5.18. In the following simulations for $\lambda = 0$, the Schrödinger Poisson solitons M_s undergo the same parametric resonance and qualitative behavior, which is expected for the $\lambda = -m_a^2/f_a^2$ axion stars treated in this work.

The representative radio luminosity $L_{\gamma} \propto n_{\gamma} \propto \exp(2\mu t)$ from a resonant Schrödinger-Poisson soliton with $M_s = 1.04 M_{s,\gamma}$ is depicted in Fig. 5.17. Fig. 5.17 has been obtained using the rescaled units from Ref. [31] and App. A.6. The results are shown in universal units, which are fixed by the specific value of $M_s = 1.04 M_{s,\gamma}$ and the axion model with m_a , f_a , $g_{a\gamma\gamma}$. For QCD axion values $m_a = 50 \,\mu\text{eV}$, $f_a \approx 10^{11}\,\text{GeV}$ and with an axion-photon coupling $g_{a\gamma\gamma} = 10^{-12}\,\text{GeV}^{-1}$ that is enhanced compared to standard KSVZ models, this corresponds to $M_s = 1.74 \cdot 10^{-12}\,M_{\odot}$ and $R_s \simeq 24.2\,\text{km}$ following Eq. (5.35).

Overall, the time evolution of the resonating $\lambda=0$ soliton in Fig. 5.17 can be roughly split into two stages: First the stage of exponential growth in which $L_{\gamma} \propto n_{\gamma} \propto \exp(2\mu t)$ in dashed lines and secondly the late-time regime indicated by the gray region and black dotted line in Fig. 5.17. The late-time behavior is characterized by the onset of backreaction, which appears when the exponentially growing decay of axions into photons starts to deplete the total mass of the soliton. Since the photon conversion rate depends on the decaying axion field density $\rho_s(t) \sim M_{\star}/R_{\star}^3$, the backreaction eventually leads to a decrease and saturation of the luminosity in Fig. 5.17.

For the exemplary case of a resonant SP soliton with $M_s=1.04M_{s,\gamma}$ in Fig. 5.17, $g_{a\gamma\gamma}=10^{-12}\,\mathrm{GeV^{-1}}$ and QCD axion values for m_a,f_a , the peak luminosity corresponds to $L_{\gamma,\mathrm{max}}\sim 2\cdot 10^{39}\,\mathrm{erg\,s^{-1}}$. Assuming a galactic Doppler spread of $\Delta f\sim 10^{-3}m_a$ from $v_{\mathrm{vir}}\sim 10^{-3}$ and a

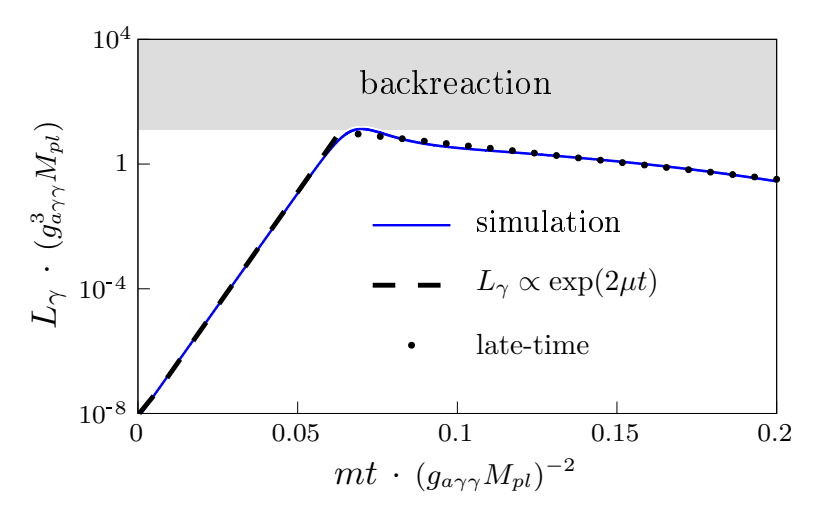


Figure 5.17: Evolution of the luminosity of a resonating soliton with $M_s = 1.04 \, M_{s,\gamma}$ from Ref. [31]. For QCD axion parameters $m_a = 50 \, \mu \text{eV}$, $f_a = 10^{11} \, \text{GeV}$ with enhanced axion-photon coupling $g_{a\gamma\gamma} = 10^{-12} \, \text{GeV}^{-1}$, this corresponds to $M_s = 1.74 \cdot 10^{-12} \, M_{\odot}$ and $R_s \simeq 24.2 \, \text{km}$. The dashed black line shows the regime, where $L_{\gamma} \propto \exp(2\mu t)$ increased exponentially, whereas the black dotted line indicates the regime after the onset of backreaction.

sensitivity of $S \sim \text{mJy}$ [191], the resulting photon flux could possibly be detected at maximum distances of $\mathcal{O}(\text{Gpc})$, see Sec. 5.6 for details.

We also demonstrate the directional dependence of the resulting electromagnetic flux predicted in Ref. [31] in Fig. 5.18. The left panel of Fig. 5.18 shows the photon flux in a cubic volume of size $L \sim 4.2r_0$ obtained from a resonant soliton with $\lambda = 0$ and increased mass $M_s = 1.36 M_{s,\gamma}$, again in rescaled units. For QCD axion values $m_a = 50 \,\mu\text{eV}$, $f_a \approx 10^{11}\,\text{GeV}$ with an enhanced axion-photon coupling $g_{a\gamma\gamma} = 10^{-12}\,\text{GeV}^{-1}$, the resonant soliton in the left panel has a mass $M_s = 2.28 \cdot 10^{-12} \,M_{\odot}$ and radius $R_s \sim 18.5\,\text{km}$. The electromagnetic flux is normalized to its maximum value $F_{\gamma,\text{max}}$, which can be estimated from Fig. 5.17 and Ref. [31] to be of order $F_{\gamma,\text{max}} \sim 10^{30}\,\text{erg}\,\text{s}^{-1}\,\text{m}^{-2}$ at a distance of $d \approx 2.1\,r_0$.

Similarly, in the second case of a collapsing soliton with attractive self-interactions $\lambda \simeq -m_a^2/f_a^2$ and non-resonant mass $M_\star = M_{\star,\lambda} < M_{\star,\gamma}$ in the right panel of Fig. 5.18, the resulting emitted flux remains qualitatively similar to that of the $\lambda = 0$ soliton in Fig. 5.17 - apart from the shifted color scale of F_γ and ρ_γ . An important difference with respect to the $\lambda = 0$ simulation on the left is the fact that the rescaling for $\lambda \neq 0$ on the right is no longer universal, since v_0 in Eq. (A.5) is fixed by the self-interaction parameter λ^7 . Accordingly, the soliton parameters in the right panel of Fig. 5.18 are set to $M_s = 2.77 \cdot 10^{-7} \, M_\odot \approx M_{\star,\lambda}$, $f_a = 1.2 \cdot 10^{14} \, \text{GeV}$, $m_a = 5 \cdot 10^{-8} \, \text{eV}$, $\lambda = -m_a^2/f_a^2$ and $g_{a\gamma\gamma} = 2.79 \cdot 10^{-15} \, \text{GeV}^{-1}$. For QCD axion parameters, the luminosity of the collapsing soliton in Fig. 5.18 was reported to saturate around

$$L_{\gamma} = 2.1 \cdot 10^{40} \left(\frac{m_a}{50 \,\mu\text{eV}}\right)^{-3} \,\text{erg s}^{-1},$$
 (5.36)

⁷For the same reason, the two panels in Fig. 5.18 show different normalizations of the coordinates and electromagnetic flux, see Ref. [31].

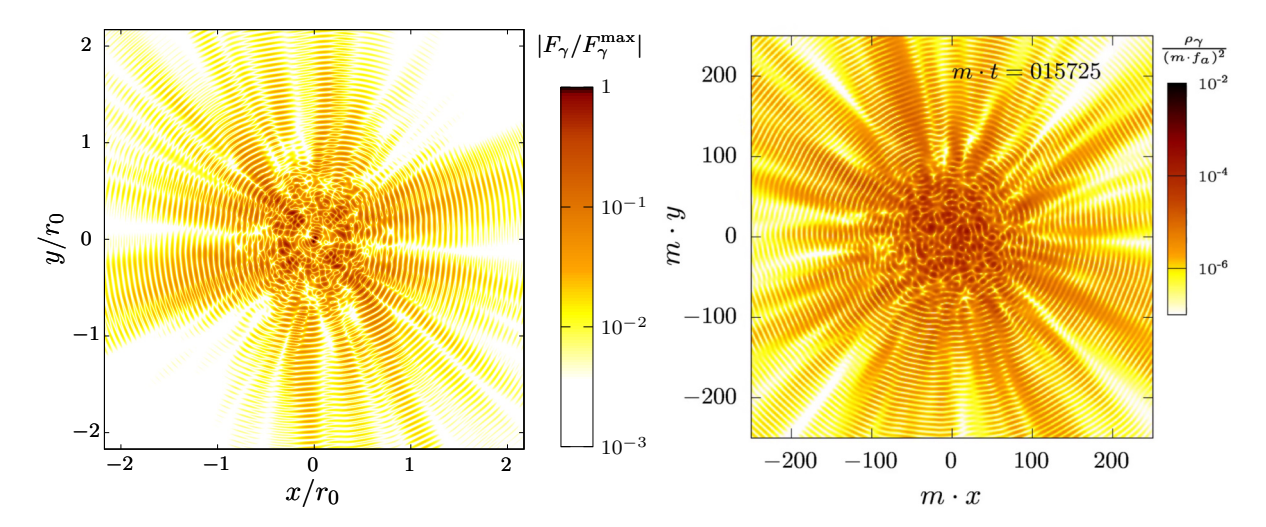


Figure 5.18: Left: Electromagnetic flux from a resonating SP soliton with mass $M_s=1.36\,M_{s,\gamma}$, radius $r_0=m_{\rm Pl}^2/(m_a^2M_s)$ [49], and for $\lambda=0$. For QCD axion values $m=m_a=50\,\mu{\rm eV},\,f_a=1.2\cdot 10^{11}\,{\rm GeV}$ with enhanced axion-photon coupling $g_{a\gamma\gamma}=10^{-12}\,{\rm GeV}^{-1}$, this corresponds to $M_s=2.28\cdot 10^{-12}\,M_\odot,\,R_s\sim 18.5\,{\rm km}$ and $F_{\gamma,{\rm max}}\sim 10^{30}\,{\rm erg\,s^{-1}\,m^{-2}}$ at $d\approx 2.1\,r_0$ (from $L_{\gamma,{\rm max}}$ in Fig. 5.17). Right: Electromagnetic flux from an off-resonant, collapsing unstable axion star with mass $M_\star=2.77\cdot 10^{-7}\,M_\odot\approx M_{\star,\lambda}$ and radius $R_\star=123\,{\rm km}$ for $\lambda\simeq -m_a^2/f_a^2$. Simulated for $f_a=1.2\cdot 10^{14}\,{\rm GeV},\,m_a=5\cdot 10^{-8}\,{\rm eV}$ and $g_{a\gamma\gamma}=2.79\cdot 10^{-15}\,{\rm GeV}^{-1}$, for which Eq. (5.36) predicts $L_\gamma\sim 10^{49}\,{\rm erg\,s^{-1}}$. Both taken from Ref. [31].

which indicates that both of the above photon conversion processes are potentially observable at $\mathcal{O}(Gpc)$ cosmological distances.

Fig. 5.18 also shows random fluctuations in the electromagnetic flux, which are caused by the spontaneous decay of axions into photons. In the simulations of Ref. [31], the quantum effects were implemented by means of randomly distributed classical waves with amplitudes set by the spontaneous decay of the soliton profile.

The important conclusion here is that the photon emission observed from the unstable axion star with $M_{\star} = M_{\star,\lambda}$ in the right panel of Fig. 5.18 occurs for a mass that lies below the resonance mass, $M_{\star} \lesssim M_{\star,\gamma}$. Equivalent results were recently confirmed in Ref. [258]. It should therefore be understood that the distinction between the relativistic axion emission from Sec. 4.4, Subsec. 5.4.1 and the parametric resonance in this section is not of physical nature. Instead, the occurrence of resonant radio emission from axion stars is expected to appear either in an isolated way for $M_{\star,\gamma} \leq M_{\star} \ll M_{\star,\lambda}$ or accompanied by the production and emission of relativistic axions for $M_{\star} \gtrsim M_{\star,\lambda}$ [253, 258] due to the self-interaction instability at $\lambda \neq 0$.

Summarizing the above two processes, we conclude that the parametric instability of resonant axion stars leads to short bursts of exponentially growing photon flux, which last until the soliton relaxes back to a sub-critical stage $M_{\star} < M_{\star,\gamma}$. The duration of these roughly isotropic radio bursts depends on the AS mass and photon coupling $g_{a\gamma\gamma}$ and was recently reported to be on the order of $\sim 0.1 \,\mathrm{s}$ in Ref. [258].

5.5.2 Abundance of parametrically resonant Axion Stars

In the previous section we have demonstrated the remarkable observational potential for the detectability of distant $\mathcal{O}(\text{Gpc})$ radio bursts from different resonant $M_{\star,\gamma}$ and collapsing $M_{\star,\lambda}$

axion stars. The next step is to estimate the galactic abundance of these signals from the mass distributions and encounter rates obtained from the ASMF considering both AS mergers and AS accretion.

Axion Star Mergers

We found in Fig. 5.15 that the rate of galactic minicluster mergers, which eventually lead to the formation of merged axion star cores with core-halo masses above the critical value $M_{\star,\lambda}$, is significant for n=1,3.34 and the \mathcal{M}_{J} -cutoff. Since the maximum stable AS mass due to self-interactions $M_{\star,\lambda}$ imposes an absolute upper limit on the existence of (stable) axion stars, the corresponding escape velocity cutoff $v_{\rm esc}(M_{\star,\lambda})$, which we applied for the bosenova rates in Subsec. 5.4.2, can also be seen as an optimistic estimate for the resonant merger rate with $v_{\rm esc}(M_{\star,\gamma}) \lesssim v_{\rm esc}(M_{\star,\lambda})$.

Therefore assuming that the two signal rates are qualitatively similar, we infer from Fig. 5.15 and Fig. 5.16 that between $\sim 1\,\mathrm{yr}^{-1}\,\mathrm{galaxy}^{-1}$ and $\sim 10^3\,\mathrm{yr}^{-1}\,\mathrm{galaxy}^{-1}$ events are predicted for $\alpha = -1/2$ and $\alpha = -0.7$ respectively. Analogous to the conclusion from Subsec. 5.4.1, the corresponding minicluster merger rates suggest that radio bursts from parametric resonance in merged solitons are sufficiently probable to be observed in our galaxy. Let us emphasize here, that this result remains true only for the range of axion-photon-couplings $g_{a\gamma\gamma}$, which are sufficiently strong for the decay mass in Eq. (4.61) to have $M_{\star,\gamma} \lesssim M_{\star,\lambda}$.

On the other hand for very weak axion-photon couplings $g_{a\gamma\gamma} \ll 10^{-17} \,\text{GeV}^{-1}$, we get $M_{\star,\gamma} \gg M_{\star,\lambda}$, which effectively prevents the parametric instability from occurring in most of the predicted mergers with $M_{\star,m} \sim M_{\star,\lambda}$ following Eq. (5.29). Note that this is also the case for most of the standard QCD axion models like the KSVZ and DFSZ axion models with $g_{a\gamma\gamma}$ and f_a fixed by Eq. (2.22) and Eq. (2.11) (see also the constraint plot in Fig. 5.19).

Axion Star Accretion

The same constraint remains true in the accretion scenarios of combined resonance and ongoing axion star mass growth, which we focus on in the following. Applying this scenario to the hypothetical ASMC population of the Milky Way has profound consequences due to two different aspects. First, we have assumed the core-halo relation from Eq. (3.57) to describe the virialized equilibrium state between the star and its host minicluster. As a direct consequence of this approach and for suitable couplings $g_{a\gamma\gamma}$, we predict a large number of stars residing in heavier miniclusters to have $M_{\star,\gamma}(g_{a\gamma\gamma}) \leq M_{\star} < M_{\star,\lambda}$. However these solitons are prevented from reaching a virialized state by the developing parametric instability and resulting mass-loss mechanism described in Subsec. 5.5.1 and Sec. 4.5.

The consequence in this scenario is an ASMC system that continuously (or repeatedly) feeds axion dark matter into its soliton core trying to reach an equilibrium state that is prohibited by the exponential decay into radio photons at $M_{\star} = M_{\star,\gamma}{}^{8}$. Similarly, in a second accretion scenario, the numerical simulations from Sec. 4.3 predict that the accretion from the host minicluster onto its axion star core continues even at late times [167, 174]. The recent semi-analytical study performed in Ref. [240] suggests that up to an order one fraction of the MC mass could

⁸One expects the axionic mass-loss due to exponential decay into photons to eventually overtake the moderate AS accretion from the MC background, soon after the resonance develops. The parametric instability then gets shut off but it can develop again after sufficient mass growth, see also Chap. 6 for details.

be absorbed by the soliton core over time. Incorporating these effects, of what we call long-time AS accretion, in composite ASMC systems leads to a continuous mass growth of the AS core until reaching either $M_{\star} = M_{\star,\gamma}$, $M_{\star} = M_{\star,\lambda}$ or $M_{\star} \simeq \mathcal{M}$. For both of these two mass growth mechanisms, a considerable fraction of the galactic axion dark matter can be converted into radio photons (and axions for $M_{\star,\lambda} \lesssim M_{\star,\gamma}$) in the narrow frequency band $f \approx m_a/(4\pi)$, where $\Delta f \sim 10^{-3} f$ is set by the galactic Doppler-shift.

It should therefore be clear, that the generic existence of galactic axion small-scale structure in KSVZ-like axion models m_a , n and its characteristic properties from Chap. 3, Chap. 4 can already be probed by existing radio telescopes. A study of the parametric resonance in accreting axion stars would require detailed estimations of the time- and mass-dependent evolution of the solitonic cores. It is therefore advisable to first infer preliminary estimates on the expected abundance and observational potential of such systems in our galaxy from the galactic ASMF in Subsec. 4.7.2, as will be done in the following.

We plot the parameter space in m_a and $g_{a\gamma\gamma}$ for which radio emission from parametric resonance can occur in the galactic ASMFs for different n in Fig. 5.19. Black background contours indicate

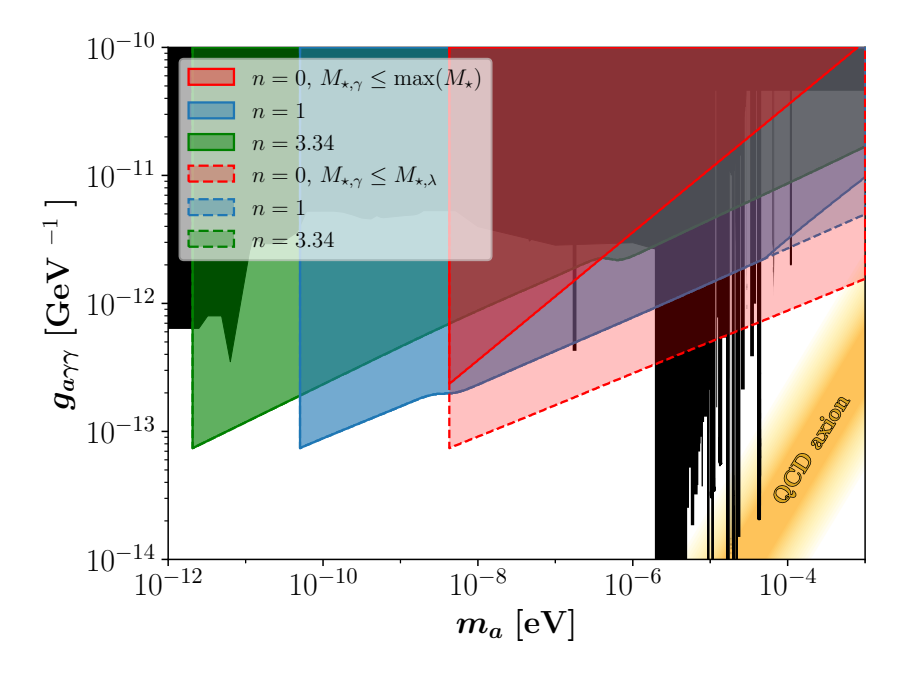


Figure 5.19: Solid colored lines and dark shades: Regions of parameter space with axion-photon coupling $g_{a\gamma\gamma}$ in GeV⁻¹ and axion mass m_a in eV, where the core-halo relation in Eq. (3.57) predicts the existence of photon-critical axion stars below the maximum AS mass in the ASMF, i.e. where $M_{\star,\gamma} \leq \max(M_{\star})|_{n,m_a}$. Dashed colored lines and light shades: axion-photon couplings, with $M_{\star,\gamma} \leq M_{\star,\lambda}$, where parametric resonance can occur before the self-interaction instability develops at $M_{\star,\lambda}$. This part of parameter space could be explored when including effects of AS accretion. Current parameter constraints are shown in black and the QCD axion band is indicated by the yellow-shaded region [262]. Taken from Ref. [1].

existing exclusions in the corresponding parameter space [262]. The dashed and solid lines in Fig. 5.19 indicate two different limitations: First in darker shades and solid lines, we plot the requirement that the present-day MCMF from the linear growth of miniclusters in Subsec. 3.6.2

predicts the existence of parametrically resonant axion stars, i.e.

$$M_{\star,\gamma}(m_a, n, g_{a\gamma\gamma}) \le \max(M_{\star})|_{m_a,n}, \tag{5.37}$$

$$\max(M_{\star}) = \min(M_{\star}(\mathcal{M}_{\max}), M_{\star \lambda}), \tag{5.38}$$

where $\max(M_{\star})$ indicates the maximum core mass in the ASMF from Fig. 4.14 for a given model m_a, n . The condition in Eq. (5.37) represents a more conservative approach since it only involves the linear growth MCMF and the core-halo relation from Eq. (3.57) to determine the soliton mass while neglecting both long-time AS accretion (see Fig. 4.6) and the previous core merger events. On a similar note, the second case in Fig. 5.19 shown by the light shades and dashed colored lines indicates the weaker constraint that

$$M_{\star,\gamma}(m_a, n, g_{a\gamma\gamma}) \le M_{\star,\lambda}(m_a, n), \tag{5.39}$$

which basically demonstrates where axion stars in models with m_a, n, f_a can experience parametric resonance before the self-interaction instability given by Eq. (4.16) starts to develop. The weaker condition in Eq. (5.39) is especially relevant when including the effects of long-time accretion from the minicluster onto its AS core, similar to what was suggested in Ref. [240]. Most importantly, the accreting solitons could eventually absorb an order one fraction of the mass of their host MCs - unless prevented by the critical masses $M_{\star,\gamma}$ and $M_{\star,\lambda}$. As a consequence, the expected mass range of the galactic population of parametrically resonant axion stars could be significantly boosted compared to the linear growth predictions from Subsec. 3.6.2 and Subsec. 4.7.2. In this late-time accretion scenario, every ASMC system with

$$\mathcal{M} \gtrsim M_{\star,\gamma} \gtrsim M_{\star,\lambda}$$
 (5.40)

could potentially serve as a site of radio conversion. We emphasize that in this case, the latetime equilibrium state between the AS core and its host minicluster has become fundamentally different from the canonical core-halo relation in Eq. (3.57). Recalling the core-halo scaling of $M_{\star} \propto \mathcal{M}^{1/3}$ in Eq. (3.57), the condition in Eq. (5.40) is therefore equivalent to a modified core-halo scaling more similar to $M_{\star} \sim \mathcal{M}$.

With the three aforementioned resonance conditions describing different predictions from the literature, we are now in a position to estimate the abundance of the corresponding radio bursts. In order to quantify the predicted number of potentially resonant axion star cores in our galaxy, we can use the integration method from Eq. (4.76) together with the conservative resonance condition in Eq. (5.37) and the optimistic prediction Eq. (5.40) due to long-time accretion. We denote the resulting number of resonant ASMC systems for which the ASMF obeys Eq. (5.37) $\mathcal{N}_{\gamma,\text{tot}}$ and plot the result for different models m_a , n at the representative value of $g_{a\gamma\gamma} = 10^{-11} \text{ GeV}$ in Fig. 5.20.

The solid lines in Fig. 5.20 show our results using the canonical core-halo relation with $M_{\star} \propto \mathcal{M}^{1/3}$, which correspond to Eq. (5.37) and solid lines in Fig. 5.19. The dashed lines on the other hand indicate the results from the more optimistic second accretion scenario from Ref. [240] with $M_{\star} \sim \mathcal{M}$, which implies Eq. (5.40) and hence larger numbers of resonant ASMC systems, as seen in Fig. 5.20. For the conservative case $M_{\star} \propto \mathcal{M}^{1/3}$, $\mathcal{N}_{\gamma,\text{tot}}$ quickly drops to zero at the point where $\max(M_{\star})|_{n,m_a} = M_{\star,\gamma}$. The detailed shape of the curves depends on the temperature-dependence n of the axion mass and on the interplay of the different cutoffs of the ASMF in Fig. 4.13 with the decay mass $M_{\star,\gamma}$.

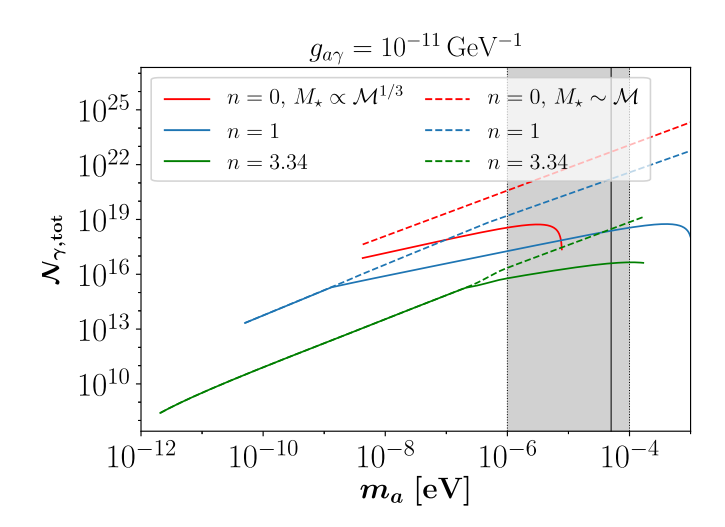


Figure 5.20: Total number of resonant ASMC systems in the Milky Way for which Eq. (5.37) holds. Shown for different axion models m_a, n with MCMF slope $\alpha = -1/2$, for an axion-photon coupling $g_{a\gamma\gamma} = 10^{-11}$ GeV and using the \mathcal{M}_0 -cutoff of the MCMF, but with different core mass relations. Solid lines show M_{\star} given by the core-halo relation in Eq. (3.57) with $M_{\star} \propto \mathcal{M}^{1/3}$, while dashed colored lines assume $M_{\star} \sim \mathcal{M}$ as suggested in Ref. [240]. Taken from Ref. [1].

Conversely, in the case $M_{\star} \sim \mathcal{M}$ in dashed lines, the number of resonant systems only vanishes at significantly larger axion masses m_a , when $M_{\star,\gamma} \geq M_{\star,\lambda}$ again depending on the temperature index n. The crucial observation for both of the discussed scenarios is the prediction of very large numbers $10^9 \lesssim \mathcal{N}_{\gamma,\text{tot}} \lesssim 10^{25}$ of potentially resonant ASMC systems in the Milky Way. Due to the resonant nature of the emission process in Subsec. 5.5.1, the diffuse radio background signal emanating from these highly abundant objects should be peaked around a narrow frequency range centered around $f \approx m_a/(4\pi)$.

We conclude that there is a significant potential in exploiting the combined effects of axion star accretion and parametric resonance in the context of galactic ASMC systems. Let us emphasize again that the occurrence of radio bursts from resonant axion stars in a given model $m_a, n, g_{a\gamma\gamma}$ is essentially limited to the color-shaded regions in Fig. 5.19, where $M_{\star,\gamma} \leq M_{\star,\lambda}$. Similar limitations are expected for the case of collapsing unstable axion stars shown in the right panel of Fig. 5.18, since the parametric instability is unlikely to be triggered far away from the resonance, i.e. for $M_{\star,\gamma} \gg M_{\star,\lambda}$.

5.6 Cosmological Event Rates

The last consideration to be inferred from the galactic ASMF and the combined signal rates from previous sections is related to extra-galactic axion small-scale structure. While the clear focus of this work lies on the analysis of different signatures from galactic ASMC systems, it is helpful to also evaluate the detectability of the resulting signals in the context of nearby galaxies. The considerations from this section will not be investigated further in this work, but should rather be seen as an estimate of the broader and cosmological scope of our results. We therefore constrain our analysis to order of magnitude estimates and leave a more detailed calculation to future research.

Throughout our estimations, we will assume other galaxies to exhibit a similar dark matter abundance, NFW halo profile and neutron star distribution from Sec. A.7. This allows us to translate the galactic signal rates from Eq. (5.2) and Eq. (5.8) onto the cosmological distribution of Milky-Way-like galaxies. For the latter, we assume a galaxy density of $n_{\rm gal} \sim 10^{-2} \,\mathrm{Mpc^{-3}}$ [263] to estimate the isotropic emission from extra-galactic AS/MC-NS and MC-MC collisions. Neglecting redshift defects, we define the *duty cycle*

$$\mathcal{D} \sim \gamma_s \frac{4\pi}{3} d_{\text{obs}}^3 t_s \,, \quad \gamma_s = n_{gal} \Gamma_s \,, \tag{5.41}$$

where the extra-galactic signal rate $\gamma_s = n_{gal}\Gamma_s$ in units of s⁻¹Mpc⁻³ is given in terms of the galactic signal rates Γ_s . Here, the typical observation distance is taken to be $d_{\rm obs} = 2\,{\rm Gpc}$, and the signal duration t_s depends on the specific encounter under consideration. The corresponding duty cycle within a beam size $\Delta\Omega$ of a given radio telescope is then simply given by $\mathcal{D}\Delta\Omega/(4\pi)$. For a typical beam size of order $\sim 1^{\circ}$ one has $\Delta\Omega/(4\pi) \simeq 3 \cdot 10^{-4}\,{\rm sr}$.

In the following, we require the duty cycle per beam $\mathcal{D}\Delta\Omega/(4\pi)$ to not be much smaller than one in order to have individual events, which are sufficiently frequent to be detectable with typical radio telescopes and accessible observation times. A rough estimate for the observed spectral flux of a single event with total emitted energy E_s and at cosmological distance $d_{\rm obs}$ is given by

$$j_s \sim \frac{E_s}{4\pi d_{\text{obs}}^2 \Delta f t_s} \simeq 10^{-13} \,\text{Jy} \left(\frac{E_s}{10^{42} \,\text{eV}}\right) \left(\frac{m_a}{50 \,\mu\text{eV}}\right)^{-1} \left(\frac{t_s}{50 \,\text{s}}\right)^{-1} \left(\frac{d_{\text{obs}}}{2 \,\text{Gpc}}\right)^{-2},$$
 (5.42)

where we assume the bandwidth $\Delta f \simeq 10^{-3} m_a$ from the galactic velocity dispersion. The next step is to enter the signal rates Γ_s based on the results from Subsec. 5.2.2 to Subsec. 5.5.2 for a QCD axion mass $m_a = 50 \,\mu\text{eV}$ combined with E_s , t_s from the single event signals in Subsec. 5.2.1 to Subsec. 5.5.1.

NS-AS Collisions

Starting with the AS-NS collisions from Fig. 5.5, we get $\gamma_s \sim 10^{-16}\,\mathrm{Mpc^{-3}s^{-1}}$ for the \mathcal{M}_J -cutoff and an MCMF slope index of $\alpha = -1/2$. The duration t_s can be inferred from the results in Fig. 5.2 by considering the signal from an AS-NS transient event with non-zero impact parameter $b = 10^3\,\mathrm{km}$. The resulting signal duration $t_s \sim 50\,\mathrm{s}$ leads to a duty cycle of roughly $\mathcal{D} \simeq 2 \cdot 10^{-4} \ll 1$. Using the same event with $b = 10^3\,\mathrm{km}$ in Fig. 5.2, we obtain the total emitted energy $E_s \sim 4\pi\,\mathrm{kpc}^2 t_s \Delta f_T \, S_T \sim 10^{42}\,\mathrm{eV}$ from the flux density $S_T \sim 10^5\,\mathrm{mJy}$ at a distance of 1 kpc. This yields an observed flux of $j_s \simeq 10^{-13}\,\mathrm{Jy}$ at $d_{\mathrm{obs}} = 2\,\mathrm{Gpc}$ in Eq. (5.42), which lies way below the sensitivity of current radio telescopes.

NS-MC Collisions

For the more common NS-MC collisions we predicted larger signal rates $\gamma_s \sim 10^{-12}\,\mathrm{Mpc^{-3}s^{-1}}$ in Fig. 5.9 for the \mathcal{M}_J -cutoff with $\alpha=-0.7$. From Fig. 5.6 and for an impact parameter of $b=10^8\,\mathrm{km}$, we find $t_s\sim 150\,\mathrm{d}$, which leads to a much larger duty cycle $\mathcal{D}\simeq 4\cdot 10^5\gg 1$ compared to the previous NS-AS case. To further estimate the observed flux density of a single NS-MC collision according to Eq. (5.42), we consult the differential fluxes from Fig. 5.6 and find that $E_s\sim 4\pi\,\mathrm{kpc}^2t_s\Delta f_T\,S_T\sim 10^{37}\,\mathrm{eV}$ from $S_T\sim 10^{-6}\,\mathrm{mJy}$ at 1 kpc distance, which yields an

essentially undetectable signal with $j_s \simeq 4 \cdot 10^{-24} \,\mathrm{Jy}$.

This result is expected since the spectral flux in Eq. (5.42) scales inversely with the signal duration t_s and linearly with S_T . The signal duration in return scales with the velocity and size of the minicluster. A consideration of the densest miniclusters with $\Phi \sim 10^4$ would therefore have advantageous effects due to both the reduced size \mathcal{R} in Eq. (3.24) and the increased central density $\rho_{\rm mc}$ in Eq. (3.23). Tracing the scalings $\mathcal{R} \propto \Phi^{4/3}$ and $\rho_{\rm mc} \propto \Phi^4$ for $\Phi \sim 10^4$ and assuming that the NS conversion rate scales linearly with the MC density, $S_T \propto \rho_{\rm mc}$, one obtains a potential boost of order $\sim 10^{21}$ for the densest miniclusters. The substantial benefit does however come at the cost of a drastically reduced collision rate, which renders such signals too rare to be searched for.

Parametric Resonance and MC-MC Merger

The last and most relevant scenario in the cosmological context is the occurrence of parametric resonance in AS core mergers following a successful minicluster merger - as was calculated in Subsec. 5.4.2 for bosenovae. For sufficiently large axion-photon coupling $g_{a\gamma\gamma}$ and $M_{\star,\gamma} \lesssim M_{\star,\lambda}$, one expects a strong radio emission following a host minicluster merger. An important detail to this scenario is the question how long it takes for the axion star cores to merge after their host miniclusters have merged. For the preliminary considerations of this section, we can estimate the typical time between two MC mergers with final mass $\mathcal{M}_1 + \mathcal{M}_2 \geq \mathcal{M}(M_{\star,\lambda})$ by dividing the corresponding rate $\Gamma_{\rm mc-mc}/N_{\star,\rm tot} \sim 10^3\,{\rm yr}^{-1}/10^{23}$ from Fig. 5.16 by the total number of MCs for $m_a = 50\,\mu{\rm eV}$, n = 3.34, $\alpha = -0.7$ in Fig. C.1, which gives $t_{\rm merg} \sim 10^{20}\,{\rm yr}$. This time should be compared to the intrinsic timescale of the ASMC system.

Note that the condensation time from Eq. (4.26), which measures the required time for soliton formation starting from random initial conditions, does not apply here since the merged host minicluster provides a distinct potential minimum for the merging AS cores. Instead we use the free-fall time of the merged miniclusters as an estimate for the timescale of the AS core merger, which gives

$$\tau_{\rm ff} = \frac{\pi \mathcal{R}^{3/2}}{4\sqrt{G\mathcal{M}(M_{\star,\lambda})}} \simeq 0.2 \,\text{yrs} \tag{5.43}$$

for QCD axion structures with $\mathcal{M}(M_{\star,\lambda}) \simeq 4 \cdot 10^{-7} \, M_{\odot}$ and $\mathcal{R} \simeq 2 \cdot 10^9 \, \mathrm{km}$ from Eq. (3.24). With the timescale of MC merger interactions $t_{\mathrm{merg}} \sim 10^{20} \, \mathrm{yr}$ being much larger than the free-fall time in Eq. (5.43), we can assume AS mergers to happen quasi-instantaneously in the following. The resulting energy emitted in a single radio burst can be estimated from the saturated axion star luminosity in Eq. (5.36) assuming a burst duration of $t_s = 0.1 \, \mathrm{s}$ as reported in Ref. [258] for $m_a \approx \mu \mathrm{eV}$. Thus expressing

$$j_s \sim \frac{L}{4\pi d_{\rm obs}^2 \Delta f} \simeq 400 \,\text{Jy} \left(\frac{L}{10^{42} \,\text{erg s}^{-1}}\right) \left(\frac{m_a}{\mu \text{eV}}\right)^{-4} \left(\frac{d_{\rm obs}}{2 \,\text{Gpc}}\right)^{-2}$$
 (5.44)

we find a significant spectral flux for $m_a = \mu \, \text{eV}$, which corresponds to $j_s \sim 0.1 \, \text{mJy sr}^{-1}$ for the QCD axion mass $m_a = 50 \, \mu \text{eV}$ with undetermined signal duration t_s . Combining the above numbers with $\gamma_s \sim 10^{-6} \, \text{Mpc}^{-3} \text{s}^{-1}$ from Fig. 5.16 for the \mathcal{M}_J -cutoff with $\alpha = -0.7$, Eq. (5.42) also yields a considerable duty cycle of $\mathcal{D} \simeq 3 \cdot 10^4$. For a beam size of $\simeq 1^{\circ}$ with $\Delta\Omega/(4\pi) \simeq$

 $3\cdot 10^{-4}$, the beam duty cycle is of order unity for the resonant MC mergers in Eq. (5.41). This means that within one beam we would expect a popcorn like signal that should be easy to distinguish from backgrounds as long as the time integrated intensity is above the sensitivity of the radio telescope considered. Note however that our above considerations predict narrow line signals with $\Delta f \simeq 10^{-3} m_a$, for which the frequency gets redshifted depending on $d_{\rm obs}$.

As an estimate, we compare the expected flux density $j_s \simeq 400\,\mathrm{Jy\,sr^{-1}}$ from Eq. (5.42) to the SKA-mid sensitivity $S \sim 10\,\mu\mathrm{Jy\,hr^{-1/2}}$ [191], which, integrated over a signal duration of $t_s = 0.1\,\mathrm{s}$ [264], gives $S \sim 2\,\mathrm{mJy}\,(0.1\,\mathrm{s/t_s})^{1/2}$. This is significantly smaller than the estimate in Eq. (5.44) for the resonant AS flux density at cosmological distances. Parametric resonance in AS core mergers therefore provides the most compelling detection mechanism in the context of extra-galactic background signals from axion small-scale structure. A particularly interesting feature of the predicted flux density in Eq. (5.44) is the strong dependence on m_a , which greatly enhances the detectability for low-mass QCD axions due to the luminosity scaling from Eq. (5.36) and Ref. [31]. We also note that a similar study involving soliton merger rates of cosmological dark matter halos with collapse redshifts $z_c \gtrsim 10$ was already performed in Ref. [34].

5.7 Implications for Axion Searches

Throughout this chapter, we have used the ASMF from Subsec. 4.7.2 to improve previous estimates on the galactic abundance and detectability of the three most anticipated AS signatures from Chap. 4: Neutron star collisions, bosenovae and radio bursts from resonating axion stars. The evaluation of the resulting signal rates paves the way for a more detailed analysis of what turns out to be the most promising axion star signatures. An improved analysis will be performed separately in the remainder of this thesis in Chap. 6 and Chap. 7. As for this section, we summarize our results for the different event rates obtained in Sec. 5.1 to Sec. 5.6 and deduce the most important implications for galactic axion searches, which aim to exploit the properties of axion small-scale structure. The following considerations thus provide a potential guideline for future and possibly more detailed research efforts.

We start with the case of resonant axion-photon conversion in the neutron star magnetosphere, which received significant attention in the recent literature [134, 135, 137, 141, 188]. While previous work on the radio flux [134] and encounter rates of NS-MC/AS transient events [135, 137, 188] determined the potential detectability of the resulting radio signals in our galaxy to be significant, our results indicate the opposite. This conclusion is first related to the fact that we assumed the population of galactic axion stars to be gravitationally bound in miniclusters, which significantly constrains their relative dark matter abundance $f_{\star} \ll 1$ in Fig. 4.16. Secondly and more importantly, the signal rates of both suitable NS-AS encounters in Fig. 5.5 and of the more probable NS-MC encounters in Fig. 5.8, Fig. 5.9 are greatly reduced by the suppression factor $f_{NS}(m_a)$ in Fig. 5.4, which accounts for the resonance condition $\omega_p \gtrsim m_a$ of the NS magnetic field. This leads to an essentially undetectable signal abundance $\Gamma_{\text{mc-NS}} \lesssim 10^{-3} \, \text{yr}^{-1}$ galaxy⁻¹ for QCD axion parameters. The strong suppression indicates that a majority of the $N_{NS} = 10^9$ galactic neutron stars assumed in this chapter are either inactive or expected to have incompatibly weak magnetic fields due to Ohmic dissipation.

We note that the first of the two previous points of small AS abundance f_{\star} may be modified in the case of enhanced axion star formation, which was suggested in Ref. [236]. Apart from

this exception, we conclude that neutron star encounters are found to be unlikely to become observable in current radio telescopes - independent of the axion model m_a , n and MCMF slope α .

In the context of bosenovae on the other hand, our results for n=3.34 in Fig. 5.15 and Fig. 5.16 suggest that MC-MC mergers can appear as often as $\sim 10\,\mathrm{yr^{-1}}$ galaxy⁻¹ for $\alpha=-1/2$ and $\sim 10^3\,\mathrm{yr^{-1}}$ galaxy⁻¹ for $\alpha=-0.7$, using the \mathcal{M}_J -cutoff. This prediction has important consequences for the future detection of AS signatures from both parametric resonance and bosenovae triggered by AS core mergers [33, 253, 264, 265] following a MC merger. A particularly important observation is the fact that this prediction remains true also for the well-motivated QCD axion with n=3.34 and $m_a=50\,\mu\text{eV}$. Conversely for the \mathcal{M}_0 -cutoff, the total number of galactic miniclusters in Fig. C.1 is significantly lower, which is why AS core mergers can not be efficiently triggered by MC collisions using this cutoff. A better understanding of the evolution of the low-mass component $\mathcal{M} < \mathcal{M}_0$ of the MCMF in Subsec. 3.5.2 is therefore crucial in improving our predictions for the detectability of AS core mergers. We also emphasize that the \mathcal{M}_0 -cutoff does not exclude the occurrence of radio/axion bursts in general since the long-time effects of ongoing accretion are expected to play a vital role in the AS evolution.

The same realization led us to develop a new emission mechanism for resonant ASMC systems with $M_{\star,\gamma} \lesssim M_{\star} \lesssim M_{\star,\lambda}$, for which the ASMF from Subsec. 4.7.2 predicts a considerable abundance in Fig. 5.20 - depending on the axion-photon coupling $g_{a\gamma\gamma}$. For these systems, we expect a continuous mass growth of the axion star core from two basic mechanisms: First the system with $\mathcal{M} > \mathcal{M}(M_{\star,\gamma})$ tries to reach a virialized state given by the (inverted) core-halo relation in Eq. (3.57) leading to an effective mass increase of M_{\star} . Similarly, in the second case, the AS core is expected to continuously accrete axion dark matter from the minicluster background as observed in Fig. 4.3, Fig. 4.7 and Ref.s [167, 170, 174, 240]. In both of the above scenarios, the total ASMC system continues to drive its solitonic core into instability at $M_{\star} = M_{\star,\gamma}$ due to parametric resonance or at $M_{\star} = M_{\star,\lambda}$ due to self-interactions - depending on $g_{a\gamma\gamma}$ and Eq. (4.61).

This has grave consequences for the observability of both radio bursts and bosenovae: The corresponding super-critical systems will not only reach the point of instability once, but repeatedly. In this case, a considerable fraction of the dark matter is contained in miniclusters, which drive their AS cores to become unstable, converting an order-one fraction of their mass M_{\star} into either photons or relativistic particles and repeat the process at a later time depending on the rate of AS accretion. The combined accretion scenario thus carries extensive observational potential, which motivates us to dedicate the remaining two chapters to a more careful investigation of AS mas growth and its consequences for radio signatures in Chap. 6 and for axion bursts in Chap. 7.

Lastly in Sec. 5.6, we have briefly discussed the potential of extra-galactic NS-AS/MC encounters and minicluster mergers with a parametrically resonant AS core. Our rough estimates suggest that NS-AS/MC signals are too faint for individual detection but that the extra-galactic radio bursts from resonant AS mergers can have large spectral fluxes of ~ 0.5 Jy even at cosmological distances of $d_{\rm obs} \simeq 2\,{\rm Gpc}$. The corresponding duty cycle can reach order-one values within a typical radio telescope beam with degree-scale opening angle suggesting potential observability of such events.

Radio Lines from Axion Stars

The evaluation of the different signal rates from Chap. 5 and their implications for the detection of axion dark matter from Sec. 5.7 motivate us to develop a combined framework of AS accretion and parametric resonance in the following. An analogous framework will be used in Chap. 7 to analyze the detectability of galactic axion bursts from the self-interaction instability, which develops at $M_{\star,\lambda}$. In this chapter, we start with the case of galactic radio line emission from resonant axion stars with $M_{\star} \geq M_{\star,\gamma}$ from Sec. 4.5 and Sec. 5.5, since the resulting background emission can be probed by existing radio telescopes. The contents of this chapter are taken from Ref. [2].

As was already mentioned in Sec. 5.7, the calculation of the background signal from the galactic population of accreting solitons with $M_{\star} \geq M_{\star,\gamma}$ requires us to employ detailed mass growth models for the AS cores. To do this, we introduce two different accretion models for composite ASMC systems: First the external minicluster accretion model in Sec. 6.2, which involves the capturing of axion dark matter from the galactic NFW background of the Milky Way and secondly the internal MC accretion model in Sec. 6.3, which utilizes the self-similar attractor solution from Eq. (4.41). For both of these models, we estimate the resulting background photon flux from resonant ASMC systems and compare it to galactic radio backgrounds in Subsec. 6.4.1. This allows us to demonstrate the possible constraints on the axion-photon coupling $g_{a\gamma\gamma}$, which can be inferred through future radio observations, in Sec.s 6.5 and 6.5.

Similar to the previous chapters, we assume at most a single axion star core to be embedded in each minicluster, where (unless stated otherwise) the mass relationship between core- and total system mass is given by the $z_{\rm eq}$ core-halo relation in Eq. (3.57). Opposed to Chap. 5, we constrain our analysis of accreting systems in Chap. 6 and Chap. 7 to the \mathcal{M}_0 -cutoff from Eq. (3.47) with an MCMF slope $\alpha = -1/2$, since the relevant ASMC population with coremasses $M_{\star} \sim M_{\star,\gamma}$ and $M_{\star} \sim M_{\star,\lambda}$ is mostly independent of the low-mass component with $\mathcal{M} < \mathcal{M}_0$. We extend our analysis of the MCMF by additionally scanning through the (\mathcal{M} -independent) parameter range $\Phi \in (0, 10^4]$ of the initial MC overdensity from Sec. 3.2 and where Φ follows the distribution from Fig. 3.1. The resulting ASMF cutoffs constraining the existence of resonant ASMC systems in this approach are summarized in Sec. 6.1.

For the expected radio signals of the resonant AS cores, we assume a conversion efficiency of order-one between the mass excess $\delta M_{\star} = M_{\star} - M_{\star,\gamma}$ at $M_{\star} \geq M_{\star,\gamma}$ and the energy of the emitted photons with resonance frequency $f = m_a/(4\pi)$ of half the axion mass. Although the single event luminosity is expected to modulate significantly over observation timescales as shown in Fig. 5.17, we employ an averaged approach by assuming a constant emission rate, which is proportional to the accreted mass excess δM_{\star} . The validity of the averaged radio emission of the total resonant AS population is essentially ensured by the large number of resonating systems, e.g. $\mathcal{N}_{\gamma,\mathrm{tot}} \gtrsim 10^9$ for $g_{a\gamma\gamma} = 10^{-11}\,\mathrm{GeV}^{-1}$ in Fig. 5.20.

6.1 Mass Distribution of resonant Systems

We start by specifying the fundamental approach with which we determine the galactic abundance of resonating ASMC systems from the MCMF of the Milky Way in Subsec. 3.6.2. For this, we essentially follow the low-mass cutoff $M_{\star, \min}$ of the ASMF in Eq. (6.1), but with the definition $\mathcal{M}_{\min} = \mathcal{M}_{0,\min}$ specifically. An important distinction to previous considerations is the fact that we vary Φ alongside \mathcal{M} , which implies that the radius cutoff mass from Eq. (4.70) is promoted to Φ -dependent quantity $\mathcal{M}_{R,\min}(\Phi)$. Tracing the scaling $\mathcal{M}_{R,\min}(\Phi) \propto \Phi^2$ for large $\Phi \gg 1$, it can be seen that the radius cutoff becomes especially important for the densest miniclusters in the population, see also Fig. 4.13. The effective low-mass cutoff at $\mathcal{M}_{\min} = \mathcal{M}_{0,\min}$ takes the form

$$\mathcal{M}_{\star,\min}(\Phi) = \max[\mathcal{M}_{0,\min}, \mathcal{M}_{h,\min}, \mathcal{M}_{R,\min}(\Phi)], \qquad (6.1)$$

where we highlight the dependence on Φ , which we discuss at the end of this section. Another obvious constraint on the resonant ASMC population is provided by the $g_{a\gamma\gamma}$ -dependent decay mass from Eq. (4.61). Combining this with the high-mass ASMF cutoff due to the existence of the maximum stable AS mass $M_{\star,\lambda}$ from Eq. (4.16), we obtain the effective low- and high-mass cutoffs

$$\mathcal{M}_{\gamma,\min}(g_{a\gamma\gamma}, \Phi) = \max[\mathcal{M}_{\gamma}(g_{a\gamma\gamma}), \mathcal{M}_{\star,\min}(\Phi)],$$
 (6.2)

$$\mathcal{M}_{\gamma,\text{max}} = \min[\mathcal{M}(M_{\star,\lambda}), \mathcal{M}_{\text{max}}]$$
 (6.3)

of the resonating ASMC population, where $\mathcal{M}_{\gamma} = \mathcal{M}(M_{\star,\gamma})$ is expressed using the inverted corehalo relation. Examples for the $\Phi = 1$ case of this population were already shown in Fig. 5.20. An important question for the understanding of the resonant ASMC population relates to the hierarchy of the different low-mass cutoffs in Eq. (6.2).

It was already mentioned that the $\propto \Phi^2$ -scaling of the radius cutoff $\mathcal{M}_{R,\text{min}}$ from Eq. (4.70) at large Φ makes it the dominant low-mass cutoff for $\mathcal{M}_{\star,\text{min}}$ in Eq. (6.1). As seen by the blue and dashed lines of the ASMF cutoff comparison in Fig. 4.13, the takeover in Φ , for which $\mathcal{M}_{\star,\text{min}}(\Phi) > \mathcal{M}_{0,\text{min}}$, is generally model-dependent¹. Additional axion model-dependence arises from the scaling of \mathcal{M}_{γ} and $\mathcal{M}_{\star,\gamma}$ from Eq. (4.61) with the axion-photon coupling $g_{a\gamma\gamma}$. Putting the above relations together, the relevant hierarchy in Eq. (6.2) is governed by the interplay between $\mathcal{M}_0(n)$, $\mathcal{M}_{R,\text{min}}(\Phi)$ and $\mathcal{M}_{\gamma}(g_{a\gamma\gamma})$, where only the dependence on the most relevant parameters is indicated. We performed a qualitative analysis of the different scalings and briefly summarize our findings in the following.

For very weak axion-photon couplings $g_{a\gamma\gamma} \lesssim 10^{-14} \,\mathrm{GeV}^{-1}$, the decay MC mass \mathcal{M}_{γ} takes over as the dominant cutoff, which combined with the maximum stable AS mass $M_{\star,\lambda}$ prevents the existence of resonant systems altogether. At larger values of $g_{a\gamma\gamma}$ and for moderate overdensities $\Phi \lesssim 10$, $\mathcal{M}_{0,\mathrm{min}}$ becomes the most relevant. The densest miniclusters with $\Phi \gtrsim 10^3$ on the other hand are strongly constrained by the radius cutoff $\mathcal{M}_{R,\mathrm{min}}(\Phi)$ and their suppressed abundance from the probability distribution $p_{\Phi}(\Phi)$ in Eq. (3.27). We checked the impact of the $\mathcal{M}_{R,\mathrm{min}}$ -cutoff and found that it does not affect our qualitative predictions, since the major contribution to the radio emission is given by ASMC systems with Φ in the intermediate density range

¹More specifically and for the \mathcal{M}_0 -cutoff, it depends mainly on the temperature index n, since all low-mass cutoffs scale roughly as $\mathcal{M}_{i,\min} \propto m_a^{-3/2}$ [58].

 $1 \lesssim \Phi \lesssim 100$.

We also mention for completeness that we neglect contributions from parameter regions Φ , \mathcal{M} , $g_{a\gamma\gamma}$, where $\mathcal{M}_{\gamma} < \mathcal{M}_{\star,\text{min}}$ since the long-term stability of such systems is questionable. Conveniently, the large values of $g_{a\gamma\gamma}$, where the above detail becomes relevant, are already excluded by helioscopes and other observations [118].

Summarizing the above considerations, the number of resonant ASMC systems in the Milky Way can be calculated from the galactic MCMF according to the relation

$$\mathcal{N}_{\gamma,\text{tot}} = 4\pi \int_{R_{\text{surv}}}^{R_{200}} dr \, r^2 \int_0^{10^4} d\Phi \, p_{\Phi}(\Phi) \mathcal{P}_{\text{surv}}(\Phi) \int_{\mathcal{M}_{\gamma,\text{min}}(\Phi)}^{\mathcal{M}_{\gamma,\text{max}}} d\mathcal{M} \, \frac{dn}{d\mathcal{M}}(r)$$
(6.4)

for $\alpha = -1/2$, $\mathcal{M}_{\min} = \mathcal{M}_{0,\min}$ and where the Milky Way volume in Eq. (3.53) is absorbed in the spatial integral over the galactocentric radius r. Note that here, the renormalization constant $C_n(r)$ was promoted to a function of r set by the NFW profile of the dark matter halo. The boundaries of the spatial integral are given by the minicluster survival cutoff due to stellar disruption from Eq. (3.54) and the radius R_{200} of the DM halo. Another survival probability is contained in the Φ -integral, which follows the distribution from Eq. (3.27) and the minicluster survival probability $\mathcal{P}_{\text{surv}}(\Phi)$ at $r = R_{\odot}$ from Eq. (3.56) and Ref. [196].

With the galactic abundance of parametrically resonant ASMC systems being prescribed by Eq. (6.4), the next step in determining the background signal is to infer the signal strength of the individual resonant systems. This will be done by introducing different accretion models in the next two sections.

6.2 External Minicluster Accretion Model

We start with the external minicluster accretion model - sometimes referred to as 'external accretion' - in this section. As the name suggests, the source of the accreted core mass growth in this scenario is external with respect to the total ASMC system. The fundamental assumption that motivates the development of this non-isolated model is related to the simulated abundance $f_{\rm mc}=0.75$ of axion dark matter in gravitationally bound structures like miniclusters [29, 30]. Translating the above MC dark matter abundance to the NFW halo of the Milky Way, one expects a background dark matter field with mass density

$$\rho_{a,f}(r) = (1 - f_{\text{mc}}) \,\rho_{\text{NFW}}(r) = 0.25 \,\rho_{\text{NFW}}(r) \tag{6.5}$$

to be present in our galaxy, next to the NFW-distributed minicluster population. Physically, such a background field can be provided by tidal streams from disrupted minicluster remnants [42, 149, 150] or by 'free-streaming' axions within the dark matter halo.

As a consequence, galactic miniclusters with typical velocities $v_{\rm mc} \sim v_{\rm vir} \sim 100\,{\rm km\,s^{-1}}$ are expected to encounter and potentially capture a fraction of the background axions over time. Note here that in this approach, we neglect MC-MC encounters for simplicity, since the resulting collision dynamics and effective mass growth or loss depend sensitively on the combination of parameters $\mathcal{M}_1, \Phi_1, \mathcal{M}_2, \Phi_2$ of the binary system.

We lay out the resulting accretion scenario involving gravitationally bound miniclusters and background DM particles in the schematic representation in Fig. 6.1. In this figure, the host minicluster and its density are indicated by the blue spherical shades, where the dense, yellow

AS core is embedded in its center. This composite ASMC systems moves through the galactic DM halo and encounters axions from the background field $\rho_{a,f}(r)$ in Eq. (6.5), shown by the black dashed arrows. Depending on the minicluster size \mathcal{R} , mass \mathcal{M} and density Φ , a mass

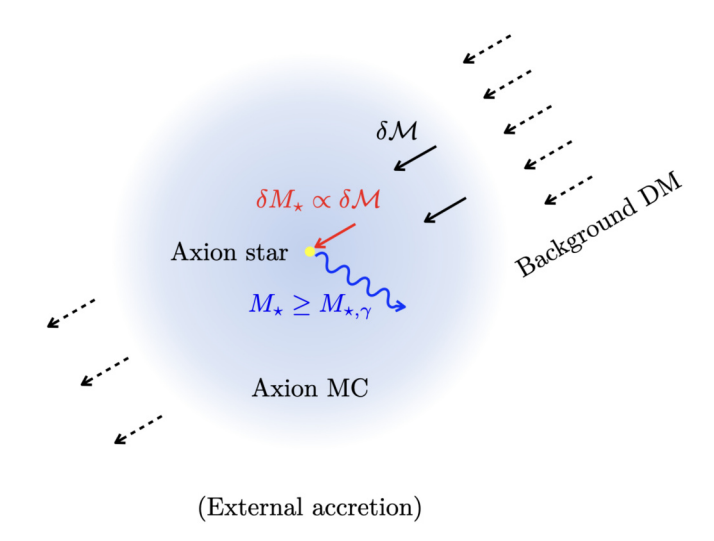


Figure 6.1: Schematic representation of the external minicluster accretion model for axion star cores, taken from Ref. [2]. In this scenario, the composite ASMC system in blue shades travels through the dark matter background of the galactic NFW halo with mass density in Eq. (6.5), shown in dashed arrows. It encounters background axions with relative velocities $v \sim v_{\rm vir}$ and captures a fraction of the colliding particles as indicated by the solid black arrows. A fraction of the acquired DM mass $\delta \mathcal{M}$ captured by the minicluster is subsequently accreted onto the axion star core in yellow, see red arrow. The resulting mass excess $\delta M_{\star} \propto \delta \mathcal{M}$ can be converted into the blue radio photons for suitable core masses $M_{\star} \geq M_{\star,\gamma}$.

excess $\delta \mathcal{M}$ of the incoming particles can be captured by the MC, shown by black solid arrows. In a secondary stage of this accretion process, a fraction of the accreted mass can be transferred onto the axion star core, which induces the core mass growth $\delta M_{\star} \propto \delta \mathcal{M}$ indicated by the red arrow. Importantly, the resonating systems of our interest are expected to host an AS core with mass $M_{\star} \approx M_{\star,\gamma}$. In such systems, the mass excess δM_{\star} can be resonantly converted into radio photons shown by the blue wave in Fig. 6.1. The corresponding conversion-efficiency of the axion DM decay into photons will be introduced together with the resulting photon flux in the following.

It should be emphasized at this point that the typical velocities $v_{\rm rel} \sim v_{\rm vir}$ in an average encounter are very large compared to the typical escape velocities $v_{\rm esc}(10^{-12}\,M_\odot) \sim 0.1\,{\rm m\,s^{-1}}$ of ASMC systems. We therefore start by developing a simplified geometrical capture model, which utilizes the \mathcal{M} - and Φ -dependent escape velocities of the total system, in the following. Defining the corresponding cross section $\sigma_{\rm mc} = 4\pi\mathcal{R}(\Phi,\mathcal{M})^2$ of the total system with negligible gravitational enhancement, we can write the external MC accretion rate at a radial position r in terms of $\rho_{a,f}(r)$ as [2]

$$\frac{\delta \mathcal{M}}{\delta t}(\Phi, \mathcal{M}, r) = 4\pi \mathcal{R}(\Phi, \mathcal{M})^2 \rho_{a,f}(r) \langle v_{\text{cap}}(\Phi, \mathcal{M}, r) \rangle, \qquad (6.6)$$

where $\mathcal{R}(\Phi, \mathcal{M})$ obeys Eq. (3.24), and the average relative velocity of the captured particles $\langle v_{\text{cap}}(\Phi, \mathcal{M}, r) \rangle$ is defined in terms of the relative velocity distribution $f_v(r)$

$$\langle v_{\rm cap}(\Phi, \mathcal{M}, r) \rangle = \int_0^{v_{\rm esc}(\Phi, \mathcal{M})} dv \, v \, f_v(r) \,,$$
 (6.7)

such that particles with $v > v_{\rm esc}(\Phi, \mathcal{M})$ are considered to withstand the gravitational capturing. We assume a one-dimensional Gaussian distribution for the spatially dependent relative velocities in $f_v(r)$ given by

$$f_v(r) = \frac{1}{\sqrt{2\pi} v_{\text{vir}}(r)} \exp\left(-\frac{v^2}{2v_{\text{vir}}(r)^2}\right), \qquad v \in (-\infty, \infty),$$
(6.8)

where the virial velocity $v_{\rm vir}(r) \sim 239 \, {\rm km/s}$ is computed from the spatially dependent velocity dispersion of the Milky Way rotation curve in Ref. [194]. Entering the Gaussian distribution for $f_v(r)$ in Eq. (6.7), the average capture velocity is found to be [2]

$$\langle v_{\rm cap}(\Phi, \mathcal{M}, r) \rangle = \frac{v_{\rm vir}(r)}{\sqrt{2\pi}} \left[1 - \exp\left(-\frac{v_{\rm esc}(\Phi, \mathcal{M})^2}{2v_{\rm vir}(r)^2}\right) \right],$$
 (6.9)

$$\approx \frac{1}{2\sqrt{2\pi}} \frac{v_{\rm esc}(\Phi, \mathcal{M})^2}{v_{\rm vir}(r)} \,. \tag{6.10}$$

In general, the r-dependent velocity integral in Eq. (6.10) would need to be evaluated at every point of the parameter space in \mathcal{M}, Φ, r . However as can be checked numerically, the velocity $v_{\rm vir}(r) \sim 200\,{\rm km\,s^{-1}}$ is roughly constant in the relevant radial range from 1 kpc to $\mathcal{O}(100)\,{\rm kpc}$ [194, 266, 267]. We therefore simplify our numerical calculations by assuming $v_{\rm vir}(r) \approx 239\,{\rm km\,s^{-1}}$ as approximately constant and find that it does not affect our qualitative results in the following

In the above framework, axion DM particles encountering the ASMC system with relative velocities $v \leq v_{\rm esc}$ are considered to get captured by the minicluster. The MC accretion efficiency $f_{\rm cap}$ with respect to the background field $\rho_{a,f}(r)$ can be estimated for typical QCD axion parameters $\mathcal{M} \sim 10^{-12} M_{\odot}$, $\Phi \sim 1$, $\mathcal{R} \sim 10^{7}$ km by considering the ratio

$$f_{\rm cap}(\mathcal{M}, \Phi) \sim \frac{v_{\rm esc}(\mathcal{M}, \Phi)}{v_{\rm vir}} \sim \frac{0.1 \,\mathrm{m \, s^{-1}}}{100 \,\mathrm{km \, s^{-1}}} \sim 10^{-6} \,,$$
 (6.11)

which gives $f_{\rm cap} \ll 1$ for most \mathcal{M}, Φ . Note also that while large values of Φ increase $v_{\rm esc}$ and $f_{\rm cap}$, they simultaneously decrease the cross section $\sigma_{\rm mc}$ in Eq. (6.6). Overall, the dominant scaling of $\delta \mathcal{M}$ in Eq. (6.6) effectively benefits from small values of Φ , which increase \mathcal{R} in Eq. (3.24) and thus the geometric cross section of the total system.

In a more general context, the highly overdense ASMC system can also capture particles through repeated scattering in the gravitational AS/MC potential - a process which we neglect in our approach. For the considerations in this work, Eq. (6.6) provides a qualitative estimation for the expected mass growth of MCs in the galactic dark matter halo.

In order to obtain a radio signal from the MC accretion rate $\delta \mathcal{M}/\delta t$ in Eq. (6.6), the next step is the derivation of the corresponding core mass growth rate $\delta M_{\star}/\delta t$. We assume the core-halo mass relation from Eq. (3.57) to provide the virial equilibrium configuration of the composite

ASMC system. This interpretation is in agreement with the virialization condition in Eq. (4.62) and it provides an intuitive connection between the mass growth of the host minicluster and its AS core.

The corresponding virialization condition can straight-forwardly be exploited by differentiating the core-halo relation with respect to time. Combining the resulting relation of the mass growth rates with the definition of $d\mathcal{M}/\delta t$ in Eq. (6.6), we obtain the AS accretion rate [2]

$$\frac{\delta M_{\star}^{ext}}{\delta t}(\Phi, \mathcal{M}, r) = \frac{1}{3} \left(\frac{\mathcal{M}}{\mathcal{M}_{h, \min}}\right)^{-\frac{2}{3}} \frac{\delta \mathcal{M}}{\delta t}(\Phi, \mathcal{M}, r), \tag{6.12}$$

$$= \frac{4\pi}{3} \left(\frac{\mathcal{M}}{\mathcal{M}_{h,\min}} \right)^{-\frac{2}{3}} \mathcal{R}(\Phi, \mathcal{M})^2 \rho_{a,f}(r) \langle v_{\text{cap}}(\Phi, \mathcal{M}, r) \rangle, \tag{6.13}$$

$$\simeq \frac{\sqrt{2\pi}}{3} \left(\frac{\mathcal{M}}{\mathcal{M}_{h,\min}} \right)^{-\frac{2}{3}} \mathcal{R}(\Phi, \mathcal{M})^2 \rho_{a,f}(r) \frac{v_{\rm esc}(\Phi, \mathcal{M})^2}{v_{\rm vir}(r)}$$
(6.14)

in the external minicluster model. We emphasize that our approach of using the core-halo relation at formation redshift $z=z_{\rm eq}$ is conservative because we tend to underestimate the abundance of resonating ASMC systems by neglecting the long-time mass growth $\delta \mathcal{M}/\delta t \cdot t_H$ over a Hubble time t_H and its impact on the core mass M_{\star} .

The possible enhancement of the accretion rate in Eq. (6.14) due to long-time AS accretion motivates us to introduce the effective efficiency factor

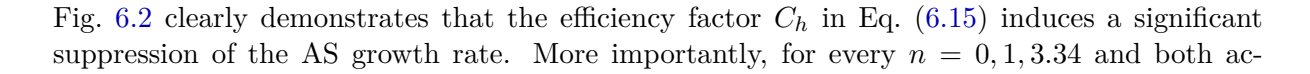
$$C_h = \left(\frac{\mathcal{M}}{\mathcal{M}_{h,\min}}\right)^{-\frac{2}{3}},\tag{6.15}$$

which is a direct consequence of the $z=z_{\rm eq}$ core-halo relation in Eq. (3.57). We introduce a second, external MC accretion model in which the core mass growth is increased by setting $C_h=1$ in Eq. (6.14) and Eq. (6.15). We call this specific scenario with increased growth rate

$$\frac{\delta M_{\star}^{enh}}{\delta t}(\Phi, \mathcal{M}, r) = \frac{\sqrt{2\pi}}{3} \mathcal{R}(\Phi, \mathcal{M})^2 \rho_{a,f}(r) \frac{v_{\rm esc}(\Phi, \mathcal{M})^2}{v_{\rm vir}(r)}.$$
 (6.16)

and $C_h = 1$ the enhanced external MC accretion model in the following. This enhanced growth rate prediction can be seen as a less conservative estimate on the expected (late-time) virialization rate of ASMC systems in an NFW background. In the following, we compare our predictions from the conservative external scenario in Eq. (6.6) and its enhanced equivalent in Eq. (6.16). Before continuing with the resulting radio emission of these systems, we investigate the predicted growth rates in some more detail.

A natural consistency check of our models can be obtained by comparing the predicted mass accretion of the AS core, $\delta M_{\star}/\delta t \cdot t_H$ over a Hubble time t_H to the mass \mathcal{M} of the total system. When the relative fraction $\delta \mathcal{M}/\delta t \cdot t_H/\mathcal{M}$ exceeds order unity, the NFW background $\rho_{a,f}(r)$ is expected to be depleted at present-day redshift z=0. Since $\delta \mathcal{M}=\delta M_{\star}/3$ in the enhanced model in Eq. (6.16), the above statement is equivalently true for the core mass growth rate $\delta M_{\star}/\delta t$ in Eq. (6.14), Eq. (6.16). We present the corresponding mass fractions for typical ASMC systems with a predicted core mass $M_{\star,\lambda}$ and $\Phi=1$ in Fig. 6.2. Here, the conservative external model from Eq. (6.14) is indicated by the solid colored lines, while dashed lines correspond to the enhanced case from Eq. (6.16) with $C_h=1$.



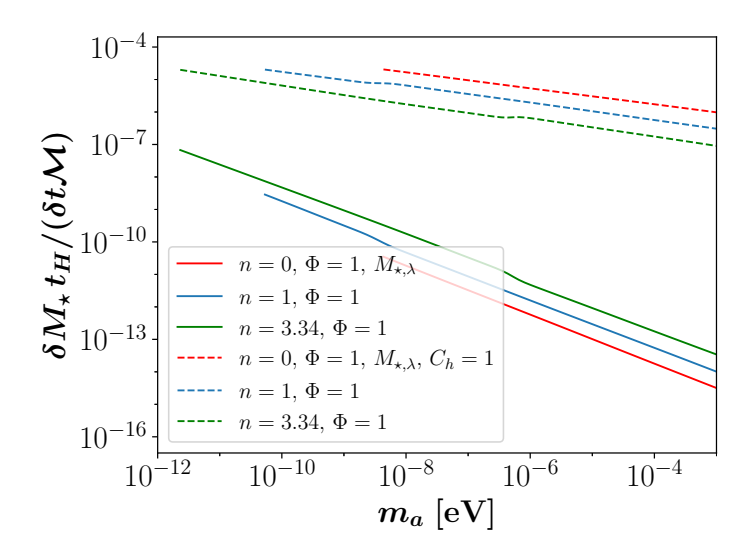


Figure 6.2: Relative fraction of accreted mass $\delta M_{\star}/\delta t \cdot t_H/\mathcal{M}$ over a Hubble time $t_H \simeq 1.3 \cdot 10^{10}$ yrs, normalized by the total mass \mathcal{M} of the ASMC system with core mass $M_{\star} = M_{\star,\lambda}$ and $\Phi = 1$. Both given for the *external* MC accretion model from Eq. (6.14) as a function of m_a, n , with the enhanced case $C_h = 1$ indicated by dashed colored lines.

cretion models, the relative mass gain over t_H is found to be non-substantial, thus ensuring possible mass growth in the present-day galaxy without depletion of the NFW background $\rho_{a,f}$. For better comprehensibility, we also present the absolute growth rates at two different values of the initial MC overdensity $\Phi = 1, 10^3$ in Fig. 6.3. Solid lines correspond to typical values $\Phi = 1$, while dashed lines show some of the densest miniclusters with $\Phi = 10^3$. As previously mentioned for the scaling of \mathcal{R} and $\delta \mathcal{M}/\delta t$ with Φ in Eq. (6.14), the growth rates benefit from smaller values of Φ , which increase the MC radius in Eq. (3.24) and its geometric cross section. On the other hand, the survival probability function $\mathcal{P}_{\text{surv}}(\Phi)$ from Eq. (3.56) strongly constrains the abundance of the $\Phi \ll 1$ population, so that the dominant contribution is given by the $\Phi \sim 1$ component nevertheless. Lastly, the increased mass growth at low axion masses m_a and fixed n in Fig. 6.3 is related to the increased mass and escape velocity of typical structures with $\mathcal{M}_0 \propto m_a^{-3/2}$ in Eq. (3.50).

In the last step of the depicted accretion process, the AS core can serve as a powerful site of radio conversion when it reaches the decay mass, $M_{\star,\gamma}$ and any mass excess $\delta M_{\star} = M_{\star} - M_{\star,\gamma}$ is converted into photons with a frequency $f \simeq m_a/(4\pi)$. We continue to estimate the resulting radio flux emitted from the accreting galactic ASMC systems with resonant core masses $M_{\star} \geq M_{\star,\gamma}$. The accretion-induced flux $F_{\star,s} \propto \delta M_{\star}/\delta t$ received from a single resonant axion star depends on three different parameters: on the initial overdensity parameter Φ , the host MC mass \mathcal{M} , and the galactic position \mathbf{r} . This simplified dependence can be expressed as

$$F_{\star,s} = \eta_{a\gamma\gamma} \frac{c^2}{4\pi d_{\text{obs}}(\mathbf{r})^2} \frac{\delta M_{\star}}{\delta t} (\Phi, \mathcal{M}, r), \tag{6.17}$$

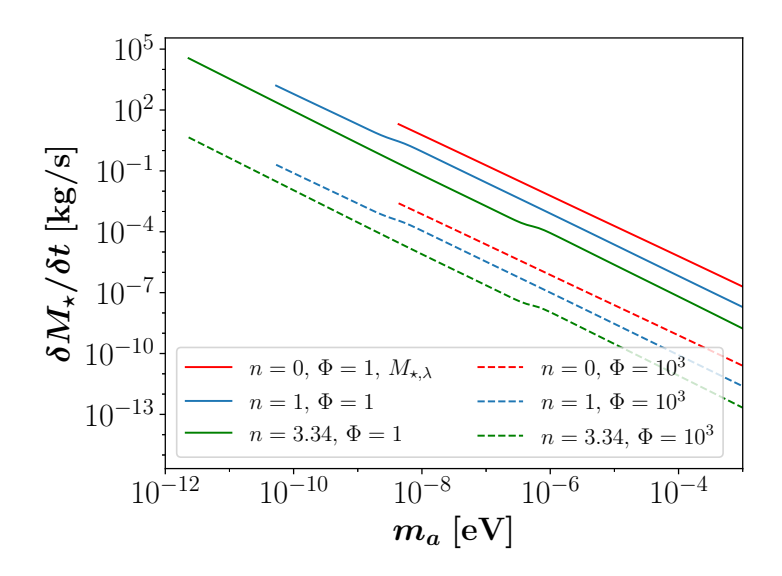


Figure 6.3: Absolute accretion rates of a critical ASMC system with maximum stable core mass $M_{\star} =$ $M_{\star,\lambda}$ in kg s⁻¹. Shown for different n, at $\Phi=1$ in solid and $\Phi=10^3$ in dashed colored lines.

where $d_{\text{obs}}(\mathbf{r})$ is the distance to the observer and the factor of c^2 is written to indicate the conversion from core mass excess to radiated energy. The coefficient $\eta_{a\gamma\gamma} = 1$ in Eq. (6.17) denotes the order-one efficiency of the resonant axion-photon conversion. In the most general sense, $\eta_{a\gamma\gamma}$ is expected to encode the onset of backreaction, the luminosity evolution $L_{\gamma}(t)$ with time and its dependence on the axion-photon coupling $g_{a\gamma\gamma}$, as depicted in Fig. 5.17.

In this work, we are mostly interested in the averaged galactic background signal arising from the $\mathcal{N}_{\gamma,\mathrm{tot}} \gg 10^8$ resonant ASMC systems, which is why we set $\eta_{a\gamma\gamma} = 1$ for simplicity. The overall flux observed from the total population of resonating systems can be obtained by integrating the single event flux $F_{\star,s}$ over \mathcal{M}, Φ and the galactic radial position \mathbf{r} , similar to what was done in Eq. (6.4) for $\mathcal{N}_{\gamma,\text{tot}}$. An important difference to Eq. (6.4) is the consideration of the threedimensional position \mathbf{r} to account for the random nature of the observed distances $d_{\text{obs}}(\mathbf{r})$ of the different single event fluxes. Thus considering the full spatial dependence, we obtain the total flux estimate [2]

$$F_{\star,\text{tot}} \simeq \int_{0}^{10^{4}} d\Phi \, p_{\Phi}(\Phi) \mathcal{P}_{\text{surv}}(\Phi) \int_{\mathcal{M}_{\gamma,\text{min}}(\Phi)}^{\mathcal{M}_{\gamma,\text{max}}} d\mathcal{M} \int_{|\mathbf{r}| > R_{\text{surv}}} d^{3}r \, \frac{dn}{d\mathcal{M}}(\mathbf{r}) \, F_{\star,s}, \tag{6.18}$$
$$= \eta_{a\gamma\gamma} c^{2} \int_{0}^{10^{4}} d\Phi \, p_{\Phi}(\Phi) \mathcal{P}_{\text{surv}}(\Phi) \int_{\mathcal{M}_{\gamma,\text{min}}(\Phi)}^{\mathcal{M}_{\gamma,\text{max}}} d\mathcal{M} \tag{6.19}$$

$$= \eta_{a\gamma\gamma} c^2 \int_0^{10^4} d\Phi \, p_{\Phi}(\Phi) \mathcal{P}_{\text{surv}}(\Phi) \int_{\mathcal{M}_{\gamma, \min}(\Phi)}^{\mathcal{M}_{\gamma, \max}} d\mathcal{M}$$
 (6.19)

$$\times \int_{|\mathbf{r}| > R_{\text{surv}}} d^3 r \, \frac{1}{4\pi d_{\text{obs}}(\mathbf{r})^2} \frac{dn}{d\mathcal{M}}(\mathbf{r}) \, \frac{\delta M_{\star}}{\delta t}, \tag{6.20}$$

where $dn/d\mathcal{M}(\mathbf{r})$ is the MC distribution defined in terms of the MCMF in Eq. (3.51). In the above expression, the spatial dependence of the distance $d_{\rm obs}(\mathbf{r}) = |\mathbf{r} - \mathbf{R}_E| \simeq \max(r, R_{\odot})$ between a single event and the observer can be simplified by averaging over two limiting cases of observation distances: first $\langle d_{\text{obs}}(\mathbf{r}) \rangle_{r \leq R_{\odot}} \simeq R_{\odot}$ in the central region and $\langle d_{\text{obs}}(\mathbf{r}) \rangle_{R_{\odot} \leq r} \simeq r$ beyond the solar radial position, which gives

$$F_{\star,\text{tot}} \simeq \eta_{a\gamma\gamma} c^2 \int_0^{10^4} d\Phi \, p_{\Phi}(\Phi) \mathcal{P}_{\text{surv}}(\Phi) \int_{\mathcal{M}_{\gamma,\text{min}}(\Phi)}^{\mathcal{M}_{\gamma,\text{max}}} d\mathcal{M} \int_{R_{\text{surv}}}^{R_{200}} dr \, \left[\frac{r}{\text{max}(r, R_{\odot})} \right]^2 \frac{dn}{d\mathcal{M}}(r) \, \frac{\delta M_{\star}}{\delta t} \, . \tag{6.21}$$

Subsequently entering the external accretion rate from Eq. (6.14), one arrives at the total flux

$$F_{\star,\text{tot}}^{ext} \simeq \frac{\sqrt{2\pi}}{3} \eta_{a\gamma\gamma} c^2 \int_0^{10^4} d\Phi \, p_{\Phi}(\Phi) \mathcal{P}_{\text{surv}}(\Phi) \int_{\mathcal{M}_{\gamma,\text{min}}(\Phi)}^{\mathcal{M}_{\gamma,\text{max}}} d\mathcal{M} \left(\frac{\mathcal{M}}{\mathcal{M}_{h,\text{min}}}\right)^{-\frac{2}{3}} \times \mathcal{R}(\Phi, \mathcal{M})^2 \frac{v_{\text{esc}}(\Phi, \mathcal{M})^2}{v_{\text{vir}}} \int_{R_{\text{surv}}}^{R_{200}} dr \left[\frac{r}{\text{max}(r, R_{\odot})}\right]^2 \rho_{a,f}(r) \frac{dn}{d\mathcal{M}}(r), \quad (6.22)$$

of the external MC accretion model, which we calculate numerically using the results from Sec. 3.6 and Sec. 6.1. Note here that the contribution to radio signals from the galactic center $r \lesssim R_{\rm surv}$ is suppressed by the MC survival from Fig. 3.9 and similarly for the periphery beyond 100 kpc due to the low density $\rho_{a,f}(r)$ and the large distances $d_{\rm obs}$ to earth.

Lastly, we can perform the same calculation from Eq. (6.22) for the case $C_h = 1$ in Eq. (6.16) to infer the total flux

$$F_{\star,\text{tot}}^{enh} = \frac{\sqrt{2\pi}}{3} \eta_{a\gamma\gamma} c^2 \int_0^{10^4} d\Phi \, p_{\Phi}(\Phi) \mathcal{P}_{\text{surv}}(\Phi) \int_{\mathcal{M}_{\gamma,\text{min}}(\Phi)}^{\mathcal{M}_{\gamma,\text{max}}} d\mathcal{M} \, \mathcal{R}(\Phi, \mathcal{M})^2 \frac{v_{\text{esc}}(\Phi, \mathcal{M})^2}{v_{\text{vir}}} \times \int_{R_{\text{surv}}}^{R_{200}} dr \left[\frac{r}{\max(r, R_{\odot})} \right]^2 \rho_{a,f}(r) \frac{dn}{d\mathcal{M}}(r).$$
(6.23)

of the enhanced minicluster accretion model with order-one mass translation onto the AS core. The remaining step at this point is to evaluate the detectability of the corresponding radio flux densities with different telescopes. Before doing so, we continue to introduce a second class of accretion scenarios in the following section.

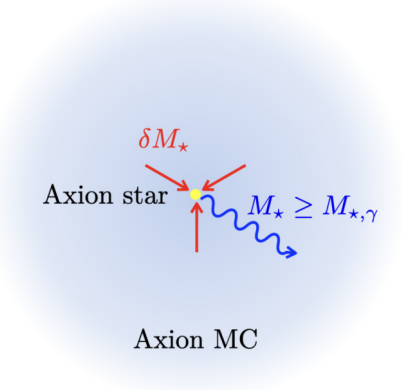
6.3 Internal Minicluster Accretion Model

This second class of models focuses on isolated ASMC systems, where the source of the accreted AS core mass is given by the minicluster itself. To make clear the distinction to the non-isolated external accretion model from the previous section, we call this second accretion scenario the *internal MC accretion model* in the following. The physical motivation for this accretion process comes from the long-time evolution of isolated ASMC systems in the numerical simulations of Subsec. 4.3.2 and Ref. [240].

According to the predictions from Ref. [240], the axion star mass growth obeys the time evolution from Eq. (4.41) after soliton condensation around $t \sim \tau_{\rm gr}$, where the condensation time $\tau_{\rm gr}$ is given by Eq. (4.26). The resulting mass growth is depicted in Fig. 4.6 for different values of ϵ in Eq. (4.43), which in turn is defined in terms of the minicluster parameters \mathcal{M}, Φ and the axion mass m_a . Most importantly for the considerations in this chapter, we can obtain the time-dependent mass growth rate of the self-similar system by taking the time derivative of Eq. (4.41). The resulting internal MC accretion rate in Eq. (4.42) and Fig. 4.7 will be used to

determine the total flux of the resonant ASMC population in the following - analogous to the computation of $F_{\star,\text{tot}}$ performed in Sec. 6.2.

We demonstrate the fundamental accretion mechanism of the internal model in Fig. 6.4, which shows the total ASMC system composed of the yellow AS core and the blue minicluster. The



(Internal accretion)

Figure 6.4: Schematic representation of the internal minicluster accretion model for axion star cores, taken from Ref. [2]. In this scenario, the isolated ASMC system exhibits a continuous mass growth of the axion star core, predicted from Eq. (4.41) and Eq. (4.7). The resulting mass excess δM_{\star} in red arrows can be converted into the blue radio photons for suitable core masses $M_{\star} \geq M_{\star,\gamma}$.

major distinction between Fig. 6.4 and Fig. 6.1 is the absence of the background DM field $\rho_{a,f}$. As mentioned before, the core mass growth δM_{\star} in red is sourced by the corresponding mass-loss of its surrounding minicluster background with mass $\mathcal{M} - M_{\star}$. A more complete scenario of AS accretion would be given by the combined contributions from internal and external mass growth. We leave a more sophisticated treatment of this combined process up to future research and instead explore the possibility of the two major mechanisms separately.

According to Eq. (4.42) and Eq. (4.43), the core mass growth rate $\delta M_{\star}/\delta t$ in the internal accretion model is fixed by a set of five different quantities: The minicluster parameters \mathcal{M}, Φ , the axion model m_a, n setting the former through \mathcal{M}_0 and the core mass M_{\star} . In the context of our approach using the ASMF prediction from Subsec. 4.7.2, the core mass M_{\star} is fixed by the $z=z_{\rm eq}$ core-halo relation in Eq. (3.57). An alternative modeling of the corresponding core mass growth could be obtained by using the initial soliton mass $M_{\star,0}$ at the time of formation $t \sim \tau_{\rm gr}$ and the present-day time coordinate t_0 of the system. In this way, the present-day core mass M_{\star} would be predicted by evolving the system in Eq. (4.41) until t_0 .

We note here that a similar study of the long-time mass growth of soliton cores without self-interactions $\lambda=0$ was recently performed in Ref. [252]. Since the self-similar attractor model faces fundamental uncertainties after reaching the critical masses $M_{\star}=M_{\star,\gamma}$ or $M_{\star}=M_{\star,\lambda}$ and since our previous approach to the ASMF was determined for the conservative core mass estimate at $z=z_{\rm eq}$ in Eq. (3.57), we use a different way to determine the soliton mass in the following.

We take the present-day parametrization of the linear growth MCMF from Subsec. 3.5.2 and derive the core masses from the core-halo relation at $z=z_{\rm eq}$ like before. This approach takes into account the linear long-time mass growth of miniclusters but not the long-time (internal) mass growth of their AS cores. Thus assuming M_{\star} to be given by the conservative initial estimate from the canonical core-halo relation, we can compute the corresponding mass growth rate from Eq. (4.42) for a given model m_a , n while integrating over the distributions of \mathcal{M} and Φ , similar to Eq. (6.21). More specifically, the resonating systems of our interest are expected to have

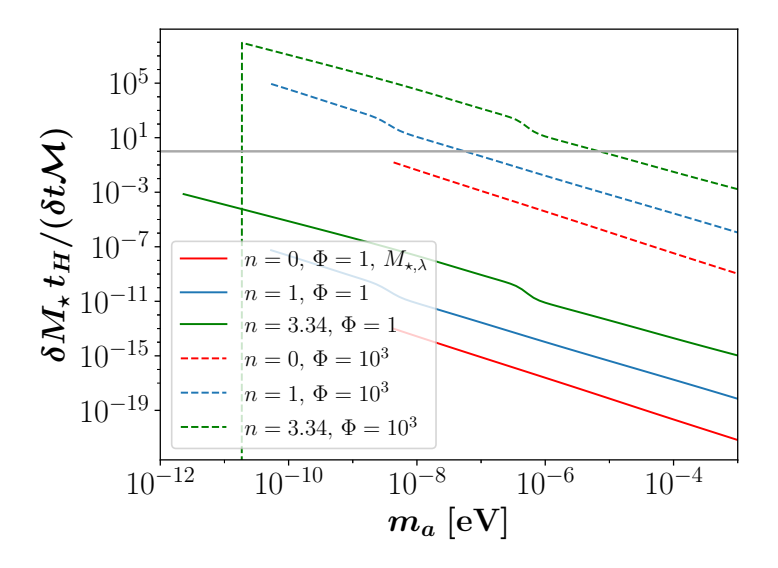


Figure 6.5: Relative fraction of accreted mass $\delta M_{\star}/\delta t \cdot t_H/\mathcal{M}$ over $t_H \simeq 1.3 \cdot 10^{10}$ yrs, normalized by the total mass \mathcal{M} of the accreting system with core mass $M_{\star} = M_{\star,\lambda}$. Both given for the *internal* MC accretion model from Eq. (4.42) for n = 0, 1, 3.34, for $\Phi = 1$ in solid and $\Phi = 10^3$ in dashed colored lines.

 $M_{\star}=M_{\star,\gamma}$, where larger core masses are prohibited by the parametric instability from Sec. 4.5. This way, the mass growth rate of the internal accretion model in Eq. (4.42) is fixed by the parameters $\mathcal{M}, \Phi, M_{\star,\gamma}$ for each axion model m_a, n . We demonstrate the long-time stability of the accreting systems in Fig. 6.5 by plotting the relative mass gain $\delta M_{\star}/\delta t \cdot t_H/\mathcal{M}$. The typical overdensity $\Phi=1$ is indicated by the solid colored lines, while dashed lines correspond to some of the densest miniclusters with $\Phi=10^3$. Fig. 6.5 demonstrates that the long-time stability $\delta M_{\star}/\delta t \cdot t_H/\mathcal{M} \ll 1$ of the systems is guaranteed for the most abundant ASMC systems with $\Phi \sim 1$.

The same statement does not hold true however for the densest miniclusters $\Phi = 10^3$, for which the mass fraction in Fig. 6.5 exceeds order one for the smallest m_a and largest n in the sample. This is mostly due to the increased absolute mass of the structures as seen from \mathcal{M}_0 in Fig. 3.7. To ensure the consistency of the accreting systems in the ASMF at large Φ , we introduce an additional requirement for the resonating ASMC population in the internal accretion model. The resulting condition ensures the long-time survival of the respective systems through linear extrapolation of the mass growth rate at $M_{\star} = M_{\star,\gamma}$, which can be expressed

through multiplication with a Heaviside function in Eq. (6.4) according to

$$\mathcal{N}_{\gamma,\text{tot}}^{int} = 4\pi \int_{R_{\text{surv}}}^{R_{200}} dr \, r^2 \int d\Phi \, p_{\Phi}(\Phi) \mathcal{P}_{\text{surv}}(\Phi) \int_{\mathcal{M}_{\gamma,\text{min}(\Phi)}}^{\mathcal{M}_{\gamma,\text{max}}} d\mathcal{M} \frac{C_n(r)}{\mathcal{M}} \left(\frac{\mathcal{M}}{\mathcal{M}_{0,\text{min}}} \right)^{-1/2} \times \Theta \left(\mathcal{M} - \frac{\delta M_{\star}^{int}}{\delta t} \Big|_{M_{\star} = M_{\star,\gamma}} t_H - \mathcal{M}_{\gamma} \right) ,$$
(6.24)

where the Θ function equates both the combined AS mass and its accreted mass after $t = t_H$ with the minicluster mass \mathcal{M} . Let us also mention for completeness, that in all applications of the internal accretion rate, we check the kinetic regime condition from Eq. (4.22) for consistency. From the above assumptions and with the internal mass growth rate given by Eq. (4.42), it is straight forward to obtain the overall AS flux of the internal accretion model equivalent to the procedure in Eq. (6.21). The expected total flux can then be estimated from the expression [2]

$$F_{\star,\text{tot}}^{int} \simeq \eta_{a\gamma\gamma} c^{2} \int_{0}^{10^{4}} d\Phi \, p_{\Phi}(\Phi) \mathcal{P}_{\text{surv}}(\Phi) \int_{\mathcal{M}_{\gamma,\text{min}}(\Phi)}^{\mathcal{M}_{\gamma,\text{max}}} d\mathcal{M} \int_{R_{\text{surv}}}^{R_{200}} dr \left(\frac{r}{\text{max}(r,R_{\odot})}\right)^{2} \times \frac{dn}{d\mathcal{M}}(r) \frac{\delta M_{\star}^{int}}{\delta t} \bigg|_{M_{\star} = M_{\star,\gamma}} \Theta \left(\mathcal{M} - \frac{\delta M_{\star}^{int}}{\delta t} \bigg|_{M_{\star} = M_{\star,\gamma}} t_{H} - \mathcal{M}_{\gamma}\right), \quad (6.25)$$

where we have neglected the mass-loss backreaction of having increased M_{\star}/\mathcal{M} and thus decreased accretion rates $\delta M_{\star}/\delta t$ at late times $t \sim t_H$.

Similar to the definition of the enhanced external accretion model in Sec. 6.2, it is helpful to introduce a less conservative modification to the expected signal in Eq. (6.25). In this case the so far neglected long-time mass growth of the AS cores over t_H can lead to a significant boost of the expected number of resonating systems in Eq. (6.24) and Eq. (6.25). We explore the resulting phenomenological potential by introducing a fourth type of scenario in which the initial core-halo relation at $z = z_{\rm eq}$ from Eq. (3.57) is relaxed to account for the prediction $M_{\star} \sim \mathcal{M}$ in Ref. [240]. This can be achieved by parametrizing the late-time core mass relation of the internal model in terms of a constant $C_{\rm acc} \leq 1$ according to

$$M_{\star} = C_{\rm acc} \mathcal{M} \,, \tag{6.26}$$

where we set $C_{\text{acc}} = 1/2$, such that the AS core can absorb up to 50% of the total mass \mathcal{M} . Since in this case, the core-halo relation is effectively replaced by the relation in Eq. (6.26), we also drop the corresponding cutoffs $\mathcal{M}_{h,\text{min}}$ in Eq. (6.1) and $\mathcal{M}_{R,\text{min}}$ for consistency. As a consequence, the late-time relation Eq. (6.26) leads to an effective decrease of the low-mass cutoff $\mathcal{M}_{\gamma,\text{min}}$ in Eq. (6.2). The corresponding total flux predicted by the *enhanced internal accretion model* is then found by additionally expressing \mathcal{M}_{γ} through Eq. (6.26), which yields

$$F_{\star,\text{tot}}^{int,\text{acc}} \simeq F_{\star,\text{tot}}^{int}(\mathcal{M}_{\gamma} = M_{\star,\gamma}/C_{\text{acc}})$$
 (6.27)

with modified $\mathcal{M}_{\gamma,\min} = \max(\mathcal{M}_{0,\min}, \mathcal{M}_{\gamma})$ as outlined above. We use the above enhanced internal accretion model to estimate the potential detectability of resonant axion stars with improved accretion modeling at late times.

We also note for completeness that the condensation time $\tau_{\rm gr}$ in Eq. (4.26) can become larger

than t_H for some parameters. This observation does not contradict the existence of axion stars in such systems since τ_{gr} was derived for random homogeneous initial conditions, which are different from the gravitational collapse of the large overdensities in Sec. 3.2. As mentioned in Ref. [167], the time of AS formation can be significantly enhanced in the early universe.

6.4 Line Emission & galactic Radio Backgrounds

In the previous sections, we have introduced two major accretion models - internal and external - which each contain a conservative and an enhanced estimate on the expected accretion rates. The purpose of this section is to investigate the resulting signal flux densities in more detail. In the following analysis, we compare the expected flux rates from Eq. (6.21) to galactic radio backgrounds over a range of observable radio frequencies.

Subsec. 6.4.1 introduces a phenomenological fit to the galactic radio backgrounds, which we use to evaluate the detectability of external and internal signal rates in Subsec. 6.4.2 and Subsec. 6.4.3. We also discuss the possible detuning of the parametric resonance in the gravitational potential of the Milky Way in Subsec. 6.4.4 and demonstrate the directional dependence of the AS line signal in Subsec. 6.5.4.

6.4.1 Galactic Radio Background

The strength of galactic radio backgrounds is accounted for by using the power-law fit for the observed thermodynamic background temperature $T_{\rm bkg}$ from Ref. [268]. The phenomenological fit in Ref. [268] was obtained by matching data from different radio surveys in the range from 22 MHz to 10.49 GHz. It is essentially composed of the blackbody temperature $T_{\rm CMB} = 2.722\,{\rm K}$ of the cosmic microwave background and of a temperature power-law found from the observed, averaged radio excess. The resulting fit for predicting the background temperature at different frequencies f is [268]

$$T_{\text{bkg}}(f) = T_{\text{CMB}} + T_{R,0} \left(\frac{f}{f_{R,0}}\right)^{\beta_f} = T_{\text{CMB}} + 30.4 \,\text{K} \left(\frac{f}{310 \,\text{MHz}}\right)^{-2.58} ,$$
 (6.28)

where $T_{R,0} = 30.4 \,\mathrm{K}$ is the background reference temperature at a reference frequency of $f_{R,0} = 310 \,\mathrm{MHz}$ and $\beta_f = -2.58$ the spectral index of the power law. In order to compare our flux rate predictions from Eq. (6.21) to the background emission from Eq. (6.28), we convert T_{bkg} and $F_{\star,\mathrm{tot}}$ into spectral flux densities. We use Planck's law to convert the thermodynamic temperature predictions from Ref. [268] into the background flux density

$$S_{\text{bkg}}(f) = \frac{8\pi h f^3}{c^3} \frac{1}{\exp\left(\frac{hf}{k_B T_{\text{bkg}}} - 1\right)}$$
 (6.29)

with T_{bkg} from Eq. (6.28). The resulting flux density has units of power per unit area and frequency, integrated over the solid angle Ω . Similarly, we can compare the units of $F_{\star,\text{tot}}$ in Eq. (6.21), which are power per unit area integrated over solid angle, to find the corresponding spectral flux density $S_{\star,\text{tot}}$.

Since the leading-order conversion process in resonating axion stars produces a nearly monochromatic emission, for which the narrow bandwidth $\Delta f \propto g_{a\gamma\gamma}$ is given by Eq. (4.53), we can simply

divide $F_{\star,\mathrm{tot}}$ by Δf to obtain its spectral equivalent $S_{\star,\mathrm{tot}}$. For the axion-photon couplings under consideration, the corresponding frequency width of the expected signal is dominated by the Doppler broadening in the Milky Way gravitational potential. Using the velocity dispersion of the galactic disc and DM halo for the relative velocities of the resonating ASMC systems, we find $v_{\mathrm{rel}} \simeq v_{\mathrm{vir}} \simeq \mathcal{O}(200\,\mathrm{km/s})$, which results in $\Delta f/f \simeq v_{\mathrm{rel}}/c \simeq 10^{-3}$, as before . Therefore writing $\Delta f = 10^{-3} f$ with $f = m_a/(4\pi)$, we obtain the total spectral flux density [2]

$$S_{\star,\text{tot}}(m_a = 4\pi f) \simeq \frac{F_{\star,\text{tot}}(m_a)}{10^{-3} m_a/(4\pi)}$$
 (6.30)

emitted from the galactic population of resonating axion stars over the entire sky. Finally expressing the center frequency $f = m_a/(4\pi)$ of the expected radio line background in Eq. (6.29), we can directly compare the magnitude of S_{bkg} and $S_{\star,\text{tot}}$ for different axion models m_a, n . This will be done for a representative value of $g_{a\gamma\gamma}$ in the next section.

6.4.2 Spectral Flux from External Accretion

Starting with the scenario of external minicluster accretion from Eq. (6.22) and Eq. (6.23), we show the resulting spectral fluxes obtained for a representative axion-photon coupling of $g_{a\gamma\gamma} = 10^{-11} \,\text{GeV}^{-1}$ in Fig. 6.6. The frequency range in MHz encompasses axion masses in the range $10^{-8} \,\text{eV} \le m_a \le 10^{-2} \,\text{eV}$, which can potentially be probed by terrestrial radio telescopes. We extend the considered range of m_a beyond these frequencies to demonstrate predicted signals in units of MJy, which could potentially be searched by space-borne telescopes.

On a more general note in Fig. 6.6 and in the following plots, we show the *conservative* estimate in the left panel together with the *enhanced* accretion scenario on the right. The black solid line in Fig. 6.6 indicates the radio backgrounds predicted by the power law fit in Eq. (6.28) and Eq. (6.29). We have separated the black body spectrum of the CMB from the overall fit as indicated by the gray dashed line at lower frequencies $f \lesssim 1\,\mathrm{GHz}$. Note that in Fig. 6.6 and in following figures, the colors were changed with respect to the representation of n=0,1,3.34 in previous chapters.

It can clearly be seen by comparing the black solid to the colored lines at different temperature indices n, that the expected spectral fluxes can become orders of magnitude larger than the backgrounds. This is especially true away from the CMB peak around $f \simeq 160\,\mathrm{GHz}$ and for lower frequencies of $f \lesssim 1\,\mathrm{GHz}$ corresponding to $m_a \lesssim 5\mu\mathrm{eV}$. We emphasize here that each point in Fig. 6.6 corresponds to a narrow line, for which the central frequency is set by Eq. (4.53) and the amplitude by the axion model m_a, n following Eq. (6.22), Eq. (6.23). The narrow radio line nature of the expected signal is mainly responsible for the increasingly large flux densities $S_{\star,\mathrm{tot}} \gg 1\,\mathrm{GJy}$ at small $f \propto m_a$. Two major reasons for this observation are the scaling $S_{\star,\mathrm{tot}} \propto m_a^{-1}$ in Eq. (6.30) and the increased accretion rates from Eq. (6.14) for heavier and larger structures $\mathcal{M}_0 \propto m_a^{-3/2}$, $\mathcal{R} \propto \mathcal{M}^{1/3}$, see Eq. (3.50), Eq. (3.24).

Furthermore, a comparison of the conservative and enhanced models in the left and right panels of Fig. 6.6 reveals the strong impact of the efficiency factor $C_h = (\mathcal{M}/\mathcal{M}_{h,\min})^{-3/2}$ in Eq. (6.14). This observation does not only demonstrate the benefit of improved understanding of the (time-dependent) core-halo relation of composite ASMC systems, but it also indicates a significant potential for enhancements of the expected signals through additional consideration of long-

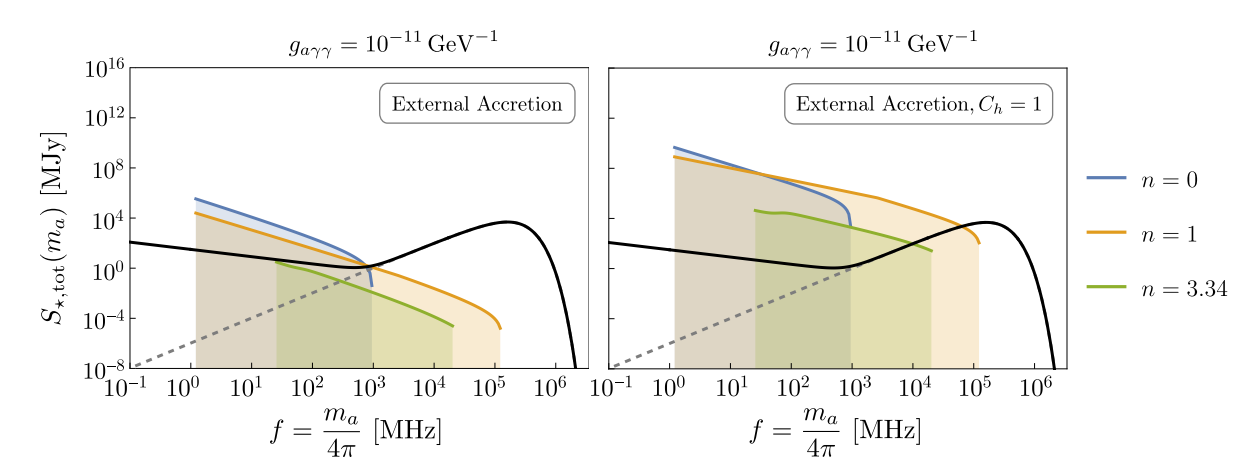


Figure 6.6: Spectral flux density $S_{\star,\text{tot}}(m_a)$ of the external accretion models in Eq. (6.14) (left) and Eq. (6.16) (right) in MJy, taken from Ref. [2]. Calculated from Eq. (6.22) and Eq. (6.23) for an axion-photon coupling of $g_{a\gamma\gamma} = 10^{-11} \,\text{GeV}^{-1}$, where each point represents a narrow line centered around the frequency $f = m_a/(4\pi)$ of the axion mass m_a . The black solid line describes the radio backgrounds, including the cosmic microwave background (dashed) and observed radio excesses, parametrized by Eq. (6.28).

time accretion². The important conclusion from Fig. 6.6 is that the external MC accretion model provides spectral fluxes, which are comparable to galactic backgrounds for a large range of axion models m_a , n - especially for the enhanced scenario in the right panel.

On a technical side, the amplitudes of $S_{\star,\text{tot}}$ at different n in Fig. 6.6 arise due to a mixing of the following effects: the modified ranges of the ASMF in Fig. 4.14, the different abundance of the objects in Fig. 5.20 and their different scalings compared to $M_{\star,\gamma}$ in Eq. (4.61), which is approximately constant for different n^3 . Effectively, the high-frequency cutoffs in Fig. 6.6 are given by regions of m_a, n , where the resonant AS mass $M_{\star,\gamma} > \max(M_{\star})$ grows beyond the range of the ASMF. Lastly, the scaling of the spectral flux densities in different accretion models can be understood from the relation

$$S_{\star, \text{tot}} \propto \int d\mathcal{M} \frac{dn}{d\mathcal{M}} \frac{\delta M_{\star}}{\delta t} \propto \int d\mathcal{M} \, \mathcal{M}^{-3/2} \mathcal{M}^p \,,$$
 (6.31)

where $p \simeq 2/3$ for the conservative external MC accretion and $p \simeq 4/3$ due to the absence of C_h in Eq. (6.14) for the enhanced external accretion scenario. The scaling of $S_{\star,\text{tot}}$ with \mathcal{M} in Eq. (6.31) and p > 1 indicates that the dominant contribution to the total galactic radio flux from resonating ASMC systems is given by the high-mass component of the MCMF with large $\mathcal{M} > \mathcal{M}_0$. Note however that we apply a stability cutoff to the largest MC masses with predicted core masses $M_{\star} \geq M_{\star,\lambda}$ due to the unknown late-time evolution after occurring of the self-interaction instability from Sec. 4.4.

To conclude, we highlight that the external accretion model from Sec. 6.2 provides a promising mechanism and strong expected radio line emission for a large range of axion models m_a , n.

²This is because the factor C_h essentially relates the mass distribution of the AS core and its host minicluster, where $C_h \sim 1$ corresponds to increased or late-time AS core masses as predicted by Ref. [240].

³This is because the second term under the square root in Eq. (4.61) is negligible for most models m_a , n so that M_{\star} is essentially independent of $f_a(n)$ in Fig. 3.6.

6.4.3 Spectral Flux from Internal Accretion

Next we examine the detectability of the spectral flux density given by the flux in Eq. (6.25) and Eq. (6.27) for the (enhanced) internal accretion scenario. Analogous to the previous section, we plot the resulting flux density predictions for different models m_a , n with representative axion-photon coupling $g_{a\gamma\gamma} = 10^{-11} \,\text{GeV}^{-1}$ compared to the galactic radio backgrounds from Eq. (6.29) in Fig. 6.7. As before, black solid and dashed lines show the total and CMB components of the

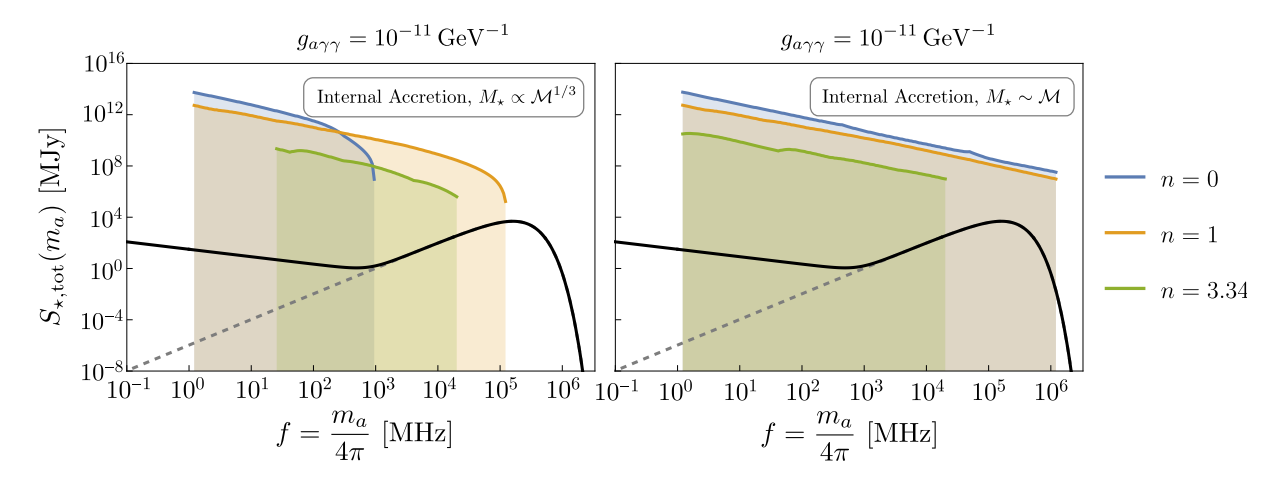


Figure 6.7: Spectral flux density $S_{\star,\text{tot}}(m_a)$ of the internal accretion models in Eq. (4.42) with the coremass given by Eq. (3.57) and $M_{\star} \propto \mathcal{M}^{1/3}$ (left) and $M_{\star} \sim \mathcal{M}$ in Eq. (6.26) (right) in MJy, taken from Ref. [2]. Calculated from Eq. (6.25) and Eq. (6.27) for an axion-photon coupling of $g_{a\gamma\gamma} = 10^{-11} \,\text{GeV}^{-1}$, where each point represents a narrow line centered around the frequency $f = m_a/(4\pi)$ of the axion mass m_a . The black-solid line describes the radio backgrounds, including the cosmic microwave background (dashed) and observed radio excesses, parametrized by Eq. (6.28).

backgrounds while different colors indicate axion models with different temperature evolution index n. The left panel of Fig. 6.7 shows the standard internal accretion model, which uses the canonical core-halo relation from Eq. (3.57) to fix the mass range of the ASMF. In contrast, the right panel of Fig. 6.7 depicts the same results for the enhanced internal accretion, which is given by the modified mass relation in Eq. (6.26).

Remarkably, both internal accretion models show significantly larger spectral flux densities compared to the external scenarios in Fig. 6.6. A major reason for this boost in signal amplitude is given by the increased accretion rates, which can become particularly large for dense $\Phi \gg 1$ and heavy $\mathcal{M} > \mathcal{M}_0$ miniclusters. Opposed to the external accretion rates in Eq. (6.6), which benefit from small values of Φ , the survival probabilities $\mathcal{P}_{\text{surv}}(\Phi)$ for large Φ are not suppressed, see Fig. 3.10. This leads to an increased survival of the most strongly emitting ASMC systems in the internal models.

Comparing the left and right panels of Fig. 6.7, one observes that the major distinction between the conservative and enhanced accretion models is the extended observable frequency range at large m_a on the right. This can simply be explained by the relaxed low-mass cutoff of the resonant MCMF population given by Eq. (6.26). The important conclusion for the internal accretion scenarios in Fig. 6.7 is that the observability of the radio line emission is essentially limited by the existence of resonating ASMC systems in the galaxy altogether. If this population is present, as predicted by the cutoffs from Eq. (6.2), Eq. (6.3) and Eq. (6.26) respectively, the

received spectral flux is expected to be overwhelmingly strong compared to galactic backgrounds.

6.4.4 Gravitational Detuning

Before we investigate the parameter constraints in the next section, we turn to briefly discuss the potential detuning of the AS resonance from Sec. 4.5 in the galactic gravitational potential, as presented in Ref. [269] and Ref. [2]. Physically, Ref. [269] investigated two fundamental detuning mechanisms, which were shown to suppress the exponential growth of stimulated photon decay in some configurations.

The first mechanism relates to the momentum spread δ_p of the axion field, which should not exceed the characteristic length scale of the resonance for the instability to develop. If the momentum spread is much larger than the resonance length, an average emitted photon will be prevented from triggering further stimulated emission due to the significant change in axion energy across its trajectory. In the framework of Ref. [269], the momentum spread of a coherent clump is given by the inverse length scale, $\delta_p \sim 1/R_{\star}$, and the resonance length $1/\mu_H$ is defined as the inverse of the growth factor μ_H from Eq. (4.56), which sets the physical scale of the parametric resonance.

The second source of potential detuning is given by the gravitational redshift of photons in an external potential like that of the Milky Way dark matter halo. When the gravitational redshift changes the photon energy sufficiently over the resonance length $1/\mu_H$, an average photon will be detuned with respect to the energy of the axions it is supposed to stimulate. Both of the above mechanisms can be formulated into two requirements for the resonance condition, as done in Ref. [269]. Defining the detuning distance of a photon as the spatial distance it has to travel in a constant external potential $\Phi_{\rm ext}$ to be shifted out of resonance from the resulting energy loss, the two criteria can be summarized as [269]

- 1. The axion momentum spread $\delta_p \sim 1/R_{\star}$ should be smaller than the growth factor, $\delta_p < \mu_H$ (i.e. smaller than the inverse resonance length $1/\mu_H^{-1}$ as formulated in Ref. [269])
- 2. The detuning distance Δz of the gravitational redshift should be longer than the resonance length $1/\mu_H$, so that $\Delta z > 1/\mu_H$

Note that the first point is equivalent to the resonance condition $\mu_H > \mu_{\rm esc}$ from Eq. (4.56) and Eq. (4.58) with $\mu_{\rm esc} = 1/(2R_{\star})$. It is therefore sufficient to test the validity of the second requirement in the following. For this, we can express the second condition by writing $\mu_H \Delta z > 1$ in terms of the effective axion momentum $p_{\rm eff} = \sqrt{p_{\star}^2 - 2m_a^2 \Phi_{\rm ext}}$ in the roughly constant external potential $\Phi_{\rm ext}$ as [269]

$$\mu_H \Delta z = \frac{4\mu_H^2}{m_a^2} \frac{p_{\text{eff}}}{|\partial_r \Phi_{\text{ext}}(r)|} = \frac{g_{a\gamma\gamma}^2 \rho_{\star}}{2m_a^2} \frac{\sqrt{-2m_a^2 \Phi_{\text{ext}}}}{|\partial_r \Phi_{\text{ext}}(r)|} > 1, \qquad (6.32)$$

where $\rho_{\star} \simeq M_{\star}/(4\pi/3R_{\star}^3)$ and $p_{\star} \ll 2m_a^2\Phi_{\rm ext}$ is the typical momentum of the clump in a dominant external potential. The properties of $\Phi_{\rm ext}$ can be estimated from the corresponding Poisson equation as $\Phi_{\rm ext}(r) \simeq -4\pi G\rho_{\rm ext}r^2$ and $\partial_r\Phi_{\rm ext} \simeq -8\pi G\rho_{\rm ext}r$, where $\rho_{\rm ext}$ is the dominant matter density sourcing the overall potential $\Phi_{\rm ext}$.

In the case of diffuse axions, $\rho_{\rm ext}$ is set by the Milky Way potential, whereas for the overdense axion clumps of our interest $\rho_{\rm ext} \approx \rho_{\star}$ [2]. Thus considering the gravitational redshift induced

by the dominant AS matter density ρ_{\star} , we can rearrange Eq. (6.32) for the radius R_{\star} to obtain the resonance condition

$$R_{\star} \lesssim \left(\frac{1}{8\pi} \sqrt{\frac{3}{2}}\right)^{2/3} \left(\frac{g_{a\gamma\gamma}^4 M_{\star}}{m_a^2 G}\right)^{1/3} \sim \left(\frac{g_{a\gamma\gamma}^4 M_{\star}}{m_a^2 G}\right)^{1/3}. \tag{6.33}$$

due to gravitational detuning [2]. Apart from the order-one numerical prefactors, the scaling in Eq. (6.33) is identical to the scaling of the resonating AS radius $R_{\star,\gamma} = R_{\star}(M_{\star,\gamma})$ obtained from Eq. (4.17) and Eq. (4.61). We therefore conclude, that the two detuning mechanisms from Ref. [269] are (1.) already included in our formalism and (2.) only expected to differ within order-one ranges, which are well within uncertainties of the galactic MCMF and ASMF. Effectively, a potential change of the resonance condition in Eq. (4.58) by order-one factors would drive the corresponding mass $M_{\star,\gamma}$ slightly above the values in our consideration, which does not affect our qualitative results. Opposed to the case of diffuse axion configurations in Ref. [269], we summarize that the coherent clumps of our interest are not considerably affected by gravitational detuning.

6.5 Constraints on the Axion-photon Coupling

With the exemplary signal flux densities evaluated in the previous sections, a straight-forward next step is to explore the potential constraints, which can be inferred from exclusion of the corresponding signals. For this, we follow the approach in Ref. [2] by employing two different criteria for the detectability of the total AS line emission: First, a simple background comparison based on the galactic radio backgrounds from Subsec. 6.4.1 and secondly a dedicated signal search using different radio telescopes and their respective sensitivities. Both of these criteria will be introduced in Subsec. 6.5.1 before applying them separately for the external MC accretion models in Subsec. 6.5.2 and the internal MC accretion scenario in Subsec. 6.5.3.

6.5.1 Approaches to Background Comparison

In the general context of this chapter, we scan the axion models m_a, n from Subsec. 3.6.1 across an axion mass range $10^{-8} \,\mathrm{eV} \le m_a \le 10^{-2} \,\mathrm{eV}$ and for n=0,1,3.34 as before. The resulting signal fluxes from Eq. (6.21) and Eq. (6.30) depend sensitively on the model m_a, n and on the axion-photon coupling $g_{a\gamma\gamma}$, which in our considerations spans across the range $10^{-17} \,\mathrm{GeV}^{-1} \le g_{a\gamma\gamma} \le 10^{-8} \,\mathrm{GeV}^{-1}$ - independent of m_a, n . For each model m_a, n , we use the abundance of resonating ASMC systems from Eq. (6.4) together with the internal and external accretion rates to obtain a corresponding signal flux in Eq. (6.21), which we compare both with radio backgrounds from Eq. (6.28) and with telescope sensitivities. Same as in Fig. 6.6 and Fig. 6.7, we use the black-body radiation law in Eq. (6.29) and Eq. (6.30) to convert from temperature and flux to spectral flux densities in units of MJy.

The corresponding signal flux densities of the galactic AS radio line emission is then compared to sensitivity requirements from two different approaches to be introduced in the following. As a major result for each of the two signal comparisons, we obtain the potential constraints in the parameter space of m_a , $g_{a\gamma\gamma}$ at a given n, which can be inferred in the future through (non-)observation of the predicted radio lines from resonating systems.

Simple Background Comparison

In the first most straight-forward approach, we employ a simple comparison of the predicted spectral flux density $S_{\star,\text{tot}}$ with the spectral flux from galactic radio backgrounds in Eq. (6.29). Accordingly, we evaluate each point $m_a, g_{a\gamma\gamma}$ in the parameter space at given n by calculating the different galactic flux densities numerically (analogous to Fig. 6.6, Fig. 6.7 for $g_{a\gamma\gamma} = 10^{-11} \,\text{GeV}^{-1}$), and determine the parameter space in $m_a, g_{a\gamma\gamma}$, where

$$S_{\star, \text{tot}}(m_a, n) > \left(\frac{S}{N}\right) S_{\text{bkg}}(m_a).$$
 (6.34)

The resulting two-dimensional parameter plots of potentially constrainable regions are given for a signal-to-noise ratio of S/N=5 with n=0,1,3.34 and correspond to axion models $m_a, n, g_{a\gamma\gamma}$, for which the galactic line emission from resonating axion stars is expected to be detectable. Importantly, the predicted constraints of the simple background comparison in Eq. (6.34) do only depend on the signal-to-noise ratio S/N and not on the experimental properties of a given telescope. They can therefore be seen as a preliminary estimate on the observational potential that can be probed with current and future radio telescopes.

We show the exclusion potential obtained from this approach in Fig. 6.8 and Fig. 6.10 and evaluate the results in detail in Subsec. 6.5.2 and Subsec. 6.5.3 respectively. Before moving on to potential constraints, we continue with the second, experimentally motivated approach.

Radio Telescope Sensitivities

As seen in Fig. 6.6, the expected spectral flux of the galactic population of resonating axion stars drops below the expected radio backgrounds for some m_a, n in the external accretion scenario. It is therefore helpful to explore the possibilities of different existing and upcoming radio telescopes in this section. This is particularly relevant since the radio line emission predicted in this work needs to be either observed or excluded by astronomical observations to derive the respective constraints on the axion-photon coupling $g_{a\gamma\gamma}$. In the following, we consider four different telescopes: LOFAR [270, 271], FAST [272, 273], ALMA [274, 275] and the upcoming square kilometer array, SKA [276, 277].

The experimental requirements for a possible detection of $S_{\star,\text{tot}}$ are best understood by discussing the expected nature of the radio line signal. Owing to the NFW profile of the Milky Way dark matter halo in Eq. (A.1) and Eq. (6.5), the distribution of resonating axion stars should be roughly isotropic when observed from the galactic center. This isotropy is obviously violated at the solar position $R_{\odot} = 8.3\,\text{kpc}$, however the MC survival cutoff, which we apply at $r < R_{\text{surv}} = 1\,\text{kpc}$ in Eq. (3.54) is expected to partially reduce anisotropic effects from the central DM component at $r < R_{\odot}$. For simplicity and due to the large uncertainties in the evolution of the galactic ASMF, we will therefore assume that the line emission of resonant axion stars can be treated as approximately isotropic in the following.

We also note that, while the AS emission will be stronger towards the galactic bulge with larger $\rho_{\text{NFW}}(r)$, the radio backgrounds (and foregrounds) of the baryonic matter will also be boosted, thus complicating possible detection of our signal. The above circumstances also motivate an observation strategy in which the telescopes are *pointed away* from the Milky Way disc. This approach is especially promising, because $S_{\star,\text{tot}}$ - opposed to the signal event signal in Eq. (6.17)

- amounts to a diffuse signal, that can also be observed far away from the galactic plane⁴. Accordingly, the AS line signal is expected to be smooth over large angular scales compared to the size of the typical beam of radio telescopes.

The diffuse nature of $S_{\star,\text{tot}}$ implies that our signals do not benefit from the interferometric techniques, which LOFAR, ALMA and SKA provide. Interferometers are designed to increase the angular resolution through an array of smaller dishes with a large maximal distance between them (called the baseline), where the effective area of the dish is given by the baseline. Importantly for our considerations, the largest angular scales in the interferometric mode, which are larger than the shortest baseline and connected to our diffuse signal, will be removed. This limitation requires us to only consider the *single-dish mode* of interferometers for detection.

Lastly at the same time, we consider a large parameter range in $m_a \in [10^{-8} \,\mathrm{eV}, 10^{-2} \,\mathrm{eV}]$, which leads to the requirement of a large range of observable frequencies $f \in [f_{\min}, f_{\max}]$ for a given experiment. To summarize the above, our signal has several fundamental properties: The narrow spectral width of the line, which benefits from sufficiently small frequency bins, the diffuse nature, which requires single-dish (mode) observations and the large range of constrainable frequencies $f \in [1 \,\mathrm{MHz}, 10^3 \,\mathrm{GHz}]$. We choose the FAST telescope as a single dish with a particularly large diamter $D_{\mathrm{tel}} = 300 \,\mathrm{m}$ and the LOFAR, ALMA and upcoming SKA arrays to cover a broad range of frequencies, see Tab. 6.1 for details.

With the experimental requirements and telescope choices summarized above, the next step is to infer the potential detectability of our line predictions using the aforementioned methods. In the context of radio astronomy, the spectral flux density $S_{\star,\text{tot}}$ in Eq. (6.30) should be more commonly expressed in terms of the antenna temperature T_{ant} , which is the noise temperature of a hypothetical resistor that gives the same amount of power density as the observed signal. For this, the sky-integrated total flux density $S_{\star,\text{tot}}$ needs to be converted into the spectral flux density $S_{\star,\text{tot}}^{\text{pb}}$ within the observed solid angle $\Delta\Omega_{\text{pb}}$ of the primary beam of the telescope

$$S_{\star,\text{tot}}^{\text{pb}}(m_a) \simeq S_{\star,\text{tot}}(m_a) \frac{\Delta\Omega_{\text{pb}}}{4\pi},$$
 (6.35)

where $\Delta\Omega_{\rm pb} = 2\pi(1-\cos(\theta_{\rm pb}/2))$ is a function of the primary beam angle $\theta_{\rm pb}$ [278, 279]. Note that by applying Eq. (6.35), we have implicitly assumed that the chosen bandwidth ΔB of the given telescope is similar to the spectral width $\Delta f \simeq \Delta B$ of the AS signal. If for a given experiment, the bandwidth $\Delta B > \Delta f$ exceeds the line width, the resulting signal would be suppressed by an additional factor

$$\eta_{\Delta B} \simeq \frac{\Delta f}{\Delta B} \simeq \frac{10^{-3} \, m_a}{\Delta B}$$
(6.36)

compared to Eq. (6.35).

Then, setting the bandwidth efficiency $\eta_{\Delta B} = 1$ by employing Eq. (6.35), we can convert the observed flux density $S_{\star, \text{tot}}^{\text{pb}}$ into the corresponding antenna temperature

$$T_{\text{ant}}^{\text{pb}} = \frac{1}{2k_{\text{B}}} A_{\text{eff}} S_{\star,\text{tot}}^{\text{pb}}(m_a), \tag{6.37}$$

⁴Depending on the telescope, there will be limitations to the observable elevation of the dish and antennas, which we do not consider in the qualitative estimates of this chapter.

of the primary beam, where $A_{\text{eff}} = \eta_A A$ is the effective area of the telescope, with efficiency factor η_A and dish surface area A [278, 279]. For single dish telescopes, the detectability of the signal $S_{\star,\text{tot}}^{\text{pb}}$ inducing the antenna temperature T_{ant} in Eq. (6.37) is typically expressed by means of the radiometer equation

$$\left(\frac{S}{N}\right)_{\text{single}} = \frac{T_{\text{ant}}^{\text{pb}}}{T_{\text{min}}},
\tag{6.38}$$

where in this work S/N = 5 as before. The minimum observable temperature

$$T_{\min} = \frac{T_{\text{sys}}}{\sqrt{\Delta B \, t_{\text{obs}}}} \tag{6.39}$$

depends on the bandwidth $\Delta B \simeq \Delta f \simeq 10^{-3} m_a/(4\pi)$ and the observation time $t_{\rm obs} = 100\,\rm hrs$. Physically, $T_{\rm min}$ quantifies the noise of the system with total temperature $T_{\rm sys} = T_{\rm rec} + T_{\rm bkg}$ given by the sum of the receiver noise and the radio background temperature $T_{\rm bkg}$ from Eq. (6.28) in a given measurement. Note also that the criterion in Eq. (6.38) is valid only for single dish telescopes, i.e. for FAST in our considerations.

Telescope arrays like LOFAR, ALMA and SKA on the other hand consist of multiple, smaller single dishes which are operated together. For a telescope setup involving N_{tel} individual dishes with $N_{\text{pol}} = 2$ polarizations, the single-mode signal to noise ratio can be inferred from Eq. (6.38) according to

$$\left(\frac{S}{N}\right)_{\text{array}} = \sqrt{N_{\text{tel}} N_{\text{pol}}} \left(\frac{S}{N}\right)_{\text{single}} = \sqrt{N_{\text{tel}} N_{\text{pol}}} \frac{T_{\text{ant}}^{\text{pb}}}{T_{\text{min}}}.$$
(6.40)

For a given telescope, the detectability for S/N=5 depends on the primary beam angle $\theta_{\rm pb}$ setting $\Omega_{\rm pb}$ in Eq. (6.35), on the effective area $A_{\rm eff}$ in Eq. (6.37), the observation bandwidth and duration ΔB , $t_{\rm obs}$ and on the system temperature $T_{\rm sys}$. For telescope arrays, additional parameters are given by the number of telescopes $N_{\rm tel}$, where we set $N_{\rm pol}=2$ in Eq. (6.40). The corresponding specifications of the different telescopes considered in this work are summarized in Table 6.1 [2]. We indicate the observable frequency ranges using the lowest and highest observable frequencies $f_{\rm min}, f_{\rm max}$ of the telescopes. In the special case of the ALMA telescope, we have simplified the frequency dependence of the system temperature due to the existence of different observation bands. The system temperatures of the ten frequency bands of ALMA are shown separately in Tab. 6.2 for completeness.

In the case of the LOFAR-LBA in the first column, we have set the primary beam angle to $\pi/3$ since the LBA dipole beam covers most of the sky above an elevation of $\sim 30^{\circ}$. In the case of FAST, $N_{\rm tel}$ indicates the number of beams of the single dish telescope and the effective area an primary beam angles depend on the wavelength $\lambda = c/f$ of observation. For simplicity, we have grouped different ALMA bands in Tab. 6.2 with same $T_{\rm sys}$ together.

To summarize the above approach, we determine if the antenna temperature in Eq. (6.37) of the respective accretion- and axion model $m_a, n, g_{a\gamma\gamma}$ is sufficient to yield a signal-to-noise ratio of $S/N \geq 5$ using Eq. (6.38) for FAST and Eq. (6.40) for LOFAR, ALMA and SKA with the parameters from Tab. 6.1 and Tab. 6.2. If we find $S/N \geq 5$ for a given axion model $m_a, n, g_{a\gamma\gamma}$, we consider the corresponding point in the parameter space of $m_a, g_{a\gamma\gamma}$ constrainable through

Parameter	LOFAR-LBA	FAST	SKA-Low / Mid	ALMA
f_{\min} [MHz]	10	1050	50	35k
$f_{\rm max} [{ m MHz}]$	90	1450	14k	950k
D_{tel} [m]	81.34	300	35 / 15	12
$N_{ m tel}$	40	19	911 / 200	50
$N_{ m pol}$	2	2	2	2
$t_{\rm obs}$ [hrs]	100	100	100	100
$T_{\rm rec} [{ m K}]$	10^{4}	24	40 / 20	
$T_{\rm sys}$ [K]	$T_{\rm rec} + T_{\rm bkg}$	$T_{\rm rec} + T_{\rm bkg}$	$T_{\rm rec} + T_{\rm bkg}$	90 to 3700
$A_{ m eff}$	$\min(16\lambda_{\rm obs}^2, 4500{\rm m}^2)$	$0.55 \pi (D_{\mathrm{tel}}/2)^2$	$0.8 \pi (D_{\mathrm{tel}}/2)^2$	$0.26\pi(D_{\rm tel}/2)^2$
$ heta_{ m pb}$	$\pi/3$	$1.02 \lambda_{ m obs}/D_{ m tel}$	$1.02 \lambda_{ m obs}/D_{ m tel}$	$1.02 \lambda_{ m obs}/D_{ m tel}$

Table 6.1: Specifications of different radio telescopes: LOFAR-LBA [270, 271], FAST [272, 273], SKA [276, 277, 280] and ALMA [274, 275] taken from Ref. [2]. For ALMA, the range of $T_{\rm sys} \in [90\,{\rm K}, 3700\,{\rm K}]$ is due to the ten different frequency bands in the range of [35 GHz, 950 GHz], see Tab. 6.2. The parameters are not chosen to maximize detectability but to offer comparable estimates of the achieved sensitivity. The quantities $f_{\rm min}$, $f_{\rm max}$ indicate the observable frequency ranges, $D_{\rm tel}$ is the telescope diameter, $\lambda_{\rm obs}$ the observed wavelength and the remaining parameters are defined in accordance with the main text.

Frequency Band	Frequency Range [GHz]	$T_{\rm sys}$ [K]
B1	[35, 50]	90
B2 - B3	[67, 116]	200
B4 - B7	[125, 373]	400
B8	[385, 500]	870
B9	[602, 720]	2200
B0	[787, 950]	3700

Table 6.2: ALMA specifications from Tab. 6.1 and Ref. [2] for the ten different frequency bands under consideration [274, 275]. Frequency ranges of the respective bands are given in units of GHz, together with the different system temperatures $T_{\rm sys}$ in units of Kelvin. Where possible, bands with same system temperature have been grouped together.

(non-)observation of the expected radio signals. We do not perform the data analysis looking for AS radio lines in this work and continue our evaluation by demonstrating the resulting constraints for the external accretion models in the next section.

6.5.2 Constraints from External Accretion

Starting with the conservative (left) and enhanced (right) external MC accretion models from Eq. (6.22) and Eq. (6.23), Fig. 6.8 shows the parameter regions of $m_a, g_{a\gamma\gamma}$, where the observed signal-to-noise ratio from resonating axion stars following Eq. (6.34) is $S/N \geq 5$. The resulting plots only show the potential constraints that can be inferred through simple comparison of $S_{\star,\text{tot}}$ with galactic backgrounds, while neglecting experimental constraints like the observable frequency range $[f_{\text{min}}, f_{\text{max}}]$ from Tab. 6.1. For comparison, we also plot existing laboratory and astrophysical constraints on the axion-photon coupling in gray shades. To indicate experimental

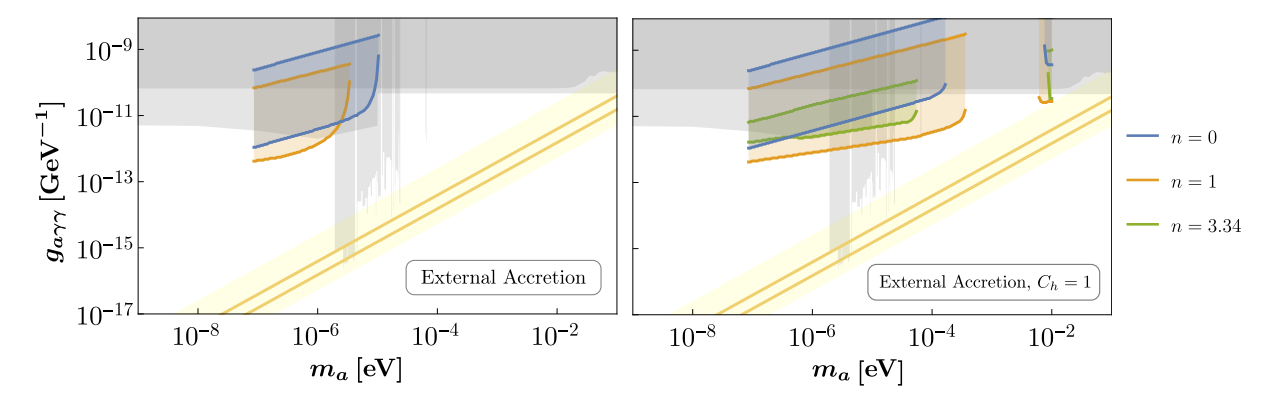


Figure 6.8: Potential constraints inferred from the external accretion model for different axion models m_a, n with couplings $g_{a\gamma\gamma}$ in the range $m_a = 10^{-7} \,\mathrm{eV} - 10^{-2} \,\mathrm{eV}$, taken from Ref. [2]. In this simple background comparison, the spectral flux densities $S_{\star,\mathrm{tot}}(m_a)$ from Fig. 6.6 and Eq. (6.22) are compared to the background spectral flux density from Eq. (6.28), requiring $S/N = S_{\star,\mathrm{tot}}^{\mathrm{pb}}/S_{\mathrm{bkg}} \geq 5$. Dark shades correspond to existing constraints and the yellow band represents the couplings of QCD axion models.

limitations of terrestrial telescopes, we impose an additional low- m_a cutoff at the radio window boundary of $f = 10 \,\mathrm{MHz}$, which corresponds to $m_a \simeq 10^{-7} \,\mathrm{eV}$. The colored regions indicate the potential constraints that can be inferred for different $m_a, g_{a\gamma\gamma}$ at a given n.

In both panels of Fig. 6.8, the constrainable regions differ depending on n, where the n=3.34 case in the left panel vanishes completely. The scaling of the flux density $S_{\star,\text{tot}}$ with the temperature index n is generally difficult to trace, since it incorporates several interdependent effects. These effects include the different mass cutoffs of the resonating MCMF in Eq. (6.2), Eq. (6.3), the dependence of the accretion rates in Eq. (6.14), Eq. (6.16) on m_a , n and the varying scalings of $\mathcal{N}_{\gamma,\text{tot}}$, $M_{\star,\gamma}$, $\max(M_{\star})$ with m_a , n, $g_{a\gamma\gamma}$ in Eq. (6.4) and Eq. (4.61).

The same statement remains true for the upper and lower boundaries of the potential constraints with respect to the range in $g_{a\gamma\gamma}$. More specifically, the high- $g_{a\gamma\gamma}$ regions are excluded because the resonance mass $M_{\star,\gamma} \propto 1/g_{a\gamma\gamma}$ drops below the predicted mass range of the ASMF, $M_{\star,\gamma} < \min(M_{\star})$. In such cases, we drop the resulting signal due to violation of the (initial) core-halo relation in Eq. (3.57) - except for the enhanced internal model from Eq. (6.26), which uses a modified mass relation altogether. Similarly, the lower boundaries of the potential constraints in $g_{a\gamma\gamma}$ appear when the decay mass exceeds the maximum core mass $M_{\star,\gamma} > \max(M_{\star})$ of the ASMF. This can either appear for $M_{\star,\gamma} > M_{\star,\lambda}$ or earlier for lower values of n with smaller high-mass cutoffs \mathcal{M}_{max} of the MCMF in Eq. (3.46).

Further comparing the conservative and enhanced external scenarios in the left and right panel of Fig. 6.8, it can be seen that the axion masses, where the potential constraints start to vanish, are larger for the enhanced model. This observation coincides with expectations from the enhanced flux densities in Fig. 6.6. In agreement with the scalings of $S_{\star,\text{tot}}(m_a)$ and $S_{\text{bkg}}(m_a)$ in Fig. 6.6, the external flux densities drop below the backgrounds around $m_a \sim 10^{-6} \,\text{eV}$, while the spectral fluxes of the enhanced model with $C_h = 1$ only vanish around the CMB peak around $m_a \sim 10^{-3} \,\text{eV}$. The same scalings between signal and background are also responsible for the appearance of the narrow regions at $m_a \lesssim 10^{-2} \,\text{eV}$ in the right panel of Fig. 6.8.

We conclude that the simple background comparison of the two flux densities at $S/N \geq 5$ demonstrates the potential for new constraints around the parameter regions $m_a \sim 10^{-6} \, \mathrm{eV}$,

 $g_{a\gamma\gamma}\sim 10^{-12}\,{\rm GeV^{-1}}$ and $m_a\sim 10^{-4}\,{\rm eV},~g_{a\gamma\gamma}\sim 10^{-11}\,{\rm GeV^{-1}}$ for the enhanced external accretion model in the right panel of Fig. 6.8. The next step is to examine the experimentally

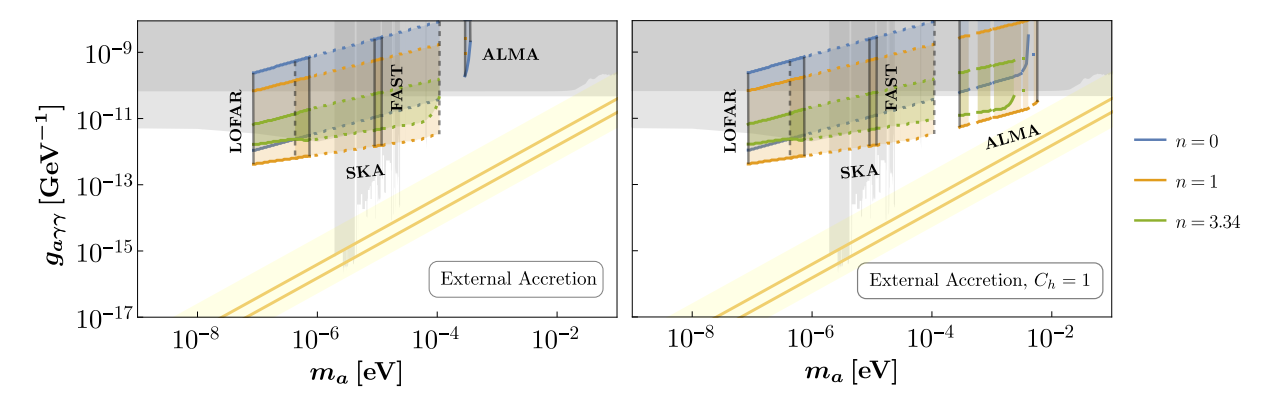


Figure 6.9: Potential constraints inferred from the external accretion model in Eq. (6.22) by comparing our signals in Fig. 6.6 with the sensitivities of different telescopes in Tab. 6.1. The spectral flux density $S_{\star,\text{tot}}(m_a)$ is translated into the antenna temperature $T_{\text{ant}}^{\text{pb}}$ in Eq. (6.37) and compared to the minimum observable temperature T_{min} in Eq. (6.39), requiring $(S/N)_{\text{array}} \geq 5$. SKA constraints are denoted by dotted lines, while all others are represented by solid lines. ALMA constraints appear as narrow strips due to the six sets of frequency bands, which have gaps between them. Dark shades correspond to existing constraints and the yellow band represents the couplings of QCD axion models. Taken from Ref. [2].

motivated comparison of the representative telescope properties from Tab. 6.1, for $S/N \geq 5$ following Eq. (6.38) and Eq. (6.40). Fig. 6.9 shows the resulting potential constraints which can be inferred with the existing telescopes LOFAR, FAST and ALMA in solid lines and with the upcoming SKA telescope in dotted lines. Same as in Fig. 6.8, colored shades denote excludable regions for different n, gray shades demonstrate existing constraints and the yellow band indicates the QCD axion parameters m_a and $g_{a\gamma\gamma}$ in eV and GeV⁻¹ respectively. Note here that overlapping regions in m_a , $g_{a\gamma\gamma}$ can amount to different axion models due to the color-dependence of n.

Overall Fig. 6.9 demonstrates the same behavior with the axion mass range being constrained by experimental limitations and the range of $g_{a\gamma\gamma}$ constrained by the scaling of $M_{\star,\gamma}$ with the cutoffs $\min(M_{\star})$, $\max(M_{\star})$ of the ASMF. The major difference compared to the simple background comparison is given by the increased range of the potential constraints in m_a and specifically the appearance of the n=3.34 models in the left panel of Fig. 6.9. The reason for this increased detectability in radio telescopes is given by the narrow spectral shape of the expected line signal, which can be distinguished from the smooth, broad emission from galactic backgrounds.

Comparing the two accretion scenarios in the left and right panel of Fig. 6.9, the accretion model-dependence of the potential constraints is reduced compared to Fig. 6.8, so that the enhanced external accretion with $C_h = 1$ only allows for an extension to the high- m_a range, which can be probed with ALMA. With respect to new constraints, the overall potential in Fig. 6.9 is qualitatively similar to that from the background comparison in Fig. 6.8 - apart from the improved coverage of ALMA around $m_a \sim 10^{-3} \, \text{eV}$ and $g_{a\gamma\gamma} \sim 10^{-11} \, \text{GeV}^{-1}$. We conclude that again, the AS line emission is either prevented by the high-mass cutoffs $M_{\star,\gamma}$, $\min(M_{\star})$, and

 $\max(M_{\star})$ or significantly larger than the background flux density $S_{\rm bkg}(m_a)^5$. For both accretion scenarios and sensitivity approaches, new experimental constraints can be inferred from dedicated searches for line emission around frequencies corresponding to $m_a \sim 10^{-6} \, {\rm eV}$ and $10^{-5} \lesssim m_a \lesssim 10^{-2} \, {\rm eV}$.

6.5.3 Constraints from Internal Accretion

In this chapter we perform an equivalent analysis of the two sensitivity approaches for the internal accretion models from Eq. (6.25) and Eq. (6.27). Like before we set the signal-to-noise ratio to $S/N \geq 5$ as a requirement for both the potential constraints in Fig. 6.10 and Fig. 6.11, which show the excludable regions inferred from the background comparison in Eq. (6.34) and Eq. (6.38), Eq. (6.40) respectively.

We begin by evaluating the simple background comparison for the internal accretion rates with the canonical core-halo relation $M_{\star} \propto \mathcal{M}^{1/3}$ in the left, and the modified mass relation with $M_{\star} \sim \mathcal{M}$ in Eq. (6.26) in the right panel of Fig. 6.10. Note here the intersections between

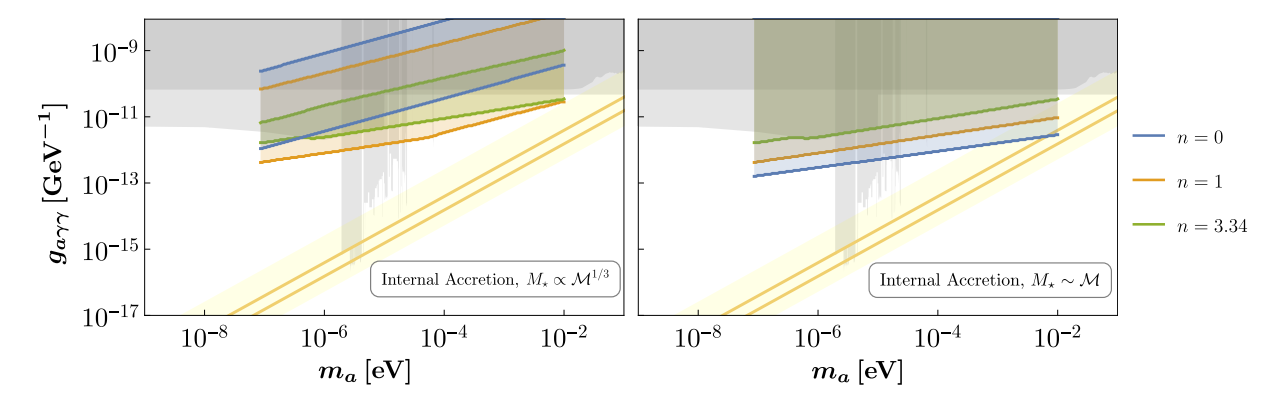


Figure 6.10: Potential constraints inferred from the internal accretion model with $M_{\star} \propto \mathcal{M}^{1/3}$ from Eq. (3.57) and $M_{\star} \sim \mathcal{M}$ from Eq. (6.26) for different $m_a, n, g_{a\gamma\gamma}$. In this simple background comparison, the spectral flux densities $S_{\star,\text{tot}}(m_a)$ from Fig. 6.7 and Eq. (6.25) are compared to the background spectral flux density from Eq. (6.28), requiring $S_{\star,\text{tot}}^{\text{pb}}/S_{\text{bkg}} \geq 5$. Dark shades correspond to existing constraints and the yellow band represents the couplings of QCD axion models. Taken from Ref. [2].

the color-shaded regions and the yellow QCD axion band in the right panel of Fig. 6.10 do not correspond to QCD axion models since the different ALP models have differing values of n. As mentioned before, the condition $M_{\star,\gamma} < \min(M_{\star})$ is not accounted for in the enhanced model due to the absence of a low-mass cutoff equivalent to $\mathcal{M}_{h,\min}$, which is why the potential constraints in the right panel extend to the largest $g_{a\gamma\gamma}$ compared to the other three accretion scenarios. While the high- $g_{a\gamma\gamma}$ region presents an uncertainty in our different approaches, its impact on the observational constraints is negligible since the corresponding couplings are already excluded by helioscopes and other experiments in gray.

Another important difference between the two core-halo scalings of the internal model in Fig. 6.10 is given by the inverted hierarchy of the lower boundaries in $g_{a\gamma\gamma}$ at different colors n. While the n=1 constraints extend to the lowest values of the axion-photon coupling for $M_{\star} \propto \mathcal{M}^{1/3}$ in

⁵This observation indicates that the impact of the chosen value S/N = 5 is low compared to the other effects mentioned in the main text of this section.

the left panel, the enhanced model with $M_{\star} \sim \mathcal{M}$ on the right has n=0 models reaching lower values of $g_{a\gamma\gamma}$. The explanation for this behavior is an increased benefit from having large numbers of low-mass miniclusters with $\mathcal{M} \sim \mathcal{M}_0$ in the n=0 case. Effectively, the mass relation in Eq. (6.26) removes the low-mass cutoff $\mathcal{M}_{h,\text{min}}$ in Eq. (6.2) and alleviates the low-mass cutoff \mathcal{M}_{γ} substantially. This modification increases the importance of the total number of miniclusters $\mathcal{N}_{\text{mc,tot}}$ for the observed flux over the range of their high-mass tail $\mathcal{M}_0 \leq \mathcal{M} \leq \mathcal{M}_{\text{max}}$. For a similar reason, the overall signal strength of the internal models is enhanced compared to the external cases, which leads to the extended ranges of inferable constraints in the colored regions of Fig. 6.10 compared to Fig. 6.8. The increase in magnitude of the predicted

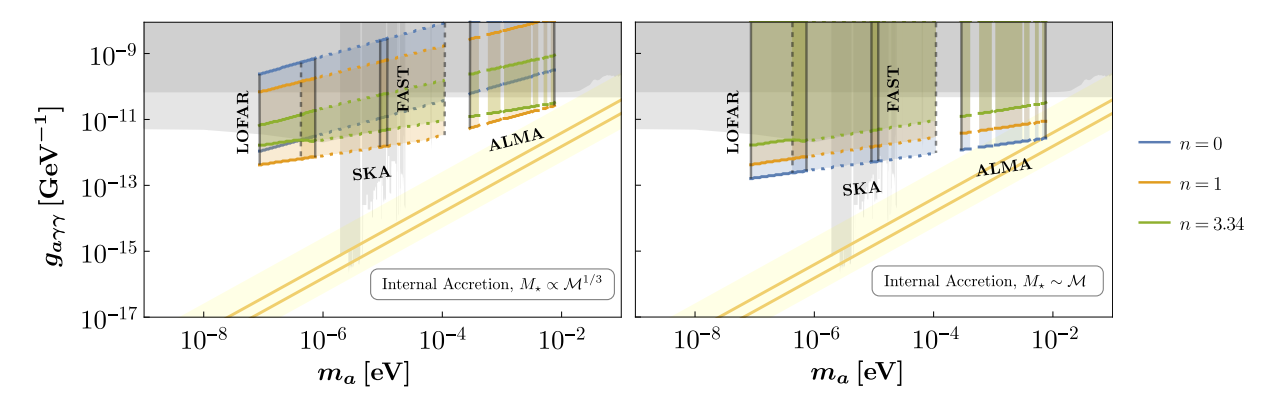


Figure 6.11: Potential constraints for the internal accretion model in Eq. (6.25) with $M_{\star} \propto \mathcal{M}^{1/3}$ from Eq. (3.57) and $M_{\star} \sim \mathcal{M}$ from Eq. (6.26). Inferred by comparing our signals in Fig. 6.7 with the sensitivities of different telescopes in Tab. 6.1, requiring $(S/N)_{\text{array}} \geq 5$. SKA constraints are denoted by dotted lines, while all others are represented by solid lines. ALMA constraints appear as narrow strips due to the six sets of frequency bands, which have gaps between them. Dark shades correspond to existing constraints and the yellow band represents the couplings of QCD axion models. Taken from Ref. [2].

flux density $S_{\star,\text{tot}}$ is also responsible for the fact that the telescope sensitivity approach does not considerably improve the excludable parameter space in Fig. 6.11 - apart from the largest couplings $g_{a\gamma\gamma}$, which are already ruled out.

Especially in the case of the internal and enhanced external accretion scenarios, the nature of the predicted AS signals is best understood in terms of an on-off-pattern: Either the resonance mass $M_{\star,\gamma}$ is present in the ASMF of a given axion model $m_a, n, g_{a\gamma\gamma}$ and the resulting signal becomes detectable, or $M_{\star,\gamma}$ lies below or above the mass range of the ASMF and no signal is expected.

To summarize, the numerically motivated internal exclusion models provide enhanced accretion rates and resulting flux densities $S_{\star,\text{tot}}$, which can be measured using earth-based experiments for a wide range of axion models $m_a, n, g_{a\gamma\gamma}$. Similar to the prospects inferred from the enhanced external model in Fig. 6.9, both internal accretion models can be used to provide novel constraints on the axion-photon coupling $g_{a\gamma\gamma}$ for axion masses in the ranges $m_a \sim 10^{-6} \,\text{eV}$ and $10^{-5} \lesssim m_a \lesssim 10^{-2} \,\text{eV}$.

6.5.4 Directional Dependence of resonant Emission

As emphasized before, the potential constraints in Subsec. 6.5.2 and Subsec. 6.5.3 need to be combined with dedicated radio line searches in order to obtain actual information on the parameter space of the axion-photon coupling $g_{a\gamma\gamma}$. On the experimental side, a dedicated analysis of astronomical radio data may require careful identification of galactic foregrounds, backgrounds and specifically an identification of atomic and molecular transition lines, which could exhibit similar features to our signal predictions. While we do not perform an analysis of the corresponding radio data in this work, we present additional information on the directional dependence of the signal, which should prove helpful in the development of future search strategies for galactic AS line emission.

The spatial distribution of galactic ASMC systems (and the background density $\rho_{a,f}(r)$ in the external accretion model) follows the spherically symmetric NFW profile of the Milky Way. It is therefore possible to express the simplified directional dependence of the total emitted flux $F_{\star,\text{tot}}$ in terms of the observed polar angle $\theta_{\rm E}$ on earth. For this, we assume the earth to be aligned with the galactic plane as shown in the right panel of Fig. 6.12. Defining the flux density, which

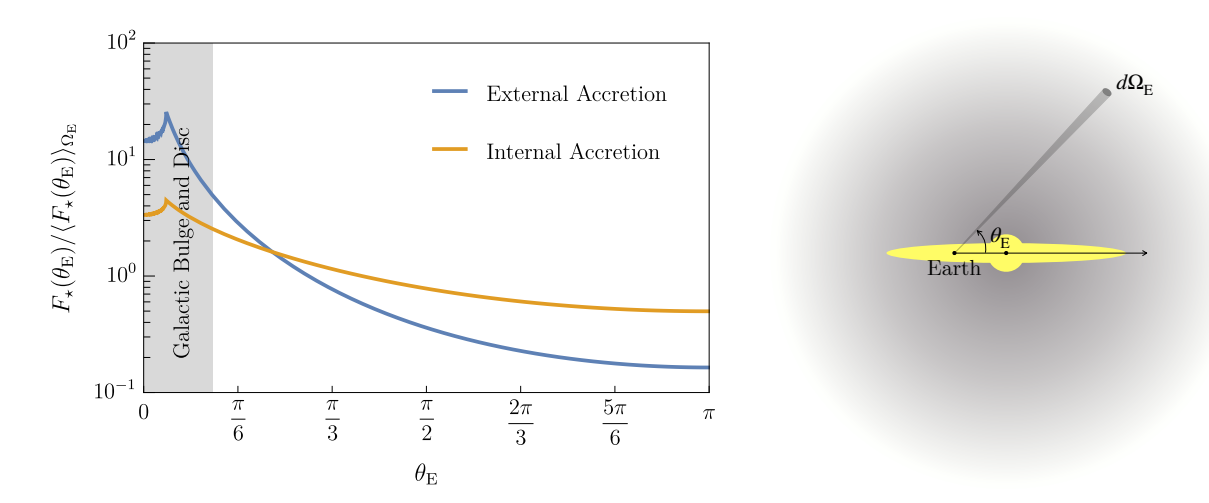


Figure 6.12: Left: Flux density per solid angle as a function of the polar angle θ_E at the earth, normalized by its average value, $F_{\star,\text{tot}}/(4\pi)$. The blue line shows the directional dependence of the external accretion models from Eq. (6.22), Eq. (6.23), while the orange line shows the angular dependence of the internal accretion model in Eq. (6.25). Gray shades represent the observing direction towards the galactic bulge, where galactic foregrounds could easily overwhelm the expected signals. Right: Schematic representation of the observation angle θ_E at earth with the NFW DM halo in gray shades and the galactic disc and bulge in yellow. Both taken from Ref. [2].

is observed within a solid angle $d\Omega_{\rm E}$ at polar angle $\theta_{\rm E}$, as $F_{\star,\rm E}(\theta_{\rm E})d\Omega_{\rm E}$ gives the flux density per solid angle $F_{\star,\rm E}(\theta_{\rm E})$ along the line of sight.

We plot the angular dependence of the flux density per solid angle $F_{\star,E}(\theta_{\rm E})$ in the left panel of Fig. 6.12, where blue and orange lines indicate the external and internal accretion models in Eq. (6.22) and Eq. (6.25) respectively. The quantity $F_{\star,E}(\theta_{\rm E})$ in Fig. 6.12 is normalized by the

sky-averaged flux density

$$\langle F_{\star}(\theta_{\rm E})\rangle_{\Omega_{\rm E}} \equiv \frac{1}{4\pi} \int d\Omega_{\rm E} F_{\star}(\theta_{\rm E}) = \frac{1}{4\pi} F_{\star,\rm tot}$$
 (6.41)

and the polar angle $\theta_{\rm E}$ is given in unit of radians. Gray shades in Fig. 6.12 indicate the galactic center at $r\lesssim 3\,{\rm kpc}$, where the NFW-distributed dark matter density yields the largest flux densities. Note that here $F_{\star,\rm E}(\theta_{\rm E})$ peaks at $\theta_E>0$ due to the applied survival cutoff $R_{\rm surv}$ from Eq. (3.54), which prevents the existence of gravitationally bound miniclusters in the galactic bulge.

Effectively, the direction dependent flux density $F_{\star,\rm E}(\theta_{\rm E})$ depends on the product of the total number of resonating axion stars $\mathcal{N}_{\gamma,\rm tot}$ and on the model-dependent accretion rate $\delta M_{\star}/\delta t$. The different slopes of the two curves in Fig. 6.12 can be explained by the additional dependence of the external accretion rate $\delta M_{\star}/\delta t$ in Eq. (6.14) on the background density $\rho_{a,f}(r)$. While the flux in the internal model is proportional to $\rho_{\rm NFW}(r)$ through the total number of objects given by the spatial number density $dn/d\mathcal{M}(r)$, the external model has a quadratic dependence $F_{\star,\rm tot} \propto \rho_{\rm NFW}(r)^2$ due to the additional background dependence of $\delta M_{\star}/\delta t$.

Importantly for future searches, the normalized angular flux density $F_{\star,E}(\theta_{\rm E})$ in Fig. 6.12 is of order one or above for $\theta_{\rm E} \lesssim \pi/3$. Telescopes in AS line searches may hence be pointed away from the galactic plane and towards polar angles of $\theta_{\rm E} \simeq \pi/3$, which allow for a significant reduction of galactic foregrounds. This is especially promising because the direction-dependent flux density in these directions is $F_{\star}(\theta_{\rm E}) \gtrsim F_{\star,{\rm tot}}/(4\pi)$, which renders our constraint predictions from Subsec. 6.5.2 and Subsec. 6.5.3 essentially valid also for $\theta_{\rm E} \simeq \pi/3$.

6.6 Outlook on Axion Star Radio Lines

In this chapter, we have combined knowledge on the present-day MCMF and ASMF from Sec. 4.7 with different predictions for the mass growth of axion star cores in our galaxy. For axion-photon couplings $g_{a\gamma\gamma}$, which render the axion star resonance mass $M_{\star,\gamma} < M_{\star,\lambda}$ smaller than the critical mass of the axion self-interaction λ , the accretion rates of the solitonic core lead to significant radio line emission at the solar position. As shown in Subsec. 6.5.2 to Subsec. 6.5.4, the predicted spectral flux densities are either non-existing or overwhelmingly strong compared to the galactic background emission from Subsec. 6.5.1.

For all of the four accretion scenarios discussed in this work, we find that new constraints on the axion-photon coupling can be inferred for parameters in the range $10^{-7} \,\mathrm{eV} \lesssim m_a \lesssim 10^{-5} \,\mathrm{eV}$ and $g_{a\gamma\gamma} \sim 10^{-11} \,\mathrm{GeV}^{-1}$, with additional dependence on the temperature evolution index n. In the case of the enhanced external and for both internal accretion models, additional exclusion potential is predicted in the range $10^{-5} \,\mathrm{eV} \lesssim m_a \lesssim 10^{-3} \,\mathrm{eV}$ and $g_{a\gamma\gamma} \gtrsim 10^{-11} \,\mathrm{GeV}^{-1}$. Most importantly, all of these parameter regions can be probed by existing radio telescopes, with the specific examples given for LOFAR, FAST, ALMA and the upcoming SKA telescope.

We have also briefly explored the directional dependence of the predicted flux densities in Subsec. 6.5.4 and found that the approximate isotropy of our signal at large polar angle $\theta_{\rm E}$ can be used to avoid galactic foreground emission while keeping an order-on intensity of the desired AS signal. Future experimental searches and additional analysis of existing radio data can directly combine observational evidence with our predictions to infer new constraints covering a significant region of currently unconstrained parameter space in $m_a, g_{a\gamma\gamma}$.

This finding is especially promising considering the fact that our modeling of the linear growth MCMF in Subsec. 3.6.2 and the use of the $z=z_{\rm eq}$ core-halo relation with $M_{\star} \propto \mathcal{M}^{1/3}$ have been conservative approaches to the late-time predictions of axion star mass distributions. More specifically, our predicted signals can potentially be boosted by additional considerations of the following effects:

- 1. The non-linear evolution of the galactic minicluster population
- 2. The consideration of the long-time mass growth of solitonic cores, which is predicted to reach substantially increased masses, $M_{\star} \sim \mathcal{M}$ for $\lambda = 0$ in simulations, see Sec. 4.3
- 3. A combined consideration of the mass growth of axion stars due to both internal and external MC accretion, which we have treated separately for simplicity
- 4. The possible survival of systems with $M_{\star} \geq M_{\star,\lambda}$, which we have neglected

Next to these major effects, which are expected to enhance the intensity of the radio emission, there are also other effects, which can reduce the radio emission and abundance of resonating systems, namely

- 1. The radio conversion efficiency $\eta_{a\gamma\gamma}$ of the resonating axion stars, which is assumed to be of order one
- 2. The time modulation of the signal described by $\eta_{a\gamma\gamma}$, which could reduce the background emission if the burst duration $\delta t_{\gamma} \ll 1/\Gamma_{\star,\gamma}$ is much smaller than the inverse rate of galactic axion bursts $\Gamma_{\star,\gamma}$ for a given model $m_a, n, g_{a\gamma\gamma}^{\ 6}$
- 3. The long-time survivability of galactic ASMC systems due to the combined
 - Parametric resonance at $M_{\star,\gamma}$
 - Self-interaction instability at $M_{\star,\lambda}$
 - \mathcal{M} -, r- and Φ -dependent tidal disruption in stellar encounters

We emphasize that according to our findings, the above effects should rather enhance than decrease the signals obtained from our conservative predictions. The process of radio emission from resonating axion stars in our galaxy hence provides a compelling mechanism to probe currently unexplored axion models. For future studies, our results can be combined with improved modeling of the evolution of miniclusters, axion stars and the triggering of the instabilities at $M_{\star,\gamma}$, $M_{\star,\lambda}$ to reinforce and extend the potential constraints presented in this chapter. We emphasize that especially the Φ -dependence of the AS mass growth rates and core-halo mass relation from Ref. [240] and Ref. [169] require further investigation. Lastly, for axion masses below $m_a \sim 10^{-7} \, \mathrm{eV}$, space-borne radio telescope can theoretically be used additionally to constrain even smaller values of $g_{a\gamma\gamma}$ and m_a .

⁶We do not perform the corresponding calculations due to a lack of numerical data on the signal duration δt_{γ} for different axion models $m_a, n, g_{a\gamma\gamma}$ and AS masses $M_{\star,\gamma}$.

Galactic Axion Novae

In the previous chapter, we have developed different accretion models for composite ASMC systems and investigated how the parametric instability at $M_{\star,\gamma}$ can lead to the emission of radio line signals at $M_{\star} \geq M_{\star,\gamma}$. The potential constraints in Sec. 6.5 remain true as long as $M_{\star,\gamma} < M_{\star,\lambda}$, whereas in the second case $M_{\star,\gamma} > M_{\star,\lambda}$, which amounts to relatively weak axion-photon couplings, the self-interaction instability develops before the AS resonance. For completeness and complementary to Chap. 7, we treat the observational consequences of the second scenario $M_{\star,\gamma} > M_{\star,\lambda}$ in more detail in this chapter. The results presented in the following are taken from Ref. [3].

Opposed to the radio line emission from resonating axion stars, the relativistic axion bursts from galactic bosenovae can not be straight-forwardly probed by existing experiments. The results of this chapter hence provide an incentive for the development of new experimental techniques for the detection of galactic axion bursts. Due to the lack of adequate observational methods at the time of writing, our treatment of the galactic bosenova rates is further simplified and less elaborate compared to the evaluation of galactic radio signals in Chap. 6. Our approximate modeling of the AS core collapse rates relies on conservative assumptions, for which we indicate possible extensions and improvements for future research at the end of this chapter.

As before, we use the galactic MCMF and ASMF from Subsec. 3.6.2 and Sec. 4.7 with a slope index $\alpha = -1/2$ and for the \mathcal{M}_0 -cutoff of the MCMF in Eq. (3.47). This means that we neglect the low-mass component of the galactic minicluster population $\mathcal{M} < \mathcal{M}_0$ since the corresponding soliton cores are the furthest away from reaching the relevant critical mass $M_{\star,\lambda}$. For simplicity, we ignore any effects of the parametric resonance at $M_{\star,\gamma} > M_{\star,\lambda}$ on the population of galactic AS cores and consider only the emission of relativistic particles from the bosenova collapse according to Sec. 4.4 and Ref. [35]¹.

For the mass growth of the AS cores, we employ the *internal accretion* model from Sec. 6.3, since it provides the largest and numerically most motivated accretion rates of the different approaches in Chap. 6. Same as in previous sections, we consider the parameters \mathcal{M}, Φ, r to be independent of each other, where \mathcal{M} is determined from the MCMF at each axion model m_a, n with $10^{-12} \,\mathrm{eV} \le m_a \le 10^{-2} \,\mathrm{eV}$ and modified temperature indices $n = 1, 2, 3.34^2$. The remaining assumptions about the survival probability of miniclusters at different r and Φ are identical to previous chapters, see Eq. (3.54), Eq. (3.56).

We summarize the modified mass growth modeling that describes the abundance of galactic bosenovae in Sec. 7.1 and combine it with the generalized sensitivity criteria from Ref. [36] to measure the expected detectability of these events in Sec. 7.2. The resulting observable

¹Note here that in the physical context and away from the case $M_{\star,\lambda} \ll M_{\star,\gamma}$, a multi-messenger signal involving both radio and axion emission is expected, see Ref.s [31, 253, 257, 258].

²We do not consider temperature-independent axion masses n=0 here since for n<1, our predictions are significantly diminished due to the non-existence of heavy axion stars with $M_{\star} \lesssim M_{\star,\lambda}$ in the ASMF, see Fig. 4.14.

parameter range in m_a depends strongly on the nature of the utilized axion coupling in a given experiment. We calculate the corresponding collapse rates in Sec. 7.3 and Sec. 7.4 and use them to infer the number of detectable bosenovae occurring within an observation time of $t_{\text{obs}} = 1 \text{ yr}$.

7.1 Mass Growth Modeling

In the context of accreting ASMC systems, the predicted number of galactic bosenovae depends mainly on three quantities: the observation time $t_{\rm obs}=1$ yr, the minicluster mass \mathcal{M} determining M_{\star} and its initial overdensity parameter Φ . As in previous chapters, we integrate over the MC mass \mathcal{M} obtained from the MCMF and over $\Phi \in (0, 10^4]$, with the probability distribution $p_{\Phi}(\Phi)$ from Eq. (3.27) and survival probability $\mathcal{P}_{\rm surv}(\Phi)$ from Eq. (3.56). We employ the internal MC accretion rate from Eq. (4.42) with the canonical core-halo relation in Eq. (3.57), where the resulting mass growth is determined by \mathcal{M}, Φ and M_{\star} at given m_a, n respectively. Integrating the MCMF over \mathcal{M}, Φ and the galactocentric radius r, the remaining quantities to be determined are the corresponding low- and high-mass cutoffs of the collapsing AS population of the Milky Way.

In the context of bosenovae, a straight-forward choice for the high-mass cutoff is given by the maximum core mass at t=0, which can be estimated from the $z=z_{\rm eq}$ core-halo relation according to

$$\mathcal{M}_{\lambda,\text{max}} = \min(\mathcal{M}_{\text{max}}, \mathcal{M}_{\lambda}), \qquad (7.1)$$

where the minicluster mass $\mathcal{M}_{\lambda} = \mathcal{M}(M_{\star,\lambda})$ is obtained by inverting Eq. (3.57). Note here that the above high-mass cutoff is conservative in the sense that it neglects the long-time accretion of axion stars, which likely sets $\mathcal{M}_{\lambda,\max} = \mathcal{M}_{\lambda}$ at present-day redshift. The low-mass cutoff on the other hand needs to be inferred from the minimum core mass $M_{\star,\text{acc}}$, which can reach the critical mass $M_{\star,\lambda}$ after continuous mass growth over t_{obs} . In general, this minimum core mass needs to be determined by considering the whole range of minicluster masses \mathcal{M} for each value of Φ and for each axion model m_a, n .

To increase computational efficiency, we adopt a simplified approach for the determination of $M_{\star,\mathrm{acc}}$, which can be motivated by means of the time dependence of the internal accretion rate in Fig. 4.7. An important observation in this figure is the fact that the accretion rate obtained from Eq. (4.42) decreases monotonically with increasing M_{\star} for a given $\mathcal{M}, \Phi, \epsilon$. Accordingly, the mass growth rate of galactic axion stars with attractive self-interactions reaches its minimum at the largest stable mass $M_{\star} = M_{\star,\lambda}$.

Furthermore, the high-mass tail of the MCMF with $\mathcal{M} > \mathcal{M}_0$ provides a major contribution to the number of miniclusters hosting an AS core close to the critical mass $M_{\star} \sim M_{\star,\lambda}$. Due to the scaling $M_{\star} \propto \mathcal{M}^{1/3}$ of the core-halo relation in Eq. (3.57), these near-critical ASMC systems exhibit very small values of M_{\star}/\mathcal{M} (see also Fig. C.4, Fig. C.2), which renders the AS accretion rate $\delta M_{\star}/\delta t \propto \mathcal{M}/\tau_{\rm gr} \propto 1/\mathcal{M}$ in Eq. (4.42) smaller for larger \mathcal{M} . Together, the above observations lead us to take the simplifying but conservative assumption that every axion star accretes with a rate similar to that of a critical ASMC system, i.e. $\delta M_{\star}/\delta t \sim \delta M_{\star}(\mathcal{M}_{\lambda}, M_{\star,\lambda}, \Phi)/\delta t$. Under this assumption, we can extrapolate the minimum AS mass, which reaches criticality over

Under this assumption, we can extrapolate the minimum AS mass, which reaches criticality over an observation time t_{obs} as a function of Φ , which gives

$$M_{\star,\mathrm{acc}}(\Phi, t_{\mathrm{obs}}) = M_{\star,\lambda} - \frac{\delta M_{\star}(\mathcal{M}_{\lambda}, M_{\star,\lambda}, \Phi)}{\delta t} t_{\mathrm{obs}},$$
 (7.2)

at the critical mass $M_{\star,\lambda}$ and corresponding MC mass \mathcal{M}_{λ} , where the internal growth rate reaches its lowest value. We derive the corresponding minicluster threshold mass corresponding to the AS mass $M_{\star,\mathrm{acc}}$ from the core-halo relation, i.e.

$$\mathcal{M}_{\lambda,\mathrm{acc}} \equiv \mathcal{M}(M_{\star,\mathrm{acc}})$$
. (7.3)

For typical miniclusters with $\Phi \sim 1$, $\mathcal{M}_{\lambda,\mathrm{acc}}$ in Eq. (7.3) provides the dominant low-mass cutoff of the ASMF. However at the largest overdensities $\Phi \sim 10^4$, the internal accretion rates $\delta M_{\star}(\mathcal{M}_{\lambda}, M_{\star,\lambda}, \Phi)/\delta t$ can increase substantially so that the low-mass cutoffs of the MCMF become relevant. It is therefore important to consider the effective low-mass cutoff of a given ASMC system with overdensity parameter Φ to be composed out of the combination

$$\mathcal{M}_{\lambda,\min} \equiv \max[\mathcal{M}_{0,\min}, \mathcal{M}_{h,\min}, \mathcal{M}_{\lambda,acc}(\Phi, t_{obs})],$$
 (7.4)

where $\mathcal{M}_{0,\text{min}}$ is the \mathcal{M}_{0} -cutoff and $\mathcal{M}_{h,\text{min}}$ is the core-halo minimum mass threshold from Eq. (3.58). In this approach, any axion star with initial mass $M_{\star} \geq M_{\star,\text{acc}}(t_{\text{obs}})$ will accrete enough axion dark matter from its surrounding minicluster within a given time t_{obs} to become super-critical $M_{\star} \geq M_{\star,\lambda}$.

Note that in Eq. (7.4) we have neglected the AS radius cutoff, since for the densest MCs with $\Phi \sim 10^4$, the mass scaling of the canonical core-halo relation in Eq. (3.57) used to derive the AS radius cutoff in Eq. (4.70) can arguably be modified. A direct application of the AS radius cutoff would diminish the predicted collapse rates, because many of the densest MCs with $\Phi \gg 10$ would be removed from the sample. There are however physical considerations from which a modification of the cutoff scaling is expected.

Following the virialization condition $v_{\star, \text{vir}} \simeq v_{\text{mc,vir}}$ that can be used to derive the canonical core-halo scaling $M_{\star} \propto \mathcal{M}^{1/3}$, the virial velocity of the minicluster is generally a function of \mathcal{M} and Φ , since $v_{\text{mc,vir}} \simeq \sqrt{G\mathcal{M}/\mathcal{R}(\Phi)}$ according to Eq. (4.35) and Eq. (3.24). Tracing the scalings with Φ one obtains $v_{\text{mc,vir}} \propto \Phi^{2/3}$ for $\Phi \gg 1$, which implies that the increased central density ρ_{mc} increases the virial velocity of the total system. The above scaling would lead to an increased AS core mass and a relaxation of the AS radius cutoff in Eq. (4.70) compared to our considerations. In order to resolve this uncertainty, future studies can extend the numerical analysis of the core-halo mass relation performed in Ref. [169] to account for variable MC densities Φ .

Therefore neglecting the AS radius cutoff and using the effective ASMF cutoffs from Eq. (7.1), Eq. (7.4), the number of expected bosenovae expected in super-critical ASMC systems can be calculated from the MCMF according to

$$\mathcal{N}_{\text{Nova}}(t_{\text{obs}}) = 4\pi \int_{\text{R}_{\text{surv}}}^{R_{200}} dr \, r^2 \int_0^{10^4} d\Phi \, p_{\Phi}(\Phi) \mathcal{P}_{\text{surv}}(\Phi) \int_{\mathcal{M}_{\lambda, \text{min}}(\Phi, t_{\text{obs}})}^{\mathcal{M}_{\lambda, \text{max}}} d\mathcal{M} \, \frac{dn}{d\mathcal{M}}(r) \,, \tag{7.5}$$

where the lower boundary of the mass-integral has to be evaluated at each value of Φ in the distribution. From the scaling $\delta M_{\star} \propto \tau_{\rm gr}^{-1} \propto \Phi^4$ in Eq. (4.42), we can already see that the strongest contribution to $\mathcal{N}_{\rm Nova}$ is given by the densest miniclusters, which have $\Phi \lesssim 10^4$. In some extreme cases with $\Phi \approx 10^4$, the accretion rates can become large enough for $M_{\star,\rm acc}$ in Eq. (7.2) to reach negative values, when $\delta M_{\star}/\delta t \cdot t_{\rm obs} > M_{\star,\lambda}$. In the following, we drop the corresponding ASMC population with $\{\mathcal{M}, \Phi\}$ predicting $M_{\star,\rm acc} < 0$, due to uncertainties about their long-time stability. We also note that in principle, the AS cores of the heaviest miniclusters with $\mathcal{M} > \mathcal{M}_{\lambda}$, which we have neglected by applying Eq. (7.1), can additionally contribute to

the number of bosenovae through repeated collapse events.

For QCD axion parameters with n=3.34, $m_a=50\,\mu\text{eV}$, critical masses $M_{\star,\lambda}\simeq 2\cdot 10^{-13}\,M_\odot$ and $\mathcal{M}_{\lambda}\simeq 2\cdot 10^{-7}\,M_\odot$, we find that typical systems with $\Phi\simeq 1$ should have $\delta M_{\star}(\mathcal{M}_{\lambda},M_{\star,\lambda},\Phi)/\delta t\simeq 2\cdot 10^{-38}\,M_\odot\,\text{s}^{-1}$, which implies $M_{\star,\text{acc}}\approx M_{\star,\lambda}$. On the other hand, for the densest miniclusters with $\Phi\simeq 10^4$ we obtain $\delta M_{\star}(\mathcal{M}_{\lambda},M_{\star,\lambda},\Phi)/\delta t\simeq 10^{-22}\,M_\odot\,\text{s}^{-1}$, which gives $\delta M_{\star}/\delta t\cdot t_{\text{obs}}\simeq 4\cdot 10^{-15}\,M_\odot$ for the accreted mass in Eq. (7.3) after $t_{\text{obs}}=1\,\text{yr}$, corresponding to an order one percent mass growth.

We illustrate the total number of galactic bosenovae derived from Eq. (7.5) for three different values of n = 1, 2, 3.34 in Fig. 7.1. The sharp turn-arounds arise from the m_a -dependence of the

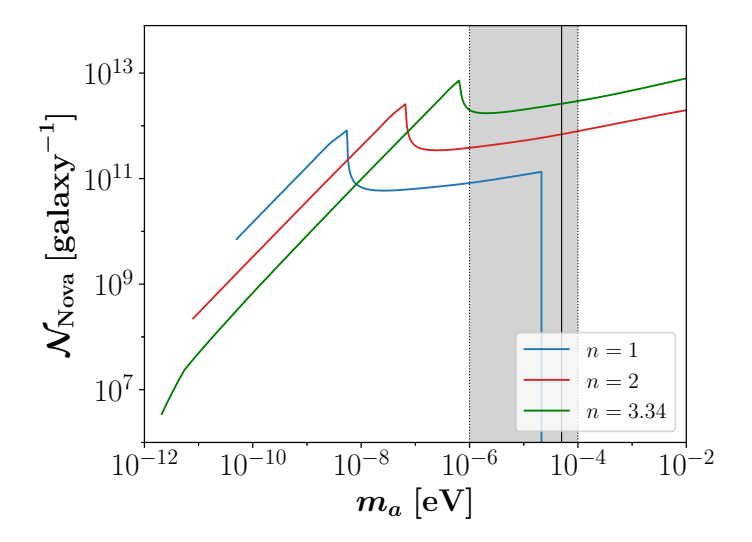


Figure 7.1: Predicted number of bosenovae occurring within the Milky Way DM halo for $t_{\rm obs} = 1$ yr for the \mathcal{M}_0 -cutoff, i.e. without the low- \mathcal{M} tail of the MCMF. Colors denote axion models with different temperature evolution n according to Eq. (2.34). As before, the gray shaded region denotes the cosmological QCD axion mass band with 10^{-6} eV $\leq m_a \leq 10^{-4}$ eV and the black solid vertical indicates the QCD axion mass $m_a \approx 50 \,\mu\text{eV}$ assumed in this work. Taken from Ref. [3]

accretion-induced low-mass cutoff $\mathcal{M}_{\lambda,\text{acc}}$ derived from Eq. (7.2) and from the cutoff-dependence of $\mathcal{M}_{\lambda,\text{min}}$, $\mathcal{M}_{\lambda,\text{max}}$ following Eq. (7.4) and Eq. (7.1). Notably, the number of galactic bosenovae increases with larger n. The different scaling of the peaks in Fig. 7.1 is related to two competing effects: First, the increased number of composite ASMC systems $\mathcal{N}_{\star,\text{tot}} \propto 1/\mathcal{M}_0$ for smaller n and \mathcal{M}_0 , and secondly the increased accretion rates for larger n.

The first of these effects is a direct consequence of the normalization of the MCMF, which is set to match the total DM mass of the Milky Way, hence $\mathcal{N}_{\text{tot}} \propto 1/\mathcal{M}_0$, where \mathcal{N}_{tot} is the total MC number (see Fig. 3.7 and Fig. C.3). The second effect on the other hand relates to the scaling of the critical mass $M_{\star,\lambda} \propto f_a$ in Eq. (4.16), which inherits an implicit temperature dependence from the n-dependent decay constant f_a in Fig. 3.6. We demonstrate the scaling of $M_{\star,\lambda}$ with three representative temperature indices n = 0, 1, 3.34 together with the resulting accretion rates $\delta M_{\star,\lambda}/\delta t = \delta M_{\star}/\delta t(M_{\star,\lambda},\mathcal{M}_{\lambda})$ of the critical ASMC systems at m_a , n in the left and right panel of Fig. 7.2.

For larger n, Eq. (4.16) yields smaller critical AS masses $M_{\star,\lambda}$, which turn out to boost the accretion rates of the self-similar attractor in Eq. (4.42) and Fig. 7.2. The enhanced accretion

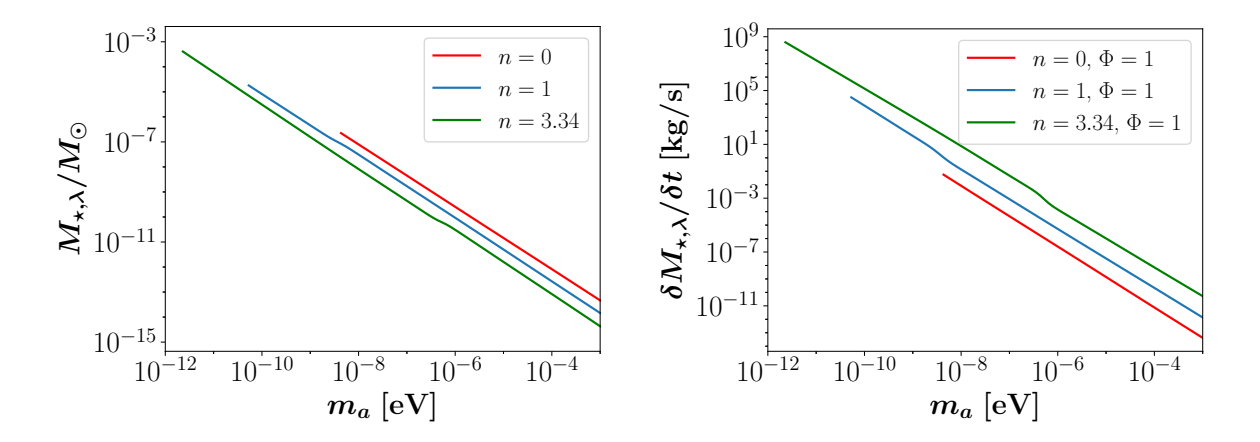


Figure 7.2: Left: Maximum stable AS masses $M_{\star,\lambda}$ from Eq. (4.16) for different axion models m_a, n with colors indicating n = 0, 1, 3.34. Right: Internal accretion rates $\delta M_{\star,\lambda}/\delta t$ from Eq. (4.42) in kg s⁻¹ for critical ASMC systems with core mass $M_{\star} = M_{\star,\lambda}$, $\mathcal{M} = \mathcal{M}_{\lambda}$ and $\Phi = 1$ at different m_a, n .

rates for smaller $M_{\star,\lambda}$ in Fig. 7.2 can be qualitatively understood as a shifting of the monotonically decreasing mass growth rate from Fig. 4.7 towards earlier times with smaller $M_{\star,\lambda}$. As can be seen by the scaling of $\mathcal{N}_{\text{Nova}}$ with larger n in Fig. 7.1, the benefit of having larger accretion rates and smaller $M_{\star,\lambda}$ is dominant over the scaling of \mathcal{N}_{tot} . Lastly and in the case of small n=1 in blue, a sudden drop in $\mathcal{N}_{\text{Nova}}$ arises from the different scalings of \mathcal{M}_{max} and \mathcal{M}_{λ} . Eventually at some m_a , the accretion-induced critical mass $\mathcal{M}_{\lambda,\text{acc}} > \mathcal{M}_{\text{max}}$ grows beyond the range of the initial ASMF, yielding $\mathcal{N}_{\text{Nova}} = 0$.

We also mention for completeness, that the results in Fig. 7.1 imply that the number of bosenovae occurring within a Hubble time can become as large as $\mathcal{N}_{\text{Nova}} t_H \gg \mathcal{N}_{\text{tot}}$ for some (m_a, n) . This observation indicates that a large number of axion stars are expected to collapse repeatedly on cosmological timescales. In fact, we can consider the exemplary case of the QCD axion with $m_a = 50 \,\mu\text{eV}$ and n = 3.34 to find that $M_{\star,\lambda}/\mathcal{M}_{\lambda} \sim 10^{-6}$, which means that a typical ASMC system with near-critical AS/MC-masses can undergo $\sim 10^6$ bosenovae until it is eventually depleted of its total mass.

Answering the question of how many of the ASMC systems are expected to shed their initial mass within t_H requires investigation of the full time evolution of the MCMF, ASMF and corehalo relation - all of which are beyond the scope of this work. We also refer to Ref. [281] for a similar study, which constrains axion models through significant depletion of cold dark matter following repeated bosenovae in the cosmological context. Our analysis complements the work in Ref. [281] by using the direct observation of relativistic axions from galactic bosenovae in different axion dark matter searches.

7.2 Detectability of galactic Axion Bursts

With the number of galactic axion bursts over $t_{\rm obs} = 1\,\rm yr$ being determined by Eq. (7.5), the next step lies in the derivation of approximate criteria for the detectability of such bursts in different earth-based experiments. We approach the derivation of an experimentally independent sensitivity criterion in this section by first recalling the fundamental properties of the relativistic

axion bursts from Sec. 4.4 and their propagation following Ref.s [3, 35, 36]. After a brief introduction about burst wave spreading, we define the resulting maximal observable distance, which can be used to infer the number of observable bursts for experiments exploiting both axion-photon and axion-fermion couplings of the form in Eq. (2.17) and Eq. (2.18).

7.2.1 Burst Properties and Propagation

The intensity of a given axion burst is mainly determined by the total energy \mathcal{E} , which is emitted during the relativistic collapse. We follow the numerical results from Ref. [35] and Eq. (4.45), which stated that the typical energy loss is approximately 30% of the critical AS mass. In this approach, one can simply estimate the total energy output of the axion burst by defining the mass loss fraction $f_{\rm em}=0.3$, where $f_{\rm em}\simeq0.2-0.5$ according to simulations [35], and write

$$\mathcal{E} \simeq f_{\rm em} M_{\star,\lambda} \sim 10^{43} \,\text{GeV} \left(\frac{f_a}{10^{11} \,\text{GeV}}\right) \left(\frac{m_a}{50 \,\mu\text{eV}}\right)^{-1} \tag{7.6}$$

for QCD axion parameters. The local burst density $\rho_{\star,d}$ measured at the detector corresponding to Eq. (7.6) will be diluted by two major effects. First, from the propagation of the spherical waves over a distance $d_{\rm obs}$ to the observer, the resulting signal is reduced by a relative factor of $\rho_{\star,d} \propto d_{\rm obs}^{-2}$. Secondly, the emission of relativistic axions with an energy spectrum following the one in Fig. 4.10 implies a range of particle momenta $k=qm_a$ with $q\gtrsim 1$. Since particles with larger q will reach the detector sooner than axions with $q\simeq 1$, the burst signal experiences an additional temporal spread, that leads to the measured burst duration δt at the detector. In general, the temporal and spatial dilution of the signal varies depending on the spread δk of the emitted axion momenta. The scalings of these three quantities can be obtained from the relativistic axion dispersion relation

$$\omega = \sqrt{k^2 + m_a^2},\tag{7.7}$$

which can be rephrased in terms of the velocity $v = \partial \omega / \partial k$ as

$$v^2 = \frac{k^2}{k^2 + m_a^2} = \frac{q^2}{q^2 + 1} \,, (7.8)$$

where we have used $k = qm_a$ in the last equation. Applying differentials one both sides one obtains [36]

$$v\delta v = \frac{q\delta q}{(q^2+1)^2},\tag{7.9}$$

which can be written in terms of the relative velocity spread $\delta v/v$ as

$$\frac{\delta v}{v} = \frac{\delta q}{q} \frac{1}{q^2 + 1} = \frac{\delta k}{k} \frac{m_a^2}{\omega^2} = \frac{\delta k}{k} \frac{m_a^2}{k^2 + m_a^2}.$$
 (7.10)

For an instantaneous burst centered at k_0 with a negligible momentum spread $\delta k/k \ll 1$, the relative spatial spread $\delta x/x$ with $x=d_{\rm obs}$ is equal to the velocity spread in Eq. (7.9), which

yields the observed signal length δx [36]

$$\frac{\delta x}{x} = \frac{\delta x}{d_{\text{obs}}} = \frac{\delta v \, t}{v t} = \frac{\delta v}{v} \tag{7.11}$$

$$\Leftrightarrow \delta x = \frac{\delta v}{v} d_{\text{obs}} \approx \frac{\delta k}{k_0} \frac{m_a^2}{k_0^2 + m_a^2} d_{\text{obs}} = \frac{\delta k}{m_a} \frac{d_{\text{obs}}}{q(q^2 + 1)}. \tag{7.12}$$

The observed signal duration δt at the detector from an axion burst with $\delta k/k \ll 1$ is straightforwardly approximated from Eq. (7.12) as

$$\delta t = \frac{\delta x}{v} \approx \frac{\delta k}{m_a} \frac{d_{\text{obs}}}{g^2 \sqrt{g^2 + 1}} \sim 80 \,\mathrm{d} \left(\frac{d_{\text{obs}}}{1 \,\mathrm{pc}}\right) \,, \tag{7.13}$$

where in the last expression we have entered q=2.4 and $\delta k \simeq m_a$ from Fig. 4.10. An important question is whether the above wave spreading effects are expected to considerably modify the signal properties at galactic distances $d_{\rm obs} \sim 1\,{\rm pc}$. Notably, the minimum momentum spread δk is given by the uncertainty principle $\delta k \gtrsim 1/\delta x_0$, where δx_0 is the original burst duration at the source. We can use this observation as a lower boundary on the spatial broadening δx in Eq. (7.12) to estimate the ratio of the observed signal duration δx at the detector over the actual burst duration δx_0 by writing

$$\frac{\delta x}{\delta x_0} \gtrsim \frac{\delta k}{m_a} \frac{d_{\text{obs}}}{q(q^2+1)\delta x_0^2} \simeq \frac{5 \cdot 10^{13}}{q(q^2+1)} \left(\frac{d_{\text{obs}}}{\text{pc}}\right) \left(\frac{m_a}{50 \,\mu\text{eV}}\right),\tag{7.14}$$

where in the last equation we have used that $\delta x_0 \approx 400/m_a$ according to the simulations in Ref. [35]. Taking the leading peak at $k/m_a \approx 2.4$ from the same simulation in Fig. 4.10, with $\delta k/m_a \sim 1$ and $q \approx 2.4$, the wave spreading effect described by δx in Eq. (7.12) dominates over the intrinsic burst duration δx_0 for $m_a \gtrsim 10^{-15} \, \text{eV}$ and $d_{\text{obs}} \gtrsim 0.03 \, \text{pc}$ [36].

We therefore continue to evaluate the burst properties by only considering the spatial and temporal dilution due to wave spreading according to Eq. (7.12) and Eq. (7.13) in the following. An important realization in the above approach is that for relativistic particles with $v \sim 1$, the spatial and temporal spread of the observed signal are approximately equal

$$\delta x \simeq \delta t \simeq \frac{\delta k_a}{m_a} \frac{d_{\text{obs}}}{q^3} \,,$$
 (7.15)

where we have used that $q^2 + 1 \simeq q^2$ [3, 36]. Therefore replacing the temporal dilution of the observed signal $\rho_{\star,d} \propto 1/\delta t$ with δx , the observed burst density $\rho_{\star,d}$ at the detector from a bosenova event with total energy output \mathcal{E} from Eq. (7.6) can be written as [3, 36]

$$\rho_{\star,d} \simeq \frac{\mathcal{E}}{4\pi d_{\text{obs}}^2 \delta x} \sim 3 \cdot 10^{-12} \frac{\text{GeV}}{\text{cm}^3} \left(\frac{d_{\text{obs}}}{1 \text{ pc}}\right)^{-3} \left(\frac{f_a}{10^{11} \text{ GeV}}\right) \left(\frac{m_a}{50 \,\mu\text{eV}}\right)^{-1} ,\qquad (7.16)$$

where d_{obs} is the distance to the bosenova, and $\delta x \simeq \delta t$ for relativistic particles. The local axion matter density $\rho_{\star,d}$ can be probed by different axion search experiments, like the axion DM searches from Sec. 2.7.1 and the spin precession experiments from Subsec. 2.7.2.

Taking the first relativistic momentum peak in the bosenova spectrum in Fig. 4.10 with $q \approx 2.4$ and $\delta k_a \simeq m_a$, it can be seen from Eq. (7.15) that the temporal spread is $\delta t \simeq 10^{-2} d_{\rm obs}$, which implies a long duration of the observed signal at the detector $\delta t \sim 80\,\mathrm{d}$ for $d_{\rm obs} \sim \mathrm{pc}$. Lastly and as mentioned in Ref. [36], the momentum spread of the burst δk is much larger than for the cold DM case (where $\delta k_a \simeq 10^{-3} m_a$), indicating that broadband searches are most suitable for detecting bosenovae, rather than resonant-type searches.

7.2.2 Burst Sensitivity and Detection

The wave spreading of the relativistic axion burst in Eq. (7.12) provides an approximate estimate on the observed signal shape from the properties of the emission process, which was simulated in Ref. [35]. In this section, we will use the corresponding burst properties at the detector together with additional considerations on the temporal scaling of the sensitivities in axion search experiments. For this, we will define two additional time parameters - next to the observed burst duration δt from Eq. (7.13). The first important time scale is the observed coherence time [36]

$$\tau_{\star} \sim \frac{2\pi}{\delta\omega} \approx \frac{2\pi d_{\text{obs}}}{q^3 m_a \delta t_b} \simeq \frac{\pi d_{\text{obs}}}{200q^3} \sim 1 \,\mathrm{d}\left(\frac{d_{\text{obs}}}{1 \,\mathrm{pc}}\right)$$
 (7.17)

of the burst, which is dominated by wave spreading in the limit in Eq. (7.14) and Eq. (7.15) under consideration. In the last equality of Eq. (7.17), we have used that the burst duration at the source is $\delta t_b \approx 400/m_a$ following Eq. (4.46). The coherence time at the detector given by Eq. (7.17) is important for the sensitivity of a given experiment, as we will explain in the following.

Continuing with the second important timescale for the sensitivity approach from Ref. [36], we introduce the equivalent coherence time of the cold dark matter background ρ_a , which is given by the de-Broglie wavelength $\lambda_{\rm dB} = 2\pi/(m_a v_{\rm vir})$ from Eq. (3.8) as

$$\tau_a \simeq \frac{2\pi}{m_a v_{\rm vir}^2} \sim 10^{-4} \,\mathrm{s} \left(\frac{50 \,\mu\text{eV}}{m_a}\right) \,,$$
(7.18)

where as before $v_{\text{vir}} \approx 239 \, \text{km s}^{-1}$ is the virial velocity of the galactic dark matter halo [130]. The two coherence times from Eq. (7.17), Eq. (7.18) will be combined with the observed burst duration δt from Eq. (7.15) and the observation time $t_{\text{obs}} = 1 \, \text{yr}$ in order to determine the time scaling of the relative sensitivity to axion bursts. We define the sensitivity in a given experiment in terms of the *minimum detectable coupling* $g_{i,\text{min}}$ of a signal 'i' probed in terms of a given interaction Lagrangian. In the concrete example of the axion-photon coupling from Eq. (2.17), we can write the axion-photon interaction as

$$\mathcal{L}_{a\gamma\gamma} \sim g_{a\gamma\gamma} \phi_i F^{\mu\nu} \tilde{F}_{\mu\nu} \,, \tag{7.19}$$

where $\phi_i = \sqrt{\rho_i}$ is the axion field observed from either the burst i = b or the cold dark matter density i = a. As in Eq. (2.20), we set $g_{a\gamma\gamma} \propto C_{a\gamma\gamma}/f_a$ for different axion models, where the model-dependent coefficient $C_{a\gamma\gamma}$ may be chosen arbitrarily, except in the case of the QCD axion with $m_a = 50 \,\mu\text{eV}$, n = 3.34 and $C_{a\gamma\gamma} = E/N - 1.92$ following Eq. (2.21).

Defining the ratio of the bosenova sensitivity over the sensitivity to cold axion DM as $g_{\star,\min}/g_{a,\min}$, it can be seen from Eq. (7.19) that the corresponding sensitivity ratio is proportional to the inverse of the respective field values ϕ_i , which implies $g_{\star,\min}/g_{a,\min} \sim \sqrt{\rho_a/\rho_{\star,d}}$. Another important scaling is that of the relative burst sensitivity $g_{\star,\min}/g_{a,\min}$ with the observation time t_{obs} . Complementary to the density scaling from Eq. (7.19), the time scaling can be motivated heuristically using the above timescales δt , τ_a and τ_{\star} .

Starting with the time scaling of the cold dark matter background, the minimum detectable coupling should scale as $g_{a,\text{min}} \propto t_{\text{obs}}^{-1/2}$ for a coherently oscillating signal, i.e. for $t_{\text{obs}} < \tau_a$. On the other hand in the temporally incoherent regime $t_{\text{obs}} > \tau_a$, the sensitivity scales with the

measurement time as $g_{a,\mathrm{min}} \propto t_{\mathrm{obs}}^{-1/4}$ [36, 282]. Combining the above two cases, we may write $g_{a,\mathrm{min}} \propto t_{\mathrm{obs}}^{-1/4} \min(t_{\mathrm{obs}}^{1/4}, \tau_a^{1/4})^{-1}$. Analogously for the axion burst with duration δt and coherence time τ_{\star} , one obtains each a sensitivity improvement $\propto t_{\mathrm{obs}}^{-1/4}$ if $t_{\mathrm{obs}} < \delta t$ and one if $t_{\mathrm{obs}} < \tau_{\star}$. This means that the burst sensitivity may be written in terms of the minimum coupling as $g_{\star,\min} \propto \min(t_{\text{obs}}^{1/4}, \delta t^{1/4})^{-1} \min(t_{\text{obs}}^{1/4}, \tau_{\star}^{1/4})^{-1}$. Both of the above statements were used to motivate the approximate scaling of the relative burst sensitivity in terms of the minimal couplings [36]

$$\frac{g_{\star,\min}}{g_{a,\min}} \simeq \sqrt{\frac{\rho_a}{\rho_{\star,d}}} \frac{t_{\text{obs}}^{1/4} \min\left[t_{\text{obs}}^{1/4}, \tau_a^{1/4}\right]}{\min\left[t_{\text{obs}}^{1/4}, \delta t^{1/4}\right] \min\left[t_{\text{obs}}^{1/4}, \tau_{\star}^{1/4}\right]},$$
(7.20)

where in our case we set $t_{\rm obs} = 1\,{\rm yr}$. While the burst duration δt and burst coherence time τ_{\star} are of order 1 d and 100 d, the coherence time of cold dark matter is $\tau_a \sim 10^{-4}$ s, which indicates that the time scaling of Eq. (7.20) is $\propto t_{\rm obs}^{1/4}$ for $t_{\rm obs} = 1\,{\rm yr}$. Concerning the scaling of the densities, ρ_a is close to the canonical cold dark matter value

 $\rho_a = 0.4 \,\mathrm{GeV/cm^3}$. Without tidal streams, the local DM density is a factor of 4 smaller, arising from the minicluster DM abundance of $f_{\rm mc} = 0.75$, which we assume following Ref.s [28, 30]. This gives $\rho_a = (1 - f_{\rm mc}) \, 0.4 \, {\rm GeV/cm^3}$ for the local DM background. According to Eq. (7.20), this would change $g_{\star,\min}/g_{a,\min}$ by a factor of 1/2 thus improving the detectability of bosenovae compared to the cold DM case.

The burst density $\rho_{\star,d}$ at the detector in Eq. (7.16) on the other hand depends strongly on the observation distance $d_{\rm obs}$ and on the mass of the axion star $M_{\star,\lambda}$. For smaller axion masses m_a , one obtains larger $M_{\star,\lambda}$, larger emitted energies $\mathcal{E} \propto M_{\star,\lambda}$ and thus larger densities $\rho_{\star,d}$, which reduce the sensitivity ratio in Eq. (7.20) and thereby improve the relative burst detectability. Therefore bosenovae are detectable at larger distances d_{obs} for smaller m_a .

Note that at this point, the only unknown in Eq. (7.20) is the observation distance, since all other parameters either depend on d_{obs} or on the axion model m_a, n . This allows us to formulate a simplified criterion for the detectability of observed bosenova events by defining the maximum observable sensitivity ratio $(g_{\star,\min}/g_{a,\min})_{\max} = 1$ as

$$\frac{g_{\star,\min}}{g_{a,\min}} \le \left(\frac{g_{\star,\min}}{g_{a,\min}}\right)_{\max} \equiv 1, \tag{7.21}$$

where the point of equality introduces an upper bound on $d_{\rm obs}$. The distance of equality can be found by recalling the scaling of the different temporal quantities $t_{\rm obs} = 1 \, {\rm yr}$, $\tau_a \sim 10^{-4} \, {\rm s}$, $\delta t \propto 80 \,\mathrm{d}\,d_{\mathrm{obs}}/\mathrm{pc}$ and $\tau_{\star} \propto 1 \,\mathrm{d}\,d_{\mathrm{obs}}/\mathrm{pc}$, which indicates that t_{obs} is typically the dominant temporal scale. We can therefore simplify the time scaling from Eq. (7.20) and enter $\rho_{\star,d}$ from Eq. (7.16) together with the expressions for τ_a , δt and τ_{\star} , which yields

$$\left(\frac{g_{\star,\min}}{g_{a,\min}}\right)_{\max} \simeq \sqrt{\frac{\rho_a}{\rho_{\star,d}}} \left(\frac{t_{\text{obs}}\tau_a}{\delta t \, \tau_{\star}}\right)^{1/4} \simeq \sqrt{\frac{200 d_{\text{obs}}^3 \rho_a}{f_{\text{em}} M_{\star,\lambda}}} \left(\frac{400 q^6 t_{\text{obs}}}{d_{\text{obs}}^2 m_a v_{\text{vir}}^2}\right)^{1/4} , \quad t_{\text{obs}} > \delta t \qquad (7.22)$$

as long as $t_{\rm obs} > \delta t$ as argued above. Rearranging the above equation for $d_{\rm obs}$, we obtain the maximum observable distance, which gives $g_{\star, \rm min}/g_{a, \rm min} = 1$

$$d_{\text{max}} \simeq \sqrt{\frac{f_{\text{em}} M_{\star,\lambda} v_{\text{vir}}}{200q^3 \rho_a}} \left(\frac{m_a}{400 t_{\text{obs}}}\right)^{1/4} \left(\frac{g_{\star,\text{min}}}{g_{a,\text{min}}}\right)_{\text{max}} , \quad t_{\text{obs}} > \delta t$$
 (7.23)

$$\simeq 7 \cdot 10^{-4} \,\mathrm{pc} \left(\frac{f_a}{10^{11} \,\mathrm{GeV}} \right)^{1/2} \left(\frac{m_a}{50 \,\mu\mathrm{eV}} \right)^{-1/4} \left(\frac{t_{\mathrm{obs}}}{1 \,\mathrm{yr}} \right)^{-1/4} \left(\frac{v_{\mathrm{vir}}}{239 \,\mathrm{km \, s^{-1}}} \right)^{1/2} \tag{7.24}$$

for a typical bosenova signal and QCD axion parameters m_a , f_a . Typically, the maximal distance is a few orders of magnitude smaller than a parsec for couplings of the form in Eq. (7.19), and somewhat larger for axion-fermion-like couplings similar to Eq. (2.18), depending on the input parameters.

The former type of couplings are exploited in the spin precession experiments introduced in Subsec. 2.7.2. Due to the presence of the spatial derivative $\partial_{\mu}\phi$ in Eq. (2.18), we call these interactions derivative couplings, with the typical example given by the axion-fermion coupling

$$\mathcal{L} \sim g_{aff}(\partial_{\mu}\phi_i)\bar{\Psi}\gamma^{\mu}\gamma^5\Psi\,,\tag{7.25}$$

where Ψ is a standard model fermion field and ϕ_i is the field density of the burst and cold dark matter field respectively. A crucial difference of derivative couplings compared to the non-derivative axion-photon coupling in Eq. (7.19) is the fact that the corresponding sensitivity ratio $g_{\star,\min}/g_{a,\min}$ receives an additional factor of $v_{\text{vir}}/v_{\star} \sim v_{\text{vir}}$ from the gradient of the axion field $\nabla \phi_i$ in Eq. (7.25). This factor suppresses the sensitivity by $v_{\text{vir}}^{-1} \sim 10^3$ in the non-relativistic DM case, giving searches for relativistic fields a comparative advantage. The corresponding sensitivity ratio with derivative couplings takes the form [36]

$$\left(\frac{g_{\star,\min}}{g_{a,\min}}\right)^{\nabla} \simeq v_{\text{vir}} \sqrt{\frac{\rho_a}{\rho_{\star,d}}} \frac{t_{\text{obs}}^{1/4} \min\left[t_{\text{obs}}^{1/4}, \tau_a^{1/4}\right]}{\min\left[t_{\text{obs}}^{1/4}, \delta t^{1/4}\right] \min\left[t_{\text{obs}}^{1/4}, \tau_{\star}^{1/4}\right]},$$
(7.26)

where we use the index 'V' to indicate the distinction from the non-derivative couplings in Eq. (7.19). As we will see in the next section, this factor of $\sim 10^3$ enhancement in sensitivity ratio motivates ongoing and future experiments searching for axions with derivative couplings, e.g. CASPEr [142, 282], which is under development but designed for resonant searches. Note also that since $g_{\star,\min}/g_{a,\min}$ is a ratio of sensitivities, the results in Eqs. (7.20) and (7.26) are independent of the properties of a particular broadband-type experiment.

Similar to the derivation of d_{max} in Eq. (7.23), we can follow the same steps in order to obtain the maximum observable distance of derivative coupling interactions

$$d_{\text{max}}^{\nabla} \simeq v_{\text{vir}}^{-1} \sqrt{\frac{f_{\text{em}} M_{\star,\lambda} v_{\text{vir}}}{200q^3 \rho_a}} \left(\frac{m_a}{400 t_{\text{obs}}}\right)^{1/4} \left(\frac{g_{\star,\text{min}}}{g_{a,\text{min}}}\right)_{\text{max}}^{\nabla} = v_{\text{vir}}^{-1} d_{\text{max}} \quad , \quad t_{\text{obs}} > \delta t \,, \qquad (7.27)$$

which is boosted by a factor of $\sim 10^3$ compared to the non-derivative case in Eq. (7.23) and where the detectability threshold $(g_{\star,\min}/g_{a,\min})_{\max}^{\nabla} = 1$ is defined analogously to Eq. (7.21). In the above framework of detectability, we can compare the maximum observable distances d_{\max} , d_{\max}^{∇} to the typical observation distance of galactic axion bursts, which can be inferred

from the abundance of $\mathcal{N}_{\text{Nova}}$ in Eq. (7.5). Since the maximum observable distance derived from Eq. (7.20) is small $d_{\text{max}} \lesssim 1 \,\text{pc}$ compared to galactic length scales $\sim 1 \,\text{kpc}$, we can estimate the typical distance between two bosenovae by writing

$$\langle d \rangle \sim \left(\frac{V_{\odot}}{\mathcal{N}_{\text{Nova}}|_{r < R_{\odot}}} \right)^{1/3} \sim \left(\frac{4\pi R_{\odot}^3/3}{f_{\odot} \mathcal{N}_{\text{Nova}}} \right)^{1/3} ,$$
 (7.28)

where $V_{\odot} = 4\pi R_{\odot}^3/3$, with the solar position $R_{\odot} = 8.3$ kpc and where $f_{\odot} \approx 0.032$ is the fraction of galactic MCs contained within $r \leq R_{\odot}$. Physically, Eq. (7.28) gives the average distance between $f_{\odot}\mathcal{N}_{\text{Nova}}$ events within a spherical volume of radius R_{\odot} , where the NFW distributed nature of the events is accounted for by f_{\odot} and $\mathcal{N}_{\text{Nova}}$ from Eq. (7.5). From this we define the average observed burst distance as

$$\langle d_{\rm obs} \rangle = \frac{\langle d \rangle}{2} \,, \tag{7.29}$$

which differs from Eq. (7.28) only by the geometrical factor of 1/2. Summarizing the above approach for each axion model m_a, n , the AS properties derived from the ASMF in Fig. 4.14 and the internal accretion rate in Eq. (4.42) yield a fixed average observation distance $\langle d_{\text{obs}} \rangle$ defined by $\mathcal{N}_{\text{Nova}}$ in Eq. (7.5), which needs to be compared to the maximum observable distance d_{max} . As we will show in the following, the sensitivity ratios of these experiments, given by Eq. (7.20) and Eq. (7.26), depend strongly on the axion model and coupling.

7.3 Non-Derivative Couplings

In this and in the following section, we consider the detectability of galactic bosenovae with different axion interactions separately. Starting with the axion-photon interaction from Eq. (2.17), or more generally with non-derivative type couplings of the form in Eq. (7.19), we show the results for d_{max} from Eq. (7.23) and $\langle d_{\text{obs}} \rangle$ from Eq. (7.29) at different axion models m_a, n in Fig. 7.3. More specifically, colored dashed lines show the n-dependent contour lines, where $g_{\star,\min}/g_{a,\min}(d_{\text{obs}})=1$ and the axion bursts emitted from collapsing ASs are sufficiently close to become distinguishable from the background DM. The contour lines are determined numerically and are well-fit by the analytic expression for d_{\max} in Eq. (7.23).

As mentioned before, the maximum observable distance needs to be compared with the average expected distance of galactic bosenovae in solid lines. In this approach and for given n = 1, 2, 3.34, regions of m_a with $\langle d_{\rm obs} \rangle \leq d_{\rm max}$ can potentially be probed by current and upcoming broadband experiments. The solid lines in Fig. 7.3 thus demonstrate, that using the MCMF from Sec. 3.5 and for composite ASMC systems obeying the core-halo relation in Eq. (3.57), bosenovae occur too rarely to be detected in axion DM searches.

Nevertheless, there are several considerations that can improve these predictions. First and mainly, we have neglected long-time AS accretion, which is expected to significantly boost the number of bosenovae within $t_{\rm obs}$. Secondly, the relative burst sensitivity of future telescopes could be improved, for example by including spectral information about the signal or by performing dedicated axion burst searches, thus enhancing the maximum observable distance $d_{\rm max}$ for bosenovae detection. And lastly, there have been recent studies, namely Ref.s [236] and [252], which suggest that an order-one fraction of the total galactic dark matter may be contained in the form of axion stars, rather than miniclusters as we have assumed. We can equivalently

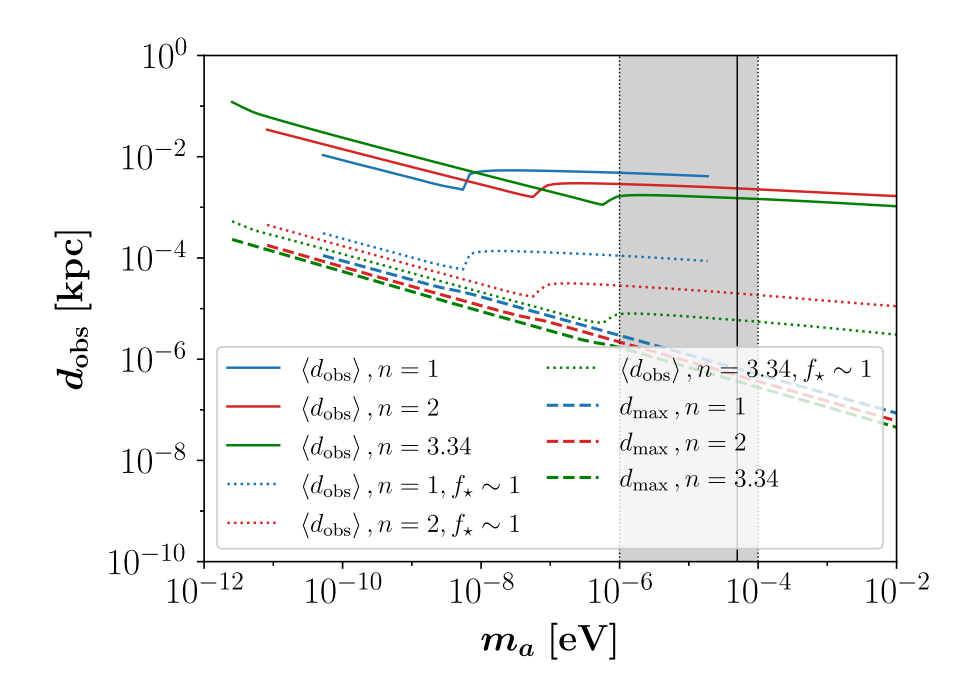


Figure 7.3: Typical observation distance $\langle d_{\rm obs} \rangle$ of galactic bosenovae in solid colored lines, the same for the case that $f_{\star} \sim 1$ in dotted lines, and maximum observable distance $d_{\rm max}$ for $g_{\star, \rm min}/g_{a, \rm min} = 1$ in dashed lines. Colors denote axion models with different temperature evolution n = 1, 2, 3.34. Shown for axions with non-derivative couplings in Eq. (7.19) using the \mathcal{M}_0 -cutoff of the MCMF. The gray shaded region denotes the cosmological QCD axion mass band with 10^{-6} eV $\leq m_a \leq 10^{-4}$ eV and the black solid vertical line indicates the QCD axion mass $m_a \approx 50 \,\mu\text{eV}$ assumed in this work. Taken from Ref. [3].

evaluate these models by setting the relative DM abundance f_{\star} of axion stars from Eq. (4.79) equal to one, $f_{\star} = 1$.

Recalling the results from Subsec. 3.6.2 and Fig. 4.16, our approach predicts $f_{\star} \sim 10^{-7}$ to $f_{\star} \sim 10^{-4}$, depending on n. Setting $f_{\star} \sim 1$ would thus boost the total number of ASs (and thus also $\mathcal{N}_{\mathrm{Nova}}$) by a linear factor of f_{\star}^{-1} . According to Eq. (7.28), this can significantly lower the expected average distance of galactic bosenovae. The resulting reduction is of order $\sim 10^{-2}$ for the average distance $\langle d_{\mathrm{obs}} \rangle \propto f_{\star}^{1/3}$. We plot the corresponding predictions from setting $f_{\star} = 1$ in dotted colored lines in Fig. 7.3 and find that such an enhanced AS abundance can potentially allow for the detection of axion bursts with only minor improvements in the sensitivity ratio $g_{\star,\mathrm{min}}/g_{a,\mathrm{min}}$ and for axion models with small $m_a < 10^{-6}$ eV. Therefore, relativistic axion bursts can specifically be used to constrain the most optimistic predictions for the abundance of AS dark matter through the development of dedicated axion burst searches.

Note that our predictions for $\langle d_{\rm obs} \rangle$ in Fig. 7.3 and the remainder of this chapter are based on the initial ASMF from Sec. 4.7 without the long-time AS mass growth predicted in Eq. (4.36) and Ref. [240]. Incorporating long-time accretion effects on the AS cores could lead to a pile-up of axion star masses around $M_{\star} \approx M_{\star,\lambda}$ thus enhancing the expected number of galactic bosenovae $\mathcal{N}_{\rm Nova}$, and presumably reducing the predicted values $\langle d_{\rm obs} \rangle$ below the threshold of observability $d_{\rm max}$. Better understanding of AS mass growth could therefore still yield observable signatures even in the case of axion-photon couplings.

7.4 Derivative Couplings

Moving on to the second scenario, we can exploit derivative type couplings like the axion-fermion interaction from Eq. (2.18) for the possible detection of galactic bosenovae following Eq. (7.26) and Eq. (7.27). This consideration is especially promising because the sensitivity ratio $(g_{\star,\min}/g_{a,\min})_{\nabla}$ of DM search experiments utilizing derivative-type axion couplings is boosted by the ratio of non-relativistic to relativistic burst speeds, roughly $v_{\text{vir}}/v_{\star} \simeq 10^{-3}$. As shown

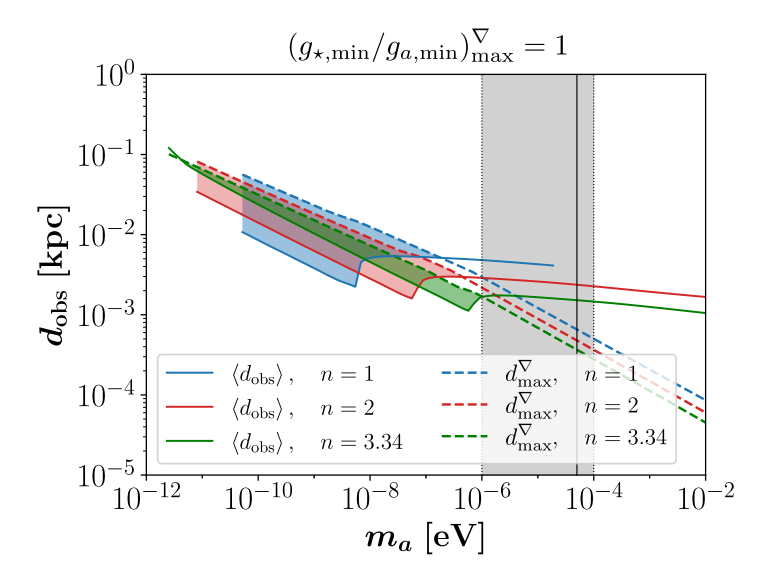


Figure 7.4: Typical observation distance $\langle d_{\text{obs}} \rangle$ of galactic bosenovae in solid colored lines and maximum observable distance d_{max} given by $(g_{\star,\text{min}}/g_{a,\text{min}})_{\text{max}}^{\nabla} = 1$ and Eq. (7.27) in dashed lines. Calculated for axions with derivative couplings as in Eq. (7.25), using the \mathcal{M}_0 -cutoff. Color-shaded regions indicate the axion mass range, where bosenovae are detectable, i.e. where $\langle d_{\text{obs}} \rangle \leq d_{\text{max}}$. Taken from Ref. [3].

in Eq. (7.27) and by the dashed lines in Fig. 7.4, this circumstance increases the maximum observable distance d_{max} determined from setting $(g_{\star,\text{min}}/g_{a,\text{min}})_{\text{max}}^{\nabla} = 1$ by a factor of $\sim 10^3$. For visualization, regions of m_a with $\langle d_{\text{obs}} \rangle \leq d_{\text{max}}$ are highlighted by colored shades, indicating that the resulting boost in relative burst sensitivity is sufficient to render a large part of the axion mass range detectable.

As argued in Sec. 7.1, the detailed scaling of d_{max}^{∇} with n in solid colored lines in Fig. 7.4 arises from a combination of the scaling of the decay constant f_a fixed by Eq. (2.64), the scaling of the characteristic MC mass \mathcal{M}_0 from Eq. (3.25) and the internal accretion rate from Eq. (4.42) used to determine $M_{\star,\text{acc}}$ in Eq. (7.2). Coincidentally, the cosmological axion band indicated by the gray-shaded regions in Fig. 7.4 is just beyond detectability for d_{max} set by $(g_{\star,\text{min}}/g_{a,\text{min}})_{\text{max}}^{\nabla} = 1$. In the future, dedicated bosenova searches using information on the energy spectrum of the burst could be used to improve the sensitivity g_{\star} in Eq. (7.26) relative to the cold DM sensitivity $g_{a,\text{min}}$ (see Ref. [36] for discussion).

We can therefore estimate the prospects of axion burst DM searches with increased sensitivity ratios, assuming an improvement of order 10, which is equivalent to increasing the maximum sensitivity ratio in Eq. (7.27) to $(g_{\star,\min}/g_{a,\min})_{\max}^{\nabla} = 10$ as depicted in Fig. 7.5. In this scenario, the maximum observable distance d_{\max} of galactic bosenovae is sufficiently enhanced to allow probes of axion models in the cosmological axion band $10^{-6} \text{ eV} \leq m_a \leq 10^{-4} \text{ eV}$ using axion

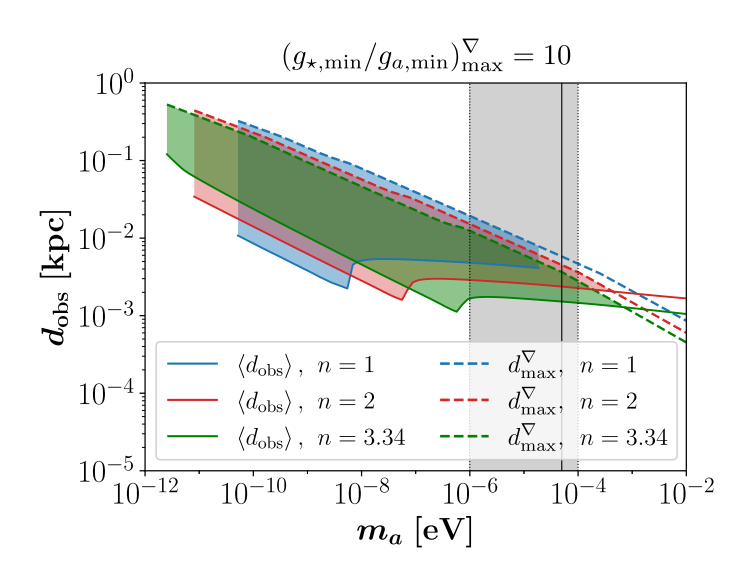


Figure 7.5: Typical observation distance $\langle d_{\text{obs}} \rangle$ of galactic bosenovae in solid colored lines and projected maximum observable distance d_{max} of future experiments with $(g_{\star,\text{min}}/g_{a,\text{min}})_{\text{max}}^{\nabla} = 10$ in dashed lines. Shown for axions with derivative couplings in Eq. (7.25) using the \mathcal{M}_0 -cutoff. Color-shaded regions indicate the axion mass range, where bosenovae are detectable, i.e. $\langle d_{\text{obs}} \rangle \leq d_{\text{max}}$. Taken from Ref. [3].

bursts. Conveniently, the case n = 3.34 with QCD-like temperature dependence of m_a in green lines and shades covers nearly the entire range of the axion mass. Even axion models with n = 1, 2 in blue and red can be probed for a wide range of axion masses. This enhancement in the case of axion-fermion coupling searches motivates further innovation and potentially dedicated searches for bosenovae in future broadband experiments.

For future improvements and potential experimental searches, we also provide the estimated number of bosenovae occurring within an observation volume $V_{\rm obs} = 4\pi d_{\rm max}^3/3$ assuming a constant DM density over the volume $V_{\odot} = 4\pi R_{\odot}^3/3$, given by

$$\mathcal{N}_{\text{obs}} \sim b \frac{V_{\text{obs}}}{V_{\odot}} f_{\odot} \mathcal{N}_{\text{Nova}} = b \left(\frac{d_{\text{max}}}{R_{\odot}}\right)^3 f_{\odot} \mathcal{N}_{\text{Nova}},$$
 (7.30)

where $b = 6/\pi$ is an order one coefficient introduced to set $\mathcal{N}_{\text{obs}} = 1 \text{ galaxy}^{-1}$ when $\langle d_{\text{obs}} \rangle = d_{\text{max}}$ for consistency using our definition of $\langle d_{\text{obs}} \rangle$ in Eq. (7.29).

We show the resulting number of observable bosenovae \mathcal{N}_{obs} , which pass the sensitivity thresholds $(g_{\star,\min}/g_{a,\min})_{\max}^{\nabla} = 1$ in solid and $(g_{\star,\min}/g_{a,\min})_{\max}^{\nabla} = 10$ in dashed colored lines for $t_{\text{obs}} = 1$ yr in Fig. 7.6. While a more sophisticated treatment of the detectability and galactic distribution of bosenovae is required to give more concrete predictions, our rough estimations demonstrate that bosenova signals are expected to occur even within smaller observation times than $t_{\text{obs}} = 1$ yr. In the case of order-one sensitivity thresholds in solid lines, \mathcal{N}_{obs} ranges from order one to roughly 100 observable events depending on (m_a, n) . Assuming a roughly constant collapse rate for simplicity, this suggests that required observation times range from $t_{\text{obs}} \sim 1$ yr for n = 3.34 down to $t_{\text{obs}} \sim 3$ d for n = 1.

The temporal requirement is further relaxed in the case of $(g_{\star,\min}/g_{a,\min})_{\max}^{\nabla} = 10$ in dashed lines, where all axion models (m_a, n) allow $t_{\text{obs}} \lesssim \mathcal{O}(10)$ days for $m_a \lesssim 10^{-4} \, \text{eV}$. The cosmological axion band and the canonical QCD axion parameters $m_a \approx 50 \, \mu\text{eV}$ are expected to yield $\mathcal{N}_{\text{obs}} \sim 10$,

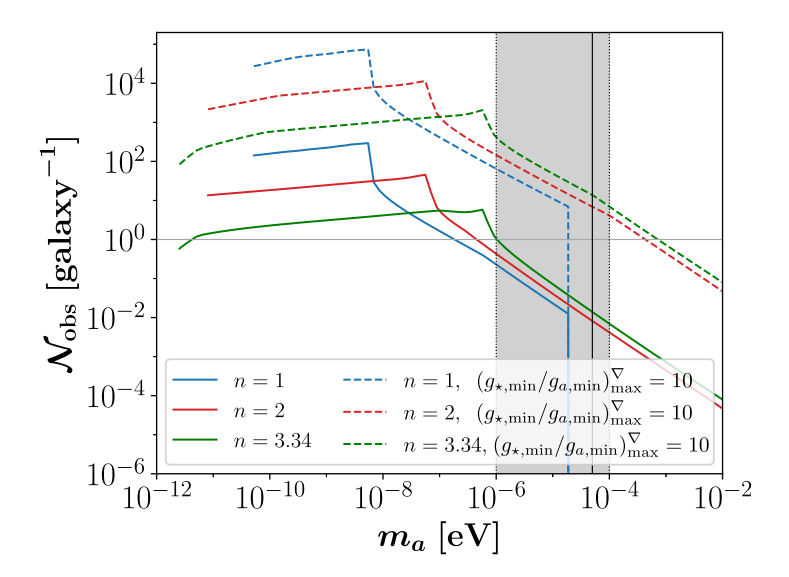


Figure 7.6: Expected number of galactic bosenovae \mathcal{N}_{obs} occurring within a maximum observable distance d_{max} from Eq. (7.27), given by $(g_{\star,\text{min}}/g_{a,\text{min}})_{\text{max}}^{\nabla} = 1$ in solid and $(g_{\star,\text{min}}/g_{a,\text{min}})_{\text{max}}^{\nabla} = 10$ in dashed colored lines. Shown for axions with derivative couplings from Eq. (7.25), using the \mathcal{M}_0 -cutoff and $t_{\text{obs}} = 1$ yr. The gray horizontal line indicates $\mathcal{N}_{\text{obs}} = 1$ galaxy⁻¹. Taken from Ref. [3].

which implies a required observation time of about a month. We note for completeness that the detailed time-dependence of \mathcal{N}_{obs} depends sensitively on the detailed accretion and reformation rates before and after the AS collapse, which we have neglected in our estimates.

7.5 Outlook on Detection of Bosenovae

Summarizing the results from Sec. 7.3 and Sec. 7.4, we find that in axion models with non-derivative couplings like the axion-photon coupling in Eq. (2.17), bosenovae are unlikely to be detected in current axion DM searches. Nevertheless, we have shown that with minor improvements in the relative burst sensitivity, our approach can be used to test predictions involving large AS abundance $f_{\star} \sim 1$ as suggested in Ref.s [236] and [252]. For $f_{\star} \sim 1$ and different temperature evolution of m_a , axion masses with $m_a \lesssim 10^{-6}$ eV could be probed in future broadband experiments. Importantly, our conservative treatment of the present-day ASMF from Sec. 4.7 does not exclude the occurrence of bosenovae in experimental searches using the axion-photon coupling, since the number of burst signals can be significantly enhanced under additional considerations of long-time AS mass growth.

Even without consideration of the long-time core accretion and using conservative assumptions, we find that galactic bosenovae in axion models with derivative couplings, like the axion-fermion coupling in Eq. (2.18), could be probed experimentally for a wide range of axion masses, ranging up to $10^{-12} \, \text{eV} \le m_a \le 10^{-6} \, \text{eV}$, depending on the temperature index n. Most importantly, our analysis suggests that moderate increases in the relative sensitivity of future broadband telescopes can potentially probe the QCD axion model with n = 3.34 and $m_a \simeq 50 \, \mu\text{eV}$ as well as ALPs with n = 3.34 up to the cosmological mass band $10^{-6} \, \text{eV} \le m_a \le 10^{-4} \, \text{eV}$. We emphasize however that the detection of the spectrally broad bosenova signals benefits from broadband

axion DM searches and that the exemplary CASPEr experiment using derivative couplings is of resonant type. Our predictions thus motivate further innovation in broadband DM experiments, both for axion-photon and axion-fermion couplings. Since the detection of galactic axion bursts provides a complementary mechanism to the radio emission from resonant AS cores in Chap. 6, the development of new experiments and dedicated axion burst searches can be seen as a promising additional method to probe the axion parameter space in Fig. 5.19.

On the experimental side, there exist several current and planned broadband-type axion experiments which exploit the axion-photon interaction $\mathcal{L}_{a\gamma\gamma}$ and could thus potentially be used for bosenova searches. These experiments include dish antenna setups like BRASS [124, 125] and BREAD [126, 133], which can probe axion masses in the range $50\,\mu\text{eV} \lesssim m_a \lesssim \text{meV}$ and $20\,\text{meV} \lesssim m_a \lesssim 0.1\,\text{eV}$, respectively. Other potentially suitable broadband experiments are ABRACADABRA [283, 284], which utilizes a superconducting toroidal magnet to search for axion masses in sub- μeV ranges and WISPLC [285], which uses an LC circuit for axion masses around the $\mathcal{O}(\text{neV})$ range. Since our predictions in Fig. 7.3 favor lower masses $m_a \lesssim 10^{-4}\,\text{eV}$, mainly BRASS, ABRACADABRA and WISPLC could reach the relevant parameter space for $f_{\star} \sim 1$ and n = 3.34. At distances $d_{\text{obs}} \leq d_{\text{max}} \sim 10^{-3}\,\text{pc}$ for $m_a \sim \mu\text{eV}$, $f_a \sim 2 \cdot 10^{11}\,\text{GeV}$ in Eq. (7.23), the signal duration would be $\delta t \lesssim 2\,\text{hrs}$ and the density at the detector is $\rho_{\star,d} \gtrsim 0.01\,\text{GeV}\,\text{cm}^{-3}$, according to Eq.s (7.15) and (7.16). The corresponding spectral width following Ref.s [35, 36] and Fig. 4.10 would be approximately $\delta k \sim m_a$ for the leading peak at $k/m_a \approx 2.4$ and $\delta k \sim 7m_a$ for the overall bosenova spectrum.

Lastly and for possible extensions of our work, we list the most important uncertainties in our modeling of galactic AS collapse rates. Most of these uncertainties are directly inherited from the linear growth predictions of the MCMF in Sec. 3.6 and Ref. [58], as well as from the semi-analytic predictions for the mass growth of AS cores from Sec. 6.3 and Ref. [240]. We refer to the conclusion of the mass growth modeling from Sec. 6.5 for detailed explanations and only add specific uncertainties, which differ from the parametric resonance case in Chap. 6.

First, the bosenova rates exhibit a stronger dependence on the initial overdensity parameter Φ , compared to the parametric resonance in Chap. 6. This is mainly due to our simplified modeling of the AS collapse rates, which neglect the mass-loss backreaction on the AS accretion rate. Secondly, we have not taken into account the possibility of multiple bosenovae occurring inside a single ASMC system for simplicity. We do however find evidence for such systems since the internal accretion rates scale as $\delta M_{\star}/\delta t \sim \tau_{\rm gr}^{-1} \sim \Phi^4$. For the densest MCs in the MCMF with $\Phi > 10$, which dominate the contribution to $\mathcal{N}_{\rm Nova}$, multiple axion bursts within $t_{\rm obs} = 1$ yr are possible.

A more careful study of the galactic AS collapse rates including the effects of long-time AS accretion would hence provide a promising extension of our work. Finally, a more reliable prediction of the galactic bosenova rates would also require additional consideration of the anisotropic distribution, long-time core mass growth and long-time stability of galactic ASMC systems.

Conclusion & Outlook

To summarize the results of this work, we put our combined predictions for galactic axion dark matter substructure into context with existing literature in Sec. 8.1. We also discuss extensions of our work and its implications for future research on signatures of axion dark matter in Sec. 8.2.

8.1 Conclusion

In Chap.s 2 to 4, we have gathered results of earlier investigations on the properties and time evolution of axion miniclusters together with the stability of their AS cores in order to infer the first predictions for the combined present-day mass distribution of galactic axion stars with attractive self-interactions $\lambda < 0$. For this, we have employed a generalized approach for the description of axion-like particles following Ref. [58], which allowed us to extend the corresponding predictions to a broad range of light scalar dark matter candidates, including the QCD axion with n = 3.34 and $m_a = 50 \,\mu\text{eV}$. Our application of the canonical core-halo relation in the gravitational limit of stable axion stars with attractive self-interactions indicates that their relative DM abundance $10^{-7} \lesssim f_{\star} \lesssim 10^{-4}$ is generally much smaller than was commonly assumed in the literature with $f_{\star} \lesssim 1$ [33, 135, 137]. We emphasize that this result is not particular to our modeling of the mass distributions but that it is a general finding for single-core ASMC structures in which the stable core mass is much lighter than the total mass of the structure.

A second crucial result of this work is the mass-integrated calculation of the spatially distributed collision- and signal rates for the most promising signatures of galactic axion stars in Chap. 5. In this chapter and in the corresponding publication, Ref. [1], we have performed the currently most detailed calculation of the abundance and detectability of galactic axion star encounters with astrophysical objects. We extended previous calculations by additionally considering the exact mass- and size distribution of these objects while keeping track of the different low-mass cutoffs and slope indices $\alpha = -1/2, -0.7$ of the MCMF.

In the context of resonant axion conversion in galactic NS-AS/MC transients, we confirmed previous findings that the collision rates of these events are considerable for a large range of axion models [135–137, 188], especially for larger axion masses. Crucially, our additional modeling of the resonance criterion between axion mass and typical NS plasma frequencies indicates that the signal rates from the above encounters are substantially diminished, rendering NS-AS/MC collisions effectively undetectable - independent of the MCMF cutoffs and slope index α .

A more positive conclusion could be inferred for the case of galactic AS core mergers in composite, merging ASMC systems. In this case and including the low-mass MC component, we found that the rate of AS core mergers can reach up to $\sim 3\,\mathrm{d}^{-1}\,\mathrm{galaxy}^{-1}$ for $\alpha = -0.7$, and $\sim 10\,\mathrm{yr}^{-1}\,\mathrm{galaxy}^{-1}$ for $\alpha = -1/2$, both for the QCD axion. Minicluster mergers can hence lead to frequent emission of radio bursts or to relativistic axion emission, where the signal properties

depend on the detailed merger dynamics outside of the scope of this work. We also performed simple estimations demonstrating that the resulting radio bursts become observable even over cosmological distance $d_{\text{obs}} \sim 2 \,\text{Gpc}$.

Most importantly for this work, the analysis from Chap. 5 indicated a remarkable potential for scenarios of combined AS accretion and triggering of radio- or axion bursts at the respective instabilities. We investigated the corresponding mass growth and resulting radio line backgrounds in more detail in Chap. 6 and Ref. [2]. Our analytical modeling of the external MC accretion from the NFW halo of the Milky Way and the semi-analytical predictions from numerical simulations of isolated ASMC systems both indicate that the expected radio signals are overwhelmingly strong if present. For both of the above accretion scenarios we estimated their potential detectability using different radio telescopes and found that dedicated line searches can be used to infer new constraints in ranges of up to $10^{-7} \,\mathrm{eV} \lesssim m_a \lesssim 10^{-2} \,\mathrm{eV}$ and $g_{a\gamma\gamma} \gtrsim 10^{-12} \,\mathrm{GeV}^{-1}$. The combined scenarios of AS resonance and core mass growth hence provide a compelling new mechanism to probe previously unexplored axion-parameter space with existing radio telescopes.

Lastly and complementary to the previous analysis, we also investigated the occurrence of repeated bosenovae in the Milky Way in Chap. 7 and Ref. [3]. While the observable distance of axion bursts is generally low, $d_{\rm obs} \lesssim 1\,{\rm pc}$, the large (internal) accretion rates of ASMC systems with density parameters in the range $1 \lesssim \Phi \lesssim 10^4$ are sufficient to potentially become detectable over observation times on the order of years. More specifically for experiments, which probe the axion-photon coupling, we find that optimistic predictions with order-one AS dark matter abundance $f_{\star} \sim 1$ can be probed by dedicated axion burst searches. The detectability of axion bursts is further enhanced for experiments exploiting derivative couplings like the axion-fermion interaction, which could potentially yield observable signatures up to QCD axion masses, $m_a \lesssim 10^{-4}\,{\rm eV}$. However at the time of writing, there exist no suitable broadband experiments, which utilize derivative axion couplings.

8.2 Outlook & Implications for Future Research

Summarizing the above findings, the investigations in this work greatly diminished prospects on the detection of NS-AS/MC collisions, but on the other hand opened up new promising observational methods for composite ASMC systems, especially when the mass growth of the AS core is accounted for. A particularly appealing possibility is given by the combined use of analytical radio line predictions from this work together with future, dedicated line searches with existing radio telescopes, as suggested in Chap. 6. Similarly, broadband experiments like BRASS [124, 125], ABRACADABRA [283, 284] and WISPLC [285] can potentially be used to constrain axion models with large AS abundance f_{\star} through development of dedicated axion burst searches. A major benefit from such methods is the fact that they can be performed with comparatively low financial expenditure. However, the financial benefit comes at the cost of large theoretical uncertainties so that these searches should be seen as a promising addition to existing laboratory and astrophysical searches.

In future studies, the corresponding large uncertainties can be reduced through improved understanding of the evolution of galactic axion DM substructure. For possible extensions of our studies, we conclude by listing 1. the major uncertainties inherent to our modeling of the mass

distributions and corresponding accretion rates and 2. the fundamental dependence of our results on different assumptions and parameters.

First and mainly, we have used the canonical $\lambda=0$ core-halo relation from Ref. [169] in the gravitational limit and the Press-Schechter theory predictions from Ref. [58] for the present-day minicluster distributions. The most relevant uncertainties in the Press-Schechter model include the low- \mathcal{M} cutoff of the MCMF, the initial power spectrum and non-linear effects of structure formation. There is also ongoing research on the MCMF slope α , the \mathcal{M} -, Φ -scaling of the $\lambda=0$ core-halo relation and on the Φ -dependence of AS accretion rates. For all of these uncertainties we have used the most well-tested assumptions, but we emphasize that our approaches can be straight-forwardly updated by using modified versions of the above relations without loss of generality. We continue to briefly elaborate about the impact of such modifications on the predictions in this work.

Starting with the canonical $\lambda=0$ core-halo relation, we have used different analytical estimations finding that the impact of weak attractive self-interactions on the equilibrium configuration of the ASMC system lies below uncertainties from the mass growth of these structures. Considering a modified core mass scaling $M_{\star} \propto \mathcal{M}^{\beta}$, where $1/3 \leq \beta \leq 7/9$ has been found in different literature [167–169, 172, 201–206, 247–249, 251, 286–290], we can summarize that larger β would increase the abundance of high-mass axion stars in MCs of mass $\mathcal{M} > \mathcal{M}_0$. Therefore our predictions based on the instabilities of axion stars from Chap.s 6 and 7 benefit from larger values of β .

Additional uncertainty arises from the *long-time AS mass growth* after the collapse of composite ASMC systems around matter-radiation equality when the core-halo relation is established [167]. On one hand, we have demonstrated how modified core mass relations of the form in Eq. (6.26) can significantly enhance the number of resonant and critical systems. On the other hand, any of these scenarios of late-time accretion quickly raise additional questions about the stability and time evolution of AS cores after triggering one of the two AS instabilities. We emphasize that such uncertainties are inherent to any study aiming to exploit axion star collapse- or resonance rates and that additional simulations are required to resolve these uncertainties.

Conveniently for the different low-mass cutoffs of the MCMF, we found in Chap. 5 that the largest and phenomenologically most relevant AS masses are mostly independent of the low-mass MC population. This also led us to solely consider the \mathcal{M}_0 -cutoff in Chap.s 6, 7. The only exception of this rule is given by the merger rates of ASMC systems in Fig. 5.15, which benefit from numerous capturing of light miniclusters. Similarly, the MCMF slope index $\alpha = -1/2, -0.7$ controls the abundance of the lightest miniclusters, which is why the MCMF with $\alpha = -0.7$ enhances the expected MC merger rates in Fig. 5.16. On the other hand, a flatter MCMF slope of $\alpha = -1/2$ would increase the relative abundance of high-mass miniclusters, thus boosting the abundance of near-critical systems in Chap.s 6, 7.

Another crucial ASMC parameter is the *initial overdensity* parameter $\Phi \in (0, 10^4]$ considered in Chap.s 6 and 7. While the effect of $\Phi > 1$ on collision and merger rates is expected to be small, the resulting impact on some of the most promising detection mechanisms involving axion star accretion was found to be substantial. In the external MC accretion model, the geometric cross section favors smaller values of $\Phi \lesssim 1$, whereas for the numerically tested internal accretion model, the radio signals are dominated by larger overdensities of $1 \lesssim \Phi \lesssim 100$. The latter statement also remains true for the collapse rates of ASs in Chap. 7, which benefits from having large $\Phi \gtrsim 10^3$ and thereby enhanced AS accretion- and collapse- rates.

A

Cosmological Context

A.1 Table of important Parameters

Quantity	Explanation	Definition
$ ho_{ m mc}$	Characteristic MC density	Eq. (3.23)
Φ	MC overdensity parameter	$\Phi = \delta \rho_a / \rho_a$
\mathcal{M}_0	Characteristic MC mass	Eq. (3.25)
$\mathcal R$	Spherically homogeneous MC radius	Eq. (3.24)
$\mathcal{M}_{J, ext{min}}$	Low-mass MCMF cutoff from the Jeans mass \mathcal{M}_J	Eq. (3.45)
$\mathcal{M}_{0, ext{min}}$	Low-mass MCMF cutoff from the characteristic MC mass \mathcal{M}_0	Eq. (3.47)
\mathcal{M}_{\min}	Applied low-mass MCMF cutoff at $z = 0$	$\mathcal{M}_{0/J, ext{min}}$
$\mathcal{M}_{ ext{max}}$	High-mass MCMF cutoff at $z = 0$	Eq. (3.46)
$\mathcal{M}_{h, ext{min}}$	MC mass of ASMF cutoff from core-halo relation	Eq. (3.58)
$\mathcal{M}_{R, ext{min}}$	MC mass of ASMF radius cutoff where $\mathcal{R} = R_{\star}$	Eq. (4.70)
$\mathcal{M}_{\star, \mathrm{min}}$	Effective low-mass cutoff of the ASMF	Eq. (6.1)
$\mathcal{M}_{\gamma, ext{min}}$	Combined \mathcal{M} -, Φ -cutoff of the Φ -integrated resonant MCMF	Eq. (6.2)
$\mathcal{M}_{\gamma, ext{max}}$	High-mass cutoff of the above resonant MCMF	Eq. (6.3)
$\mathcal{M}_{\lambda,\mathrm{acc}}$	MCMF high-mass cutoff due to accretion over $t_{\rm obs}$	Eq. (7.3)
$\mathcal{M}_{\lambda, ext{min}}$	Combined \mathcal{M} -, Φ -cutoff of the Φ -integrated accreting MCMF	Eq. (7.4)
$\mathcal{M}_{\lambda, ext{max}}$	High-mass cutoff of the above accreting MCMF	Eq. (7.1)
$\mathcal{M}_{ ext{tot}}$	Total mass of MCs in the MW	Eq. (3.52)
$\mathcal{N}_{\mathrm{tot}}$	Total number of MCs in the MW	Eq. (3.53)
$\mathcal{N}_{\gamma, ext{tot}}$	Number of MCs hosting a resonant AS with $M_{\star} \geq M_{\star,\gamma}$	Eq. (6.4)
$\mathcal{N}_{ ext{Nova}}$	Total number of galactic bosenovae occurring within $t_{\rm obs}$	Eq. (7.5)
$M_{\star,\lambda}$	Maximum stable AS mass imposed by self-interactions	Eq. (4.16)
$R_{\star,\lambda}$	Minimum stable AS radius imposed by self-interactions	Eq. (4.16)
$M_{\star,h}$	Low-mass ASMF cutoff from core-halo relation	$\mathcal{M}_{h, ext{min}}$
$M_{\star,R}$	Low-mass ASMF radius cutoff where $\mathcal{R} = R_{\star}$	Eq. (4.68)
$M_{\star,\gamma}$	Decay mass of ASs triggering parametric resonance	Eq. (4.61)
$M_{\star,\mathrm{acc}}$	ASMF high-mass cutoff due to accretion over $t_{\rm obs}$	Eq. (7.2)
$M_{\star,\mathrm{tot}}$	Total mass of ASs in the MW	Eq. (4.75)
$N_{\star,\mathrm{tot}}$	Total number of ASs in the MW	Eq. (4.76)
f_{\star}	Fraction of total MW mass contained in ASs	Eq. (4.79)
$arepsilon_{m{\star}}$	Parameter describing the typical AS mass	Eq. (4.79)

Table A.1: Different minicluster (top) and axion star parameters (bottom) used in this work.

In Tab. A.1 we summarize the different minicluster (top part) and axion star parameters (bottom part) used in this thesis together. For each parameter, a short explanation is provided together with the corresponding equation of definition in the right row. In the specific case of the minimum mass $M_{\star,h}$ imposed by the core-halo relation in Eq. (3.58), we emphasize that $M_{\star,h} = \mathcal{M}_{h,\min}$ by definition of $\mathcal{M}_{h,\min}$.

A.2 Schematic Summary of Contents

Fig. A.1 depicts a graphical summary of the contents of this work highlighting the logical struc-

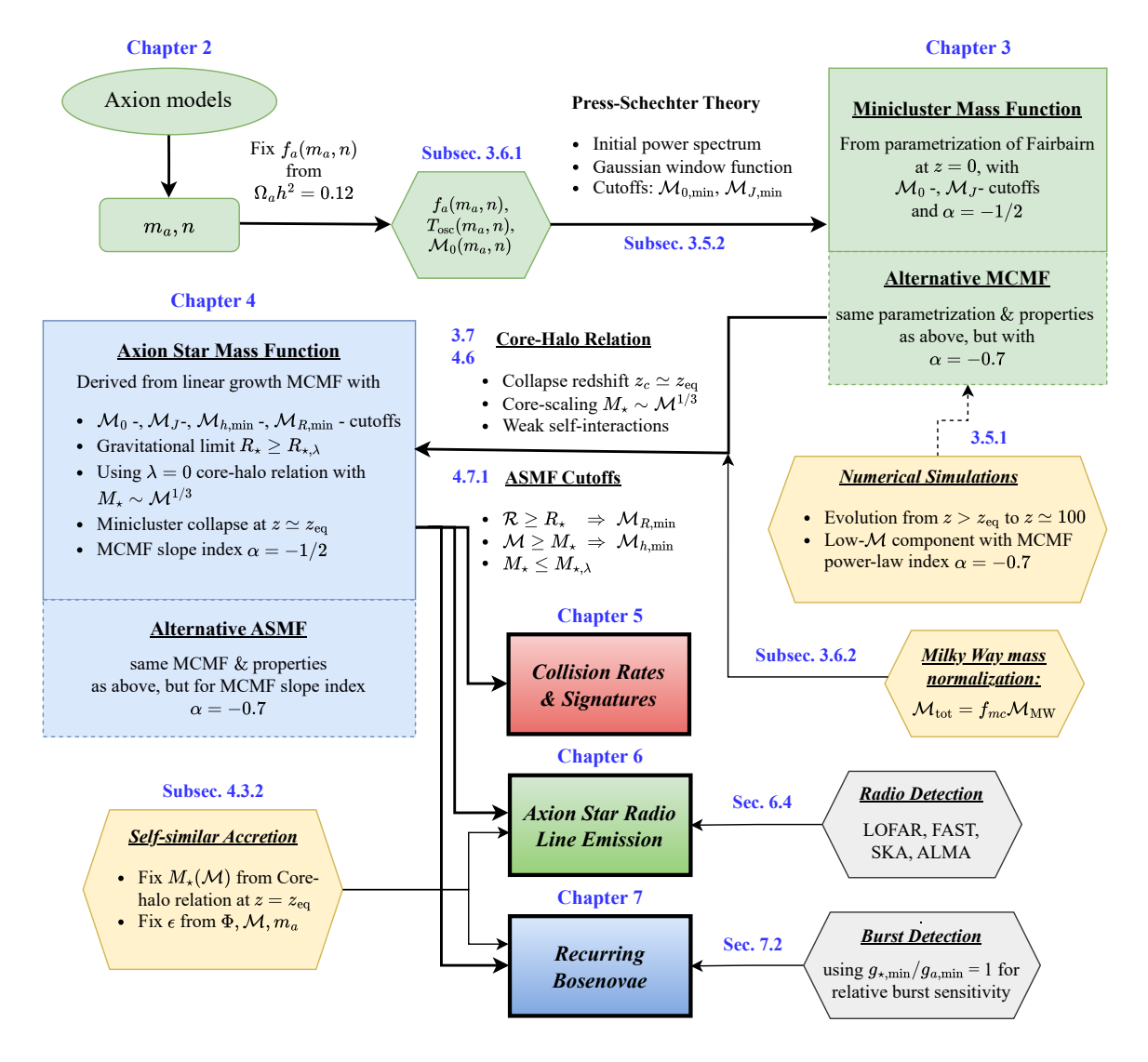


Figure A.1: Schematic representation of the structure of this thesis, modified from the scheme in Ref. [1]. Green panels indicate methods derived from Ref. [58], yellow panels relate to other literature [30, 194, 240], while black-framed colored elements indicate the results obtained in this work and Ref.s [1–3]. Underlying assumptions are explained by text items and the corresponding sections are shown in blue. Gray panels indicate additional considerations of experimental requirements.

ture of the different chapters. Corresponding chapters and sections are indicated in dark blue numbers, green panels indicate the approach from Ref. [58], light blue panels show the results taken from Ref. [1] and black rectangles indicate phenomenological implications corresponding to the three publications, Ref.s [1–3] in Chap.s 5, 6, 7, respectively. Yellow and gray panels indicate additional input from numerical simulations and experimental instrumentation.

To summarize the overall structure in a few sentences: The green panels indicate the derivation of the present-day properties of axion miniclusters for different axion models m_a , n from Sec. 3.6. Combining the minicluster properties with the core-halo relation from Eq. (3.57) together and additional consistency requirements in Sec. 4.7.1, we obtain the present-day mass distribution of axion stars in the Milky Way after normalization to the total mass of the NFW DM halo. The inferred knowledge on axion stars is thereafter applied to existing (Chap. 5) and novel signatures (in Chap.s 6 and 7) of galactic axion stars and miniclusters.

A.3 Relativistic Degrees of Freedom

In order to obtain the oscillation temperature $T_{\rm osc}$ numerically from the condition $m_a(T_{\rm osc}) = 3H(T_{\rm osc})$, we employ the fits to the relativistic and entropic degrees of freedom from Ref. [54], analogous to what was done in Ref. [58]. The corresponding fit parameters used in Eq. (2.52) are summarized in Tab. A.2.

$\underline{}$ j	1	2	3	4	5
a_0^R	1.21				
$a_{j,1}^R$	0.572	0.330	0.579	0.138	0.108
$a_{j,2}^R$	-8.77	-2.95	-1.80	-0.162	3.76
$a_{j,3}^R$	0.682	1.01	0.165	0.934	0.869
a_0^S	1.36				
$a_{j,1}^S$	0.498	0.327	0.579	0.140	0.109
$a_{j,2}^S$	-8.74	-2.89	-1.79	-0.102	3.82
$a_{j,3}^S$	0.693	1.01	0.155	0.963	0.907

Table A.2: Parameters for the fits of the relativistic 'R' and entropic 'S' degrees of freedom as a function of temperature following Eq. (2.52), taken from Ref. [54].

A.4 Navarro-Frank-White Profile

For the profile of the galactic DM halo we use the Navarro-Frank-White (NFW) profile [291]

$$\rho_{\text{NFW}}(r) = \frac{\rho_0}{\frac{r}{R_s} \left(1 + \frac{r}{R_s}\right)^2},$$
(A.1)

with characteristic density $\rho_0 = \rho_a = 0.32 \,\mathrm{GeV/cm^3}$ and core radius $R_s = 20.2 \,\mathrm{kpc}$ [194].

A.5 Ground States of the Schrödinger-Poisson System

Complementary to our analytical calculations of the soliton properties in Sec. 4.1, there have been numerous studies about the numerical computation of the exact groundstates of the Schrödinger-Poisson system, e.g. in Ref.s [49, 235, 292–294]. The groundstate properties of the lowest energy eigenstates with n=0 are commonly used for the derivation of the core-halo mass relation in Eq. (3.57) [171] and for other qualitative $\lambda=0$ soliton properties, e.g. in Eq. (5.35).

For the considerations in this work and for completeness, we briefly recall the fundamental results from Ref. [49] for the parameters of the lowest five $0 \le n \le 4$ eigenstates of the SP system with

$$R_s = \frac{1}{GM_s m_a^2} f_n \qquad , \qquad E_s = -\left(GM m_a\right)^2 \epsilon_n \,, \tag{A.2}$$

$$\rho_s = (Gm_a^2)^3 M^4 \rho_n, \quad , \quad v_{\text{s,vir}} = GM_s m_a w_n^{1/2}.$$
(A.3)

Note that the half-mass radius in Eq. (A.2) describes an effective mass-radius relation for $\lambda = 0$, analogous to the $\lambda < 0$ case in Eq. (4.17). The dimensionless constants ρ_n , f_n , ϵ_n , and w_n are determined numerically and taken from Ref. [49]. Together with the relation $w_n = \frac{2}{3}\epsilon_n$, the corresponding parameters are summarized in Tab. A.3.

n	$ ho_n$	f_n	ϵ_n	w_n
0	0.00440	3.9251	0.16277	0.10851
1	0.000180	23.562	0.03080	0.02053
2	0.000031	60.903	0.012526	0.008351
3	$9.400 \cdot 10^{-6}$	116.18	0.006747	0.004498
4	$3.733 \cdot 10^{-6}$	178.60	0.004209	0.002806

Table A.3: Properties of the lowest energy eigenstates of the Schrödinger-Poisson equation [49].

A.6 Rescaling of the Schrödinger Poisson system

Similar to the $\lambda \neq 0$ case of the GPP system in Eq. (4.7) and Eq. (4.8), there exists a class of transformations, which excludes the physical parameters m_a, G from the system Eq. (3.14), Eq. (3.15). The corresponding rescaling can be achieved by normalization of the system properties with the de-Broglie wavelength $(m_a v_0)^{-1}$ and coherence time $\sim (m_a v_0^2)^{-1}$ according to [170]

$$x = \widetilde{x}/(m_a v_0), \qquad \qquad t = \widetilde{t}/(m_a v_0^2), \qquad (A.4)$$

$$\psi = v_0^2 \sqrt{m_a/G} \,\widetilde{\psi} \,, \qquad \qquad \Phi_N = v_0^2 \,\widetilde{\Phi}_N \,, \qquad (A.5)$$

where as in the main text the tilde indicates the dimensionless, rescaled quantities. The resulting rescaled Schrödinger-Poisson system is

$$i\frac{\partial\widetilde{\psi}}{\partial\widetilde{t}} = -\frac{1}{2}\widetilde{\Delta}\widetilde{\psi} + \widetilde{\Phi}_N\widetilde{\psi}, \qquad (A.6)$$

$$\widetilde{\Delta}\widetilde{\Phi}_N = 4\pi |\widetilde{\psi}|^2 \,, \tag{A.7}$$

which is equivalent to Eq. (4.9) and Eq. (4.10) for $\lambda = 0$ as expected. Note here that the $\lambda < 0$ rescaling from Eq. (4.7) and Eq. (4.8) is essentially a special case of the SP rescaling for $v_0 = f_a \sqrt{G}/c_{\lambda}$, where v_0 is fixed by the self-interaction strength λ [35].

A.7 Galactic Neutron Star Distribution

We model the galactic neutron star distribution using the phenomenological fit from Ref. [259]

$$n_{NS}(\rho,\ell) = \frac{C_{NS}}{2\pi\rho} p_{\varrho}(\varrho) p_{\ell}(\varrho,\ell) , \qquad (A.8)$$

$$p_{\varrho}(\varrho) = A_{0,\varrho} + A \frac{\varrho^{\gamma - 1}}{\lambda^{\gamma}} e^{-\varrho/\lambda}, \qquad (A.9)$$

$$p_{\ell}(\varrho, \ell) = A_{0,\ell} \,\theta(\ell - 0.1 \text{kpc}) + A_{1,\ell} e^{-\ell/h_1(\varrho)} + A_{2,\ell} e^{-\ell/h_2(\varrho)}, \tag{A.10}$$

where $\theta(x)$ is a Heaviside function. The scale heights $h_{1,2}(\rho)$ are defined by

$$h_1(\varrho) = k_1 \varrho + b_1, \tag{A.11}$$

$$h_2(\varrho) = \begin{cases} k_2^{<} \varrho + b_2^{<}, & \varrho \le 4.5 \text{kpc} \\ k_2^{>} \varrho + b_2^{>}, & \varrho \ge 4.5 \text{kpc} \end{cases}$$
(A.12)

with the relevant parameters summarized in Tab. A.4.

Parameter	Value	
γ	1.83	
$A_{0,\ell}$	$1.8 \cdot 10^{-5} \text{ kpc}^{-1}$	
$A_{1,\ell}$	$1.87 \; {\rm kpc^{-1}}$	
$A_{2,\ell}$	$35.6 \cdot 10^{-3} \text{ kpc}^{-1}$	
k_1	$13 \cdot 10^{-3}$	
$k_2^{<}$	$18.4 \cdot 10^{-3}$	
$k_2^>$	0.05	

Parameter	Value
A	$95.6 \cdot 10^{-3}$
λ	$4.48~\mathrm{kpc}$
b_1	$12.8 \cdot 10^{-3} \text{ kpc}$
$b_2^{<}$	$0.03~{\rm kpc}$
$b_2^>$	$0.65~\mathrm{kpc}$
$A_{0,\varrho}$	$5 \cdot 10^{-3} \; \mathrm{kpc^{-1}}$

Table A.4: Best-fit parameters obtained from Ref. [259] for the galactic neutron star distribution of the Milky Way used for the calculation of the total mass-integrated collision rates Γ_{i-NS} in Eq. (5.8), Sec. 5.2 and Sec. 5.3.

A.8 Madelung Transformation

In the context of N-body simulations, it is useful to rewrite the wavefunction of the SP equations as [171, 295]

$$\psi = \sqrt{\frac{\rho}{m_a}} e^{im_a \theta_p/\hbar} = \sqrt{n} e^{im_a \theta_p/\hbar} , \qquad (A.13)$$

where the velocity amounts to the phase gradient $\mathbf{v} = \nabla \theta_p$. We keep track of powers of \hbar in this section to indicate the connection between the Schrödinger equation and the hydrodynamical

representation in the following. In this approach, the first line of Eq. (3.14) takes a form analogous to the mass- and momentum conservation equations in fluid dynamics. The corresponding transformation is called the *Madelung transformation* and it yields the equations

$$\partial_t \rho + \nabla(\rho \mathbf{v}) = 0, \tag{A.14}$$

$$\partial_t \mathbf{v} + (\mathbf{v}\nabla)\mathbf{v} = -\nabla\Phi_N + \frac{\hbar^2}{2m_a^2}\nabla\left(\frac{\nabla^2\sqrt{\rho}}{\sqrt{\rho}}\right). \tag{A.15}$$

Comparing Eq. (A.14) with the Euler equations of fluid dynamics, one finds that the only difference is given by the last term, which encodes the contribution of scalar field gradients to the change of momentum:

$$Q = -\frac{\hbar^2}{2m_a^2} \frac{\nabla^2 \sqrt{\rho}}{\sqrt{\rho}}.$$
 (A.16)

The extra term in Eq. (A.16) is often referred to as a *quantum pressure term*, since it is derived from the Schrödinger-Poisson equations. We note however that it is neither a pressure nor of real quantum nature in the context of the classical axion field equations derived in Sec. 3.1.

Numerical Methods

 \mathbf{B}

This chapter summarizes the numerical techniques used for the non-relativistic three-dimensional simulations, which are employed in Subsec. 4.3.1 and Subsec. 5.4.1 following Ref.s [170, 239]. Numerical simulations of the SP and GPP system have been performed in numerous studies, e.g. Ref.s [27, 32, 33, 166, 167, 170, 172, 174, 175, 202, 213, 231, 296–301], using either N-body simulations or pseudo-spectral methods. The fundamental goal in all of these simulations is to evolve the rescaled wavefunction $\widetilde{\psi}$ in the rescaled Gross-Pitaesvskii-Poisson system

$$i\frac{\partial\widetilde{\psi}}{\partial\widetilde{t}} = -\frac{1}{2}\widetilde{\Delta}\widetilde{\psi} + \widetilde{\Phi}_N\widetilde{\psi} - \frac{1}{8}|\widetilde{\psi}|^2\widetilde{\psi}, \qquad (B.1)$$

$$\widetilde{\Delta}\widetilde{\Phi}_N = 4\pi(|\widetilde{\psi}|^2 - \widetilde{n}), \qquad (B.2)$$

starting from random homogeneous initial conditions for $\widetilde{\psi}_0 = \widetilde{\psi}(\widetilde{t}=0)$ as argued in Subsec. 4.3.1. Note that the rescaled number density $\widetilde{n} = \widetilde{N}/\widetilde{L}^3$ in the dimensionless Poisson equation in Eq. (B.2) is related to the periodic boundary conditions in Sec. B.2, B.3. In the case of periodic boundary conditions, one can show that the volume integral over the source term needs to vanish. This is ensured by subtracting the average over $|\widetilde{\psi}|^2$, given by n.

We introduce the pseudo-spectral operator-splitting method, which allows for high-performant parallel computations, in Sec. B.1 following Ref. [239]. The operator splitting scheme decomposes the time evolution operator from Eq. (4.27) into diagonal components on the corresponding position- and Fourier space grids from Sec. B.2. Combining the numerical grid setup with the discrete Fourier transformation from Sec. B.3 and the overall summary of the resulting algorithmic scheme in Sec. B.4, we apply our simulations to the case of axion star condensation in Sec. B.5, Subsec. 4.3.1 and to non-relativistic AS core mergers in Subsec. 5.4.1.

B.1 Operator-Splitting Methods

As mentioned in Sec. B.5, the time evolution of cold axion dark matter, described by $\widetilde{\psi}(\widetilde{\mathbf{x}}, \widetilde{t} + \Delta \widetilde{t})$, can be determined from the time evolution operator

$$\widetilde{\mathcal{U}} = \widetilde{T} \exp\left(-i \int_{\widetilde{t}}^{\widetilde{t} + \Delta \widetilde{t}} d\widetilde{t}' \widetilde{\mathcal{H}}\right) = \widetilde{T} \exp\left\{-i \int_{\widetilde{t}}^{\widetilde{t} + \Delta \widetilde{t}} d\widetilde{t}' \left[\frac{\widetilde{\mathbf{k}}^2}{2} + \widetilde{\Phi}_N - \frac{1}{8}|\widetilde{\psi}|^2\right]\right\}$$
(B.3)

of the rescaled GPP system in Eq. (B.1), Eq. (B.2), where \widetilde{T} is a time ordering operator. A crucial realization in Eq. (B.3) is the fact that the Hamiltonian of the system may be separated

into exponentials of the spatial and momentum components $\widetilde{\mathcal{H}}_{\widetilde{x}},\,\widetilde{\mathcal{H}}_{\widetilde{k}}$ according to

$$\widetilde{\mathcal{H}} = -\frac{\widetilde{\nabla}^2}{2} + \widetilde{\Phi}_N - \frac{1}{8}|\widetilde{\psi}|^2 = \widetilde{\mathcal{H}}_{\widetilde{\mathbf{x}}} + \widetilde{\mathcal{H}}_{\widetilde{\mathbf{k}}},$$
 (B.4)

$$\widetilde{\mathcal{H}}_{\widetilde{\mathbf{x}}} = \widetilde{\Phi}_N - \frac{1}{8} |\widetilde{\psi}|^2 \quad , \quad \widetilde{\mathcal{H}}_{\widetilde{\mathbf{k}}} = -\frac{\widetilde{\nabla}^2}{2} \,.$$
 (B.5)

The decomposition in Eq. (B.4) can be used to facilitate the calculation of different expectation values in the corresponding eigenspace, i.e. in position and in Fourier space, where $\langle \widetilde{\psi} | \widetilde{\mathcal{H}}_{\mathbf{x}} | \widetilde{\psi} \rangle$ and $\langle \widetilde{\psi}_{\widetilde{\mathbf{k}}} | \widetilde{\mathcal{H}}_{\widetilde{\mathbf{k}}} | \widetilde{\psi}_{\widetilde{\mathbf{k}}} \rangle$ become diagonal. By means of the above separation of the Hamiltonian, the wave function $\widetilde{\psi}(\widetilde{\mathbf{x}}, \widetilde{t} + \Delta \widetilde{t}) = \widetilde{\mathcal{U}}\widetilde{\psi}(\widetilde{t})$ may be evolved in time by multiplication with exponentials $\exp \widetilde{\mathcal{H}}_i$ of the Hamiltonian components $\widetilde{\mathcal{H}}_{\widetilde{\mathbf{x}}}$ and $\widetilde{\mathcal{H}}_{\widetilde{\mathbf{k}}}$ in the corresponding eigenspace i. focusing on a single step $\Delta \widetilde{t}$ in Eq. (B.3) for simplicity, the time evolution operator $\exp(-i\widetilde{\mathcal{H}}\Delta\widetilde{t})$ needs to be decomposed into a series of products of $\exp(-i\widetilde{\mathcal{H}}_{\widetilde{\mathbf{x}}}\Delta\widetilde{t})$ and $\exp(-i\widetilde{\mathcal{H}}_{\widetilde{\mathbf{k}}}\Delta\widetilde{t})$. Since the commutator of the two eigenbases is non-vanishing $[\widetilde{\mathbf{x}},\widetilde{\mathbf{k}}] \neq 0$, a specific decomposition into the above products can only be accurate up to a certain order in time.

In the simplest case, $\exp(-i\widetilde{\mathcal{H}}\Delta\tilde{t}) = \exp(-i\widetilde{\mathcal{H}}_{\tilde{x}}\Delta\tilde{t}) \cdot \exp(-i\widetilde{\mathcal{H}}_{\tilde{k}}\Delta\tilde{t}) + \mathcal{O}(\Delta\tilde{t}^2)$ the resulting error is quadratic in the timestep size $\Delta\tilde{t}$. Another particularly simple and well-known scheme is the so-called *Strang-splitting* [302]

$$\exp\left[-i(\widetilde{\mathcal{H}}_{\widetilde{\mathbf{x}}} + \widetilde{\mathcal{H}}_{\widetilde{\mathbf{k}}})\Delta\widetilde{t}\right] = \exp\left(-i\frac{\widetilde{\mathcal{H}}_{\widetilde{\mathbf{k}}}}{2}\Delta\widetilde{t}\right)\exp\left(-i\widetilde{\mathcal{H}}_{\widetilde{\mathbf{x}}}\Delta\widetilde{t}\right)\exp\left(-i\frac{\widetilde{\mathcal{H}}_{\widetilde{\mathbf{k}}}}{2}\Delta\widetilde{t}\right) + \mathcal{O}(\Delta\widetilde{t}^{3}), \quad (B.6)$$

which is accurate up to $\mathcal{O}(\Delta \tilde{t}^3)$. This can best be seen by applying the Baker-Campbell Hausdorff formula [239, 303], which states that the general product of the exponentials

$$\exp(X)\exp(Y) = \exp(Z) \tag{B.7}$$

of two arbitrary non-commuting operators X and Y may be expressed as

$$Z = X + Y + \frac{1}{2}[X, Y] + \frac{1}{12}[X, [X, Y]] + \frac{1}{12}[Y, [Y, X]] + \frac{1}{24}[X, [Y, [Y, X]]] + \dots$$
 (B.8)

Applying the Baker-Campbell-Hausdorff formula twice to the Strang product [239]

$$e^{\frac{X}{2}}e^{Y}e^{\frac{X}{2}} = \exp\left\{\frac{X}{2} + Y + \frac{X}{2} + \frac{1}{2}\left[\frac{X}{2}, Y\right] + \frac{1}{2}\left[Y, \frac{X}{2}\right] + \mathcal{O}(dt^{3})\right\} = e^{X+Y} + \mathcal{O}(\Delta \tilde{t}^{3}) \quad (B.9)$$

one finds that the $\mathcal{O}(\Delta \tilde{t}^2)$ contributions given by the commutator of $X = -i\widetilde{\mathcal{H}}_{\tilde{\mathbf{k}}}\Delta \tilde{t}$ and $Y = -i\widetilde{\mathcal{H}}_{\tilde{\mathbf{k}}}\Delta \tilde{t}$ cancel each other. More specifically, it can be shown that all other commutators, which correspond to even orders in time, also vanish. Following Ref. [239], one can apply Eq. (B.8) repeatedly at higher orders and write

$$\exp\left(\frac{X}{2}\right)\exp(Y)\exp\left(\frac{X}{2}\right) = \exp(W) \tag{B.10}$$

with

$$W = X + Y + \frac{1}{12}[Y, [Y, X]] - \frac{1}{24}[X, [X, Y]] + \frac{7}{5760}[X, [X, [X, [X, Y]]]] - \frac{1}{720}[Y, [Y, [Y, [Y, X]]]] + \frac{1}{360}[X, [Y, [Y, [Y, X]]]] + \frac{1}{360}[Y, [X, [X, [X, Y]]]] - \frac{1}{480}[X, [X, [Y, [Y, X]]]] + \frac{1}{120}[Y, [Y, [X, [X, Y]]]] + \dots$$
(B.11)

Defining the time-independent operators $A = X/\Delta \tilde{t}$ and $B = Y/\Delta \tilde{t}$, Eq. (B.10) implies that the second-order integrator from Eq. (B.9) may be expressed in odd powers of $\Delta \tilde{t}$ as

$$S_2(\Delta \tilde{t}) \equiv \exp\left(\frac{A}{2}\Delta \tilde{t}\right) \exp\left(B\Delta \tilde{t}\right) \exp\left(\frac{A}{2}\Delta \tilde{t}\right)$$
$$= \exp\left(\alpha_1 \Delta \tilde{t} + \alpha_3 \Delta \tilde{t}^3 + \alpha_5 \Delta \tilde{t}^5 + \ldots\right), \tag{B.12}$$

where the corresponding coefficients α_i can be read off from Eq. (B.11), namely

$$\alpha_1 = A + B, \quad \alpha_3 = \frac{1}{12} [B, [B, A]] - \frac{1}{24} [A, [A, B]],$$
(B.13)

$$\alpha_5 = \frac{7}{5760}[A, [A, [A, [A, B]]]] + \dots$$
 (B.14)

As argued in Ref. [239], the vanishing of even powers in S_2 is a direct consequence of the fact that the operator is symmetric and time reversible, $S_2(\Delta \tilde{t})S_2(-\Delta \tilde{t}) = 1$.

Crucially for the splitting schemes used in this work, the fundamental operator S_2 can be used to derive higher order splitting schemes

$$S_{2n+2}(\Delta \tilde{t}) := S_{2n} \left(z_1 \Delta \tilde{t} \right) S_{2n} \left(z_0 \Delta \tilde{t} \right) S_{2n} \left(z_1 \Delta \tilde{t} \right) =, \tag{B.15}$$

where the effective time arguments $z_i \Delta \tilde{t}$ of S_{2n} with $n \in \mathbb{N}$ introduce two coefficients z_0 and z_1 , which must satisfy the conditions¹

$$z_0 + 2z_1 = 1, \quad z_0^{2n+1} + 2z_1^{2n+1} = 0$$
 (B.16)

in order for the higher order product $S_{2n+2}(\Delta \tilde{t})$ to produce an operator of order $\mathcal{O}(\Delta \tilde{t}^{2n+2})$ in the time coordinate $\Delta \tilde{t}$. Ref. [239] used the inductive method in Eq. (B.15) to derive operators of up to eight order in time. For arbitrary A, B the resulting schemes S_{2n+2} can equivalently be characterized by a product series of the form

$$\exp\left[\Delta \tilde{t}(A+B)\right] = \prod_{i=1}^{k} \exp\left(c_i \Delta \tilde{t}A\right) \exp\left(d_i \Delta \tilde{t}B\right) + \mathcal{O}\left(\Delta \tilde{t}^{n+1}\right), \tag{B.17}$$

where the products are ordered from left to right and the splitting parameters c_i , d_i are determined from repeated application of Eq.s (B.15) and (B.16) respectively. For the case of interest, $A = -i\widetilde{\mathcal{H}}_{\mathbf{k}}$ and $B = -i\widetilde{\mathcal{H}}_{\mathbf{k}}$ as mentioned before. Geometrically Eq. (B.17) separates each time step $\Delta \tilde{t}$ into two sets of sub-intervals $\{c_i\Delta \tilde{t}, d_i\Delta \tilde{t}\}$, which correspond to the kinetic and potential

¹This can be straight-forwardly shown by repeated application of the identity in Eq. (B.12) for S_{2n} at n=0 combined with induction arguments.

components of the rescaled Hamiltonian in Eq. (B.4).

Specifically, for the fourth-order splitting scheme the coefficients are [239]

$$c_1 = c_4 = \frac{1}{2(2 - 2^{1/3})}, \quad c_2 = c_3 = \frac{1 - 2^{1/3}}{2(2 - 2^{1/3})},$$
 (B.18)

$$d_1 = d_3 = \frac{1}{2 - 2^{1/3}}, \quad d_2 = -\frac{2^{1/3}}{2 - 2^{1/3}}, \quad d_4 = 0.$$
 (B.19)

Importantly for the numerical algorithm in this thesis, we find that the fourth-order splitting has the best combination of computational efficiency and resulting numerical errors. We briefly elaborate on numerical efficiency of our simulations at the end of this section and continue with the higher order splitting schemes.

At higher orders, the splitting schemes are often characterized by a set of m equivalent coefficients w_i , which are related to the coefficients c_i , d_i in Eq. (B.17) via the conditions

$$\sum_{i=1}^{k} c_i = \sum_{i=1}^{k} d_i = 1,$$
(B.20)

together with the coefficient relations

$$c_j = c_{k+1-j} = \frac{1}{2}(w_{m+2-j} + w_{m+1-j})$$
 , $w_{m+1} = 0$ (B.21)

$$d_j = d_{k-j} = w_{m+1-j} \quad , \quad d_k = 0 \,,$$
 (B.22)

where k = 2m + 2 is the number of parameters $c_i, d_i, 1 \le j \le (m+1)/2$ and m = 3, 7 for $\mathcal{O}(6)$ and $\mathcal{O}(8)$ in this work [170, 239]. We implement the above approach of using different sets of w_i from the literature for operators of order $\mathcal{O}(\Delta \tilde{t}^n)$ for n = 4, 6, 8. At each n, we compared the results from various literature [239, 304–307] to find the best splitting scheme with coefficients w_i for our simulations.

Crucially, we find that higher orders in time reduce numerical errors but simultaneously lead to an $\mathcal{O}(2)$ increase of the required steps, namely k=4,8,16 for n=4,6,8. It is therefore advisable to choose lower orders n in time together with smaller stepsizes $\Delta \tilde{t}$, which after adequate choice for $\Delta \tilde{t}$, turns out to yield the best combination of numerical performance and computational error control. The corresponding time stepping scheme is introduced in Sec. B.2.

w_i	n = 6, m = 3	n = 8, m = 7
w_1	-1.17767998417887	0.315293092396767
w_2	0.235573213359359	0.334624918245298
w_3	0.784513610477560	0.299064181303656
w_4		-0.573862471116082
w_5		0.190754710296238
w_6		-0.409100825800032
w_7		0.741670364350613

Table B.1: Splitting coefficients $w_i, ..., w_m$ at different orders n determining the k = 2m + 2 splitting steps in Eq. (B.17). The n = 6 scheme was taken from Ref. [239] and the n = 8 scheme from Ref. [304].

Before, we finish this section by listing the optimal sets of w_i determined from different literature and optimization tests to our problem in Tab. B.1. The time splitting schemes in Eq.s (B.18), (B.19) and Tab. B.1 contribute operator splitting methods at orders n = 4, 6, 8 in time. The remaining choice of the time step size Δt will be discussed together with the spatial grid setup in the next section.

B.2 Three-dimensional Grid Setup

Starting with the spatial grid setup, we use three-dimensional, evenly spaced grids for both position space, where $\widetilde{\psi}_{\widetilde{\mathbf{x}}}(\widetilde{t})$ is multiplied by components $\exp(-id_i\widetilde{\mathcal{H}}_{\widetilde{\mathbf{x}}}\Delta\widetilde{t})$ of $\widetilde{\mathcal{U}}$, and momentum space, where $\widetilde{\psi}_{\widetilde{\mathbf{k}}}(\widetilde{t})$ is evolved using $\exp(-ic_i\widetilde{\mathcal{H}}_{\widetilde{\mathbf{k}}}\Delta\widetilde{t})$. Each axis of the \widetilde{x} - and \widetilde{k} -grids has the maximum values \widetilde{x}_{\max} , \widetilde{k}_{\max} and grid spacing $\Delta\widetilde{x}$, $\Delta\widetilde{k}$ given by

$$\widetilde{x}_{\max} = \frac{\widetilde{L}}{2}$$
 , $\widetilde{k}_{\max} = \frac{\pi N_{\text{res}}}{\widetilde{L}}$ (B.23)

$$\Delta \widetilde{x} = \frac{\widetilde{L}}{N_{\text{res}}} \quad , \quad \Delta \widetilde{k} = \frac{2\pi}{\widetilde{L}} \,,$$
 (B.24)

where \widetilde{L} is the rescaled grid length and $N_{\rm res}$ its resolution. In the simulations, \widetilde{L} and $N_{\rm res}$ are specified by user input, from which the grid parameters are inferred. Note here that due to the zero-points of the grid, there is an asymmetry for the even grid resolution $N_{\rm res} = 256$ which we use². In the algorithm, the slightly asymmetric grid axes are set up as

$$-\widetilde{x}_{\max} + \Delta \widetilde{x} \leq \widetilde{x}_i \leq \widetilde{x}_{\max}, \qquad (B.25)$$

$$-\widetilde{k}_{\max} \leq \widetilde{k}_i \leq \widetilde{k}_{\max} - \Delta \widetilde{k}, \qquad (B.26)$$

where we note that the periodic boundary condition $\widetilde{\psi}(\widetilde{\mathbf{x}}) = \widetilde{\psi}(\widetilde{\mathbf{x}} + L\mathbf{n}_{\widetilde{x}}\widetilde{\mathbf{x}})$ is fulfilled. The asymmetry of the Fourier space grid requires the vanishing of modes with large $\widetilde{k} \sim \widetilde{k}_{\text{max}}$, where the asymmetry becomes relevant. This can either be achieved by increasing the resolution N_{res} or by decreasing the grid length \widetilde{L} according to Eq. (B.25).

Our code performs automated consistency checks at specified timesteps to ensure that the modes in the system fulfill $\tilde{k} < \tilde{k}_{\text{max}}$. This can straight-forwardly done by computing the expectation value of the total momentum operator $\tilde{P}(\tilde{t})$ of the system in Eq. (4.13), since the initial conditions to be specified in the following are isotropic in Fourier space and since \tilde{P} is a conserved quantity of the rescaled GPP system.

Moving on to the isotropic initial conditions of the three-dimensional simulations, we emphasize that the final state of the system is completely determined by the initial state $\psi_0(\mathbf{x})$ and the time evolution specified by the operator splitting schemes in Eq. (B.17) and Tab. B.1. The initial wavefunction in return is specified in Fourier space, where we employ two approaches that are common in the literature [170, 174, 213]. First the Gaussian initial distribution

$$\widetilde{\psi}_0(\widetilde{\mathbf{k}}) = 2\sqrt{2}\pi^{3/4}\sqrt{\widetilde{N}}\exp\left(-\frac{\widetilde{\mathbf{k}}^2}{2} + i\theta_r(\widetilde{\mathbf{k}})\right)$$
 (B.27)

²It is important to choose powers of 2 for the fast Fourier transform algorithm to perform efficiently.

where the initial phases $\theta_r(\mathbf{k}) \in [0, 2\pi]$ are randomly drawn from a uniform distribution at each point \mathbf{k} on the momentum space grid. And secondly, the δ -distributed wave function

$$|\psi_0(\mathbf{k})|^2 \propto \delta_D(|\mathbf{k}| - m_a v_0), \tag{B.28}$$

which constitutes the surface of a sphere with radius $|\mathbf{k}| = m_a v_0$ equal to the characteristic momentum $k_0 = m_a v_0$ of the system and again with random phases $\theta_r \in [0, 2\pi]$. For the Gaussian and δ -distributions considered in this section, we obtained b = 0.9 and b = 0.6 respectively, which agrees with the predictions from the original work, Ref. [170]. On the technical side, we also allow for variable radii of the initial momentum sphere by employing the delta distribution as $|\widetilde{\psi}(\mathbf{k})|^2 \propto \delta_D(|\widetilde{\mathbf{k}}| - c_0|\widetilde{\mathbf{k}}_0|)$ with $c_0\widetilde{k}_0 = c_0 = 0.6$ for the simulations in this work.

As mentioned in the main text, we demonstrate the initial configuration and subsequent evolution of a δ -distributed field $\widetilde{\psi}_0(\widetilde{\mathbf{x}})$ in Fig. 4.2, which was obtained using the pseudo-spectral operator splitting method in App. B. The simulations in this work were set up with a resolution of $N_x = 256^3$ and initialized with a δ -distributed initial field for a rescaled system size $\widetilde{L} = 44$ and particle number $\widetilde{N} = 55$ shown in the top left panel.

After specification of the initial wavefunction $\psi(\mathbf{k})$ according to the above procedure, the next step is to initialize the three-dimensional operator field $\widetilde{\Phi}_N(\widetilde{\mathbf{x}})$, which determines the position space component $\widetilde{\mathcal{H}}_{\widetilde{\mathbf{x}}}$ in Eq. (B.4) and thereby the time evolution in Eq. (B.17). In order to obtain the Newtonian potential from the source term $\propto |\widetilde{\psi}(\widetilde{\mathbf{x}})|^2$ in Eq. (B.2), we use Fourier transforms to calculate $\widetilde{\Phi}_N(\widetilde{\mathbf{k}})$ in momentum space. The procedure and numerical implementation of the Fourier transformation is presented in Sec. B.3.

Before, we summarize the numerical grid setup of this section by introducing the *adaptive time* stepping scheme obtain from the Courant–Friedrichs–Lewy condition [308, 309] of the system:

$$\Delta \tilde{t} = \min \left\{ \frac{\Delta \tilde{x} \tilde{L}}{\pi^2 c_k}, \frac{1}{c_x \max \left[\tilde{\Phi}_N(\tilde{\mathbf{x}}) \right]} \right\}, \tag{B.29}$$

where $\max[\widetilde{\Phi}_N(\widetilde{\mathbf{x}})]$ is the absolute maximum of the Newotnian position space potential and $\Delta \widetilde{x}$ is the spatial cell size from Eq. (B.26). The numerical constants $c_k = c_x$ depend on the system at hand, where for the simulations in this work $c_k = c_x = 10$ provides the best results. Upon initialization, our numerical algorithm allows the determination of a constant number of timesteps N_t together a fixed, temporal step size $\Delta \widetilde{t}$. When the step size $\Delta \widetilde{t}$ is omitted upon initialization, the adaptive method from Eq. (B.29) is employed automatically.

For long-time simulations like the results in Fig. 4.2 and Sec. B.5, the best approach is to first perform a test simulation of the condensation process with adaptive $\Delta \tilde{t}$ until $\tilde{t} \gtrsim \tilde{\tau}_{\rm gr}$ to obtain a suitable step size from the data output. This step size can then be used to re-calculate the same simulation with improved $\Delta \tilde{t}$ to enhance the numerical stability at large $\tilde{t} \gg \tilde{\tau}_{\rm gr}$. The simple reason for the resulting improvement is the fact that at the time of rapid collapse during condensation, the position term $\max[\tilde{\Phi}_N(\tilde{\mathbf{x}})]$ can change considerably between two time steps $\Delta \tilde{t}$ in Eq. (B.29).

B.3 Discrete Fourier Transform and Discrete Observables

As mentioned in the previous sections, the kinetic components $\propto \exp(-id_i\widetilde{\mathcal{H}}_{\widetilde{k}}\Delta \tilde{t})$ of the time evolution operator in Eq. (B.17) need to be applied in Fourier space. Similarly, the Newtonian

potential $\widetilde{\Phi}_N$ needs to be computed using Fourier transformations as will be specified in the following. In this section, we summarize the implementation and application of the *discrete Fourier transformation* (DFT) in the numerical algorithm.

For the implementation of the DFT, we use the FFTW library [310] in C++17, which we normalize according to

$$\widetilde{\psi}(\widetilde{\mathbf{k}}) = \sqrt{\frac{1}{N_{\text{res}}^3}} \sum_{\widetilde{\mathbf{x}}} \widetilde{\psi}(\widetilde{\mathbf{x}}) e^{-i\widetilde{\mathbf{k}}\widetilde{\mathbf{x}}} = \sqrt{\frac{\Delta \widetilde{x}^3}{\widetilde{L}^3}} \sum_{\widetilde{\mathbf{x}}} \widetilde{\psi}(\widetilde{\mathbf{x}}) e^{-i\widetilde{\mathbf{k}}\widetilde{\mathbf{x}}},$$
(B.30)

where the sum goes over all N_{res}^3 discrete points $\tilde{\mathbf{x}}$ of the position space grid. Similarly, the inverse discrete Fourier transform (IDFT) is defined with the same normalization constant

$$\widetilde{\psi}(\widetilde{\mathbf{x}}) = \sqrt{\frac{1}{N_{\text{res}}^3}} \sum_{\widetilde{\mathbf{k}}} \widetilde{\psi}(\widetilde{\mathbf{k}}) e^{i\widetilde{\mathbf{k}}\widetilde{\mathbf{x}}} = \sqrt{\frac{\Delta \widetilde{x}^3}{\widetilde{L}^3}} \sum_{\widetilde{\mathbf{k}}} \widetilde{\psi}(\widetilde{\mathbf{k}}) e^{i\widetilde{\mathbf{k}}\widetilde{\mathbf{x}}},$$
(B.31)

which yields a factor of $N_{\rm res}^{-3}$ after consecutive application of the DFT and IDFT. The discrete Fourier transforms are applied using periodic boundary conditions and the above FFTW algorithm to allow for CPU parallelization, for which we find that generally 64 CPU threads yield the best performance.

After initialization of the $\tilde{t}=0$ wavefunction in \tilde{k} -space, the Fourier transform of the Newtonian potential $\tilde{\Phi}_N$ can be computed from the Poisson equation in Eq. (B.2) according to

$$\widetilde{\Phi}_N(\widetilde{\mathbf{k}}) = \frac{-4\pi |\widetilde{\psi}(\widetilde{\mathbf{k}})|^2}{|\widetilde{\mathbf{k}}|^2} \quad , \quad \widetilde{\Phi}_N(|\widetilde{\mathbf{k}}| = 0) = 0 \,, \tag{B.32}$$

where we have set the $\tilde{\mathbf{k}} = 0$ mode to zero, as in Ref. [170]. The coordinate representation $\widetilde{\Phi}_N(\widetilde{\mathbf{x}})$ is then simply obtained by applying the inverse DFT to the field in Eq. (B.32). In the case of adaptive time stepping in Eq. (B.29), the maximum of $\widetilde{\Phi}_N(\widetilde{\mathbf{x}})$ is used to determine $\Delta \tilde{t}$ for the next propagation length in time.

On a different note about Fourier transformations, we employ the evolution operator decomposition in Eq. (B.17) to the total Hamiltonian in Eq. (B.4) and its components $\widetilde{\mathcal{H}}_{\tilde{\mathbf{x}}}$. This implies that the propagation of the wavefunction $\widetilde{\psi}(\tilde{t} + \Delta \tilde{t})$ at each timestep $\Delta \tilde{t}$ requires k = 2m + 2 applications of the DFT and IDFT respectively in order to switch between position and momentum space, where the split steps c_i and d_i in Eq. (B.17) are performed.

Simultaneously, the algorithm computes the expectation values for different observables of the system. The first such quantity is the rescaled total particle number

$$\widetilde{N} = \Delta \widetilde{x}^3 \sum_{\widetilde{\mathbf{x}}} |\widetilde{\psi}(\widetilde{\mathbf{x}})|^2 = \Delta \widetilde{x}^3 \sum_{\widetilde{\mathbf{k}}} |\widetilde{\psi}(\widetilde{\mathbf{k}})|^2,$$
(B.33)

which can either be computed in position or in Fourier space and which is equal to the total mass in rescaled coordinates. Another important conserved quantity is the total energy of the system

$$\widetilde{E} = \Delta \widetilde{x}^3 \sum_{\widetilde{\mathbf{k}}} \frac{\widetilde{\mathbf{k}}^2}{2} |\widetilde{\psi}(\widetilde{\mathbf{k}})|^2 + \frac{\Delta \widetilde{x}^3}{2} \sum_{\widetilde{\mathbf{x}}} \widetilde{\Phi}_N(\widetilde{\mathbf{x}}) |\widetilde{\psi}(\widetilde{\mathbf{x}})|^2 + \frac{\Delta \widetilde{x}^3}{2} \sum_{\widetilde{\mathbf{x}}} \widetilde{\lambda} |\widetilde{\psi}(\widetilde{\mathbf{x}})|^4, \qquad (B.34)$$

which is composed out of the kinetic, gravitational and self-interaction energy of the system, equivalent to Eq.s (4.2), (4.3), (4.4). Crucially for our checks of the numerical stability, the relative energy

$$\frac{\Delta \widetilde{E}(\widetilde{t})}{\widetilde{E}(\widetilde{t}=0)} = \frac{\widetilde{E}(\widetilde{t}) - \widetilde{E}(0)}{\widetilde{E}(0)}$$
(B.35)

can be used to check the conservation of energy in the system (see Fig. B.1). We ensure that none of our simulations exceed $\Delta \widetilde{E}/\widetilde{E}(0) \sim 10^{-3}$ for consistency.

A third conserved quantity of the rescaled GPP system is the total momentum

$$\widetilde{P} = \Delta \widetilde{x}^3 \sum_{\widetilde{\mathbf{k}}} \widetilde{\mathbf{k}} |\widetilde{\psi}(\widetilde{\mathbf{k}})|^2, \qquad (B.36)$$

which is computed numerically in Fourier space. As mentioned in Sec. B.2, the initial wavefunction at $\tilde{t}=0$ is specified with $\tilde{P}(0)=0$ in Fourier space, so that the conservation of momentum can simply be checked by ensuring that $\tilde{P}(\tilde{t})\ll 1$ over time. In each simulation and at different specified time steps, the numerical algorithm computes all three of the above expectation values, provides them as live output during runtime and raises warnings if any of the conservation laws are considerably violated. In order for a simulation to be considered numerically stable, all three of the above quantities need to be conserved at all \tilde{t} .

B.4 Pseudo-spectral Operator-splitting Scheme

With the basic numerical techniques of our simulations being specified in Sec.s B.1 to B.3, we continue to briefly summarize how these techniques are combined in the schematic structure of the algorithm. For later use, the documentation of the numerical C++ code is contained in the respective '.cpp' files and in the main file. We also mention some technical details about parallelization, data output and operating systems at the end of this section.

Starting with the schematic summary of the algorithm, each simulation can be broadly summarized by the following points:

- 1. Initialize the spatial grid with \widetilde{N} , \widetilde{L} and resolution $N_{\rm res}$
- 2. Set the number N_t and size $\Delta \tilde{t}$ of timesteps to be performed
- 3. Initialize $\tilde{t} = 0$ wavefunction $\widetilde{\psi}_0(\tilde{\mathbf{k}})$ in **Fourier space** (either Gaussian or δ -distributed, see Eq.s (B.27), (B.28))
- 4. Perform kinetic evolution through multiplication of $\widetilde{\psi}(\mathbf{k})$ by $\exp(-ic_i\widetilde{\mathcal{H}}_{\mathbf{k}}\Delta \tilde{t})$
- 5. Fourier transform to **position space** to compute the source term in Eq. (B.2) with $\tilde{n} = \tilde{N}/\tilde{L}^3$ from $\tilde{\psi}(\tilde{\mathbf{x}})$ and Eq. (B.33)
- 6. Transform back to **Fourier space** with DFT
- 7. Compute the Poisson potential in Fourier space from Eq. (B.32)
- 8. IDFT to **position space** and evolve $\widetilde{\psi}(\widetilde{\mathbf{x}})$ through multiplication with $\exp(-id_i\widetilde{\mathcal{H}}_{\widetilde{\mathbf{x}}}\Delta\widetilde{t})$

- 9. Repeat steps 4. to 8. until k=2m+2 and the product series in Eq. (B.17) is complete for a given time step $\Delta \tilde{t}$
- 10. Calculate expectation values \widetilde{E} , \widetilde{P} and \widetilde{N} from Eq.s (B.34), (B.36) and (B.33)
- 11. Save expectation values to data and print to user output
- 12. Repeat steps 4. to 11. for each of the N_t time steps with step size $\Delta \tilde{t}$
- 13. Save final density field $\widetilde{\psi}(\tilde{t}_f)$ to output for later simulations

The above enumeration demonstrates the importance of the computational efficiency of the DFT in Eq. (B.30), (B.31). In principle the parallelization can also be performed on graphics processing units as for example done in Ref.s [170, 174]. As mentioned before, in our code we use CPU parallelization, which is implemented with the FFTW library [310] using 64 cores and the OpenMP library using arbitrary multiples of 2 for the thread number.

The code also allows for controlled data output at dedicated steps by tracing the axion star in the \tilde{z} -plane through determination of the point with maximum density $\max(|\tilde{\psi}|^2)$ in $\tilde{\mathbf{x}}$. This allows to significantly reduce data output through saving only the corresponding \tilde{z} -plane in position space at specified steps $n\Delta \tilde{t}$ with $n \in \mathbb{N}$.

Other utility functions include the time dependent output of the projected Fourier spectrum $|\widetilde{\psi}(|\widetilde{\mathbf{k}}|)|^2$ as a function of $|\widetilde{\mathbf{k}}|$, the output and animation of the radial profile $\widetilde{\psi}(\widetilde{r},\widetilde{t})$ over time and the implementation of absorbing boundary conditions for AS mergers similar to what was done in Ref.s [33, 172]. The absorbing potential is defined in terms of an overall amplitude V_0 with center L_c and width $\delta_{\rm abs}$ according to [33]

$$V_{\rm abs}(\widetilde{\mathbf{x}}) = -\frac{iV_0}{2} \left[2 + \frac{\tanh\left(\max(\widetilde{x}, \widetilde{y}, \widetilde{z}) - L_c\right)}{\delta_{\rm abs}} - \tanh\left(\frac{L_c}{\delta_{\rm abs}}\right) \right]. \tag{B.37}$$

This potential was used in the non-relativistic AS merger simulation from Fig.s 5.10 and 5.11 to prevent back-reflection of emitted waves, where we choose $V_0 = 100$, $L_c = 22$ and $\delta_{\rm abs} = 0.5$ from optimization of the collision process. It is implemented as an external addition to the Newtonian potential $\widetilde{\Phi}_N$ and added to the position space Hamiltonian $\widetilde{\mathcal{H}}$ in Eq. (B.4). Note here that we have omitted the tilde for some variables since they do not have a physical equivalent, namely V_0, L_c and $\delta_{\rm abs}$.

In the specific case of the AS merger from Fig. 5.10, we have added a second axion star through implementation of the best-fit, spherically symmetric sech-profile [33, 231]

$$\widetilde{\psi}(\widetilde{r}) = \sqrt{\frac{3\widetilde{M}_{\star}}{\pi^3 R_0^3}} \operatorname{sech}\left(\frac{\widetilde{r}}{\widetilde{R}_0}\right),$$
(B.38)

where $R_0 \sim 1$ is a length scale which sets the profile shape of the sech-fit and where we use $M_{\star} = 6$. As part of the thesis in Ref. [235], the numerical code in this work was also extended by an implementation of the exact, spherically symmetric soliton solutions, which were calculated in Ref. [231]. The stability analysis in Ref. [235] using improved exact profiles compared to the sech-fit in Eq. (B.38) showed that there exist transition regions in the stable and dilute branches of axion stars in Fig. 4.1. This realization can be interested for transition between the two branches and future research on long-time stability of axion stars.

To conclude this section, we mention that all of the simulation figures in this thesis and several from Ref. [235] were produced using a fully automated plotting routine in Python, which uses the C++ output data and a Python-C++ interface.

B.5 Application to Axion Star Condensation

We continue with the application of the above numerical simulations to axion star condensation, which was already shown in the main text in Sec. 4.2 and Sec. 4.3.1. The simulations in this thesis are performed for $\lambda=0$, $\widetilde{L}=44$, $\widetilde{N}=55$ on a $N_x=256^3$ grid with timesteps $\Delta \widetilde{t}=0.01$ and predicted condensation time $\widetilde{\tau}_{\rm gr}\simeq 1445$. For computational efficiency, the order of the time splitting scheme was chosen as four, corresponding to Eq.s (B.18) and (B.19), and the time step size $\Delta \widetilde{t}=0.01$ was found from previous test simulations.

Fig. B.1 clearly shows that all of the relevant observables remain precisely conserved up to deviations of order $\mathcal{O}(\Delta) \sim 10^{-4}$ or lower. The largest relative violation of conservation laws

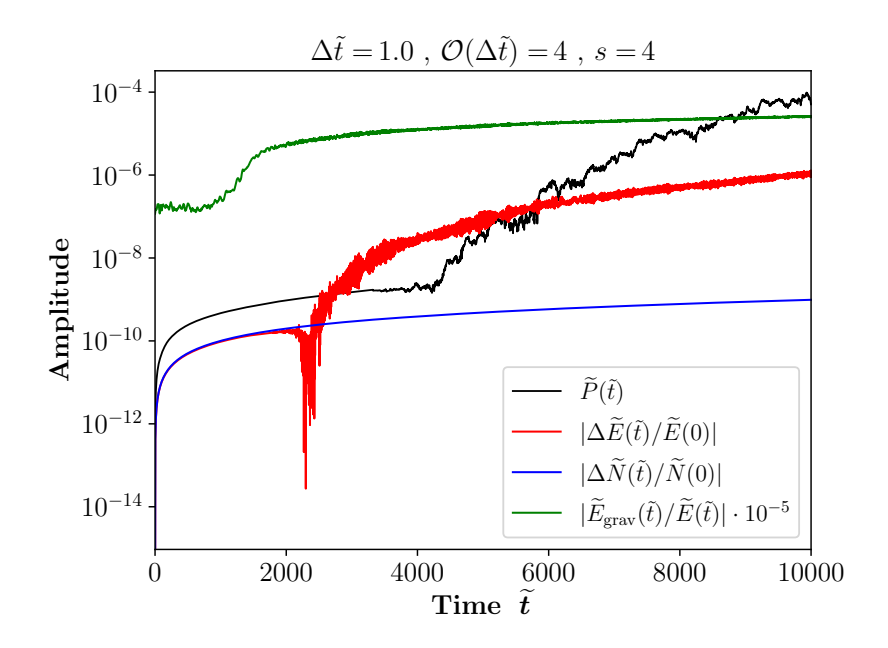


Figure B.1: Time-dependent numerical consistency checks for different conserved observables of the GPP system in Eq.s (B.36), (B.34) and (B.33) with the conserved dimensionless total momentum $\widetilde{P}(\tilde{t})$ shown in black lines. The violation of energy- and mass-conservation are measured by the relative energy shift $|\Delta \widetilde{E}(\tilde{t})/\widetilde{E}(0)|$ in red and by the relative shift $|\Delta \widetilde{N}(\tilde{t})/\widetilde{N}(0)|$ of the total particle number in blue lines. The green line indicates the relative potential binding energy $|\widetilde{E}_{\text{grav}}(\tilde{t})/\widetilde{E}(\tilde{t})|$ of the dilute system, which is dominated by E_{grav} in Eq.s (4.3) and (B.34). Prior to the point of condensation around $\tilde{t} \sim \widetilde{\tau}_{\text{gr}} \simeq 1445$, the potential energy can be seen to rapidly increase, see also Fig. 4.2.

is seen for the total momentum $\widetilde{P}(\widetilde{t})$ in black, which indicates that the asymmetry of the \widetilde{k} -space grid is a dominant effect in the simulations. On the other hand, the particle number $\widetilde{N}(\widetilde{t})$ is well-preserved since it only inherits numerical errors through repeated application of the DFT and IDFT in Eq.s (B.30), (B.31), as argued in Ref. [170].

Another useful tool for the considerations of axion star mass growth is given by the radial profile

 $\widetilde{\psi}(|\widetilde{\mathbf{r}}|,\widetilde{t})$, which can be saved and animated automatically. The corresponding soliton profiles of the long-time simulation with $\lambda=0$ from Fig. 4.2 and B.1 are depicted by colored lines at different times \widetilde{t} in Fig. B.2. Importantly and in accordance with the mass-radius relation of stable axion stars $M_{\star} \propto 1/R_{\star}$, the profile can be seen to increase in amplitude and decrease in radius during the mass growth at larger \widetilde{t} .

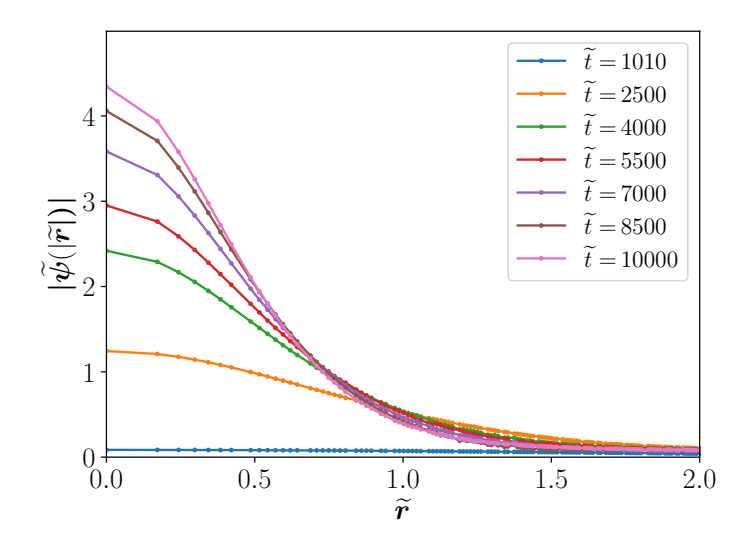


Figure B.2: Radial axion star profile $\widetilde{\psi}(|\widetilde{\mathbf{r}}|, \widetilde{t})$ over time obtained from the simulations in Fig.s 4.2 and B.1. At $\widetilde{t} < \widetilde{\tau}_{\rm gr} \simeq 1440$ in blue, the automated algorithm determines the maximum density from the background fluctuations, which gives a roughly homogeneous $\widetilde{\psi}(|\widetilde{\mathbf{r}}|, \widetilde{t})$.

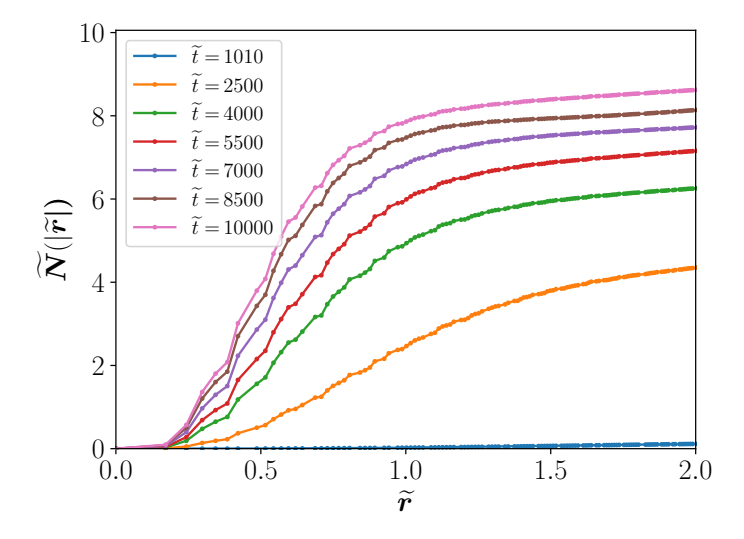


Figure B.3: Integrated rescaled mass (i.e. particle number) of the axion star over time in the simulations from Fig.s 4.2, B.1 and B.3. At $\tilde{t} < \tilde{\tau}_{\rm gr} \simeq 1440$ in blue, the automated algorithm determines the maximum density from the background fluctuations, which gives a roughly constant mass $\tilde{N}(|\tilde{r}|, \tilde{t})$.

The wave-like features in the cumulative radial AS mass in Fig. B.3 are essentially caused by the spherically symmetric quasi-particle fluctuations in the excited surrounding region of the condensed soliton, see also Fig. 4.2.

B.6 Outlook on numerical Simulations for Future Research

We conclude the summary of the numerical simulations from this thesis by listing the most promising fields of its application for future studies. It should be clear from the theory part in Chap. 4, that the field of axion star condensation from isotropic initial conditions is well-established at the time of writing. Accordingly, mass growth simulations of interest to scientific publications require enhanced performance with GPU acceleration and use of large computer clusters, both beyond the scope of our simulations. Instead, there are some other, less straightforward directions, which can be explored using the numerical techniques from this appendix.

- 1. Through implementation of the redshift-dependent Schrödinger-Poisson equations in an expanding universe, the virialization of composite ASMC systems around matter-radiation equality could be explored, similar to what was done in Ref.s [30, 169], but with special emphasis on the Φ -dependence of the core-halo mass relation from Eq. (3.57). This dependence was also mentioned as one of the major uncertainties for ASMC phenomenology in the conclusions in Sec.s 6.5, 7.5.
- 2. The numerical study of the stability of exact spherically symmetric solutions of axion stars in Ref. [235] using this code demonstrated that the dilute and stable branch regions around the critical value $M_{\star} \sim M_{\star,\lambda}$ should not be understood as absolutely distinguishable. Instead the simulations in Ref. [235] showed that quasi-stable solutions can exist on the top of the dense branch, and that transitions between the two branches can be induced through external perturbation, e.g. through external gravitational fields in transient events. Such stability simulations have not been published to date and would be worth exploring.
- 3. The interference effects in axion star mergers from Fig. 5.11 suggested possible constructive interference with the minicluster background, which could have considerable effect on the merger dynamics. While such effects have been observed in the collisions of isolated solitons before, for example in Ref.s [33, 172], the interaction of the minicluster background has not been taken into account so far. Constructive interference effects could prove beneficial for the development of parametric resonance or Bosenovae following MC mergers and would contribute to the current understanding of composite ASMC systems.

Overall, the combined phenomenology of axion stars in galactic miniclusters allows for a range of new scientific studies, which can be performed with three-dimensional solvers like the one developed in this thesis. The modular and automated nature of the corresponding algorithm and its data output hence allows for simple extensions of our work in future investigations.

Additional Information on Mass Distributions

This chapter provides additional information on our results for different AS-/MC-properties inferrred from the MCMF and ASMF in Subsec.s 3.6.2 and 4.7.2, respectively. Sec. C.1 shows the total number, average masses and radii of miniclusters obtained for different axion models m_a , n considered in this work. Similarly, Sec. C.2 contains the same quantities inferred from the core-halo relation in Eq. (3.57) for axion stars at different m_a , n.

C.1 Properties of galactic Miniclusters

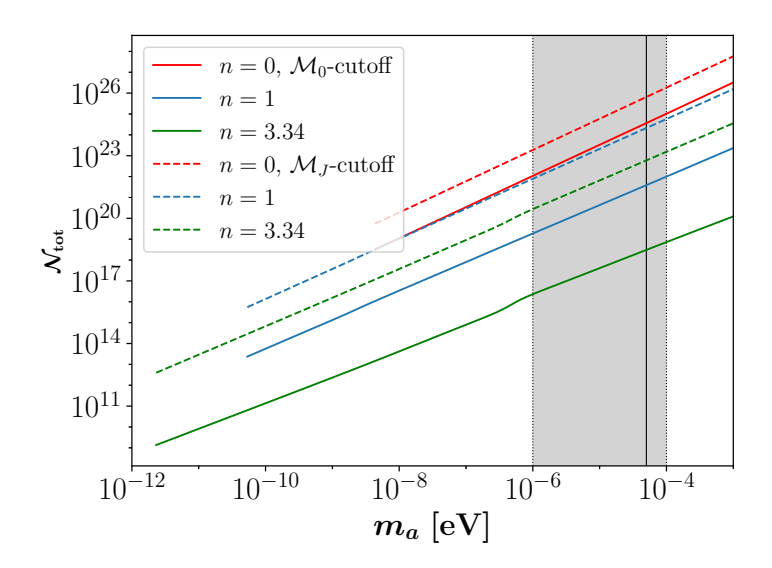


Figure C.1: Total number of galactic axion miniclusters for different axion models m_a , n from Subsec. 3.6.1, obtained from the linear growth MCMF from Sec. 3.6. Shown for both MCMF low-mass cutoffs from Subsec. 3.5.2 in solid and dashed lines. Taken from Ref. [1].

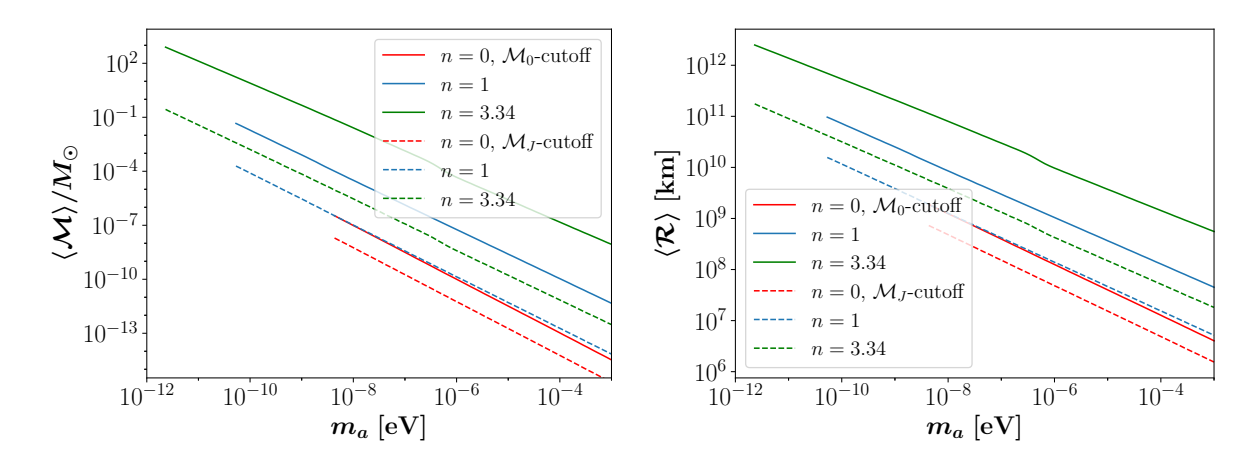


Figure C.2: Average mass (left) and radius (right) of galactic axion miniclusters from Eq.s (4.77), (4.78) for different axion models m_a , n from Subsec. 3.6.1. Obtained from the linear growth MCMF from Sec. 3.6 for both MCMF low-mass cutoffs from Subsec. 3.5.2 in solid and dashed lines.

C.2 Properties of galactic Axion Stars

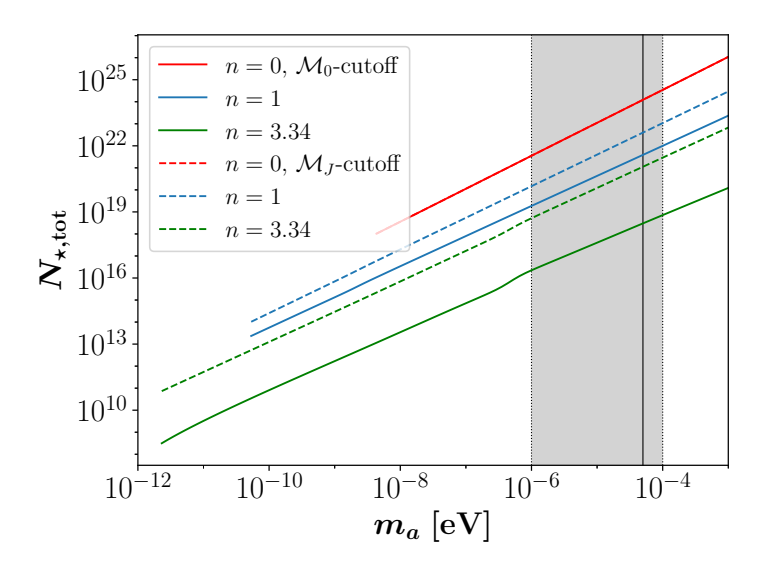


Figure C.3: Total number of galactic axion stars for different axion models m_a , n from Subsec. 3.6.1, obtained from the linear growth MCMF and the core-halo relation in Eq. (3.57). Shown for both MCMF low-mass cutoffs from Subsec. 3.5.2 in solid and dashed lines. For n = 0, the AS number is independent of the low- \mathcal{M} cutoffs. Taken from Ref. [1].

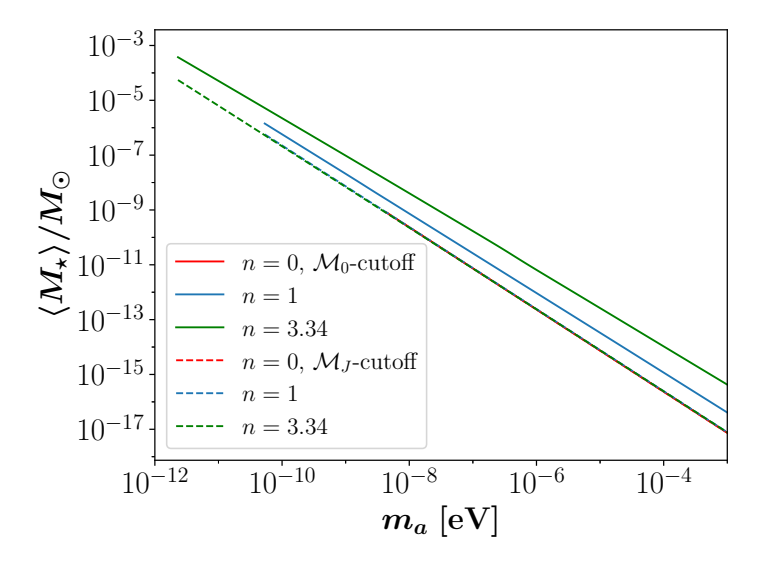


Figure C.4: Average mass of galactic axion stars for different axion models m_a , n from Subsec. 3.6.1, obtained from the linear growth MCMF and the core-halo relation in Eq. (3.57). The different \mathcal{M}_J -cutoffs in dashed lines and the n=0 \mathcal{M}_0 -cutoff in red solid lines yield almost identical results. Taken from Ref. [1].

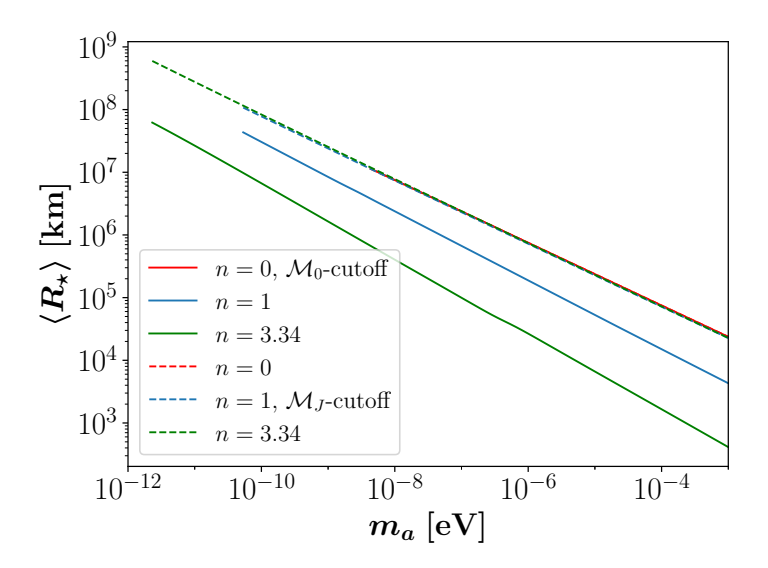


Figure C.5: Average radius of galactic axion stars for different axion models m_a, n from Subsec. 3.6.1, obtained from the linear growth MCMF and the core-halo relation in Eq. (3.57). The different \mathcal{M}_J -cutoffs in dashed lines and the n=0 \mathcal{M}_0 -cutoff in red solid lines yield almost identical results. Taken from Ref. [1].

Analytical Calculations on Axion Stars

D.1 Parametric Resonance

In this chapter, we summarize the derivation of the AS resonance criterion from Sec. 4.5 following Ref. [32]. The first step is to start from the Lagrangian $\mathcal{L}_{a\gamma\gamma}$ from Eq. (2.17), which describes the interaction of the electromagnetic field in the presence of an axion field ϕ . Varying the Lagrangian in Eq. (2.17) with respect to the four vector potential $A^{\mu} = (A_0, \mathbf{A})$ and neglecting the gradients of the non-relativistic axion field ϕ , which is slowly varying in space, one obtains the equation of motion

$$\ddot{\mathbf{A}} - \nabla^2 \mathbf{A} + g_{a\gamma\gamma} \nabla \left(\partial_t \phi \mathbf{A} \right) = 0 \tag{D.1}$$

for the two degrees of freedom of the propagating photon described by \mathbf{A} . Note that Eq. (D.1) is formulated in the Coulomb gauge $\nabla \cdot \mathbf{A}$, as indicated by the fact that the time-derivative $\partial_t \phi$ is contained inside the brackets and spatial derivative ∇ . In Fourier space, Eq. (D.1) may be expressed in terms of the electromagnetic modes in k-space as

$$\ddot{\mathbf{A}}_{\mathbf{k}} + k^2 \mathbf{A}_{\mathbf{k}} + g_{a\gamma\gamma} i \mathbf{k} \int \frac{d^3 k'}{(2\pi)^3} \partial_t \phi_{\mathbf{k} - \mathbf{k}'} \mathbf{A}_{\mathbf{k}'} = 0, \qquad (D.2)$$

where again gradient terms have been neglected compared to the time-derivatives of the axion field, $|\nabla \phi| \ll |\partial_t \phi|$.

The next step is to insert the time- and k-dependence of the axion field into Eq. (D.2). As was shown in the detailed studies of Ref. [32], the fundamental dynamics of the soliton resonance we are interested in may also be captured by assuming a homogeneous axion field

$$\phi(t) = \phi_0 \cos(\omega_0 t) \tag{D.3}$$

with field amplitude ϕ_0 and an oscillation frequency $\omega_0 \approx m_a$. While the system in Eq. (D.3) is by nature unstable against gravitational collapse and soliton formation, it allows for a simplified analytical treatment. Importantly for this work, the condition for resonant axion-photon conversion inside the soliton is derived from the properties of the homogeneous axion field in Eq. (D.3). Therefore using the above approach for $\phi(t)$ in Eq. (D.2), the electromagnetic modes decouple in Fourier space, yielding the simplified EOM

$$\ddot{A}_{\mathbf{k}} + k^2 A_{\mathbf{k}} - g_{a\gamma\gamma} \,\omega_0 \,\phi_0 \sin(\omega_0 \,t) \,i \,\mathbf{k} A_{\mathbf{k}} = 0 \tag{D.4}$$

for the vector potential **A**, whose Fourier transform can be expressed in terms of the time-dependent mode functions $s_{\mathbf{k}}(t)$

$$\mathbf{A}_{\mathbf{k}}(t) = \sum_{\lambda = \pm} \left[a_{\mathbf{k},\lambda} \, \boldsymbol{\epsilon}_{\mathbf{k},\lambda} \, s_{\mathbf{k}}(t) + a_{\mathbf{k},\lambda}^{\dagger} \, \boldsymbol{\epsilon}_{\mathbf{k},\lambda}^{*} \, s_{\mathbf{k}}^{*}(t) \right] , \qquad (D.5)$$

where $\epsilon_{\mathbf{k},\lambda=\pm}$ are vectors describing the circular polarization and $a_{\mathbf{k},\lambda}$ and $a_{\mathbf{k},\lambda}^{\dagger}$ are annihilation and creation operators. Finally writing $i\mathbf{k}\epsilon_{\mathbf{k},\lambda} = k \epsilon_{\mathbf{k},\lambda}$, the two polarizations in Eq. (D.4) decouple so that the mode functions $s_{\mathbf{k}}(t)$ satisfy the *Mathieu equation*

$$\ddot{s}_{\mathbf{k}} + \left[k^2 - g_{a\gamma\gamma} \,\omega_0 \, k \,\phi_0 \sin(\omega_0 \, t) \right] \, s_{\mathbf{k}} = 0 \,, \tag{D.6}$$

which describes an oscillator with a periodic pump frequency $\omega_k^2(t) = \omega_k^2(t+T)$ and period $T = 2\pi/\omega_0$. Defining the effective frequency $\omega_k^2(t) = A + B\sin(\omega_0 t)$, Eq. (D.6) reduces to

$$\ddot{s}_{\mathbf{k}} + \omega_k^2(t)s_{\mathbf{k}} = 0, \tag{D.7}$$

where the coefficients

$$A = k^2 \qquad , \qquad B = -g_{a\gamma\gamma} \,\phi_0 \,k \,\omega_0 \tag{D.8}$$

will prove useful at a later point in the calculation. Due to the periodicity of the pump, the system exhibits a resonance for modes with certain values of k. To see this in general, the Mathieu equation, needs to be solved numerically, see also Ref. [32] for a detailed analysis. For the purpose of this work, it is sufficient to perform a small amplitude analysis, in which the pumping term stays relatively small. The corresponding solutions to Eq. (D.6), Eq. (D.7) can be written in the general form

$$s_{\mathbf{k}}(t) = P_{\mathbf{k}}(t)e^{\mu_k t} + P_{\mathbf{k}}(-t)e^{-\mu_k t},$$
 (D.9)

where $P_{\mathbf{k}}(t)$ is a periodic function of time and the parameter μ_k is the Floquet exponent describing the stability of the solution. As stated in the main text, the real component of the Floquet exponent μ_k is responsible for the exponentially growing modes. At small amplitudes, $k/\omega_0 \gg g_{a\gamma\gamma}\phi_0/2$, the resulting spectrum of narrow resonant bands is composed of equally spaced lines at $k^2 \approx (n\omega_0/2)^2$ for $n \in \mathbb{N}^+$.

Next, taking advantage of the small amplitudes of the periodic pump, one can write the mode functions from Eq. (D.9) in terms of the harmonic expansion

$$s_{\mathbf{k}}(t) = \sum_{\omega = -\infty}^{+\infty} e^{i\,\omega\,t} f_{\omega}(t), \qquad (D.10)$$

where the frequencies ω are summed over the range of $\omega = \pm n\omega_0/2$. Inserting the harmonic expansion Eq. (D.10) into Eq. (D.6) and dropping terms $\propto \ddot{f}_{\omega}$, gives [32]

$$4 i \omega \dot{f}_{\omega}(t) + 2(A - \omega^{2}) f_{\omega}(t) - i B \left[f_{\omega - \omega_{0}}(t) - f_{\omega + \omega_{0}}(t) \right] = 0$$
 (D.11)

for the differential equations at different frequency bands $\omega = \pm n\omega_0/2$. Then focusing on the dominant instability in the n=1 band and the lowest frequencies $\omega = \pm \omega_0/2$, one obtains the coupled pair of differential equations

$$\frac{d}{dt} \begin{bmatrix} f_{\frac{\omega_0}{2}}(t) \\ f_{-\frac{\omega_0}{2}}(t) \end{bmatrix} = \frac{i}{m} \begin{bmatrix} A - \frac{\omega_0^2}{4} & -i\frac{B}{2} \\ -i\frac{B}{2} & -A + \frac{\omega_0^2}{4} \end{bmatrix} \begin{bmatrix} f_{\frac{\omega_0}{2}}(t) \\ f_{-\frac{\omega_0}{2}}(t) \end{bmatrix}.$$
(D.12)

According to standard matrix theory, the system Eq. (D.12) exhibits an exponential growth $\propto \exp(\pm \mu_k t)$ where the growth rate μ_k is given by the eigenvalues of the above matrix. Solving

the coupled differential equations in Eq. (D.12), and inserting the expressions for A and B in Eq. (D.8), yields the exponential growth rate

$$\mu_k^{(1)} = \sqrt{\frac{g_{a\gamma\gamma}^2 k^2 \phi_0^2}{4} - \frac{\left(k^2 - \frac{\omega_0^2}{4}\right)^2}{\omega_0^2}}$$
 (D.13)

of the dominant n = 1 instability band. Since the width an growth factors $\mu_k^{(n)}$ of higher order instabilities decrease with larger n, it is sufficient to consider the leading n = 1 instability for AS resonance, as done in the remaining steps in Sec. 4.5.

D.2 Derivation of Axion Star Resonance Mass

This appendix contains the derivation of the decay mass from Eq. (4.61) for the Gaussian profile, analogous to what was done in Ref.s [33, 231] for the sech-profile in Eq. (B.38). As argued in Sec. 4.5, the condition for the parametric instability to develop in a given soliton can be inferred from the growth exponent Eq. (4.55) of the first instability band for the homogeneous axion field in Eq. (D.3). Requiring $\mu_H > \mu_{\rm esc}$ with μ_H from Eq. (4.55) and $\mu_{\rm esc} \approx 1/(2R_{\star})$ [231], one obtains

$$\frac{g_{a\gamma\gamma}m_a}{4}\phi_0 > \frac{1}{2R_+},\tag{D.14}$$

where the central density $\phi_0 = \phi(r=0)$ can be obtained from Eq. (3.10) for the Gaussian profile in Eq. (4.1), which gives $\phi_0 = \sqrt{2M_\star/(\pi^{3/2}m_a^2R_\star^3)}$ in Eq. (4.57). This leads to the AS resonance condition

$$\frac{g_{a\gamma\gamma}m_a}{4}\sqrt{\frac{2M_{\star}}{\pi^{3/2}m_a^2R_{\star}^3}} > \frac{1}{2R_{\star}},$$
 (D.15)

$$\Leftrightarrow g_{a\gamma\gamma}\sqrt{\frac{M_{\star}}{2\pi^{3/2}R_{\star}}} > 1, \qquad (D.16)$$

where the rescaling from Eq. (4.7) and Eq. (4.8) can be used to write

$$\frac{M_{\star}}{R_{\star}} = \frac{m_{\rm Pl} f_a}{m_a c_{\lambda}^{1/2}} \frac{m_a f_a \widetilde{M}_{\star}}{m_{\rm Pl} c_{\lambda}^{1/2} \widetilde{R}_{\star}} = \frac{f_a^2}{c_{\lambda}} \frac{\widetilde{M}_{\star}}{\widetilde{R}_{\star}}. \tag{D.17}$$

This leads to the condition

$$g_{a\gamma\gamma}f_{a} > \left(2\pi^{3/2}\right)^{1/2} \sqrt{\frac{\widetilde{R}_{\star}}{\widetilde{M}_{\star}}} c_{\lambda}$$

$$= \sqrt{2}\pi^{3/4} \left[\frac{g(\alpha_{\star})c_{\lambda}}{\alpha_{\star}}\right]^{1/2} \sqrt{\frac{\widetilde{R}_{\star,\lambda}}{\widetilde{M}_{\star,\lambda}}} \equiv \beta_{\star} \left[\frac{g(\alpha_{\star})c_{\lambda}}{\alpha_{\star}}\right]^{1/2} \tag{D.18}$$

from Eq. (4.58), where in the last two equations, we have expressed the AS quantities M_{\star} , R_{\star} in terms of the critical quantities $M_{\star,\lambda}$, $R_{\star,\lambda}$ by introducing an additional parameter $\alpha_{\star} \in (0,1]$,

which parametrizes the mass-radius relation according to Eq. (4.59) and Eq. (4.60) with $g(\alpha_{\star}) = (1 + \sqrt{1 - \alpha_{\star}^2})/\alpha_{\star}$ [33]. Just like the critical quantities $M_{\star,\lambda}$, $R_{\star,\lambda}$ from Eq. (4.16), the parameter

$$\beta_{\star} = \sqrt{2}\pi^{3/4} \sqrt{\frac{\widetilde{R}_{\star,\lambda}}{\widetilde{M}_{\star,\lambda}}} \approx 0.42$$
 (D.19)

in Eq. (D.18) depends on the chosen ansatz for the radially symmetric wavefunction, where $\beta_{\star} \approx 0.42$ for the Gaussian profile in Eq. (4.1) used in this work. In rescaled coordinates, the critical quantities take the values

$$\widetilde{M}_{\star,\lambda} = 10.88\,,\tag{D.20}$$

$$\widetilde{R}_{\star,\lambda} = 0.173. \tag{D.21}$$

With the above relations we can derive the decay mass, beyond which the parametric resonance develops. Rearranging the point of equality given by Eq. (D.18) in terms of the mass parameter α_{\star} from Eq. (4.59) leads to

$$g_{a\gamma\gamma}f_a = \beta_\star \left[\frac{c_\lambda g(\alpha_\star)}{\alpha_\star} \right]^{1/2}$$
 (D.22)

$$\Leftrightarrow g_{a\gamma\gamma}^2 f_a^2 = \beta_{\star}^2 c_{\lambda} \frac{1 + \sqrt{1 - \alpha_{\star}^2}}{\alpha_{\star}^2}$$
 (D.23)

$$\Leftrightarrow 1 + \sqrt{1 - \alpha_{\star}^2} = \alpha_{\star}^2 \frac{g_{a\gamma\gamma}^2 f_a^2}{\beta_{\star}^2 c_{\lambda}}$$
 (D.24)

$$\Leftrightarrow 1 - \alpha_{\star}^2 = \alpha_{\star}^4 \frac{g_{a\gamma\gamma}^4 f_a^4}{\beta_{\star}^4 c_{\lambda}^2} + 1 - 2\alpha_{\star}^2 \frac{g_{a\gamma\gamma}^2 f_a^2}{\beta_{\star}^2 c_{\lambda}}$$
 (D.25)

$$\Leftrightarrow \alpha_{\star}^{2} \frac{g_{a\gamma\gamma}^{4} f_{a}^{4}}{\beta_{\star}^{4} c_{\lambda}^{2}} = \frac{2g_{a\gamma\gamma}^{2} f_{a}^{2}}{\beta_{\star}^{2} c_{\lambda}} - 1 \tag{D.26}$$

$$\Leftrightarrow \alpha_{\star} = \sqrt{\frac{2c_{\lambda}\beta_{\star}^{2}}{g_{a\gamma\gamma}^{2}f_{a}^{2}} - \frac{\beta_{\star}^{4}c_{\lambda}^{2}}{g_{a\gamma\gamma}^{4}f_{a}^{4}}} = \frac{M_{\star}}{M_{\star,\lambda}}.$$
 (D.27)

Then expressing $M_{\star,\lambda}$ in terms of its rescaled equivalent from Eq. (D.20) and rearranging for $M_{\star} = M_{\star,\gamma}$, we obtain the Gaussian profile decay mass

$$M_{\star,\gamma} = \widetilde{M}_{\star,\lambda} \frac{m_{\rm Pl} f_a}{m_a} \frac{\sqrt{2c_{\lambda}} \beta_{\star}^2}{g_{a\gamma\gamma}^2 f_a^2} \sqrt{\frac{g_{a\gamma\gamma}^2 f_a^2}{\beta_{\star}^2 c_{\lambda}} - \frac{1}{2}}$$
(D.28)

$$= \widetilde{M}_{\star,\lambda} \frac{m_{\rm Pl}}{m_a} \frac{\sqrt{2}\beta_{\star}^2}{g_{a\gamma\gamma}^2 f_a} \sqrt{\left(\frac{g_{a\gamma\gamma} f_a}{\beta_{\star}}\right)^2 - \frac{c_{\lambda}}{2}}$$
(D.29)

$$= \widetilde{M}_{\star,\lambda} \frac{m_{\rm Pl}}{m_a} 2\sqrt{2} \pi^{3/2} \frac{\widetilde{R}_{\star,\lambda}}{\widetilde{M}_{\star,\lambda}} \frac{1}{g_{a\gamma\gamma}^2 f_a} \sqrt{\left(\frac{g_{a\gamma\gamma} f_a}{\beta_{\star}}\right)^2 - \frac{c_{\lambda}}{2}}$$
 (D.30)

$$= 5.94 \cdot 10^{-14} M_{\odot} \left(\frac{50 \,\mu\text{eV}}{m_a} \right) \left(\frac{10^{-11} \text{GeV}^{-1}}{g_{a\gamma\gamma}} \right)^2 \left(\frac{10^{11} \text{GeV}}{f_a} \right) \sqrt{\left(\frac{g_{a\gamma\gamma} f_a}{0.42} \right)^2 - \frac{c_{\lambda}}{2}} \quad (D.31)$$

from Eq. (4.61) and Ref. [2].

D.3 Derivation of Axion Star Radius Cutoff

The axion star radius cutoff masses $\mathcal{M}_{R,\min}$, $M_{\star,R}$ from Eq. (4.70), Eq. (4.68) can be derived from the condition Eq. (4.66), as will be shown in this chapter. For ease of computation, it is useful to first rewrite the spherically homogeneous minicluster radius from Eq. (3.24) in terms of a Φ -dependent function $f_{\Phi}(\Phi)$ according to

$$\mathcal{R} = \frac{3.4 \cdot 10^7 \,\mathrm{km}}{\Phi (1 + \Phi)^{1/3}} \left(\frac{\mathcal{M}}{10^{-12} \,M_{\odot}} \right)^{1/3} \equiv f_{\Phi}(\Phi) \,\mathcal{M}^{1/3} \,. \tag{D.32}$$

Similarly, we define the function $f_z(z)$ as the power of $\mathcal{M}_{h,\text{min}}$ in Eq. (3.57), Eq. (3.58) which relates the AS core mass

$$M_{\star}(z) = \mathcal{M}_{h,\min}^{2/3}(z)\mathcal{M}^{1/3} \equiv f_z(z)\mathcal{M}^{1/3}$$
 (D.33)

to the mass \mathcal{M} of its host minicluster. Note also that we defined the physical radius of the soliton to be given by the radius

$$R_{\star,90} = C_{\star,90} R_{\star} \quad , \quad C_{\star,90} = 1.76796$$
 (D.34)

containing 90% of the total soliton mass at position $r \to \infty$, and where $C_{\star,90}$ is a profile-dependent constant. For the Gaussian profile in Eq. (4.1) assumed in this work, $C_{\star,90} = 1.76796$ [159]. This way, we can express the equality of axion star core and host minicluster size in Eq. (4.66) as

$$R_{\star,90} = C_{\star,90} R_{\star} \stackrel{!}{=} \mathcal{R} \,.$$
 (D.35)

Lastly, we express the scale radius R_{\star} in the above equation in terms of the AS mass M_{\star} through the mass-radius relation Eq. (4.17) and write the MC radius in terms of its mass \mathcal{M} , which gives

$$\frac{\alpha_{\rm kin}}{\alpha_{\rm grav} G m_a^2 M_{\star}} \pm \sqrt{\left(\frac{\alpha_{\rm kin}}{\alpha_{\rm grav} G m_a^2 M_{\star}}\right)^2 - \frac{3\alpha_{\rm int}}{\alpha_{\rm grav} G m_a^2 f_a^2}} = \frac{f_{\Phi}(\Phi) \mathcal{M}^{1/3}}{C_{\star,90}} \,. \tag{D.36}$$

The axion star mass can be eliminated from Eq. (D.36) by using the core-halo relation from Eq. (3.57), which after re-arranging yields

$$\left(\frac{f_{\Phi}(\Phi)\mathcal{M}^{1/3}}{C_{\star,90}} - \frac{\alpha_{\text{kin}}}{\alpha_{\text{grav}}Gm_a^2 f_z(z)\mathcal{M}^{1/3}}\right)^2 = \frac{f_{\Phi}^2(\Phi)\mathcal{M}^{2/3}}{C_{\star,90}^2} - \frac{2\alpha_{\text{kin}} f_{\Phi}(\Phi)}{\alpha_{\text{grav}}Gm_a^2 f_z(z)C_{\star,90}} + \left(\frac{\alpha_{\text{kin}}}{\alpha_{\text{grav}}Gm_a^2 f_z(z)\mathcal{M}^{1/3}}\right)^2 = \left(\frac{\alpha_{\text{kin}}}{\alpha_{\text{grav}}Gm_a^2 f_z(z)\mathcal{M}^{1/3}}\right)^2 - \frac{3\alpha_{\text{int}}\alpha_{\text{kin}}^2}{\alpha_{\text{grav}}Gm_a^2 f_a^2} \qquad (D.37)$$

$$\Leftrightarrow \frac{f_{\Phi}^2(\Phi)\mathcal{M}^{2/3}}{C_{\star,90}^2} = \frac{2\alpha_{\text{kin}} f_{\Phi}(\Phi)}{\alpha_{\text{grav}}Gm_a^2 f_z(z)C_{\star,90}} - \frac{3\alpha_{\text{int}}\alpha_{\text{kin}}^2}{\alpha_{\text{grav}}Gm_a^2 f_a^2}. \qquad (D.38)$$

Solving the above equation for the minicluster mass \mathcal{M} at the point of equality, $R_{\star,90} = \mathcal{R}$, and re-entering the helper functions f_{Φ} and f_z , we obtain the final low-mass cutoff

$$\mathcal{M}_{R,\min} = \left(\frac{2\alpha_{\text{kin}}C_{\star,90}}{\alpha_{\text{grav}}Gm_a^2 f_z(z)f_{\Phi}(\Phi)} - \frac{3\alpha_{\text{int}}\alpha_{\text{kin}}^2 C_{\star,90}^2}{\alpha_{\text{grav}}Gm_a^2 f_a^2 f_{\Phi}(\Phi)^2}\right)^{3/2}$$

$$= \left(\frac{2\alpha_{\text{kin}}C_{\star,90}\Phi(1+\Phi)^{1/3}(10^{-12} M_{\odot})^{1/3}}{\alpha_{\text{grav}}Gm_a^2 \mathcal{M}_{h,\min}(z)^{2/3} \cdot 3.4 \cdot 10^7 \text{ km}}\right)^{3/2}$$

$$- \frac{3\alpha_{\text{int}}\alpha_{\text{kin}}^2 C_{\star,90}^2 \Phi^2(1+\Phi)^{2/3}(10^{-12} M_{\odot})^{2/3}}{\alpha_{\text{grav}}Gm_a^2 f_a^2(3.4 \cdot 10^7 \text{ km})^2}\right)^{3/2}$$

$$= \left(\frac{2\alpha_{\text{kin}}\Phi(1+\Phi)^{1/3}C_{\star,90}}{\alpha_{\text{grav}}} 1.28 \cdot 10^8 \text{ kg}^{2/3} \left(\frac{50 \,\mu\text{eV}}{m_a}\right)^2 \left(\frac{1+z}{1+z_{\text{eq}}}\right)^{1/2} \left(\frac{\xi(z)}{\xi(z_{\text{eq}})}\right)^{1/6}$$

$$- \frac{3\alpha_{\text{int}}\alpha_{\text{kin}}^2 \Phi^2(1+\Phi)^{2/3}C_{\star,90}^2}{\alpha_{\text{grav}}} 8.82 \text{ kg}^{2/3} \left(\frac{50 \,\mu\text{eV}}{m_a}\right)^2 \left(\frac{6 \cdot 10^{11} \,\text{GeV}}{f_a}\right)^2\right)^{3/2}$$
(D.41)

of the ASMF. The complete relation in Eq. (D.41) contains a modification term $\propto \alpha_{\rm int}$ that arises due to the weak attractive self-interactions $\lambda = -m_a^2/f_a^2$ considered in this thesis. Comparing the corresponding coefficients we find that the condition for the self-interaction term to be negligible is

$$\frac{3\alpha_{\rm int}\alpha_{\rm kin}\Phi(1+\Phi)^{1/3}C_{\star,90}}{2}\frac{8.82}{1.3\cdot10^8} \left(\frac{m_a}{50\,\mu\text{eV}}\right) \left(\frac{1+z}{1+z_{\rm eq}}\right)^{1/2} \left(\frac{\xi(z)}{\xi(z_{\rm eq})}\right)^{1/6} \left(\frac{6\cdot10^{11}\,\text{GeV}}{f_a}\right)^2 \ll 1\,,$$
(D.42)

which for the axion models m_a , n from Subsec. 3.6.1 can be formulated in terms of the symmetry breaking constant f_a to obtain the condition

$$f_a \gg 18 \,\text{GeV} \,\sqrt{\Phi} (1+\Phi)^{1/6} \left(\frac{m}{50 \,\mu\text{eV}}\right)^{1/2} \left(\frac{1+z}{1+z_{\text{eq}}}\right)^{1/4} \left[\frac{\zeta(z)}{\zeta(z_{\text{eq}})}\right]^{1/12} \,.$$
 (D.43)

We checked that the condition in Eq. (D.43) remains valid for all of the axion models with $10^{-12}\,\mathrm{eV} \le m_a \le 10^{-2}\,\mathrm{eV}$ and n=0,1,2,3.34 considered in this work. We note that this statement can also be read off from Fig. 3.6 and that it coincides with our definition of weak self-interactions. Physically, Eq. (D.43) demonstrates, that the self-interaction is indeed negligible for the dilute and large solitons on the stable branch of Fig. 4.1, which have $R_{\star} \gg R_{\star,\lambda}$ and are hence dominated by gravity.

Therefore neglecting the $\propto \alpha_{\rm int}$ term in Eq. (D.41), we finally obtain the minicluster mass

$$\mathcal{M}_{R,\min} \approx 4.9 \cdot 10^{-17} \, M_{\odot} \, \sqrt{\Phi} (1+\Phi)^{1/6} \, \left(\frac{\alpha_{\rm kin} C_{\star,90}}{\alpha_{\rm grav}} \right)^{1/2} \left(\frac{1+z}{1+z_{\rm eq}} \right)^{1/4} \left[\frac{\zeta(z)}{\zeta(z_{\rm eq})} \right]^{1/12} \left(\frac{50 \, \mu \text{eV}}{m_a} \right)^{3/2}$$
(D.44)

corresponding to the ASMF radius cutoff in Eq. (4.70). Note that after entering $f_z(z)$ in the above expressions, the radius cutoff masses become dependent on the core-halo relation. Additional dependence on the assumed soliton profile is indicated by the constants α_i and $C_{\star,90}$.

Bibliography

- [1] Dennis Maseizik and Günter Sigl. "Distributions and collision rates of ALP stars in the Milky Way". In: *Phys. Rev. D* 110.8 (2024), p. 083015. DOI: 10.1103/PhysRevD.110.083015. arXiv: 2404.07908 [astro-ph.CO].
- [2] Dennis Maseizik et al. "Radio lines from accreting axion stars". In: Journal of Cosmology and Astroparticle Physics 2025.05 (2025), p. 033. DOI: 10.1088/1475-7516/2025/05/033. arXiv: 2409.13121 [hep-ph].
- [3] Dennis Maseizik et al. "Detectability of accretion-induced bosenovae in the Milky Way". In: Phys. Rev. D 111.6 (2025), p. 063017. DOI: 10.1103/PhysRevD.111.063017. arXiv: 2410.13082 [hep-ph].
- [4] Günter Sigl, Dennis Maseizik, and Hyeonseok Seong. "Glowing Axion Stars at Radio Frequencies". In: *PoS* COSMICWISPers (2024), p. 026. DOI: 10.22323/1.454.0026.
- [5] Adam G. Riess et al. "Observational Evidence from Supernovae for an Accelerating Universe and a Cosmological Constant". In: *The Astronomical Journal* 116.3 (Sept. 1998), pp. 1009–1038. ISSN: 0004-6256. DOI: 10.1086/300499.
- [6] Eleonora Di Valentino et al. "In the realm of the Hubble tension—a review of solutions". In: Class. Quant. Grav. 38.15 (2021), p. 153001. DOI: 10.1088/1361-6382/ac086d. arXiv: 2103.01183 [astro-ph.CO].
- [7] F. Zwicky. "Die Rotverschiebung von extragalaktischen Nebeln". In: *Helv. Phys. Acta* 6 (1933), pp. 110–127. DOI: 10.1007/s10714-008-0707-4.
- [8] Vera C. Rubin and W. Kent Ford Jr. "Rotation of the Andromeda Nebula from a Spectroscopic Survey of Emission Regions". In: Astrophys. J. 159 (1970), pp. 379–403. DOI: 10.1086/150317.
- [9] V. C. Rubin, W. K. Ford Jr., and N. Thonnard. "Rotational properties of 21 SC galaxies with a large range of luminosities and radii, from NGC 4605 (R=4kpc) to UGC 2885 (R=122kpc)." In: *The Astrophysical Journal* 238 (June 1980), pp. 471–487. DOI: 10.1086/158003.
- [10] Jaan Einasto, Ants Kaasik, and Enn Saar. "Dynamic evidence on massive coronas of galaxies". In: *Nature* 250.5464 (1974), pp. 309–310. DOI: 10.1038/250309a0.
- [11] M. Markevitch et al. "A Textbook Example of a Bow Shock in the Merging Galaxy Cluster 1E 0657-56". In: *The Astrophysical Journal* 567.1 (Feb. 2002), pp. L27–L31. ISSN: 1538-4357. DOI: 10.1086/339619.
- [12] Douglas Clowe, Anthony Gonzalez, and Maxim Markevitch. "Weak lensing mass reconstruction of the interacting cluster 1E0657-558: Direct evidence for the existence of dark matter". In: *Astrophys. J.* 604 (2004), pp. 596–603. DOI: 10.1086/381970. arXiv: astroph/0312273.
- [13] G. F. Smoot et al. "Structure in the COBE Differential Microwave Radiometer First-Year Maps". In: *The Astrophysical Journal Letters* 396 (Sept. 1992), p. L1. DOI: 10.1086/186504.

- [14] P. A. R. Ade et al. "Planck2015 results: XIII. Cosmological parameters". In: Astronomy & Astrophysics 594 (Sept. 2016), A13. ISSN: 1432-0746. DOI: 10.1051/0004-6361/201525830.
- [15] R. D. Peccei and Helen R. Quinn. "CP Conservation in the Presence of Pseudoparticles". In: *Phys. Rev. Lett.* 38 (25 June 1977), pp. 1440–1443. DOI: 10.1103/PhysRevLett.38. 1440.
- [16] R. D. Peccei and Helen R. Quinn. "Constraints imposed by CP conservation in the presence of pseudoparticles". In: *Phys. Rev. D* 16 (6 Sept. 1977), pp. 1791–1797. DOI: 10.1103/PhysRevD.16.1791.
- [17] Steven Weinberg. "A New Light Boson?" In: *Phys. Rev. Lett.* 40 (4 Jan. 1978), pp. 223–226. DOI: 10.1103/PhysRevLett.40.223.
- [18] F. Wilczek. "Problem of Strong P and T Invariance in the Presence of Instantons". In: Phys. Rev. Lett. 40 (5 Jan. 1978), pp. 279–282. DOI: 10.1103/PhysRevLett.40.279.
- [19] Michael Dine and Willy Fischler. "The Not So Harmless Axion". In: *Phys. Lett. B* 120 (1983). Ed. by M. A. Srednicki, pp. 137–141. DOI: 10.1016/0370-2693(83)90639-1.
- [20] John Preskill, Mark B. Wise, and Frank Wilczek. "Cosmology of the Invisible Axion". In: Phys. Lett. B 120 (1983). Ed. by M. A. Srednicki, pp. 127–132. DOI: 10.1016/0370–2693(83)90637-8.
- [21] L. F. Abbott and P. Sikivie. "A Cosmological Bound on the Invisible Axion". In: *Phys. Lett. B* 120 (1983). Ed. by M. A. Srednicki, pp. 133–136. DOI: 10.1016/0370-2693(83) 90638-X.
- [22] Edward W. Kolb. *The Early Universe*. Vol. 69. Taylor and Francis, May 2019. ISBN: 978-0-429-49286-0, 978-0-201-62674-2. DOI: 10.1201/9780429492860.
- [23] Edward W. Kolb and Igor I. Tkachev. "Axion miniclusters and Bose stars". In: *Physical Review Letters* 71.19 (Nov. 1993), pp. 3051–3054. ISSN: 0031-9007. DOI: 10.1103/physrevlett.71.3051.
- [24] Edward W. Kolb and Igor I. Tkachev. "Large-amplitude isothermal fluctuations and high-density dark-matter clumps". In: *Physical Review D* 50.2 (July 1994), pp. 769–773. ISSN: 0556-2821. DOI: 10.1103/physrevd.50.769.
- [25] Edward W. Kolb and Igor I. Tkachev. "Axion miniclusters and Bose stars". In: *Physical Review Letters* 71.19 (Nov. 1993), pp. 3051–3054. ISSN: 0031-9007. DOI: 10.1103/physrevlett.71.3051.
- [26] Remo Ruffini and Silvano Bonazzola. "Systems of Self-Gravitating Particles in General Relativity and the Concept of an Equation of State". In: *Phys. Rev.* 187 (5 Nov. 1969), pp. 1767–1783. DOI: 10.1103/PhysRev.187.1767.
- [27] Benedikt Eggemeier et al. "Gravitational collapse in the postinflationary Universe". In: *Physical Review D* 105.2 (Jan. 2022). ISSN: 2470-0029. DOI: 10.1103/physrevd.105.023516.
- [28] Alejandro Vaquero, Javier Redondo, and Julia Stadler. "Early seeds of axion miniclusters". In: *Journal of Cosmology and Astroparticle Physics* 2019.04 (Apr. 2019), pp. 012–012. ISSN: 1475-7516. DOI: 10.1088/1475-7516/2019/04/012.

- [29] Huangyu Xiao, Ian Williams, and Matthew McQuinn. "Simulations of axion minihalos". In: *Physical Review D* 104.2 (July 2021). ISSN: 2470-0029. DOI: 10.1103/physrevd.104.023515.
- [30] Benedikt Eggemeier et al. "First Simulations of Axion Minicluster Halos". In: *Physical Review Letters* 125.4 (July 2020). arXiv:1911.09417 [astro-ph], p. 041301. ISSN: 0031-9007, 1079-7114. DOI: 10.1103/PhysRevLett.125.041301.
- [31] D. G. Levkov, A. G. Panin, and I. I. Tkachev. "Radio-emission of axion stars". In: *Physical Review D* 102.2 (July 2020). ISSN: 2470-0029. DOI: 10.1103/physrevd.102.023501.
- [32] Mark P. Hertzberg and Enrico D. Schiappacasse. "Dark matter axion clump resonance of photons". In: *Journal of Cosmology and Astroparticle Physics* 2018.11 (Nov. 2018), pp. 004–004. ISSN: 1475-7516. DOI: 10.1088/1475-7516/2018/11/004.
- [33] Mark P. Hertzberg, Yao Li, and Enrico D. Schiappacasse. "Merger of dark matter axion clumps and resonant photon emission". In: *Journal of Cosmology and Astroparticle Physics* 2020.07 (July 2020), pp. 067–067. ISSN: 1475-7516. DOI: 10.1088/1475-7516/2020/07/067.
- [34] Xiaolong Du et al. "Soliton merger rates and enhanced axion dark matter decay". In: *Physical Review D* 109.4 (Feb. 2024). ISSN: 2470-0029. DOI: 10.1103/physrevd.109.043019.
- [35] D. G. Levkov, A. G. Panin, and I. I. Tkachev. "Relativistic Axions from Collapsing Bose Stars". In: *Physical Review Letters* 118.1 (Jan. 2017). ISSN: 1079-7114. DOI: 10.1103/ physrevlett.118.011301.
- [36] Joshua Eby et al. "Probing relativistic axions from transient astrophysical sources". In: *Physics Letters B* 825 (Feb. 2022), p. 136858. ISSN: 0370-2693. DOI: 10.1016/j.physletb. 2021.136858.
- [37] Roberto D. Peccei. "The Strong CP Problem and Axions". In: *Axions*. Springer Berlin Heidelberg, 2008, pp. 3–17. ISBN: 9783540735182. DOI: 10.1007/978-3-540-73518-2_1.
- [38] Jihn E. Kim and Gianpaolo Carosi. "Axions and the strong *CP* problem". In: *Rev. Mod. Phys.* 82 (1 Mar. 2010), pp. 557–601. DOI: 10.1103/RevModPhys.82.557.
- [39] Michael Dine et al. "Axions, instantons, and the lattice". In: *Physical Review D* 96.9 (Nov. 2017). ISSN: 2470-0029. DOI: 10.1103/physrevd.96.095001.
- [40] Pierre Sikivie. "Axion Cosmology". In: *Axions*. Springer Berlin Heidelberg, 2008, pp. 19–50. ISBN: 9783540735182. DOI: 10.1007/978-3-540-73518-2_2.
- [41] David J.E. Marsh. "Axion Cosmology". In: *Physics Reports* 643 (July 2016), pp. 1–79. ISSN: 0370-1573. DOI: 10.1016/j.physrep.2016.06.005.
- [42] Ciaran O'Hare. "Cosmology of axion dark matter". In: Proceedings of 1st General Meeting and 1st Training School of the COST Action COSMIC WSIPers PoS(COSMICWISPers). COSMICWISPers. Sissa Medialab, Apr. 2024. DOI: 10.22323/1.454.0040.
- [43] Giovanni Grilli di Cortona et al. "The QCD axion, precisely". In: Journal of High Energy Physics 2016.1 (Jan. 2016). ISSN: 1029-8479. DOI: 10.1007/jhep01(2016)034.
- [44] Andreas Ringwald. Review on Axions. 2024. arXiv: 2404.09036 [hep-ph].

- [45] Igor G. Irastorza and Javier Redondo. "New experimental approaches in the search for axion-like particles". In: *Progress in Particle and Nuclear Physics* 102 (Sept. 2018), pp. 89–159. ISSN: 0146-6410. DOI: 10.1016/j.ppnp.2018.05.003.
- [46] Luca Di Luzio et al. "The landscape of QCD axion models". In: *Physics Reports* 870 (July 2020), pp. 1–117. ISSN: 0370-1573. DOI: 10.1016/j.physrep.2020.06.002.
- [47] Günter Sigl. Astroparticle Physics: Theory and Phenomenology. Vol. 1. Atlantis Studies in Astroparticle Physics and Cosmology. Springer, 2017. ISBN: 978-94-6239-242-7, 978-94-6239-243-4. DOI: 10.2991/978-94-6239-243-4.
- [48] G. Raffelt and A. Caputo. "Astrophysical Axion Bounds: The 2024 Edition". In: Proceedings of 1st General Meeting and 1st Training School of the COST Action COSMIC WSIPers PoS(COSMICWISPers). COSMICWISPers. Sissa Medialab, Mar. 2024, p. 041. DOI: 10.22323/1.454.0041.
- [49] Lam Hui et al. "Ultralight scalars as cosmological dark matter". In: *Physical Review D* 95.4 (Feb. 2017). ISSN: 2470-0029. DOI: 10.1103/physrevd.95.043541.
- [50] R. Jackiw and C. Rebbi. "Vacuum Periodicity in a Yang-Mills Quantum Theory". In: *Phys. Rev. Lett.* 37 (1976). Ed. by J. C. Taylor, pp. 172–175. DOI: 10.1103/PhysRevLett. 37.172.
- [51] R. J. Crewther et al. "Chiral Estimate of the Electric Dipole Moment of the Neutron in Quantum Chromodynamics". In: *Phys. Lett. B* 88 (1979). [Erratum: Phys.Lett.B 91, 487 (1980)], p. 123. DOI: 10.1016/0370-2693(79)90128-X.
- [52] C. Abel et al. "Measurement of the Permanent Electric Dipole Moment of the Neutron". In: Physical Review Letters 124.8 (Feb. 2020). ISSN: 1079-7114. DOI: 10.1103/physrevlett.124.081803.
- [53] Particle Data Group et al. "Review of Particle Physics". In: Progress of Theoretical and Experimental Physics 2020.8 (Aug. 2020), p. 083C01. ISSN: 2050-3911. DOI: 10.1093/ptep/ptaa104. eprint: https://academic.oup.com/ptep/article-pdf/2020/8/083C01/34673722/ptaa104.pdf.
- [54] Olivier Wantz and E. P. S. Shellard. "Axion cosmology revisited". In: *Physical Review D* 82.12 (Dec. 2010). ISSN: 1550-2368. DOI: 10.1103/physrevd.82.123508.
- [55] David J. Gross, Robert D. Pisarski, and Laurence G. Yaffe. "QCD and instantons at finite temperature". In: *Rev. Mod. Phys.* 53 (1 Jan. 1981), pp. 43–80. DOI: 10.1103/RevModPhys.53.43.
- [56] Sz. Borsanyi et al. "Calculation of the axion mass based on high-temperature lattice quantum chromodynamics". In: *Nature* 539.7627 (2016), pp. 69–71. DOI: 10.1038/nature20115. arXiv: 1606.07494 [hep-lat].
- [57] Sz. Borsanyi et al. Lattice QCD for Cosmology. 2016. arXiv: 1606.07494 [hep-lat].
- [58] Malcolm Fairbairn et al. "Structure formation and microlensing with axion miniclusters". In: Physical Review D 97.8 (Apr. 2018). ISSN: 2470-0029. DOI: 10.1103/physrevd.97.083502.
- [59] T. W. Donnelly et al. "Do Axions Exist?" In: *Phys. Rev. D* 18 (1978), p. 1607. DOI: 10.1103/PhysRevD.18.1607.

- [60] A. Zehnder. "Axion Search in a Monochromatic γ Transition: A New Lower Limit for the Axion Mass". In: *Phys. Lett. B* 104 (1981). Ed. by R. J. Cence, E. Ma, and A. Roberts, pp. 494–498. DOI: 10.1016/0370-2693(81)90522-0.
- [61] Jihn E. Kim. "Weak Interaction Singlet and Strong CP Invariance". In: *Phys. Rev. Lett.* 43 (1979), p. 103. DOI: 10.1103/PhysRevLett.43.103.
- [62] Mark Srednicki. "Axion couplings to matter: (I). CP-conserving parts". In: Nuclear Physics B 260.3 (1985), pp. 689–700. ISSN: 0550-3213. DOI: https://doi.org/10.1016/0550-3213(85)90054-9.
- [63] Sanghyeon Chang and Kiwoon Choi. "Hadronic axion window and the big-bang nucleosynthesis". In: *Physics Letters B* 316.1 (Oct. 1993), pp. 51–56. ISSN: 0370-2693. DOI: 10.1016/0370-2693(93)90656-3.
- [64] H. Peter Nilles and Stuart Raby. "Supersymmetry and the strong CP problem". In: *Nuclear Physics B* 198.1 (1982), pp. 102–112. ISSN: 0550-3213. DOI: https://doi.org/10.1016/0550-3213(82)90547-8.
- [65] Asimina Arvanitaki et al. "String axiverse". In: Physical Review D 81.12 (June 2010). ISSN: 1550-2368. DOI: 10.1103/physrevd.81.123530.
- [66] Michele Cicoli, Mark D. Goodsell, and Andreas Ringwald. "The type IIB string axiverse and its low-energy phenomenology". In: *Journal of High Energy Physics* 2012.10 (Oct. 2012). ISSN: 1029-8479. DOI: 10.1007/jhep10(2012)146.
- [67] Peter Svrcek and Edward Witten. "Axions in string theory". In: *Journal of High Energy Physics* 2006.06 (June 2006), pp. 051–051. ISSN: 1029-8479. DOI: 10.1088/1126-6708/2006/06/051.
- [68] Andreas Ringwald. Exploring the Role of Axions and Other WISPs in the Dark Universe. 2012. arXiv: 1210.5081 [hep-ph].
- [69] G. W. Gibbons and S. W. Hawking. "Cosmological event horizons, thermodynamics, and particle creation". In: *Phys. Rev. D* 15 (10 May 1977), pp. 2738–2751. DOI: 10.1103/PhysRevD.15.2738.
- [70] E. Armengaud et al. "Physics potential of the International Axion Observatory (IAXO)".
 In: Journal of Cosmology and Astroparticle Physics 2019.06 (June 2019), pp. 047–047.
 ISSN: 1475-7516. DOI: 10.1088/1475-7516/2019/06/047.
- [71] Jack J. Bennett et al. "Towards a precision calculation of the effective number of neutrinos Neff in the Standard Model. Part II. Neutrino decoupling in the presence of flavour oscillations and finite-temperature QED". In: *Journal of Cosmology and Astroparticle Physics* 2021.04 (Apr. 2021), p. 073. ISSN: 1475-7516. DOI: 10.1088/1475-7516/2021/04/073.
- [72] Maria Archidiacono et al. "Future cosmological sensitivity for hot dark matter axions". In: Journal of Cosmology and Astroparticle Physics 2015.05 (May 2015), pp. 050–050. ISSN: 1475-7516. DOI: 10.1088/1475-7516/2015/05/050.
- [73] P. J. E. Peebles. "Large-scale background temperature and mass fluctuations due to scale-invariant primeval perturbations". In: *The Astrophysical Journal Letters* 263 (Dec. 1982), pp. L1–L5. DOI: 10.1086/183911.

- [74] Michael S. Turner. "Coherent scalar-field oscillations in an expanding universe". In: *Phys. Rev. D* 28 (6 Sept. 1983), pp. 1243–1247. DOI: 10.1103/PhysRevD.28.1243.
- [75] Andreas Pargner. "Phenomenology of Axion Dark Matter". 51.03.06; LK 01. PhD thesis. Karlsruher Institut für Technologie (KIT), 2019. 137 pp. DOI: 10.5445/IR/1000092362.
- [76] Peter W. Graham and Adam Scherlis. "Stochastic axion scenario". In: *Physical Review D* 98.3 (Aug. 2018). ISSN: 2470-0029. DOI: 10.1103/physrevd.98.035017.
- [77] Sebastian Hoof et al. "Axion global fits with Peccei-Quinn symmetry breaking before inflation using GAMBIT". In: *Journal of High Energy Physics* 2019.3 (Mar. 2019). ISSN: 1029-8479. DOI: 10.1007/jhep03(2019)191.
- [78] Raymond T. Co, Lawrence J. Hall, and Keisuke Harigaya. "Axion Kinetic Misalignment Mechanism". In: *Physical Review Letters* 124.25 (June 2020). ISSN: 1079-7114. DOI: 10.1103/physrevlett.124.251802.
- [79] Cem Eröncel et al. "ALP dark matter from kinetic fragmentation: opening up the parameter window". In: *Journal of Cosmology and Astroparticle Physics* 2022.10 (Oct. 2022), p. 053. ISSN: 1475-7516. DOI: 10.1088/1475-7516/2022/10/053.
- [80] Cem Eröncel and Géraldine Servant. "ALP dark matter mini-clusters from kinetic fragmentation". In: Journal of Cosmology and Astroparticle Physics 2023.01 (Jan. 2023), p. 009. ISSN: 1475-7516. DOI: 10.1088/1475-7516/2023/01/009.
- [81] Cem Eröncel et al. Model implementations of axion dark matter from kinetic misalignment. 2024. arXiv: 2408.08355 [hep-ph].
- [82] T W B Kibble. "Topology of cosmic domains and strings". In: *Journal of Physics A: Mathematical and General* 9.8 (Aug. 1976), p. 1387. DOI: 10.1088/0305-4470/9/8/029.
- [83] Alexander Vilenkin. "Cosmic strings and domain walls". In: *Physics Reports* 121.5 (1985), pp. 263–315. ISSN: 0370-1573. DOI: https://doi.org/10.1016/0370-1573(85)90033-X.
- [84] M B Hindmarsh and T W B Kibble. "Cosmic strings". In: Reports on Progress in Physics 58.5 (May 1995), pp. 477–562. ISSN: 1361-6633. DOI: 10.1088/0034-4885/58/5/001.
- [85] Takashi Hiramatsu et al. "Production of dark matter axions from collapse of string-wall systems". In: *Phys. Rev. D* 85 (2012). [Erratum: Phys.Rev.D 86, 089902 (2012)], p. 105020. DOI: 10.1103/PhysRevD.85.105020. arXiv: 1202.5851 [hep-ph].
- [86] T. W. B. Kibble. "Some Implications of a Cosmological Phase Transition". In: *Phys. Rept.* 67 (1980), p. 183. DOI: 10.1016/0370-1573(80)90091-5.
- [87] Richard Lynn Davis. "Cosmic Axions from Cosmic Strings". In: Phys. Lett. B 180 (1986), pp. 225–230. DOI: 10.1016/0370-2693(86)90300-X.
- [88] Malte Buschmann et al. "Dark matter from axion strings with adaptive mesh refinement". In: *Nature Communications* 13.1 (Feb. 2022). ISSN: 2041-1723. DOI: 10.1038/s41467-022-28669-y.
- [89] David H. Lyth. "Estimates of the cosmological axion density". In: *Physics Letters B* 275.3 (1992), pp. 279–283. ISSN: 0370-2693. DOI: https://doi.org/10.1016/0370-2693(92)91590-6.
- [90] Giovanni Pierobon et al. *Miniclusters from axion string simulations*. 2023. arXiv: 2307. 09941 [hep-ph].

- [91] Ciaran A. J. O'Hare et al. "Simulations of axionlike particles in the postinflationary scenario". In: *Physical Review D* 105.5 (Mar. 2022). ISSN: 2470-0029. DOI: 10.1103/physrevd.105.055025.
- [92] Diego Harari and P. Sikivie. "On the Evolution of Global Strings in the Early Universe".
 In: Phys. Lett. B 195 (1987), pp. 361–365. DOI: 10.1016/0370-2693(87)90032-3.
- [93] Masahide Yamaguchi, Jun'ichi Yokoyama, and M. Kawasaki. "Evolution of a global string network in a matter-dominated universe". In: *Physical Review D* 61.6 (Feb. 2000). ISSN: 1089-4918. DOI: 10.1103/physrevd.61.061301.
- [94] Takashi Hiramatsu et al. "Improved estimation of radiated axions from cosmological axionic strings". In: *Physical Review D* 83.12 (June 2011). ISSN: 1550-2368. DOI: 10.1103/physrevd.83.123531.
- [95] Marco Gorghetto, Edward Hardy, and Giovanni Villadoro. "More axions from strings". In: SciPost Physics 10.2 (Feb. 2021). ISSN: 2542-4653. DOI: 10.21468/scipostphys.10. 2.050.
- [96] Heejoo Kim, Junghyeon Park, and Minho Son. Axion Dark Matter from Cosmic String Network. 2024. arXiv: 2402.00741 [hep-ph].
- [97] Marco Gorghetto, Edward Hardy, and Giovanni Villadoro. "Axions from strings: the attractive solution". In: *Journal of High Energy Physics* 2018.7 (July 2018). ISSN: 1029-8479. DOI: 10.1007/jhep07(2018)151.
- [98] Masahiro Kawasaki et al. "Long-term dynamics of cosmological axion strings". In: *Progress of Theoretical and Experimental Physics* 2018.9 (Sept. 2018). ISSN: 2050-3911. DOI: 10.1093/ptep/pty098.
- [99] Vincent B. Klaer and Guy D. Moore. "The dark-matter axion mass". In: Journal of Cosmology and Astroparticle Physics 2017.11 (Nov. 2017), pp. 049–049. ISSN: 1475-7516. DOI: 10.1088/1475-7516/2017/11/049.
- [100] Richard Lynn Davis. "Goldstone bosons in string models of galaxy formation". In: *Phys. Rev. D* 32 (12 Dec. 1985), pp. 3172–3177. DOI: 10.1103/PhysRevD.32.3172.
- [101] R. A. Battye and E. P. S. Shellard. "Axion String Constraints". In: *Phys. Rev. Lett.* 73 (22 Nov. 1994), pp. 2954–2957. DOI: 10.1103/PhysRevLett.73.2954.
- [102] R. A. Battye and E. P. S. Shellard. "Axion String Constraints [Phys. Rev. Lett. 73, 2954 (1994)]". In: Phys. Rev. Lett. 76 (12 Mar. 1996), pp. 2203–2204. DOI: 10.1103/PhysRevLett.76.2203.
- [103] Masahiro Kawasaki, Ken'ichi Saikawa, and Toyokazu Sekiguchi. "Axion dark matter from topological defects". In: *Physical Review D* 91.6 (Mar. 2015). ISSN: 1550-2368. DOI: 10.1103/physrevd.91.065014.
- [104] Peter Cox et al. "Classification of three-family flavoured DFSZ axion models that have no domain wall problem". In: *Journal of High Energy Physics* 2024.2 (Feb. 2024). ISSN: 1029-8479. DOI: 10.1007/jhep02(2024)011.
- [105] Benedikt Eggemeier et al. "Axion minivoids and implications for direct detection". In: *Physical Review D* 107.8 (Apr. 2023). ISSN: 2470-0029. DOI: 10.1103/physrevd.107.083510.

- [106] Duane A. Dicus et al. "Astrophysical Bounds on the Masses of Axions and Higgs Particles". In: *Phys. Rev. D* 18 (1978), p. 1829. DOI: 10.1103/PhysRevD.18.1829.
- [107] P. Sikivie. "Experimental Tests of the Invisible Axion". In: *Phys. Rev. Lett.* 51 (1983). Ed. by M. A. Srednicki. [Erratum: Phys.Rev.Lett. 52, 695 (1984)], pp. 1415–1417. DOI: 10.1103/PhysRevLett.51.1415.
- [108] F Hoogeveen and T Ziegenhagen. "Production and detection of light bosons using optical resonators". In: *Nuclear Physics B* 358.1 (1991), pp. 3–26. ISSN: 0550-3213. DOI: https://doi.org/10.1016/0550-3213(91)90528-6.
- [109] Yukio Fukuda et al. "Production and detection of axions by using optical resonators". In: Progress in Crystal Growth and Characterization of Materials 33.1 (1996), pp. 363–366. ISSN: 0960-8974. DOI: https://doi.org/10.1016/0960-8974(96)83672-2.
- [110] Guido Mueller et al. "Detailed design of a resonantly enhanced axion-photon regeneration experiment". In: *Physical Review D* 80.7 (Oct. 2009). ISSN: 1550-2368. DOI: 10.1103/physrevd.80.072004.
- [111] R Bähre et al. "Any light particle search II Technical Design Report". In: *Journal of Instrumentation* 8.09 (Sept. 2013), T09001–T09001. ISSN: 1748-0221. DOI: 10.1088/1748-0221/8/09/t09001.
- [112] Klaus Ehret et al. "New ALPS results on hidden-sector lightweights". In: *Physics Letters B* 689.4–5 (May 2010), pp. 149–155. ISSN: 0370-2693. DOI: 10.1016/j.physletb.2010. 04.066.
- [113] R. Ballou et al. "New exclusion limits on scalar and pseudoscalar axionlike particles from light shining through a wall". In: *Physical Review D* 92.9 (Nov. 2015). ISSN: 1550-2368. DOI: 10.1103/physrevd.92.092002.
- [114] Pierre Sikivie. "Invisible axion search methods". In: Reviews of Modern Physics 93.1 (Feb. 2021). ISSN: 1539-0756. DOI: 10.1103/revmodphys.93.015004.
- [115] Javier Redondo. "Solar axion flux from the axion-electron coupling". In: *Journal of Cosmology and Astroparticle Physics* 2013.12 (Dec. 2013), pp. 008–008. ISSN: 1475-7516. DOI: 10.1088/1475-7516/2013/12/008.
- [116] K Barth et al. "CAST constraints on the axion-electron coupling". In: Journal of Cosmology and Astroparticle Physics 2013.05 (May 2013), pp. 010–010. ISSN: 1475-7516. DOI: 10.1088/1475-7516/2013/05/010.
- [117] Georg G. Raffelt. "Astrophysical Axion Bounds". In: Axions. Springer Berlin Heidelberg, pp. 51–71. ISBN: 9783540735182. DOI: $10.1007/978-3-540-73518-2_3$.
- [118] "New CAST limit on the axion–photon interaction". In: *Nature Physics* 13.6 (May 2017), pp. 584–590. ISSN: 1745-2481. DOI: 10.1038/nphys4109.
- [119] A. Abeln et al. "Conceptual design of BabyIAXO, the intermediate stage towards the International Axion Observatory". In: *JHEP* 05 (2021), p. 137. DOI: 10.1007/JHEP05(2021) 137. arXiv: 2010.12076 [physics.ins-det].
- [120] E Armengaud et al. "Conceptual design of the International Axion Observatory (IAXO)". In: Journal of Instrumentation 9.05 (May 2014), T05002–T05002. ISSN: 1748-0221. DOI: 10.1088/1748-0221/9/05/t05002.

- [121] J I Read. "The local dark matter density". In: Journal of Physics G: Nuclear and Particle Physics 41.6 (May 2014), p. 063101. ISSN: 1361-6471. DOI: 10.1088/0954-3899/41/6/063101.
- [122] C. Bartram et al. "Search for Invisible Axion Dark Matter in the 3.3–4.2 μ eV Mass Range". In: *Phys. Rev. Lett.* 127.26 (2021), p. 261803. DOI: 10.1103/PhysRevLett.127. 261803. arXiv: 2110.06096 [hep-ex].
- [123] David Alesini et al. "The future search for low-frequency axions and new physics with the FLASH resonant cavity experiment at Frascati National Laboratories". In: *Physics of the Dark Universe* 42 (Dec. 2023), p. 101370. ISSN: 2212-6864. DOI: 10.1016/j.dark. 2023.101370.
- [124] Dieter Horns et al. "Searching for WISPy cold dark matter with a dish antenna". In: Journal of Cosmology and Astroparticle Physics 2013.04 (Apr. 2013), pp. 016–016. ISSN: 1475-7516. DOI: 10.1088/1475-7516/2013/04/016.
- [125] Fayez Bajjali et al. "First results from BRASS-p broadband searches for hidden photon dark matter". In: *Journal of Cosmology and Astroparticle Physics* 2023.08 (Aug. 2023), p. 077. ISSN: 1475-7516. DOI: 10.1088/1475-7516/2023/08/077.
- [126] Stefan Knirck et al. "First Results from a Broadband Search for Dark Photon Dark Matter in the 44 to 52 μeV Range with a Coaxial Dish Antenna". In: Phys. Rev. Lett. 132.13 (2024), p. 131004. DOI: 10.1103/PhysRevLett.132.131004. arXiv: 2310.13891 [hep-ex].
- [127] Allen Caldwell et al. "Dielectric Haloscopes: A New Way to Detect Axion Dark Matter". In: *Physical Review Letters* 118.9 (Mar. 2017). ISSN: 1079-7114. DOI: 10.1103/physrevlett.118.091801.
- [128] B. Ary dos Santos Garcia et al. "First search for axion dark matter with a Madmax prototype". In: (Sept. 2024). arXiv: 2409.11777 [hep-ex].
- [129] B. Majorovits et al. "MADMAX: A new road to axion dark matter detection". In: *J. Phys. Conf. Ser.* 1342.1 (2020). Ed. by Ken Clark et al., p. 012098. DOI: 10.1088/1742-6596/1342/1/012098. arXiv: 1712.01062 [physics.ins-det].
- [130] Alexander J. Millar et al. "Dielectric haloscopes to search for axion dark matter: theoretical foundations". In: *Journal of Cosmology and Astroparticle Physics* 2017.01 (Jan. 2017), pp. 061–061. ISSN: 1475-7516. DOI: 10.1088/1475-7516/2017/01/061.
- [131] S. Beurthey et al. MADMAX Status Report. 2020. arXiv: 2003.10894 [physics.ins-det].
- [132] P. Brun et al. "A new experimental approach to probe QCD axion dark matter in the mass range above 40 μ eV". In: Eur. Phys. J. C 79.3 (2019), p. 186. DOI: 10.1140/epjc/s10052-019-6683-x. arXiv: 1901.07401 [physics.ins-det].
- [133] Jesse Liu et al. "Broadband Solenoidal Haloscope for Terahertz Axion Detection". In: Physical Review Letters 128.13 (Mar. 2022). ISSN: 1079-7114. DOI: 10.1103/physrevlett. 128.131801.
- [134] Samuel J. Witte et al. "Transient radio lines from axion miniclusters and axion stars". In: *Physical Review D* 107.6 (Mar. 2023). ISSN: 2470-0029. DOI: 10.1103/physrevd.107.063013.

- [135] Yang Bai, Xiaolong Du, and Yuta Hamada. "Diluted axion star collisions with neutron stars". In: *Journal of Cosmology and Astroparticle Physics* 2022.01 (Jan. 2022), p. 041. ISSN: 1475-7516. DOI: 10.1088/1475-7516/2022/01/041.
- [136] Thomas D. P. Edwards et al. "Transient Radio Signatures from Neutron Star Encounters with QCD Axion Miniclusters". In: *Physical Review Letters* 127.13 (Sept. 2021). ISSN: 1079-7114. DOI: 10.1103/physrevlett.127.131103.
- [137] Joshua Eby et al. "Collisions of dark matter axion stars with astrophysical sources". In: Journal of High Energy Physics 2017.4 (Apr. 2017). ISSN: 1029-8479. DOI: 10.1007/jhep04(2017)099.
- [138] Benoît Cerutti and Andrei Beloborodov. "Electrodynamics of pulsar magnetospheres". In: *Space Sci. Rev.* 207.1-4 (2017), pp. 111–136. DOI: 10.1007/s11214-016-0315-7. arXiv: 1611.04331 [astro-ph.HE].
- [139] Peter Goldreich and William H. Julian. "Pulsar Electrodynamics". In: *The Astrophysical Journal* 157 (Aug. 1969), p. 869. DOI: 10.1086/150119.
- [140] Anson Hook et al. "Radio Signals from Axion Dark Matter Conversion in Neutron Star Magnetospheres". In: *Physical Review Letters* 121.24 (Dec. 2018). ISSN: 1079-7114. DOI: 10.1103/physrevlett.121.241102.
- [141] Dion Noordhuis et al. Axion Clouds around Neutron Stars. Oct. 2024. DOI: 10.1103/ PhysRevX.14.041015.
- [142] D. F. Jackson Kimball et al. Overview of the Cosmic Axion Spin Precession Experiment (CASPEr). 2018. arXiv: 1711.08999 [physics.ins-det].
- [143] Peter W. Graham and Surjeet Rajendran. "New observables for direct detection of axion dark matter". In: *Physical Review D* 88.3 (Aug. 2013). ISSN: 1550-2368. DOI: 10.1103/physrevd.88.035023.
- [144] Jonas Enander, Andreas Pargner, and Thomas Schwetz. "Axion minicluster power spectrum and mass function". In: *Journal of Cosmology and Astroparticle Physics* 2017.12 (Dec. 2017), pp. 038–038. ISSN: 1475-7516. DOI: 10.1088/1475-7516/2017/12/038.
- [145] Edward Hardy. "Miniclusters in the axiverse". In: *Journal of High Energy Physics* 2017.2 (Feb. 2017). ISSN: 1029-8479. DOI: 10.1007/jhep02(2017)046.
- [146] E. W. Kolb and I. I. Tkachev. "Femtolensing and Picolensing by Axion Miniclusters". In: The Astrophysical Journal 460.1 (Mar. 1996). arXiv:astro-ph/9510043. ISSN: 0004637X. DOI: 10.1086/309962.
- [147] C. J. Hogan and M. J. Rees. "Axion Miniclusters". In: Phys. Lett. B 205 (1988), pp. 228–230. DOI: 10.1016/0370-2693(88)91655-3.
- [148] Kathryn M. Zurek, Craig J. Hogan, and Thomas R. Quinn. "Astrophysical effects of scalar dark matter miniclusters". In: *Physical Review D* 75.4 (Feb. 2007). ISSN: 1550-2368. DOI: 10.1103/physrevd.75.043511.
- [149] Peter Tinyakov, Igor Tkachev, and Konstantin Zioutas. "Tidal streams from axion miniclusters and direct axion searches". In: *Journal of Cosmology and Astroparticle Physics* 2016.01 (Jan. 2016), pp. 035–035. ISSN: 1475-7516. DOI: 10.1088/1475-7516/2016/01/035.

- [150] V. I. Dokuchaev, Yu. N. Eroshenko, and I. I. Tkachev. "Destruction of axion miniclusters in the Galaxy". In: *Journal of Experimental and Theoretical Physics* 125.3 (Sept. 2017), pp. 434–442. ISSN: 1090-6509. DOI: 10.1134/s1063776117080039.
- [151] Chris Kouvaris, Tao Liu, and Kun-Feng Lyu. "Radio signals from axion star-neutron star binaries". In: *Phys. Rev. D* 109 (2 Jan. 2024), p. 023008. DOI: 10.1103/PhysRevD.109.023008.
- [152] Benjamin R. Safdi, Zhiquan Sun, and Alexander Y. Chen. "Detecting axion dark matter with radio lines from neutron star populations". In: *Physical Review D* 99.12 (June 2019). ISSN: 2470-0029. DOI: 10.1103/physrevd.99.123021.
- [153] R. A. Battye et al. "Dark matter axion detection in the radio/mm waveband". In: *Physical Review D* 102.2 (July 2020). ISSN: 2470-0029. DOI: 10.1103/physrevd.102.023504.
- [154] Mikaël Leroy et al. "Radio signal of axion-photon conversion in neutron stars: A ray tracing analysis". In: *Physical Review D* 101.12 (June 2020). ISSN: 2470-0029. DOI: 10.1103/physrevd.101.123003.
- [155] Joshua W. Foster et al. "Green Bank and Effelsberg Radio Telescope Searches for Axion Dark Matter Conversion in Neutron Star Magnetospheres". In: *Physical Review Letters* 125.17 (Oct. 2020). ISSN: 1079-7114. DOI: 10.1103/physrevlett.125.171301.
- [156] R. A. Battye et al. "Radio line properties of axion dark matter conversion in neutron stars". In: *Journal of High Energy Physics* 2021.9 (Sept. 2021). ISSN: 1029-8479. DOI: 10.1007/jhep09(2021)105.
- [157] Joshua W. Foster et al. "Extraterrestrial Axion Search with the Breakthrough Listen Galactic Center Survey". In: *Physical Review Letters* 129.25 (Dec. 2022). ISSN: 1079-7114. DOI: 10.1103/physrevlett.129.251102.
- [158] Pierre-Henri Chavanis. "Phase transitions between dilute and dense axion stars". In: *Physical Review D* 98.2 (July 2018). ISSN: 2470-0029. DOI: 10.1103/physrevd.98.023009.
- [159] Pierre-Henri Chavanis. "Mass-radius relation of Newtonian self-gravitating Bose-Einstein condensates with short-range interactions. I. Analytical results". In: *Physical Review D* 84.4 (Aug. 2011). ISSN: 1550-2368. DOI: 10.1103/physrevd.84.043531.
- [160] Pierre-Henri Chavanis. "Maximum mass of relativistic self-gravitating Bose-Einstein condensates with repulsive or attractive $|\varphi|4$ self-interaction". In: *Phys. Rev. D* 107.10 (2023), p. 103503. DOI: 10.1103/PhysRevD.107.103503. arXiv: 2211.13237 [gr-qc].
- [161] Borna Salehian et al. "Beyond Schrödinger-Poisson: nonrelativistic effective field theory for scalar dark matter". In: *Journal of High Energy Physics* 2021.9 (Sept. 2021). ISSN: 1029-8479. DOI: 10.1007/jhep09(2021)050.
- [162] David J. Kaup. "Klein-Gordon Geon". In: *Phys. Rev.* 172 (5 Aug. 1968), pp. 1331–1342. DOI: 10.1103/PhysRev.172.1331.
- [163] Steven Weinberg. Cosmology. 2008. ISBN: 978-0-19-852682-7.
- [164] Eric Braaten, Abhishek Mohapatra, and Hong Zhang. "Classical nonrelativistic effective field theories for a real scalar field". In: *Physical Review D* 98.9 (Nov. 2018). ISSN: 2470-0029. DOI: 10.1103/physrevd.98.096012.

- [165] Yasusada Nambu and Misao Sasaki. "Quantum treatment of cosmological axion perturbations". In: *Phys. Rev. D* 42 (12 Dec. 1990), pp. 3918–3924. DOI: 10.1103/PhysRevD. 42.3918.
- [166] M. A. Rego-Monteiro. "Generalized nonlinear Schrödinger equation: Conservation of energy and solitary-wave solutions". In: J. Math. Phys. 61.5 (2020), p. 052101. DOI: 10.1063/5.0006799.
- [167] Benedikt Eggemeier and Jens C. Niemeyer. "Formation and mass growth of axion stars in axion miniclusters". In: *Physical Review D* 100.6 (Sept. 2019). arXiv:1906.01348 [astro-ph], p. 063528. ISSN: 2470-0010, 2470-0029. DOI: 10.1103/PhysRevD.100.063528.
- [168] Hsi-Yu Schive, Tzihong Chiueh, and Tom Broadhurst. "Cosmic structure as the quantum interference of a coherent dark wave". In: *Nature Physics* 10.7 (June 2014), pp. 496–499. ISSN: 1745-2481. DOI: 10.1038/nphys2996.
- [169] Hsi-Yu Schive et al. "Understanding the Core-Halo Relation of Quantum Wave Dark Matter from 3D Simulations". In: *Physical Review Letters* 113.26 (Dec. 2014). ISSN: 1079-7114. DOI: 10.1103/physrevlett.113.261302.
- [170] D. G. Levkov, A. G. Panin, and I. I. Tkachev. "Gravitational Bose-Einstein Condensation in the Kinetic Regime". In: *Physical Review Letters* 121.15 (Oct. 2018). ISSN: 1079-7114. DOI: 10.1103/physrevlett.121.151301.
- [171] Jens C. Niemeyer. "Small-scale structure of fuzzy and axion-like dark matter". In: *Progress in Particle and Nuclear Physics* 113 (July 2020), p. 103787. ISSN: 0146-6410. DOI: 10.1016/j.ppnp.2020.103787.
- [172] Bodo Schwabe, Jens C. Niemeyer, and Jan F. Engels. "Simulations of solitonic core mergers in ultralight axion dark matter cosmologies". In: *Physical Review D* 94.4 (Aug. 2016). ISSN: 2470-0029. DOI: 10.1103/physrevd.94.043513.
- [173] Sacha Davidson and Thomas Schwetz. "Rotating drops of axion dark matter". In: *Physical Review D* 93.12 (June 2016). ISSN: 2470-0029. DOI: 10.1103/physrevd.93.123509.
- [174] Jiajun Chen et al. "New insights into the formation and growth of boson stars in dark matter halos". In: *Phys. Rev. D* 104.8 (2021), p. 083022. DOI: 10.1103/PhysRevD.104.083022. arXiv: 2011.01333 [astro-ph.CO].
- [175] Benedikt Eggemeier, Ananthu Krishnan Anilkumar, and Klaus Dolag. "Evidence for axion miniclusters with an increased central density". In: *Physical Review D* 110.4 (Aug. 2024). ISSN: 2470-0029. DOI: 10.1103/physrevd.110.043530.
- [176] David Ellis et al. "Structure of axion miniclusters". In: *Physical Review D* 106.10 (Nov. 2022). ISSN: 2470-0029. DOI: 10.1103/physrevd.106.103514.
- [177] Jai-chan Hwang and Hyerim Noh. "Axion as a cold dark matter candidate". In: *Physics Letters B* 680.1 (Sept. 2009), pp. 1–3. ISSN: 0370-2693. DOI: 10.1016/j.physletb.2009. 08.031.
- [178] Renée Hlozek et al. "A search for ultralight axions using precision cosmological data". In: *Physical Review D* 91.10 (May 2015). ISSN: 1550-2368. DOI: 10.1103/physrevd.91. 103512.

- [179] William H. Press and Paul Schechter. "Formation of galaxies and clusters of galaxies by selfsimilar gravitational condensation". In: *Astrophys. J.* 187 (1974), pp. 425–438. DOI: 10.1086/152650.
- [180] David Ellis, David J. E. Marsh, and Christoph Behrens. "Axion miniclusters made easy". In: *Physical Review D* 103.8 (Apr. 2021). ISSN: 2470-0029. DOI: 10.1103/physrevd.103.083525.
- [181] Andrew R. Liddle and D. H. Lyth. Cosmological inflation and large scale structure. 2000. ISBN: 978-0-521-57598-0, 978-0-521-82849-9. DOI: 10.1017/CB09781139175180.
- [182] Houjun Mo, Frank C. van den Bosch, and Simon White. *Galaxy Formation and Evolution*. 2010. DOI: 10.1017/CB09780511807244.
- [183] Ravi K. Sheth, H. J. Mo, and Giuseppe Tormen. "Ellipsoidal collapse and an improved model for the number and spatial distribution of dark matter haloes". In: *Mon. Not. Roy. Astron. Soc.* 323 (2001), p. 1. DOI: 10.1046/j.1365-8711.2001.04006.x. arXiv: astro-ph/9907024.
- [184] Malte Buschmann, Joshua W. Foster, and Benjamin R. Safdi. "Early-Universe Simulations of the Cosmological Axion". In: *Physical Review Letters* 124.16 (Apr. 2020). ISSN: 1079-7114. DOI: 10.1103/physrevlett.124.161103.
- [185] Volker Springel et al. "Simulating cosmic structure formation with the <scp>gadget</scp>-4 code". In: *Monthly Notices of the Royal Astronomical Society* 506.2 (July 2021), pp. 2871–2949. ISSN: 1365-2966. DOI: 10.1093/mnras/stab1855.
- [186] G. Efstathiou and J. R. Bond. "Isocurvature cold dark matter fluctuations". In: Mon. Not. Roy. Astron. Soc. 218.1 (1986), pp. 103–121. DOI: 10.1093/mnras/218.1.103.
- [187] Jie Wang and Simon D. M. White. "Discreteness effects in simulations of Hot/Warm dark matter". In: *Mon. Not. Roy. Astron. Soc.* 380 (2007), pp. 93–103. DOI: 10.1111/j.1365-2966.2007.12053.x. arXiv: astro-ph/0702575.
- [188] Bradley J. Kavanagh et al. "Stellar disruption of axion miniclusters in the Milky Way". In: *Physical Review D* 104.6 (Sept. 2021). ISSN: 2470-0029. DOI: 10.1103/physrevd.104.063038.
- [189] Evan Berkowitz, Michael I. Buchoff, and Enrico Rinaldi. "Lattice QCD input for axion cosmology". In: *Physical Review D* 92.3 (Aug. 2015). ISSN: 1550-2368. DOI: 10.1103/physrevd.92.034507.
- [190] P. A. R. Ade et al. "Improved Constraints on Cosmology and Foregrounds from BICEP2 and Keck Array Cosmic Microwave Background Data with Inclusion of 95 GHz Band". In: *Physical Review Letters* 116.3 (Jan. 2016). ISSN: 1079-7114. DOI: 10.1103/physrevlett. 116.031302.
- [191] SKA-mid Sensitivity Calculator. https://sensitivity-calculator.skao.int/mid. Accessed: 08.04.2024. 2024.
- [192] María Beltrán, Juan García-Bellido, and Julien Lesgourgues. "Isocurvature bounds on axions revisited". In: *Physical Review D* 75.10 (May 2007). ISSN: 1550-2368. DOI: 10.1103/physrevd.75.103507.

- [193] Mark P. Hertzberg, Max Tegmark, and Frank Wilczek. "Axion cosmology and the energy scale of inflation". In: *Physical Review D* 78.8 (Oct. 2008). ISSN: 1550-2368. DOI: 10.1103/physrevd.78.083507.
- [194] Paul J. McMillan. "Mass models of the Milky Way". In: *Monthly Notices of the Royal Astronomical Society* 414.3 (July 2011). arXiv:1102.4340 [astro-ph], pp. 2446–2457. ISSN: 00358711. DOI: 10.1111/j.1365-2966.2011.18564.x.
- [195] Paul J. McMillan. "The mass distribution and gravitational potential of the Milky Way". In: Monthly Notices of the Royal Astronomical Society 465.1 (Feb. 2017). arXiv:1608.00971 [astro-ph], pp. 76–94. ISSN: 0035-8711, 1365-2966. DOI: 10.1093/mnras/stw2759.
- [196] Virgile Dandoy, Thomas Schwetz, and Elisa Todarello. "A self-consistent wave description of axion miniclusters and their survival in the galaxy". In: *Journal of Cosmology and Astroparticle Physics* 2022.09 (Sept. 2022), p. 081. ISSN: 1475-7516. DOI: 10.1088/1475-7516/2022/09/081.
- [197] Xuejian Shen et al. "Disruption of Dark Matter Minihalos in the Milky Way Environment: Implications for Axion Miniclusters and Early Matter Domination". In: *The Astrophysical Journal* 962.1 (Feb. 2024), p. 9. DOI: 10.3847/1538-4357/ad12c6.
- [198] Xiaolong Du et al. "Tidal disruption of fuzzy dark matter subhalo cores". In: *Physical Review D* 97.6 (Mar. 2018). ISSN: 2470-0029. DOI: 10.1103/physrevd.97.063507.
- [199] Gregor Wentzel. "Eine Verallgemeinerung der Quantenbedingungen für die Zwecke der Wellenmechanik". In: Z. Phys. 38.6 (1926), pp. 518–529. DOI: 10.1007/BF01397171.
- [200] H. A. Kramers. "Wellenmechanik und halbzahlige Quantisierung". In: Z. Phys. 39.10 (1926), pp. 828–840. DOI: 10.1007/BF01451751.
- [201] Xiaolong Du et al. "Core-halo mass relation of ultralight axion dark matter from merger history". In: *Physical Review D* 95.4 (Feb. 2017). ISSN: 2470-0029. DOI: 10.1103/physrevd. 95.043519.
- [202] Jan Veltmaat, Jens C. Niemeyer, and Bodo Schwabe. "Formation and structure of ultralight bosonic dark matter halos". In: *Physical Review D* 98.4 (Aug. 2018). ISSN: 2470-0029. DOI: 10.1103/physrevd.98.043509.
- [203] Philip Mocz et al. "First Star-Forming Structures in Fuzzy Cosmic Filaments". In: *Physical Review Letters* 123.14 (Oct. 2019). ISSN: 1079-7114. DOI: 10.1103/physrevlett. 123.141301.
- [204] Philip Mocz et al. "Galaxy formation with BECDM I. Turbulence and relaxation of idealized haloes". In: *Monthly Notices of the Royal Astronomical Society* 471.4 (July 2017), pp. 4559–4570. ISSN: 1365-2966. DOI: 10.1093/mnras/stx1887.
- [205] Yusuke Manita, Takuya Takahashi, and Atsushi Taruya. Soliton self-gravity and core-halo relation in fuzzy dark matter halos. 2024. arXiv: 2411.14614 [astro-ph.CO].
- [206] Kfir Blum et al. Bracketing the soliton-halo relation of ultralight dark matter. 2025. arXiv: 2504.16202 [astro-ph.C0].
- [207] Greg L. Bryan and Michael L. Norman. "Statistical Properties of X-Ray Clusters: Analytic and Numerical Comparisons". In: *The Astrophysical Journal* 495.1 (Mar. 1998), p. 80. DOI: 10.1086/305262.

- [208] P. Sikivie and Q. Yang. "Bose-Einstein Condensation of Dark Matter Axions". In: *Physical Review Letters* 103.11 (Sept. 2009). ISSN: 1079-7114. DOI: 10.1103/physrevlett.103.111301.
- [209] Joshua Eby et al. "Collapse of axion stars". In: *Journal of High Energy Physics* 2016.12 (Dec. 2016). ISSN: 1029-8479. DOI: 10.1007/jhep12(2016)066.
- [210] Joshua Eby, Peter Suranyi, and L. C. R. Wijewardhana. "The lifetime of axion stars". In: $Modern\ Physics\ Letters\ A\ 31.15$ (May 2016), p. 1650090. ISSN: 1793-6632. DOI: 10. 1142/s0217732316500905.
- [211] I. I. Tkachev. "On the possibility of Bose star formation". In: *Phys. Lett. B* 261 (1991), pp. 289-293. DOI: 10.1016/0370-2693(91)90330-S.
- [212] Luca Visinelli et al. "Dilute and dense axion stars". In: *Physics Letters B* 777 (Feb. 2018), pp. 64–72. ISSN: 0370-2693. DOI: 10.1016/j.physletb.2017.12.010.
- [213] Jiajun Chen et al. "Relaxation times for Bose-Einstein condensation by self-interaction and gravity". In: *Physical Review D* 106.2 (July 2022). ISSN: 2470-0029. DOI: 10.1103/physrevd.106.023009.
- [214] James H. Buckley et al. "Fast radio bursts from axion stars moving through pulsar magnetospheres". In: *Physical Review D* 103.4 (Feb. 2021). ISSN: 2470-0029. DOI: 10.1103/physrevd.103.043015.
- [215] Kay Kirkpatrick, Anthony E. Mirasola, and Chanda Prescod-Weinstein. "Relaxation times for Bose-Einstein condensation in axion miniclusters". In: *Physical Review D* 102.10 (Nov. 2020). ISSN: 2470-0029. DOI: 10.1103/physrevd.102.103012.
- [216] Hsi-Yu Schive, Tzihong Chiueh, and Tom Broadhurst. "Cosmic structure as the quantum interference of a coherent dark wave". In: *Nature Physics* 10.7 (June 2014), pp. 496–499. ISSN: 1745-2481. DOI: 10.1038/nphys2996.
- [217] Eric Braaten, Abhishek Mohapatra, and Hong Zhang. "Dense Axion Stars". In: *Physical Review Letters* 117.12 (Sept. 2016). ISSN: 1079-7114. DOI: 10.1103/physrevlett.117. 121801.
- [218] David A. Feinblum and William A. McKinley. "Stable States of a Scalar Particle in Its Own Gravational Field". In: *Phys. Rev.* 168 (5 Apr. 1968), pp. 1445–1450. DOI: 10.1103/PhysRev.168.1445.
- [219] Edward Seidel and Wai-Mo Suen. "Formation of solitonic stars through gravitational cooling". In: *Physical Review Letters* 72.16 (Apr. 1994), pp. 2516–2519. ISSN: 0031-9007. DOI: 10.1103/physrevlett.72.2516.
- [220] Miguel Escudero et al. "Axion star explosions: A new source for axion indirect detection". In: Physical Review D 109.4 (Feb. 2024). ISSN: 2470-0029. DOI: 10.1103/physrevd.109.043018.
- [221] Monica Colpi, Stuart L. Shapiro, and Ira Wasserman. "Boson Stars: Gravitational Equilibria of Self-Interacting Scalar Fields". In: *Phys. Rev. Lett.* 57 (20 Nov. 1986), pp. 2485—2488. DOI: 10.1103/PhysRevLett.57.2485.

- [222] Edward W. Kolb and Igor I. Tkachev. "Nonlinear axion dynamics and the formation of cosmological pseudosolitons". In: *Physical Review D* 49.10 (May 1994), pp. 5040–5051. ISSN: 0556-2821. DOI: 10.1103/physrevd.49.5040.
- [223] Joshua Eby et al. "Global view of axion stars with nearly Planck-scale decay constants". In: *Physical Review D* 103.6 (Mar. 2021). ISSN: 2470-0029. DOI: 10.1103/physrevd.103.063043.
- [224] Andrew R. Liddle and Mark S. Madsen. "The Structure and formation of boson stars". In: Int. J. Mod. Phys. D 1 (1992), pp. 101–144. DOI: 10.1142/S0218271892000057.
- [225] James Y. Widdicombe et al. "Formation of relativistic axion stars". In: *Journal of Cosmology and Astroparticle Physics* 2018.10 (Oct. 2018), pp. 005–005. ISSN: 1475-7516. DOI: 10.1088/1475-7516/2018/10/005.
- [226] Joshua Eby et al. "Boson stars from self-interacting dark matter". In: Journal of High Energy Physics 2016.2 (Feb. 2016). ISSN: 1029-8479. DOI: 10.1007/jhep02(2016)028.
- [227] Felix Kling and Arvind Rajaraman. "Profiles of boson stars with self-interactions". In: *Physical Review D* 97.6 (Mar. 2018). ISSN: 2470-0029. DOI: 10.1103/physrevd.97.063012.
- [228] Paul Tod and Irene M Moroz. "An analytical approach to the Schrödinger-Newton equations". In: *Nonlinearity* 12.2 (Mar. 1999), p. 201. DOI: 10.1088/0951-7715/12/2/002.
- [229] Eric Braaten and Hong Zhang. Axion Stars. 2018. arXiv: 1810.11473 [hep-ph].
- [230] Pierre-Henri Chavanis and Luca Delfini. "Mass-radius relation of Newtonian self-gravitating Bose-Einstein condensates with short-range interactions. II. Numerical results". In: *Physical Review D* 84.4 (Aug. 2011). ISSN: 1550-2368. DOI: 10.1103/physrevd.84.043532.
- [231] Enrico D. Schiappacasse and Mark P. Hertzberg. "Analysis of dark matter axion clumps with spherical symmetry". In: *Journal of Cosmology and Astroparticle Physics* 2018.01 (Jan. 2018), pp. 037–037. ISSN: 1475-7516. DOI: 10.1088/1475-7516/2018/01/037.
- [232] Joshua Eby et al. "Axion stars in the infrared limit". In: Journal of High Energy Physics 2015.3 (Mar. 2015). ISSN: 1029-8479. DOI: 10.1007/jhep03(2015)080.
- [233] Edward Seidel and Wai-Mo Suen. "Dynamical evolution of boson stars: Perturbing the ground state". In: *Phys. Rev. D* 42 (2 July 1990), pp. 384–403. DOI: 10.1103/PhysRevD. 42.384.
- [234] Jason Arakawa et al. "Bosenovae with Quadratically-Coupled Scalars in Quantum Sensing Experiments". In: *In preparation* (Feb. 2024). arXiv: 2402.06736 [hep-ph].
- [235] Dennis Einfeldt. "Stability of Axion Stars". MA thesis. Hamburg University, 2023.
- [236] Marco Gorghetto, Edward Hardy, and Giovanni Villadoro. *More Axion Stars from Strings*. 2024. arXiv: 2405.19389 [hep-ph].
- [237] D. V. Semikoz and I. I. Tkachev. "Condensation of bosons in the kinetic regime". In: *Phys. Rev. D* 55 (2 Jan. 1997), pp. 489–502. DOI: 10.1103/PhysRevD.55.489.
- [238] Alan H. Guth, Mark P. Hertzberg, and C. Prescod-Weinstein. "Do dark matter axions form a condensate with long-range correlation?" In: *Phys. Rev. D* 92 (10 Nov. 2015), p. 103513. DOI: 10.1103/PhysRevD.92.103513.

- [239] Haruo Yoshida. "Construction of higher order symplectic integrators". In: *Physics Letters* A 150.5 (1990), pp. 262–268. ISSN: 0375-9601. DOI: https://doi.org/10.1016/0375-9601(90)90092-3.
- [240] A. S. Dmitriev et al. "Self-Similar Growth of Bose Stars". In: *Phys. Rev. Lett.* 132 (9 Feb. 2024), p. 091001. DOI: 10.1103/PhysRevLett.132.091001.
- [241] Nitsan Bar et al. "Galactic rotation curves versus ultralight dark matter: Implications of the soliton-host halo relation". In: *Physical Review D* 98.8 (Oct. 2018). ISSN: 2470-0029. DOI: 10.1103/physrevd.98.083027.
- [242] Jason Arakawa et al. Detection of Bosenovae with Quantum Sensors on Earth and in Space. 2023. arXiv: 2306.16468 [hep-ph].
- [243] Thomas Helfer et al. "Black hole formation from axion stars". In: Journal of Cosmology and Astroparticle Physics 2017.03 (Mar. 2017), pp. 055–055. ISSN: 1475-7516. DOI: 10. 1088/1475-7516/2017/03/055.
- [244] Florent Michel and Ian G. Moss. "Relativistic collapse of axion stars". In: *Physics Letters* B 785 (Oct. 2018), pp. 9–13. ISSN: 0370-2693. DOI: 10.1016/j.physletb.2018.07.063.
- [245] N.W. McLachlan. Theory and Application of Mathieu Functions. Clarendon Press, 1951.
- [246] L. D. Landau and E. M. Lifshitz. *Mechanics, Third Edition: Volume 1 (Course of Theoretical Physics)*. 3rd ed. Butterworth-Heinemann, Jan. 1976. ISBN: 0750628960.
- [247] Luis E. Padilla et al. "Core-halo mass relation in scalar field dark matter models and its consequences for the formation of supermassive black holes". In: *Physical Review D* 103.6 (Mar. 2021). ISSN: 2470-0029. DOI: 10.1103/physrevd.103.063012.
- [248] J. Luna Zagorac et al. "Soliton formation and the core-halo mass relation: An eigenstate perspective". In: *Physical Review D* 107.8 (Apr. 2023). ISSN: 2470-0029. DOI: 10.1103/physrevd.107.083513.
- [249] Pierre-Henri Chavanis. "Derivation of the core mass-halo mass relation of fermionic and bosonic dark matter halos from an effective thermodynamical model". In: *Physical Review D* 100.12 (Dec. 2019). ISSN: 2470-0029. DOI: 10.1103/physrevd.100.123506.
- [250] Pin-Yu Liao et al. Deciphering the Soliton-Halo Relation in Fuzzy Dark Matter. 2025. arXiv: 2412.09908 [astro-ph.CO].
- [251] Atsushi Taruya and Shohei Saga. "Analytical approach to the core-halo structure of fuzzy dark matter". In: *Physical Review D* 106.10 (Nov. 2022). ISSN: 2470-0029. DOI: 10.1103/physrevd.106.103532.
- [252] Jae Hyeok Chang, Patrick J. Fox, and Huangyu Xiao. "Axion stars: mass functions and constraints". In: *JCAP* 08 (2024), p. 023. DOI: 10.1088/1475-7516/2024/08/023. arXiv: 2406.09499 [hep-ph].
- [253] Liina Chung-Jukko, Eugene A. Lim, and David J. E. Marsh. *Multimessenger signals from compact axion star mergers*. 2024. arXiv: 2403.03774 [astro-ph.CO].
- [254] Mustafa A. Amin et al. "Dipole radiation and beyond from axion stars in electromagnetic fields". en. In: *Journal of High Energy Physics* 2021.6 (June 2021), p. 182. ISSN: 1029-8479. DOI: 10.1007/JHEP06(2021)182.

- [255] Igor I. Tkachev. "Fast Radio Bursts and Axion Miniclusters". In: JETP Letters 101.1 (Jan. 2015). arXiv:1411.3900 [astro-ph], pp. 1–6. ISSN: 0021-3640, 1090-6487. DOI: 10.1134/S0021364015010154.
- [256] Stuart Raby. "Axion star collisions with neutron stars and fast radio bursts". In: *Physical Review D* 94.10 (Nov. 2016). ISSN: 2470-0029. DOI: 10.1103/physrevd.94.103004.
- [257] Liina M. Chung-Jukko et al. "Electromagnetic instability of compact axion stars". In: *Phys. Rev. D* 108 (6 Sept. 2023), p. L061302. DOI: 10.1103/PhysRevD.108.L061302.
- [258] Haoran Di, Haihao Shi, and Zhu Yi. "Detection of dilute axion stars with stimulated decay". In: *Physical Review D* 111.2 (Jan. 2025). ISSN: 2470-0029. DOI: 10.1103/physrevd. 111.023011.
- [259] Ali Taani et al. "Modeling the Spatial Distribution of Neutron Stars in the Galaxy". In: Astrophysics and Space Science 340 (May 2012), pp.147–153. DOI: 10.1007/S10509(012) 1121–7.
- [260] Miguel Gullón et al. "Population synthesis of isolated neutron stars with magnetorotational evolution". In: *Monthly Notices of the Royal Astronomical Society* 443.3 (July 2014), pp. 1891–1899. ISSN: 0035-8711. DOI: 10.1093/mnras/stu1253.
- [261] S. B. Popov et al. "Population synthesis studies of isolated neutron stars with magnetic field decay". In: *Monthly Notices of the Royal Astronomical Society* 401.4 (Feb. 2010), pp. 2675–2686. ISSN: 1365-2966. DOI: 10.1111/j.1365-2966.2009.15850.x.
- [262] Ciaran O'Hare. cajohare/AxionLimits: AxionLimits. https://cajohare.github.io/AxionLimits/. Version v1.0. July 2020. DOI: 10.5281/zenodo.3932430.
- [263] J. R. Weaver et al. "COSMOS2020: The galaxy stellar mass function: The assembly and star formation cessation of galaxies at $0.2 < z \le 7.5$ ". In: Astronomy & Astrophysics 677 (Sept. 2023), A184. ISSN: 1432-0746. DOI: 10.1051/0004-6361/202245581.
- [264] Haoran Di. Stimulated Decay of Collapsing Axion Stars and Fast Radio Bursts. 2023. arXiv: 2311.06860 [hep-ph].
- [265] Mustafa A. Amin and Zong-Gang Mou. "Electromagnetic bursts from mergers of oscillons in axion-like fields". In: *Journal of Cosmology and Astroparticle Physics* 2021.02 (Feb. 2021), pp. 024–024. ISSN: 1475-7516. DOI: 10.1088/1475-7516/2021/02/024.
- [266] Andreas Irrgang et al. "Milky Way Mass Models for Orbit Calculations". In: Astron. Astrophys. 549 (Jan. 2013), A137. ISSN: 1432-0746. DOI: 10.1051/0004-6361/201220540. arXiv: 1211.4353 [astro-ph.GA].
- [267] Pijushpani Bhattacharjee, Soumini Chaudhury, and Susmita Kundu. "Rotation Curve of the Milky Way out to ~ 200 kpc". In: *Astrophys. J.* 785.1 (Mar. 2014), p. 63. ISSN: 1538-4357. DOI: 10.1088/0004-637X/785/1/63. arXiv: 1310.2659 [astro-ph.GA].
- [268] Jayce Dowell and Greg B. Taylor. "The Radio Background below 100 MHz". In: *The Astrophysical Journal Letters* 858.1 (May 2018), p. L9. ISSN: 2041-8213. DOI: 10.3847/2041-8213/aabf86.

- [269] Ariel Arza, Thomas Schwetz, and Elisa Todarello. "How to suppress exponential growth—on the parametric resonance of photons in an axion background". In: *Journal of Cosmology and Astroparticle Physics* 2020.10 (Oct. 2020), pp. 013–013. ISSN: 1475-7516. DOI: 10. 1088/1475-7516/2020/10/013.
- [270] M. P. van Haarlem et al. "LOFAR: The LOw-Frequency ARray". In: *Astron. Astrophys.* 556 (2013), A2. DOI: 10.1051/0004-6361/201220873. arXiv: 1305.3550 [astro-ph.IM].
- [271] LOFAR Imaging capabilities and sensitivity. https://science.astron.nl/telescopes/lofar/lofar-system-overview/observing-modes/lofar-imaging-capabilities-and-sensitivity/.
- [272] Peng Jiang et al. "The fundamental performance of FAST with 19-beam receiver at L band". In: Research in Astronomy and Astrophysics 20.5, 064 (May 2020), p. 064. DOI: 10.1088/1674-4527/20/5/64. arXiv: 2002.01786 [astro-ph.IM].
- [273] Lei Qian et al. "FAST: Its Scientific Achievements and Prospects". In: *The Innovation* 1.3, 100053 (Nov. 2020), p. 100053. DOI: 10.1016/j.xinn.2020.100053. arXiv: 2011.13542 [astro-ph.IM].
- [274] ALMA Sensitivity Calculator. https://almascience.eso.org/proposing/sensitivity-calculator.
- [275] ALMA Technical Handbook. https://almascience.eso.org/proposing/technical-handbook.
- [276] SKA Design Baseline Description. https://www.skao.int/en/science-users/122/relevant-documents.
- [277] SKA Sensitivity Calculator. https://www.skao.int/en/science-users/ska-tools/493/ska-sensitivity-calculators.
- [278] Thomas L. Wilson, Kristen Rohlfs, and Susanne Hüttemeister. *Tools of Radio Astronomy*. 2013. DOI: 10.1007/978-3-642-39950-3.
- [279] Bernard F. Burke, Francis Graham-Smith, and Peter N. Wilkinson. *An Introduction to Radio Astronomy*. 4th ed. Cambridge University Press, 2019. DOI: 10.1017/9781316987506.
- [280] Robert Braun et al. "Anticipated Performance of the Square Kilometre Array Phase 1 (SKA1)". In: (Dec. 2019). arXiv: 1912.12699 [astro-ph.IM].
- [281] Patrick J. Fox, Neal Weiner, and Huangyu Xiao. "Recurrent axion stars collapse with dark radiation emission and their cosmological constraints". In: *Physical Review D* 108.9 (Nov. 2023). ISSN: 2470-0029. DOI: 10.1103/physrevd.108.095043.
- [282] Dmitry Budker et al. "Proposal for a Cosmic Axion Spin Precession Experiment (CASPEr)". In: *Physical Review X* 4.2 (May 2014). ISSN: 2160-3308. DOI: 10.1103/physrevx.4.021030.
- [283] Yonatan Kahn, Benjamin R. Safdi, and Jesse Thaler. "Broadband and Resonant Approaches to Axion Dark Matter Detection". In: *Physical Review Letters* 117.14 (Sept. 2016). ISSN: 1079-7114. DOI: 10.1103/physrevlett.117.141801.
- [284] Chiara P. Salemi. "First Results from ABRACADABRA-10cm: A Search for Low-Mass Axion Dark Matter". In: 54th Rencontres de Moriond on Electroweak Interactions and Unified Theories. 2019, pp. 229–234. arXiv: 1905.06882 [hep-ex].

- [285] Zhongyue Zhang, Dieter Horns, and Oindrila Ghosh. "Search for dark matter with an LC circuit". In: *Physical Review D* 106.2 (July 2022). ISSN: 2470-0029. DOI: 10.1103/physrevd.106.023003.
- [286] Mattia Mina, David F. Mota, and Hans A. Winther. "Solitons in the dark: First approach to non-linear structure formation with fuzzy dark matter". In: *Astronomy and Astro-physics* 662 (June 2022), A29. ISSN: 1432-0746. DOI: 10.1051/0004-6361/202038876.
- [287] Matteo Nori and Marco Baldi. "Scaling relations of fuzzy dark matter haloes I. Individual systems in their cosmological environment". In: *Monthly Notices of the Royal Astronomical Society* 501.1 (Dec. 2020), pp. 1539–1556. ISSN: 1365-2966. DOI: 10.1093/mnras/staa3772.
- [288] I-Kang Liu, Nick P Proukakis, and Gerasimos Rigopoulos. "Coherent and incoherent structures in fuzzy dark matter haloes". In: *Monthly Notices of the Royal Astronomical Society* 521.3 (Feb. 2023), pp. 3625–3647. ISSN: 1365-2966. DOI: 10.1093/mnras/stad591.
- [289] Pierre-Henri Chavanis. "A predictive model of BEC dark matter halos with a solitonic core and an isothermal atmosphere". In: *Physical Review D* 100.8 (Oct. 2019). arXiv:1810.08948 [astro-ph, physics:gr-qc], p. 083022. ISSN: 2470-0010, 2470-0029. DOI: 10.1103/PhysRevD.100.083022.
- [290] Pierre-Henri Chavanis. "Core mass halo mass relation of bosonic and fermionic dark matter halos harbouring a supermassive black hole". In: *Physical Review D* 101.6 (Mar. 2020). arXiv:1911.01937 [astro-ph, physics:gr-qc], p. 063532. ISSN: 2470-0010, 2470-0029. DOI: 10.1103/PhysRevD.101.063532.
- [291] Julio F. Navarro, Carlos S. Frenk, and Simon D. M. White. "The Structure of Cold Dark Matter Halos". In: *The Astrophysical Journal* 462 (May 1996). arXiv:astro-ph/9508025, p. 563. ISSN: 0004-637X, 1538-4357. DOI: 10.1086/177173.
- [292] Remo Ruffini and Silvano Bonazzola. "Systems of Self-Gravitating Particles in General Relativity and the Concept of an Equation of State". In: *Phys. Rev.* 187 (5 Nov. 1969), pp. 1767–1783. DOI: 10.1103/PhysRev.187.1767.
- [293] A numerical study of the Schrödinger-Newton equations. Jan. 2003. DOI: 10.1088/0951-7715/16/1/307.
- [294] F. Siddhartha Guzmán and L. Arturo Ureña-López. "Evolution of the Schrödinger-Newton system for a self-gravitating scalar field". In: *Phys. Rev. D* 69 (12 June 2004), p. 124033. DOI: 10.1103/PhysRevD.69.124033.
- [295] E. Madelung. "Quantentheorie in hydrodynamischer Form". In: Z. Phys. 40.3 (1927), pp. 322–326. DOI: 10.1007/BF01400372.
- [296] Eniko J. M. Madarassy and Viktor T. Toth. "Evolution and dynamical properties of Bose-Einstein condensate dark matter stars". In: *Physical Review D* 91.4 (Feb. 2015). ISSN: 1550-2368. DOI: 10.1103/physrevd.91.044041.
- [297] M. Garny and T. Konstandin. "Gravitational collapse in the Schrödinger-Poisson system". In: Journal of Cosmology and Astroparticle Physics 2018.01 (Jan. 2018), pp. 009–009. ISSN: 1475-7516. DOI: 10.1088/1475-7516/2018/01/009.

- [298] Mathias Garny, Thomas Konstandin, and Henrique Rubira. "The Schrödinger-Poisson method for Large-Scale Structure". In: *Journal of Cosmology and Astroparticle Physics* 2020.04 (Apr. 2020), pp. 003–003. ISSN: 1475-7516. DOI: 10.1088/1475-7516/2020/04/003.
- [299] F. Siddhartha Guzman and L. Arturo Urena-Lopez. "Evolution of the Schrodinger-Newton system for a selfgravitating scalar field". In: Phys. Rev. D 69 (2004), p. 124033. DOI: 10.1103/PhysRevD.69.124033. arXiv: gr-qc/0404014.
- [300] I. M. Moroz, Roger Penrose, and P. Tod. "Spherically symmetric solutions of the Schrodinger-Newton equations". In: Class. Quant. Grav. 15 (1998), pp. 2733–2742. DOI: 10.1088/0264-9381/15/9/019.
- [301] Matteo Nori and Marco Baldi. "AX-GADGET: a new code for cosmological simulations of Fuzzy Dark Matter and Axion models". In: *Monthly Notices of the Royal Astronomical Society* 478.3 (May 2018), pp. 3935–3951. ISSN: 1365-2966. DOI: 10.1093/mnras/sty1224.
- [302] Gilbert Strang. "On the Construction and Comparison of Difference Schemes". In: SIAM Journal on Numerical Analysis 5.3 (1968), pp. 506–517. DOI: 10.1137/0705041. eprint: https://doi.org/10.1137/0705041.
- [303] V. S. Varadarajan. *Lie Groups, Lie Algebras, and Their Representations*. Springer, 1984. ISBN: 978-0-387-90969-1, 978-1-4612-7016-4, 978-1-4612-1126-6. DOI: 10.1007/978-1-4612-1126-6.
- [304] Sergio Blanes, Fernando Casas, and Ander Murua. Splitting and composition methods in the numerical integration of differential equations. 2008. arXiv: 0812.0377 [math.NA].
- [305] S. Blanes, F. Casas, and A. Murua. "On the Numerical Integration of Ordinary Differential Equations by Processed Methods". In: SIAM Journal on Numerical Analysis 42.2 (2004), pp. 531–552. DOI: 10.1137/S0036142902417029. eprint: https://doi.org/10.1137/S0036142902417029.
- [306] Robert Mclachlan. "On the Numerical Integration of Ordinary Differential Equations by Symmetric Composition Methods". In: SIAM J. Sci. Comp. 16 (Jan. 1995), pp. 151—DOI: 10.1137/0916010.
- [307] Mark Sofroniou and Giulia Spaletta. "Derivation of symmetric composition constants for symmetric integrators". In: *Optimization Methods and Software* 20 (Aug. 2005), pp. 597–613. DOI: 10.1080/10556780500140664.
- [308] Andrew Eberhardt et al. "Investigating the use of field solvers for simulating classical systems". In: *Physical Review D* 101.4 (Feb. 2020). ISSN: 2470-0029. DOI: 10.1103/physrevd.101.043011.
- [309] Muhammad Adeel Ajaib. Numerical Methods and Causality in Physics. 2013. arXiv: 1302.5601 [physics.comp-ph].
- [310] M. Frigo and S.G. Johnson. "The Design and Implementation of FFTW3". In: *Proceedings of the IEEE* 93.2 (2005), pp. 216–231. DOI: 10.1109/JPROC.2004.840301.

Acknowledgments

The last words of this thesis are dedicated to all the different people who supported me on the long way to an academic career as a physicist. First and foremost I would like to thank my supervisor, Günter Sigl, for providing me with the unique opportunity to embark on a doctorate in the exciting field of axion dark matter research and for giving me the opportunity to develop myself as a researcher. I am grateful for his swift advice and our numerous talks during the course of my studies. Apart from his mentorship and scientific guidance, I especially appreciate being given the freedom to develop my research interests and to explore my own ideas and approaches. Without his guidance this work would have not been possible.

I also want to thank Robi Banerjee for being the second reviewer of this thesis and for taking the time to read through this admittedly long manuscript.

Then I want to deeply thank my family for a lifetime of unconditional support, for their unwavering understanding of my personal journey and for the countless wonderful memories that we share. I thank both my family and friends for their ongoing encouragement on the way that took me to write this thesis, for their time, advice and support that made my academic and personal development possible to begin with.

Finally, I would like to acknowledge my collaborators, Hyeonseok Seong, Sagnik Mondal, Dennis Einfeldt and Joshua Eby, whose expertise, ideas, and creativity have greatly enriched this work. I thank them for their determination and hard work that led us together through countless hours of scientific puzzles, and I greatly appreciate their reliability and kindness, which gave me the feeling of working together with friends.

I also want to express my gratitude for all the other collaborators and colleagues, who have accompanied me on the unique academic journey that was my doctorate. I thank Benedikt Eggemeier for extremely helpful discussions on axion miniclusters, on the core-halo relation and on the formation of axion stars in cosmological simulations. I also want to acknowledge the valuable guidance on the properties of neutron stars that was provided to me by Samuel Witte and which greatly enriched our paper on the signal rates of neutron-star-axion-star collisions.

I thank Dieter Horns, Marios Maroudas and Josep Batllori Berenguer for fruitful discussions on radio and axion experiments. And lastly, I thank Marvin Beck, Simone Rossoni, Julien Manshanden, Oindrila Ghosh, Suman Dey, Danelise de Oliveira Franco, Karoly Seller and my other colleagues, who were always sure to provide valuable and entertaining company - in hard and in good times.